Middle-Late Jurassic Cu-Pb-Zn-bearing and W-bearing granitoids and their skarn mineralization in the Nanling Range, South China : the Tongshanling and Weijia deposits

Xu-Dong Huang

ÉCOLE DOCTORALE
ENERGIE, MATERIAUX, SCIENCES DE LA TERRE ET DE L'UNIVERS

Institut des Sciences de la Terre d'Orléans

School of Earth Sciences and Engineering, Nanjing University

THÈSE EN COTUTELLE INTERNATIONALE présentée par:

Xu-Dong HUANG

soutenue le **28 Octobre 2018**

pour obtenir le grade de:

Docteur de l'Université d'Orléans et de l'Université de Nanjing

Discipline/Spécialité: Sciences de la Terre et de l'Univers

Middle-Late Jurassic Cu-Pb-Zn-bearing and W-bearing granitoids and their skarn mineralization in the Nanling Range, South China: the Tongshanling and Weijia deposits

THÈSE dirigée par:

Jian-Jun LU	Professeur, Nanjing University
Stanislas SIZARET	Professeur, Université d'Orléans

RAPPORTEURS:

Mei-Fu ZHOU	Professeur, The University of Hong Kong
Xiao-Ming SUN	Professeur, Sun Yat-Sen University

JURY (*y reporter tous les membres de jury présents à la soutenance*)**:**

Zhen-Min JIN	Professeur, China University of Geosciences, Wuhan
Ru-Cheng WANG	Professeur, Nanjing University
Mei-Fu ZHOU	Professeur, The University of Hong Kong
Yan CHEN	Professeur, Université d'Orléans
Alain CHAUVET	Chercheur, Université Montpellier 2, CNRS
Stanislas SIZARET	Professeur, Université d'Orléans

Extended English abstract

Granitoids and their related mineralization is always the highly focused topic for geologists all over the world. The Nanling Range in South China is one of the most famous metallogenic belts around the world, especially for its large-scale W-Sn mineralization. Middle-Late Jurassic is the most important epoch for granitic magmatism and associated mineralization in this region. Although numerous studies have been carried out on the petrogenesis and metallogenesis of the Middle-Late Jurassic ore-bearing granitoids in the Nanling Range, there are still great controversies and problems remaining to be solved, especially on the Cu-Pb-Zn-bearing and W-bearing granitoids and their skarn mineralization. Four main scientific problems are proposed as follows: (1) What are the petrogenetic differences and links between the Middle-Late Jurassic Cu-Pb-Zn-bearing and W-bearing granitoids in the Nanling Range? (2) How do the skarn deposits structurally connect to the Middle-Late Jurassic ore-bearing granitoids in the Nanling Range? (3) What are the genetic links between different mineralization types and the formation mechanism of complex zonation in the Middle-Late Jurassic Cu-Pb-Zn skarn deposits in the Nanling Range? (4) What are the key factors controlling the occurrence of unusual magnesian skarn W mineralization during Late Jurassic in the Nanling Range? The Tongshanling-Weijia area in the western part of the Nanling Range is selected as the study area. The main research objects of this Ph.D. thesis are the Tongshanling Cu-Pb-Zn and Weijia W skarn deposits.

The South China Block is a major continental component with a complex history of tectonic evolution in East Asia. It was constructed through a Neoproterozoic (1.0 – 0.8 Ga) amalgamation of the Yangtze and Cathaysia Blocks. In Phanerozoic, the South China Block mainly experienced three tectonothermal events, i.e., the Early Paleozoic (460 – 390 Ma) intracontinental orogeny, the Early Mesozoic (240 – 200 Ma) intracontinental compressional deformation, and the Late Mesozoic (Jurassic to Cretaceous) palaeo-Pacific plate subduction. As a consequence, the corresponding multiple-aged (i.e., Neoproterozoic, Early Paleozoic, Triassic, Jurassic, and Cretaceous) granitoids and associated polymetallic mineral deposits are widely developed in South China. In the Nanling Range of South China, the most extensive

Middle-Late Jurassic (165 – 150 Ma) ore-bearing granitoids can be divided into W-bearing, Sn-bearing, Nb-Ta-bearing, and Cu-Pb-Zn-bearing granitoids. Skarn is one of the most important mineralization types for the Middle-Late Jurassic polymetallic mineral deposits especially the Cu-Pb-Zn and W deposits in the Nanling Range.

The Tongshanling-Weijia area is situated in southern Hunan Province. The exposed strata in this area include Ordovician to Triassic systems except for the absence of Silurian system and Upper Permian to Lower Triassic series and are dominated by Devonian and Carboniferous systems. The Middle Devonian Qiziqiao Formation, the Upper Devonian Shetianqiao and Xikuangshan Formations, and the Shidengzi Member of the Upper Carboniferous Datang Stage are the main ore-bearing horizons in the Tongshanling-Weijia area. The structural framework of this area is south-north- to southwest-northeast-trending on the whole. The Tongshanling granodiorite and the Weijia granite are the dominant magmatic rocks in this area, which are genetically related to Cu-Pb-Zn and W mineralization, respectively. The Tongshanling Cu-Pb-Zn deposit, Jiangyong Pb-Zn-Ag deposit, and Yulong Mo deposit are distributed around the Tongshanling intrusion and constitute the Tongshanling Cu-Mo-Pb-Zn-Ag ore district. The Weijia W deposit is located 15 km to the northeast of the Tongshanling polymetallic ore district.

The Middle-Late Jurassic Cu-Pb-Zn-bearing and W-bearing granitoids in the Nanling Range are distinctly different in mineralogy and geochemistry. The Cu-Pb-Zn-bearing granitoids are dominated by weakly fractionated metaluminous I-type amphibole-bearing granodiorites, which have higher $CaO/(Na_2O+K_2O)$ ratios, light/heavy rare earth element (LREE/HREE) ratios, and δEu values, lower Rb/Sr ratios, and weak Ba, Sr, P, and Ti depletions. The W-bearing granites are mainly highly differentiated peraluminous S-type granites, which have lower $CaO/(Na_2O+K_2O)$ ratios, LREE/HREE ratios, and δEu values, higher Rb/Sr ratios, and strong Ba, Sr, P, and Ti depletions. The Cu-Pb-Zn-bearing and W-bearing granitoids were formed predominantly between 155.2 Ma and 167.0 Ma (peak value: 160.6 Ma) and between 151.1 Ma and 161.8 Ma (peak value: 155.5 Ma), respectively. There is a time gap of about 5 Ma between the two different types of ore-bearing granitoids. Based on detailed geochronological and geochemical studies of both the Tongshanling

Cu-Pb-Zn-bearing and Weijia W-bearing granitoids and combined with a comparison between the Middle-Late Jurassic Cu-Pb-Zn-bearing and W-bearing granitoids in the Nanling Range, a genetic model of the two different types of ore-bearing granitoids has been proposed. The underplated basaltic magmas induced by the subduction of the palaeo-Pacific plate provided heat to firstly cause partial melting of the mafic amphibolitic basement in the lower crust, resulting in the formation of Cu-Pb-Zn mineralization related granodioritic magmas. With the development of basaltic magma underplating, the muscovite-rich metasedimentary basement in the upper-middle crust was then partially melted to generate W-bearing granitic magmas. The non-simultaneous partial melting of one source followed by the other brought about a time gap of about 5 Ma between the Cu-Pb-Zn-bearing and W-bearing granitoids.

The microgranular enclaves in the Tongshanling granodiorite have dioritic compositions with a mineralogy dominated by plagioclase, amphibole, and biotite. Abundant residual materials, such as mafic mineral clots, inherited and metamorphic zircon, and Ca-rich core plagioclase, occur in the enclaves and are in favor of a restite origin. The amphibole-rich clots are considered as vestiges of residual pyroxene-rich precursors from the source. Three types of amphibole, i.e., magmatic, metamorphic, and magma reworked metamorphic amphibole, have been recognized in the granodiorite and its enclaves according to their different occurrences, textures, and compositions. The zonal amphibole-rich clots exhibit increasing Al and decreasing Si contents from interior amphibole to exterior amphibole and also from core to rim in amphibole grains, and the outer parts of enclave magmatic zircon have higher ThO_2+UO_2 contents and lower Zr/Hf ratios than the inner parts, showing the process of magma reworking of the restite enclaves. Based on the textural and compositional evidence, these microgranular enclaves are thought to be reworked restite enclaves. This is also supported by thermobarometric calculation. A model illustrating the formation process of reworked restite enclave has been proposed. Combined with previous experimental studies of partial melting, the Tongshanling granodiorite is deduced to be derived from dehydration melting of amphibolite in the mafic lower crust. The fertile amphibolitic source is beneficial to the formation of Cu-Pb-Zn-bearing granodiorites in the Nanling Range.

Magma emplacement-induced structural control on skarn formation at the Tongshanling

Cu-Pb-Zn deposit was studied by structural analysis, Raman spectroscopy of carbonaceous material (RSCM) thermometry, and electron backscatter diffraction (EBSD) mapping. In the Tongshanling area, the regional normal faults were in all probability formed during the Late Triassic to Early Jurassic decompression and are not related to the emplacement of the Middle-Late Jurassic Tongshanling granodiorite. The emplacement of the Tongshanling granodiorite induced strong marbleization and deformation of the surrounding carbonate rocks. The wall-rock foliation cuts the bedding and is parallel to the intrusion boundary with a gradually decreased density outward from the contact zone. RSCM thermometry shows an outward trend of gradually decreased metamorphic temperature from ca. 620 °C to ca. 300 °C. EBSD mapping reveals that the deformed calcite in the contact zone has strong shape preferred orientation (SPO) and crystallographic preferred orientation (CPO). The exoskarn and sulfide-quartz veins of the Tongshanling Cu-Pb-Zn deposit strike and dip consistently with the foliation of the deformed wall rocks. Combined with the RSCM and EBSD results, it is concluded that the exoskarn and sulfide-quartz veins were controlled by the magma emplacement-induced wall-rock deformation which significantly increased wall-rock permeability to promote the infiltration of magmatic fluids along fractures.

The Tongshanling Cu-Pb-Zn deposit shows a well-developed outward zonation from proximal endoskarn through proximal exoskarn to sulfide-quartz veins and then to distal skarn, additionally with a few late Pb-Zn sulfide-quartz veins and carbonate replacement Pb-Zn sulfide veins distributed in the proximal part. The Jiangyong Pb-Zn-Ag deposit and Yulong Mo deposit are dominated by carbonate replacement and skarn mineralization, respectively. Garnet U-Pb dating yields a $^{207}Pb/^{235}U$-$^{206}Pb/^{238}U$ concordia age of 162.0 ± 3.7 Ma with a weighted average $^{206}Pb/^{238}U$ age of 162.4 ± 4.2 Ma for the proximal exoskarn in the Tongshanling Cu-Pb-Zn deposit. Molybdenite Re-Os dating of the Tongshanling Cu-Pb-Zn deposit and Yulong Mo deposit yields ^{187}Re-^{187}Os isochron ages of 161.8 ± 1.7 Ma and 160.0 ± 5.8 Ma with weighted average model ages of 161.9 ± 1.1 Ma and 160.1 ± 0.8 Ma, respectively. U-Pb dating of the hydrothermal titanite in the altered granodiorite yields lower intercept ages of 155.5 ± 3.1 Ma and 155.6 ± 3.1 Ma in the Wetherill and Tera-Wasserburg U-Pb concordia plots, respectively, with a weighted average $^{206}Pb/^{238}U$ age of 154.4 ± 1.9 Ma.

S, Pb, and H-O isotopic studies reveal that the ore-forming materials and fluids of the Tongshanling polymetallic ore district were derived from the Tongshanling intrusion. The Cu and Zn were most probably released from the mafic amphibolitic lower crust by partial melting, whereas, the Pb was extracted from the upper crust by the ascending granodioritic magma. Based on the geological, geochronological, and isotopic geochemical studies, it is concluded that the different mineralization types and ore deposits in the Tongshanling ore district are genetically linked together and are the productions of evolution and zonation of the same skarn system associated with the Tongshanling granodioritic intrusion. A comparison of the Middle-Late Jurassic Cu-Pb-Zn and W deposits in the Nanling Range further supports the petrogenetic model of non-simultaneous partial melting illustrating the origins of the Cu-Pb-Zn-bearing and W-bearing granitoids.

The Weijia scheelite skarn deposit comprises dominant magnesian skarn and subordinate calcic skarn with abundant fluorite and is genetically related to a highly fractionated porphyritic granite with a felsitic to fine-grained matrix. The magnesian skarn generally occurs as stockwork veinlets in dolostone with a mineralogy dominated by serpentine and phlogopite. Wollastonite, garnet, and pyroxene are the main calcic skarn minerals. Scheelite is mostly distributed in the magnesian and calcic skarns as disseminated grains. Biotite fluorimetry indicates that the Weijia granite was crystallized from a F-rich magma. The high fluorine activity of granitic melts results in a low magmatic viscosity to enable the prolonged crystal fractionation and tungsten enrichment of the granitic magma to a relatively low temperature, finally with the porphyritic Weijia granite formed under a water-saturated condition. During the magmatic to hydrothermal evolution, F-rich hydrosaline melts were firstly separated from magma by liquid immiscibility followed by the exsolution of F-poor hydrothermal fluids. Both of the F-rich hydrosaline melts and F-poor hydrothermal fluids have transported tungsten from the magma into the wall rocks for subsequent skarn mineralization. RSCM thermometry indicates a distinctly lower temperature of magnesian skarnization than calcic skarnization. The relatively low temperature and high fluorine activity during magnesian skarnization are not favorable for the development of anhydrous prograde skarn minerals, such as forsterite and spinel, and lead to the formation of the special

F-rich garnet. As the shared precipitant of fluorine and tungsten, calcium could be the critical factor to induce the positive correlation between the WO_3 and CaF_2 grades of skarn ores. The higher WO_3 grades of the calcic skarn than those of the magnesian skarn are controlled by the higher calcium activity during skarnization in limestone than that in dolostone.

Main conclusions of this Ph.D. thesis are summarized as follows: (1) The Middle-Late Jurassic Cu-Pb-Zn-bearing and W-bearing granitoids in the Nanling Range were derived from non-simultaneous partial melting of the mafic amphibolitic basement and the muscovite-rich metasedimentary basement, respectively; (2) The microgranular enclaves of the Tongshanling granodiorite are reworked restite enclaves derived from partial melting of the mafic amphibolitic source; (3) The exoskarn and sulfide-quartz veins in the Tongshanling Cu-Pb-Zn deposit are structurally controlled by the magma emplacement-induced wall-rock deformation; (4) The different mineralization types and ore deposits in the Tongshanling polymetallic ore district are genetically linked together and are the productions of evolution and zonation of the same skarn system associated with the Tongshanling granodioritic intrusion; (5) The key factors controlling the occurrence of unusual magnesian skarn W mineralization during Late Jurassic in the Nanling Range mainly include an enriched source, a fluorine-rich magma, a strong crystal fractionation, and a fluorine-rich hydrosaline melt.

Keywords: Cu-Pb-Zn-bearing granitoids; W-bearing granites; Microgranular enclaves; Skarn; Magmatic-hydrothermal system; Zonation; Structural control; Permeability; Petrogenesis; Metallogenesis; Middle-Late Jurassic; Nanling Range

Table of contents

List of figures and tables

Figures

Tables

Chapter 1. Introduction

1.1. Research background and scientific problems

1.1.1. Research background

Granitoids and their related mineralization is always the highly focused topic for geologists all over the world (Hsu et al., 1963a, 1963b; Einaudi et al., 1981; Xu et al., 1982; Černý et al., 2005; Linnen and Cuney, 2005; Meinert et al., 2005; Seedorff et al., 2005; Sillitoe, 2010; Chen et al., 2013; Mao et al., 2013a; Wu et al., 2017). In the past decade, numerous studies concerning granitoids and their related mineralization have been carried out on the aspects of origin and evolution of granitoids (e.g., Tartèse and Boulvais, 2010; Huang and Jiang, 2014; Romer and Kroner, 2015, 2016; Simons et al., 2016, 2017; Jiang and Zhu, 2017; Wu et al., 2017; Zhang et al., 2017a), spatiotemporal and genetic links between granitoids and ore deposits (e.g., Chiaradia et al., 2009; Feng et al., 2011a, 2015; Zhang et al., 2015a, 2017b, 2017c; Naranjo et al., 2018), geochemical behaviors of ore elements during magmatic to hydrothermal evolution (e.g., Che et al., 2013; Ballouard et al., 2016; Hulsbosch et al., 2016; Schmidt, 2018; Wolf et al., 2018), descriptive deposit geology and structural analysis (e.g., Soloviev, 2011, 2015; Soloviev et al., 2013; Mahjoubi et al., 2016; Ducoux et al., 2017; Soloviev and Kryazhev, 2017; Naranjo et al., 2018; Yang et al., 2018), sources of ore-forming materials and fluids (e.g., Vallance et al., 2009; Shu et al., 2013; Soloviev et al., 2013; Xie et al., 2015; Ding et al., 2016a; Zhou et al., 2016), physicochemical evolution during ore-forming process (e.g., Vallance et al., 2009; Shu et al., 2013; Mao et al., 2017), hydrothermal fluid dynamics (e.g., Sizaret et al., 2009; Mahjoubi et al., 2016; Launay et al., 2018), numerical modeling (e.g., Eldursi et al., 2009; Ingebritsen and Appold, 2012; Schöpa et al., 2017), metallogenic mechanism (e.g., Lecumberri-Sanchez, 2017; Korges et al., 2018; Zhang et al., 2018a), etc. Hence, there is no doubt that granitoid-related ore deposits are the final products of comprehensive effect by various factors which include the sources of granitoids, generation of granitoid magmas, evolution of magmatic to hydrothermal systems, influence of accidental materials and fluids, migration of ore-bearing fluids, fluid-rock

reaction, structural controls, etc.

The Nanling Range in South China is one of the most famous metallogenic belts around the world, especially for its large-scale W-Sn mineralization. A great number of granitoids and associated mineral deposits are widely developed in the Nanling Range (Fig. 1-1). Although these granitoids and related ore deposits were formed in multiple periods, i.e., Early Paleozoic, Triassic, Jurassic, and Cretaceous (Fig. 1-1), Middle-Late Jurassic is the most important epoch for granitic magmatism and associated mineralization in this region (Mao et al., 2007, 2013a; Chen et al., 2013; Fu et al., 2013; Li et al., 2013). Four dominant types of Middle-Late Jurassic ore-bearing granitoids in the Nanling Range, i.e., W-bearing (e.g., Yaogangxian, Dengfuxian, Weijia, Xihuashan, Dajishan, etc., Fig. 1-1), Sn-bearing (e.g., Huashan-Guposhan, Jiuyishan, Qitianling, Qianlishan, Hehuaping, etc.), Nb-Ta-bearing (e.g., Dajishan, Jianfengling, Laiziling, etc.), and Cu-Pb-Zn-bearing (e.g., Shuikoushan, Baoshan, Tongshanling, Dabaoshan, etc., Fig. 1-1) granitoids, have been recognized by previous studies (Chen et al., 2008, 2013; Fu et al., 2013; Li et al., 2013). Although numerous studies have been carried out on the petrogenesis of these Middle-Late Jurassic ore-bearing granitoids (e.g., Wang et al., 2003a; Zhang, 2004; Li et al., 2007a; Chen et al., 2008, 2013; Jiang et al., 2009; Fu et al., 2013; Li et al., 2013; Xie et al., 2013; Dong et al., 2014; Zhang, 2014; Zuo et al., 2014; Yang et al., 2016; Zhao et al., 2016a, 2016b; Wu et al., 2017; Zhang et al., 2017a), there are still great controversies remaining to be solved, especially on the origins of the Cu-Pb-Zn-bearing and W-bearing granitoids.

Based on the occurrence of dark microgranular enclaves and the interpretation of geochronological and geochemical data, it is generally considered that the Middle-Late Jurassic Cu-Pb-Zn-bearing granitoids in the Nanling Range, which are dominated by I-type amphibole-bearing granodiorites, were formed by mixing of crust-derived and mantle-derived magmas (Wang et al., 2003a; Jiang et al., 2009; Li et al., 2013; Xie et al., 2013; Zhao et al., 2016b). However, these microgranular enclaves do not show any credible evidence, except for some Sr-Nd isotopes (Xie et al., 2013), supporting magma mixing and detailed petrographic and mineralogical studies of these microgranular enclaves are absent. It is noteworthy that the zircon Hf isotopic compositions of these microgranular enclaves are similar to those of their

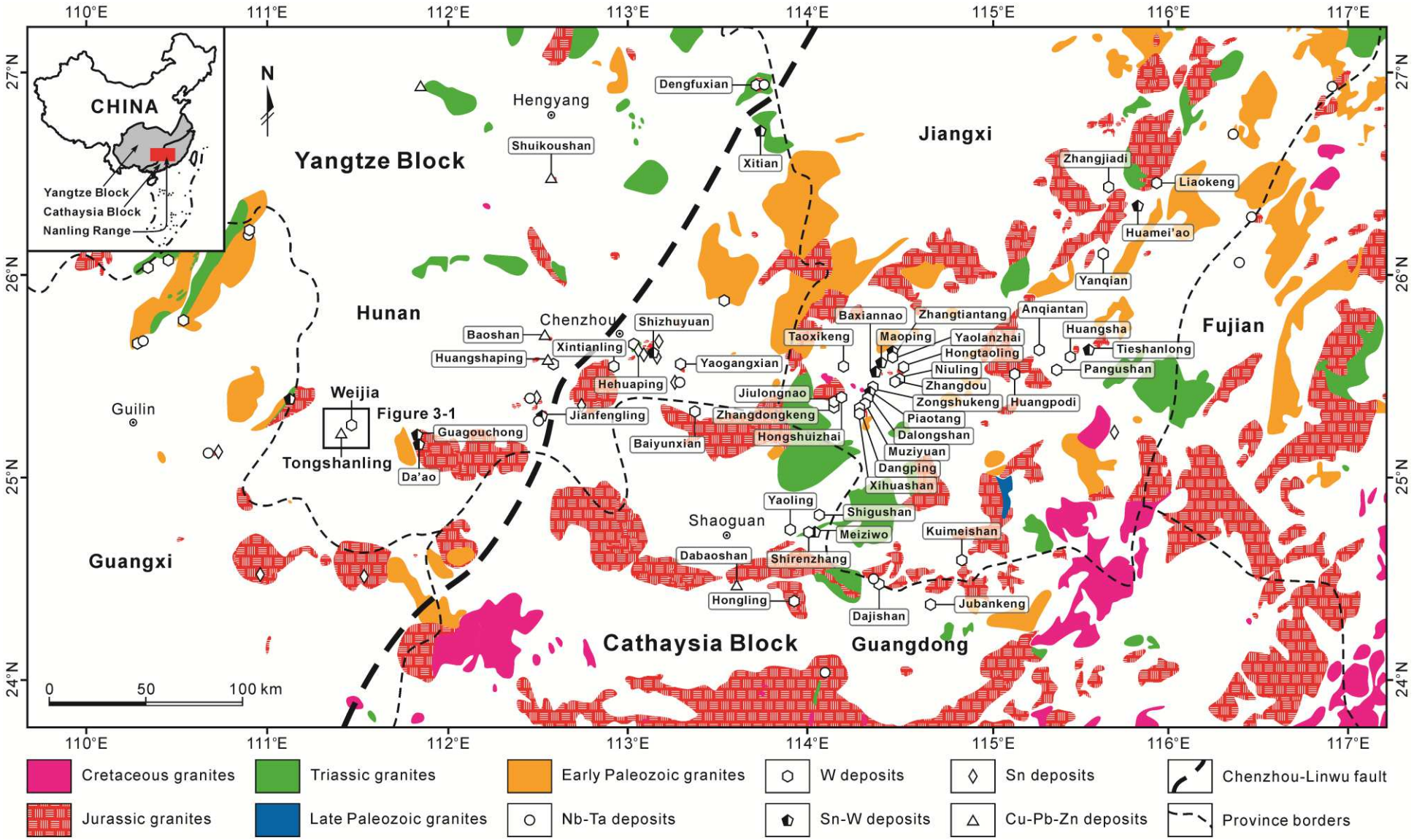

Figure 1-1. Distribution of multiple-aged granitoids and related mineral deposits in the Nanling Range of South China (modified after Chen et al., 2008, 2013).

host granitoids, both of which show typical crust-derived features (Jiang et al., 2009; Xie et al., 2013; Zuo et al., 2014; Yang et al., 2016; Zhao et al., 2016b). Zuo et al. (2014) and Yang et al. (2016) proposed that the Shuikoushan granodiorite was derived from partial melting of the mafic lower crust. Thus, the petrogenesis of these Cu-Pb-Zn-bearing granitoids is still disputable and needs further investigations.

For the Late Jurassic W-bearing granites in the Nanling Range, it is widely accepted that they are dominated by highly fractionated S-type two-mica, muscovite, and biotite granites and were mainly derived from partial melting of crustal metasedimentary rocks (Zhang, 2004; Chen et al., 2008, 2013; Fu et al., 2013; Dong et al., 2014; Zhang, 2014; Jiang and Zhu, 2017). However, some researchers thought that these W-bearing granites are highly fractionated I-type granites and were mainly derived from partial melting of crustal meta-igneous rocks (Li et al., 2007a; Wu et al., 2017; Zhang et al., 2017a). Li et al. (2007a) pointed out that the Jurassic amphibole-bearing granodiorite, biotite monzogranite, K-feldspar granite, and two-mica (muscovite) granite constitute a metaluminous to weakly peraluminous evolution series of I-type granites. It is reasonable that the highly fractionated properties of the W-bearing granites enhance the difficulty of distinguishing their source rocks (Chappell, 1999; Gao et al., 2016; Wu et al., 2017). Therefore, the petrogenesis of these W-bearing granites and the relationship between the W-bearing granites and the Cu-Pb-Zn-bearing granodiorites require further studies.

The Middle-Late Jurassic Cu-Pb-Zn-bearing and W-bearing granitoids related mineral deposits in the Nanling Range are dominated by skarn, greisen, quartz vein, and carbonate replacement mineralization in which only skarn is of great importance to both of the Cu-Pb-Zn and W deposits (Chen et al., 2008; Mao et al., 2009a, 2013a; Fu et al., 2013). A number of Middle-Late Jurassic Cu-Pb-Zn and W skarn deposits appear in the western part of the Nanling Range. Study on the genesis and ore-forming processes of these Cu-Pb-Zn and W skarn deposits is beneficial to understanding the differences between Cu-Pb-Zn and W skarn mineralization and the regional metallogenic regularities of Cu-Pb-Zn and W in the Nanling Range.

The Middle-Late Jurassic Cu-Pb-Zn skarn deposits in the Nanling Range, such as the

Tongshanling, Baoshan, Shuikoushan, Dabaoshan, and Huangshaping deposits, commonly have the characteristic of association of different mineralization types which include skarn, carbonate replacement, sulfide-quartz vein, etc. (Wang, 2010; Zhu et al., 2012; Lu et al., 2013, 2015; Bao et al., 2014; Qu et al., 2014; Cai et al., 2015; Dai et al., 2015; Huang et al., 2015; Xie et al., 2015; Ding et al., 2016a). In addition, complex zonation of metals and mineralization types may occur in an individual Cu-Pb-Zn skarn deposit or ore district. For instance, the Tongshanling Cu-Mo-Pb-Zn-Ag skarn ore district is constituted by three ore deposits, i.e., the Tongshanling Cu-Pb-Zn, Jiangyong Pb-Zn-Ag, and Yulong Mo deposits, distributing around the Tongshanling granodioritic intrusion (Huang and Lu, 2014; Zhao et al., 2016b). The Tongshanling Cu-Pb-Zn deposit shows a zonation of proximal skarn (endoskarn and exoskarn), distal skarn, and sulfide-quartz veins between them (Huang and Lu, 2014; Cai et al., 2015; Lu et al., 2015). The Jiangyong Pb-Zn-Ag deposit is composed of proximal skarn and distal carbonate replacement (Yi and Xu, 2006; Huang and Lu, 2014). The Yulong Mo deposit comprises only skarn (Huang and Lu, 2014; Zhao et al., 2016b). Although numerous geochronological and geochemical studies have been carried out on these Middle-Late Jurassic Cu-Pb-Zn skarn deposits (e.g., Lu et al., 2006, 2015; Qu et al., 2014; Cai et al., 2015; Huang et al., 2015), the links between different mineralization types and the genesis of complex zonation are still poorly understood.

Essentially, all economic W skarns are calcic throughout the world (Kwak, 1987), such as the well-known Zhuxi (China), Xintianling (China), Shizhuyuan (China), Yaogangxian (China), CanTung (Canada), Pine Creek (USA), King Island (Australia), Salau (France), and Los Santos (Spain) deposits (Meinert et al., 2005; Pan et al., 2017). Magnesian W skarns are uncommon and have been rarely reported (Guy, 1979; Casquet and Tornos, 1984; Kwak, 1987; Dubru et al., 1988; Vander Auwera and Andre, 1991). However, the discovery of the Late Jurassic super-large Weijia W deposit (ca. 300,000 t WO_3) in the Nanling Range that comprises predominant magnesian W skarn (ca. 240,000 t WO_3) and subordinate calcic W skarn (ca. 60,000 t WO_3) demonstrates and highlights the importance of magnesian skarn for W mineralization. Scientifically the Weija deposit presents a special case of W skarn deposit. Such unusual economic mineralization is of great interest to economic geologists and

provides an excellent opportunity for further understanding of W skarn mineralization. Since the concealed Weijia W deposit is still unmined, however, very few studies have been carried out on its metallogenesis and mineralization process, except for some publications of deposit geology and ore-bearing granite (e.g., Li et al., 2012a; Hu et al., 2015; Zhao et al., 2016a, 2016b). No genetic model has been proposed for this particular W skarn deposit so far and the key factors that control magnesian skarn W mineralization are still unknown.

Although numerous geochronological and geochemical studies have revealed that the Middle-Late Jurassic Cu-Pb-Zn and W skarn deposits in the Nanling Range are genetically associated with granitoids (e.g., Bi et al., 1988; Li et al., 1996; Liu et al., 2006; Lu et al., 2006, 2015; Ma et al., 2007; Yao et al., 2007; Lei et al., 2010; Huang and Lu, 2014; Qu et al., 2014; Zhu et al., 2014; Cai et al., 2015; Huang et al., 2015; Shuang et al., 2016; Zhao et al., 2016a, 2016b), the detailed structural connecting process between them is still unclear. Previous studies on skarn deposits mainly focused on metasomatism, zonation, skarn mineralogy, geochemistry, and petrogenesis (Meinert et al., 2005). However, little attention has been paid to structural control (e.g., Love et al., 2004; Li et al., 2014a; Ducoux et al., 2017), especially the magma emplacement related one, on skarn formation. Magma emplacement-induced structural control is crucial to understanding the process of skarnization and can provide important information for prospecting and exploration. In addition, the roles of some other key parameters affecting skarn formation, such as permeability, were also rarely considered. The anisotropy of permeability in country rocks, which could be derived from magma emplacement-induced structures, may control the location and scale of skarnization to a certain extent. Thus, except for geochemical studies, studies on magma emplacement-induced structural control and permeability constraint are also of great importance and will be beneficial to further understanding the mechanism of skarn formation.

1.1.2. Scientific problems

Under on the research background mentioned above, four main scientific problems concerning the Middle-Late Jurassic Cu-Pb-Zn-bearing and W-bearing granitoids and associated skarn deposits in the Nanling Range are proposed as follows.

(1) What are the petrogenetic differences and links between the Middle-Late Jurassic Cu-Pb-Zn-bearing and W-bearing granitoids in the Nanling Range?

(2) How do the skarn deposits structurally connect to the Middle-Late Jurassic ore-bearing granitoids in the Nanling Range?

(3) What are the genetic links between different mineralization types and the formation mechanism of complex zonation in the Middle-Late Jurassic Cu-Pb-Zn skarn deposits in the Nanling Range?

(4) What are the key factors controlling the occurrence of unusual magnesian skarn W mineralization during Late Jurassic in the Nanling Range?

1.2. Topic selection and research contents

1.2.1. Topic selection

The Tongshanling-Weijia area in the western part of the Nanling Range is an ideal region for studying the Middle-Late Jurassic Cu-Pb-Zn-bearing and W-bearing granitoids and associated skarn deposits. In the Tongshanling-Weijia area, the Tongshanling granodiorite and Weijia granite are spatially adjacent with a distance of 15 km and are genetically associated with Cu-Pb-Zn and W skarn mineralization, respectively. These Cu-Pb-Zn-bearing and W-bearing granitoids and related skarn deposits were formed contemporaneously in Middle-Late Jurassic (Jiang et al., 2009; Huang and Lu, 2014; Lu et al., 2015; Zhao et al., 2016a, 2016b). As described above, the Tongshanling Cu-Mo-Pb-Zn-Ag skarn ore district exhibits a complex zonation of metals and different mineralization types and the Weijia W skarn deposit contains dominant magnesian W skarn and subordinate calcic W skarn. Therefore, the Tongshanling-Weijia area is selected as the study area of this Ph.D. thesis. The Tongshanling and Weijia deposits, which act as a window of the Middle-Late Jurassic Cu-Pb-Zn-bearing and W-bearing granitoids and related skarn deposits in the Nanling Range, are the main research objects of this Ph.D. thesis. Consequently, this Ph.D. thesis is entitled "Middle-Late Jurassic Cu-Pb-Zn-bearing and W-bearing granitoids and their skarn mineralization in the Nanling Range, South China: the Tongshanling and Weijia deposits".

1.2.2. Research contents

This Ph.D. thesis mainly contains the following research contents.

(1) Petrogenesis of the Tongshanling Cu-Pb-Zn-bearing granodiorite and Weijia W-bearing granite. Comparison of the Middle-Late Jurassic Cu-Pb-Zn-bearing and W-bearing granitoids in the Nanling Range.

(2) Petrogenesis and formation process of the microgranular enclaves in the Tongshanling granodiorite.

(3) Regional structural features in the Tongshanling-Weijia area. Local structural control on skarn formation at the Tongshanling Cu-Pb-Zn deposit induced by magma emplacement.

(4) Zonation and genesis of the Tongshanling Cu-Mo-Pb-Zn-Ag skarn ore district which includes the Tongshanling Cu-Pb-Zn, Jiangyong Pb-Zn-Ag, and Yulong Mo deposits.

(5) Ore-forming process of the Weijia W skarn deposit. Key factors controlling the unusual magnesian skarn W mineralization in the Weijia deposit.

1.3. Research methodology and technical route

1.3.1. Research methodology

This Ph.D. thesis was finished mainly through the following research methods.

(1) Field observation, sample collection, and sample processing: regional and local structural analyses, deposit geological study, mineral separation, thin section making, whole-rock powder preparation, etc.

(2) Structural study: deformation analysis, RSCM thermometry, and calcite EBSD mapping.

(3) Petrographic study: optical microscope and scanning electron microscope observations.

(4) Mineralogical study: SEM elemental mapping, EMP analysis of major elements, and LA-ICP-MS analysis of trace elements.

(5) Geochronological study: zircon, garnet, and titanite U-Pb and molybdenite Re-Os dating.

(6) Petrogeochemical study: whole-rock major elements, trace elements, and Sr-Nd isotopes and zircon Hf isotope.

(7) Ore deposit geochemical study: S and Pb isotopes of sulfide minerals and H-O isotopes of quartz.

1.3.2. Technical route

Petrogenesis of granitoids was studied by zircon U-Pb dating and Hf isotope and whole-rock geochemistry. Petrogenesis of microgranular enclaves was studied through petrography and mineralogy. Magma emplacement-induced structural control on skarn formation was studied by structural analysis, RSCM thermometry, and EBSD mapping. Zonation and genesis of the Tongshanling polymetallic ore district were studied through molybdenite Re-Os and garnet and titanite U-Pb dating and S, Pb, H-O isotopes. Metallogenesis of the Weijia W deposit and key factors controlling the unusual magnesian W skarn were studied by RSCM thermometry, whole-rock geochemistry, and mineralogy.

1.4. Workload and research achievements

1.4.1. Workload

The details of completed workload during my Ph.D. study are listed in Table 1-1.

1.4.2. Main findings and innovations

Main findings and innovations of this Ph.D. thesis are listed as follows.

(1) The Middle-Late Jurassic Cu-Pb-Zn-bearing and W-bearing granitoids in the Nanling Range were derived from non-simultaneous partial melting of the mafic amphibolitic basement and the muscovite-rich metasedimentary basement, respectively.

(2) The microgranular enclaves of the Tongshanling granodiorite are reworked restite enclaves derived from partial melting of the mafic amphibolitic source.

(3) The exoskarn and sulfide-quartz veins in the Tongshanling Cu-Pb-Zn deposit are structurally controlled by the magma emplacement-induced wall-rock deformation.

(4) The different mineralization types and ore deposits in the Tongshanling polymetallic ore district are genetically linked together and are the productions of evolution and zonation of the same skarn system associated with the Tongshanling granodioritic intrusion.

(5) The key factors controlling the occurrence of unusual magnesian skarn W mineralization during Late Jurassic in the Nanling Range mainly include an enriched source, a fluorine-rich magma, a strong crystal fractionation, and a fluorine-rich hydrosaline melt.

Table 1-1. List of completed workload during my Ph.D. study

Subject	Content	Quantity	unit	Persons and/or organizations attending/completing this work
Field observation	➢ 2012.10.12 – 2012.10.21 Tongshanling Cu-Mo-Pb-Zn-Ag ore district and Weijia W deposit	10	days	Cheng, C.Z., Huang, X.D., Liu, Z., etc.
	➢ 2013.04.27 Magnetite-apatite deposits in the Ning-Wu Basin	1	day	Lu, J.J., Wang, L.J., Huang, X.D., etc.
	➢ 2013.06.04 – 2013.06.05 Magnetite-apatite deposits in the Ning-Wu Basin	2	days	Lu, J.J., Wang, L.J., Huang, X.D., etc.
	➢ 2013.07.13 – 2013.08.01 Tongshanling Cu-Pb-Zn deposit, Yulong Mo deposit, Weijia W deposit, Baoshan Pb-Zn deposit, and Huangshaping Pb-Zn-W-Mo deposit	20	days	Lu, J.J., Ma, D.S., Ding, T., Huang, X.D., Sun, Z.Y., etc.
	➢ 2013.11.17 – 2013.11.25 Weijia granite, Jiangyong Pb-Zn-Ag deposit, and Tongshanling Cu-Pb-Zn deposit	9	days	Huang, X.D., Sun, Z.Y., etc.
	➢ 2014.01.25 – 2014.01.26 Zhuxi W deposit	2	days	Wang, R.C., Lu, J.J., Lu, X.C., Shu, L.S., Chen, G.H., Huang, X.D., Yu, Q., etc.
	➢ 2014.08.01 – 2014.08.08 Tongshanling granodiorite, Yulong Mo deposit, Jiangyong Pb-Zn-Ag deposit, and Weijia W deposit	8	days	Huang, X.D., Zhao, X., etc.
	➢ 2014.08.23 – 2014.08.24 Beiya Au deposit and Jinding Pb-Zn deposit	2	days	Meinert, L.D., Lentz, D.R., Huang, X.D., Yao, C.Y., etc.
	➢ 2014.09.28 – 2014.10.06 Weijia W deposit, Tongshanling Cu-Pb-Zn deposit, and Jiuyishan, Jianfengling, and Huashan-Guposhan granites	9	days	Chen, Y., Faure, M., Scaillet, B., Lu, J.J., Sizaret, S., Wang, B., Guo, C.L., Liu, H.S., Huang, F.F., Huang, X.D., Zhao, X., Zhu, X., etc.
	➢ 2014.12.08 – 2014.12.18 Tongshanling Cu-Pb-Zn deposit	11	days	Huang, X.D., Tuo, X.S., etc.
	➢ 2015.09.08 – 2015.09.14 Jurassic granites in Fujian Province	7	days	Liu, H.S., Huang, X.D., etc.
	➢ 2015.09.27 – 2015.10.15 Regional geology of the Tongshanling-Weijia area, Tongshanling Cu-Pb-Zn deposit, and Muguayuan W deposit	19	days	Lu, J.J., Chauvet, A., Sizaret, S., Barbanson, L., Guo, C.L., Huang, X.D., Zhang, Q., Zhao, X., Xiang, L., Li, X.Y., etc.
	➢ 2016.05.24 – 2016.05.29 Granites and associated Mineralization in the French Massif Central	6	days	Chen, Y., Faure, M., Wang, R.C., Li, X.H., Xu, X.S., Yang, J.H., Chauvet, A., Lin, W., Qiu, J.S., Sizaret, S., Li, Q.L., Xie, L., Liu, X.C., Liu, H.S., Xue, Z.H., Huang, F.F., Zhu, Z.Y., Huang, X.D., etc.

(*To be continued on the next page*)

Table 1-1. (*Continued*)

Subject	Content	Quantity	unit	Persons and/or organizations attending/completing this work
	➢ 2016.09.13 – 2016.09.16 Jiaodong Au deposits	4	days	Fan, H.R., Fontboté, L., Rhys, D., Liu, X., Qiu, K.F., Huang, X.D., etc.
	➢ 2016.10.12 – 2016.10.21 Regional geology of the Tongshanling-Weijia area, Tongshanling Cu-Pb-Zn deposit, and Weijia W deposit	10	days	Chauvet, A., Barbanson, L., Huang, X.D., Chen, G.H., etc.
	● Total	120	days	
Sample collection	➢ From surface outcrops	120	pieces	Huang, X.D., etc.
	➢ From underground galleries	246	pieces	Huang, X.D., etc.
	➢ From drill cores	227	pieces	Huang, X.D., etc.
	➢ From ore plots	147	pieces	Huang, X.D., etc.
	● Total	740	pieces	
Sample processing	Mineral separation			
	➢ Zircon	7	pieces	Langfang Geoservices Co. Ltd.
	➢ Sulfide minerals	116	pieces	Huang, X.D. and Cheng, C.Z.
	➢ Scheelite	30	pieces	Langfang Geoservices Co. Ltd.
	➢ Quartz	37	pieces	Huang, X.D. and Cheng, C.Z.
	● Total	190	pieces	
	Polished epoxy resin discs holding zircon	4	pieces	Beijing GeoAnalysis Co. Ltd.
	Polished sections	65	pieces	Langfang Geoservices Co. Ltd., NJU, and ISTO
	Thin sections			
	➢ Covered thin sections	316	pieces	Langfang Geoservices Co. Ltd. and NJU
	➢ Uncovered thin sections	476	pieces	Langfang Geoservices Co. Ltd., ISTO, and NJU
	➢ Thin sections for fluid inclusion study	77	pieces	Langfang Geoservices Co. Ltd. and ISTO
	● Total	869	pieces	
	Whole-rock powder	54	pieces	Langfang Geoservices Co. Ltd. and NJU
	Sample preparation for permeability experiment	8	pieces	Huang, X.D. and Sizaret, S. at ISTO
Isotopic dating	LA-ICP-MS Zircon U-Pb dating	4 114	pieces points	Huang, X.D. at LAMD, NJU
	Molybdenite Re-Os dating	13	pieces	National Research Center of Geoanalysis, CAGS, Beijing
	LA-ICP-MS Titanite U-Pb dating	1 21	piece points	Huang, X.D. at Nanjing FocuMS Technology Co. Ltd.
Petrographic observation	By optical microscope	803	pieces	Huang, X.D. at LAMD, NJU and ISTO
	By SEM (BSE and CL images)	80 23	pieces days	Huang, X.D. at LAMD, NJU and ISTO and Beijing GeoAnalysis Co. Ltd.

(*To be continued on the next page*)

Table 1-1. (*Continued*)

Subject	Content	Quantity	unit	Persons and/or organizations attending/completing this work
Mineral CPO determination	Calcite EBSD mapping	8	pieces	Barou, F., Huang, X.D., and Chauvet, A. at Géosciences Montpellier
Composition analysis	Whole-rock composition			
	➢ Whole-rock major elements	54	pieces	Analysis Center of No. 230 Research Institute of the China National Nuclear Corporation, Changsha
	➢ Whole-rock trace elements	54	pieces	Huang, X.D. and Liu, Q. at LAMD, NJU
	➢ Whole-rock Sr-Nd isotopes	17	pieces	Huang, X.D. at LAMD, NJU
	In-situ mineral composition			
	➢ Point and line analyses and elemental mapping by SEM	80 23	pieces days	Huang, X.D. at LAMD, NJU and ISTO
	➢ Major elements by EMP	5856	points	Huang, X.D. at LAMD, NJU and ISTO
	➢ Trace elements by LA-ICP-MS	411	points	Huang, X.D. at Nanjing FocuMS Technology Co. Ltd.
	➢ Zircon Hf isotope by LA-ICP-MS	4 83	pieces points	Huang, X.D. at LAMD, NJU
	Mineral and fluid isotopic composition			
	➢ S isotope of sulfide minerals	112	pieces	Ministry of Education Key Laboratory of Nuclear Resources and Environment, East China University of Technology
	➢ Pb isotope of sulfide minerals	41	pieces	Analytical Laboratory of the Beijing Research Institute of Uranium Geology
	➢ H-O isotopes of quartz	37	pieces	Analytical Laboratory of the Beijing Research Institute of Uranium Geology and LAMD, NJU
Temperature measurement	RSCM thermometry	47	pieces	Huang, X.D. at BRGM
	Fluid inclusion thermometry	11	pieces	Huang, X.D. at LAMD, NJU
Experimental study	Crystal growth experiment	20	rounds	Huang, X.D. and Sizaret, S. at Polytech Orléans
	Permeability experiment	6	rounds	Huang, X.D., Sizaret, S., and Champallier, R. at ISTO
Numerical modeling	Crystal growth and magma emplacement-induced fluid flow	2	cases	Huang, X.D. and Sizaret, S. at ISTO

Notes: BRGM: Bureau de Recherches Géologiques et Minières, France; BSE: backscattered electron; CAGS: Chinese Academy of Geological Sciences; CL: cathodoluminescence; CPO: crystallographic preferred orientation; EBSD: electron backscatter diffraction; EMP: electron microprobe; ISTO: Institut des Sciences de la Terre d'Orléans, France; LA-ICP-MS: laser ablation-inductively coupled plasma-mass spectrometry; LAMD: State Key Laboratory for Mineral Deposits Research, China; NJU: Nanjing University, China; RSCM: Raman spectroscopy of carbonaceous material; SEM: scanning electron microscope.

Chapter 2. Geological setting

2.1. South China

South China is world famous for the widespread multiple-aged granitoids and related polymetallic mineral deposits, especially the extremely abundant W-Sn deposits, and has attracted great interests of numerous geologists and scientific research institutes to carry out countless studies on its geodynamic evolution, magmatism, and mineralization (Hsu, 1943; Hsu et al., 1960, 1963a, 1963b; Institute of Geochemistry, CAS, 1979; Mo et al., 1980; Department of Geology, NJU, 1981; Xu et al., 1982, 1983; Chen et al., 1989a, 2008, 2013; The Granitoid Research Group of the Nanling Project, MGMR, 1989; Hua and Mao, 1999; Zhou and Li, 2000; Shu and Zhou, 2002; Wang and Zhou, 2002; Hua et al., 2003, 2005; Sun et al., 2005; Sun, 2006; Zhou et al., 2006a, 2018; Li and Li, 2007; Li et al., 2007a, 2009, 2013, 2016, 2017, 2018a; Wang et al., 2007a, 2013, 2017a; Zaw et al., 2007; Zhou, 2007; Mao et al., 2008a, 2009a, 2011a, 2011b, 2013a; Faure et al., 2008, 2009, 2016a, 2016b, 2017; Shu et al., 2009, 2015; Wan, 2010; Hu and Zhou, 2012; Shu, 2012; Zhao and Cawood, 2012; Pirajno, 2013; Zhang et al., 2013; Hu et al., 2017; Zhao et al., 2017). As one of the main continental fragments disaggregated from the Gondwana supercontinent that assembled together with Siberia to construct the present Eurasia (Metcalfe, 2013), the South China Block is a major continental component with a complex history of tectonic evolution in East Asia (Zhou and Li, 2000; Shu and Zhou, 2002; Li and Li, 2007; Wang et al., 2007a, 2013, 2017a; Faure et al., 2008, 2009, 2016a, 2016b, 2017; Li et al., 2009, 2016, 2017, 2018a; Shu et al., 2009, 2015; Wan, 2010; Shu, 2012; Zhao and Cawood, 2012; Zhang et al., 2013). The South China Block is generally considered to link with the North China Block through the Qinling-Dabie-Sulu orogen to the north, connect with the Indochina Block by the Jinshajiang-Ailaoshan-Song Ma suture zone to the southwest, joint with the Songpan-Gantze Block through the Longmenshan fault to the northwest, and is bounded by the Pacific plate to the east (Fig. 2-1). Faure et al. (2016a) proposed a hypothetic Triassic suture to the east of Hainan Island as the southern offshore of the South China Block (Fig. 2-1).

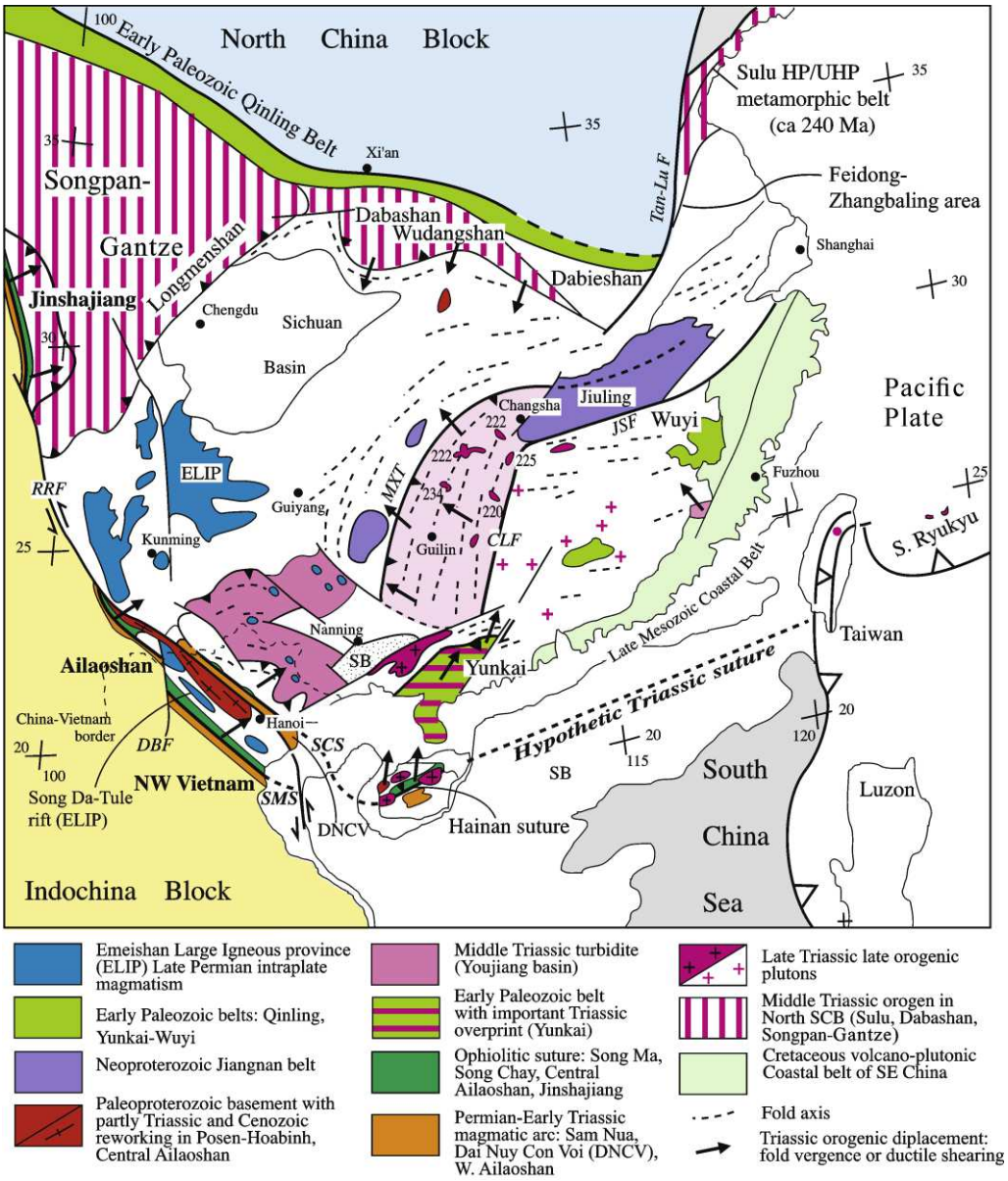

Figure 2-1. Structural map showing the tectonic location and main tectonic elements of the South China Block (cited from Faure et al., 2017).

2.1.1. Geodynamic evolution

It is generally accepted that the South China Block was constructed through a Neoproterozoic amalgamation of the Yangtze Block and the Cathaysia Block with the Jiangnan Orogen as the suture zone between them (Figs. 2-2 and 2-3a), although the precise time of the amalgamation is still controversial from 1.0 Ga to 0.8 Ga (Li et al., 2002, 2003, 2007b, 2008, 2009, 2014b; Wang and Li, 2003; Shu et al., 2006a, 2011; Zhou et al., 2006b;

Wang et al., 2007a; Cawood et al., 2013; Yao et al., 2014a). After the collision of the Yangtze Block and the Cathaysia Block, the South China Block experienced a regional-scale extension during Late Neoproterozoic which led to the formation of rift basins that contain a set of siliciclastic sediments coeval with bimodal volcanic rocks (800 – 690 Ma; Fig. 2-3b) (Wang and Li, 2003; Shu et al., 2011; Li et al., 2014b). Then the Cathaysia Block underwent a stable intraplate neritic-bathyal depositional stage from Sinian to Early Paleozoic (690 – 460 Ma; Fig. 2-3c) during which thick siliciclastic sediments were formed (Shu et al., 2014) without volcanic magmatism and any evidence for the input of mantle-derived materials.

In Phanerozoic, the South China Block mainly experienced three tectonothermal events, i.e., Early Paleozoic, Triassic, and Jurassic-Cretaceous events, which were generally referred to as "Caledonian or Kwangsian", "Indosinian", and "Yanshanian" movements by Chinese

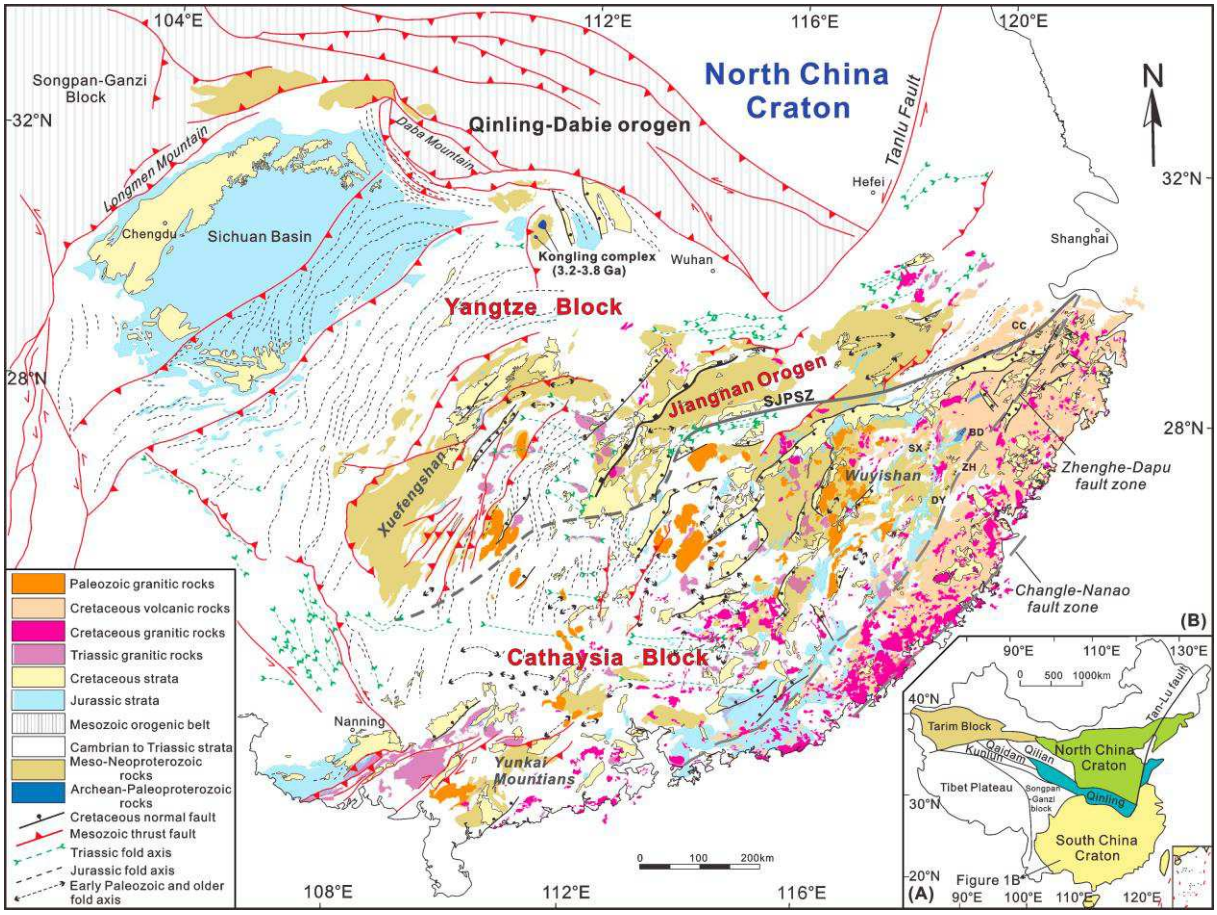

Figure 2-2. (a) Sketch map showing the tectonic location of South China. (b) Simplified geological map of South China illustrating the distributions of main Phanerozoic structures and igneous rocks (cited from Li et al., 2017).

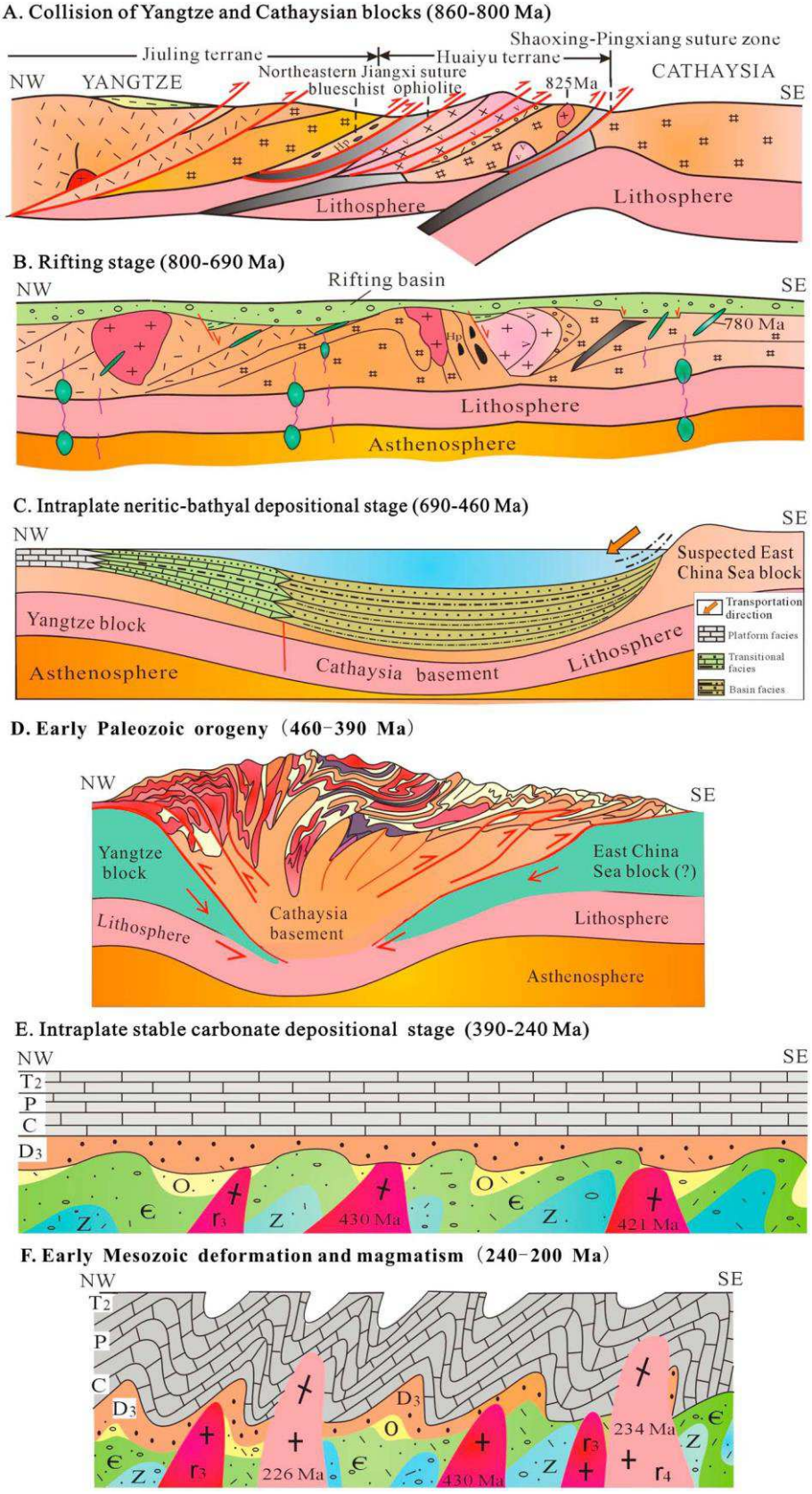

Figure 2-3. Schematic model illustrating the geodynamic evolution of South China from Neoproterozoic to Early Mesozoic (cited from Shu et al., 2015).

geologists, respectively (Ting, 1929; Hsu et al., 1960, 1963a, 1963b; Ren, 1991; Hua and Mao, 1999; Zhou and Li, 2000; Hua et al., 2003, 2005; Wang et al., 2005a, 2010, 2011a, 2013; Zhou et al., 2006a; Chen et al., 2010, 2013). The Early Paleozoic tectonic movement was commonly recognized according to the presence of a conspicuous unconformity between the Middle Devonian and Silurian strata, pervasive shortening deformation, and high-grade metamorphism (Grabau, 1924; Ting, 1929; Lin et al., 2008; Faure et al., 2009; Charvet et al., 2010; Li et al., 2010, 2016, 2017; Charvet, 2013; Wang et al., 2013; Shu et al., 2015). It is now commonly interpreted as an intracontinental orogeny due to the lack of ophiolitic rocks, accretionary complexes, volcanic rocks with arc affinities, and the input of mantle-derived components in granitic magmatism (Faure et al., 2009; Charvet et al., 2010; Li et al., 2010; Charvet, 2013; Wang et al., 2013; Shu et al., 2015). Three competing tectonic models have been proposed to explain the origin of the Early Paleozoic orogeny, i.e., (1) northwestward intracontinental subduction of the northwestern Cathaysia Block beneath the southeastern Yangtze Block (Fig. 2-4a; Faure et al., 2009), (2) northwestward intraplate overthrusting of the northwestern Cathaysia Block atop the southeastern Yangtze Block (Fig. 2-4b; Li et al.,

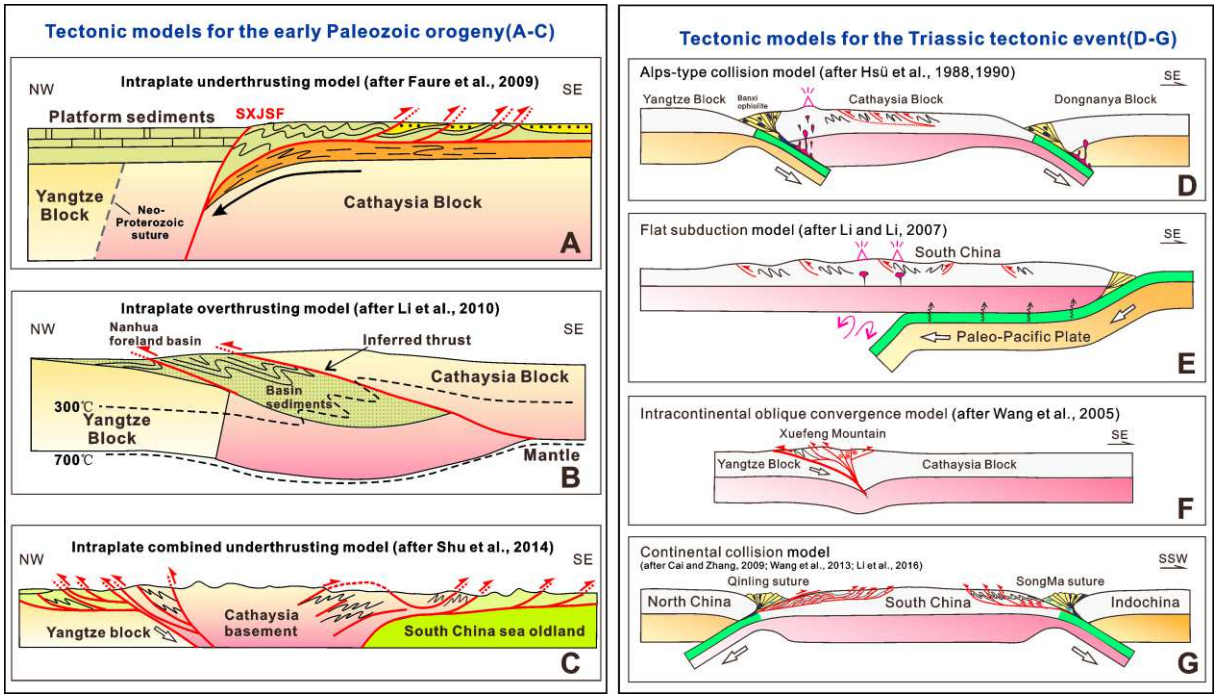

Figure 2-4. Schematic models illustrating the geodynamic mechanism of the (a–c) Early Paleozoic and (d–g) Triassic tectonic events in the South China Block (cited from Li et al., 2017).

2010), and (3) combined northwestward underthrusting of an inferred East China Sea Block and southeastward underthrusting of the Yangtze Block both beneath the Cathaysia Block (Figs. 2-3d and 2-4c; Shu et al., 2014, 2015). This tectonic event was constrained in chronology by newly grown mica $^{40}Ar/^{39}Ar$ dating at 450 – 390 Ma with contemporaneous anatectic granites dated at 460 – 390 Ma (Shu et al., 1999, 2015; Charvet et al., 2010; Shu, 2012; Li et al., 2016, 2017). During Late Paleozoic from 390 Ma to 240 Ma, the South China Block underwent a stable intraplate carbonate depositional stage in a littoral-neritic environment resulting in the formation of a series of limestone, dolomite, and clastic rocks (Fig. 2-3e; Shu et al., 2006b, 2008, 2009).

Triassic is the main period for the development of the South China tectonic framework (Faure et al., 2016a, 2017). The Triassic tectonic movement was initially recognized due to the Late Triassic (Norian) angular unconformity of conglomerate and sandstone overlaying folded and metamorphosed rocks in Vietnam of the Indochina Block (Deprat, 1914, 1915; Fromaget, 1932, 1941). In South China, the Triassic event is recorded as a regional Late Triassic unconformity, folding, thrusting, ductile shearing, metamorphism, and granitic magmatism (Wang et al., 2005a, 2013; Lin et al., 2008; Shu et al., 2008, 2015; Zhang and Cai, 2009; Chu et al., 2012a, 2012b; Faure et al., 2016a, 2016b, 2017; Li et al., 2016, 2017). An Alps-type collision model (Fig. 2-4d) was proposed by Hsü et al. (1988, 1990) to explain the origin of this tectonic event based on interpreting the Banxi Group as a Mesozoic ophiolitic mélange. However, subsequent studies revealed that the Banxi Group is composed of a Neoproterozoic turbidite sequence (Gu et al., 2002; Wang and Li, 2003; Wang et al., 2007a). Although it is now widely accepted that the Triassic tectonic movement in the South China Block is an intraplate deformation event (Lin et al., 2008; Shu et al., 2008, 2015; Chu et al., 2012a, 2012b; Faure et al., 2014), the geodynamic mechanism of this event is still disputed with the following models: (1) flat-slab subduction model of the palaeo-Pacific plate (Figs. 2-4e and 2-5a–d) proposed by Li and Li (2007), (2) intraplate oblique convergence of the Yangtze Block and the Cathaysia Block (Fig. 2-4f) proposed by Wang et al. (2005a), and (3) collision of the South China Block with the Indochina Block and/or the North China Block (Figs. 2-4g and 2-6a–b) (Lepvrier et al., 2004; Faure et al., 2008; Cai and Zhang, 2009; Wang

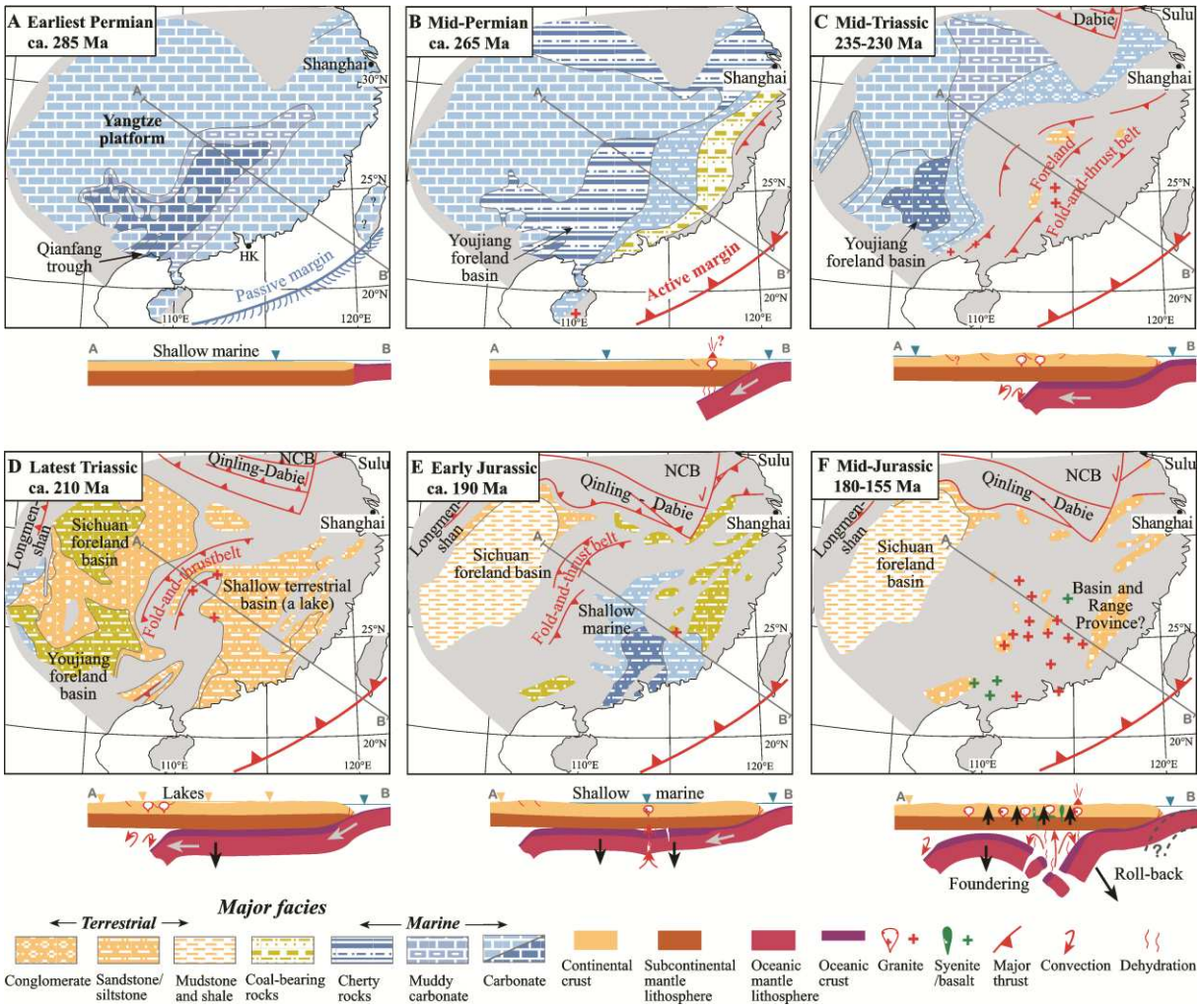

Figure 2-5. Paleogeographic evolution of the South China Block from Permian to Jurassic, the flat-slab subduction model of the palaeo-Pacific plate, and postorogenic magmatism induced by slab foundering and retreating (cited from Li and Li, 2007).

et al., 2013; Shu et al., 2015; Li et al., 2016). Wang et al. (2013) emphasized that the interaction between the South China Block and the surrounding blocks/plates provided the first-order driving force for the Triassic intracontinental deformation across the South China Block. The third tectonic model is becoming more and more popular than the former two, however, the influence of the palaeo-Pacific plate subduction during Triassic is still uncertain (Wang et al., 2013).

During Late Mesozoic (Jurassic-Cretaceous), the South China Block was dominated by an extensional tectonic regime, which is demonstrated by the occurrence of abundant granitoid rocks with an evident input of juvenile mantle-derived components, the wide

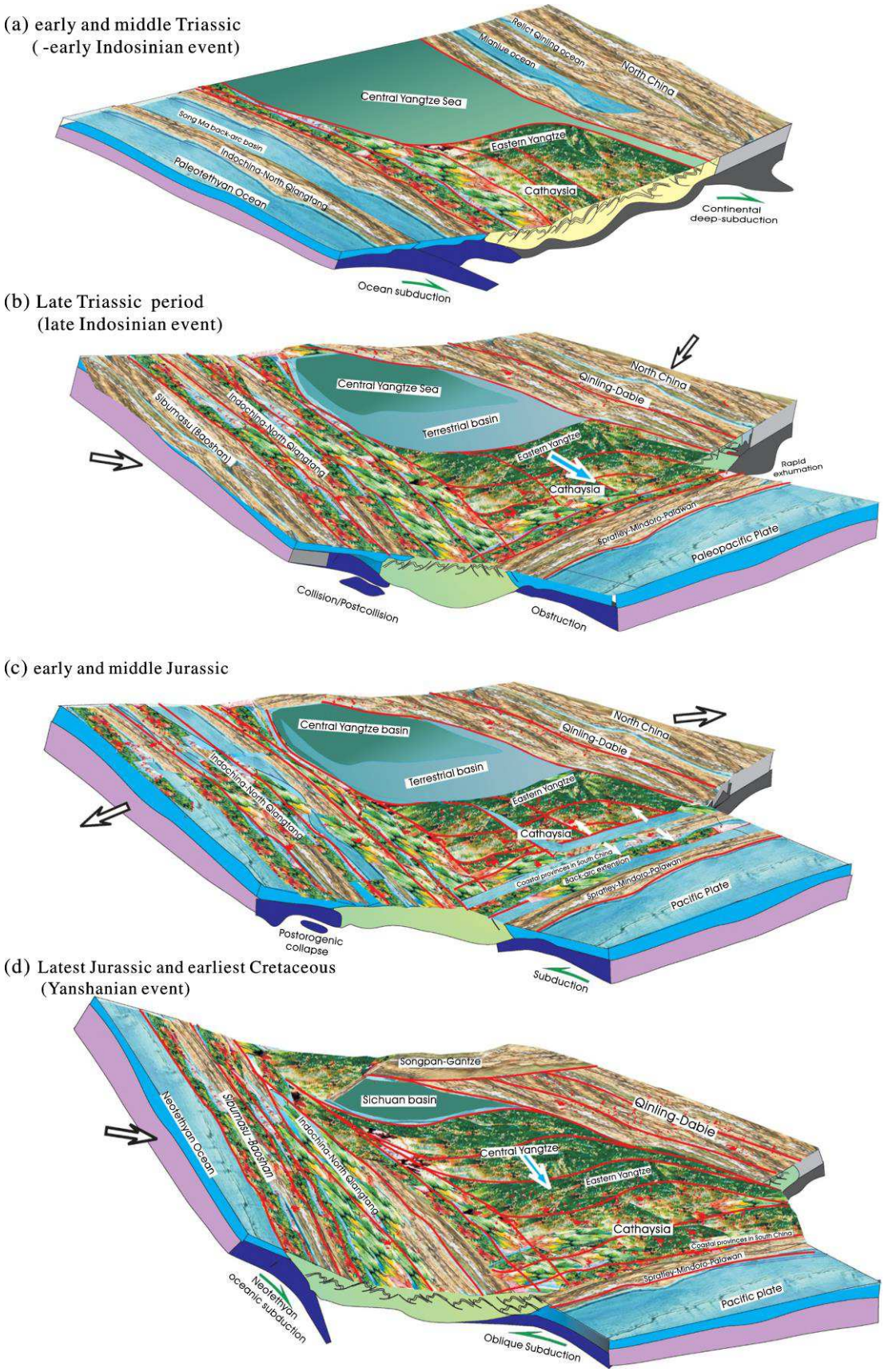

Figure 2-6. Schematic model illustrating the driving mechanisms for the geodynamic evolution of the South China Block during Mesozoic (cited from Wang et al., 2013).

distribution of extensional basins, the existence of extensional tectonomagmatic associations, the extensional information recorded by magma emplacement processes, and the absence of compressional deformation structures (Shu and Zhou, 2002; Shu et al., 2006b, 2009; Shu, 2012; Wang and Shu, 2012; Wang et al., 2013; Wei et al., 2014a, 2014b, 2016). Zhou and Li (2000) firstly proposed the model of palaeo-Pacific plate subduction with changing angles (Fig. 2-7) to understand the origin of the large-scale Late Mesozoic granitic magmatism in Southeastern China. A combination of the palaeo-Pacific plate subduction induced back-arc extensional setting, asthenosphere upwelling, basaltic magmas underplating, and crustal anatexis is thought to be the key mechanism for the generation of these Late Mesozoic granitoid rocks (Shu and Zhou, 2002; Zhou et al., 2006a). A transition of regional tectonic regime from the Tethysian domain to the palaeo-Pacific domain is suggested to occur in Early-Middle Jurassic (Shu and Zhou, 2002; Zhou et al., 2006a; Shu, 2012). Li and Li (2007) interpreted the Late Mesozoic granitoid rocks as a result of postorogenic magmatism induced

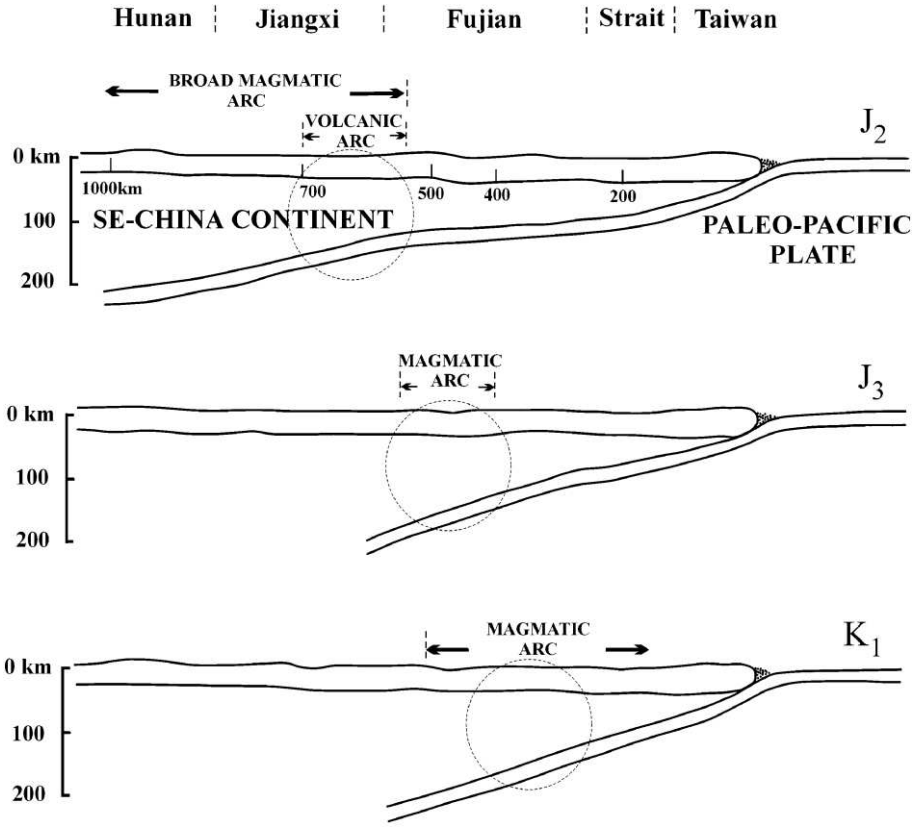

Figure 2-7. Schematic model illustrating the palaeo-Pacific plate subduction with changing angles in Southeastern China during Late Mesozoic (cited from Zhou and Li, 2000).

by slab foundering and retreating in their flat-slab subduction model of the palaeo-Pacific plate (Fig. 2-5e and f). Wang et al. (2013) pointed that the post-orogenic collapse after the Triassic compressive deformation and the back-arc extension resulted from the westward subduction of the palaeo-Pacific plate probably jointly controlled the Early-Middle Jurassic tectonic regime of the South China Block (Fig. 2-6c), and the palaeo-Pacific plate subduction and the blocking with the Indochina Block to the southwest and the North China Block to the north might dominate the tectonic regime of the South China Block since Late Jurassic (Fig. 2-6d). However, the geophysical study on granite emplacement mechanism carried out by Liu et al. (2018) revealed that the Late Jurassic Qitianling pluton in South China was formed during a period of tectonic quiescence. Therefore, the Jurassic tectonic setting in South China remains a subject of controversy that need to be solved by further studies.

2.1.2. Multiple-aged granitoids and volcanic rocks

The outcrop area of the multiple-aged granitoids in the South China Block is about 169,690 km^2, in which the Neoproterozoic, Early Paleozoic, Late Paleozoic, Triassic, Jurassic, and Cretaceous granitoids occupy about 9,950 km^2, 22,110 km^2, 1,480 km^2, 23,230 km^2, 61,460 km^2, and 51, 460 km^2, respectively (Fig. 2-8; according to a recently revised version of the map from Sun, 2006). In addition, the Jurassic and Cretaceous volcanic rocks have outcrop areas of 1,170 km^2 and 89,620 km^2, respectively (Fig. 2-8; Zhou et al., 2006a). These multiple-aged granitoids and volcanic rocks in the South China Block respectively have unique spatial distributions, chronological features, structural characteristics, mineralogical and geochemical compositions, and relations with tectonic events.

The Neoproterozoic granitoids mostly occur as peraluminous granite batholiths along the southeastern margin of the Yangtze Block in southern Anhui, northern Jiangxi, southern Hubei, and northern Guangxi Provinces (Fig. 2-8), such as the Xucun, Jiuling, Motianling, and Yuanbaoshan granites. They were partially deformed as gneissoid granites and coexist with a set of slightly earlier formed Neoproterozoic island-arc volcanic-sedimentary sequence (Zhou, 2003; Sun, 2006). These Neoproterozoic granites generally contain aluminum-rich minerals, such as cordierite, muscovite, tourmaline, and garnet, and are considered as S-type granites (Li et al., 2003; Zhou, 2003). Some Neoproterozoic I-type granitoids also appear in

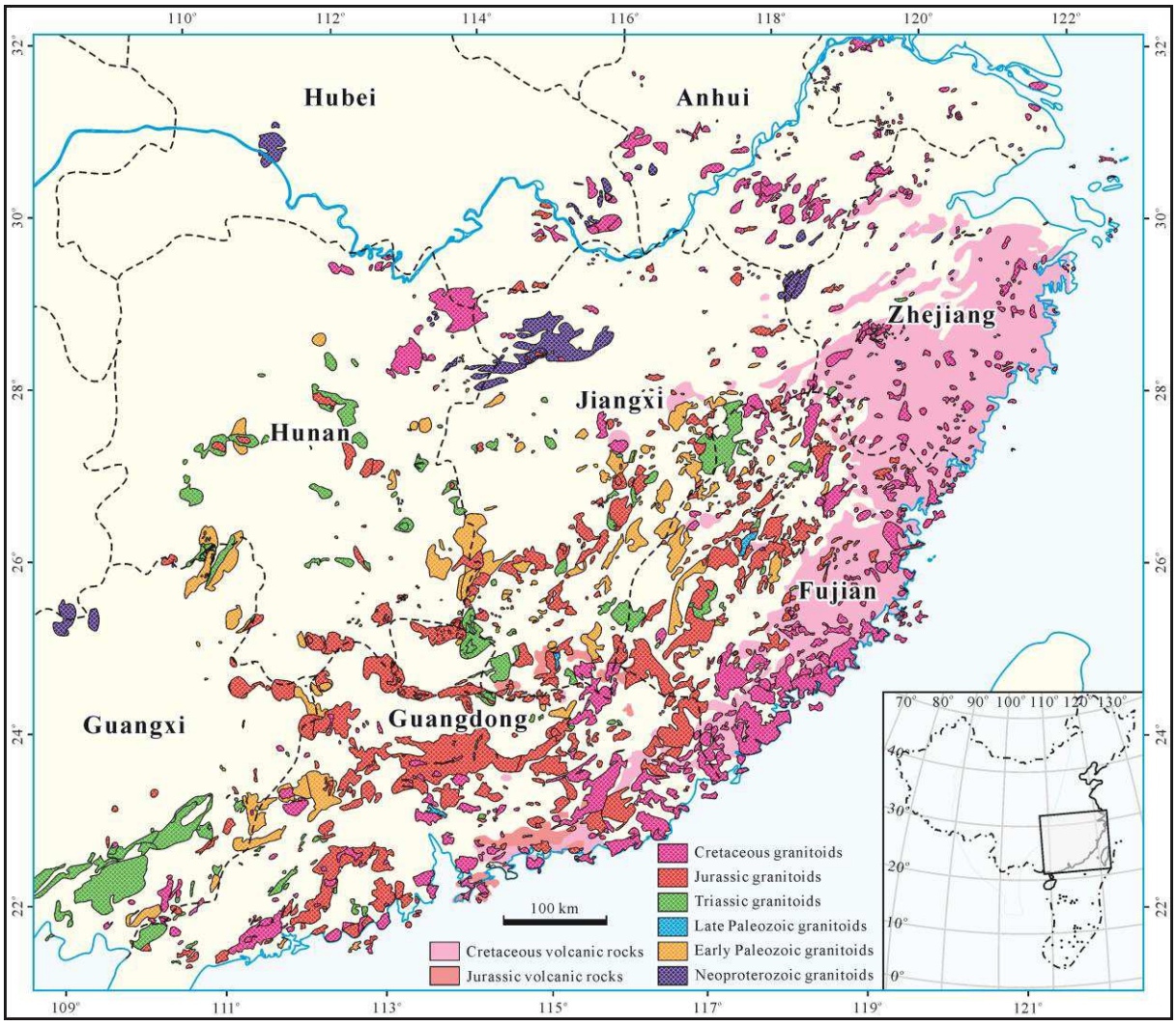

Figure 2-8. Distribution of multiple-aged granitoids and volcanic rocks in South China (modified after Sun, 2006 and Zhou et al., 2006a).

the South China Block, such as the Huangling complex in western Hubei Province (Fig. 2-8) which is comprised of dominant Na-rich tonalite-trondhjemite-granodiorite association and minor K-rich calc-alkaline intrusions (Li et al., 2003). The Neoproterozoic granitoids were mostly formed at ca. 830 Ma and were derived from partial melting of various crustal sources with different influences by juvenile mantle-derived components (Li et al., 2003; Zhou, 2003; Sun, 2006; Yao et al., 2014a; Zhang et al., 2016a; Wang et al., 2017a; Xiang et al., 2018). Li et al (2003) introduced a model of mantle plume beneath South China to interpret the origin of these Neoproterozoic granitoids, however, it is now more accepted that the generation of these Neoproterozoic granitoids was related to the amalgamation of the Yangtze and

Cathaysia Blocks and its post-orogenic extension (Zhou, 2003; Sun, 2006; Yao et al., 2014a; Wang et al., 2017a).

The Early Paleozoic granitoids are mainly distributed in the boundary areas between Jiangxi and Fujian, Jiangxi and Hunan, Hunan and Guangxi, and Guangxi and Guangdong Provinces (Fig. 2-8). However, Early Paleozoic volcanic rocks and associated mafic intrusions are poor in the South China Block interior (Zhou, 2003; Sun, 2006; Wang et al., 2013; Zhang et al., 2017d). These Early Paleozoic granitoids can be divided into relatively earlier gneissoid granites and relatively later massive granitoids with respective peak ages of ca. 440 Ma and ca. 420 Ma (Sun, 2006; Wang et al., 2013; Shu et al., 2014, 2015). The gneissoid granites are less voluminous than the massive granitoids and generally contain muscovite, garnet, and tourmaline. The massive granitoids mostly occur as large-volume batholiths and laccoliths and are characterized by peraluminous biotite monzonitic granites, two-mica monzonitic granites, and muscovite-(garnet) granites (Wu et al., 2008; Charvet et al., 2010; Li et al., 2010; Wang et al., 2013). There are also some biotite granodiorites and hornblende-bearing granites. For the petrogenesis of these Early Paleozoic granitoids, Sun (2006) pointed out that the gneissoid granites were formed through crustal partial melting by a combined compression, ductile deformation, and migmatization mechanism, whereas, the massive granitoids were formed by partial melting of dominant crustal materials with possible input of mantle-derived components under an extensional tectonic setting. Zhang et al. (2010, 2012) and Wang et al. (2011a) proposed that these Early Paleozoic granitoids probably originated from partial melting of Proterozoic metapelite and meta-igneous rocks with poor input of juvenile mantle-derived components. Li et al. (2010) and Wang et al. (2011a) interpreted their origin to be related to increased thermal weakening of the thickened continental crust during Early Paleozoic.

The Late Paleozoic magmatic rocks in the South China Block are dominated by the voluminous Emeishan basalts and related intrusions in Southwest China which were formed at ca. 260 Ma in Late Permian (Xu et al., 2001; Fan et al., 2008; Zhou et al., 2008). However, the Late Paleozoic granitoids are rarely exposed and are dominantly distributed in southern Hainan Island. These Late Paleozoic granitoids in Hainan are characterized by calc-alkaline

gneissoid granites which have ages of 267 – 252 Ma, show the geochemical features of I-type granites, and are thought to be related to a continental arc setting (Li et al., 2006; Chen et al., 2011). They are temporally similar to the gneissoid granodiorites in the Ailaoshan-Song Ma suture zone between the South China Block and the Indochina Block (Lan et al., 2000; Carter et al., 2001; Carter and Clift, 2008).

The Triassic granitoids are mainly spread in southeastern Guangxi, Hunan, northern Guangdong, southern Jiangxi, and western Fujian Provinces (Fig. 2-8). However, Triassic volcanic rocks are almost absent in the South China Block. Two series of Triassic granitoids have been recognized as follows: (1) minor gneissoid granites dominantly along the Yunkai domain at the southern margin of the South China Block with ages of 250 – 242 Ma; (2) voluminous peraluminous massive granitoids with two peak ages of ca. 240 Ma and ca. 220 Ma (Wang and Zhou, 2002; Li et al., 2005; Wang et al., 2005b, 2007b, 2013; Peng et al., 2006a; Zhou et al., 2006a; Zhou, 2007; Zhang et al., 2014). Except for the garnet- and cordierite-bearing granites in the Darongshan-Shiwandashan and northern Yunkai domains, most of these peraluminous massive granitoids are biotite monzonitic granites, two-mica monzonitic granites, and muscovite granites (Zhou and Yu, 2001; Wang and Zhou, 2002; Zhou et al., 2006a; Zhou, 2007). The Triassic granitoids contain both S-type and I-type granites and are dominated by S-type granites. It is generally accepted that these granitoids were derived from partial melting of crustal metamorphic basements without significant addition of juvenile mantle-derived components (Ge, 2003; Deng et al., 2004; Wang et al., 2007b). For the petrogenetic mechanism of these Triassic granitoids, Wang et al. (2002a, 2007b) emphasized the importance of isostatic adjustment of the thickened continental crust, with heat supplied from in-situ radiogenic heating in the thickened continental crust, and subsequent heating by underplated basaltic magmas. Zhou et al. (2006a) interpreted the earlier gneissoid granites as syn-collisional granites and the later massive granitoids as late collisional granitoids.

The Jurassic granitoids occupy the largest exposure area of the whole multiple-aged granitoids in South China and are mostly distributed in Guangdong, Hunan, Jiangxi, and Fujian Provinces far away from the southeast coastline (Fig. 2-8). These Jurassic granitoids

show a southwest-northeast trend of spatial distribution overall and exhibit a west-east extending trend in the Nanling Range made up of three distinguishable belts which are the northern Qitianling-Jiufeng belt, the middle Dadongshan-Guidong belt, and the southern Fogang-Xinfengjiang belt (Fig. 2-8; Sun, 2006; Zhou et al., 2006a; Wang et al., 2013). These Jurassic granitoids were mainly formed from 165 Ma to 150 Ma and are composed of I-type, S-type, and A-type granitoids and minor syenites (Zhou and Li, 2000; Hua et al., 2003, 2005; Sun et al., 2005; Sun, 2006; Zhou et al., 2006a; Li and Li, 2007; Zhou, 2007; Chen et al., 2008, 2013; Jiang et al., 2008; Mao et al., 2008a, 2013a; Zhu et al., 2008; Wang et al., 2013; Huang et al., 2017a). Compared with the Jurassic granitoids, the Jurassic volcanic rocks are obviously less exposed and are mostly spread in southern Hunan, southern Jiangxi, northeastern Guangdong, and southwestern Fujian Provinces with a rough west-east trend. They were dominantly formed in Early-Middle Jurassic from 195 Ma to 170 Ma and are mainly composed of bimodal magmatic assemblages of basalt and rhyolite with similar abundances (Zhou et al., 2006a; Wang et al., 2013).

The Cretaceous granitoids occupy the second largest exposure area of the whole multiple-aged granitoids in South China and are mainly spread in the coastal Guangdong, Fujian, and Zhejiang Provinces with a southwest-northeast extending trend, and also in the Lower Yangtze northern Hunan, southern Hubei, and southern Anhui Provinces with a west-north-east trend of spatial distribution (Fig. 2-8). These Cretaceous granitoids were mainly formed from 135 Ma to 80 Ma with two peak ages of 125 Ma and 93 Ma and are composed of I-type, S-type, and A-type granitoids, and minor alkaline rocks (Zhou and Li, 2000; Wang and Zhou, 2002; Hua et al., 2003, 2005; Sun, 2006; Zhou et al., 2006a; Li and Li, 2007; Zhou, 2007; Mao et al., 2008a, 2013a; Wang et al., 2013; Yan et al., 2017). Compared with the Cretaceous granitoids, the Cretaceous volcanic rocks are much more voluminous and are mainly distributed in the coastal Zhejiang, Fujian, and Guangdong Provinces constituting a northeast-trending volcanic zone (Fig. 2-8). They were mainly formed from 130 Ma to 85 Ma and are dominated by granitic volcanic-subvolcanic-intrusive assemblages with minor mafic rocks (Zhou et al., 2006a; Wang et al., 2013).

The Early-Middle Jurassic volcanic rocks in the South China Block were interpreted as

to genetically associated with crust-mantle interaction under a rift-like setting in response to the far-field effect induced by the palaeo-Pacific plate subduction (Zhou et al., 2006a, 2006c; Zhou, 2007; He et al., 2010; Wang et al., 2013). Zhou et al. (2006a) proposed that the formation of these Early-Middle Jurassic volcanic rocks might mark the ending of the old Tethysian tectonic regime and the beginning of the new palaeo-Pacific tectono-magmatic cycle. The explosive formation of the Late Mesozoic granitoids and the Cretaceous volcanic rocks is widely considered as a result of the palaeo-Pacific plate subduction, asthenosphere upwelling, basaltic magmas underplating, and crustal anatexis, and maybe also post-orogenic extension (Zhou and Li, 2000; Shu and Zhou, 2002; Wang and Zhou, 2002; Zhou et al., 2006a; Li and Li, 2007; Zhou, 2007; Mao et al., 2013a; Wang et al., 2013; Huang et al., 2017a; Li et al., 2018a). Compared with the Early Paleozoic and Triassic granitoids, the Late Mesozoic granitoids distinctly contain more juvenile mantle-derived components (Zhou et al., 2006a; Wang et al., 2013).

2.1.3. Polymetallic mineralization

Numerous mineral deposits of W, Sn, rare metals, base metals, and precious metals have been discovered in the South China Block, which are characterized by multiple-aged (Neoproterozoic, Early Paleozoic, Triassic, Jurassic, and Cretaceous) mineralization and are dominated by Mesozoic especially Late Mesozoic mineralization (Figs. 2-9 and 2-10; Hua and Mao, 1999; Hua et al., 2003, 2005; Mao et al., 2007, 2008a, 2009a, 2009b, 2011a, 2011b, 2013a; Zaw et al., 2007; Chen et al., 2008, 2013, 2015a; Ma, 2008; Pei et al., 2008; Cheng et al., 2010; Hu and Zhou, 2012; Fu et al., 2013; Li et al., 2013; Pirajno, 2013; Sheng et al., 2015; Hu et al., 2016, 2017; Zhao et al., 2017; Zhou et al., 2017, 2018). The vast majority of these multiple-aged mineral deposits are temporally and spatially closely associated with the multiple-aged granitoids in the South China Block (Fig. 2-10; Hua et al., 2003; Mao et al., 2007, 2008a, 2009a, 2009b, 2011a, 2011b, 2013a; Chen et al., 2008, 2013; Ma, 2008; Pei et al., 2008; Cheng et al., 2010; Hu and Zhou, 2012; Fu et al., 2013; Li et al., 2013; Hu et al., 2016, 2017; Zhao et al., 2017; Zhou et al., 2017, 2018).

The Neoproterozoic mineralization has been discovered mainly in the Jiangnan Orogen between the Yangtze and Cathaysia Blocks so far. They are dominated by Sn and also some

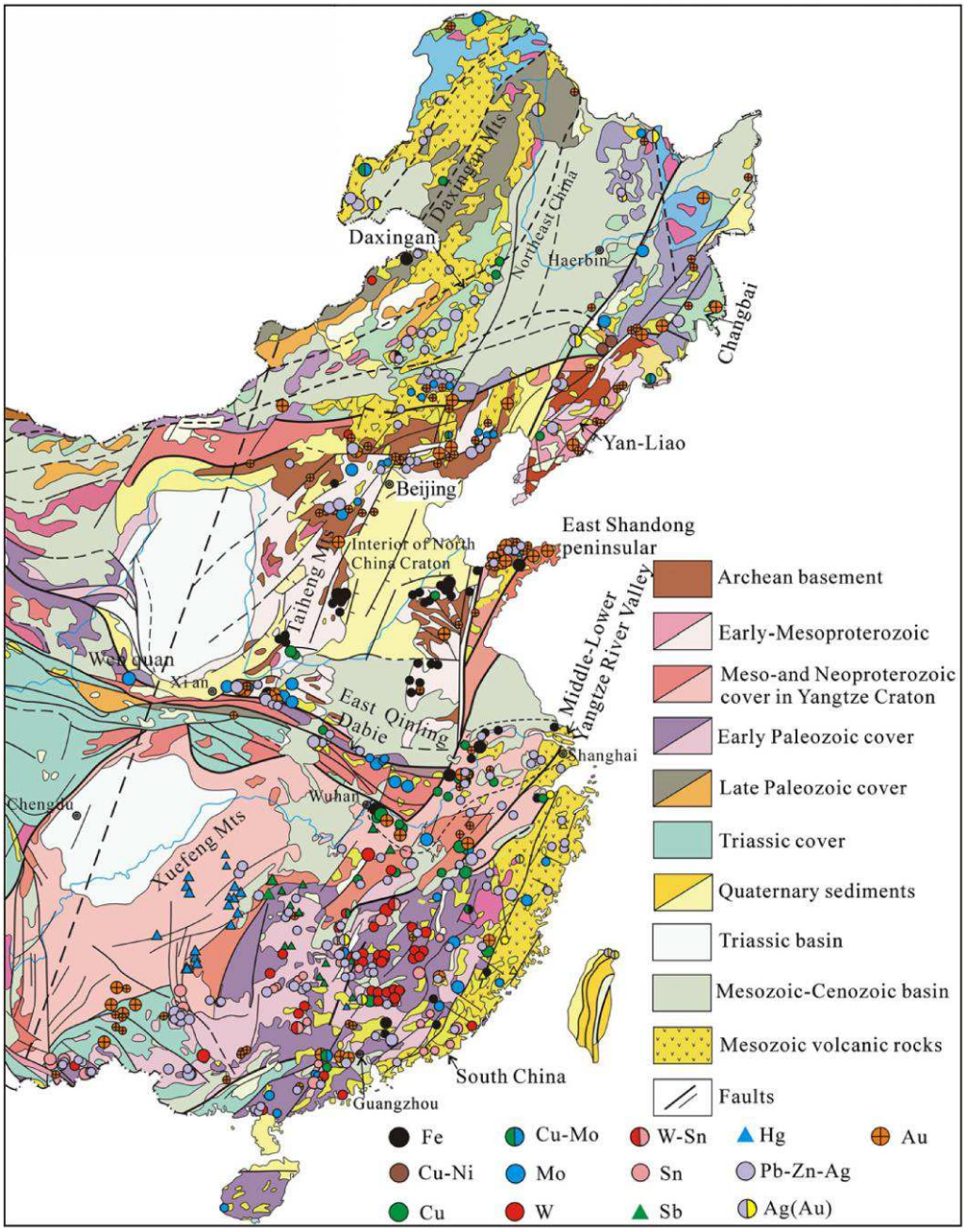

Figure 2-9. Distribution of the Mesozoic mineral deposits in East China (Southeast China and Northeast China) (cited from Mao et al., 2011a).

W deposits which are related to the Neoproterozoic granites in the Jiangnan Orogen, such as the Baotan Sn orefield associated with the Pingying granite (Zhang et al., 2016a; Chen et al., 2018), the Jiumao Sn deposit associated with the Yuanbaoshan granite (Yao et al., 2014a; Xiang et al., 2018), the Biaoshuiyan and Heiwanhe Sn-W deposits associated with the Fanjingshan granite (Xia, 1985; Zhu, 2010; Wang et al., 2011b), the Nanjia and Wuya W

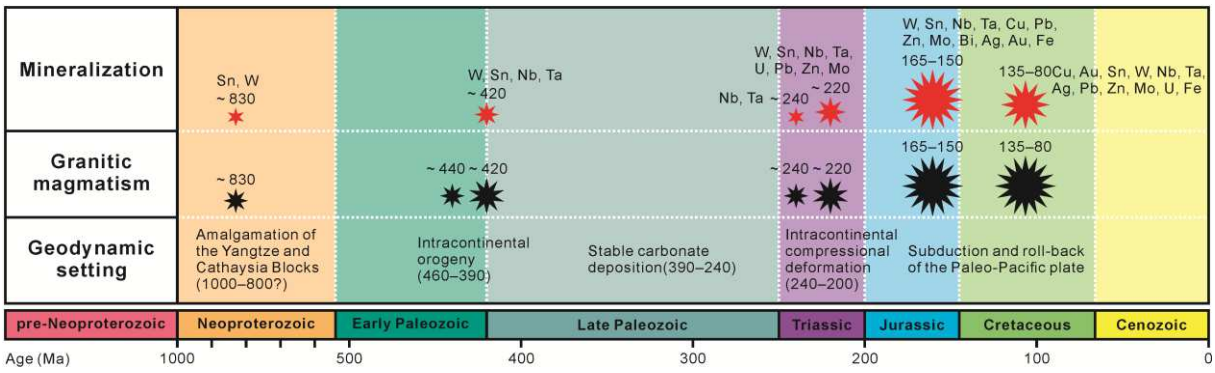

Figure 2-10. Summary of the geodynamic evolution, granitic magmatism, and related mineralization in South China.

deposits associated with the Motianling granite (Pan and Hu, 2014; Liu et al., 2016a, 2016b), and the Huashandong W deposit associated with the Jiuling granite (Zhong et al., 2005; Liu et al., 2015). Chen et al. (2018) published a cassiterite U-Pb age of 829 ± 19 Ma by LA-ICP-MS analysis for the Menggongshan Sn deposit in the Baotan Sn orefield. Xiang et al. (2018) obtained two metallogenic ages of 831 ± 11 Ma and 828 ± 12 Ma for the Jiumao Sn deposit by LA-ICP-MS cassiterite U-Pb dating. Liu et al. (2015) constrained the formation time of the Huashandong W deposit at 805 ± 5 Ma by molybdenite Re-Os dating.

The Early Paleozoic mineral deposits in South China discovered until now are mainly W (Sn) and also some Nb-Ta deposits and are temporally and spatially related to the later (ca. 420 Ma) Early Paleozoic granites (Fig. 2-10). The Yuechengling granitic complex in northern Guangxi Province is a typical case of the Early Paleozoic W-bearing granites. Yang et al. (2014) published a zircon U-Pb age of 421.8 ± 2.4 Ma and a scheelite Sm-Nd age of 421 ± 24 Ma for the Niutangjie W deposit at the southern margin of the Yuechengling granite. Chen et al. (2016) identified an Early Paleozoic W mineralization event in the Dushiling W deposit at the northeastern margin of the Yuechengling granite by zircon U-Pb dating (422.9 ± 2.1 Ma, 423.2 ± 2.4 Ma, 420.9 ± 2.3 Ma, 421.5 ± 2.5 Ma), scheelite Sm-Nd dating (417 ± 35 Ma), and titanite U-Pb dating (424 ± 13 Ma, 425 ± 12 Ma). The Penggongmiao granitic batholith in southern Hunan Province was previously also regarded as an Early Paleozoic W-bearing granite. A dozen of scheelite-quartz veins have been detected at the southern contact zone between the Penggongmiao granite and country rocks in the Zhangjialong W deposit. Two

crystallization ages of 435.3 ± 2.7 Ma and 436.2 ± 3.1 Ma and a crystallization age of 426.5 ± 2.5 Ma for the Penggongmiao medium to coarse grained biotite granite and the magmatic scheelite-bearing aplite veins therein, respectively, were obtained by Zhang et al. (2011a) through LA-ICP-MS zircon U-Pb dating. However, Yuan et al. (2018) recently pointed out that the Zhangjialong W deposit was formed during Late Jurassic with a molybdenite Re-Os age of 160.2 ± 2.2 Ma and a muscovite 40Ar/39Ar age of 153.5 ± 1.0 Ma. The Xigang Nb-Ta deposit in eastern Jiangxi Province was recently confirmed as an Early Paleozoic (422 ± 3 Ma, 420 ± 4 Ma, 424 ± 5 Ma) deposit by LA-ICP-MS coltan U-Pb dating (Che et al., 2018).

During Triassic, some Nb-Ta deposits were formed at ca. 240 Ma and more W-Sn, Nb-Ta, and also U, Pb-Zn, Mo deposits were formed at ca. 220 Ma (Fig. 2-10). The LA-ICP-MS coltan U-Pb geochronological study of Che et al. (2018) confirmed that the Guangning Nb-Ta deposits in Guangdong Province were formed during Early Triassic (Houxi: 248 ± 4 Ma; Chunxin: 247 ± 3 Ma, 246 ± 3 Ma; Dongtounan: 247 ± 3 Ma, 246 ± 3 Ma; Shenkeng: 245 ± 3 Ma). The Late Triassic mineral deposits in South China mainly contain the Wangxianling W deposit (zircon U-Pb age: 226 – 222 Ma, molybdenite Re-Os age: 228 – 221 Ma, muscovite $^{40}Ar/^{39}Ar$ age: 214 Ma, Zhang et al., 2015a), Limu Sn-W-Nb-Ta deposit (zircon U-Pb age: 218 – 214 Ma, muscovite $^{40}Ar/^{39}Ar$ age: 213 Ma, Feng et al., 2013; zircon U-Pb age: 225 Ma, Zhang et al., 2014; coltan U-Pb age: 219 – 217 Ma, Che et al., 2018), Qingshuitang Pb-Zn deposit (zircon U-Pb age: 203 Ma, Miao et al., 2014), Youmaling W deposit (zircon U-Pb age: 215 – 212 Ma, Yang et al., 2013; zircon U-Pb age: 225 – 220 Ma, scheelite Sm-Nd age: 212 Ma, Zhang et al., 2015b; coltan U-Pb age: 204 Ma, Che et al., 2018), Yuntoujie W-Mo deposit (zircon U-Pb age: 217 Ma, molybdenite Re-Os age: 217 Ma, Wu et al., 2012), Caojiaba W deposit (titanite U-Pb age: 206 – 196 Ma, Xie et al., 2018), Muguayuan W deposit (Li et al., 2018b), etc.

Late Mesozoic (Yanshanian) is the most important metallogenic period in South China (Fig. 2-10). The Late Mesozoic mineralization is characterized by widespread, large-scale, and polymetallic (W, Sn, Nb, Ta, Cu, Pb, Zn, Au, Ag, Mo, Bi, U, Fe, etc.) mineralization (Fig. 2-10). Thus, it was called Late Mesozoic “metallogenic explosion” by Hua and Mao (1999). Mao et al. (2013a) discussed the temporal-spatial distribution features of these Late

Mesozoic mineral deposits. Here, the general regularities of the Late Mesozoic mineralization are further summarized as follows: (1) Middle-Late Jurassic (175 – 155 Ma) calc-alkaline granitoids associated porphyry, skarn Cu (Au, Mo) and hydrothermal Pb-Zn-Ag systems in the Qinzhou-Hangzhou metallogenic belt; (2) Late Jurassic (160 – 150 Ma) metaluminous to peraluminous granites related W-Sn-Mo-Bi-Nb-Ta systems dominated by skarn, quart-vein, greisen, and pegmatite mineralization in the Nanling Range metallogenic belt and adjacent areas; (3) Early Cretaceous (145 – 120 Ma) porphyry-skarn Cu-Mo-Au, skarn Fe and Fe-Cu, and magnetite-apatite deposits associated with the I-type calc-alkaline granitoids (gabbro, diorite, and granodiorite) and A-type granitoids in the Middle-Lower Yangtze metallogenic belt; (4) Middle-Late Cretaceous (120 – 80 Ma) porphyry-epithermal Cu-Mo-Au, epithermal Au (Ag), hydrothermal Pb-Zn-Ag, porphyry Sn, quartz-vein W, and granite-related U deposits in the southeastern coastal metallogenic belt and granite-related Sn polymetallic, W, and Carlin-type Au deposits in the Youjiang basin. It is noteworthy that the recently discovered giant Dahutang veinlet-disseminated W deposit (> 1.31 Mt WO_3, zircon U-Pb age: 170 – 160 Ma for granodiorite porphyry, ca. 150 Ma for porphyritic biotite granite, ca. 144 Ma for fine-grained biotite granite, and ca. 130 Ma for granite porphyry, molybdenite Re-Os age: 150 – 140 Ma; Mao et al., 2013c, 2015; Huang and Jiang, 2014; Zhang et al., 2018a, 2018b) and Zhuxi skarn W deposit (2.86 Mt WO_3, zircon U-Pb age: 151 – 148 Ma, scheelite Sm-Nd age: ca. 144 Ma, molybdenite Re-Os age: ca. 145 Ma, muscovite $^{40}Ar/^{39}Ar$ age: ca. 150 Ma; Chen et al., 2015b; Liu et al., 2017; Pan et al., 2017; Wang et al., 2017b; He et al., 2018) in northern Jiangxi Province have changed the distribution framework of tungsten resources in South China.

2.2. Nanling Range

The Nanling Range covers a total area of about 200,000 km^2 in the central-southern part of South China from 111° E to 117° E and from 23°20’ N to 26°40’ N and includes southern Hunan, southern Jiangxi, northern Guangdong, northeastern Guangxi, and western Fujian Provinces (Fig. 1-1; Shu et al., 2006b; Zhou, 2007; Chen et al., 2013). It holds the largest W production of South China and also of the whole world. Since the first question of “Where is

the Nanling Range?" raised by Li (1942), systematic studies of the different types of granitoids and their related mineralization in the Nanling Range have never been interrupted (Hsu, 1943; Hsu et al., 1960, 1963a, 1963b; Institute of Geochemistry, CAS, 1979; Mo et al., 1980; Department of Geology, NJU, 1981; Xu et al., 1982, 1983; Chen et al., 1989a, 2008, 2013; The Granitoid Research Group of the Nanling Project, MGMR, 1989; Hua and Mao, 1999; Hua et al., 2003, 2005; Li et al., 2007a, 2013; Mao et al., 2007, 2008a, 2009a, 2011a, 2013a; Zaw et al., 2007; Ma, 2008; Pei et al., 2008; Hu and Zhou, 2012; Fu et al., 2013; Pirajno, 2013; Hu et al., 2017; Huang et al., 2017a; Zhao et al., 2017; Zhou et al., 2018). Although multiple-aged (Early Paleozoic, Triassic, Jurassic, and Cretaceous) granitoids and associated polymetallic (W, Sn, Nb, Ta, Cu, Pb, Zn, etc.) mineral deposits are widely developed in the Nanling Range (Fig. 1-1), Middle-Late Jurassic is the most important period for granitic magmatism and related mineralization in this region (Chen et al., 2013; Li et al., 2013; Mao et al., 2013a; Huang et al., 2017a).

2.2.1. Middle-Late Jurassic ore-bearing granitoids

The Middle-Late Jurassic ore-bearing granitoids in the Nanling Range can be divided into four different types, i.e., W-bearing, Sn-bearing, Nb-Ta-bearing, and Cu-Pb-Zn-bearing granitoids, according to the association of ore-forming elements, petrographic features, and geochemical characteristics (Chen et al., 2008, 2013; Huang et al., 2017a; Wang et al., 2017c). Main features of these ore-bearing granitoids are summarized in Table 2-1. The W-bearing granites are dominated by S-type two-mica, muscovite, and biotite granites, such as the Yaogangxian, Dengfuxian, Taoxikeng, Xihuashan, and Dajishan granites (Fig. 1-1). The Sn mineralization is mainly associated with two different types of granites, i.e., aluminous A-type (A_2-type) biotite granites, such as the Huashan-Guposhan, Jiuyishan, and Qitianling granites, and S-type two-mica, muscovite, and biotite granites, such as the Maoping, Piaotang, Baxiannao, and Huamei'ao granites (Fig. 1-1). The Nb-Ta-bearing granites are mostly highly fractionated albite and muscovite granites which are genetically associated with S-type W-bearing and Sn-bearing granites, such as the Jianfengling, Laiziling, Dengfuxian, and Dajishan granites (Fig. 1-1). The Cu-Pb-Zn mineralization is predominantly related to metaluminous calc-alkaline I-type granodioritic rocks, such as the Shuikoushan, Baoshan,

Tongshanling, and Dabaoshan granodiorites (Fig. 1-1). All of these different types of ore-bearing granitoids were formed from 165 Ma to 150 Ma. Dark microgranular enclaves and amphibole are commonly observed in the Cu-Pb-Zn-bearing granodioritic rocks and the Huashan-Guposhan and Qitianling A_2-type Sn-bearing biotite granites but are absent in the other Sn-bearing granites and also the W-bearing and Nb-Ta-bearing granites. The Fe-Ti oxide minerals of the Cu-Pb-Zn-bearing granodiorites and the Huashan-Guposhan and Qitianling Sn-bearing granites are dominated by magnetite, whereas, the other ore-bearing granites mainly contain ilmenite. These different types of ore-bearing granitoids have various associations of accessory minerals. They also have different features in mineralization types. The Cu-Pb-Zn mineralization mainly consists of skarn, carbonate replacement, and sulfide-quartz vein. Skarn, greisen, and quartz vein are the dominant types for W and Sn mineralization. Besides, chloritized granite is also important for Sn mineralization. The Nb-Ta mineralization mainly comprises albite granite, greisen, and pegmatite.

Table 2-1. Main features of the Middle-Late Jurassic ore-bearing granitoids in the Nanling Range (summarized from Chen et al., 2008, 2013; Huang et al., 2017a; Wang et al., 2017c)

Ore-bearing granitoid	Cu-Pb-Zn	Sn	W	Nb-Ta
Tectonic setting		Intraplate extension		
Rock type	I-type granodioritic rocks	A(A_2)-type biotite granites and S-type two-mica, muscovite, and biotite granites	S-type two-mica, muscovite, and biotite granites	Highly fractionated albite and muscovite granites
Age		165 – 150 Ma		
Dark enclaves	Observed	Observed or not	Not observed	Not observed
Amphibole	Observed	Observed or not	Not observed	Not observed
Fe-Ti oxide minerals	Mainly magnetite	Mainly Magnetite or mainly ilmenite	Mainly ilmenite	Mainly ilmenite
Accessory minerals	Titanite, allanite, apatite, sulfide minerals	Titanite, allanite, apatite, cassiterite or monazite, xenotime, apatite, cassiterite	Monazite, xenotime, apatite, wolframite, scheelite	Columbite-tantalite, monazite, xenotime, ferberite
Mineralization type	Skarn, carbonate replacement, sulfide-quartz vein	Skarn, greisen, quartz vein, chloritized granite	Skarn, greisen, quartz vein	Albite granite, greisen, pegmatite

2.2.2. Middle-Late Jurassic skarn deposits

Skarn is one of the most important mineralization types for the Middle-Late Jurassic Cu-Pb-Zn, W, and Sn deposits in the Nanling Range (Table 2-1). The skarn Cu-Pb-Zn deposits mainly include the Tongshanling (Cai et al., 2015; Lu et al., 2015; Wang et al., 2017d), Baoshan (Lu et al., 2006; Bao et al., 2014; Xie et al., 2015), Shuikoushan (Liu, 1994; Lu et al., 2013; Huang et al., 2015), Dabaoshan (Wang, 2010; Qu et al., 2014; Dai et al., 2015), and Huangshaping (Xi et al., 2009; Zhu et al., 2012; Ding et al., 2016a) deposits (Fig. 1-1). The skarn W deposits mainly include the Yaogangxian (Peng et al., 2006b; Zhu et al., 2014), Shizhuyuan (Liu et al., 2006; Wu et al., 2016), Xintianling (Bi et al., 1988; Zhang, 2014; Shuang et al., 2016), and Weijia (Hu et al., 2015; Huang et al., 2017a) deposits (Fig. 1-1). The skarn Sn deposits mainly include the Shizhuyuan (Li et al., 1996; Liu et al., 2006), Jinchuantang (Liu et al., 2014), and Hehuaping (Yao et al., 2014b) deposits (Fig. 1-1). These Middle-Late Jurassic skarn deposits are mostly distributed in the western part of the Nanling Range (Fig. 1-1). Association of different mineralization types is a common feature of these skarn deposits. Carbonate replacement and sometimes sulfide-quartz vein are also important mineralization types in the skarn Cu-Pb-Zn deposits. For instance, the Tongshanling Cu-Pb-Zn deposit is composed of skarn Cu (Mo), skarn Cu-Pb-Zn, sulfide-quartz vein Cu-Pb-Zn, and carbonate replacement Pb-Zn orebodies (Cai et al., 2015; Lu et al., 2015; Wang et al., 2017d). Quartz vein and greisen are also important mineralization types in the skarn W and Sn deposits. For instance, the Yaogangxian W deposit mainly contains scheelite skarn and wolframite-quartz vein orebodies (Peng et al., 2006b; Zhu et al., 2014). Another remarkable feature of these skarn deposits is the association of different ore-forming elements. For instance, the Huangshaping deposit is dominated by skarn W-Mo and carbonate replacement Pb-Zn mineralization (Xi et al., 2009; Zhu et al., 2012; Ding et al., 2016a) and the Shizhuyuan deposit is characterized by Sn-W-Mo-Bi polymetallic mineralization (Li et al., 1996; Liu et al., 2006; Wu et al., 2016). Among these Middle-Late Jurassic skarn deposits in the Nanling Range, the spatially adjacent Tongshanling Cu-Pb-Zn and Weijia W skarn deposits in the Tongshanling-Weijia area are selected as the research objects of this Ph.D. thesis.

Chapter 3. Geology of the Tongshanling-Weijia area

In geography, the Tongshanling-Weijia area is situated in southern Hunan Province about 120 km to the east of Guilin (Fig. 1-1) and at the boundary region among Daoxian, Jiangyong, and Jianghua Counties. In geology, it is located in the conjunction zone between the Yangtze and Cathaysia Blocks, in the western part of the Nanling Range metallogenic belt (Fig. 1-1), and also in the southwestern part of the Qinzhou-Hangzhou metallogenic belt. The Haiyangshan-Dupangling, Jiuyishan, and Huashan-Guposhan plutons are distributed to the west, east, and south of the Tongshanling-Weijia area, respectively.

3.1. Stratigraphy

In the Tongshanling-Weijia area, the exposed strata include Ordovician to Triassic systems except for the absence of Silurian system and Upper Permian to Lower Triassic series and are dominated by Devonian and Carboniferous systems (Figs. 3-1 and 3-2). The Upper Ordovician strata mainly occur in the northwestern part of the Tongshanling-Weijia area (Fig. 3-1) with a thickness larger than 782 m and are composed of low-grade metasandstone with interbedded slate (Fig. 3-2). The Lower Devonian strata overlay the Upper Ordovician strata by an angular unconformity and comprise conglomerate, pebbled sandstone, quartz sandstone, and siltstone with a thickness of ca. 120 m (Fig. 3-2). The Middle Devonian series contains the lower Tiaomajian Formation and the upper Qiziqiao Formation with thicknesses of ca. 530 m and ca. 1080 m, respectively (Figs. 3-1 and 3-2). The Tiaomajian Formation is constituted by a ca. 390-m-thick Lower Member of siltstone and silty shale with intercalated quartz sandstone and shale and a ca. 140-m-thick Upper Member of siltstone and quartz sandstone with intercalated shale and mudstone (Fig. 3-2). The Qiziqiao Formation consists of a ca. 340-m-thick Lower Member of limestone, carbonaceous limestone, and marly limestone, a ca. 390-m-thick Middle Member of dolostone with intercalated dolomitic limestone, and a ca. 350-m-thick Upper Member of limestone with intercalated marly limestone (Fig. 3-2). The Upper Devonian series contains the lower Shetianqiao Formation and the upper Xikuangshan Formation with thicknesses of 233 – 499 m and 198 – 345 m, respectively (Figs. 3-1 and 3-2).

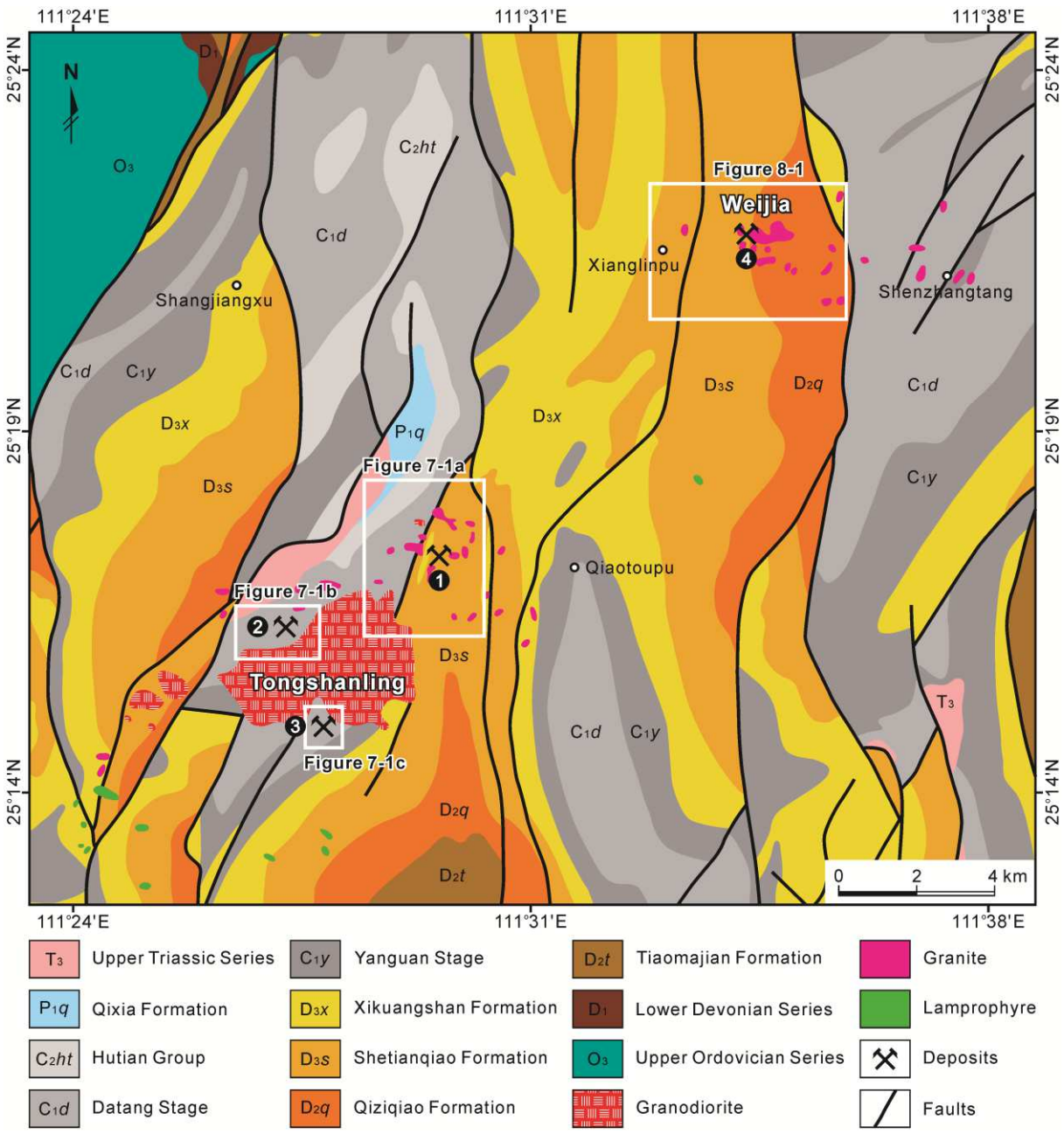

Figure 3-1. Geological map of the Tongshanling-Weijia area in southern Hunan Province (modified after Regional Geological Survey Team of Hunan Geology Bureau, 1975a, 1975b). 1: Tongshanling Cu-Pb-Zn deposit; 2: Jiangyong Pb-Zn-Ag deposit; 3: Yulong Mo deposit; 4: Weijia W deposit.

The Shetianqiao Formation is made up of limestone and dolomitic limestone with intercalated dolostone lumps (Fig. 3-2). The Xikuangshan Formation is composed of a 133 – 269-m-thick Lower Member of limestone and dolomitic limestone with intercalated marl and marly limestone and a 65 – 76-m-thick Upper Member of siltstone, shale, and marl (Fig. 3-2). The Lower Carboniferous series contains the lower Yanguan Stage and the upper Datang Stage

System	Series	Stage/ Group/ Formation	Member	Sequence	Thickness (m)	Description	Mineralization
Triassic	Upper				> 60	Conglomerate, marl, and shale	
Permian	Lower	Qixia			> 40	Chert-bearing limestone	
Carboniferous	Upper	Hutian			> 170	Dolostone	
	Lower	Datang	Zimenqiao		~ 146	Limestone with intercalated dolomitic limestone	
			Ceshui		19 ~ 44	Shale with intercalated marl	
			Shidengzi		251 ~ 370	Chert-bearing limestone with intercalated shale and dolomitic limestone	Carbonated replacement Pb-Zn-Ag and calcic skarn Mo mineralization
		Yanguan	Upper		4 ~ 66	Marl, marly limestone, and sillcalite	
			Lower		287 ~ 463	Limestone and dolomitic limestone	
Devonian	Upper	Xikuangshan	Upper		65 ~ 76	Siltstone, shale, and marl	
			Lower		133 ~ 269	Limestone and dolomitic limestone with intercalated marl and marly limestone	Calcic skarn Cu-Pb-Zn mineralization
		Shetianqiao			233 ~ 499	Limestone and dolomitic limestone with intercalated dolostone lumps	Sulfide-quartz vein Cu-Pb-Zn mineralization
	Middle	Qiziqiao	Upper		~ 350	Limestone with intercalated marly limestone	Calcic skarn Cu-Pb-Zn, W, and sulfide-quartz vein Cu-Pb-Zn mineralization
			Middle		~ 390	Dolostone with intercalated dolomitic limestone	Magnesian skarn W mineralization
			Lower		~ 340	Limestone, carbonaceous limestone, and marly limestone	
		Tiaomajian	Upper		~ 140	Siltstone and quartz sandstone with intercalated shale and mudstone	
			Lower		~ 390	Siltstone and silty shale with intercalated quartz sandstone and shale	
	Lower				~ 120	Conglomerate, pebbled sandstone, quartz sandstone, and siltstone	
Ordovician	Upper				> 782	Low-grade metasandstone with interbedded slate	

Figure 3-2. Stratigraphic column of the Tongshanling-Weijia area (according to Regional Geological Survey Team of Hunan Geology Bureau, 1975a, 1975b).

with thicknesses of 291 – 529 m and 416 – 560 m, respectively (Figs. 3-1 and 3-2). The Yanguan Stage comprises a 287 – 463-m-thick Lower Member of limestone and dolomitic limestone and a 4 – 66-m-thick Upper Member of marl, marly limestone, and sillcalite (Fig. 3-2). The Datang Stage is constituted by the 251 – 370-m-thick Shidengzi Member of chert-bearing limestone with intercalated shale and dolomitic limestone, the 19 – 44-m-thick Ceshui Member of shale with intercalated marl, and the ca. 146-m-thick Zimenqiao Member of limestone with intercalated dolomitic limestone (Fig. 3-2). The Upper Carboniferous strata, i.e., the Hutian Group, consists of dolostone with a thickness larger than 170 m (Fig. 3-2). The Lower Permian strata, i.e., the Qixia Formation, is made up of chert-bearing limestone with a

thickness larger than 40 m (Fig. 3-2). The Upper Triassic strata overlay the Lower Permian and Carboniferous strata by an angular unconformity and are composed of conglomerate, marl, and shale with a thickness larger than 60 m (Fig. 3-2).

3.2. Structures

The structural framework of the Tongshanling-Weijia area is south-north- to southwest-northeast-trending on the whole (Fig. 3-1). The folds in this area comprise alternatively appeared anticlines and synclines which are cut through by faults (Fig. 3-1). A vast majority of the faults are thrust and strike-slip faults and several ones are normal faults. The folded and metamorphosed Ordovician strata and the angular unconformity between the Lower Devonian and Upper Ordovician strata record the Early Paleozoic intracontinental orogen in the South China Block. The Devonian and Carboniferous strata have been folded and faulted through the Triassic intracontinental compressive deformation in South China which also led to the angular unconformity of the Upper Triassic strata overlaying the folded Lower Permian and Carboniferous strata. The south-north- to southwest-northeast-trending structural framework in the Tongshanling-Weijia area was established dominantly by the Triassic tectonic event. During Middle-Late Jurassic, the Tongshanling and Weijia granitoids intruded into the folded and faulted Devonian and Carboniferous carbonate strata as stocks, dikes, apophyses, etc. (Fig. 3-1).

3.3. Magmatism

The Tongshanling granodiorite porphyry and the Weijia granite porphyry are the main magmatic rocks in the Tongshanling-Weijia area (Fig. 3-1). The Tongshanling granodiorite porphyry was emplaced as stocks with a total exposure area of 12 km^2 (Fig. 3-1). It is composed of plagioclase (ca. 45 vol%), K-feldspar (ca. 22 vol%), quartz (ca. 20 vol%), biotite (ca. 10 vol%), and amphibole (ca. 3 vol%). Some dark microgranular enclaves are found in the Tongshanling granodiorite porphyry. The Weijia granite porphyry is located 15 km to the northeast of the Tongshanling intrusion (Fig. 3-1). It was emplaced as scattered bosses, ductoliths, apophyses, and dikes with a total exposure area of 1.3 km^2 (Fig. 3-1). The Weijia

granite porphyry consists of K-feldspar (ca. 37 vol.%), quartz (ca. 35 vol.%), albite (ca. 25 vol.%), and minor muscovite (ca. 2 vol.%) and biotite (ca. 1 vol.%). Dark microgranular enclaves are absent in the Weijia granite porphyry. There are some other granite porphyry swarms, i.e., the Tongshanling granite porphyry, appearing in the northeastern part of the Tongshanling intrusion (Fig. 3-1) and cutting the Tongshanling granodiorite porphyry and related skarn. This kind of granite porphyry is petrographically different from the Weijia granite porphyry with a distinctly finer grain size. Its phenocrysts are composed of plagioclase (ca. 35 vol%), K-feldspar (ca. 30 vol%), quartz (ca. 30 vol%), and biotite (ca. 5 vol%). Some mafic rocks also occur in this area and its adjacent area. They are the Huziyan high-Mg basalt in Daoxian County (ca. 150 Ma; Li et al., 2004) and the Huilongxu lamprophyre in Jiangyong County (ca. 170Ma; Wang et al., 2003b) (Fig. 3-1).

3.4. Mineralization

The polymetallic mineralization in the Tongshanling-Weijia area contains Cu-Pb-Zn and W mineralization associated with the Tongshanling granodiorite porphyry and the Weijia granite porphyry, respectively (Fig. 3-1). The Tongshanling Cu-Pb-Zn deposit, Jiangyong Pb-Zn-Ag deposit, and Yulong Mo deposit, which are distributed around the Tongshanling granodioritic intrusion, constitute the Tongshanling Cu-Mo-Pb-Zn-Ag ore district (Fig. 3-1). The Tongshanling polymetallic ore district is one of the oldest mines in the Nanling Range. The ore-bearing horizons of these mineral deposits are the Middle Devonian Qiziqiao Formation, the Upper Devonian Shetianqiao Formation and Xikuangshan Formation, and the Shidengzi Member of the Upper Carboniferous Datang Stage (Fig. 3-2). The mineralization types of these mineral deposits include skarn, sulfide-quartz vein, and carbonate replacement with the Tongshanling Cu-Pb-Zn deposit dominated by skarn and sulfide-quartz vein mineralization, the Jiangyong Pb-Zn-Ag deposit dominated by carbonate replacement mineralization, and the Yulong Mo deposit dominated by skarn mineralization (Fig. 3-2). The Weijia W deposit is a recently discovered super-large scheelite skarn deposit in the Nanling Range. It is distributed in the contact zone between the Weijia granite porphyry and wall rocks (Fig. 3-1) and is mainly composed of magnesian and calcic skarn W orebodies, which

appear in the Middle Member (dolostone) and Upper Member (limestone) of the Qiziqiao Formation, respectively (Fig. 3-2). The Weijia scheelite skarn deposit is a special case that is characterized by large-scale magnesian skarn mineralization and is significantly different from the other scheelite skarn deposits in the Nanling Range and also around the world which are mostly dominated by calcic skarn mineralization.

Chapter 4. Different origins of the Cu-Pb-Zn-bearing and W-bearing granitoids

4.1. Introduction

The Nanling Range of South China is world famous for its widely developed multiple-aged granitic magmatism (Early Paleozoic, Triassic, Jurassic, and Cretaceous) and related polymetallic mineralization (W, Sn, Nb, Ta, Cu, Pb, Zn, etc.) (Fig. 1-1) and thus has been of interest to geologists for a long time. Relative to Early Paleozoic, Triassic, and Cretaceous granitoids, Jurassic granitoids and related mineral deposits are the most important in the Nanling Range (Chen et al., 2013; Li et al., 2013; Mao et al., 2013a). According to the association of ore-forming elements, petrographic and geochemical characteristics, the Jurassic ore-bearing granitoids in the Nanling Range can be divided into four different types: W-bearing, Sn-bearing, Nb-Ta-bearing, and Cu-Pb-Zn-bearing. The W-bearing granites are dominated by crust-derived S-type two-mica, muscovite, and biotite granites (Chen et al., 2013). The Sn mineralization is mainly associated with aluminous A-type (A_2-type) granites (Jiang et al., 2008; Zhu et al, 2008; Chen et al., 2013). The Nb-Ta-bearing granites are mostly highly fractionated albite granites (Chen et al., 2008). The Cu-Pb-Zn mineralization is predominantly related to amphibole-bearing metaluminous calc-alkaline granodiorites (Wang et al., 2003a; Li et al., 2013). Various kinds of granitoids have distinct diversities in terms of metallogenic specialization. A comparative study of different types of ore-bearing granitoids will not only improve the understanding of the mechanism that controls metallogenic specialization, but also has important implications for prospecting and exploration.

The Middle-Late Jurassic Cu-Pb-Zn-bearing and W-bearing granitoids in the Nanling Range are obviously different in terms of their petrography and geochemistry. However, the mechanism that created these differences is still not well understood. Numerous studies have been conducted on these two types of ore-bearing granitoids. The W-bearing granites are considered to be products of the partial melting of an old metasedimentary basement (Zhang, 2004; Chen et al., 2013; Dong et al., 2014; Zhang, 2014), however, the petrogenesis of the

Cu-Pb-Zn-bearing granitoids is still controversial. Wang et al. (2003a) held an opinion that the diorites-granodiorites in southeastern Hunan Province mainly originated from basaltic rocks from depleted mantle and were contaminated by some old crustal materials. Another opinion proposed by Jiang et al. (2009) based on the Tongshanling granodiorite is that this type of granitoid was produced by the mixing of dominant melts from the partial melting of metasedimentary basement and some mantle-derived basaltic magmas. Yang et al. (2016) considered that the Shuikoushan granodiorite originated from amphibole-dehydration melting of mafic rocks in the middle-lower crust. Although the Jurassic Cu-Pb-Zn-bearing and W-bearing granitoids in the Nanling Range were both predominantly formed during the Middle-Late Jurassic (165 – 150 Ma), the W-bearing granites (ca. 155 Ma) were formed slightly later than the Cu-Pb-Zn-bearing granitoids (ca. 160 Ma). The cause of this time gap requires further investigation. Whether or not these two types of ore-bearing granitoids are products of the same original magma in different fractionation stages is also unclear.

This study focused on the magmatism of the Tongshanling-Weijia area in southern Hunan Province and undertook a comparison of the Middle-Late Jurassic Cu-Pb-Zn-bearing granitoids (Shuikoushan, Baoshan, Huangshaping, Tongshanling, Dabaoshan intrusions, etc.) and W-bearing granites (Yaogangxian, Xintianling, Dengfuxian, Weijia, Xihuashan, Muziyuan, Piaotang, Dajishan intrusions, etc.) in the Nanling Range. Based on a summary of the main features and differences of the two different types of ore-bearing granitoids, a petrogenetic model has been proposed.

4.2. Petrography of granitoids

4.2.1. Tongshanling granodiorite porphyry

The Tongshanling granodiorite is porphyritic and has a medium-fine granitic texture (Fig. 4-1a–c). Phenocrysts are generally 1 – 5cm in size and locally some plagioclase megacrysts can be greater than 10 cm. Rock-forming minerals are dominated by plagioclase (45 vol.%), K-feldspar (22 vol.%), quartz (20 vol.%), biotite (10 vol.%), and amphibole (3 vol.%). Accessory minerals include mainly apatite, zircon, titanite, allanite, rutile, sulfides, and Fe-Ti oxide minerals. The Fe-Ti oxide minerals are mainly magnetites. Plagioclases with An%

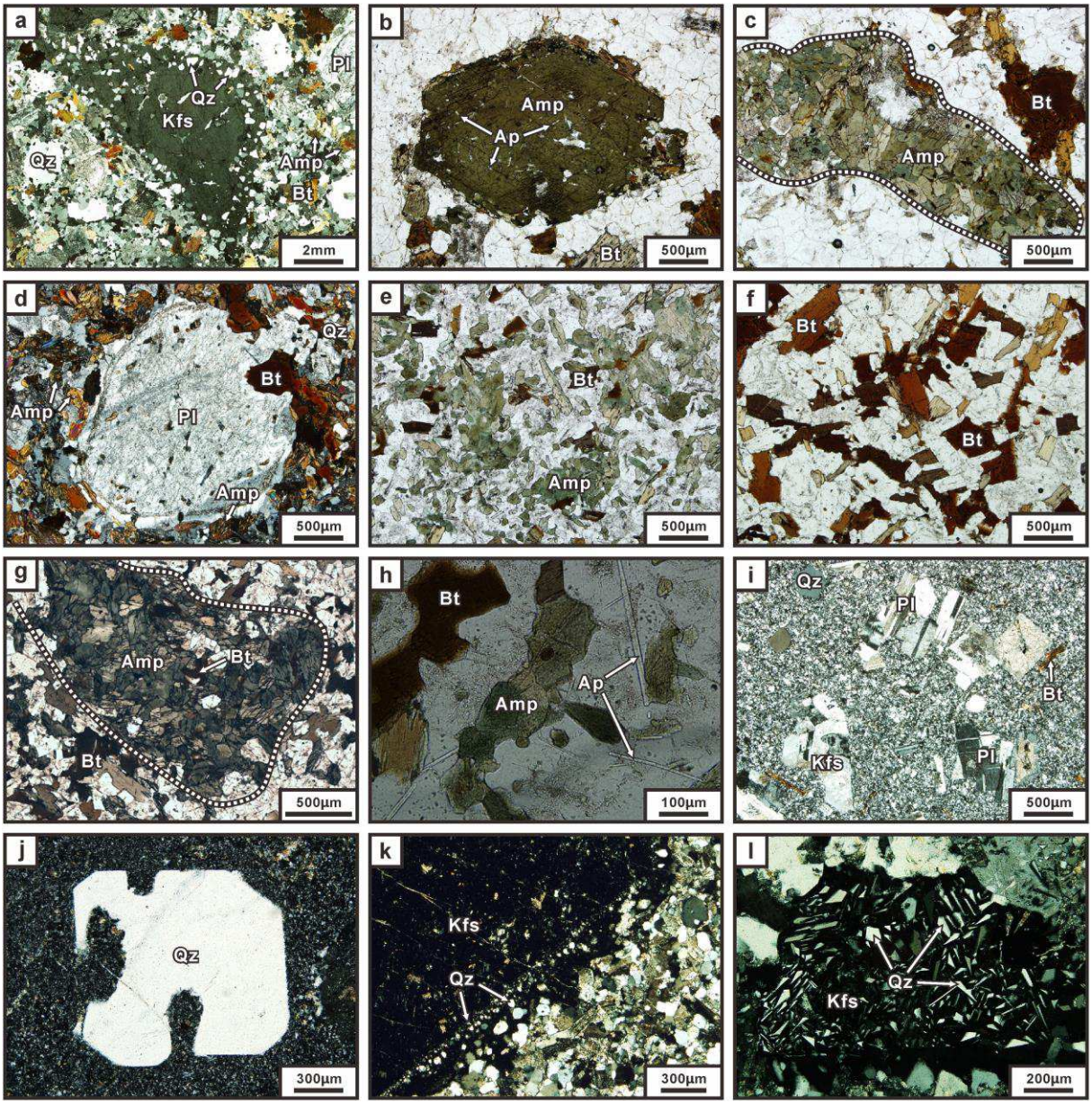

Figure 4-1. Petrographic photomicrographs of granitoids from the Tongshanling-Weijia area. (a–c) Tongshanling granodiorite porphyry; (d–h) Dioritic dark enclaves; (i) Tongshanling granite porphyry; (j–l) Weijia granite porphyry. (a) "Pearlitic margin" texture of` K-feldspar phenocryst, the size of microgranular quartz grains is 200 – 500 μm, crossed-polarized light. (b) Single-grained amphibole with short prismatic apatite inclusions, plane-polarized light. (c) Amphibole-rich clot, plane-polarized light. (d) Reaction rim of plagioclase phenocryst, crossed-polarized light. (e) Amphibole as the predominant dark mineral, plane-polarized light. (f) Biotite as the predominant dark mineral, plane-polarized light. (g) Amphibole-rich clot, plane-polarized light. (h) Needle-like or elongated prismatic apatites, plane-polarized light. (i) Porphyritic texture, the matrix has a felsitic texture, crossed-polarized light. (j) Hexagonal bipyramidal quartz phenocryst with resorption texture, crossed-polarized

light. (k) “Pearlitic margin” texture of K-feldspar phenocryst, the size of microgranular quartz grains is 10 – 100 μm, and increases from inside to outside, crossed-polarized light. (l) Micrographic texture, crossed-polarized light. Mineral abbreviations: Qz = quartz, Kfs = K-feldspar, Pl = plagioclase, Amp = amphibole, Bt = biotite, Ap = apatite.

values of 21 – 48 commonly have a zonal texture and sericitized calcium-rich cores. Some K-feldspar phenocrysts have a “pearlitic margin” texture, which is made up of 200 – 500 μm quartz grains (Fig. 4-1a). Biotites are brown and generally contain mineral inclusions of apatite and zircon. Amphiboles are green hornblendes and generally contain apatite inclusions (Fig. 4-1b). Locally, amphibole-rich clots appear (Fig. 4-1c). Apatites have short prismatic shapes. Magnetite is sometimes associated with allanite (Fig. 4-2a), and in some cases occurs as inclusions in allanite and biotite (Fig. 4-2b and c). Magnetite in biotite occasionally has pyrite inclusions (Fig. 4-2c).

4.2.2. Dioritic dark enclaves

Dioritic dark enclaves are commonly observed in the Tongshanling granodiorite porphyry. They are mostly ellipsoidal and several to dozens of centimeters in size. There is no quenched boundary between the enclaves and their host rocks. The enclaves have a fine granular texture and occasionally contain plagioclase phenocryst, which generally has a reaction rim (Fig. 4-1d). The mineral assemblage of the enclaves is the same as the host granodiorite porphyry, but the abundance of mafic minerals in the enclaves can reach 50 vol%. The ratios of amphibole to biotite in the enclaves are quite variable. In most cases amphiboles are more than biotites (Fig. 4-1e), except for a few enclaves in which mafic minerals are dominated by biotites (Fig. 4-1f). Amphibole-rich clots (Fig. 4-1g) are common in the dark enclaves. Plagioclases have a zonal texture, An% values of 22 – 45, and mostly show sericitized calcium-rich cores. Apatites have a needle-like or elongated prismatic shape (Fig. 4-1h).

4.2.3. Tongshanling granite porphyry

The Tongshanling granite porphyry has a porphyritic texture (Fig. 4-1i) and phenocrysts

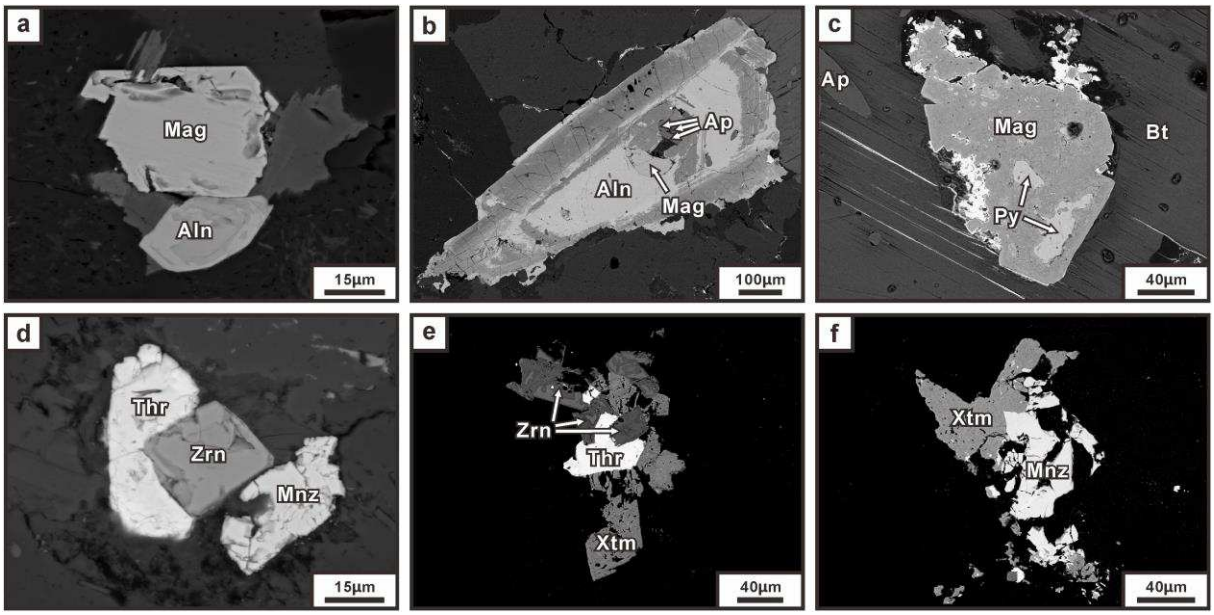

Figure 4-2. Backscattered electron (BSE) images of accessory minerals in the Tongshanling granodiorite porphyry and Weijia granite porphyry. (a–c) Tongshanling granodiorite porphyry; (d–f) Weijia granite porphyry. (a) Intergrowth of magnetite and allanite. (b) Magnetite and apatite inclusions in allanite. (c) Pyrite inclusions of magnetite in biotite. (d) Intergrowth of zircon, thorite, and monazite. (e) Intergrowth of zircon, thorite, and xenotime. (f) Intergrowth of monazite and xenotime. Mineral abbreviations: Mag = magnetite, Aln = allanite, Ap = apatite, Py = pyrite, Bt = biotite, Zrn = zircon, Thr = thorite, Mnz = monazite, Xtm = xenotime.

are mainly 0.2 – 3 mm sized plagioclase (35 vol%), K-feldspar (30 vol%), quartz (30 vol%), and biotite (5 vol%). The matrix exhibits a fine-granular to felsitic texture (Fig. 4-1i). Accessory minerals include mainly zircon and apatite. An embayed resorption texture is common for quartz phenocrysts. Biotites are brown and generally contain apatite inclusions.

4.2.4. Weijia granite porphyry

The Weijia granite porphyry is light red or off-white in outcrops at the surface and has a porphyritic texture. Phenocrysts are 30 – 50 vol% in content and are comprised of quartz, K-feldspar, albite, and minor biotite. The phenocryst granularity is 0.5 – 5 mm except for a few phenocrysts larger than 1 cm. The matrix has a fine granular to felsitic texture (Fig. 4-1j and k) and contains a few muscovites. Quartz phenocrysts generally have a hexagonal bipyramidal shape and resorption texture (Fig. 4-1j). In the rim of some K-feldspar phenocrysts, microgranular quartz grains, with a grain size of 10 – 100 μm, constitute a

"Pearlitic margin" texture (Fig. 4-1k), and the size of these quartz grains increases from inside to outside. A micrographic texture (Fig. 4-1l) can be found in K-feldspars. Accessory minerals include zircon, thorite, xenotime, monazite (Fig. 4-2d–f), niobite, samarskite, fergusonite, scheelite, parisite, and ilmenite.

4.3. Sampling and analytical methods

The samples of the Tongshanling granodiorite porphyry and its dioritic dark enclaves, the Tongshanling and Weijia granite porphyries were collected from outcrops at the surface and in the adits of mines.

Zircons were extracted by standard density and magnetic separation techniques. Intact and transparent zircon grains were handpicked under a binocular microscope, then mounted in an epoxy resin disc and polished. Cathodoluminescence (CL) image was obtained using a JEOL JSM-6510 scanning electron microscope equipped with a Gatan Mini-CL detector at the Beijing GeoAnalysis Co. Ltd. Whole-rock trace and rare earth element (REE), Sr-Nd isotope, and zircon U-Pb and Hf isotope analyses were performed at the State Key Laboratory for Mineral Deposits Research, Nanjing University.

The U-Pb isotope of zircons was determined by an Agilent 7500a ICP-MS equipped with a New Wave UP213 laser sampler. Analysis was performed with a beam diameter of 25 μm, 5 Hz repetition rate, energy of 10-20 J/cm^2, acquisition time of 60 s, and background measurement of 40 s. Zircon Lu-Hf isotope was analyzed using a Neptune Plus MC-ICP-MS attached to a New Wave UP193FX laser ablation system. Analysis was performed with a beam diameter of 35 μm, 10 Hz repetition rate, acquisition time of 60 s, and acquisition number of 200 times. The detailed analytical procedures and data processing methods followed Zhang et al. (2014).

Whole-rock powder was dissolved in Teflon vessel using a HF+HNO_3 mixture for trace element, rare earth element and Sr-Nd isotope analyses. Trace and rare earth elements were determined by a Finnigan MAT Element II HR-ICP-MS. The analytical conditions and procedure followed Gao et al. (2003). The analytical precision for most elements was better than 5 %. A cation-exchange resin was used to separate and purify Sr and Nd using the

method described by Pu et al. (2005). The Sr and Nd isotopic ratios were determined by a Neptune Plus MC-ICP-MS. The parameters for mass fractionation correction and data processing were the same as those described by Xie et al. (2013) and Zhang et al. (2014).

Whole-rock major element compositions were measured using a wet chemical method at the Analysis Center of No. 230 Research Institute of the China National Nuclear Corporation, Changsha. The analytical precision for all elements was better than 5 %. The detailed procedures are described in the China National Standards GB/T 14506.3-2010 – GB/T 14506.14-2010.

4.4. Results

4.4.1. Zircon U-Pb age

Zircons of granitoids from the Tongshanling-Weijia area are mainly colorless and transparent through to light brown and subtransparent, and euhedral to subhedral prismatic grains with pyramidal termination, and exhibit well-developed growth zoning in CL images (Fig. 4-3). The analytical results of zircon U-Pb isotopes are listed in Appendix 4-1. Magmatic zircons from the Tongshanling granodiorite porphyry have a weighted mean $^{206}Pb/^{238}U$ age of 162.5 ± 1.0 Ma (Fig. 4-4a), representing its crystallization age. Magmatic zircons in the dioritic dark enclaves generally consist of cores with a bright CL image and rims with a dark CL image. The rims have higher Th and U contents than the cores and both have the same $^{206}Pb/^{238}U$ ages (Fig. 4-3b), giving a weighted mean value of 160.6 ± 1.4 Ma (Fig. 4-4b). The weighted mean $^{206}Pb/^{238}U$ age of the Tongshanling granite porphyry is 158.8 ± 1.2 Ma (Fig. 4-4c), which is slightly younger than the granodiorite porphyry. There are two kinds of zircons in the Weijia granite porphyry. One has a bright CL image (Fig. 4-3d) and good transparency without cracks, while the other has a dark CL image (Fig. 4-3d) and is subtransparent with cracks. Metamictization happened in zircons with a dark CL image. Therefore, in this study zircons with a bright CL image were selected for dating. Their $^{206}Pb/^{238}U$ ages vary from 157 Ma to 160 Ma and yield a weighted mean value of 158.3 ± 2.2 Ma (Fig. 4-4d). Old inherited cores are common in magmatic zircons of the granitoids from this study area. Inherited cores usually have a rounded shape (Fig. 4-3) and their $^{206}Pb/^{238}U$

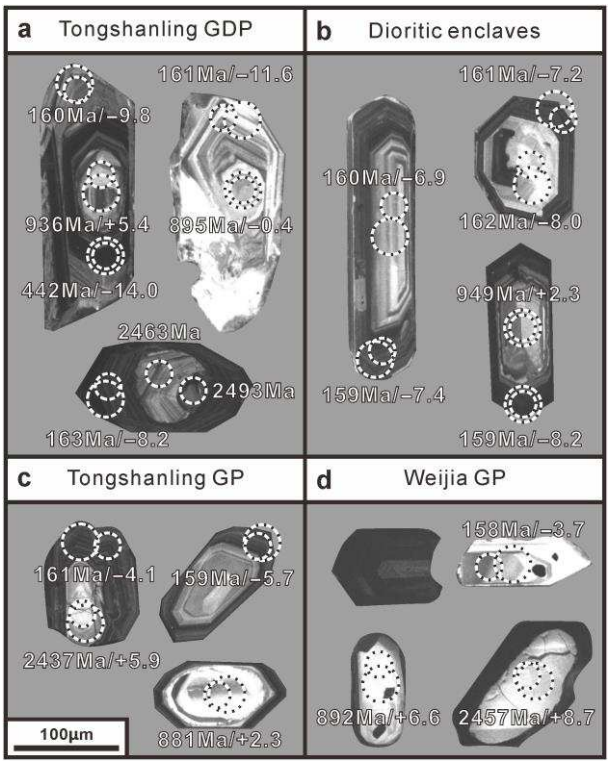

Figure 4-3. Zircon CL images of granitoids from the Tongshanling-Weijia area. GDP: granodiorite porphyry; GP: granite porphyry. The smaller and larger circles represent the analytical spots of U-Pb and Hf isotope, respectively, and the numbers are U-Pb age and ε_{Hf} (t) value.

ages are concentrated in range of 800 – 1200 Ma and 2350 – 2500 Ma (Appendix 4-1).

4.4.2. Zircon Hf isotope

The analytical results of zircon Hf isotope are listed in Appendix 4-2. The Tongshanling granodiorite porphyry and its dioritic dark enclaves have consistent zircon ε_{Hf} (t) values (–11.6 – –6.3 and –9.3 – –6.9, respectively) and Hf model ages (1.60 – 1.94 Ga and 1.64 – 1.79 Ga, respectively) (Fig. 4-5a–d). The Tongshanling granite porphyry has a larger variation of zircon ε_{Hf} (t) and T_{DM}^{C} (Hf) values (–16.1 – –0.2 and 1.22 – 2.22 Ga, respectively) (Fig. 4-5e and f). The values of zircon ε_{Hf} (t) and T_{DM}^{C} (Hf) of the Weijia granite porphyry change in range of –4.6 – –1.7 and 1.31 – 1.50 Ga (Fig. 4-5g and h), respectively. The 800 – 1200 Ma inherited zircon cores mainly have ε_{Hf} (t) values of –0.4 – +6.9 (mostly above +2.3) and T_{DM}^{C} (Hf) values of 1.18 – 1.55 Ga. The 2350 – 2500 Ma inherited zircon cores have ε_{Hf} (t) values of +5.9 – +8.7 and T_{DM}^{C} (Hf) values of 2.44 – 2.53 Ga.

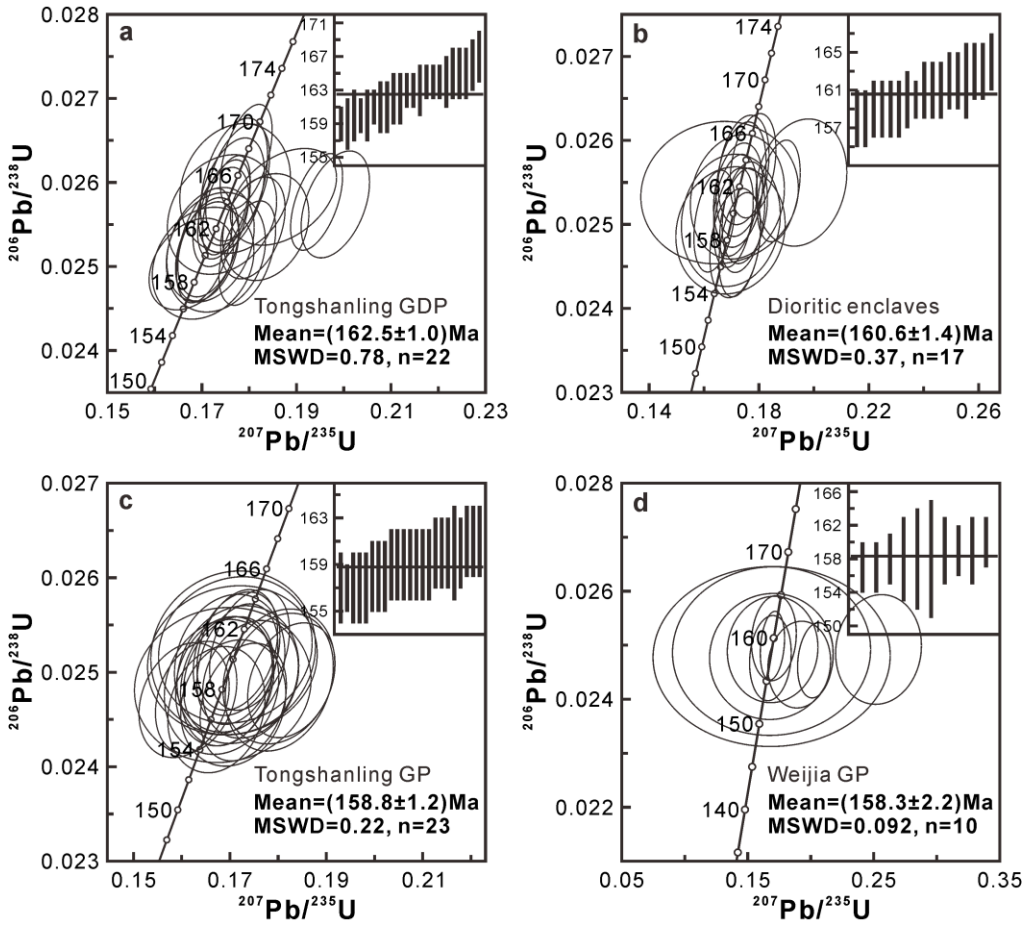

Figure 4-4. Zircon $^{206}Pb/^{238}U$-$^{207}Pb/^{235}U$ concordia diagrams of granitoids from the Tongshanling-Weijia area. GDP: granodiorite porphyry; GP: granite porphyry.

4.4.3. Whole-rock major elements

The analytical results of whole-rock major element, trace and rare earth element and Sr-Nd isotopic compositions of granitoids from the Tongshanling-Weijia area are listed in Appendix 4-3 and the main geochemical features are shown in Table 4-1. In the TAS diagram (Fig. 4-6a), the Tongshanling granodiorite porphyry samples are plotted in the granodiorite field, the dark enclaves mainly in the monzodiorite to diorite fields, and the Tongshanling and Weijia granite porphyries in the granite field. The Tongshanling granodiorite porphyry and its dioritic dark enclaves are metaluminous calc-alkaline rocks and the Tongshanling and Weijia granite porphyries are peraluminous alkaline granites (Fig. 4-6b and c). In the ACF diagram (Fig. 4-6d), the Tongshanling granodiorite porphyry and its dark enclaves are plotted in the

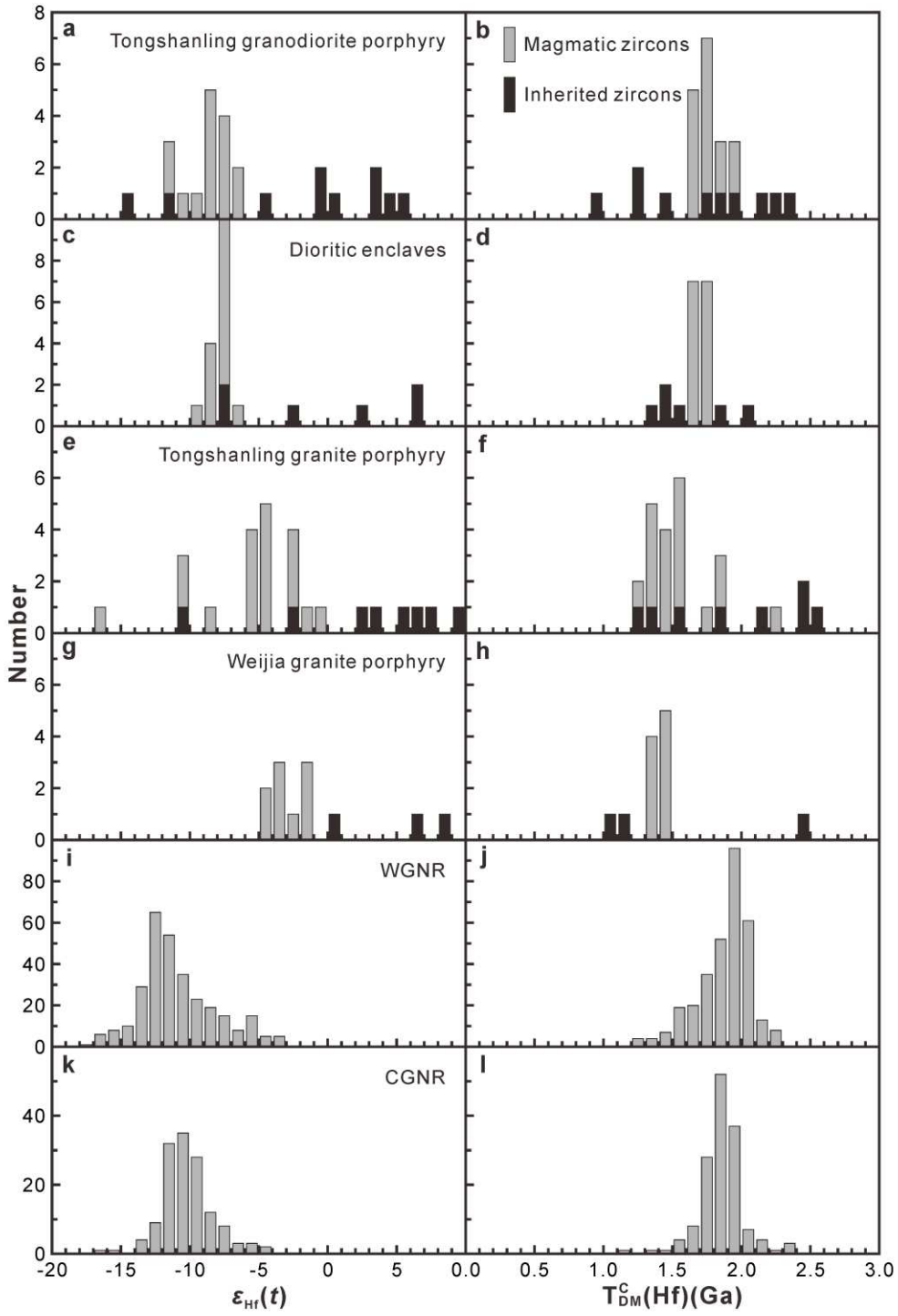

Figure 4-5. Histograms for zircon ε_{Hf} (t) and T^{C}_{DM} (Hf) (Ga) values of granitoids from the Tongshanling-Weijia area. The zircon Hf isotopic data of the Middle-Late Jurassic Cu-Pb-Zn-bearing granitoids in the Nanling Range (CGNR) are from Xie et al. (2013), Zuo et al. (2014), Zhao et al. (2016b), and unpublished data from our research group; the zircon Hf isotopic data of the Late Jurassic W-bearing granites in the Nanling Range (WGNR) are from Chen et al. (2013).

Table 4-1. Main geochemical features of granitoids from the Tongshanling-Weijia area

Geochemical indexes	Tongshanling granodiorite porphyry	Dioritic dark enclaves	Tongshanling granite porphyry	Weijia granite porphyry
SiO_2 (wt.%)	63.71 – 70.09	53.38 – 59.35	71.35 – 74.34	73.86 – 76.73
$CaO/(Na_2O+K_2O)$	0.32 – 0.60	0.70 – 1.22	0.09 – 0.31	0.01 – 0.09
Mg/(Mg+Fe)	0.42 – 0.48	0.42 – 0.47	0.31 – 0.41	0.04 – 0.32
ASI[a]	0.91 – 1.03	0.83 – 0.94	0.97 – 1.17	1.00 – 1.18
DI[b]	68 – 80	42 – 58	83 – 90	94 – 97
Rb/Sr	0.5 – 1.3	0.5 – 0.9	0.5 – 1.2	10.3 – 21.6
Zr/Hf	30.6 – 34.5	28.8 – 32.9	27.4 – 32.8	14.0 – 16.9
δEu[c]	0.64 – 0.97	0.37 – 0.73	0.73 – 0.83	0.03 – 0.05
ΣREE (ppm)	82 – 111	107 – 202	124 – 158	55 – 100
LREE/HREE	6.0 – 7.7	2.9 – 7.3	13.4 – 15.9	1.8 – 3.4
HFSE[d] (ppm)	184 – 241	219 – 275	228 – 261	142 – 179
T_{Zr}[e] (°C)	747 – 770	702 – 764	763 – 784	718 – 741
$(^{87}Sr/^{86}Sr)_i$	0.708955 – 0.710682	0.710023 – 0.711200	0.707011 – 0.708124	
ε_{Nd} (t) value	–6.9 – –4.2	–6.7 – –5.2	–2.8 – –2.1	–5.4 – –4.5
T^C_{DM} (Nd) (Ga)	1.29 – 1.51	1.38 – 1.49	1.12 – 1.18	1.32 – 1.39
Zircon ε_{Hf} (t) value	–11.6 – –6.3	–9.3 – –6.9	–16.1 – –0.2	–4.6 – –1.7
Zircon T^C_{DM} (Hf) (Ga)	1.60 – 1.94	1.64 – 1.79	1.22 – 2.22	1.31 – 1.50

Notes: [a] ASI: aluminum saturation index, $n(Al_2O_3)/n(CaO+Na_2O+K_2O)$. [b] DI: differentiation index, the sum of CIPW normative minerals Q, Or, Ab, Ne, Lc, and Kp. [c] $\delta Eu = 2Eu_N/(Sm_N+Gd_N)$. [d] HFSE: high field strength elements (Zr+Nb+Ce+Y). [e] T_{Zr}: zircon saturation temperature, calculated by the method of Miller et al. (2003).

I-type granite field and the Tongshanling and Weijia granite porphyries are plotted in the S-type granite field.

4.4.4. Whole-rock trace and rare earth elements

The Tongshanling granodiorite porphyry has low Rb/Sr ratios, high Zr/Hf ratios, and weak Ba, Nb, P, and Ti depletions as shown in the spider diagram (Fig. 4-7a). Its REE patterns slope to the right, without obvious Eu negative anomalies (Fig. 4-7b). Compared with the granodiorite porphyry, the dioritic dark enclaves have a distinctly higher ΣREE abundance and more visible Sr and Eu depletions (Fig. 4-7c and d). The Tongshanling granite porphyry has similar Rb/Sr and Zr/Hf ratios to the Tongshanling granodiorite porphyry, and exhibits

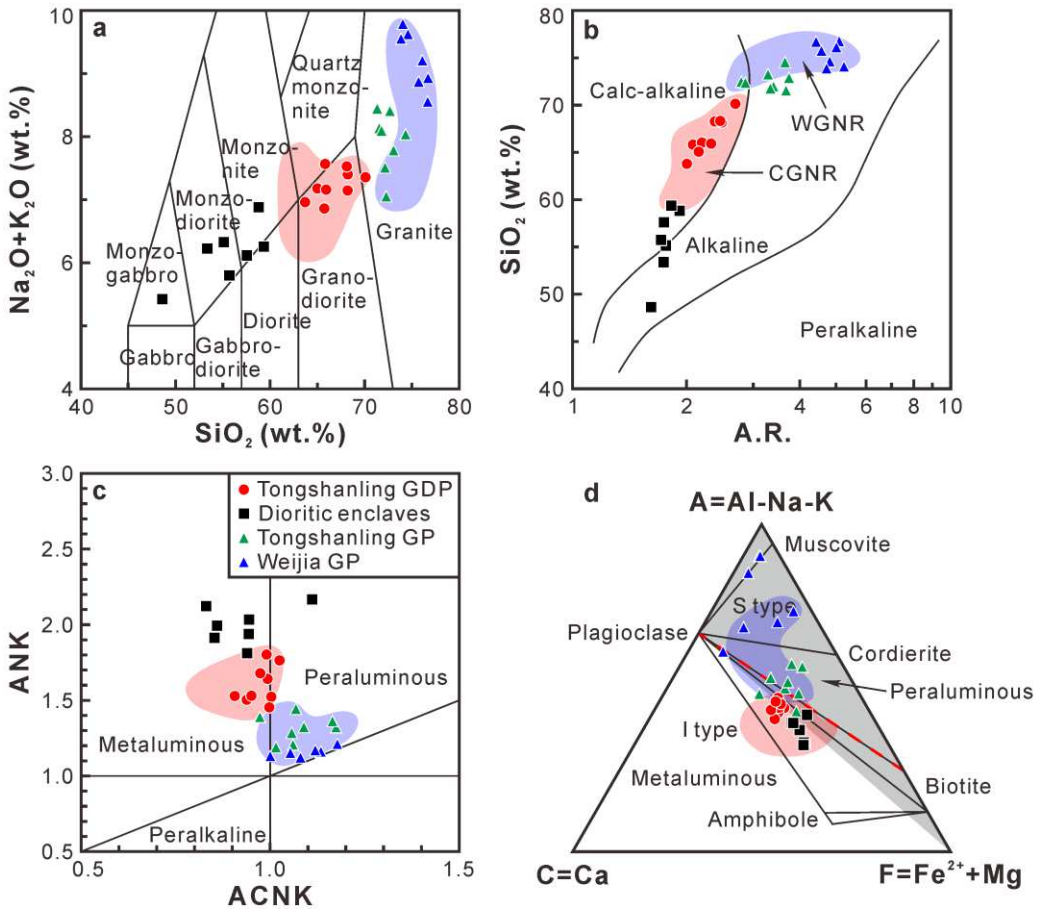

Figure 4-6. Major element diagrams of granitoids from the Tongshanling-Weijia area. (a) TAS [(Na_2O+K_2O) (wt.%)-SiO_2 (wt.%)] classification diagram, after Middlemost (1994). (b) SiO_2 (wt.%)-A.R. diagram, after Wright (1969). (c) ANK-ACNK diagram. (d) ACF diagram, after Hine et al. (1978). GDP: granodiorite porphyry; GP: granite porphyry. The whole-rock geochemical data of the Middle-Late Jurassic Cu-Pb-Zn-bearing granitoids in the Nanling Range (CGNR) are from Wang et al. (2003a), Jiang et al. (2009), Xie et al. (2013), Zuo et al. (2014), Zhao et al. (2016b), and unpublished data from our research group; the whole-rock geochemical data of the Late Jurassic W-bearing granites in the Nanling Range (WGNR) are from Zhang (2004), Zhang (2014), Zhao et al. (2016b), and unpublished data from our research group.

obvious Ba, Sr, P, and Ti depletions (Fig. 4-7e), high LREE/HREE ratios of 13.4 – 15.9, weak Eu negative anomalies (Fig. 4-7f), and high HFSE abundances. The Weijia granite porphyry is characterized by high Rb/Sr ratios, low Zr/Hf ratios, low ΣREE and HFSE abundances, strong Ba, Sr, P, and Ti depletions, obvious Nd positive anomalies (Fig. 4-7g), flat REE patterns, and strong Eu negative anomalies (Fig. 4-7h).

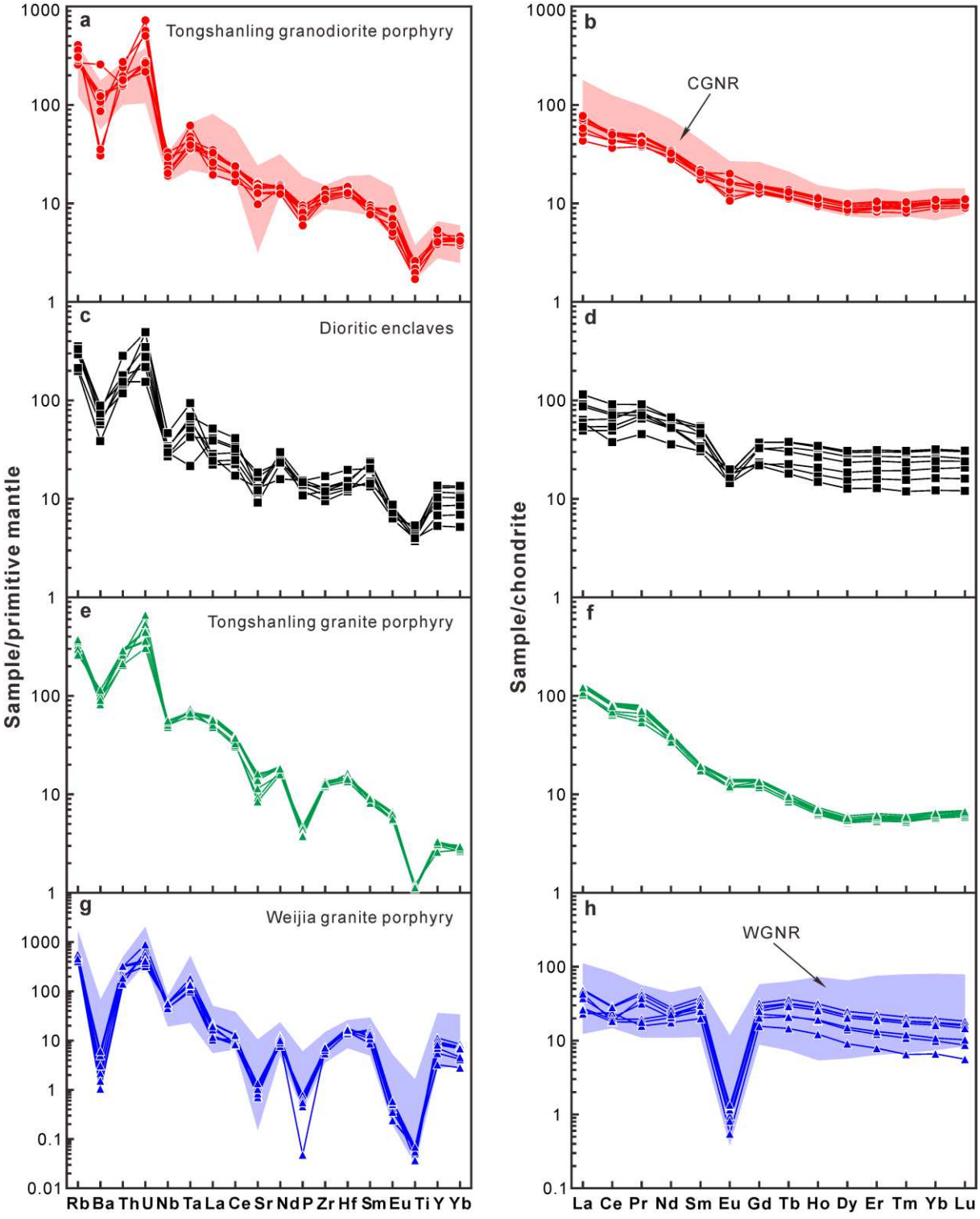

Figure 4-7. Primitive mantle-normalized (Sun and Mcdonough, 1989) spider diagrams and chondrite-normalized (Boynton, 1984) REE patterns of granitoids from the Tongshanling-Weijia area. The legends and data sources of the Middle-Late Jurassic Cu-Pb-Zn-bearing (CGNR) and W-bearing (WGNR) granitoids in the Nanling Range are the same as Figure 4-6.

4.4.5. Whole-rock Sr-Nd isotopes

The Tongshanling granodiorite porphyry and its dioritic dark enclaves have $(^{87}Sr/^{86}Sr)_i$ ratios of 0.708955 – 0.710682 and 0.710023 – 0.711200, ε_{Nd} (t) values of –6.9 – –4.2 and –6.7 – –5.2, and Nd model ages of 1.29 – 1.51 Ga and 1.38 – 1.49 Ga, respectively. The Tongshanling granite porphyry has lower $(^{87}Sr/^{86}Sr)_i$ ratios (0.707011 – 0.708124), higher ε_{Nd} (t) values (–2.8 – –2.1) (Fig. 4-8a), and younger Nd model ages (1.12 – 1.18 Ga). It is difficult to thoroughly extract Rb from the samples of the Weijia granite porphyry which have high Rb/Sr ratios. Therefore, its Sr isotopic composition has not been determined. The ε_{Nd} (t) values of the Weijia granite porphyry are –5.4 – –4.5 and are plotted above the evolution region of the Precambrian metasedimentary basement of the Nanling Range (Fig. 4-8b). Its T_{DM}^{C} (Nd) values are 1.32 – 1.39 Ga.

4.5. Discussion

4.5.1. Timing of granitoids

Wang et al. (2002b) reported a U-Pb age of 178.9 ± 1.7 Ma for the Tongshanling granodiorite porphyry by single-grain zircon dating. The SHRIMP zircon U-Pb dating results from Wei et al. (2007) and Jiang et al. (2009) are 149 ± 4 Ma and 163.6 ± 2.1 Ma, respectively. Zhao et al. (2016b) obtained three LA-ICP-MS zircon U-Pb ages of 160.7 ± 0.5 Ma, 160.5 ± 0.9 Ma and 159.7 ± 0.8 Ma. Zircon dating of the Tongshanling granodiorite porphyry and its dark enclaves in this study gives consistent U-Pb ages of 162.5 ± 1.0 Ma and 160.6 ± 1.4 Ma (Fig. 4-4a and b), respectively, which are in accordance with the ages published by Jiang et al. (2009) and Zhao et al. (2016b). The zircon U-Pb age of the Weijia granite porphyry obtained in this study is 158.3 ± 2.2 Ma (Fig. 4-4d) and is consistent with the result of 157.8 ± 0.9 Ma acquired by Zhao et al. (2016a). The Tongshanling granite porphyry has a zircon U-Pb age of 158.8 ± 1.2 Ma (Fig. 4-4c). From the above discussion, it is concluded that the Tongshanling granodiorite porphyry and both the Weijia and Tongshanling granite porphyries were formed at 160 – 164 Ma and about 158 Ma and 158.8 Ma, respectively, and that the granite porphyries are slightly younger than the granodiorite porphyry. The metallogenic ages of the Tongshanling Cu-Pb-Zn deposit and Weijia W deposit obtained by Huang and Lu (2014) and

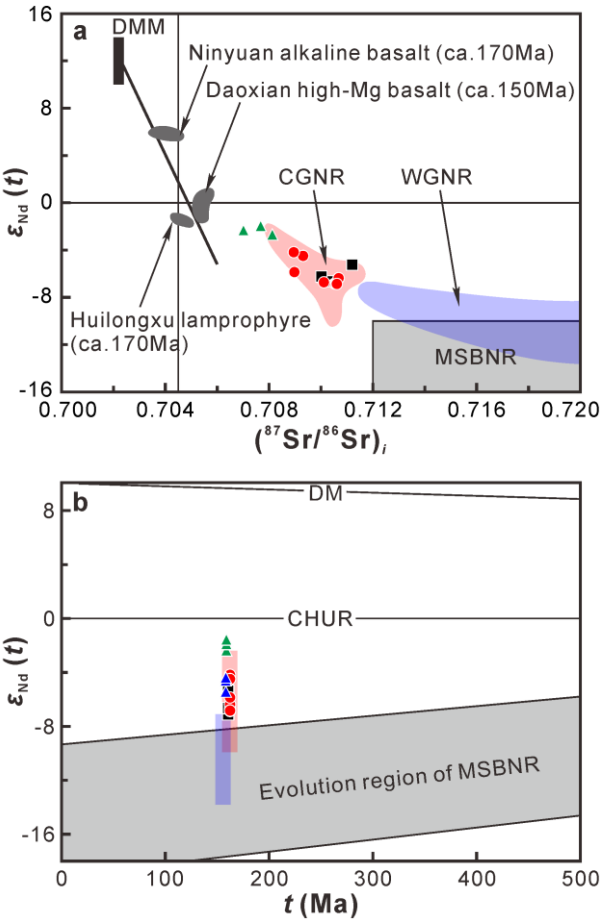

Figure 4-8. Sr-Nd isotopic compositions of granitoids from the Tongshanling-Weijia area. (a) ε_{Nd} (t)-($^{87}Sr/^{86}Sr)_i$ diagram, the Sr-Nd isotopic compositions of the Precambrian metasedimentary basement of the Nanling Range (MSBNR) are from Zhu et al. (2008) and Xie et al. (2013), the Ninyuan alkaline basalt and Daoxian high-Mg basalt are from Li et al. (2004) and Jiang et al. (2009), and the Huilongxu lamprophyre are from Wang et al. (2003b). (b) ε_{Nd} (t)-t (Ma) diagram, the Nd isotopic evolution region of the Precambrian metasedimentary basement of the Nanling Range are from Sun et al. (2005). The legends and data sources of the Middle-Late Jurassic Cu-Pb-Zn-bearing (CGNR) and W-bearing (WGNR) granitoids in the Nanling Range are the same as Figure 4-6.

Zhao et al. (2016b) by molybdenite Re-Os dating are 161.8 ± 1.7 Ma and 159.0 ± 5.6 Ma, respectively. They are consistent with zircon U-Pb ages of the Tongshanling granodiorite porphyry and Weijia granite porphyry, respectively, indicating that the Cu-Pb-Zn and W mineralization in the Tongshanling-Weijia area are closely associated with granitoids.

4.5.2. Degree of fractionation

The Tongshanling granodiorite porphyry is an amphibole-bearing metaluminous calc-alkaline granitoid, and has low differentiation indexes and Rb/Sr ratios, high CaO/(Na_2O+K_2O) ratios and δEu values (Table 4-1 and Fig. 4-9a), and weak Ba, Sr, P, and Ti depletions (Fig. 4-7a), showing a low degree of fractionation. The Weijia granite porphyry is a high-silica peraluminous alkaline granite, and has very high differentiation indexes, low CaO/(Na_2O+K_2O) ratios, high Rb/Sr ratios (Table 4-1 and Fig. 4-9a), strong Ba, Sr, P, and Ti depletions (Fig. 4-7g), and obvious Eu negative anomalies (Fig. 4-7h), indicating a higher degree of fractionation than the Tongshanling granodiorite porphyry and belonging to a highly evolved granite. The Tongshanling granite porphyry has distinctly different petrological characteristics from the Cu-Pb-Zn-bearing Tongshanling granodiorite porphyry and is a peraluminous alkaline granite. This granite porphyry has low Rb/Sr ratios, high Zr/Hf and LREE/HREE ratios (Table 4-1), and weak Eu negative anomalies (Fig. 4-7f), with an evidently lower fractionation degree than the W-bearing Weijia granite porphyry.

4.5.3. Petrogenesis

The Tongshanling granodiorite porphyry has typical crust-derived Sr-Nd-Hf isotopic signatures (Table 4-1), indicating an origin from the partial melting of crustal materials. The existence of hornblende and hornblende-rich dioritic dark enclaves, low aluminum saturation indexes and $(^{87}Sr/^{86}Sr)_i$ ratios (Table 4-1), rightward sloping REE patterns, and weak depletions of Ba, Sr, P, Ti, and Eu (Fig. 4-7a and b) exhibit the characteristics of I-type granite, and in the ACF diagram (Fig. 4-6d) the Tongshanling granodiorite porphyry is plotted in the I-type granite field. The high Mg/(Mg+Fe) ratios (0.42 – 0.48) indicate a mafic source. In the AMF-CMF diagram (Fig. 4-9c), the Tongshanling granodiorite porphyry is plotted in the field of partial melts from metabasaltic to metatonalitic sources. All these features suggest that the Tongshanling granodiorite porphyry might be derived from the partial melting of the basaltic to tonalitic mafic lower crust.

The dioritic dark enclaves have a zircon U-Pb age and Sr-Nd-Hf isotopic compositions that are consistent with the host granodiorite porphyry (Table 4-1 and Figs. 4-4, 4-5 and 4-8),

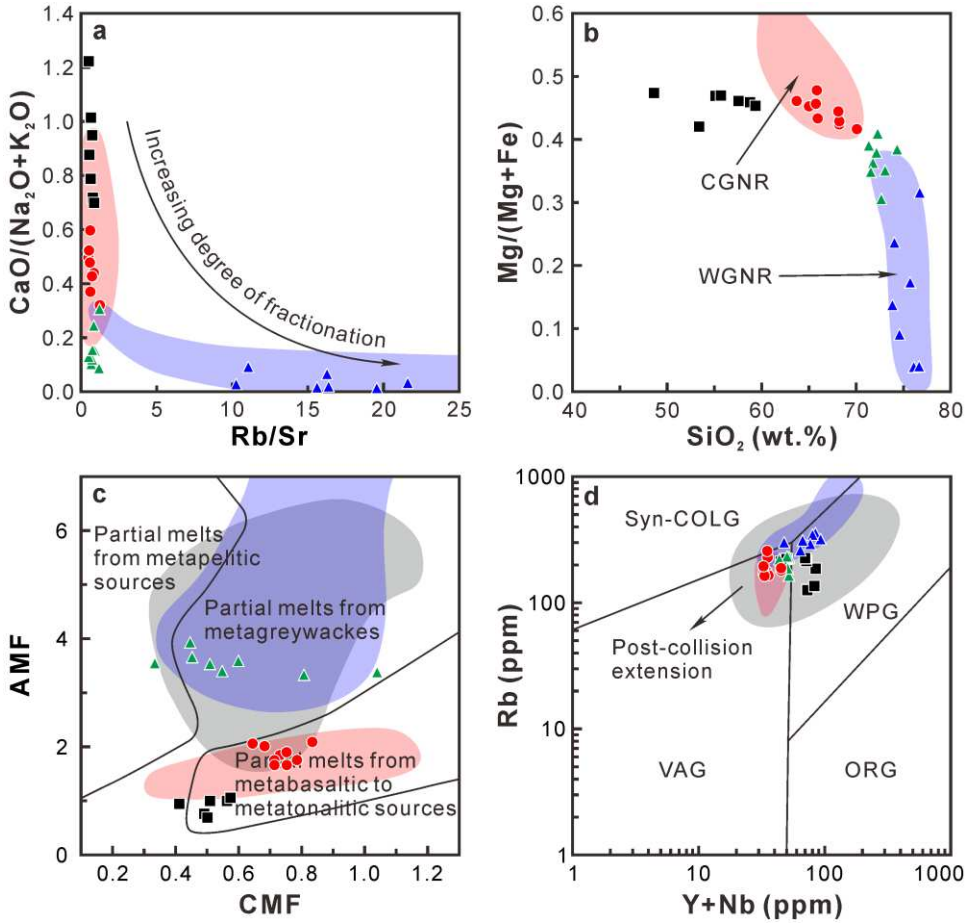

Figure 4-9. (a) $CaO/(Na_2O+K_2O)$-Rb/Sr diagram. (b) $Mg/(Mg+Fe)$-SiO_2 (wt.%) diagram. (c) AMF-CMF diagram, after Altherr et al. (2000), AMF = molar $Al_2O_3/(MgO+FeO_{Total})$, CMF = molar $CaO/(MgO+FeO_{Total})$. (d) Rb (ppm)-(Y+Nb) (ppm) diagram, after Pearce et al. (1984) and Förster et al. (1997), Syn-COLG: syn-collision granites; VAG: volcanic arc granites; WPG: within plate granites; ORG: ocean ridge granites. The legends and data sources of the Middle-Late Jurassic Cu-Pb-Zn-bearing (CGNR) and W-bearing (WGNR) granitoids in the Nanling Range are the same as Figure 4-6.

indicating they have the same source. The aggregated amphiboles in the dark enclaves and granodiorite porphyry (Fig. 4-1c and g) generally contain actinolitic cores (Al_2O_3: 2.5 – 3.7 wt.%) and hornblende rims (Al_2O_3: 4.7 – 8.9 wt.%). This phenomenon is common in calc-alkaline granodiorites and their dark enclaves, and was considered to be the result of a reaction between unmelted residual pyroxenes and melts based on studies of mineral chemistry, REE and isotopes (Castro and Stephens, 1992; Sial et al., 1998; Stephens, 2001; Martin, 2007). Because the plagioclase crystallized from dioritic and granodioritic magmas is

generally andesine to oligoclase, the calcium-rich cores (An% > 70) of plagioclase from the dark enclaves and granodiorite porphyry might be the residue from source going through partial melting. The reaction rim of plagioclase phenocrysts from the enclaves (Fig. 4-1d) implies that these phenocrysts originated from the host magmas and that there is mass exchange between the enclaves and host magmas. CL images of magmatic zircons from the enclaves show the texture of dark rim and bright core (Fig. 4-3b). Relative to the bright core, the dark rim has higher Th and U concentrations (ThO_2+UO_2 contents of rim and core: 0.12 – 0.32 wt.% and 0.04 – 0.21 wt.%, respectively), and lower Zr/Hf ratios (rim: 74 – 86, core: 86 – 110), which are similar to those of the magmatic zircons from the host granodiorite porphyry (ThO_2+UO_2 contents: 0.01 – 0.44 wt.%, Zr/Hf ratios: 68 – 94), also indicating a mass exchange between the enclaves and host magmas. Therefore, it is very likely that the dioritic dark enclaves are reaction products of the restites from source after partial melting and granodioritic magmas.

Both the Tongshanling and Weijia granite porphyries were formed slightly later than the Tongshanling granodiorite porphyry (Fig. 4-4c and d), and have similar Nd and zircon Hf isotopic compositions with crust-derived signatures (Table 4-1 and Figs. 4-5 and 4-8). These granite porphyries are peraluminous alkaline granites and are plotted in the S-type granite field of the ACF diagram (Fig. 4-6d). In the AMF-CMF diagram (Fig. 4-9c), the Tongshanling granite porphyry is plotted in the field of partial melts from metagreywackes. The Weijia granite porphyry does not fall into the diagram due to its high degree of fractionation (AMF: 11.88 – 69.08, CMF: 0.23 – 3.14). Its low Mg/(Mg+Fe) ratios (0.04 – 0.32) indicate that it might be product of the partial melting of metasedimentary rocks. Its spider diagram and REE patterns are similar to those of the typical S-type W-bearing Yaogangxian granite in the Nanling Range (Dong et al., 2014). Thus, both the Tongshanling and Weijia granite porphyries are S-type granite. They might be derived from the partial melting of metasedimentary rocks in the upper-middle crust. The Weijia granite porphyry went through a high degree of differentiation, whereas the Tongshanling granite porphyry is a weakly fractionated granite.

4.5.4. Sources of the Cu-Pb-Zn-bearing and W-bearing granitoids

The main features of the Middle-Late Jurassic Cu-Pb-Zn-bearing and W-bearing granitoids in the Nanling Range are summarized in Table 4-2. The Cu-Pb-Zn-bearing granitoids were mainly formed at 155.2 – 167.0 Ma, with a peak value of 160.6 Ma, and the W-bearing granites were predominantly formed at 151.1 – 161.8 Ma, with a peak value of 155.5 Ma (Appendix 4-4 and Fig. 4-10). Overall, these two different types of ore-bearing granitoids were formed in the Middle-Late Jurassic, however, the W-bearing granites were formed about 5 Ma later than the Cu-Pb-Zn-bearing granitoids. The Cu-Pb-Zn-bearing granitoids are mostly metaluminous calc-alkaline amphibole-bearing granodiorites, with low degrees of fractionation (Wang, 2010; Xie et al., 2013; Yang et al., 2016). The W-bearing granites are peraluminous alkaline granites and are highly differentiated (Chen et al., 2008; Dong et al., 2014) (Figs. 4-6, 4-7 and 4-9a).

The Middle-Late Jurassic Cu-Pb-Zn-bearing and W-bearing granitoids in the Nanling Range have $(^{87}Sr/^{86}Sr)_i$ ratios of 0.708 – 0.712 and > 0.712, ε_{Nd} (t) values of –10 – –2 (peak value: –7 – –6) and –14 – –7 (peak value: –10 – –9), and zircon ε_{Hf} (t) values of –13 – –7 (peak value: –11 – –10) and –14 – –8 (peak value: –13 – –12), respectively, indicating that they were both derived from the partial melting of continental crust.

The Middle-Late Jurassic Cu-Pb-Zn-bearing granitoids in the Nanling Range have the features of I-type granites. They are plotted in the I-type granite field of the ACF diagram (Fig. 4-6d) and are plotted in the field of partial melts from metabasaltic to metatonalitic sources in the AMF-CMF diagram (Fig. 4-9c). These granitoids have high Mg/(Mg+Fe) ratios (Fig. 4-9b). All these features show that they were derived from the partial melting of mafic rocks. This type of ore-bearing granitoids has an average zircon saturation temperature of 750 °C (Table 4-2), which is distinctly lower than the formation temperature (840 – 1139 °C) of the granulitic mafic xenoliths in the Daoxian basalt (Kong et al., 2000; Dai et al., 2008), indicating that the source of this type of granitoids is not a granulitic basement. According to the experimental study of Beard and Lofgren (1991), dehydration melting of amphibolites would generate water-unsaturated weakly peraluminous to metaluminous granodioritic melts, with residual plagioclase and pyroxene, whereas partial melting in water-saturated conditions

Table 4-2. Main features of the Middle-Late Jurassic Cu-Pb-Zn-bearing and W-bearing granitoids in the Nanling Range

	Cu-Pb-Zn-bearing granitoids[a]	W-bearing granites[b]
Location	Western part of the Nanling Range (South Hunan, North Guangdong)	Eastern part of the Nanling Range (South Hunan, South Jiangxi, North Guangdong)
Age (Ma)	155.2 – 167.0 (peak value: 160.6)	151.1 – 161.8 (peak value: 155.5)
Tectonic setting	Intraplate extension	Intraplate extension
Rock type	Granodiorites with the signatures of I-type granites	S-type two-mica, muscovite, and biotite granites
Source	Mainly mafic amphibolitic basement in the lower crust	Mainly muscovite-rich metasedimentary basement in the upper-middle crust
Dark enclaves	Observed	Not observed
Amphibole	Observed	Not observed
Fe-Ti oxide minerals	Mainly magnetite	Mainly ilmenite
Accessory minerals	Zircon, titanite, allanite, etc.	Zircon, monazite, xenotime, thorite, etc.
Redox condition	Oxidized	Reduced
Degree of fractionation	Weakly fractionated	Highly fractionated
ASI	0.8 – 1.0	1.0 – 1.2
$CaO/(Na_2O+K_2O)$	0.3 – 0.8	<0.2
Rb/Sr	<2	10 – 250
δEu	0.6 – 1.0	<0.15
ΣREE (ppm)	100 – 240	60 – 180
LREE/HREE	5 – 13	0.5 – 3
HFSE (ppm)	180 – 290	150 – 300
T_{Zr} (°C)	720 – 790 (average value: 750)	690 – 760 (average value: 735)
$(^{87}Sr/^{86}Sr)_i$	0.708 – 0.712	>0.712
ε_{Nd} (t) value	Mainly –10 – –2 (peak value: –7 – –6)	Mainly –14 – –7 (peak value: –10 – –9)
Zircon ε_{Hf} (t) value	Mainly –13 – –7 (peak value: –11 – –10)	Mainly –14 – –8 (peak value: –13 – –12)

Notes: [a] The Cu-Pb-Zn-bearing granitoids include Shuikoushan, Baoshan, Huangshaping, Tongshanling, Dabaoshan intrusions, etc., the Huangshaping ore-bearing granites are mainly granite porphyry and quartz porphyry. [b] The W-bearing granites include Yaogangxian, Xintianling, Dengfuxian, Weijia, Xihuashan, Muziyuan, Piaotang, Dajishan intrusions, etc. The detailed data sources are shown in Appendix 4-4 and the captions of Figures 4-5 and 4-6.

would produce Ca-rich, and Fe-, Mg-, Ti-, and K-poor and strongly peraluminous melts, with residual amphibole. The Middle-Late Jurassic Cu-Pb-Zn-bearing granitoids in the Nanling

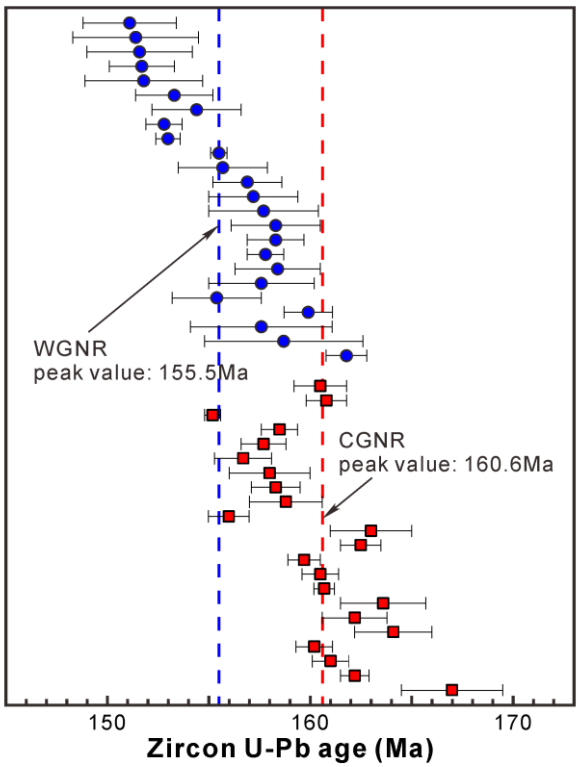

Figure 4-10. Zircon U-Pb ages of the Middle-Late Jurassic Cu-Pb-Zn-bearing (CGNR) and W-bearing (WGNR) granitoids in the Nanling Range. The data sources are shown in Appendix 4-4.

Range are Fe-, Mg-, and K-rich metaluminous granodiorites, therefore, they were in all probability derived from dehydration melting of amphibolites. The granulitic mafic xenoliths in the Daoxian basalt were formed under a pressure of 0.88 – 1.24 GPa with a corresponding depth of 29 – 41 km (Dai et al., 2008), suggesting that the lower limit of the depth of the amphibolitic basement is presumably 29 km. Yang et al. (2016) estimated the depth of the amphibolitic source of the Shuikoushan granodiorite in Hunan Province and obtained an upper limit of 25 km. Therefore, it is speculated that as the source of the Cu-Pb-Zn-bearing granitoids, the depth of the amphibolitic basement in the lower crust is 25 – 29 km. The zircon Hf model ages of the Cu-Pb-Zn-bearing granitoids (1.50 – 2.20 Ga, peak value: 1.85 Ga) indicate that the amphibolitic basement was mainly formed in the Paleoproterozoic. SHRIMP zircon U-Pb dating of the amphibolite from the Mayuan Group, which is the basement of the Cathaysia Block, yielded a Paleoproterozoic age of 1766 ± 19 Ma (Li, 1997), confirming that there is Paleoproterozoic amphibolitic basement in the Nanling Range.

The Late Jurassic W-bearing granites in the Nanling Range are plotted in the S-type

granite field of the ACF diagram (Fig. 4-6d) and in the Precambrian metasedimentary basement of the Nanling Range in the Sr-Nd isotope diagram (Fig. 4-8), and they have low Mg/(Mg+Fe) ratios (Fig. 4-9b), indicating that they originated from the partial melting of metasedimentary rocks. In the AMF-CMF diagram (Fig. 4-9c), the W-bearing granites are mainly plotted in the field of partial melts from metagreywackes. They have an average zircon saturation temperature of 735 °C (Table 4-2). According to experimental studies, metagreywackes can be partially melted to produce granitic melts only when the temperature is higher than 800 °C (Vielzeuf and Montel, 1994; Gardien et al., 1995). Under the temperature conditions of below 800 °C, muscovite is the only possible rock-forming mineral that can be greatly dehydrated (Miller et al, 2003), and muscovite-rich metapelites can be partially melted to generate granitic magmas even when the temperature is lower than 750 °C (Thompson, 1982; Gardien et al, 1995). Thus, it can be considered that the source of the W-bearing granites is a muscovite-rich metasedimentary basement in the upper-middle crust. The zircon Hf model ages of the W-bearing granites (1.50 – 2.30 Ga, peak value: 1.95 Ga) indicate that the metasedimentary basement which as the W-bearing granite source was mainly formed in the Paleoproterozoic.

4.5.5. Genetic model of the Cu-Pb-Zn-bearing and W-bearing granitoids

The Middle-Late Jurassic Cu-Pb-Zn-bearing and W-bearing granitoids in the Nanling Range are plotted in the post-collision extension field of the Rb-(Y+Nb) tectonic discrimination diagram (Fig. 4-9d), indicating that they were formed in an extensional tectonic setting. The palaeo-Pacific plate subduction model was proposed by Zhou and Li (2000) and Zhou et al. (2006a) to explain the geodynamical mechanism of the Late Mesozoic large-scale granitic magmatism in South China. The extensional tectonic setting caused by the palaeo-Pacific plate subduction induced asthenosphere upwelling and basaltic magma underplating. Deep continental crust was partially melted by heating of the underplated basaltic magmas to generate granitic magmas. On the basis of the study of the petrogenesis and source signatures of the Middle-Late Jurassic Cu-Pb-Zn-bearing and W-bearing granitoids in the Nanling Range, we proposed a genetic model for the two different types of ore-bearing granitoids (Fig. 4-11). By extensional decompression and heating of the

underplated basaltic magmas, the mafic amphibolitic basement in the lower crust was first partially melted to produce Cu-Pb-Zn mineralization related granodioritic magmas. With further basaltic magma underplating, the W-bearing granitic magmas were generated by the partial melting of the muscovite-rich metasedimentary basement in the upper-middle crust. The time gap of about 5 Ma between the Middle-Late Jurassic Cu-Pb-Zn-bearing and W-bearing granitoids in the Nanling Range was caused by the non-simultaneous partial melting of different granitoid sources.

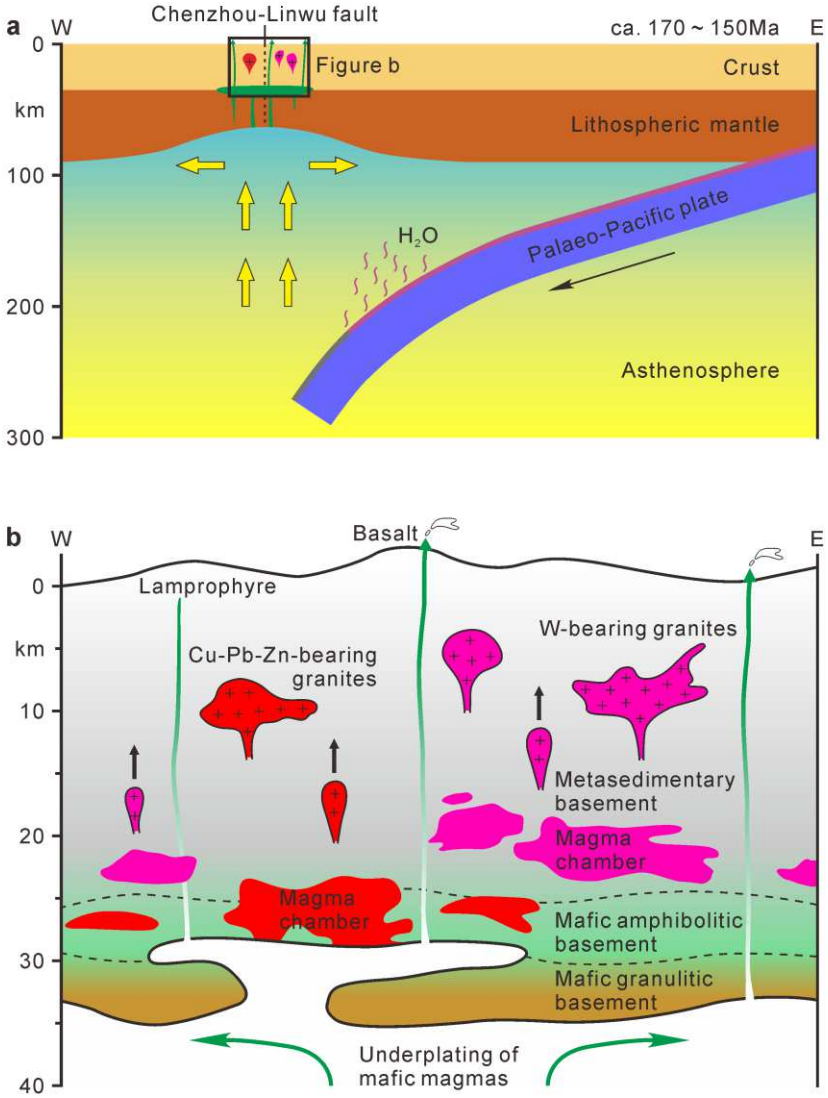

Figure 4-11. Genetic model of the Middle-Late Jurassic Cu-Pb-Zn-bearing and W-bearing granitoids in the Nanling Range. MC: magma chamber; MSB: metasedimentary basement; MAB: mafic amphibolitic basement; MGB: mafic granulitic basement.

4.6. Summary

The Tongshanling granodiorite porphyry and Weijia granite porphyry were formed at 160 – 164 Ma and about 158 Ma, respectively. The statistics of the zircon U-Pb ages indicate that the Middle-Late Jurassic Cu-Pb-Zn-bearing and W-bearing granitoids in the Nanling Range were formed mainly at about 160 Ma and 155 Ma, respectively. There is a time gap of about 5 Ma between the formation of the two different types of ore-bearing granitoids.

The Middle-Late Jurassic Cu-Pb-Zn-bearing granitoids in the Nanling Range are dominated by metaluminous amphibole-bearing granodiorites, which have a low degree of fractionation and the features of I-type granites, whereas the Late Jurassic W-bearing granites are highly differentiated peraluminous S-type granites.

A comparison of the Middle-Late Jurassic Cu-Pb-Zn-bearing and W-bearing granitoids in the Nanling Range revealed that the Cu-Pb-Zn-bearing granitoids were mainly derived from the partial melting of the mafic amphibolitic basement in the lower crust and that the W-bearing granites were predominantly derived from the partial melting of the muscovite-rich metasedimentary basement in the upper-middle crust. The time gap of about 5 Ma between the two different types of ore-bearing granitoids arose from the non-simultaneous partial melting of different granitoid sources.

Chapter 5. Reworked restite enclave

5.1. Introduction

Microgranular enclaves in granitoids have long been studied, as they can provide significant information for the petrogenetic mechanism of their host granitoids. Various models have been proposed to explain the origin of microgranular enclaves, including magma mixing, restite after partial melting, accidental xenolith, and disrupted cumulate (autolith) (Didier, 1973; Didier and Barbarin, 1991), among which magma mixing (Vernon, 1984; Dorais et al., 1990; Poli and Tommasini, 1991; Blundy and Sparks, 1992; Yang et al., 2004, 2007; Barbarin, 2005; Zhao et al., 2010; Cheng et al., 2012; Perugini and Poli, 2012; Fu et al., 2016; Zhang et al., 2016b) and restite (White and Chappell, 1977; Chappell et al., 1987; Chen et al., 1989b, 1990, 1991; Chappell and White, 1991; Chappell, 1996; White et al., 1999; Chappell and Wyborn, 2012) were the most hotly debated hypotheses. In recent years, mixing of mafic and felsic magmas was the most popular petrogenetic interpretation for dark microgranular enclaves and their host granitoids which show juvenile and evolved isotopic signatures, respectively (e.g., Yang et al., 2004, 2007; Zhao et al., 2010; Cheng et al., 2012; Fu et al., 2016). This interpretation was also frequently cited for those granitoids and enclaves with similar isotopic compositions (e.g., Jiang et al., 2009; Liu et al., 2013; Luo et al., 2015). However, it is noteworthy that magma mixing is primarily controlled by the viscosities of different end-members, and a low viscosity interval between mafic and felsic magmas favors their mixing (Sato and Sato, 2009; Perugini and Poli, 2012; Laumonier et al., 2014a, 2014b, 2015). Under experimental conditions of 300 MPa and relatively slow strain rates (10^{-5} – 10^{-3} s^{-1}), the rheological threshold for mixing of basaltic and haplotonalitic magmas under water-absent and water-saturated conditions occurs at 1160 – 1170 °C (Laumonier et al., 2014a) and around 1000 °C (Laumonier et al., 2015), respectively. It is inconceivable for most natural granitic magmas to keep such high temperatures to have a large-scale mixing with mafic magmas. Wu et al. (2007) pointed out that the existence of magmatic enclaves is indicative of a limited magma mixing.

In the Nanling Range of South China, dark microgranular enclaves are commonly observed in the Middle-Late Jurassic Cu-Pb-Zn-bearing granodiorites, such as the Tongshanling (Jiang et al., 2009) and Baoshan (Xie et al., 2013) granodiorites. Previous studies interpreted these enclaves as a result of mantle-derived mafic magma and crust-derived felsic magma mixing (Jiang et al., 2009; Xie et al., 2013), and it was widely considered that the Middle-Late Jurassic Cu-Pb-Zn-bearing granodiorites have an origin of crust-mantle mixing (e.g., Wang et al., 2003a; Jiang et al., 2009; Li et al., 2013; Xie et al., 2013; Zhao et al., 2016b). However, another hypothesis, partial melting of the mafic lower crust, has been proposed in recent years (Yang et al., 2016; Huang et al., 2017a), and gave rise to a reconsideration of the origin of the Cu-Pb-Zn-bearing granodiorites. The arguments for these two different interpretations were both primarily based on geochemistry and geochronology, but petrographic and mineralogical evidence was absent.

The Tongshanling intrusion, which is a typical Cu-Pb-Zn-bearing granodiorite containing microgranular enclaves and has been intensely studied in terms of geochronology and geochemistry, was chosen as the research target. In this study, detailed petrographic and mineralogical researches have been carried out on the Tongshanling granodiorite and its microgranular enclaves to better constrain the genesis of microgranular enclaves and provide petrogenetic implications for the Middle-Late Jurassic Cu-Pb-Zn-bearing granodiorites in the Nanling Range.

5.2. Tongshanling granodiorite and its microgranular enclaves

The Tongshanling intrusion as stock with a total exposure area of 12 km^2 (Fig. 3-1) has an approximately homogeneous composition of amphibole-bearing biotite granodiorite (Fig. 5-1a) and does not show obvious lithological zonation except for local variation of mineral granularity. It has SiO2 contents of 63.7 – 70.1 wt.% and is metaluminous (aluminum saturation index: 0.9 – 1.0), high-K calc-alkaline and weakly fractionated [$CaO/(Na_2O+K_2O)$: 0.3 – 0.6; Rb/Sr: 0.5 – 1.3], and shows characteristics of I-type granites (Huang et al., 2017a). Three deposits, the Tongshanling Cu-Pb-Zn deposit, Jiangyong Pb-Zn-Ag deposit, and Yulong Mo deposit, are distributed around this intrusion (Fig. 3-1). These deposits occur in the concealed

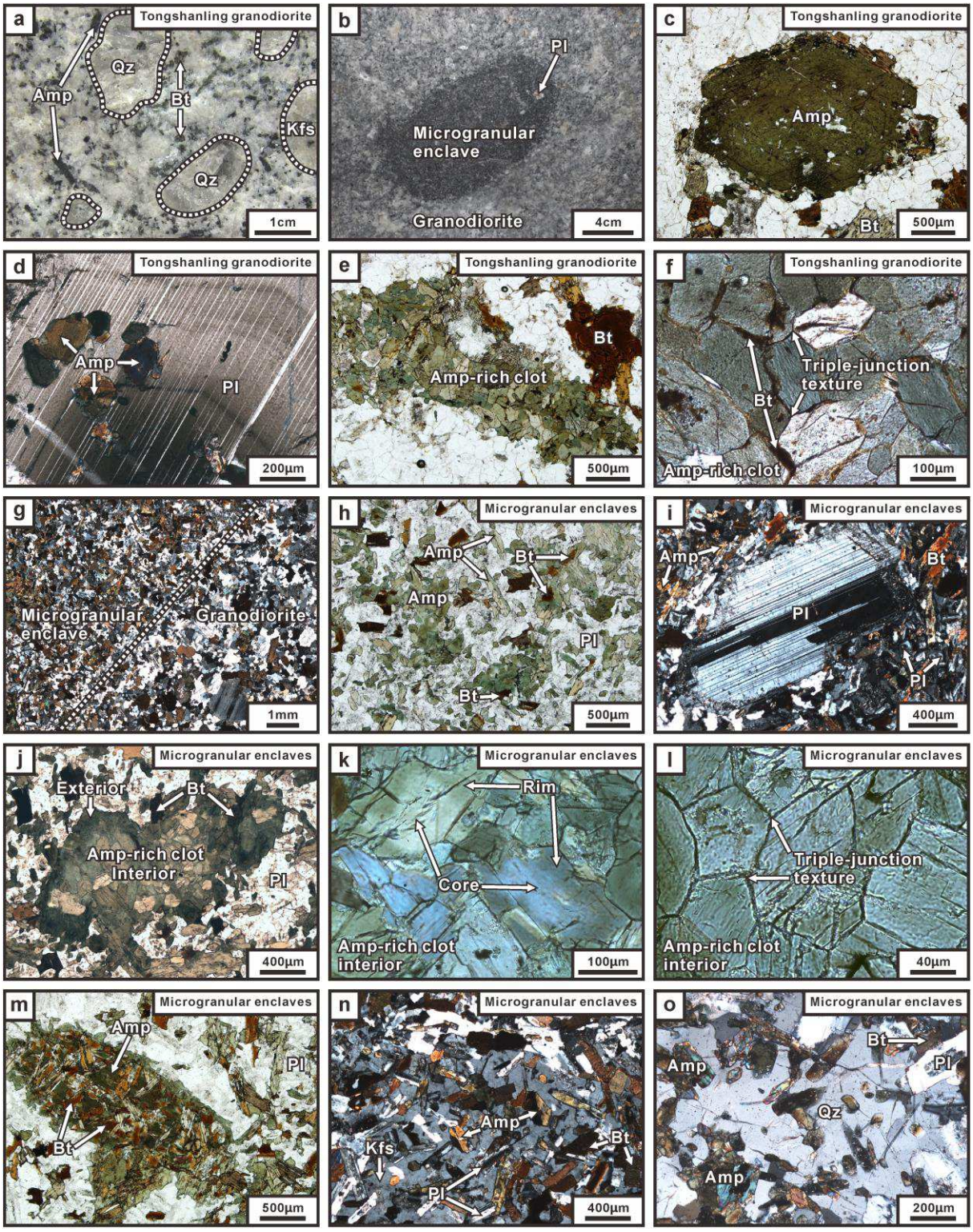

Figure 5-1. Petrographic photographs of the Tongshanling granodiorite and its microgranular enclaves. (a) Medium- to coarse-grained and porphyritic texture of the amphibole-bearing biotite granodiorite at specimen scale. (b) An ellipsoidal dark enclave in the granodiorite, which contains a few plagioclase phenocrysts, shows a gradational contact with the host, and does not have a chilled margin with magmatic flow foliation. (c) Idiomorphic and isolated amphibole in the granodiorite, plane-polarized light. (d) Enclosed amphibole in the

granodiorite, crossed-polarized light. (e) Amphibole-rich clot in the granodiorite, which is mainly comprised of aggregated fine-grained amphibole with a few biotite and plagioclase, plane-polarized light. (f) Granoblastic triple-junction texture of the amphibole-rich clot with a few interstitial anhedral biotite crystals, in the granodiorite, plane-polarized light. (g) Gradational transition from an enclave to the host granodiorite with increasing mineral granularity and decreasing proportion of mafic minerals, crossed-polarized light. (h) The enclaves are mainly composed of plagioclase, amphibole, and biotite, the mafic minerals are anhedral to subhedral and are dominated by amphibole with a few biotite, the amphibole occurs dominantly as aggregated with fewer isolated crystals, plane-polarized light. (i) Reaction rim of a plagioclase phenocryst which does not have a Ca-rich core, in the enclaves, crossed-polarized light. (j) Amphibole-rich clot in the enclaves, which has a pale-green to colorless interior and a green colored exterior, plane-polarized light. (k) Zonal amphibole crystals in the amphibole-rich clot interior with paler colored cores and deeper colored rims, in the enclaves, plane-polarized light. (l) Granoblastic triple-junction texture of the amphibole-rich clot interior without interstitial biotite, in the enclaves, plane-polarized light. (m) Intergrowth of biotite and amphibole in an amphibole-biotite clot which does not show zonal feature and granoblastic triple-junction texture, in the enclaves, plane-polarized light. (n) Poikilitic texture of a large-grained K-feldspar crystal in the enclaves, crossed-polarized light. (o) Poikilitic texture of a large-grained quartz crystal in the enclaves, crossed-polarized light. Amp = amphibole, Bt = biotite, Kfs = K-feldspar, Pl = plagioclase, Qz = quartz.

contact zone between granodiorite and carbonate rocks, and its peripheral zone. By zircon U-Pb and molybdenite Re-Os dating, it was revealed that the Tongshanling granodiorite (164 – 160 Ma; Jiang et al., 2009; Zhao et al., 2016b; Huang et al., 2017a) and its surrounding deposits (162 – 160 Ma; Huang and Lu, 2014; Lu et al., 2015; Zhao et al., 2016b) were formed contemporaneously.

Dark microgranular enclaves are commonly found scattered throughout the Tongshanling granodiorite. They occur as separate individuals, which are several to dozens of centimeters in size and generally have round to ellipsoid shapes (Fig. 5-1b). The contact of the enclaves with the host rock is gradational (Fig. 5-1b), and chilled margin and magmatic flow foliation are absent. Most enclaves are fine-grained and homogeneous, and some contain a few plagioclase phenocrysts (Fig. 5-1b). Previous zircon U-Pb geochronology showed that they were formed

at 163 – 160 Ma (Jiang et al., 2009; Huang et al., 2017a), which is identical to that of the host granodiorite. These enclaves mostly have dioritic compositions (53.4 – 59.4 wt.% SiO_2), and show similar Mg/(Mg+Fe) ratios (0.4 – 0.5) and HREE-depleted REE patterns with the host rock, but higher ΣREE contents and larger negative Eu anomalies (Huang et al., 2017a).

5.3. Petrography

5.3.1. Tongshanling granodiorite

The Tongshanling granodiorite is medium- to coarse-grained, porphyritic (Fig. 5-1a), and consists primarily of plagioclase (ca. 45 vol.%), K-feldspar (ca. 22 vol.%), quartz (ca. 20 vol.%), biotite (ca. 10 vol.%), and amphibole (ca. 3 vol.%). The phenocrysts are mainly 1 – 5 cm sized, except for some local plagioclase megacrysts with a size up to 10 cm. Plagioclase is primarily euhedral to subhedral oligoclase to andesine with zonal texture, and occasionally includes a sericitized core which has an embayed margin and generally occupies less than 30 vol.% of the whole plagioclase (Fig. 5-2a). Amphibole is green colored and mostly occurs as euhedral (Fig. 5-1c) to subhedral isolated crystals, and occasionally as mineral inclusions (i.e., enclosed amphibole) in plagioclase (Fig. 5-1d) and K-feldspar. Besides the isolated and enclosed amphibole, another rare but remarkable amphibole is aggregated crystals which

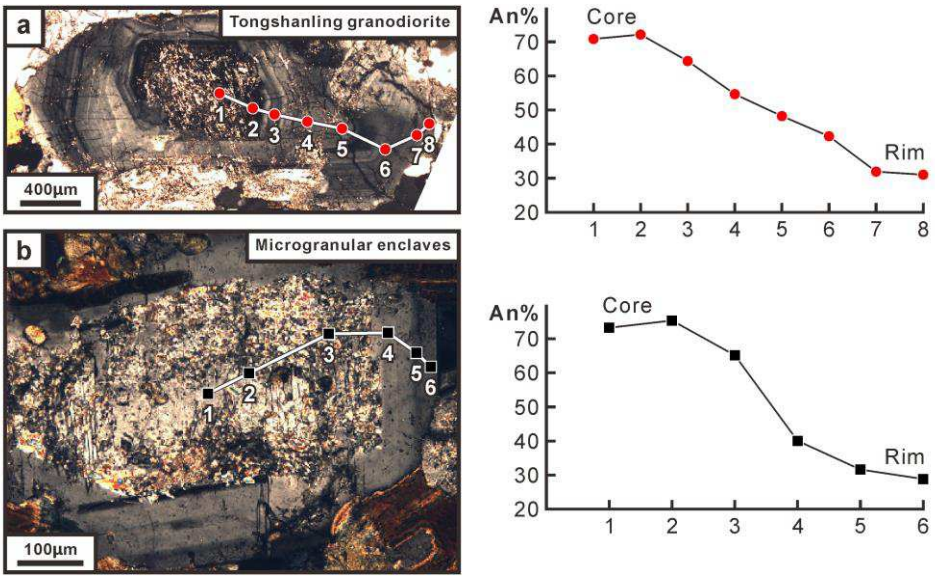

Figure 5-2. Compositional zonation of plagioclase with a Ca-rich core (analysis was performed on the unaltered part) from the Tongshanling granodiorite and its microgranular enclaves.

constitute millimetric polycrystalline amphibole-rich clots together with a few biotite and plagioclase (Fig. 5-1e). The aggregated amphibole is obviously finer grained (< 300 μm) than the isolated ones and is generally connected by a granoblastic triple-junction texture (Fig. 5-1f). Biotite is brown and dominantly distributes in the matrix as euhedral to subhedral crystals. A few anhedral biotite crystals are distributed as interstitial along the boundary between the aggregated amphibole grains (Fig. 5-1f). Accessory minerals include zircon, apatite, titanite, allanite, rutile, sulfide, and Fe-Ti oxide minerals. The Fe-Ti oxide minerals are dominated by magnetite.

5.3.2. Microgranular enclaves

The fine-grained (Fig. 5-1g) dioritic dark enclaves have the same minerals, even accessory minerals, as their host granodiorite but in different proportions. They generally have a plagioclase content of 50 – 60 vol.%, and 30 – 50 vol.% of mafic minerals (Fig. 5-1g and h), with a few K-feldspar and quartz. The mafic minerals of most enclaves are dominated by amphibole (Fig. 5-1h), with the exception of some dominated by biotite. At the contact between the enclaves and their host rock, the mineral granularity and proportion of mafic minerals change gradually rather than sharply (Fig. 5-1g). Plagioclase is mainly subhedral to anhedral and sometimes euhedral crystals which mostly consist of a sericitized core with an irregular margin and a fresh rim with zonal texture (Fig. 5-2b). The sericitized core accounts for at least 60 vol.% of the whole plagioclase (Fig. 5-2b). Notably, the quantity of core-bearing plagioclase and the proportion of sericitized core in the enclaves are much more than those in the host granodiorite. The plagioclase phenocrysts with a reaction rim and no sericitized cores (Fig. 5-1i) appear occasionally. Biotite is brown and occurs primarily as anhedral to subhedral crystals. Compared with the host granodiorite, the majority of amphibole in the enclaves occurs as aggregated rather than isolated crystals (Fig. 5-1h). The ratio of the aggregated and isolated amphibole contents is about 5:1. The aggregated amphibole, which mainly constitutes amphibole-rich clots together with a few biotite, is anhedral and has a similar grain size (< 300 μm) with the most other enclave minerals (Fig. 5-1h and j). The isolated amphibole is mostly anhedral to subhedral (Fig. 5-1h) and never appears as idiomorphic as that in the host granodiorite (Fig. 5-1c). Nearly half of the

amphibole-rich clots are several millimeters sized and are zoned with a pale-green to colorless interior and a deep-green colored exterior (Fig. 5-1j); the another half is smaller in size and does not show a color zonation (Fig. 5-1h). Although not always, the interior amphibole grains in the zonal clots also show a zonal feature, with the core being paler colored than the rim (Fig. 5-1k). However, the clot exterior amphibole grains do not show a color zonation. A granoblastic triple-junction texture can be commonly observed in the clot interior where only amphibole appears but no interstitial biotite does (Fig. 5-1l), whereas the clot exterior shows an anhedral granular texture of dominant amphibole and a few biotite crystals (Fig. 5-1j). The biotite in the clot exterior occupies no more than 5 vol.% of the clot. Besides the amphibole-rich clots, some rarely-occurred mafic mineral clots are composed of amphibole and abundant biotite with an intergrowth texture, and do not have zonal feature and granoblastic triple-junction texture (Fig. 5-1m). In these amphibole-biotite clots, the content of biotite is about 40 – 50 vol.%. A few large-grained K-feldspar and quartz have a poikilitic texture and include the fine-grained amphibole, biotite, and plagioclase (Fig. 5-1n and o).

5.4. Analytical methods

Major element analyses of plagioclase, amphibole, and biotite were carried out with a CAMECA SX50 electron microprobe (EMP) at Institut des Sciences de la Terre d'Orléans (ISTO), France. Zircon was analyzed by a JEOL JXA-8100M EMP at the State Key Laboratory for Mineral Deposits Research (LAMD), Nanjing University (NJU), China. The analytical conditions included an accelerating voltage of 15 kV, a beam current of 10 nA (CAMECA, ISTO) or 20 nA (JEOL, LAMD, NJU) with beam diameter of 1 μm, and counting times of 10 s for all elements and 5 s for background. The collected data were corrected by the ZAF procedures. Calibration was performed using natural minerals and synthetic compounds.

Trace element contents of amphibole and biotite were determined by an Agilent 7700× inductively coupled plasma mass spectrometry coupled to an Excite 193 nm Photon Machines laser ablation system (LA-ICP-MS) at Nanjing FocuMS Technology Co. Ltd. Each analysis was performed by a 25 – 50-μm ablating spot at 5 – 8 Hz with energy of 5 – 5.5 mJ (transmittance 80%) for 40 s after measuring the gas blank for 15 s. USGS standard reference

materials BIR-1G, BHVO-2G, and BCR-2G, NIST standard reference material 610, and Chinese Geological Standard Glasses CGSG-1 and CGSG-2 were used as external standards to plot calibration curve. GSE-1G was analyzed for quantity control of the time-dependent calibration for sensitivity drift. The off-line data processing was performed using a program called ICPMSDataCal (Liu et al., 2008b).

5.5. Analytical results

5.5.1. Plagioclase

Representative microprobe analyses of plagioclase from the Tongshanling granodiorite and its microgranular enclaves are listed in Appendix 5-1. In the granodiorite, most plagioclase crystals show an anorthite range from An_{21} to An_{48} (Fig. 5-3). The plagioclase with a sericitized core has an anorthite content of An_{71} – An_{72} and An_{31} – An_{64} at the core and rim, respectively (Fig. 5-2a). In the enclaves, the plagioclase rims have an anorthite content of An_{22} – An_{45}, similar to that of the core-free plagioclase in the host granodiorite, whereas, the sericitized cores show an anorthite range from An_{65} to An_{76} (Fig. 5-3). Thus, the enclave plagioclase shows a discontinuous compositional change from core to rim (Fig. 5-2b). The Ca-rich plagioclase cores of both the granodiorite and its enclaves are almost uniform in composition without obvious zonation (Fig. 5-2).

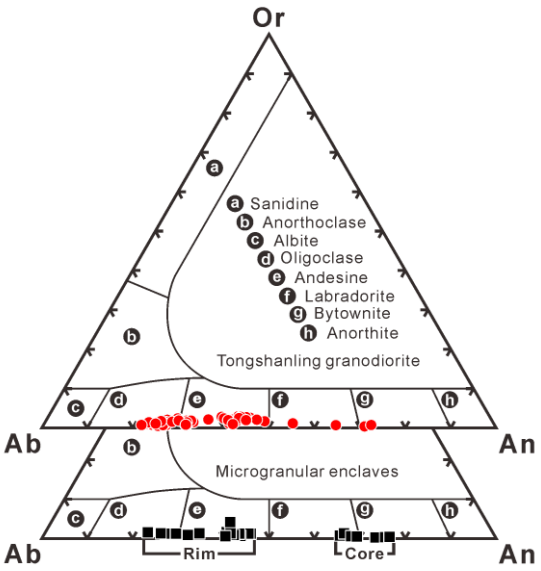

Figure 5-3. Composition of plagioclase from the Tongshanling granodiorite and its microgranular enclaves.

5.5.2. Amphibole

The different occurrences of amphibole (i.e., enclosed, isolated, and aggregated) in the Tongshanling granodiorite and its enclaves are all calcium amphibole, and show a large compositional variation, but have quite consistent Mg/(Mg+Fe) ratios (0.44 – 0.58) (Fig. 5-4; Appendix 5-2). In the classification of Hawthorne et al. (2012), for the granodiorite, the enclosed and most isolated crystals plot in the pargasite field; some isolated ones plot in the magnesio-hornblende field; the core and rim of aggregated amphibole grains plot in the transition field from tremolite to magnesio-hornblende and in the magnesio-hornblende field, respectively (Fig. 5-4a). For the enclaves, the core and rim of clot interior amphibole grains plot in the tremolite and in the transition field from tremolite to magnesio-hornblende, respectively; both the clot exterior amphibole and the isolated amphibole plot in the magnesio-hornblende field (Fig. 5-4a).

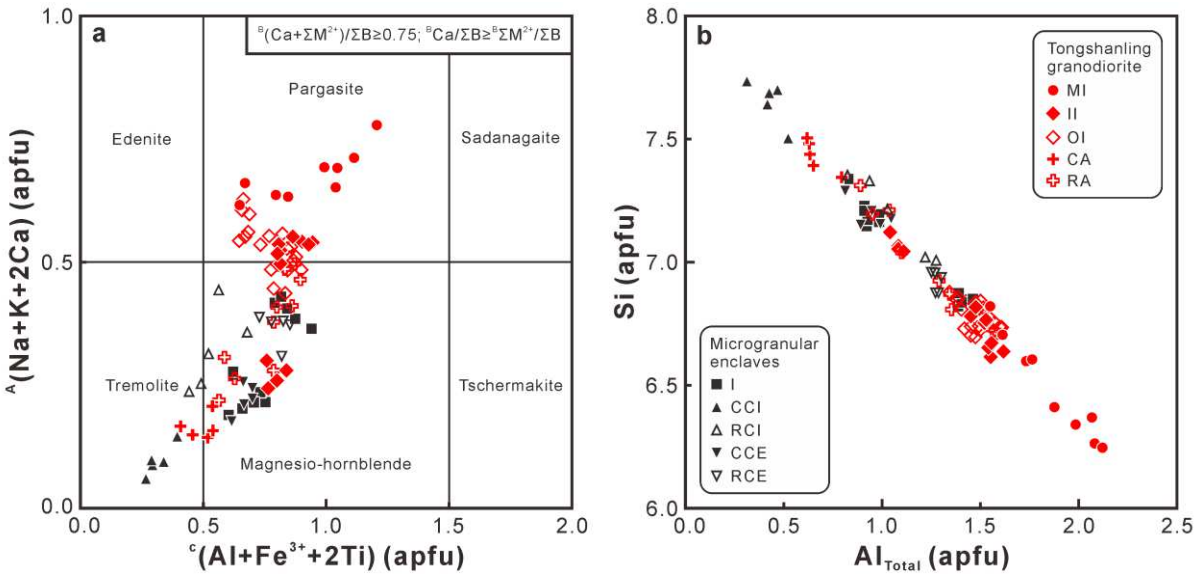

Figure 5-4. Mineral chemistry of amphibole from the Tongshanling granodiorite and its microgranular enclaves. (a) Classification diagram of amphibole [General formula: $A_{0-1}B_2C_5T_8O_{22}(OH, F, Cl)_2$, after Hawthorne et al., 2012], when $Mg/(Mg+Fe^{2+}) < 0.9$, the tremolite field represents an actinolitic composition (according to Leake et al., 1997). (b) Si (apfu)-Al_{Total} (apfu) diagram. MI: mineral inclusion; II: inner of isolated amphibole; OI: outer of isolated amphibole; CA: core of aggregated amphibole grains; RA: rim of aggregated amphibole grains; I: isolated amphibole; CCI: core of clot interior amphibole grains; RCI: rim of clot interior amphibole grains; CCE: core of clot exterior amphibole grains; RCE: rim of clot exterior amphibole grains.

Among all the different occurrences of amphibole, the enclosed amphibole in the granodiorite has the highest Al [1.55 – 2.12 apfu (atoms per formula unit)] and lowest Si (6.25 – 6.82 apfu) contents (Fig. 5-4b). Most isolated amphibole crystals in the granodiorite have Al contents of 1.34 – 1.62 apfu and Si contents of 6.62 – 6.88 apfu and a few have obviously lower Al (1.04 – 1.11 apfu) and higher Si (7.04 – 7.12 apfu) contents (Fig. 5-4b). The aggregated amphibole of both the granodiorite and its enclaves shows distinctly lower Al and higher Si contents than the enclosed and dominant isolated amphibole in the granodiorite (Fig. 5-4b). The core of aggregated amphibole grains in the granodiorite has lower Al contents (0.63 – 0.81 apfu) and higher Si contents (7.33 – 7.49 apfu) than the rim (Al: 0.90 – 1.59 apfu; Si: 6.71 – 7.31 apfu) (Fig. 5-4b). Particularly, the core of clot interior amphibole grains in the enclaves shows actinolitic compositions [$Mg/(Mg+Fe^{2+}) < 0.9$; Fig. 5-4a; Appendix 5-2] with the lowest Al (0.31 – 0.52 apfu) and highest Si (7.49 – 7.72 apfu) contents and the rim has higher Al (0.82 – 1.28 apfu) and lower Si (7.01 – 7.35 apfu) contents than the core (Fig. 5-4b). Notably, although the clot exterior amphibole grains do not show a color zonation, they have zoned compositions, with the core having lower Al contents (0.81 – 1.05 apfu) and higher Si contents (7.16 – 7.30 apfu) than the rim (Al: 1.25 – 1.30 apfu; Si: 6.88 – 6.97 apfu) (Fig. 5-4b). At clot scale, the exterior of zonal amphibole-rich clots shows more Al-enriched and Si-depleted amphibole compositions than those of the interior (Fig. 5-4b). The isolated amphibole in the enclaves can be divided into two different groups with low-Al, high-Si and high-Al, low-Si compositions, respectively (Fig. 5-4).

Trace element compositions of amphibole are listed in Appendix 5-3. The isolated amphibole in the granodiorite has flat REE patterns with weak LREE depletions and obvious Eu negative anomalies (Fig. 5-5a). The ΣREE contents are 307 – 764 ppm and the mean δEu [$\delta Eu = 2Eu_N/(Sm_N + Gd_N)$] value is 0.05. The rim of clot interior amphibole grains and the isolated amphibole in the enclaves, with ΣREE contents of 485 – 525 ppm and 317 – 549 ppm, respectively, have the similar REE patterns and mean δEu value (0.06) (Fig. 5-5b and c) to the isolated amphibole in the granodiorite. In contrast, although the core of clot interior amphibole grains in the enclaves also shows flat REE patterns with weak LREE depletions, it has distinctly lower ΣREE contents (99 – 146 ppm) and a slightly higher mean δEu value (0.09) (Fig. 5-5b).

In the trace element binary diagrams (Fig. 5-6), it is clearly separated from the other occurrences of amphibole by lower contents of Rb, Sr, Cs, Ba, Zr, Hf, Nb, Ta, Th, U, ΣREE, Y, Zn, Pb, Sn, W, V, Sc, Ga, and In.

5.5.3. Biotite

Biotite crystals of the Tongshanling granodiorite and its microgranular enclaves have similar major element compositions (Appendix 5-4). Their Mg/(Mg+Fe) ratio varies in a

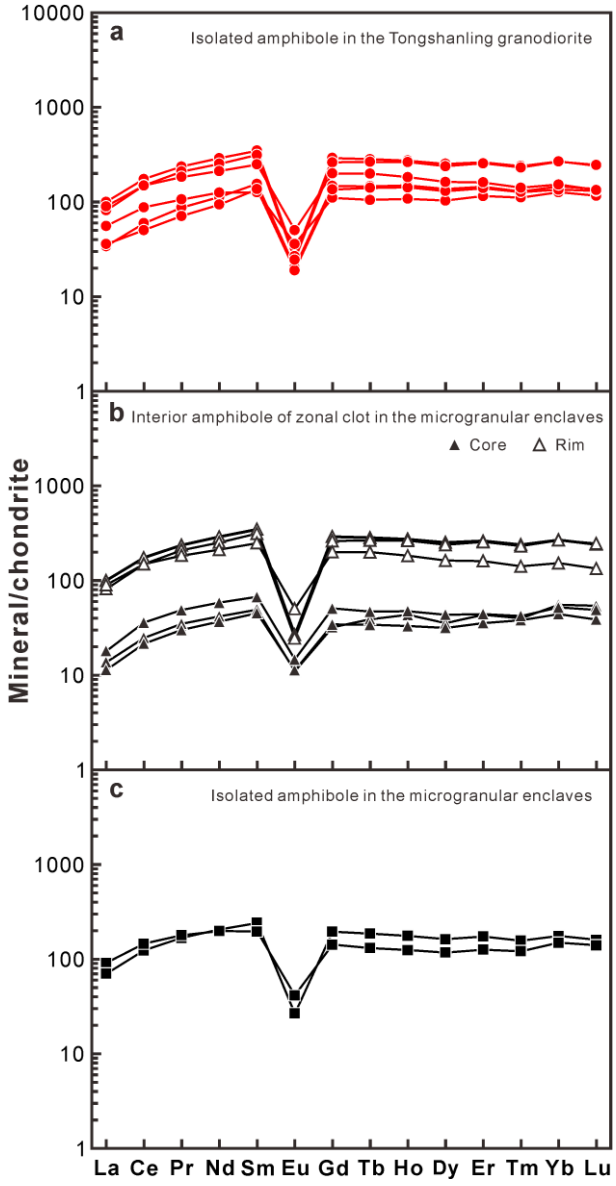

Figure 5-5. Chondrite-normalized (Boynton, 1984) REE patterns of amphibole from the Tongshanling granodiorite and its microgranular enclaves.

narrow range of 0.39 – 0.48. In the classification of Tischendorf et al. (1997), they plot dominantly in the Fe biotite field and some in the Mg biotite field (Fig. 5-7). However, they

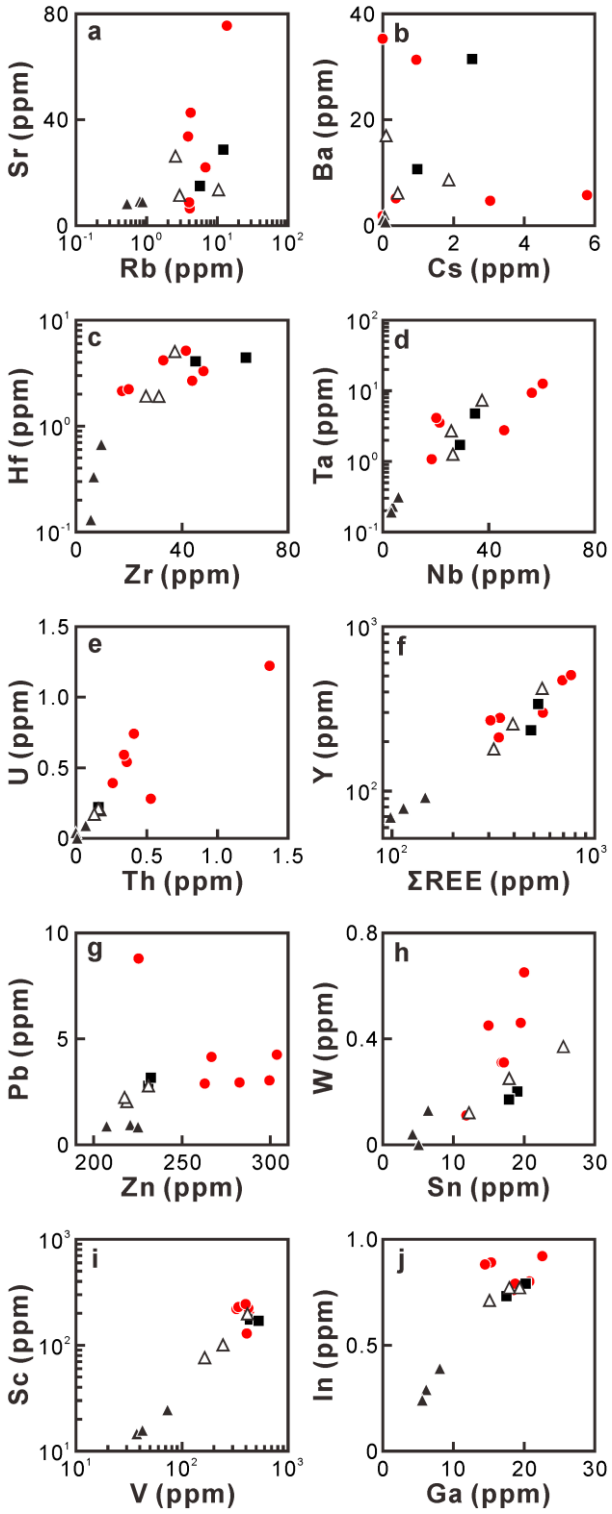

Figure 5-6. Trace element binary diagrams of amphibole from the Tongshanling granodiorite and its microgranular enclaves. Legends are the same as Figure 5-5.

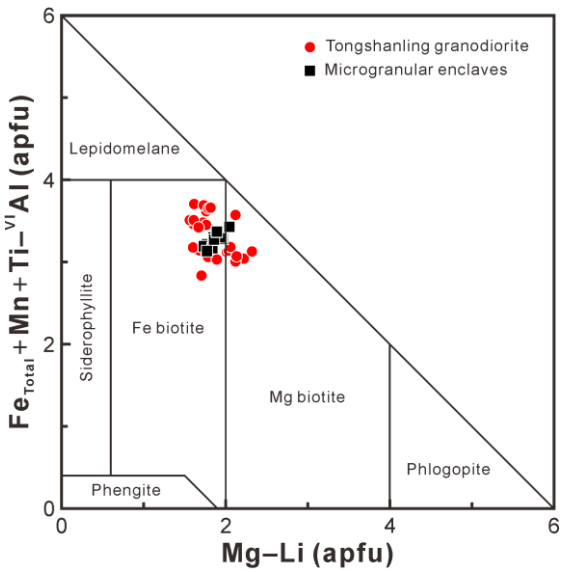

Figure 5-7. Classification diagram of biotite (after Tischendorf et al., 1997) from the Tongshanling granodiorite and its microgranular enclaves.

show some differences in the trace element compositions (Appendix 5-3). The enclave biotite has lower Sr, Ba, ΣREE, Y, Zn, Pb, W, Sc, Co, Ni, Ga, and In contents, and higher Sn and V contents than that of the granodiorite (Figs. 5-8 and 5-9).

5.5.4. Zircon

Magmatic zircon of the granodiorite shows well-developed oscillatory zoning, and generally includes an inherited core (Fig. 5-10a). Their ThO_2+UO_2 contents and Zr/Hf ratios

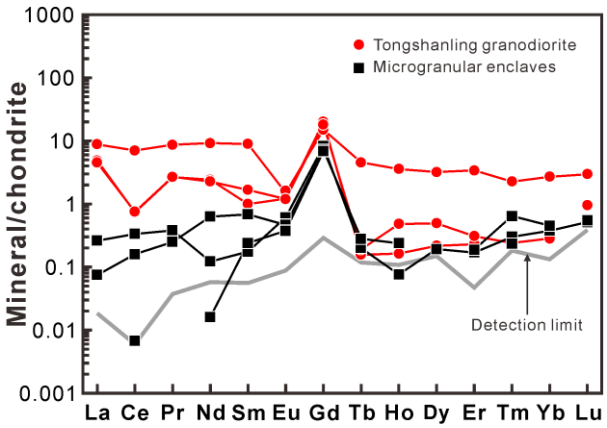

Figure 5-8. Chondrite-normalized (Boynton, 1984) REE patterns of biotite from the Tongshanling granodiorite and its microgranular enclaves.

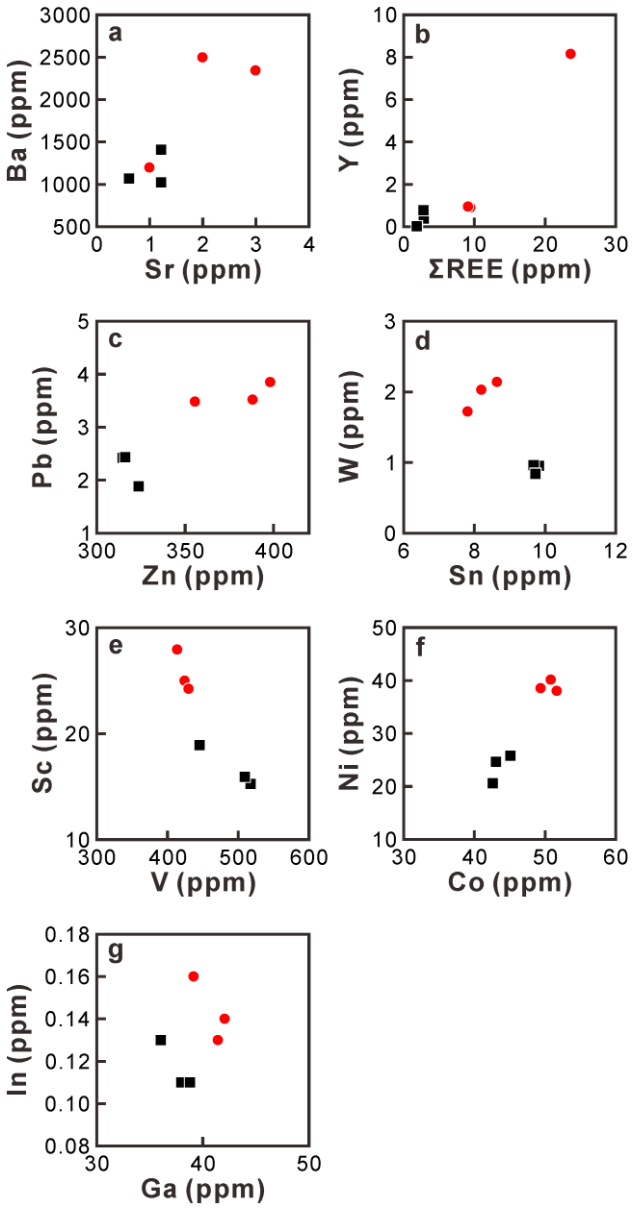

Figure 5-9. Trace element binary diagrams of biotite from the Tongshanling granodiorite and its microgranular enclaves. Legends are the same as Figures 5-7 and 5-8.

are 0.01 – 0.44 wt.% and 68 – 94, respectively (Fig. 5-10b; Appendix 5-5). In the enclaves, inherited zircon cores are also present (Fig. 5-10c). The magmatic zircon generally comprises an inner part with bright cathodoluminescence (CL) image and an outer part with dark CL image (Fig. 5-10c). The outer parts have higher ThO_2+UO_2 contents and lower Zr/Hf ratios than the inner parts and are compositionally more similar to the magmatic zircon in the host granodiorite (Fig. 5-10b; Appendix 5-5). It is worth noting that about 80% of the enclave zircon

grains show chaotic internal textures without oscillatory zoning (Fig. 5-10d and e), and sometimes are surrounded by an oscillatory-zoned magmatic rim (Fig. 5-10f).

5.6. Discussion

5.6.1. Textural evidence

5.6.1.1. Residual materials

The restite model was mostly discussed and developed by the studies of granites and their enclaves in the Lachlan Fold Belt (White and Chappell, 1977; Chappell et al., 1987; Chen et al., 1989b, 1990, 1991; Chappell and White, 1991; Chappell, 1996; White et al., 1999; Chappell and Wyborn, 2012). Restite microgranular enclaves in calc-alkaline I-type granitoids generally have some diagnostic textural features as follows: (1) remnants of refractory materials, such as

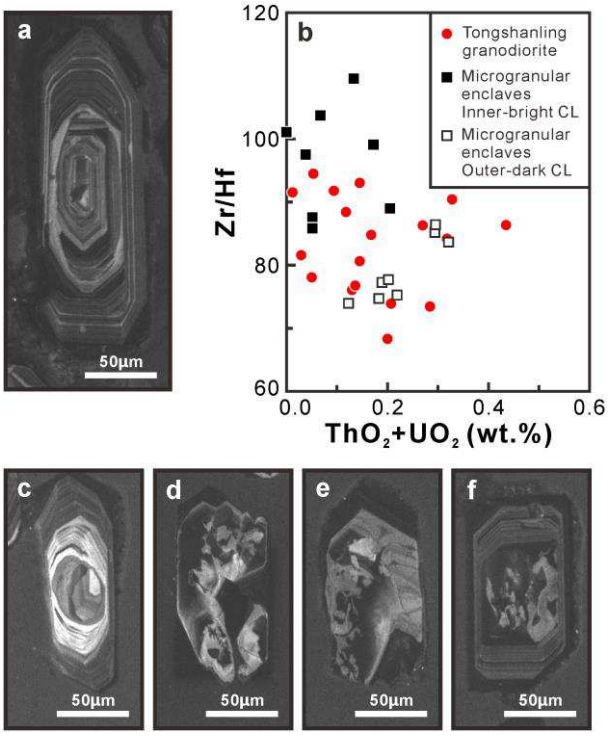

Figure 5-10. Texture and mineral chemistry of zircon from the Tongshanling granodiorite and its microgranular enclaves. (a) CL image of a magmatic zircon with an inherited core from the granodiorite. (b) Zr/Hf-ThO_2+UO_2 (wt.%) diagram of magmatic zircon from the granodiorite and its enclaves. (c) CL image showing the compositional zonation of a magmatic zircon with an inherited core from the enclaves. (d and e) Chaotic internal textures of metamorphic zircon in the enclaves. (f) Metamorphic zircon with a magmatic rim in the enclaves.

Ca-rich plagioclase, inherited zircon, and possibly pyroxene produced by dehydration melting reactions; (2) mafic mineral clots coexisted with Ca-rich plagioclase; (3) residual metamorphic texture inherited from the source.

In the enclaves of the Tongshanling granodiorite, mafic mineral clots are widely scattered (Fig. 5-1h, j, and m). These clots are comprised of anhedral to subhedral crystals and do not exhibit the typical texture of serial crystallization as in magmatic rocks. The metamorphogenic granoblastic triple-junction texture in the interior of zonal amphibole-rich clots (Fig. 5-1l) directly reflects the restite information from the metamorphic source (Castro and Stephens, 1992; Sial et al., 1998). The commonly occurred old zircon cores (Fig. 5-10c; Huang et al., 2017a) are also indicative of an inheritance from the crustal source. The chaotic internal texture of the dominant enclave zircon grains (Fig. 5-10d and e) is different from the magmatic oscillatory-zoned texture and is similar to the convoluted zoning and recrystallization texture of zircon formed by high-temperature metamorphism (Hoskin and Black, 2000; Corfu et al., 2003; Wu and Zheng, 2004; Harley et al., 2007). In all probability, this kind of zircon is metamorphic zircon maintained from the source after partial melting. With an irregular margin and almost uniform composition without zonation (Fig. 5-2b), the sericitized Ca-rich plagioclase cores are distinctly different from the fresh zonal magmatic plagioclase. The confined sericitization only in the core rather than in the rim (Fig. 5-2b) may indicate that the core plagioclase was an early existed phase which has been altered by magmatic fluids before the crystallization of rim plagioclase. Therefore, these plagioclase cores are thought to be of a restite origin. They are analogous to the residual plagioclase described by Chappell et al. (1987). The existence of these residual minerals implicates that the temperature of partial melting was insufficient to thoroughly melt the source materials. Thus, these microgranular enclaves are restite enclaves and show the same petrographic features as the restite enclaves of I-type granites in the Lachlan Fold Belt (e.g., Chen et al., 1990, 1991).

5.6.1.2. Vestiges of magma reworking

The textural vestiges of restite enclaves reworked by the host magma are evident in the microgranular enclaves. The plagioclase phenocrysts in the enclaves show identical features to the matrix plagioclase in the host granodiorite with a similar granularity and composition (An_{30}

– An_{40}, measured by optical microscope) and without Ca-rich cores (Fig. 5-1i). They were probably formed by transfer of accidental crystals from the host magma. White et al. (1999) emphasized that the restite enclaves could contain a melt phase which has been produced during partial melting but is insufficient to disaggregate the enclave into the magma. The reaction rim of plagioclase phenocryst (Fig. 5-1i) could be formed by reaction of the accidental plagioclase with the initial melt in the enclaves. Vernon (1991) pointed out that poikilitic texture results from magmatic crystallization with relatively low nucleation rates and high growth rates. Thus, the poikilitic texture of K-feldspar (Fig. 5-1n) and quartz (Fig. 5-1o) in the enclaves in all probability reflects an input of late-stage silica-rich melt from the host magma. There is a progressive change of texture and mineral proportion from the zonal amphibole-rich clot interior to exterior (Fig. 5-1j–l) and then to the amphibole-biotite clot (Fig. 5-1m), with gradually obscurer granoblastic triple-junction texture and elevated biotite content, showing a progressive reaction process of the restite with the accidental melt from the host magma. This accidental melt was also probably responsible for the formation of the magmatic rims of residual plagioclase (Fig. 5-2b) and zircon (Fig. 5-10c and f). The process of magma reworking is also reflected by the gradational contact between the enclaves and the host granodiorite (Fig. 5-1g).

5.6.2. Compositional evidence

5.6.2.1. Magmatic amphibole

Both natural amphibole (Duan and Jiang, 2017) and experimental studies (Schmidt, 1992; Ernst and Liu, 1998) have revealed that, during magmatic crystallization with decreasing pressure and temperature, the early-crystallized amphibole is more Al-enriched and Si-depleted than the late-crystallized amphibole. The dominant idiomorphic isolated amphibole in the Tongshanling granodiorite shows normal magmatic growth zonation (Appendix 5-2) and was evidently formed by magmatic crystallization. With higher Al and lower Si contents than the isolated amphibole (Fig. 5-4b), the enclosed amphibole is also of magmatic origin but was crystalized earlier than the isolated one. In the plot of the generalized tschermakite vs. edenite components (Fig. 5-11), the magmatic amphibole is distributed away from the tremolite

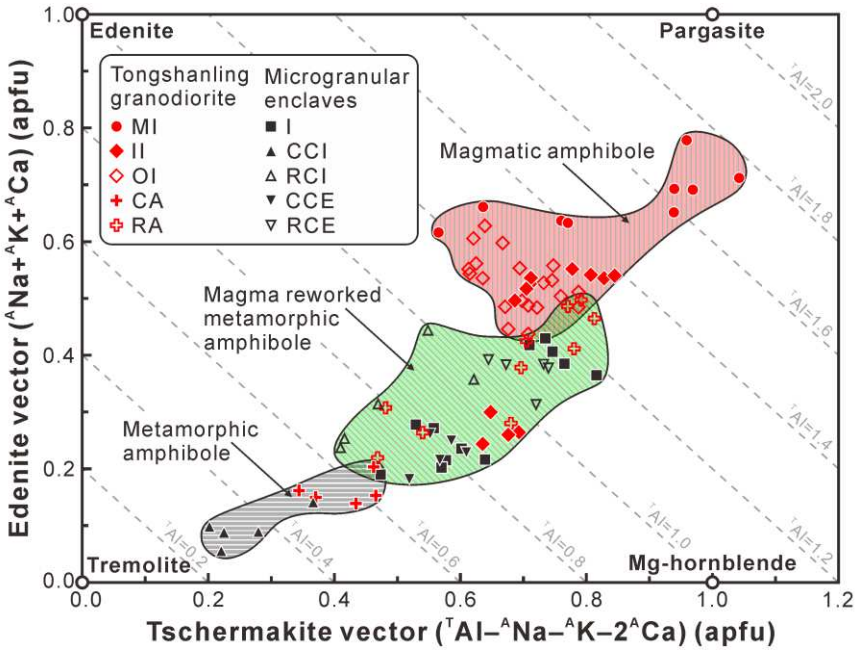

Figure 5-11. Plot of the generalized tschermakite [(^{T}Al–^{A}Na–^{A}K–2^{A}Ca) (apfu)] vs. edenite [(^{A}Na+^{A}K+^{A}Ca) (apfu)] components for amphibole from the Tongshanling granodiorite and its microgranular enclaves (after Schumacher, 2007). Legends are the same as Figure 5-4.

end-member and is obviously separated from the other occurrences of amphibole. Assuming that the whole-rock composition of the Tongshanling granodiorite is similar to the melt composition from which the magmatic amphibole was crystallized, the REE distributions of model magmatic amphibole calculated by partition coefficients in felsic (dacitic to rhyolitic) melts (Arth, 1976) are consistent with those of the isolated amphibole (Fig. 5-12), further demonstrating its magmatic origin.

5.6.2.2. Metamorphic amphibole

It is notable that, compared with the magmatic amphibole, the amphibole grains in the enclave zonal clots show a contrary compositional zonation and distinctly lower Al and higher Si contents (Fig. 5-4b; Appendix 5-2), indicating that they were not formed by magmatic crystallization. The clot interior amphibole has a granoblastic triple-junction texture (Fig. 5-11) and the grain core is compositionally close to the tremolite end-member (Fig. 5-11), thus the actinolitic core amphibole is considered to be of a metamorphic origin. A study of analogous amphibole-rich clots in granodiorite by Castro and Stephens (1992) argued that the actinolitic

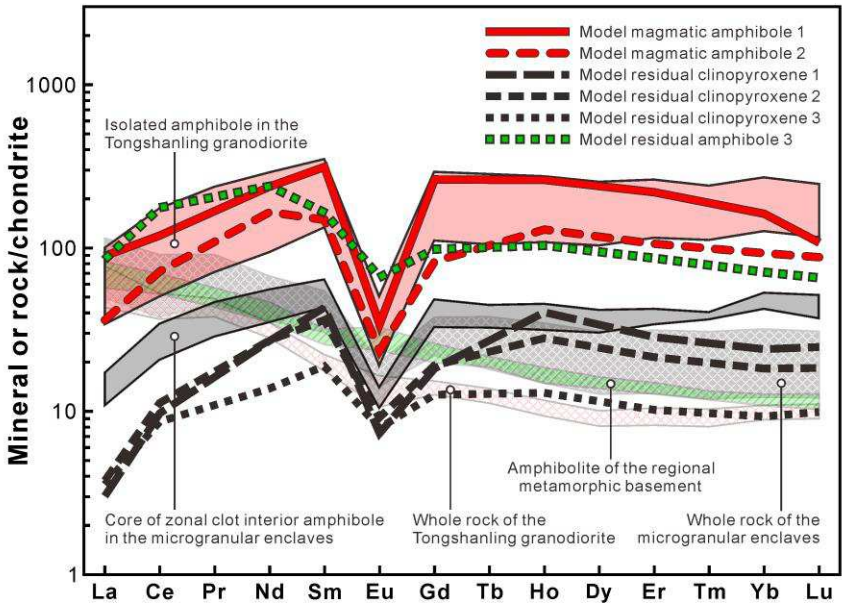

Figure 5-12. REE distribution modelling of magmatic amphibole and residual clinopyroxene and amphibole. Model magmatic amphibole 1 and 2 are calculated by partition coefficients in felsic melts with rhyolitic and dacitic compositions (Arth, 1976), respectively, assuming that the whole-rock composition of the Tongshanling granodiorite is similar to the melt composition in which magmatic amphibole has been crystallized. Model residual clinopyroxene 1, 2, and 3 are calculated by partition coefficients in dacitic melt (Arth, 1976; Fujimaki et al., 1984) in terms of 10% partial melting with a restite comprised of 30% clinopyroxene + 70% plagioclase (model 1), 50% clinopyroxene + 50% plagioclase (model 2), and 45% clinopyroxene + 45% plagioclase + 10% amphibole (model 3), respectively, using the amphibolite of the regional metamorphic basement (Li, 1997) as the source rock. Model residual amphibole 3 is calculated by the restite model 3. The whole-rock REE compositions of the Tongshanling granodiorite and its microgranular enclaves are from Huang et al. (2017a). The REE concentrations of all model residual minerals and natural samples are normalized by chondrite (Boynton, 1984).

core amphibole is actually a pseudomorph after a primary pyroxene-rich precursor, which is expected to be relatively poor in Al and has been transformed into amphibole by a complex reaction. They supposed that this reaction may have occurred by hydrogenation of the primary pyroxene with a magnesio-hornblende armor [pyroxene + fluids (OH, etc.) → actinolite] or may also have occurred as a direct discontinuous reaction of the pyroxene with the melt (pyroxene + $melt_1$ → hornblende + $melt_2$). Martin (2007) considered that the former hypothesis is more dependable. The actinolitic core amphibole in the Tongshanling microgranular

enclaves contains significantly lower REE contents than the magmatic amphibole (Fig. 5-5a and b). It is consistent with the hypothesis that the actinolitic core amphibole was transformed from primary residual pyroxene which has significantly lower REE partition coefficients than amphibole in felsic melt (Arth, 1976; Fujimaki et al., 1984). This is also responsible for the distinctly lower contents of the other incompatible elements in the actinolitic core amphibole (Fig. 5-6a–h). It is reasonable that the incompatible elements tend to concentrate in melt during partial melting and give rise to a depleted remnant. The obvious Eu negative anomalies and weak LREE depletions of the actinolitic core amphibole (Fig. 5-5b) indicate the coexistence of plagioclase in residual materials (Stephens, 2001). This has been further demonstrated by the occurrence of abundant residual Ca-rich plagioclase cores in the enclaves. As revealed by previous experimental studies, dehydration melting of amphibolite at crustal pressure and temperature usually produces a pyroxene- and plagioclase-rich restite in which the pyroxene is dominated by clinopyroxene (Beard and Lofgren, 1991; Wolf and Wyllie, 1994; Johannes and Holtz, 1996). Using the amphibolite of the regional metamorphic basement (Li, 1997) as the source rock of the Tongshanling granodiorite, the REE distributions of model residual clinopyroxene calculated in terms of 10% partial melting with a model restite comprised of different proportions of clinopyroxene, plagioclase and amphibole are similar to the actinolitic core amphibole but with lower REE contents especially when residual amphibole occurs (Fig. 5-12). However, the model residual amphibole contains distinctly higher REE contents than the actinolitic core amphibole (Fig. 5-12). Thus, the results of REE distribution modeling indicate that the actinolitic core amphibole was transformed from primary residual pyroxene by hydrogenation, during which the REE contents had increased due to its higher REE partition coefficients, rather than directly preserved as residual amphibole.

5.6.2.3. Magma reworked metamorphic amphibole

The increasing Al and decreasing Si contents from core to rim of the clot interior amphibole grains and also from interior to exterior of the whole zonal clot (Fig. 5-4b), with a trend from metamorphic amphibole to magmatic amphibole (Fig. 5-11), show the process of magma reworking of the restite enclaves. In consideration of the consistent REE patterns with the magmatic amphibole (Fig. 5-5a and b), the rim of clot interior amphibole grains may have

been formed by reaction of the actinolitic amphibole with the host magma. Castro and Stephens (1992) and Stephens (2001) considered that this reaction was induced dominantly by diffusive exchange along the grain boundaries. With a similar compositional zonation to the clot interior amphibole but higher Al and lower Si contents (Fig. 5-4), the clot exterior amphibole was formed by a more intense magma reworking than the clot interior amphibole. The isolated enclave amphibole has magma reworked compositions (Fig. 5-11) and consistent REE patterns with the magmatic amphibole (Fig. 5-5a and c), suggesting that it is also magma reworked amphibole and is deduced to be transformed from isolated residual pyroxene. The high-Al and low-Si isolated amphibole may result from a more intense reworking by a late and evolved host melt than the low-Al and high-Si isolated amphibole.

5.6.2.4. Zircon and plagioclase

The composition zonation of enclave magmatic zircon (Fig. 5-10c) has recorded two different melts existed in the enclaves. Huang et al. (2017a) reported that both the inner parts and outer parts of enclave magmatic zircon have consistent U-Pb ages and Hf isotopic compositions with the magmatic zircon in the host granodiorite, indicating that they were sequentially crystallized from different melts with the same origin. The outer parts have higher ThO_2+UO_2 contents and lower Zr/Hf ratios than the inner parts, and are more similar to those of the magmatic zircon in the host granodiorite (Fig. 5-10b), suggesting that the outer magmatic zircon was crystallized from a late and more evolved host melt, whereas, the inner parts with lower ThO_2+UO_2 contents and higher Zr/Hf ratios (Fig. 5-10b) may be crystallized from the initial melt retained in restite. The magmatic rims of enclave plagioclase may have been crystallized from the initial melt or the evolved host melt. However, the consistent compositions of magmatic plagioclase in the enclaves and their host granodiorite (Fig. 5-3) and the discontinuous compositional change within the enclave plagioclase from core to rim (Fig. 5-2b) indicate that the magmatic rim plagioclase in the enclaves was in all probability dominantly crystallized from the evolved host melt.

5.6.2.5. Biotite

The temperature of biotite dehydration melting is much lower than that of amphibole dehydration melting (Johannes and Holtz, 1996). Therefore, the enclave biotite should not be a residual phase when amphibole broke down. However, it has lower contents of ΣREE and some other incompatible elements such as Sr, Ba, Y, Zn, Pb, and W than the magmatic biotite in the host granodiorite (Figs. 5-8 and 5-9a–d), reflecting some residual information. The consistent major element compositions of biotite in the granodiorite and its enclaves (Fig. 5-7) indicate an intense reworking of the restite by the host magma.

5.6.2.6. Residual materials in the granodiorite

There are also some residual materials in the host granodiorite, such as the old zircon cores (Fig. 5-10a), the Ca-rich plagioclase cores (Fig. 5-2a), and the rarely-occurred amphibole-rich clots (Fig. 5-1e). These residual materials can be directly inherited from the source after partial melting or can be derived from disaggregation of the restite enclaves reworked by the host magma. The amphibole-rich clots also have a metamorphic triple-junction texture (Fig. 5-1f) and mainly consist of granoblastic amphibole with an actinolitic core surrounded by a magnesio-hornblende rim (Fig. 5-4a), which are similar to those in the enclaves. In the amphibole-rich clots, the amphibole rim has distinctly higher Al and lower Si contents than the core (Fig. 5-4b), showing a magma reworked signature (Fig. 5-11). The low-Al and high-Si magma reworked isolated amphibole (Figs. 5-4b and 5-11) may be derived from the disaggregation of amphibole-rich clots or transformed from isolated residual pyroxene just as in the enclaves.

5.6.2.7. Geochemical signatures

The Harker plots of the Tongshanling granodiorite and its microgranular enclaves show excellent linearities (Fig. 5-13). This phenomenon coincides with the restite model and was explained to be result from progressive separation of melt and restite (White and Chappell, 1977; Chappell et al., 1987). Previous studies showed that the microgranular enclaves have quite consistent evolved Sr-Nd and zircon Hf isotopic compositions with their host granodiorite, with both the enclaves and granodiorite having respective $(^{87}Sr/^{86}Sr)_i$ ratios of 0.710 – 0.711

and 0.709 – 0.711, ε_{Nd} (t) values of –6.7 – –5.0 and –6.9 – –4.2, and zircon ε_{Hf} (t) values of –11.5 – –6.9 and –12.2 – –6.9 (Jiang et al., 2009; Zhao et al., 2016b; Huang et al., 2017a). They are distinct from those mantle-derived enclaves which have more juvenile isotopic signatures than the host granitoids (e.g., Yang et al., 2004, 2007; Zhao et al., 2010; Cheng et al., 2012; Fu et al., 2016). The almost contemporaneous mantle-derived mafic rocks adjacent to the Tongshanling intrusion show notably more juvenile isotopic compositions than the Tongshanling granodiorite and its enclaves, such as the Huziyan high-Mg basalt [ca. 150 Ma, $(^{87}Sr/^{86}Sr)_i$: 0.705 – 0.706, ε_{Nd} (t): –1.3 – +0.7], Huilongxu lamprophyre [ca. 170 Ma, $(^{87}Sr/^{86}Sr)_i$: 0.704 – 0.705, ε_{Nd} (t): –1.7 – –1.3], and Ninyuan alkaline basalt [ca. 170 Ma, $(^{87}Sr/^{86}Sr)_i$: 0.704 – 0.705, ε_{Nd} (t): +5.4 – +6.1] (Wang et al., 2003b; Li et al., 2004; Jiang et al., 2009). It was impossible to produce these enclaves with the same isotopic signatures as their host granodiorite by crust-mantle magma mixing. These isotopic features are suggestive of a crustal origin for the enclaves and preclude

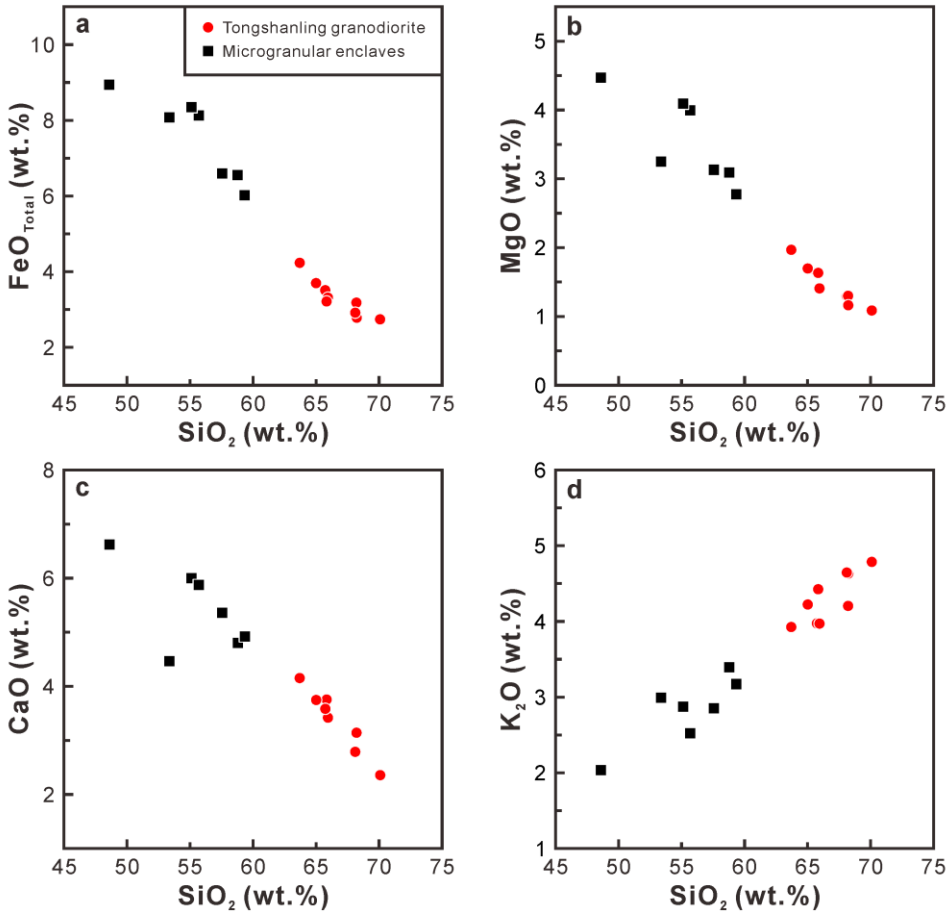

Figure 5-13. Harker plots for (a) FeO_{Total}, (b) MgO, (c) CaO, and (d) K_2O of the Tongshanling granodiorite and its microgranular enclaves showing excellent linearities. The data are from Huang et al. (2017a).

the possibility of mantle-derived mafic magmatic crystallization, which further support the interpretation of the enclaves as reworked restite.

5.6.3. Geothermobarometry

5.6.3.1. Temperature

Numerous mineral thermometers, include amphibole, plagioclase, and biotite, have been proposed to estimate the temperature conditions of magmatic process (e.g., Holland and Blundy, 1994; Henry et al., 2005; Putirka, 2005, 2008, 2016; Ridolfi and Renzulli, 2012). Various thermometers (Table 5-1) were applied for temperature calculation to test the interpretation for enclave origin. Most magma reworked amphibole crystals, except for the intensely reworked high-Al and low-Si isolated amphibole and the rim of clot exterior amphibole grains in the enclaves, were not used for calculation due to their distinct compositional disequilibrium (low Al and high Si contents) with the host melt which would inevitably lead to an underestimation of temperature. The detailed results are listed in Table 5-1. Although there are some differences between different calculation methods and some thermometers yielded overestimated (Ridolfi et al., 2010; Molina et al., 2015; Putirka, 2005; Eq. 4a of Putirka, 2016) and underestimated (Eq. 4b of Putirka, 2016) temperatures (Table 5-1), several general regularities are evident. The temperature recorded by magmatic amphibole decreases progressively from the enclosed ones through the inner and to the outer of isolated ones (Table 5-1; Fig. 5-14a and b). This is in accordance with their petrographic crystallization sequence. The actinolitic core amphibole and the Ca-rich core plagioclase record distinctly higher temperatures than the isolated magmatic amphibole and the magmatic rim plagioclase, respectively (Table 5-1). This is consistent with the restite origin of the actinolitic core amphibole and the Ca-rich core plagioclase. The magmatic rim plagioclase and biotite in the enclaves show consistent temperatures with those in the host granodiorite, respectively (Table 5-1; Fig. 5-14c), suggesting that during the process of magma reworking the enclave plagioclase and biotite were in equilibrium with the host melt. The high-Al and low-Si isolated amphibole and the rim of clot exterior amphibole grains in the enclaves have similar temperatures which are slightly lower than that of the isolated magmatic amphibole (Table 5-1;

Table 5-1. Geothermometry based on mineral chemical compositions of amphibole, plagioclase, and biotite from the Tongshanling granodiorite and its microgranular enclaves

Geothermometer	Temperature[a] (°C)		Reference
	Tongshanling granodiorite	Microgranular enclaves	
Amphibole	MI: 740 – 840; II: 700 – 770; OI: 690 – 760	I: 700 – 750; RCE: 690 – 720	Ernst and Liu (1998)
Amphibole	MI: 828 – 931; II: 818 – 844; OI: 801 – 842	I: 803 – 809; RCE: 783 – 795	Ridolfi et al. (2010)
Amphibole[b]	MI: 751 – 807; II: 683 – 744; OI: 663 – 780	I: 654 – 726; RCE: 662 – 698	Ridolfi and Renzulli (2012)
Amphibole-liquid[c]	MI: 962 – 998; II: 976 – 984; OI: 971 – 989	I: 976 – 984; RCE: 969 – 974	Molina et al. (2015)
Amphibole-liquid	MI: 897 – 919; II: 903 – 908; OI: 893 – 910	I: 879 – 886; RCE: 871 – 887	Equation 4a of Putirka (2016)
Amphibole-liquid	MI: 598 – 616; II: 596 – 603; OI: 594 – 609	I: 595 – 603; RCE: 593 – 602	Equation 4b of Putirka (2016)
Amphibole	MI: 769 – 867; II: 771 – 792; OI: 758 – 789	I: 753 – 759; RCE: 739 – 751	Equation 5 of Putirka (2016)
Amphibole	MI: 772 – 865; II: 769 – 787; OI: 757 – 788	I: 753 – 760; RCE: 740 – 752	Equation 6 of Putirka (2016)
Amphibole	MI: 764 – 858; II: 774 – 793; OI: 763 – 784	I: 755 – 763; RCE: 748 – 764	Equation 8 of Putirka (2016)
Amphibole-liquid	MI: 786 – 877; II: 796 – 809; OI: 788 – 803	I: 784 – 788; RCE: 774 – 785	Equation 9 of Putirka (2016)
Amphibole-plagioclase[d]	MI: 729 – 896; II: 710 – 782; OI: 698 – 764	I: 703 – 740; RCE: 682 – 728	Blundy and Holland (1990)
Amphibole-plagioclase (A)	MI: 709 – 863; II: 700 – 801; OI: 682 – 789	I: 682 – 729; RCE: 679 – 737	Holland and Blundy (1994)
Amphibole-plagioclase (B)	MI: 700 – 849; II: 676 – 775; OI: 661 – 770; CA: 819 – 847	I: 660 – 739; RCE: 662 – 751; CCI: 764 – 848	Holland and Blundy (1994)
Plagioclase-liquid	Core: 1017 – 1030; Intermediate: 990 – 999; Rim: 956 – 972	Core: 1025 – 1031; Intermediate: 994 – 995; Rim: 960 – 973	Putirka (2005)
Biotite	680 – 726	694 – 733	Henry et al. (2005)

Notes: [a] MI: mineral inclusion; II: inner of isolated amphibole; OI: outer of isolated amphibole; CA: core of aggregated amphibole grains; I: isolated amphibole; CCI: core of clot interior amphibole grains; RCE: rim of clot exterior amphibole grains. The low-Al and high-Si isolated amphibole was excluded for temperature calculation. [b] The pressure used for those pressure-dependent thermometers was 3 kbar for the II, OI, I, and RCE amphibole, 5 kbar for the MI amphibole, and 8 kbar for the CA and CCI amphibole. [c] The model liquid used the averaged whole-rock composition of the Tongshanling granodiorite based on the data reported by Huang et al. (2017a). [d] For the amphibole-plagioclase thermometers, the II, OI, I, and RCE amphibole, the MI amphibole, and the CA and CCI amphibole were supposed to be in equilibrium with the rim, intermediate, and core plagioclase, respectively.

Fig. 5-14a and b), indicating that the intensely reworked enclave amphibole was nearly in equilibrium with the host melt. However, they show notably lower temperatures than the early enclosed magmatic amphibole (Table 5-1; Fig. 5-14a and b), reflecting that an evolved host melt was responsible for the reworking of restite enclaves. The prediction of SiO_2 in coexisting

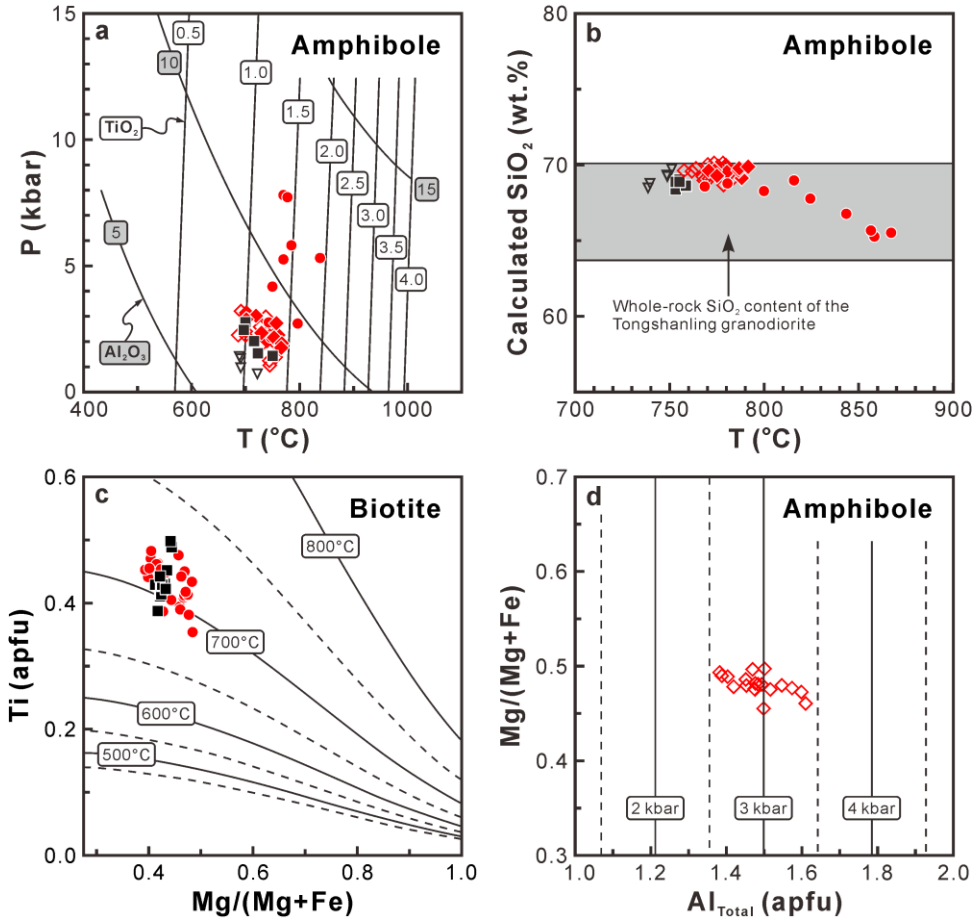

Figure 5-14. Physicochemical conditions estimated by mineral chemical compositions of amphibole and biotite from the Tongshanling granodiorite and its microgranular enclaves. (a) Semiquantitative thermobarometer of amphibole based on Al_2O_3 and TiO_2 contents (after Ernst and Liu, 1998). (b) Temperature and SiO_2 content in coexisting model melt calculated by amphibole composition based on the Equations 5 and 10 of Putirka (2016). (c) Temperature calculated by the Ti-in-biotite geothermometer according to Henry et al. (2005), the dashed curves represent intermediate 50 °C interval isotherms. (d) Pressure calculated by the Al-in-hornblende geobarometer according to Anderson and Smith (1995), the dashed curves represent intermediate 0.5 kbar interval isobars. Legends of amphibole and biotite are the same as Figure 5-4 and Figures 5-7 and 5-8, respectively.

model melt with magmatic amphibole and intensely reworked enclave amphibole (Eqs. 10 and 5 of Putirka, 2016) yielded SiO_2 contents of 65.3 – 70.1 wt.% and 68.4 – 69.7 wt.%, respectively, which match the whole-rock composition of the Tongshanling granodiorite (63.7 – 70.1 wt.%, Huang et al., 2017a) (Fig. 5-14b). It means that these amphibole crystals were basically in equilibrium with the host granodioritic magma and the temperature calculation is meaningful.

5.6.3.2. Pressure

Al-in-hornblende barometer can provide an effective approach to estimate the magma emplacement depth of near-solidus granitic systems with highly restrictive conditions (Schmidt, 1992; Anderson and Smith, 1995; Ridolfi and Renzulli, 2012; Mutch et al., 2016; Putirka, 2016). The Tongshanling granodiorite contains all the necessary equilibrium phases, i.e., hornblende + biotite + plagioclase + orthoclase + quartz + titanite + Fe-Ti oxide + melt + fluid. Based on the calibration proposed by Anderson and Smith (1995), the rim compositions of magmatic isolated amphibole [Mg/(Mg+Fe) > 0.35] in the granodiorite give a pressure of 2.6 – 3.4 (3.0 ± 0.4) kbar (calculated with T = 750 °C) (Fig. 5-14d), corresponding to a deep emplacement depth of 8.6 – 11.2 km (3.3 km/kbar) with an average value of ca. 10 km. This result is consistent with those calculated by the calibration of Mutch et al. (2016) and the Equation 7a of Putirka (2016) on the whole, which are 2.7 – 3.6 kbar and 2.5 – 3.3 kbar, respectively.

The Tongshanling granodiorite belongs to low-temperature granites in terms of the relatively low zircon saturation temperature (Table 5-2) and the occurrence of inherited zircon (Chappell et al., 2000; Miller et al., 2003). The low-temperature and deep-emplaced granodioritic magma is indicative of a relatively high viscosity to a certain extent which is favorable for carrying some residual materials from the source. Different from volcanic rocks in which the anhydrous primary residual minerals, such as pyroxene, can be commonly preserved as phenocrysts, the deep-emplaced magma is beneficial to drive an intense reworking of the residual materials during slow cooling (Chappell et al., 1987). Thus, the residual pyroxene might have been totally transformed into amphibole in such a deep-emplaced magma. This

Table 5-2. Main features of the major Middle-Late Jurassic Cu-Pb-Zn-bearing granodiorites in the Nanling Range, South China

Intrusion	Shuikoushan	Baoshan	Tongshanling	Dabaoshan
Metal association	Pb-Zn-Au-Ag	(Cu, Mo)-Pb-Zn-Ag	Cu(Mo)-Pb-Zn-Ag	Mo(W)-Cu-Pb-Zn-Fe
Dark enclaves	Have not been reported	Observed	Observed	Have not been reported
Lithology	Porphyritic to equigranular biotite granodiorite with a dominant mineralogy of plagioclase + K-feldspar + quartz + biotite ± amphibole			
Accessory minerals	Apatite, zircon, titanite, allanite, rutile, sulfide minerals, and Fe-Ti oxide minerals (mainly magnetite)			
Zircon U-Pb age (Ma)	156.0 ± 1.0, 158.8 ± 1.8, 158.3 ± 1.2	158.0 ± 2.0, 156.7 ± 1.4, 157.7 ± 1.1	163.6 ± 2.1, 160.7 ± 0.5, 160.5 ± 0.9, 159.7 ± 0.8, 162.5 ± 1.0	167.0 ± 2.5, 162.2 ± 0.7, 161.0 ± 0.9, 160.2 ± 0.9, 166.3 ± 2.0, 166.2 ± 2.7, 162.1 ± 1.6
Metallogenic age (Ma) (Molybdenite Re-Os dating)	157.8 ± 1.4	160 ± 2	161.8 ± 1.7, 160.1 ± 0.8, 161 ± 1, 162.2 ± 1.6	163.9 ± 1.3, 164.8 ± 0.8
Evolutionary degree	Low	Low	Low	Low
SiO_2 (wt.%)	59.6 – 65.2	62.6 – 68.8	63.7 – 70.1	64.4 – 72.9
ASI[a]	0.9 – 1.1	0.8 – 1.0	0.9 – 1.0	1.0 – 1.1
$CaO/(Na_2O+K_2O)$	0.3 – 0.8	0.3 – 0.9	0.3 – 0.7	0.2 – 0.8
Mg/(Mg+Fe)	0.4 – 0.6	0.4 – 0.6	0.4 – 0.5	0.3 – 0.7
Rb/Sr	0.2 – 0.4	0.5 – 2.9	0.4 – 1.3	1.2 – 2.1
δEu[b]	0.8 – 1.0	0.6 – 0.8	0.6 – 1.0	0.6 – 0.8
LREE/HREE	8.7 – 16.1	7.0 – 10.6	5.1 – 11.3	10.3 – 18.0
ΣREE (ppm)	120 – 234	124 – 271	82 – 189	134 – 236
HFSE[c] (ppm)	229 – 267	198 – 282	165 – 264	175 – 284
T_{Zr}[d] (°C)	726 – 775	722 – 760	738 – 772	739 – 774
$(^{87}Sr/^{86}Sr)_i$	0.710 – 0.711	0.710 – 0.712	0.709 – 0.711	0.704 – 0.714
$\varepsilon_{Nd}(t)$ value	–6.6 – –5.9	–7.3 – –5.0	–6.9 – –4.2	–8.2 – –6.8
Zircon $\varepsilon_{Hf}(t)$ value	–10.8 – –7.9	–12.0 – –9.2	–12.2 – –6.9	–11.8 – –7.5
References	Huang et al. (2015); Wang et al. (2003a); Yang et al. (2016); Zuo et al. (2014)	Lu et al. (2006); Wang et al. (2003a); Xie et al. (2013)	Huang and Lu (2014); Jiang et al. (2009); Lu et al. (2015); Wang et al. (2003a); Huang et al. (2017a); Zhao et al. (2016b)	Li et al. (2012b); Mao et al. (2013b); Qu et al. (2014); Huang et al. (2017b); Wang (2010); Wang et al. (2011d)

Notes: [a] Aluminum saturation index, ASI = $n(Al_2O_3)/n(CaO+Na_2O+K_2O)$. [b] $\delta Eu = 2Eu_N/(Sm_N+Gd_N)$. [c] High field strength elements, HFSE = Zr+Nb+Ce+Y. [d] Zircon saturation temperature, T_{Zr} was calculated by the method of Miller et al. (2003).

could account for the absence of residual pyroxene in the Tongshanling granodiorite and its microgranular enclaves.

5.6.4. The model for reworked restite enclave

Based on the nature of reworked restite enclaves with distinct textural and compositional features described above, the formation process of the microgranular enclaves in the Tongshanling granodiorite is deduced as follows (Fig. 5-15).

Stage 1: Formation of granodioritic melt and restite during partial melting. Partial melting of the mafic amphibolitic basement in the lower crust produced a metaluminous and high-K calc-alkaline granodioritic melt coexisted with a primary pyroxene-rich restite that mainly comprised of pyroxene, plagioclase, and also refractory accessory minerals, such as zircon. Most melt was extracted and constituted a granodioritic magma with a few residual materials. There were still a few initial melts maintained in the restite due to its high viscosity.

Stage 2: Preliminary reaction of the restite enclave with the initial melt. Some fragments of restite were carried by the ascending host magma. With the cooling of magma, the inner parts of magmatic zircon were firstly crystallized from the initial melt in the restite enclaves. The pyroxene-rich precursors were transformed into actinolite by progressive hydrogenation from exterior to interior. Some small clots had a more intense reaction with the initial melt and formed magnesio-hornblende and a few biotite in the exteriors. The isolated residual pyroxene was also transformed into magnesio-hornblende with low Al and high Si contents.

Stage 3: Further reaction of the restite enclave with the evolved host melt. The composition of the host melt was gradually evolved with crystallization. Progressive input of the evolved host melt led to a further reaction of the restite enclaves with the melt. This resulted in the formation of the outer parts of magmatic zircon and the magmatic rims around residual Ca-rich plagioclase. The exteriors of most clots had been transformed into magnesio-hornblende. The small clots showed more Al-enriched and Si-depleted compositions of magnesio-hornblende and might have a higher biotite content than the large ones due to the more intense reaction with the melt. Some low-Al and high-Si isolated amphibole crystals were transformed into high-Al and low-Si ones.

Stage 4: Formation of the reworked restite enclave. With the reaction between the restite enclaves and the host magma, the zonal amphibole-rich clots had been formed. The small clots might have been transformed into non-zoning amphibole-rich clots or amphibole-biotite clots. The input of late-stage silica-rich melt from the host magma led to the formation of the poikilitic texture of K-feldspar and quartz in the restite enclaves. After the granodioritic magma had been completely solidified, the reworked restite enclaves were survived as dark

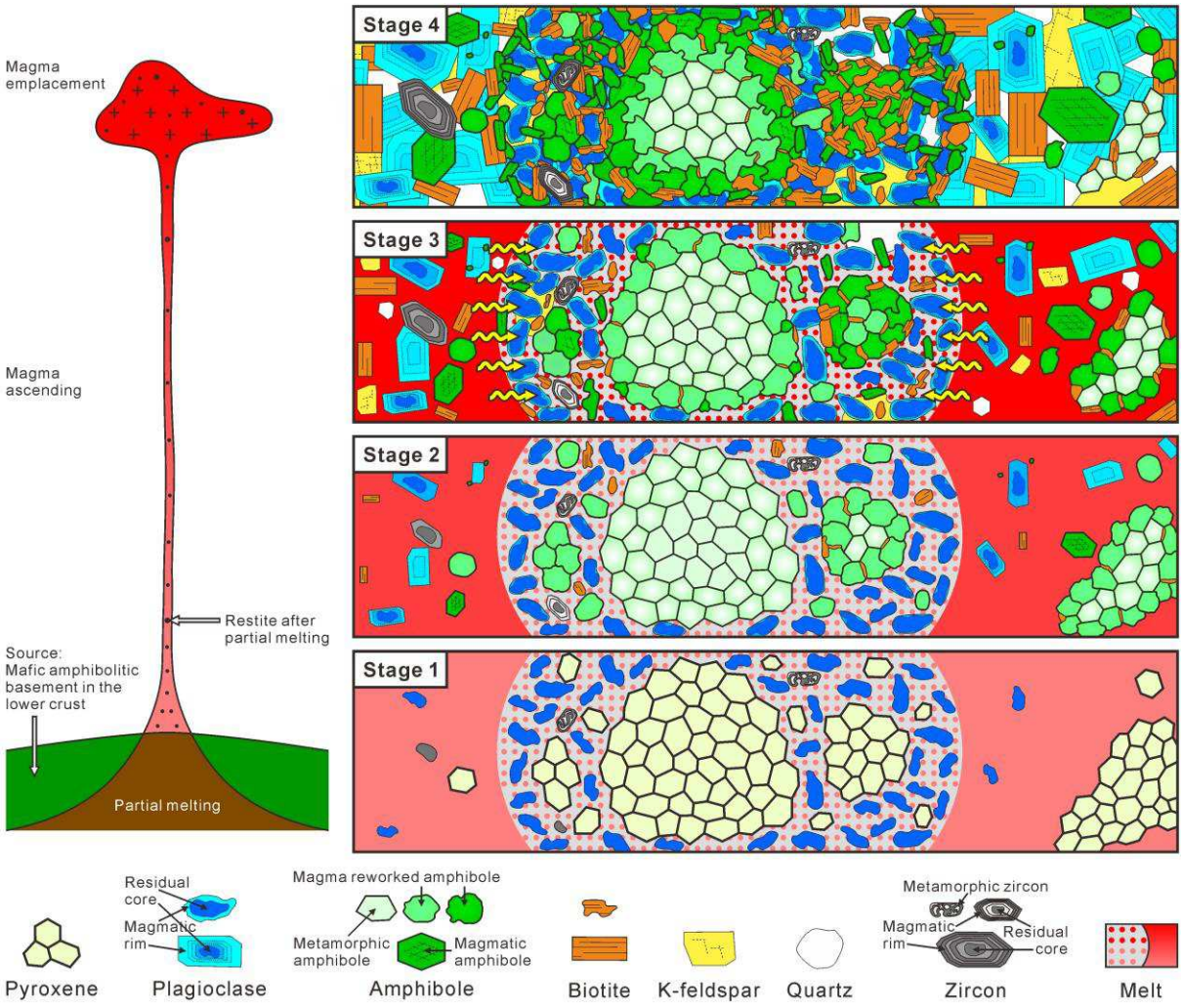

Figure 5-15. Schematic model illustrating the formation process of reworked restite enclave (see detailed description in the text). In the right diagram, the center and the surrounding parts show the evolutionary processes of the restite enclave and the host granodioritic magma, respectively. To better explain this model, the melt content in the enclave (spots in the center part of the right diagram) and the zircon size have been magnified. For the magma reworked amphibole, the deeper colored ones have a more intense reaction with the melt and higher Al contents than the paler colored ones.

microgranular enclaves in the host granodiorite.

5.7. Petrogenetic implications

Restite may provide an important indication for the source nature of the host granitoids since it is remnant of refractory material after partial melting of the source rocks. Because the Tongshanling microgranular enclaves are restite which has been partially modified by the host granodioritic magma, the primary restite should be more mafic than the dioritic compositions. The pyroxene-rich precursors of the amphibole-rich clots, which have silica-poor compositions and mainly consist of pyroxene and Ca-rich plagioclase, may represent the primary restite from the source after partial melting. To produce such a composition of primary restite and a granodioritic magma showing I-type features, the source should have a relatively mafic composition, such as amphibolite (e.g., Chen et al., 1990; Sial et al., 1998; Stephens, 2001).

Dehydration melting of amphibolite can generate metaluminous granodioritic melts with a pyroxene-rich restite at pressure lower than 10 kbar (Beard and Lofgren, 1991; Johannes and Holtz, 1996), whereas, water-saturated melting of amphibolite will produce strongly peraluminous melts with a restite dominated by amphibole (Beard and Lofgren, 1991). A pressure estimation of granulitic mafic xenoliths (8.8 – 12.4 kbar; Dai et al., 2008) in the Huziyan basalt (ca. 150 Ma), which occurs at 20 km north-northeast to the Tongshanling intrusion, suggests that the mafic amphibolitic basement should be located at a depth corresponding to a pressure lower than 8.8 kbar. Therefore, dehydration melting of amphibolite at pressure lower than 8.8 kbar was in all probability responsible for the origin of the metaluminous Tongshanling granodiorite. The zircon Hf model ages of the Tongshanling granodiorite and its microgranular enclaves (1.5 – 2.1 Ga and 1.6 – 2.0 Ga, respectively, both with a peak value of 1.75 Ga; Jiang et al., 2009; Zhao et al., 2016b; Huang et al., 2017a) indicate that the amphibolitic basement was mainly formed in Paleoproterozoic. The occurrence of the Tianjinping amphibolite (1766 ± 19 Ma; Li, 1997) from the basement of the Cathaysia Block confirms the existence of the Paleoproterozoic amphibolitic basement in the Nanling Range.

It is noteworthy that, the lower crust of South China, especially the mafic amphibolitic

basement, has fertile ore-forming metals. For instance, the amphibolites of the Tianjinping Formation and the Mayuan Group have Cu contents of 57.7 ppm and 66.5 ppm, and Zn contents of 119 ppm and 118 ppm, respectively (Li, 1997), which are distinctly higher than those of the middle and upper crusts in South China (Gao et al., 1998) and are also higher than those of the lower crust reported by Rudnick and Fountain (1995). Such a fertile source is beneficial to the formation of Cu-Pb-Zn-bearing granodiorites in the Nanling Range.

The Middle-Late Jurassic Cu-Pb-Zn-bearing granodiorites in the Nanling Range have similar mineralogical and geochemical features (Table 5-2). They are generally hornblende-bearing, metaluminous and high-K calc-alkaline rocks with high Mg/(Mg+Fe) ratios and low evolutionary degrees, and show characteristics of I-type granites (Table 5-2). They also have similar evolved Sr-Nd and zircon Hf isotopic compositions (Table 5-2). With regard to the previously proposed two different genetic models for these Cu-Pb-Zn-bearing granodiorites, i.e., crust-mantle mixing and partial melting of the mafic lower crust, our research stands by the latter and provides inspiration for the further study.

Chapter 6. Magma emplacement-induced structural control on skarn formation

6.1. Introduction

Skarn deposits, as one of the most important mineralization types for a lot of metals, have attracted a great interest of numerous geologists. Previous studies mainly focused on metasomatism, zonation, skarn mineralogy, geochemistry, and petrogenesis (Meinert et al., 2005). However, little attention has been paid to structural control (e.g., Love et al., 2004; Li et al., 2014a; Ducoux et al., 2017), especially the magma emplacement related one, on skarn formation. Magma emplacement-induced structural control is crucial to understanding the process of skarnization and can provide important information for prospecting and exploration. In South China, multiple-aged granitoids and polymetallic deposits are widely developed (Figs. 2-8–2-10, Zhou et al., 2006a; Chen et al., 2013; Mao et al., 2013a). Although numerous geochronological and geochemical studies have revealed that most mineral deposits are genetically associated with granitoids (e.g., Yang et al., 2014; Zhang et al., 2015a; Chen et al., 2016; Zhao et al., 2016b; Xiang et al., 2018), the detailed connecting process between them is still unclear. The magma-dynamic study of Liu et al. (2018) revealed that the emplacement of the Jurassic granitoids in South China was not driven by tectonic deformation. Therefore, these granitoids are good cases for the study of local wall-rock deformation induced by volume force involved in the emplacement of granitoids. This study takes the Middle-Late Jurassic Tongshanling Cu-Pb-Zn deposit in southern Hunan Province of China (Fig. 6-1a) as an excellent example to decipher magma emplacement-induced structural control on skarn formation.

6.2. Regional structural analysis

The exposed strata in the Tongshanling area are dominated by Devonian and Carboniferous carbonate rocks (Fig. 6-1). These strata have been deformed and developed a lot of north-south to northeast-southwest striking folds and faults (Fig. 6-1). The folds are

composed of alternatively appeared anticlines and synclines which are cut through by the faults (Fig. 6-1b and c). A vast majority of these faults show an east to southeast vergent thrusting or a sinistral strike-slip sense and several ones are normal faults (Fig. 6-1b–d). During Middle-Late Jurassic, the Tongshanling granodioritic magmas intruded into the carbonate strata as stock (Fig. 6-1b and c) and then caused Cu-Pb-Zn mineralization.

6.2.1. Normal fault

Both the normal faults to the west and east of the Tongshanling intrusion strike consistently with the regional thrust faults and dip to west to northwest (Figs. 6-1b and 6-2). The carbonate rocks adjacent to these normal faults do not show any deformation except for brittle fractures (Fig. 6-2). At a southern outcrop of the western normal fault, automorphic calcite accumulates along the fault plane as vein steeply cutting the bedding and broken by a later sinistral strike-slip movement (Fig. 6-2a–c). At a northern outcrop, the calcite mainly distributes in the footwall of the normal fault (Fig. 6-2d). For the eastern normal fault, two generations of calcite are recognized, with the late calcite being more coarse-grained, automorphic and pure, and having a lower hardness than the early one (Fig. 6-2e–l). Some wall-rock breccias are observed in the first-generation calcite from a southern outcrop (Fig. 6-2l).

6.2.2. Contact zone

The carbonate rocks in the contact zone close to the Tongshanling intrusion have been strongly marbleized and deformed (Fig. 6-3). The recrystallized calcite crystals mostly have an elongated shape (Fig. 6-3c, e, and h). In the northeastern contact zone, the foliation dips to north to northeast, cuts the bedding with a steeper angle, and shows a sense of normal motion (Fig. 6-3a, b, and d). From proximal to distal, the intensity of marbleization and the density of foliation gradually decrease and finally to the undeformed carbonate strata (Fig. 6-3a). The southern contact zone exhibits distinctly stronger marbleization and deformation with a higher density of foliation than the northeastern contact zone (Fig. 6-3). In the southern contact zone, the bedding is invisible and the foliation is wrinkled near the intrusion (Fig. 6-3g). Notably, the foliation rotates around the southern boundary of the intrusion and is parallelized to the

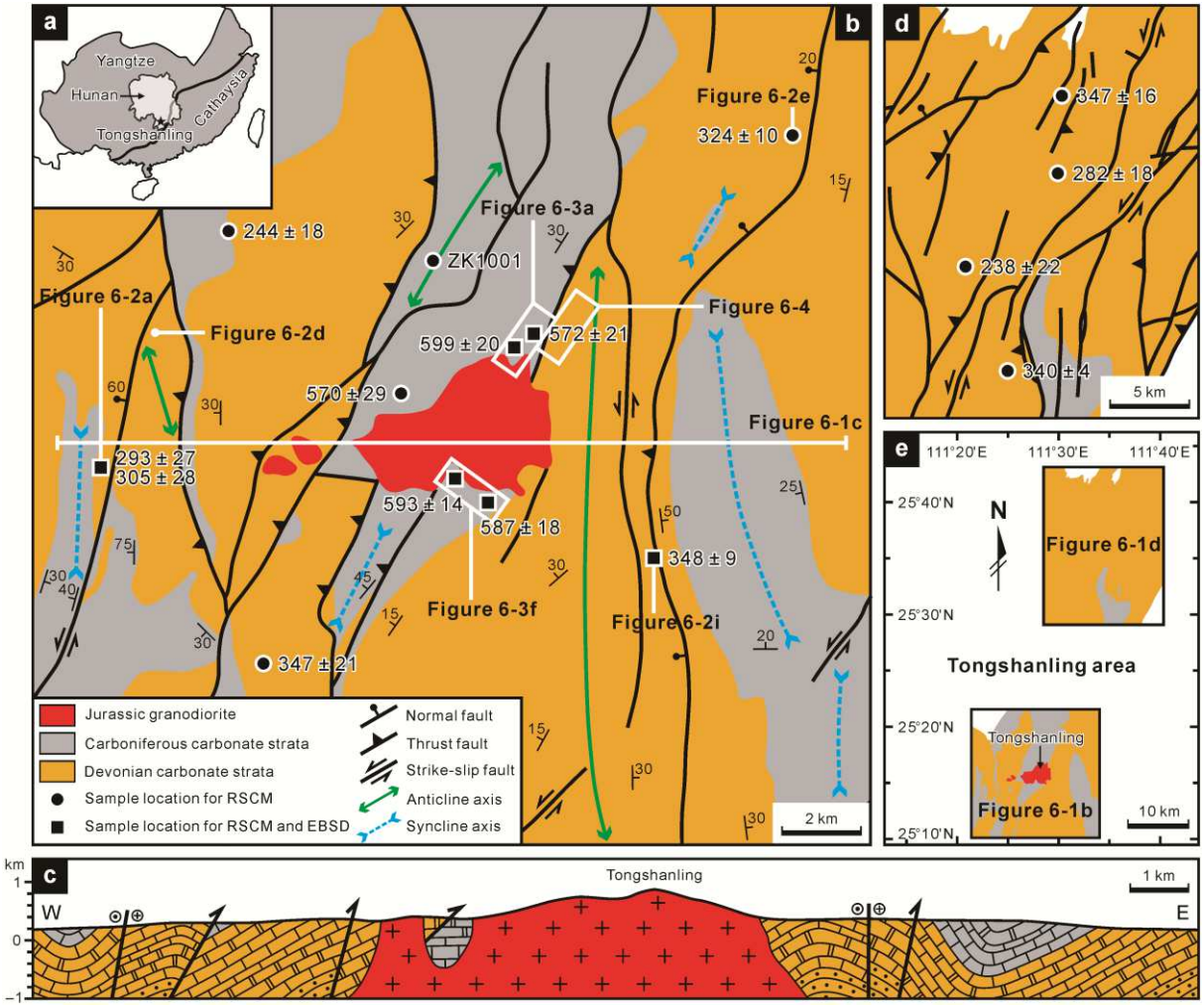

Figure 6-1. Simplified geological map of the Tongshanling area (modified after Regional Geological Survey Team of Hunan Geology Bureau, 1975a, 1975b) showing the sample locations for Raman spectroscopy of carbonaceous material (RSCM) analysis and electron backscatter diffraction (EBSD) mapping. The results of RSCM thermometry are presented as mean value ± standard deviation (°C) in Figure 6-1b and d, the same in the following figures.

contact (Fig. 6-3f, i, and j). The dip angle of foliation in the southern contact zone is larger than that in the northeastern contact zone (Fig. 6-3).

6.3. Deposit geology

The Tongshanling Cu-Pb-Zn deposit occurs in the northeastern concealed contact zone between the granodiorite and carbonate rocks and its peripheral zone (Fig. 6-4). This deposit shows an obvious zonation with a proximal skarn, a distal skarn, and sulfide-quartz veins

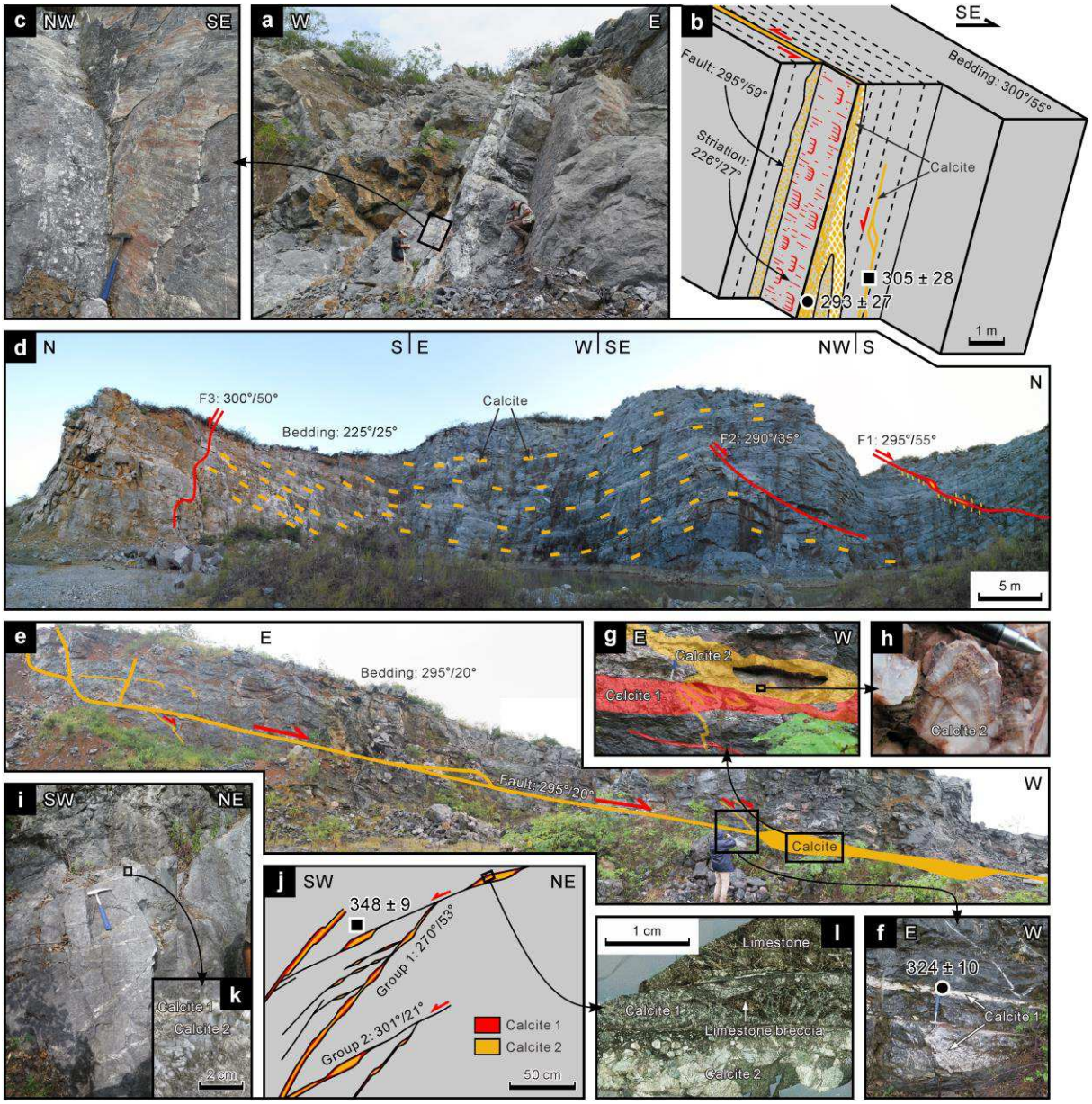

Figure 6-2. Field observations of normal faults (outcrop locations shown in Fig. 6-1b) in the Tongshanling area.

between them (Fig. 6-4). The proximal skarn is distributed in the granodiorite and in the limestone of the Middle Devonian Qiziqiao Formation and can be further divided into massive endoskarn extending along the border of granodiorite and peripheral vein exoskarn (Fig. 6-4). The sulfide-quartz veins mainly occur in the Qiziqiao limestone with minor in the Upper Devonian Shetianqiao limestone (Fig. 6-4). Differently, the distal skarn is stratiform and evidently controlled by the argillaceous limestone of the Upper Devonian Xikuangshan Formation (Fig. 6-4). The distal skarn is not the research object of this study and will not be

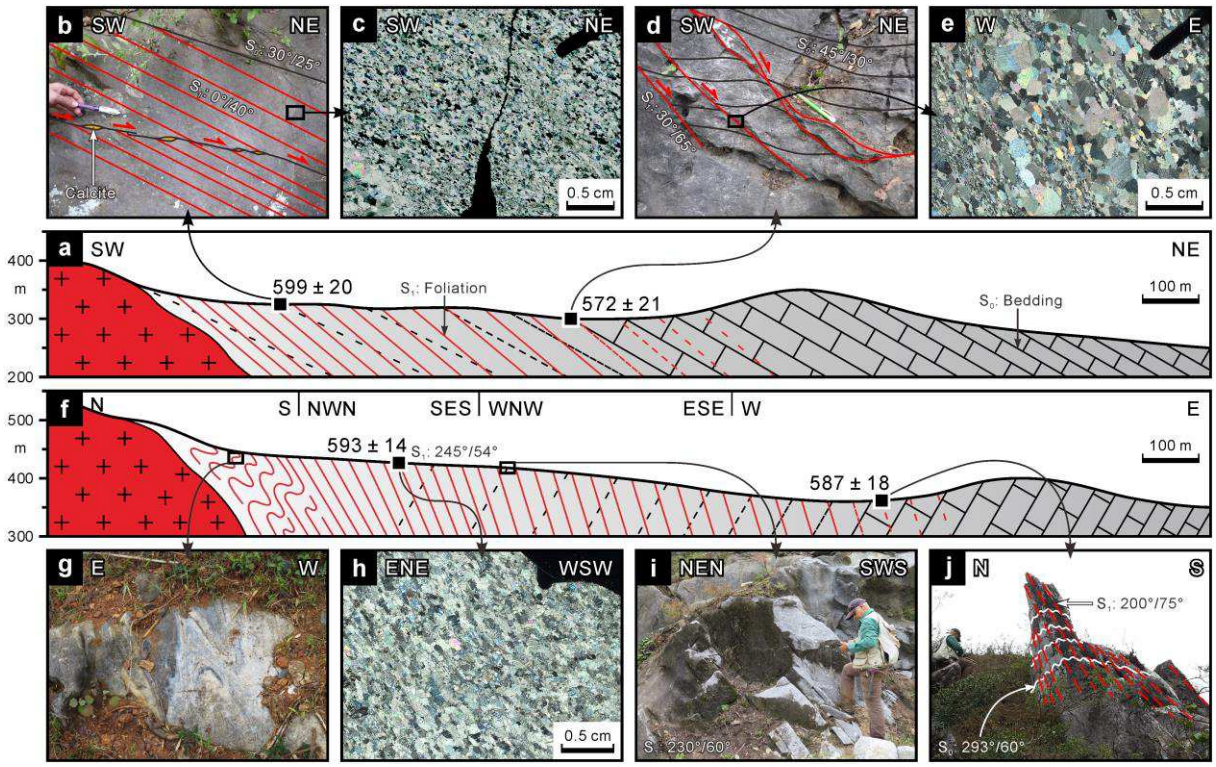

Figure 6-3. Cross sections (section lines shown in Fig. 6-1b) of the (a–e) northeastern and (f–j) southern contact zones from the Tongshanling intrusion to country rocks.

further described and discussed in the following text.

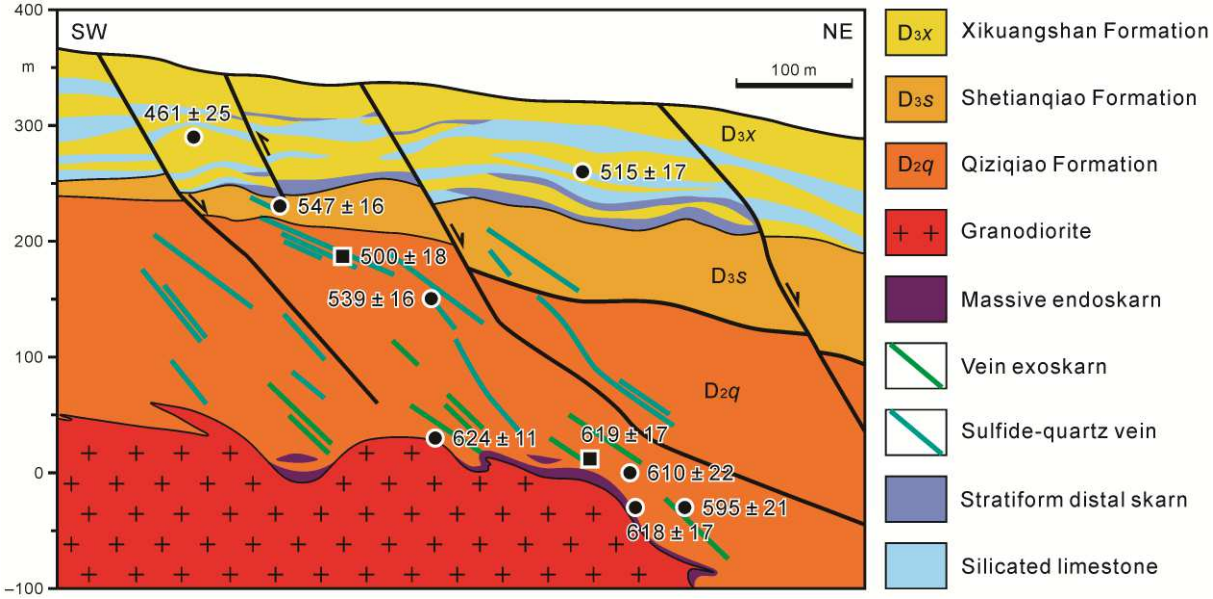

Figure 6-4. Cross section (section line shown in Fig. 6-1b) of the Tongshanling Cu-Pb-Zn deposit (modified after No. 206 Exploring Team of Hunan Metallurgical and Exploring Company, unpub. report, 1975).

6.3.1. Endoskarn

With irregular shapes, the massive endoskarn dominantly consists of garnet and pyroxene with minor retrograde minerals, such as actinolite and epidote. It has a brown color and does not show a clear zonation (Fig. 6-5a). Sulfide ore bodies in the endoskarn are composed of chalcopyrite and pyrrhotite coexisting with abundant quartz and show a banded structure (Fig. 6-5a). The sulfide and quartz bands dip to north to northeast in general (Fig. 6-5a).

6.3.2. Exoskarn

The exoskarn veins, with a width of dozens of centimeters, have a brownish green color on the whole (Figs. 6-5b–c and 6-6a). They cut across the bedding by a steeper angle and

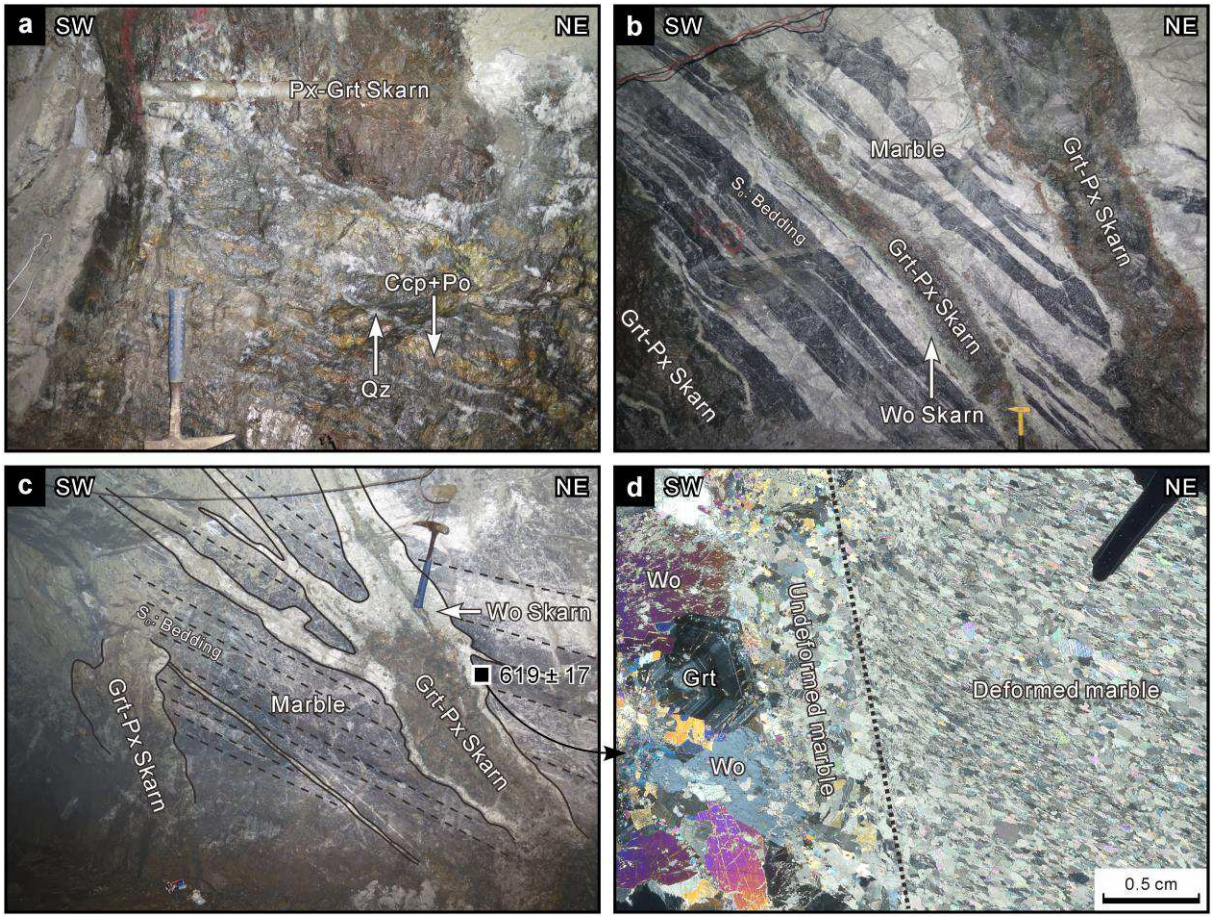

Figure 6-5. Photographs of (a) massive endoskarn, (b and c) vein exoskarn, and (d) deformed country rocks in the Tongshanling Cu-Pb-Zn deposit. Mineral abbreviations: Ccp = chalcopyrite, Grt = garnet, Po = pyrrhotite, Px = pyroxene, Qz = quartz, Wo = wollastonite.

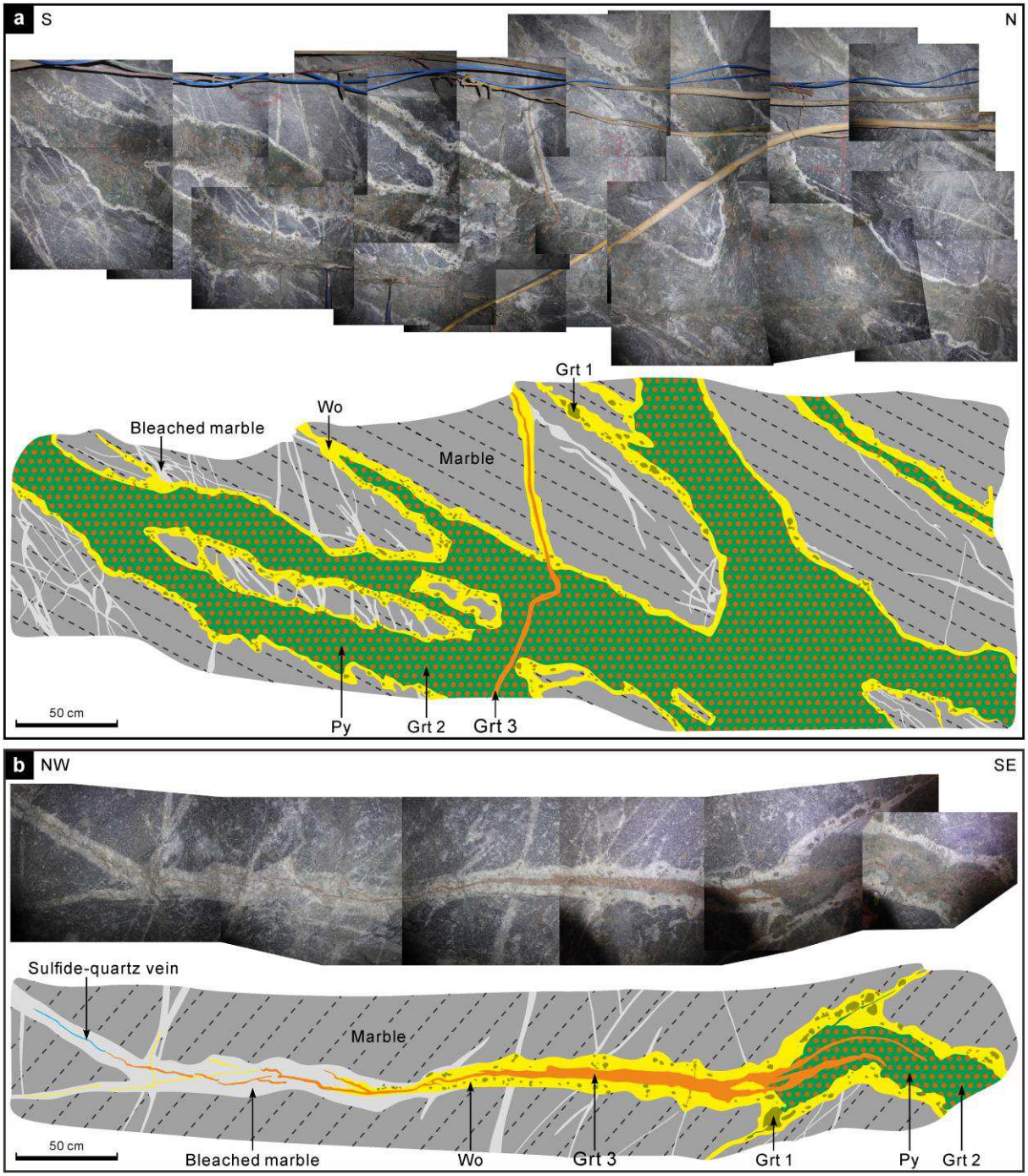

Figure 6-6. Panoramic views of exoskarn in the Tongshanling Cu-Pb-Zn deposit showing skarn zonation and evolution. Mineral abbreviations are the same as Figure 6-5.

uniformly dip to north to northeast (Figs. 6-5b–c and 6-6a). Some parts of the exoskarn veins are parallel to the bedding and construct a steplike profile with the steeper parts (Figs. 6-5c and 6-6a). The country rocks have been strongly marbleized and deformed (Fig. 6-5b–d). These exoskarn veins commonly exhibit a well-developed outward zonation from

garnet-pyroxene through wollastonite to marble (Figs. 6-5 and 6-6). Different from the deformed marble which consists of elongated calcite crystals, the marble envelope of the exoskarn comprises undeformed granular calcite crystals (Fig. 6-5d). Three generations of garnets are distinguished. They are chronologically green-brown disseminated garnet in the wollastonite skarn, brown garnet coexisting with pyroxene, and red-brown vein-like garnet cutting the garnet-pyroxene skarn (Fig. 6-6). Ore minerals are chalcopyrite, sphalerite, galena, pyrrhotite, and pyrite. Vein-like barren quartz occurs in the center of exoskarn (Fig. 6-7a) or cuts through it (Fig. 6-7b). A few sulfide-quartz veinlets appear at the distal end of exoskarn veins (Fig. 6-6b).

6.3.3. Sulfide-quartz vein

The sulfide-quartz veins are a dozen to tens of centimeters in width (Fig. 6-7c and d). They consistently dip to north to northeast and cut the bedding (Fig. 6-7c and d). Compared with the deformed marble close to exoskarn, the wall rocks of sulfide-quartz veins have not been strongly marbleized and deformed (Fig. 6-7c and d). Some outcrops show a sense of normal motion (Fig. 6-7d). Ore minerals are chalcopyrite, sphalerite, galena, pyrite, and arsenopyrite.

6.4. Sampling and analytical methods

Thirty-six carbonate samples from surface and underground outcrops and a drill core (ZK1001) to the north of the Tongshanling intrusion were collected for Raman spectroscopy of carbonaceous material (RSCM) analysis among which eight samples were further selected for electron backscatter diffraction (EBSD) mapping (sample locations shown in Figs. 6-1–6-5). Garnets in the endoskarn and exoskarn were sampled for compositional analysis by electron microprobe (EMP).

RSCM analysis was carried out by a Renishaw InVIA Reflex micro-spectrometer coupled to a DM2500 Leica microscope at Bureau de Recherches Géologiques et Minières (BRGM), Orléans, France. An argon laser with λ_0 = 514.5 nm was used as exciter. Instrument control and Raman measurements were performed by the Renishaw Wire 3.4 software. Before analysis, the spectrometer was calibrated using the 520.4 cm^{-1} line of silicon. To check

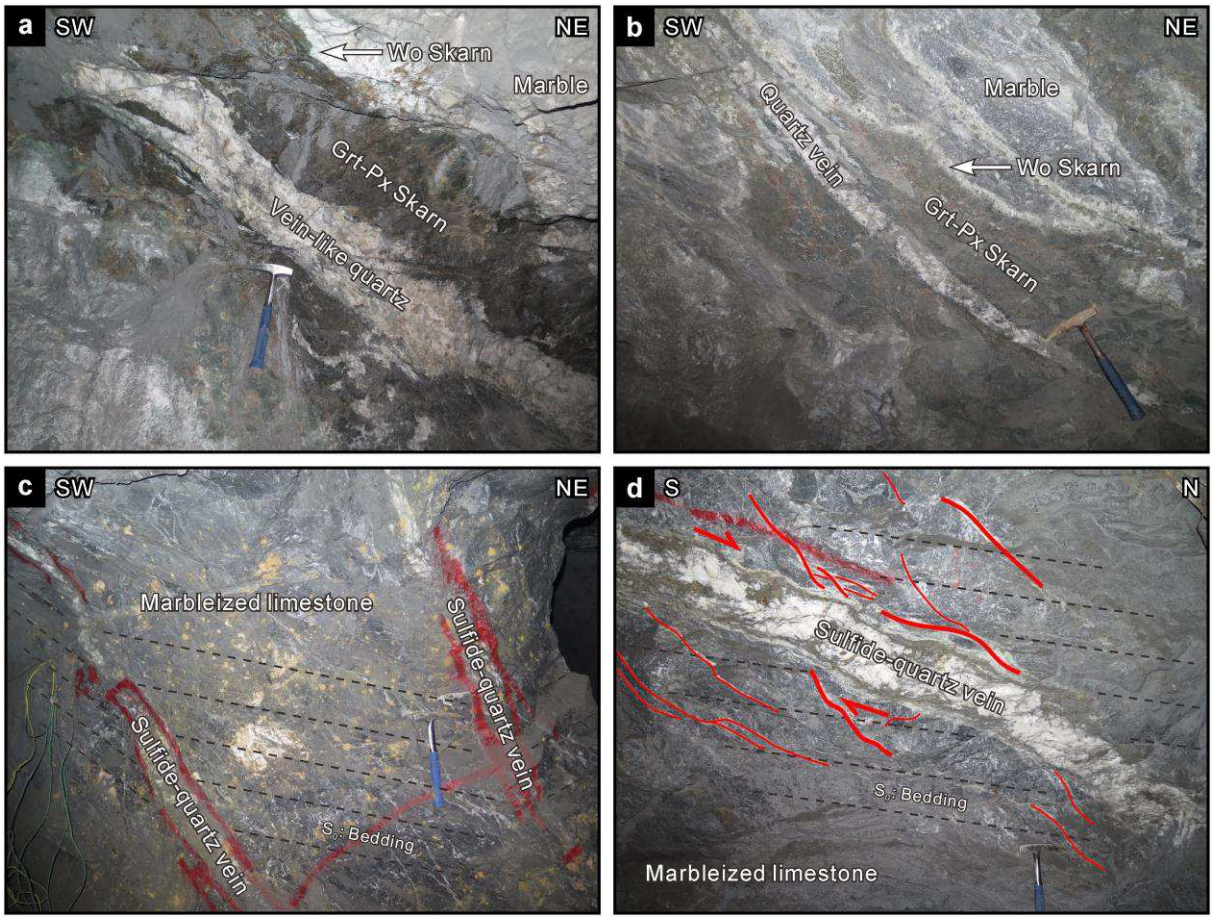

Figure 6-7. Photographs of vein-like quartz (a) in the center of exoskarn or (b) cutting through it and (c and d) sulfide-quartz veins in the peripheral strata in the Tongshanling Cu-Pb-Zn deposit. Mineral abbreviations are the same as Figure 6-5.

within-sample structural heterogeneity, at least 10 spectra were recorded for each sample. Each spectrum was acquired through 5 – 10 accumulations and an acquisition time of 10 – 20 s. The off-line data were processed using the program PeakFit v4.06 with a Voigt function.

EBSD mapping was executed by a CamScan X500FE CrystalProbe equipped with an HKL NordlysNano EBSD detector and an X-Max^N energy dispersive spectrometry (EDS) detector at Géosciences Montpellier, France. The operating conditions included an accelerating voltage of 20 kV and a working distance of 25 mm. A mapped area from 1.2 × 1.7 mm to 12.6 × 16.5 mm and a step size between 1 μm and 18 μm were used for different samples depending on their grain sizes. The acquired data were processed using the CHANNEL5 software.

Garnet was analyzed by a JEOL JXA-8100M EMP at the State Key Laboratory for

Mineral Deposits Research (LAMD), Nanjing University (NJU), China. The analytical conditions included an accelerating voltage of 15 kV, a beam current of 20 nA with beam diameter of 1 μm, and counting times of 10 s for all elements and 5 s for background. The collected data were corrected by the ZAF procedures. Calibration was performed using natural minerals and synthetic compounds.

6.5. Results

6.5.1. RSCM thermometry

Raman spectra of carbonaceous material are shown in Figure 6-8. Some parameters of the Raman spectra are listed in Appendix 6-1. Calculation of temperatures is based on the functions of Beyssac et al. (2002) and Lahfid et al. (2010). The unfractured and undeformed carbonate strata far away from the Tongshanling intrusion have undergone temperatures from 238 °C to 347 °C (Fig. 6-1b and d) with a mean value of 300 °C. The undeformed limestone adjacent to the regional normal faults gives temperature of 293 – 348 °C (Figs. 6-1b and 6-2b,

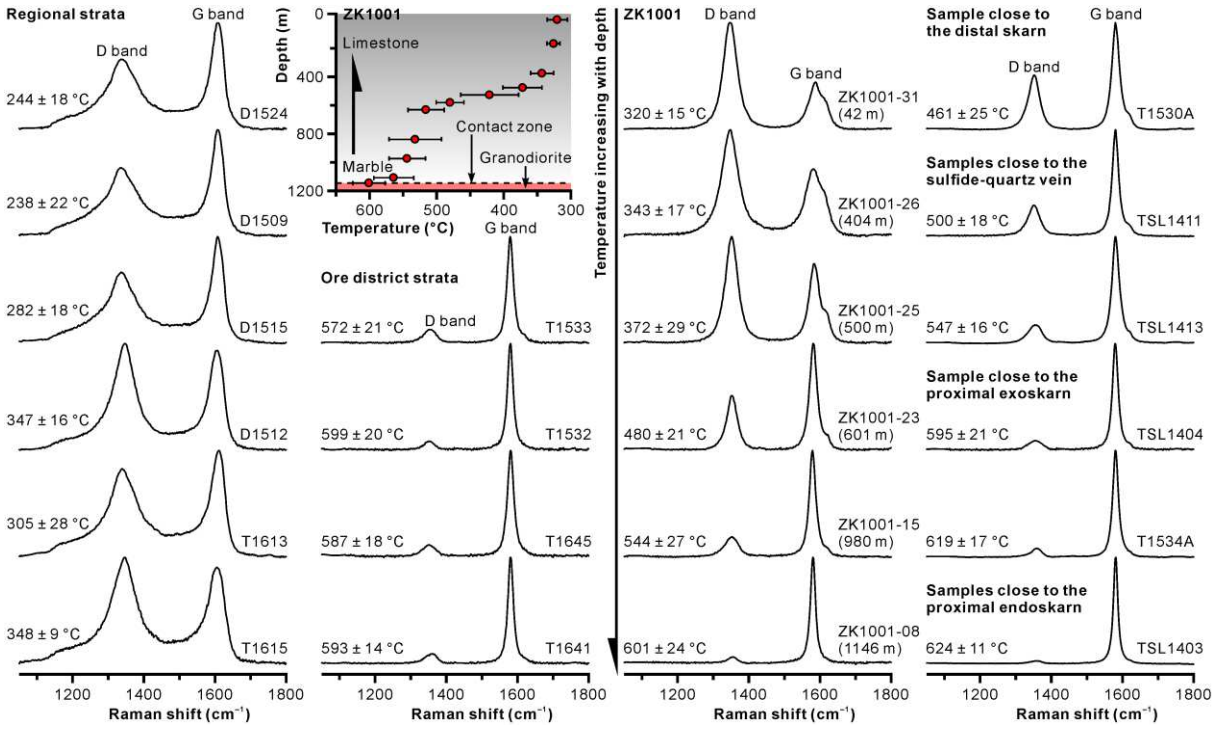

Figure 6-8. Raman spectra of carbonaceous material in carbonate rocks from the Tongshanling Cu-Pb-Zn deposit and its adjacent area and temperatures calculated by the RSCM thermometry.

f, j). The temperatures obtained by the deformed marble in the contact zone range from 570 °C to 599 °C (Figs. 6-1b and 6-3a, f). A gradational transition of lithology from marble at the contact zone to limestone near the surface with progressively decreasing temperatures from 601 °C to 320 °C is revealed by the drill core ZK1001 (Fig. 6-8). In the Tongshanling Cu-Pb-Zn deposit, from proximal to distal, the metamorphosed carbonate rocks close to the endoskarn, exoskarn, sulfide-quartz veins, and distal skarn underwent temperatures of 618 – 624 °C, 595 – 619 °C, 500 – 547 °C, and 461 – 515 °C, respectively (Fig. 6-4).

6.5.2. EBSD mapping

EBSD analytical results of carbonate samples are shown in Figure 6-9. Near the regional normal faults, the calcite grains have no shape preferred orientation (SPO) and show a weak crystallographic preferred orientation (CPO) by the smaller grains but not by the larger grains (Fig. 6-9a and b). The elongated calcite and dolomite grains in the contact zone have an obvious SPO (Fig. 6-9c–g). They mostly show a CPO with their c-axis aligned with the long axis of the grains and clockwise oblique to the Z-axis of the sample frame (Fig. 6-9c–g). The fine-grained samples (Fig. 6-9c and f–g) have a more well-defined c-axis maximum than the coarse-grained samples (Fig. 6-9d and e). In the fine-grained samples, the c-axis maximum of the smaller grains is more confined than that of the larger grains (Fig. 6-9c and f–g). In the coarse-grained samples, the c-axes of the larger grains are roughly normal to the XZ plane (Fig. 6-9d and e). The calcite grains in a calcite (20 %)-dolomite (80 %) composite sample from the southern contact zone have distinctly more perpendicular c-axes to the XZ plane than the dolomite grains (Fig. 6-9f and g). With a strong SPO, the calcite adjacent to the exoskarn at underground gallery shows a consistent CPO (Fig. 6-9h) with the calcite in the northeastern contact zone at surface (Fig. 6-9c). The calcite near the peripheral sulfide-quartz veins does not have a SPO but shows a CPO by the smaller grains, whereas, not by the larger ones (Fig. 6-9i).

6.5.3. Garnet composition

Representative EMP analyses of garnet are listed in Appendix 6-2. Both the garnets in the endoskarn and exoskarn are grandite (Py+Al+Sp < 7.8 %) (Fig. 6-10). The composition of

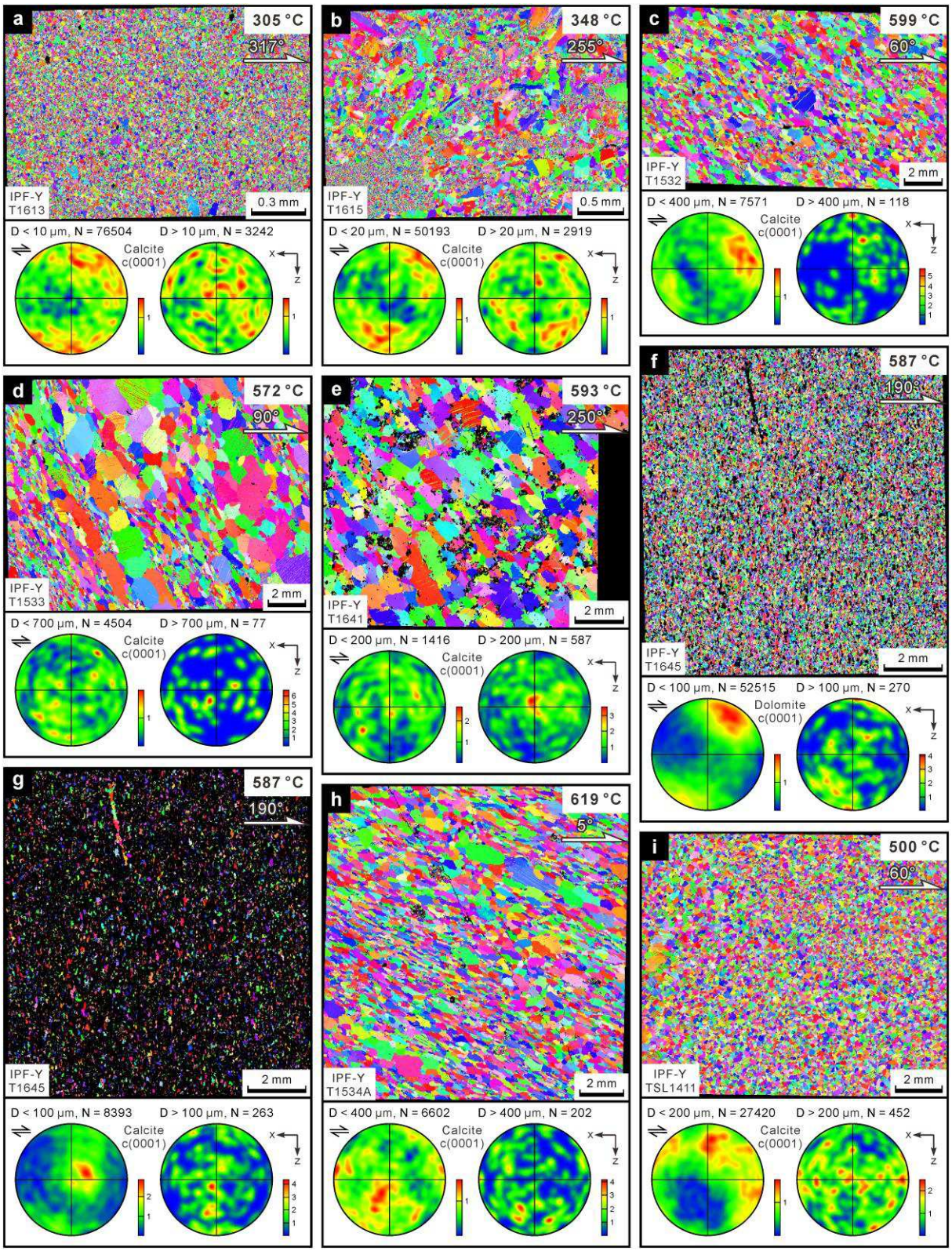

Figure 6-9. Crystallographic preferred orientation (CPO) of calcite (dolomite) from the Tongshanling Cu-Pb-Zn deposit and its adjacent area determined by EBSD mapping. All pole figures are equal-area lower hemisphere projections based on one point per grain. D and N are the size and number of grains, respectively. (a and b)

Undeformed limestone adjacent to the western (T1613) and eastern (T1615) normal faults, respectively. (c–d and e–g) Deformed marble in the northeastern (T1532 and T1533) and southern (T1641 and T1645) contact zones, respectively. (h and i) Metamorphosed carbonate rocks close to the exoskarn (T1534A) and sulfide-quartz vein (TSL1411), respectively.

garnet in the endoskarn ranges from $Gr_{57.8}Ad_{38.7}$ to $Gr_{65.2}Ad_{30.3}$ (Fig. 6-10a). Three generations of garnets in the exoskarn sequentially have respective composition of $Gr_{7.3}Ad_{91.4}$ – $Gr_{20.4}Ad_{78.2}$, $Gr_{20.2}Ad_{75.8}$ – $Gr_{29.8}Ad_{66.7}$, and $Gr_{59.0}Ad_{38.0}$ – $Gr_{68.7}Ad_{29.1}$, with progressively increasing Al and decreasing Fe contents (Fig. 6-10b). The composition of the latest garnet in the exoskarn is consistent with that of the garnet in the endoskarn (Fig. 6-10).

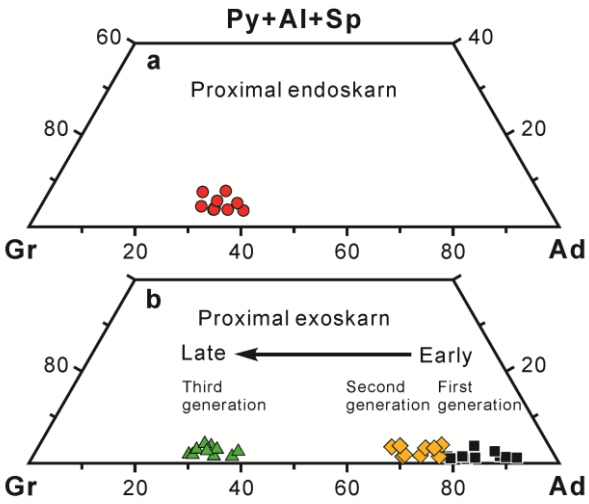

Figure 6-10. Compositions of garnets from the endoskarn and exoskarn of the Tongshanling Cu-Pb-Zn deposit. Mineral abbreviations: Ad = andradite, Al = almandine, Gr = grossularite, Py = pyrope, Sp = spessartine.

6.6. Discussion

The Early-Middle Triassic intracontinental deformation in the eastern South China Block has been generally recognized as a northwest-southeast compression associated with a series of northeast-southwest striking folds and thrust faults (Wang et al., 2013; Shu et al., 2015). In the Tongshanling area, the Early-Middle Triassic intracontinental compression caused folding and thrusting of the Devonian and Carboniferous carbonate strata which were further intruded

by the Middle-Late Jurassic granodioritic magmas (Fig. 6-1b and c). The regional west- to northwest-dipping normal faults (Figs. 6-1b and 6-2) should be formed under an extensional setting most probably induced by the Late Triassic to Early Jurassic decompression and/or the subduction of the Paleo-Pacific plate rather than the emplacement of the Tongshanling intrusion. The calcite distributed along or in the footwall of the normal faults (Fig. 6-2) may be generated by a later decompressive precipitation after an earlier pressure dissolution. At the eastern normal fault, the first-generation calcite is fine-grained with a higher hardness and contains some wall-rock breccias, whereas the second-generation calcite is automorphic, coarse-grained and pure (Fig. 6-2c and d), indicating a transition from a relatively compressive setting to a relatively extensional setting. This is in accordance with the regional tectonic evolution from Triassic compression to Jurassic extension.

The organization degree of carbonaceous material is not affected by retrogression, thus the RSCM thermometry records the peak metamorphic temperature (Beyssac et al., 2002). Since the carbonate strata far away from the Tongshanling intrusion have not been influenced by magmatic heating and also have not been deformed by regional metamorphism, the temperature recorded by the strata (ca. 300 °C) may arise from burial metamorphism corresponding to a depth of ca. 10 km (calculated by a gradient of 30 °C/km). This is comparable to the emplacement depth of the Tongshanling granodiorite (ca. 10 km) calculated by Al-in-hornblende barometer (Huang et al., 2018). The slightly higher temperature of the fractured limestone could result from local heating during normal faulting.

Combining the results of RSCM thermometry and EBSD mapping with structural analysis, it is confidently concluded that the wall-rock metamorphism and deformation around the Tongshanling intrusion was induced by magma emplacement. The critical evidence is listed as follows: (1) the wall-rock metamorphism and deformation are limited in the contact zone (Fig. 6-3); (2) the metamorphic temperature and the marbleization degree of wall rocks gradually decrease outward from the contact zone (Figs. 6-3 and 6-8); (3) the foliation of deformed marble, which cuts the bedding and shows a sense of normal motion, keeps in parallel with the intrusion boundary and dips outward (Fig. 6-3); (4) the density of foliation gradually decreases outward from the contact zone (Fig. 6-3); (5) different from the

undeformed calcite close to the regional normal faults, the calcite in the contact zone has much stronger SPO and CPO (Fig. 6-9). Compared with the northeastern contact zone, the southern contact zone has a much stronger intensity of marbleization and deformation with steeper-dipping foliation (Fig. 6-3), indicating that the magma conduit of the Tongshanling intrusion should be located in the southern part.

Rheological behaviour of naturally and experimentally deformed carbonates and microstructural evolution of calcite and dolomite during deformation have been the topics of numerous studies (e.g., Pieri et al., 2001; Barnhoorn et al., 2004; Oesterling et al., 2007; Seaton et al., 2009; Kushnir et al., 2015; Berger et al., 2016). Mineral composition, grain size, temperature, and strain greatly affect the deformation mechanism of carbonate minerals. The clockwisely oblique CPO of deformed calcite in the contact zone (Fig. 6-9c–g) is indicative of a high shear strain with subgrain rotation recrystallization and grain size reduction (as demonstrated by Pieri et al., 2001; Barnhoorn et al., 2004; Oesterling et al., 2007). The weaker CPO of the coarse-grained samples may result from post-deformational grain growth at elevated temperature (> 500 °C), possibly over a prolonged period of time. Although the experimental observation of Barnhoorn et al. (2005) revealed that post-deformational annealing does not produce a significant change of CPO in a short time (not exceed 24 hours), a natural case of Seaton et al. (2009) proved that long-term grain growth at high temperature can destroy pre-existing CPO. The deformation mechanism of calcite-dolomite composite is strongly controlled by strain partitioning between calcite and dolomite (Kushnir et al., 2015). During high-temperature deformation, dolomite is generally stronger than calcite with a dominant deformation mechanism of dislocation creep, whereas calcite undergoes dislocation creep and dynamic recrystallization (Kushnir et al., 2015; Berger et al., 2016). The dolomite in the calcite-dolomite composite sample from the southern contact zone was deformed mainly by c <a> and r slip systems (Fig. 6-9f), whereas the calcite was deformed dominantly by r <a> and f slip systems (Fig. 6-9g).

Previous molybdenite Re-Os dating revealed that the exoskarn and sulfide-quartz veins were formed contemporaneously with the emplacement of the Tongshanling intrusion (Huang and Lu, 2014; Lu et al., 2015). In comparison with the endoskarn garnet, the compositional

evolution of the three generations of exoskarn garnet (Figs. 6-6 and 6-10) indicates a progressive increase of magmatic components during the formation of the exoskarn and implies a genetical link between the exoskarn and the Tongshanling granodiorite. The exoskarn and sulfide-quartz veins strike and dip consistently with the foliation in the contact zone and cut the bedding (Figs. 6-5b–c and 6-7c–d). Both the results of RSCM thermometry and EBSD mapping of deformed marble adjacent to the exoskarn veins are comparable to those of deformed marble in the contact zone at surface (Figs. 6-8 and 6-9). The peripheral sulfide-quartz veins are actually late-stage productions during the evolution of skarn system (Figs. 6-6b and 6-7a–b) and their wall rocks were marbleized under a lower temperature (Fig. 6-8) and were deformed with a weaker CPO but no SPO (Fig. 6-9i). Therefore, the exoskarn and sulfide-quartz veins are evidently controlled by the magma emplacement-induced wall-rock deformation. The undeformed marble envelope of the exoskarn (Fig. 6-5d) may be formed by chemical recrystallization of the deformed marble during metasomatism and is suggestive of a post-deformational skarnization. The sulfide and quartz bands of the endoskarn (Fig. 6-5a), with the same strike-dip as the exoskarn and sulfide-quartz veins, also reflect some information of the magma emplacement-induced structural control.

The permeability of crust exponentially decreases with depth (Ingebritsen and Manning, 1999; Ingebritsen and Appold, 2012). Recrystallization of calcite during marbleization will further significantly decrease the permeability of carbonate rocks. With a depth of ca. 10 km, unfractured marble is almost impermeable (permeability could be lower than 10^{-20} m^2, unpublished experimental data). However, fracturing can dramatically increase the permeability of rocks (Ingebritsen and Appold, 2012; Coelho et al., 2015). Thus, the magma emplacement-induced wall-rock deformation was critically important for creating permeability to promote the infiltration of magmatic fluids along fractures and then structurally controlled the wall-rock skarnization. A schematic model illustrating the magma emplacement-induced structural control on skarn formation of the Tongshanling Cu-Pb-Zn deposit is shown in Figure 6-11.

This study provides a new viewpoint for understanding the connecting process between skarn systems and granitoids and enlightens further prospecting and exploration for mineral

deposits related to granitoids, especially the deep-emplacement granitoids, in South China and also around the world. Magma emplacement-induced wall-rock fractures are ideal permeable zones and are beneficial to hydrothermal mineralization.

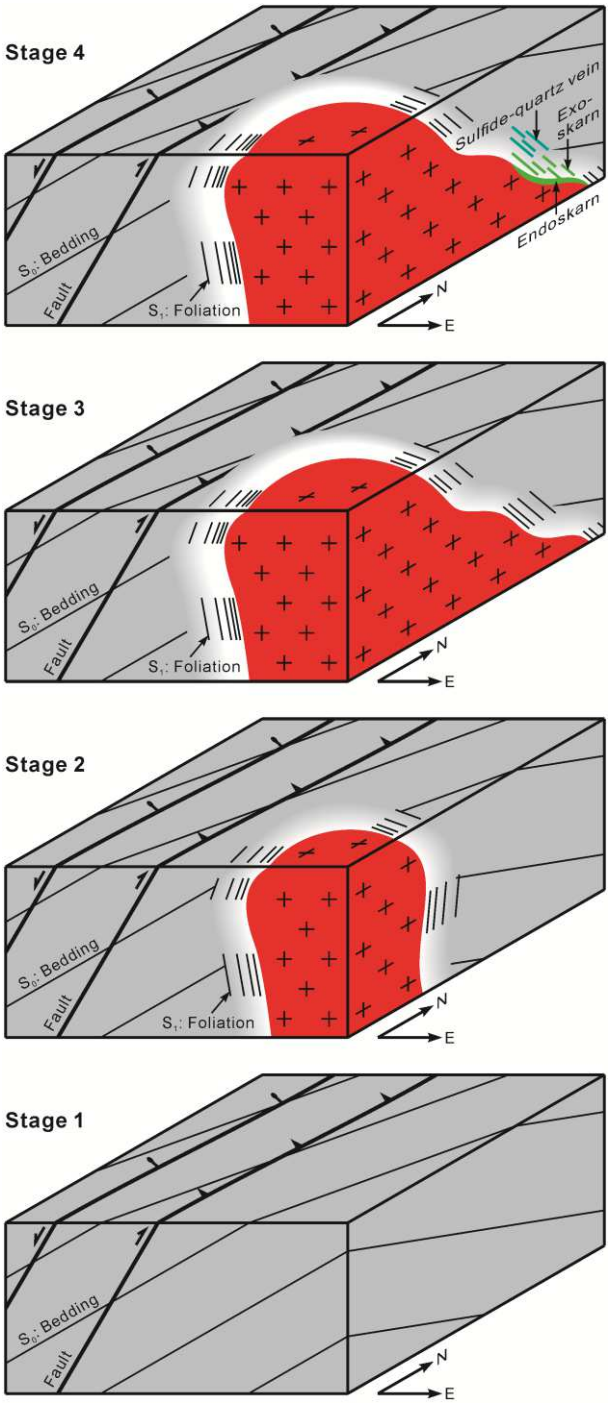

Figure 6-11. Schematic model illustrating the magma emplacement-induced structural control on skarn formation at the Tongshanling Cu-Pb-Zn deposit.

6.7. Summary

The regional normal faults in the Tongshanling area were formed under the tectonic change from Triassic compression to Jurassic extension earlier than the emplacement of the Tongshanling intrusion.

The emplacement of the Tongshanling intrusion started from the southern part and induced wall-rock marbleization and deformation in the contact zone.

The magma emplacement-induced wall-rock deformation significantly increased permeability to promote the infiltration of magmatic fluids along fractures and then structurally controlled the formation of exoskarn and sulfide-quartz veins.

Chapter 7. Zonation and genesis of the Tongshanling Cu-Mo-Pb-Zn-Ag skarn system

7.1. Introduction

Association and zonation of various alteration and mineralization types are commonly observed in natural magmatic-hydrothermal systems, such as porphyry and skarn systems (Meinert et al., 2005; Sillitoe, 2010; Soloviev, 2011, 2015; Soloviev et al., 2013; Catchpole et al., 2015; Pirajno and Zhou, 2015; Soloviev and Kryazhev, 2017). Comprehensive study on the relationship between these alteration and mineralization types through geology, geochronology, geochemistry, etc., will greatly promote the understanding of ore-forming process and is also beneficial to further prospecting and exploration. The Middle-Late Jurassic Cu-Pb-Zn deposits in the Nanling Range, South China, include the Shuikoushan, Baoshan, Tongshanling, and Huangshaping deposits in southeastern Hunan Province, and the Dabaoshan deposit in northern Guangdong Province (Fig. 1-1), are characterized by multiple mineralization types that are spatially associated and zoned (Lu et al., 2013; Qu et al., 2014; Cai et al., 2015; Xie et al., 2015; Ding et al., 2016a). For instance, carbonate replacement and skarn are the predominant mineralization types of the Shuikoushan Pb-Zn-Au-Ag (Lu et al., 2013; Huang et al., 2015), Baoshan Cu-Mo-Pb-Zn-Ag (Lu et al., 2006; Xie et al., 2015), Tongshanling Cu-Mo-Pb-Zn-Ag (Cai et al., 2015; Lu et al., 2015; Zhao et al., 2016b), and Huangshaping Pb-Zn-W-Mo (Yao et al., 2007; Ding et al., 2016a) deposits; sulfide-quartz veins are also important in the Tongshanling ore district (Cai et al., 2015; Lu et al., 2015; Zhao et al., 2016b); the Dabaoshan deposit mainly consists of porphyry Mo (W), skarn Mo-W, and stratiform Cu-Pb-Zn orebodies (Wang et al., 2011c; Qu et al., 2014; Mao et al., 2017). However, the relationship between these different mineralization types was rarely considered in previous studies. Whether they are genetically linked or not is still ambiguous.

The Tongshanling polymetallic ore district is located in the western part of the Nanling Range metallogenic belt about 120 km to the east of Guilin and in the suture zone between the Yangtze Block and Cathaysia Block (Fig. 1-1). It was discovered in 1958 and mined since

1977 and is one of the oldest mines in the Nanling Range. Ancient mineral waste residues were remained on the surface and some pottery bowls of the Jin dynasty (from A.D. 265 to A.D. 420) were found in an ancient adit. The ore district contains about 53,000 t Cu (average 1.23 wt.% Cu), 6,000 t Mo (average 0.30 wt.% Mo), 126,000 t Pb (average 2.58 wt.% Pb), 138,000 t Zn (average 3.95 wt.% Zn), and 780 t Ag (average 144 g/t Ag) (No. 206 Exploring Team of Hunan Metallurgical and Exploring Company, unpub. report, 1975; No. 409 Geological Team of Bureau of Geology and Mineral Exploration and Development of Hunan Province, unpub. report, 2008; Institute of Geological Survey of South Hunan, unpub. report, 2012). In addition, there are about 5,520 t Bi (average 0.16 wt.% Bi), 1,900 t Cd (average 0.016 wt.% Cd), 195 t Se (average 0.001 wt.% Se), and 95 t Te (average 0.003 wt.% Te) within the Cu-Pb-Zn resources. It is constituted by three ore deposits distributed around the Tongshanling granodioritic intrusion, i.e., the Tongshanling Cu-Pb-Zn deposit, Jiangyong Pb-Zn-Ag deposit, and Yulong Mo deposit (Figs. 3-1, 7-1, 7-2, and 7-3). They are dominated by skarn, sulfide-quartz vein, and carbonate replacement mineralization. Although numerous geochronological and geochemical studies have been carried out on the Tongshanling granodiorite and these surrounding deposits (Wang et al., 2003a; Yi and Xu, 2006; Wei et al., 2007; Jiang et al., 2009; Quan et al., 2013; Cai et al., 2015; Lu et al., 2015; Zhao et al., 2016b; Huang et al., 2017a; Wang et al., 2017d), the relationships of the three deposits and different mineralization types are still unknown.

In this study, new geochronological data of garnet and titanite U-Pb and molybdenite Re-Os ages and geochemical data of S, Pb, and H-O isotopic compositions are presented based on detailed geological information and paragenetic sequences to constrain the genetic links and ore-forming processes of the different deposits and mineralization types in the Tongshanling Cu-Mo-Pb-Zn-Ag ore district.

7.2. Deposit geology

7.2.1. Tongshanling Cu-Pb-Zn deposit

The Tongshanling Cu-Pb-Zn deposit occurs in the northeastern concealed contact zone between the Tongshanling granodiorite and country rocks, and its peripheral zone (Figs. 3-1,

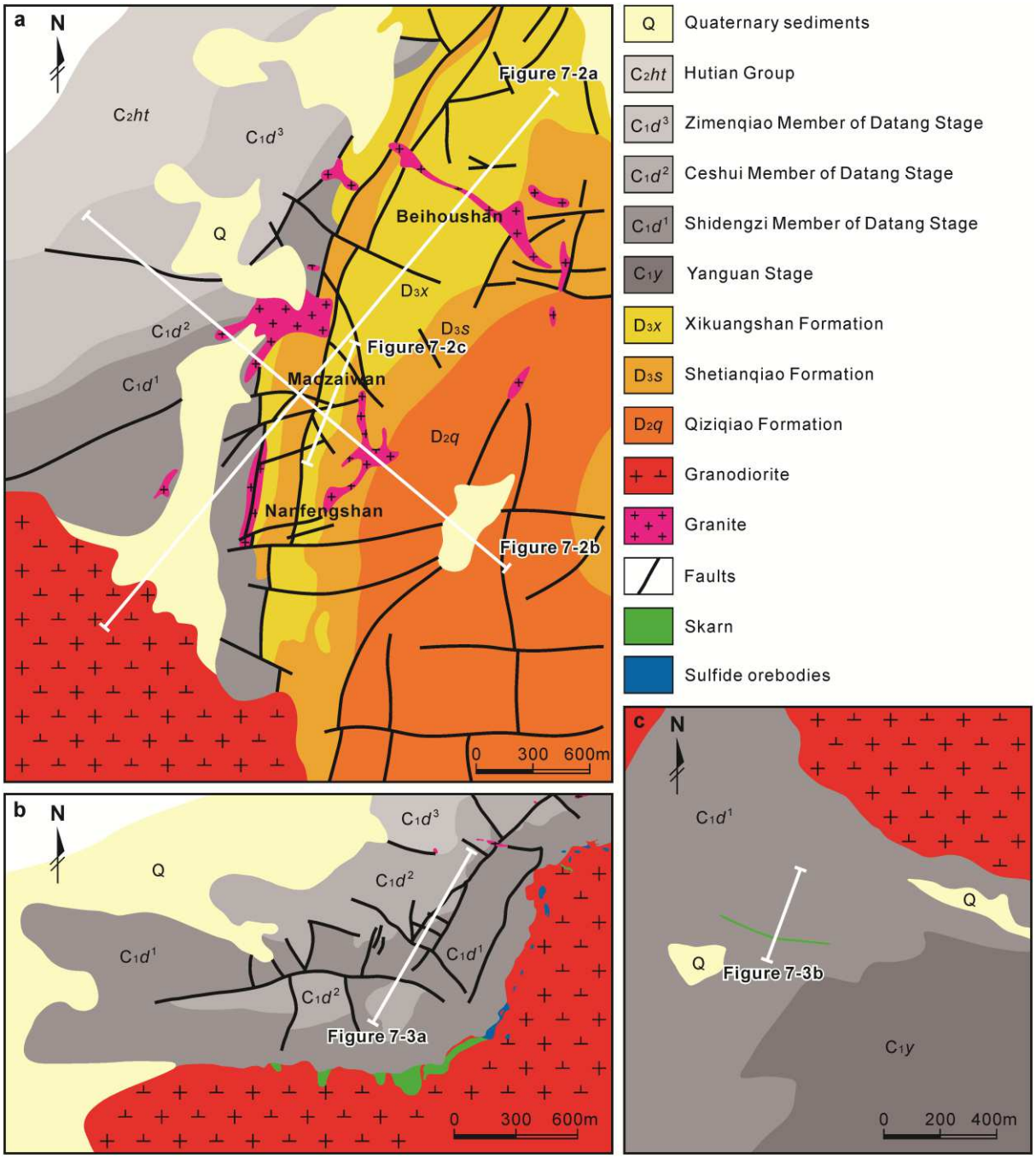

Figure 7-1. Geological maps of the (a) Tongshanling Cu-Pb-Zn deposit (modified after No. 206 Exploring Team of Hunan Metallurgical and Exploring Company, unpub. report, 1975), (b) Jiangyong Pb-Zn-Ag deposit (modified after No. 409 Geological Team of Bureau of Geology and Mineral Exploration and Development of Hunan Province, unpub. report, 2008), and (c) Yulong Mo deposit (modified after Institute of Geological Survey of South Hunan, unpub. report, 2012).

7-1a, and 7-2). Three ore sections, Nanfengshan, Maozaiwan, and Beihoushan, successfully constitute this deposit from southwest to northeast (Fig. 7-1a). The Tongshanling Cu-Pb-Zn

deposit exhibits an obvious zonation of proximal skarn, distal skarn, and sulfide-quartz veins between them (Fig. 7-2). The proximal skarn is distributed in the Nanfengshan and Maozaiwan sections (Fig. 7-2) and can be further divided into endoskarn and exoskarn which are different in geometry, mineralogy and mineralization. The sulfide-quartz veins mainly occur in the Maozaiwan section with minor in the Beihoushan section (Fig. 7-2). The distal skarn was well developed in the Beihoushan section with minor in the Maozaiwan section (Fig. 7-2).

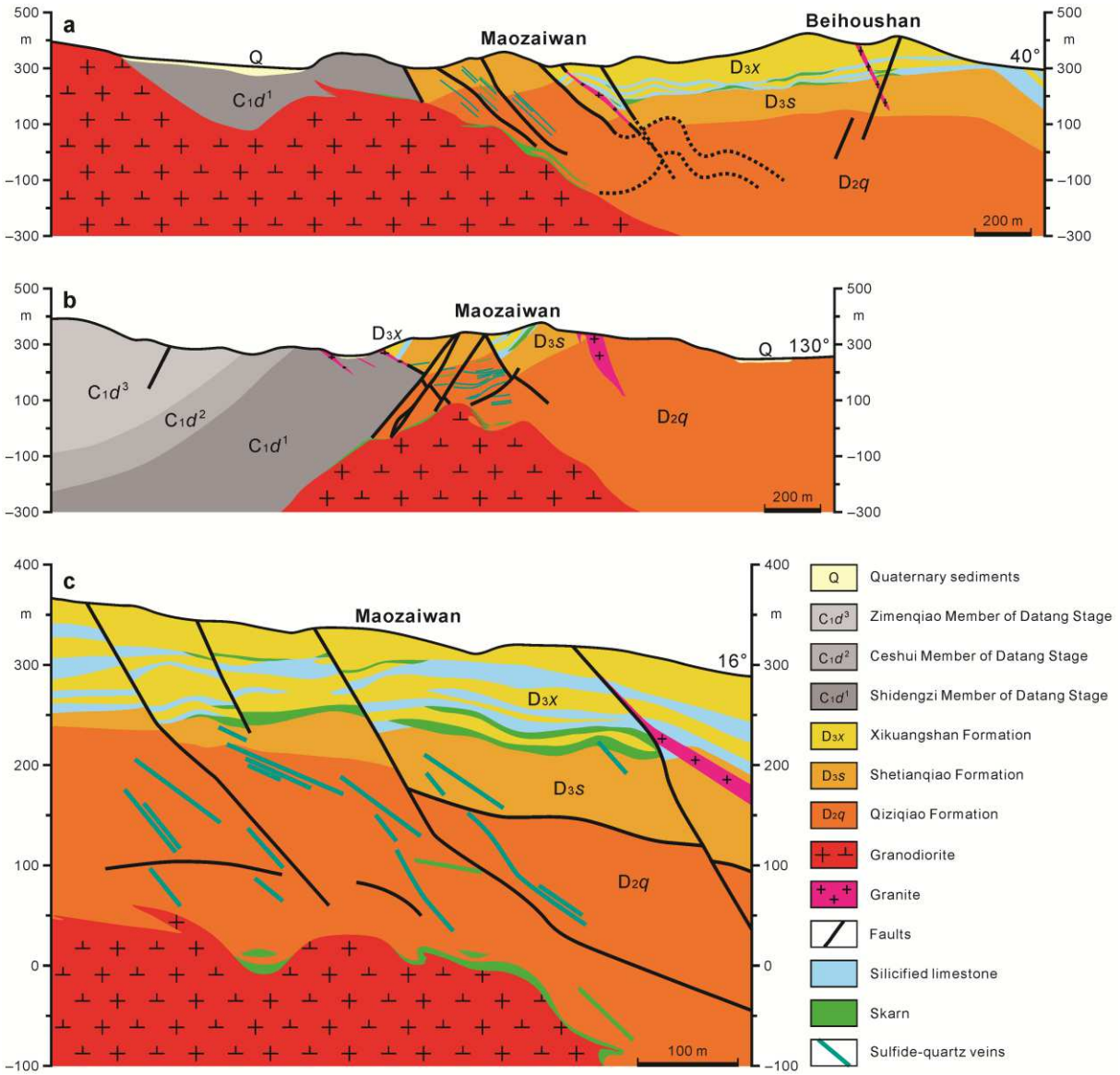

Figure 7-2. Cross sections (section lines shown in Fig. 7-1) of the Tongshanling Cu-Pb-Zn deposit (modified after No. 206 Exploring Team of Hunan Metallurgical and Exploring Company, unpub. report, 1975).

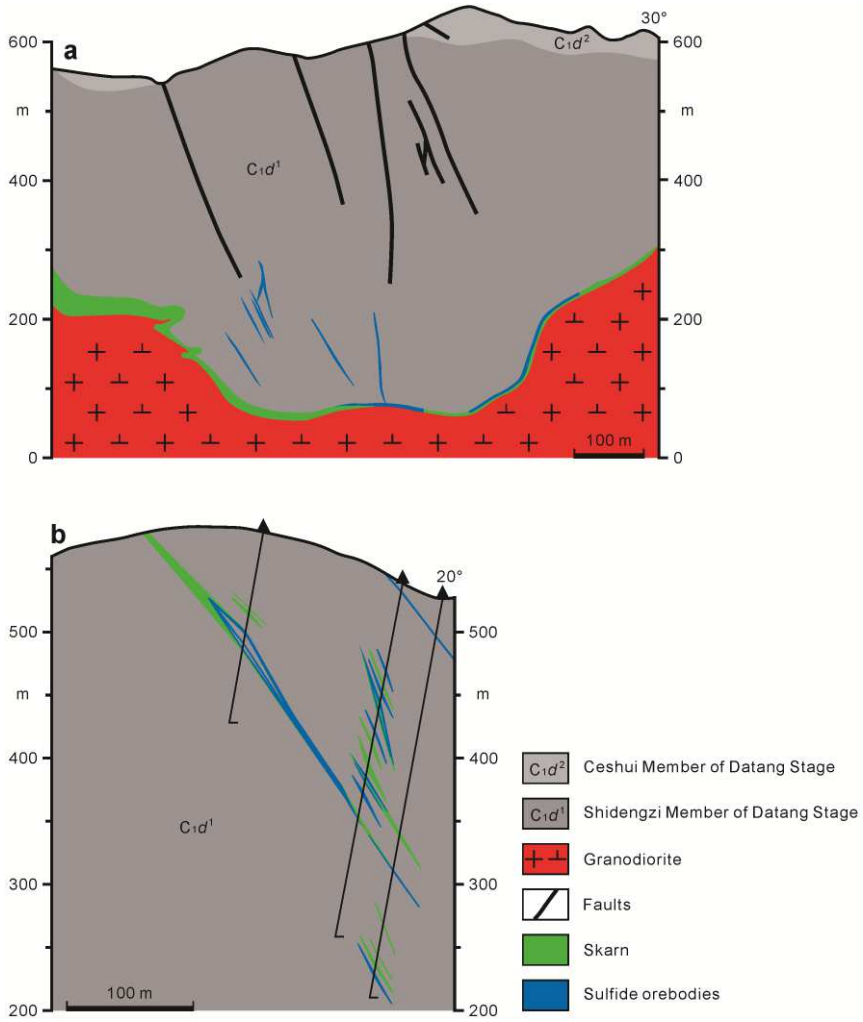

Figure 7-3. Cross sections (section lines shown in Fig. 7-1) of the (a) Jiangyong Pb-Zn-Ag deposit (modified after No. 409 Geological Team of Bureau of Geology and Mineral Exploration and Development of Hunan Province, unpub. report, 2008) and (b) Yulong Mo deposit (modified after Institute of Geological Survey of South Hunan, unpub. report, 2012).

7.2.1.1. Proximal endoskarn

The proximal endoskarn is massive (Fig. 7-4a) with irregular shapes and extends along the border of granodiorite. With a principal mineralogy of garnet and pyroxene (Figs. 7-5a and 7-6a) and minor retrograde minerals, such as actinolite and epidote, the endoskarn has a brown color in general and does not show a clear zonation (Fig. 7-4a). Chalcopyrite and pyrrhotite are the predominant ore minerals coexisting with abundant quartz in the endoskarn (Figs. 7-4a, 7-5a, and 7-6b). The chalcopyrite generally surrounds the pyrrhotite as envelopes

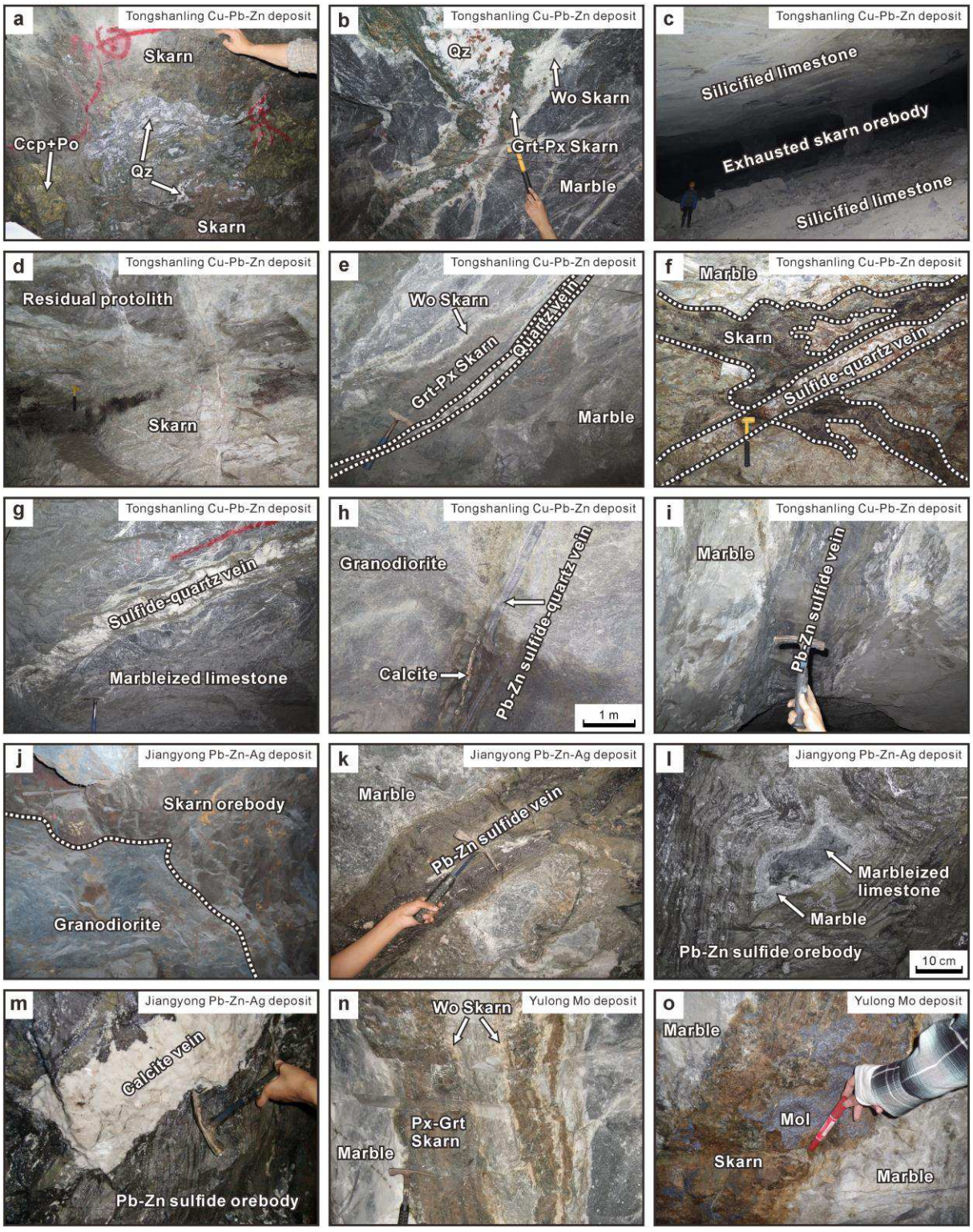

Figure 7-4. Outcrop-scale photos of different mineralization types of the (a–i) Tongshanling Cu-Pb-Zn deposit, (j–m) Jiangyong Pb-Zn-Ag deposit, and (n and o) Yulong Mo deposit. (a) Chalcopyrite + pyrrhotite mineralization accompanied by quartz in the massive proximal endoskarn. (b) Proximal exoskarn vein with an outward zonation from garnet-pyroxene through wollastonite to marble and late quartz in the center. (c) Exhausted stratiform distal skarn orebody with roof and floor of silicified limestone. (d) Residual argillaceous

limestone in the distal skarn. (e) Proximal exoskarn cut through by a quartz vein. (f) Distal skarn cut across by a sulfide-quartz vein. (g) Sulfide-quartz vein mineralization in the peripheral zone of proximal skarn. (h) Late Pb-Zn sulfide-quartz vein cutting the granodiorite. (i) Late carbonate replacement Pb-Zn sulfide vein with a banded structure. (j) Skarn orebody in the contact zone between granodiorite and country rocks. (k) Carbonate replacement Pb-Zn sulfide vein with a banded structure. (l) Residual carbonate rocks in the banded carbonate replacement Pb-Zn sulfide orebody. (m) Banded carbonate replacement Pb-Zn sulfide orebody cut by a late calcite vein. (n) Skarn vein with an outward zonation from pyroxene-garnet through wollastonite to marble. (o) Molybdenite in the skarn vein. Mineral abbreviations: Ccp = chalcopyrite, Grt = garnet, Mol = molybdenite, Po = pyrrhotite, Px = pyroxene, Qz = quartz, Wo = wollastonite.

(Fig. 7-5a). Sparse disseminated sphalerite and pyrite grains occasionally appear in the chalcopyrite. There is no galena in the endoskarn ores.

7.2.1.2. Proximal exoskarn

The proximal exoskarn mostly occurs as veins with a width of dozens of centimeters in the upper member of the Qiziqiao Formation (Fig. 7-4b). These exoskarn veins commonly exhibit a well-developed outward zonation from garnet-pyroxene through wollastonite (Fig. 7-6c) to marble and contain late quartz in the center (Fig. 7-4b). They are green-colored on the whole (Fig. 7-4b) and the pyroxene/garnet ratio is distinctly higher than that of the endoskarn. Ore minerals are chalcopyrite, sphalerite, galena, pyrrhotite, and pyrite (Figs. 7-5b and 7-6d). The (sphalerite + galena)/chalcopyrite and pyrite/pyrrhotite ratios of the exoskarn ores are remarkably higher than those of the endoskarn ores.

7.2.1.3. Distal skarn

Different form the proximal skarn, the distal skarn is evidently controlled by the argillaceous limestone of the Xikuangshan Formation and has stratiform shapes with thicknesses of several meters (Figs. 7-2 and 7-4c). Some residual protolith pieces of argillaceous limestone are observed in the distal skarn (Fig. 7-4d). The distal skarn does not show an obvious zonation. The roof and floor of the distal skarn are generally silicified limestone (Fig. 7-4c) which is widely and continuously spread in the lower member of the

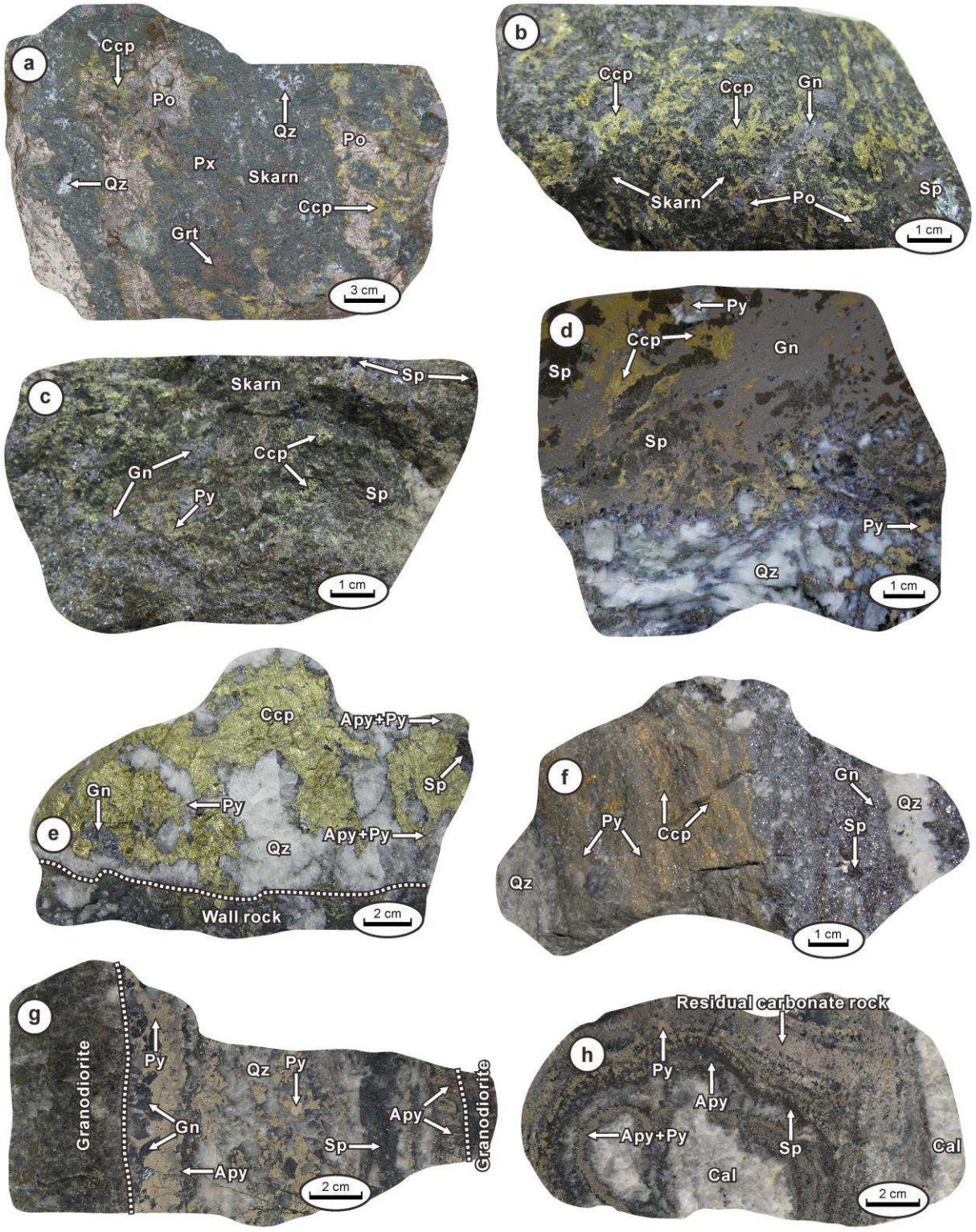

Figure 7-5. Specimen-scale photos of different ore types of the Tongshanling Cu-Pb-Zn deposit. (a) Proximal endoskarn ore. (b) Proximal exoskarn ore. (c and d) Distal skarn ore. (e) Cu-dominant sulfide-quartz vein ore. (f) Cu-Pb-Zn sulfide-quartz vein ore. (g) Pb-Zn sulfide-quartz vein ore. (h) Carbonate replacement Pb-Zn sulfide vein ore. Mineral abbreviations: Apy = arsenopyrite, Cal = calcite, Ccp = chalcopyrite, Gn = galena, Grt = garnet, Po = pyrrhotite, Px = pyroxene, Py = pyrite, Qz = quartz, Sp = sphalerite, Wo = wollastonite.

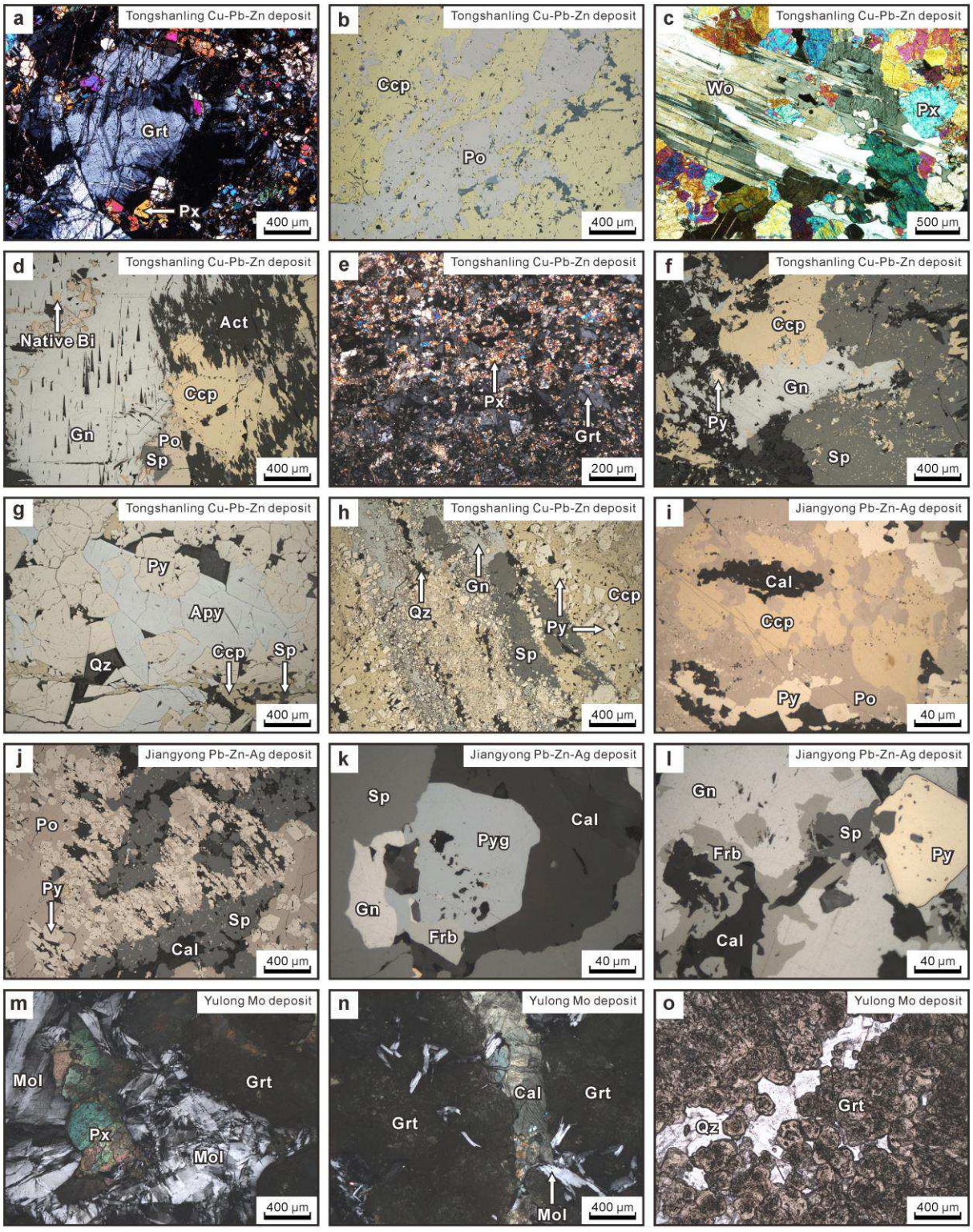

Figure 7-6. Petrographic photomicrographs of different mineralization and ore types of the (a–h) Tongshanling Cu-Pb-Zn deposit, (i–l) Jiangyong Pb-Zn-Ag deposit, and (m–o) Yulong Mo deposit. (a) Coarse-grained garnet and pyroxene in the proximal endoskarn. (b) Chalcopyrite and pyrrhotite in the proximal endoskarn ore. (c) Coarse-grained pyroxene and wollastonite in the proximal exoskarn. (d) Chalcopyrite, sphalerite, galena, pyrrhotite, native bismuth, and actinolite in the proximal exoskarn ore. (e) Fine-grained garnet and pyroxene in

the distal skarn. (f) Chalcopyrite, sphalerite, galena, and pyrite in the distal skarn ore. (g) Early euhedral arsenopyrite and pyrite cut by late chalcopyrite in the Cu-dominant sulfide-quartz vein ore. (h) Early pyrite and chalcopyrite replaced by late sphalerite and galena in the Cu-Pb-Zn sulfide-quartz vein ore. (i) Chalcopyrite, pyrrhotite, and pyrite in the skarn ore. (j) Early pyrrhotite and pyrite replaced by late sphalerite in the carbonate replacement ore. (k) Pyrargyrite, freibergite, and galena coexisting with sphalerite in the carbonate replacement ore. (l) Galena with freibergite inside enclosing sphalerite and idiomorphic pyrite in the carbonate replacement ore. (m) Flaky molybdenite aggregation in the pyroxene-garnet skarn. (n) Flaky molybdenite disseminated in the garnet skarn cut by a late calcite veinlet. (o) Early automorphic garnet and late interstitial quartz in skarn. Mineral abbreviations: Act = actinolite, Apy = arsenopyrite, Cal = calcite, Ccp = chalcopyrite, Frb = freibergite, Gn = galena, Grt = garnet, Mol = molybdenite, Po = pyrrhotite, Px = pyroxene, Py = pyrite, Pyg = pyrargyrite, Qz = quartz, Sp = sphalerite, Wo = wollastonite.

Xikuangshan Formation (Fig. 7-2). Skarn minerals are prograde garnet, pyroxene, wollastonite, and retrograde actinolite, vesuvianite, epidote, etc., which are markedly more fine-grained than those of the proximal skarn (Fig. 7-6e). Ore minerals include chalcopyrite, sphalerite, galena, pyrite (Figs. 7-5c–d and 7-6f), and sometimes pyrrhotite and arsenopyrite.

7.2.1.4. Sulfide-quartz vein

The quartz veins are a dozen to tens of centimeters in width (Fig. 7-4e–h) and are mainly distributed in the Qiziqiao and Shetianqiao Formations spatially between the proximal skarn and the distal skarn (Fig. 7-2). Both the proximal and distal skarns are cut by the quartz veins (Fig. 7-4e and f). Early vein-like quartz in the proximal exoskarn center (Fig. 7-4b) and the quartz veins cutting through the proximal exoskarn are barren (Fig. 7-4e). The peripheral mineralized quartz veins can be separated into proximal Cu-dominant sulfide-quartz veins and distal Cu-Pb-Zn sulfide-quartz veins. The ores of the latter have noticeably higher (sphalerite + galena)/chalcopyrite ratios than those of the former and both of them contain pyrite but do not have pyrrhotite (Figs. 7-5e–f and 7-6g–h). Arsenopyrite appears in the Cu-dominant sulfide-quartz vein ores (Figs. 7-5e and 7-6g) but is absent in the Cu-Pb-Zn sulfide-quartz vein ores (Figs. 7-5f and 7-6h). Some late Pb-Zn sulfide-quartz veins cut through the granodiorite (Fig. 7-4h) and contain abundant pyrite and arsenopyrite (Fig. 7-5g).

7.2.1.5. Carbonate replacement

Carbonate replacement Pb-Zn sulfide veins are rarely occurred in the proximal part. They have a width of several tens of centimeters and show a banded texture (Figs. 7-4i and 7-5h). Ore minerals are sphalerite, galena, pyrite, and arsenopyrite (Fig. 7-5h). The unique gangue mineral is calcite (Fig. 7-5h).

7.2.1.6. Ore types

Based on the zonation of mineralization and mineral association, seven different ore types of the Tongshanling Cu-Pb-Zn deposit are distinguished as follows (mineral abbreviations refer to Figs. 7-5 and 7-6):

(1) Proximal endoskarn ore (Ccp ± Sp + Po ± Py + skarn minerals + Qz) (Figs. 7-5a and 7-6a–b);

(2) Proximal exoskarn ore (Ccp + Sp + Gn + Po + Py + skarn minerals + Qz + Cal) (Figs. 7-5b and 7-6c–d);

(3) Distal skarn ore (Ccp + Sp + Gn ± Po + Py ± Apy + skarn minerals + Qz + Cal) (Figs. 7-5c–d and 7-6e–f);

(4) Cu-dominant sulfide-quartz vein ore (Ccp ± Sp ± Gn + Py + Apy + Qz) (Figs. 7-5e and 7-6g);

(5) Cu-Pb-Zn sulfide-quartz vein ore (Ccp + Sp + Gn + Py + Qz) (Figs. 7-5f and 7-6h);

(6) Pb-Zn sulfide-quartz vein ore (Sp + Gn + Py + Apy + Qz) (Fig. 7-5g);

(7) Carbonate replacement Pb-Zn sulfide vein ore (Sp + Gn + Py + Apy + Cal) (Fig. 7-5h).

7.2.1.7. Paragenesis

The paragenetic sequence of the Tongshanling Cu-Pb-Zn deposit (Fig. 7-7) is comprised of a prograde stage and a retrograde stage. Anhydrous skarn minerals wollastonite, garnet, and pyroxene were firstly formed in the prograde stage followed by a few scheelite and molybdenite. In the early retrograde stage, some hydrous skarn minerals, such as actinolite, vesuvianite, and epidote, replaced the anhydrous skarn by retrograde alteration. Sericite and chlorite were then formed by hydrothermal alteration of the granodiorite. Hydrothermal quartz, calcite, and sulfide minerals began to precipitate. The formation sequence of sulfide

minerals started from pyrrhotite and pyrite through chalcopyrite to sphalerite and then to galena overall. The content of pyrite progressively increased with time. A little native bismuth was simultaneously precipitated with galena. With the occurrence of abundant quartz, the proximal Cu-dominant sulfide-quartz veins were formed and followed by the distal Cu-Pb-Zn sulfide-quartz veins and then the late Pb-Zn sulfide-quartz veins. Some Pb-Bi sulfides were contemporaneously precipitated with galena in the sulfide-quartz veins. The carbonate replacement Pb-Zn sulfide veins were formed at the latest.

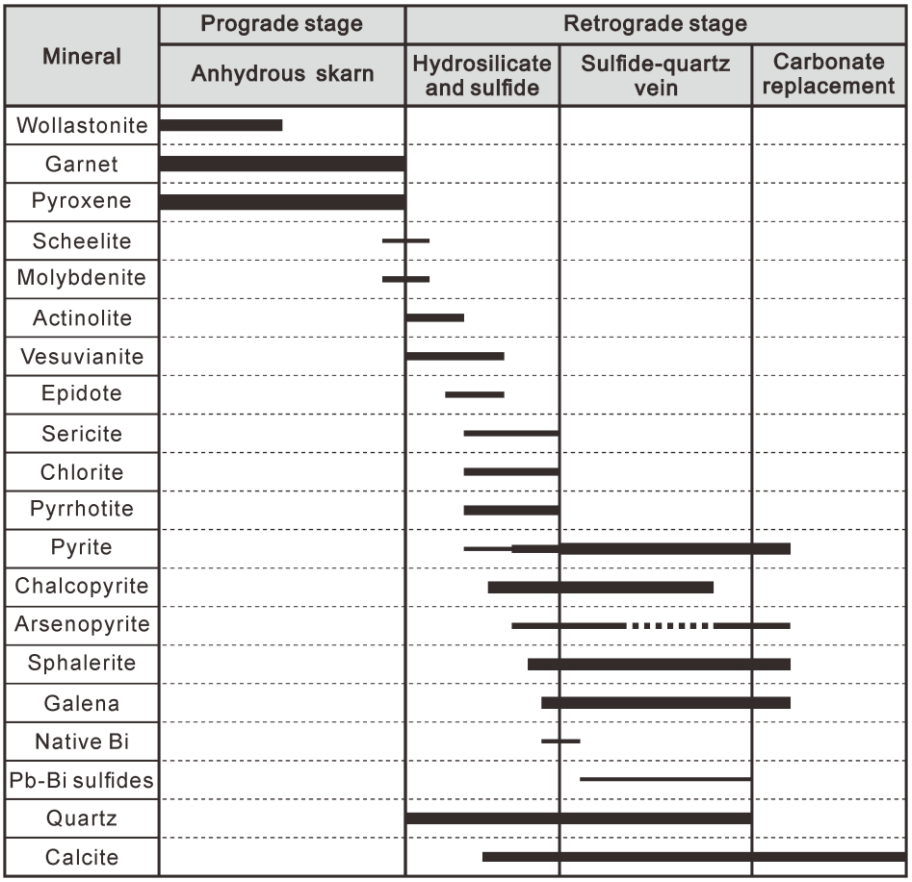

Figure 7-7. Paragenetic sequence of the Tongshanling Cu-Pb-Zn deposit.

7.2.2. Jiangyong Pb-Zn-Ag deposit

The Jiangyong Pb-Zn-Ag deposit occurs in the northwestern concealed contact zone between the Tongshanling granodiorite and country rocks, and its peripheral zone (Figs. 3-1, 7-1b, and 7-3a). It is characterized by carbonate replacement mineralization in the Shidengzi

limestone of the Upper Carboniferous Datang Stage (Fig. 7-3a). Although skarn mineralization is developed in the contact zone (Figs. 7-1b, 7-3a, and 7-4j), it is not of great economic importance. The ore minerals of the skarn orebodies are dominated by pyrrhotite and pyrite with minor chalcopyrite (Fig. 7-6i) and sphalerite. The carbonate replacement sulfide orebodies are distributed within the range of 350 m in distance from the contact zone. They generally show vein-like (Fig. 7-4k), lentiform, and sackform geometries and mostly have a banded structure (Fig. 7-4k–m). Sphalerite, galena, pyrite, pyrrhotite, and arsenopyrite are the dominant ore minerals of the carbonate replacement sulfide orebodies (Fig. 7-6j). Silver is predominantly concentrated in galena by isomorphous substitution of Pb or as independent Ag-minerals such as pyrargyrite (Fig. 7-6k), freibergite (Fig. 7-6k and l), and freieslebenite. The galena/sphalerite ratio, pyrite/pyrrhotite ratio, and Ag grade of sulfide ores show positive correlations with the distance to the contact zone.

Compared with the Tongshanling Cu-Pb-Zn deposit, the Jiangyong Pb-Zn-Ag deposit shows a relatively weak prograde anhydrous skarn stage with the formation of some wollastonite, garnet, and pyroxene in the contact zone and a strong retrograde stage dominated by carbonate replacement with the formation of abundant sulfide minerals and calcite in the peripheral zone but almost no quartz and chalcopyrite (Figs. 7-7 and 7-8). The carbonate replacement ore bodies of the Jiangyong Pb-Zn-Ag deposit are similar to those of the Tongshanling Cu-Pb-Zn deposit in geometry, ore structure, mineral association, and paragenetic sequence (Figs. 7-7 and 7-8). During Pb-Zn mineralization, galena was generally precipitated later and more distal than sphalerite. Galena/sphalerite ratio, pyrite/pyrrhotite ratio, and Ag grade progressively increased with time. Barren calcite veins were formed at the latest and cut the sulfide orebodies (Fig. 7-4m).

7.2.3. Yulong Mo deposit

The Yulong Mo deposit occurs in the periphery of the southern concealed contact zone between the Tongshanling granodiorite and country rocks (Figs. 3-1, 7-1c, and 7-3b). It is constituted by NW-SE-striking mineralized skarn veins in the Shidengzi limestone of the Datang Stage (Figs. 7-1c and 7-3b). These skarn veins are generally 0.1 – 2 m in thickness (Fig. 7-4n and o) with an interval distance of 3 – 10 m and a vertical extension of 10 – 100 m.

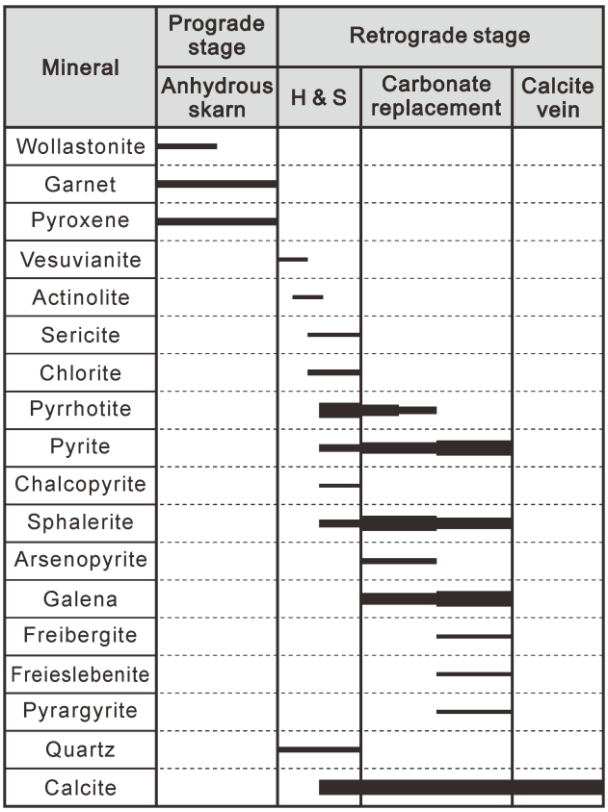

Figure 7-8. Paragenetic sequence of the Jiangyong Pb-Zn-Ag deposit. H &S = Hydrosilicate and sulfide.

They commonly have a brown color and exhibit an outward zonation from pyroxene-garnet through wollastonite to marble (Fig. 7-4n). Ore minerals are mainly molybdenite, pyrrhotite, pyrite, and minor scheelite, chalcopyrite, sphalerite, galena, and arsenopyrite. Molybdenite is distributed in pyroxene-garnet skarn as aggregations (Figs. 7-4o and 7-6m), veinlets, and disseminated (Fig. 7-6n). Late quartz and calcite occur as interstitial in skarn (Fig. 7-6o) or as veinlets cutting skarn (Fig. 7-6n).

The paragenetic sequence of the Yulong Mo deposit is shown in Figure 7-9. Compared with the Tongshanling Cu-Pb-Zn deposit and Jiangyong Pb-Zn-Ag deposit, the Yulong Mo deposit is characterized by a well-developed prograde anhydrous skarn stage with the formation of abundant wollastonite, garnet, and pyroxene and a relatively weak retrograde stage with the formation of some hydrosilicate minerals such as vesuvianite, actinolite, epidote, and chlorite and sulfide minerals but no strong sulfide-quartz vein and carbonate replacement mineralization (Figs. 7-7–7-9). The early-formed molybdenite is the unique ore mineral of economic significance.

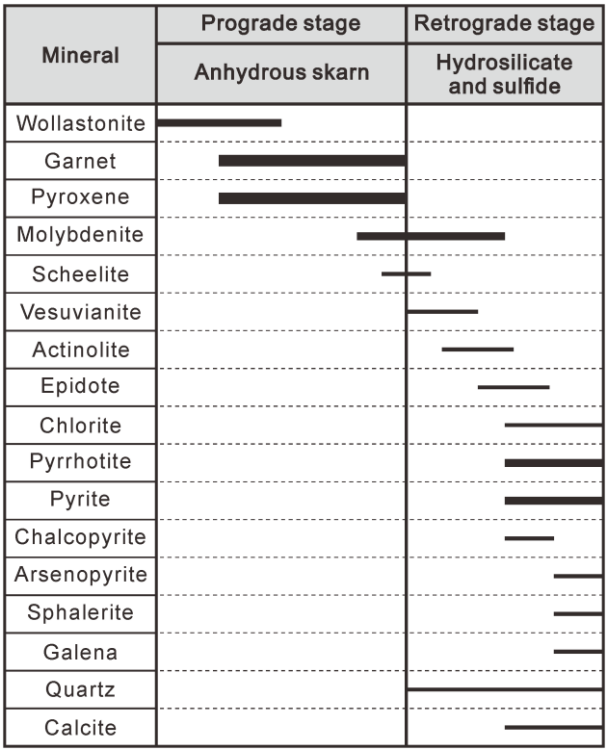

Figure 7-9. Paragenetic sequence of the Yulong Mo deposit.

7.3. Sampling and analytical methods

Proximal exoskarn and altered granodiorite from the Tongshanling Cu-Pb-Zn deposit were sampled for laser ablation-inductively coupled plasma-mass spectrometry (LA-ICP-MS) U-Pb dating of garnet and hydrothermal titanite on thin sections, respectively. Molybdenite samples of proximal endoskarn, proximal exoskarn, and distal skarn from the Tongshanling Cu-Pb-Zn deposit and skarn from the Yulong Mo deposit were collected for Re-Os dating. Sulfide minerals (chalcopyrite, sphalerite, galena, pyrite, pyrrhotite, and molybdenite) of different mineralization types from different levels of the three ore deposits were systematically sampled for S and Pb isotopic analyses. Quartz samples from the three ore deposits were collected for H-O isotopic analyses. Sulfide minerals and quartz were handpicked under a binocular microscope after crushing samples to 40 – 60 mesh. Separated grains were rinsed by absolute alcohol. Then, the sulfide minerals were ground to powder < 200 mesh for subsequent analyses.

U-Pb dating of garnet was conducted with an Agilent 7700× ICP-MS coupled to a

GeoLasPro 193 nm laser ablation system at the Guangdong Provincial Key Laboratory of Marine Resources and Coastal Engineering, Sun Yat-sen University, China. Each analysis was performed by a 32-μm ablating spot at 5 Hz with an energy density of 5 J/cm^2 for 45 s after measuring the gas blank for 20 s. Zircon 91500 (Wiedenbeck et al., 1995) was used as the external standard and garnet QC04 and OH-1 (Deng et al., 2017; Seman et al., 2017) were used to monitor the process of garnet U-Pb dating. The matrix effect of garnet U-Pb dating has been proved to be minor (Mezger et al., 1989; Deng et al., 2017; Seman et al., 2017). The off-line data processing was performed using a program called ICPMSDataCal (Liu et al., 2008b). Common lead was corrected by the ^{207}Pb method (Stern, 1997; Frost et al., 2000; Aleinikoff et al., 2002) and the ^{207}Pb-corrected ^{206}Pb/^{238}U ages were used to calculate the weighted average age.

Re-Os dating of molybdenite was carried out by a Thermo Electron TJA X-series ICP-MS in the Re-Os laboratory of the National Research Center of Geoanalysis, Chinese Academy of Geological Sciences, Beijing. The analyzed molybdenite was fine-grained (< 0.1 mm) in order to prevent decoupling of Re and ^{187}Os within large grains. Firstly, molybdenite was digested by HNO_3-HCl solution in a Carius tube followed by heating for 10 hours at 230 °C with a stainless-steel jacket. Then, the Re was separated through solvent extraction and cation-exchange resin chromatography. The detailed analytical procedures were described by Shirey and Walker (1995), Mao et al. (1999), and Du et al. (2004). Analytical blanks for Re and Os were 4.3 pg and 0.09 pg, respectively. Model ages were calculated by the following equation: $t=[\ln(1+^{187}Os/^{187}Re)]/\lambda$, in which λ is the ^{187}Re decay constant of 1.666×10^{-11}/year (Smoliar et al., 1996). The model age of the GBW04435 (JDC) molybdenite standard measured in this study is 141.0 ± 1.9 Ma and is consistent with the certified value of 139.6 ± 3.8 Ma (Du et al., 2004).

U-Pb dating of titanite was performed by an Agilent 7700× ICP-MS coupled to an Excite 193 nm Photon Machines laser ablation system at Nanjing FocuMS Technology Co. Ltd., China. Each analysis was conducted with a 40-μm ablating spot at 6 Hz with an energy density of 6.7 J/cm^2 for 45 s after measuring the gas blank for 15 s. Titanite BLR-1 (Aleinikoff et al., 2007; Mazdab, 2009) was used as the external standard and Ontario titanite

(Corfu, 1996) was used to monitor the process of U-Pb dating. NIST SRM 610 was used as the reference material to calibrate the U, Th, and Pb concentrations of titanite by using ^{43}Ca as the internal calibration. The off-line data processing was performed using a program called ICPMSDataCal (Liu et al., 2008b). Common lead was corrected by the ^{207}Pb method (Stern, 1997; Frost et al., 2000; Aleinikoff et al., 2002) and the ^{207}Pb-corrected $^{206}Pb/^{238}U$ ages were used to calculate the weighted average age. Wetherill U-Pb concordia plots of garnet and titanite, Tera-Wasserburg U-Pb concordia plots of titanite, Re-Os isochrons of molybdenite, and weighted average age calculations of garnet, molybdenite, and titanite were constructed by the software Isoplot 4.15 (Ludwig, 2012).

Sulfur isotopic compositions of sulfide minerals were analyzed by a Finnigan MAT-253 mass spectrometer coupled to a Flash EA 1112 elemental analyzer at the State Key Laboratory Breeding Base of Nuclear Resources and Environment, East China University of Technology. For each sample, 20 – 100 μg sulfide powder was heated at 1020 °C to extract SO_2 gas for S isotopic analysis. The analytical results of $^{34}S/^{32}S$ ratios are expressed as the conventional $\delta^{34}S$ values in per mil relative to the Cañon Diablo Troilite (CDT). The analytical precision was better than 0.2 ‰.

Lead isotopic compositions of sulfide minerals were measured by a GV IsoProbe-T Thermal Ionization Mass Spectrometer (TIMS) at the Analytical Laboratory of the Beijing Research Institute of Uranium Geology, China. The analytical procedure involved dissolution of sulfide powder using HF and $HClO_4$ in crucibles followed by basic anion-exchange resin chromatography to purify Pb. Lead isotopic ratios were monitored and corrected by the analytical results of the standard NIST NBS 981. The external reproducibilities of Pb isotopic ratios were 0.001 – 0.003 for $^{206}Pb/^{204}Pb$ and $^{207}Pb/^{204}Pb$, and 0.002 – 0.008 for $^{208}Pb/^{204}Pb$ at 2-sigma level.

Hydrogen-oxygen isotopic compositions of quartz were analyzed using a Finnigan MAT-253 mass spectrometer at the Analytical Laboratory of the Beijing Research Institute of Uranium Geology, China. Water was released from quartz by heating to ca. 600 °C in an induction furnace and then reacted with heated zinc powder at 400 °C to produce H_2 for hydrogen isotopic analysis. Quartz grains were ground to powder < 200 mesh and then

reacted with BrF_5 at 500 – 600 °C for 14 h to generate O_2. With the catalysis of platinum, the O_2 reacted with graphite at 700 °C to produce CO_2 for oxygen isotopic analysis. The analytical results of $^{2}H/^{1}H$ and $^{18}O/^{16}O$ ratios are expressed as the conventional δD and $\delta^{18}O$ values in per mil relative to the Standard Mean Ocean Water (SMOW) with precisions of 1 ‰ and 0.2 ‰, respectively.

7.4. Results

7.4.1. Garnet U-Pb dating

The LA-ICP-MS U-Pb dating results of garnet in the proximal exoskarn from the Tongshanling Cu-Pb-Zn deposit are listed in Appendix 7-1. Twenty-five analyses revealed that the garnet in the proximal exoskarn has U, Th, and Pb contents of 7.25 – 17.19 ppm, 0.02 – 0.20 ppm, and 0.18 – 0.61 ppm, respectively, and $^{207}Pb/^{206}Pb$, $^{207}Pb/^{235}U$, and $^{206}Pb/^{238}U$ ratios of 0.012337 – 0.122815, 0.165985 – 0.609241, and 0.023547 – 0.029738, respectively (Appendix 7-1). A concordia age of 162.0 ± 3.7 Ma is obtained by the Wetherill concordia plots of the ^{207}Pb-corrected $^{207}Pb/^{235}U$ and $^{206}Pb/^{238}U$ ratios (Fig. 7-10). The weighted average value of the ^{207}Pb-corrected $^{206}Pb/^{238}U$ ages is 162.4 ± 4.2 Ma (Fig. 7-10) which is consistent with the concordia age.

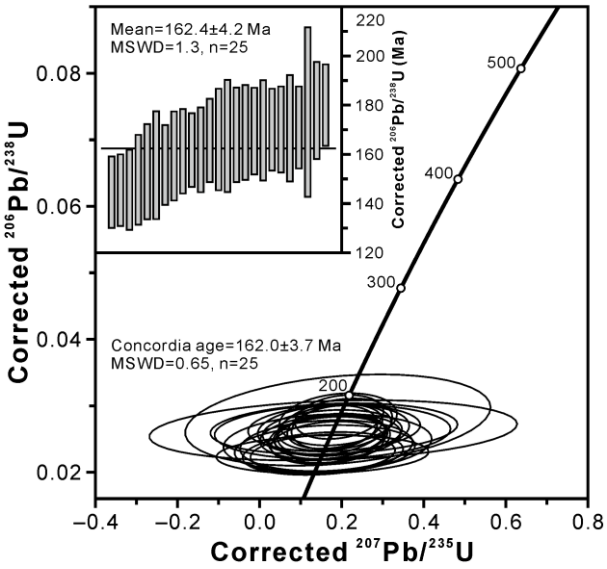

Figure 7-10. Wetherill U-Pb concordia plots and weighted average $^{206}Pb/^{238}U$ age of garnet in the proximal exoskarn from the Tongshanling Cu-Pb-Zn deposit.

7.4.2. Molybdenite Re-Os dating

The Re-Os dating results of molybdenites from the Tongshanling Cu-Pb-Zn deposit and Yulong Mo deposit are listed in Appendix 7-2. Two molybdenite samples from the proximal endoskarn, one molybdenite sample from the proximal exoskarn, and two molybdenite samples from the distal skarn of the Tongshanling Cu-Pb-Zn deposit have respective Re contents of 16.28 – 89.51 ppm, 24.60 ppm, and 47.97 – 98.23 ppm, respective ^{187}Re contents of 10.23 – 56.26 ppm, 15.46 ppm, and 30.15 – 61.74 ppm, respective ^{187}Os contents of 27.84 – 152.45 ppb, 41.32 ppb, and 81.02 – 168.46 ppb, and respective model ages of 162.4 – 163.1 Ma, 160.2 Ma, and 161.1 – 163.5 Ma (Appendix 7-2). All these five samples yield a ^{187}Re-^{187}Os isochron age of 161.8 ± 1.7 Ma and a consistent weighted average model age of 161.9 ± 1.1 Ma (Fig. 7-11a).

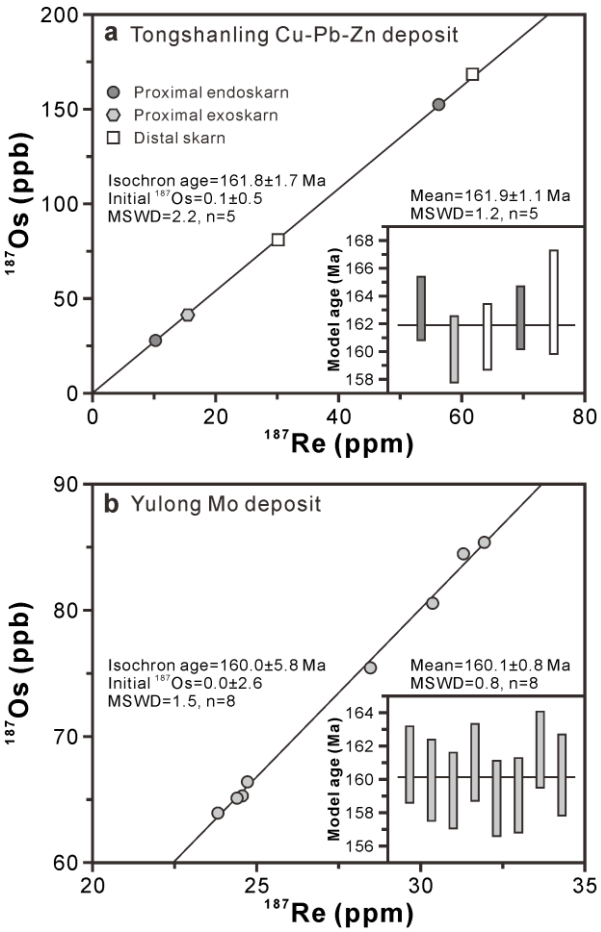

Figure 7-11. Re-Os isochrons and weighted average model ages of molybdenites from the (a) Tongshanling Cu-Pb-Zn deposit and (b) Yulong Mo deposit.

Eight molybdenite samples from the skarn of the Yulong Mo deposit have Re, ^{187}Re, and ^{187}Os contents of 37.90 – 50.82 ppm, 23.82 – 31.94 ppm, and 63.93 – 85.39 ppb, respectively (Appendix 7-2). Their Re-Os model ages vary from 158.9 Ma to 161.8 Ma and have a weighted average value of 160.1 ± 0.8 Ma (Appendix 7-2 and Fig. 7-11b). The ^{187}Re-^{187}Os isochron age of these eight molybdenite samples is 160.0 ± 5.8 Ma (Fig. 7-11b) which is consistent with the weighted average model age.

7.4.3. Titanite U-Pb dating

The titanite used for U-Pb dating occurs as pseudomorphic crystals replacing biotite or coexists with sulfide minerals as an interstitial texture in the altered granodiorite (Fig. 7-12a). This kind of titanite is evidently hydrothermal titanite formed by hydrothermal alteration of the granodiorite and is different from the automorphic and isolated magmatic titanite.

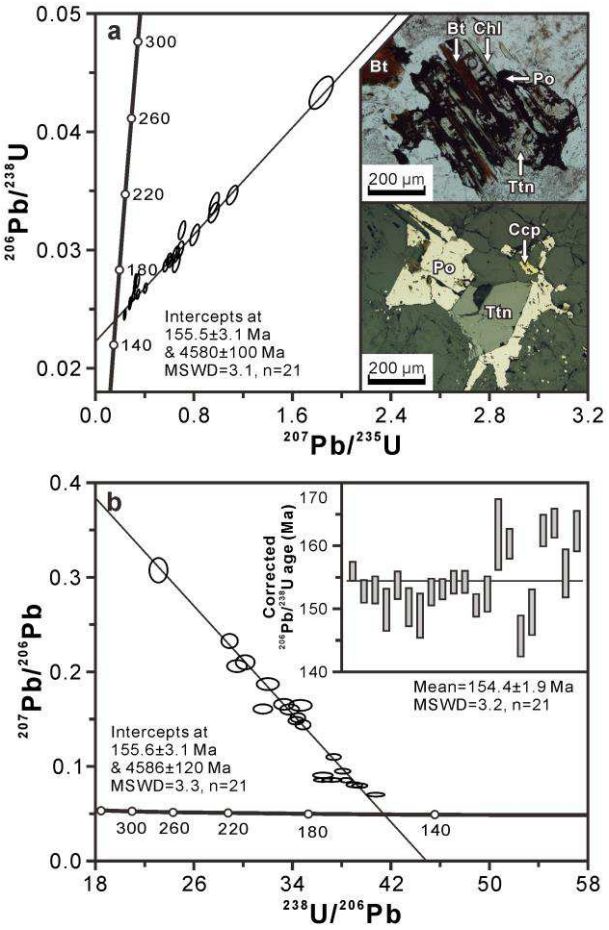

Figure 7-12. (a) Wetherill and (b) Tera-Wasserburg U-Pb concordia plots and weighted average ^{206}Pb/^{238}U age of hydrothermal titanite in the altered granodiorite from the Tongshanling Cu-Pb-Zn deposit.

The LA-ICP-MS U-Pb dating results of hydrothermal titanite in the altered granodiorite from the Tongshanling Cu-Pb-Zn deposit are listed in Appendix 7-3. Twenty-one analyses revealed that the hydrothermal titanite in the altered granodiorite has U, Th, and Pb contents of 40.6 – 404.4 ppm, 21.1 – 249.1 ppm, and 2.1 – 12.4 ppm, respectively, and $^{207}Pb/^{206}Pb$, $^{207}Pb/^{235}U$, and $^{206}Pb/^{238}U$ ratios of 0.070981 – 0.295930, 0.236849 – 1.833193, and 0.024529 – 0.043285, respectively (Appendix 7-3). A lower intercept age of 155.5 ± 3.1 Ma and an upper intercept age of 4580 ± 100 Ma are obtained by the Wetherill concordia plots of the $^{207}Pb/^{235}U$ and $^{206}Pb/^{238}U$ ratios (Fig. 7-12a). The Tera-Wasserburg concordia plots of the $^{238}U/^{206}Pb$ and $^{207}Pb/^{206}Pb$ ratios yield a lower intercept age of 155.6 ± 3.1 Ma and an upper intercept age of 4586 ± 120 Ma (Fig. 7-12b). The weighted average value of the ^{207}Pb-corrected $^{206}Pb/^{238}U$ ages is 154.4 ± 1.9 Ma (Fig. 7-12b) which is consistent with the lower intercept ages of the Wetherill and Tera-Wasserburg U-Pb concordia plots.

7.4.4. S isotope

The analytical results of S isotopic compositions of the sulfide minerals from the Tongshanling Cu-Pb-Zn deposit, Jiangyong Pb-Zn-Ag deposit, and Yulong Mo deposit are listed in Appendix 7-4 and shown in Figure 7-13. These sulfide minerals have $\delta^{34}S$ values of –0.3 – 6.3 ‰ and show a progressively decreasing trend of the $\delta^{34}S$ value from the Tongshanling Cu-Pb-Zn deposit through the Jiangyong Pb-Zn-Ag deposit to the Yulong Mo deposit on the whole (Fig. 7-13).

The $\delta^{34}S$ values of the sulfide minerals from the Tongshanling Cu-Pb-Zn deposit range from 0.2 ‰ to 5.0 ‰ and show variations of 1.9 – 3.6 ‰, 2.5 – 4.4 ‰, 1.9 – 4.6 ‰, 0.2 – 4.5 ‰, and 1.9 – 5.0 ‰ for the proximal endoskarn, proximal exoskarn, sulfide-quartz vein, distal skarn, and carbonate replacement mineralization types, respectively (Fig. 7-13). One pyrrhotite sample from the altered granodiorite has a $\delta^{34}S$ value of 3.9 ‰ (Fig. 7-13). In the proximal endoskarn ores, the $\delta^{34}S$ values of molybdenite, chalcopyrite, and pyrrhotite are 3.2 – 3.6 ‰, 2.2 – 2.4 ‰, and 1.9 – 2.1 ‰, respectively (Fig. 7-13). The chalcopyrite, sphalerite, and galena in the proximal exoskarn ores have respective $\delta^{34}S$ values of 3.4 – 4.4 ‰, 2.8 – 3.9 ‰, and 2.5 – 2.8 ‰ (Fig. 7-13). In the sulfide-quartz veins, chalcopyrite, sphalerite, and galena show respective $\delta^{34}S$ values of 2.7 – 4.6 ‰, 2.9 – 4.5 ‰, and 1.9 – 3.1 ‰ (Fig. 7-13).

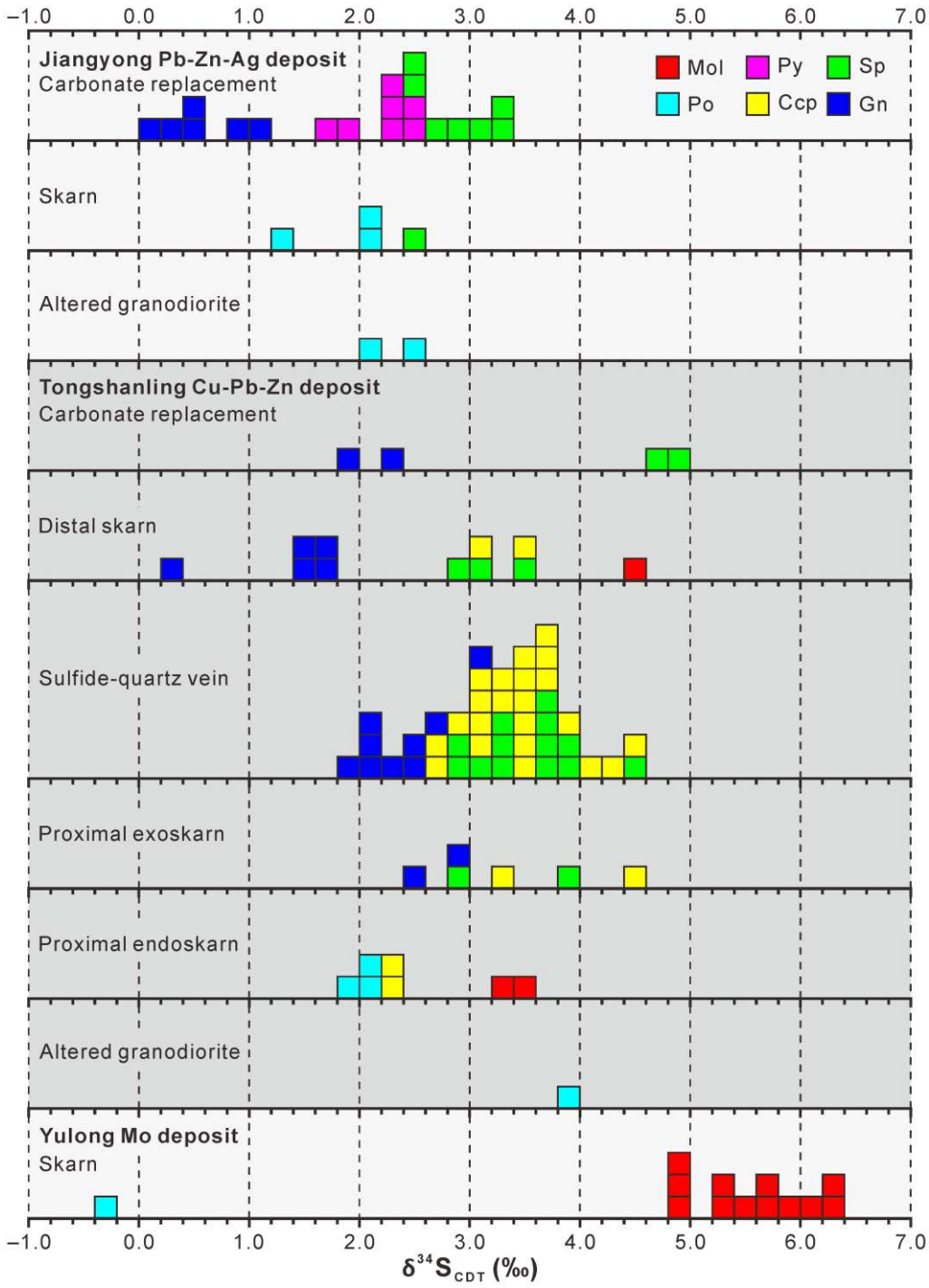

Figure 7-13. S isotopic compositions of sulfide minerals from the Tongshanling Cu-Pb-Zn deposit, Jiangyong Pb-Zn-Ag deposit, and Yulong Mo deposit. Mineral abbreviations: Ccp = chalcopyrite, Gn = galena, Mol = molybdenite, Po = pyrrhotite, Py = pyrite, Sp = sphalerite.

The molybdenite, chalcopyrite, sphalerite, and galena in the distal skarn ores have $\delta^{34}S$ values of 4.5 ‰, 3.1 – 3.6 ‰, 3.0 – 3.4 ‰, and 0.2 – 1.8 ‰, respectively (Fig. 7-13). In the carbonate replacement ores, the $\delta^{34}S$ values of sphalerite and galena are 4.7 – 5.0 ‰ and 1.9 –

2.2 ‰, respectively (Fig. 7-13).

The $\delta^{34}S$ values of the sulfide minerals from the Jiangyong Pb-Zn-Ag deposit vary from 0.2 ‰ to 3.3 ‰ and show ranges of 1.2 – 2.6 ‰ and 0.2 – 3.3 ‰ for the skarn and carbonate replacement mineralization types, respectively (Fig. 7-13). Two pyrrhotite samples from the altered granodiorite have $\delta^{34}S$ values of 2.0 ‰ and 2.5 ‰ (Fig. 7-13). In the skarn ores, one sphalerite and three pyrrhotite samples show respective $\delta^{34}S$ values of 2.6 ‰ and 1.2 – 2.2 ‰ (Fig. 7-13). The sphalerite, pyrite, and galena in the carbonate replacement ores have $\delta^{34}S$ values of 2.4 – 3.3 ‰, 1.8 – 2.6 ‰, and 0.2 – 1.1 ‰, respectively (Fig. 7-13). The $\delta^{34}S$ values of twelve molybdenite and one pyrrhotite samples from the skarn ores of the Yulong Mo deposit are 4.9 – 6.3 ‰ and –0.3 ‰, respectively (Fig. 7-13).

The sulfur isotopic fractionations and calculated temperatures of sulfide mineral pairs from the Tongshanling Cu-Pb-Zn deposit and Jiangyong Pb-Zn-Ag deposit are listed in Table 7-1. The $\delta^{34}S$ values of sulfide minerals in isotopic equilibrium should be arranged in the sequence of $\delta^{34}S_{Mol} > \delta^{34}S_{py} > \delta^{34}S_{Sp} = \delta^{34}S_{Po} > \delta^{34}S_{Ccp} > \delta^{34}S_{Gn}$ (Ohmoto and Rye, 1979). According to the $\Delta^{34}S$ values of sulfide mineral pairs, it is evidently concluded that the pyrrhotite-chalcopyrite in the proximal endoskarn ores and the sphalerite-chalcopyrite in the proximal exoskarn, sulfide-quartz vein, and distal skarn ores of the Tongshanling Cu-Pb-Zn deposit and the sphalerite-pyrrhotite in the skarn ores and the pyrite-sphalerite in the carbonate replacement ores of the Jiangyong Pb-Zn-Ag deposit were not formed in isotopic equilibrium (Table 7-1). Considering the positive $\Delta^{34}S_{Sp\text{-}Gn}$ values (Table 7-1) and the close coexistence of sphalerite and galena, they were possibly formed in isotopic equilibrium. The calculate temperatures of the sphalerite-galena pairs reveal that the carbonate replacement ore-forming processes in the Tongshanling Cu-Pb-Zn deposit and Jiangyong Pb-Zn-Ag deposit have similar temperatures which are distinctly lower than those of the skarn and sulfide-quartz vein mineralization (Table 7-1).

7.4.5. Pb isotope

The analytical results of the Pb isotopic compositions of sulfide minerals are listed in Appendix 7-4. The $^{206}Pb/^{204}Pb$, $^{207}Pb/^{204}Pb$, and $^{208}Pb/^{204}Pb$ ratios of the sulfide minerals from the Tongshanling Cu-Pb-Zn deposit vary from 18.643 to 18.785, 15.725 to 15.854, and 38.919

Table 7-1. Sulfur isotopic fractionations and calculated temperatures of sulfide mineral pairs from the Tongshanling Cu-Pb-Zn deposit and Jiangyong Pb-Zn-Ag deposit

		$\Delta^{34}S_{CDT}$ (‰) [T °C][a]						
Sample No.	Level	Py-Sp	Py-Gn	Sp-Po	Sp-Ccp	Sp-Gn	Po-Ccp	Ccp-Gn
Tongshanling Cu-Pb-Zn deposit								
Proximal endoskarn								
TSL121	00 m						–0.3	
TSL122	00 m						–0.3	
Proximal exoskarn								
TSL98	00 m				–0.6	0.3		0.9 [530]
TSL123	00 m				–0.5	1.1 [541]		1.6 [329]
Sulfide-quartz vein								
TSL04-1	60 m				0.7 [190]	1.6 [402]		0.9 [530]
TSL04-5	60 m				–0.2	1.1 [541]		1.3 [395]
TSL04-6	60 m				–0.2	1.0 [581]		1.2 [422]
TSL04-9	60 m				–0.2			
TSL04-12	60 m				–0.9			
TSL04-15	60 m				1.0 [114]			
TSL25-2	90 m				–0.2	1.0 [581]		1.2 [422]
TSL25-3	90 m				0.0	0.8 [682]		0.8 [578]
TSL26-1	120 m				0.2 [593]	1.0 [581]		0.8 [578]
TSL28-1	120 m				–0.3			
TSL28-2	120 m				–0.2	0.8 [682]		1.0 [488]
TSL28-3	120 m				0.2 [593]	1.2 [507]		1.0 [488]
TSL29-2	180 m				–0.1	1.2 [507]		1.3 [395]
Distal skarn								
TSL91	231 m				–0.1	1.3 [476]		1.4 [371]
TSL93	231 m					1.6 [402]		
TSL145	231 m				–0.5			
Carbonate replacement								
TSL17	60 m					2.8 [237]		
TSL40	231 m					2.8 [237]		
Jiangyong Pb-Zn-Ag deposit								
Skarn								
JY48	240 m			0.4				
Carbonate replacement								
JY59	200 m	–0.7						
JY47	160 m	–1.0	1.5 [556]			2.5 [267]		
JY63	160 m	–0.4	2.1 [427]			2.5 [267]		
JY50	240 m	–0.9	1.9 [463]			2.8 [237]		
JY56	200 m	–0.6	1.8 [483]			2.4 [278]		
JY58	200 m	–0.9	1.3 [617]			2.2 [303]		
JY66	240 m	–0.1	1.9 [463]			2.0 [331]		

Note: [a] Temperatures were calculated using the isotopic fractionation factors of sulfide mineral pairs from Ohmoto and Rye (1979), $\Delta^{34}S_{A\text{-}B} = C_{A\text{-}B} \times 10^6 / T\ (K)^2$, $C_{Py\text{-}Sp} = 0.30$, $C_{Py\text{-}Gn} = 1.03$, $C_{Sp\text{-}Po} = 0.00$, $C_{Sp\text{-}Ccp} = 0.15$, $C_{Sp\text{-}Gn} = 0.73$, $C_{Po\text{-}Ccp} = 0.15$, $C_{Ccp\text{-}Gn} = 0.58$. Mineral abbreviations: Ccp = chalcopyrite, Gn = galena, Po = pyrrhotite, Py = pyrite, Sp = sphalerite.

to 39.352, respectively. Nine chalcopyrite samples show $^{206}Pb/^{204}Pb$, $^{207}Pb/^{204}Pb$, and $^{208}Pb/^{204}Pb$ ratios of 18.703 – 18.785, 15.730 – 15.854, and 38.931 – 39.350, respectively. The $^{206}Pb/^{204}Pb$, $^{207}Pb/^{204}Pb$, and $^{208}Pb/^{204}Pb$ ratios of nine sphalerite samples are 18.693 – 18.752, 15.747 – 15.821, and 38.993 – 39.240, respectively. Eleven galena samples have $^{206}Pb/^{204}Pb$, $^{207}Pb/^{204}Pb$, and $^{208}Pb/^{204}Pb$ ratios of 18.643 – 18.743, 15.725 – 15.834, and 38.919 – 39.352, respectively. The $^{206}Pb/^{204}Pb$, $^{207}Pb/^{204}Pb$, and $^{208}Pb/^{204}Pb$ ratios of one molybdenite sample are 18.723, 15.770, and 39.073, respectively.

The $^{206}Pb/^{204}Pb$, $^{207}Pb/^{204}Pb$, and $^{208}Pb/^{204}Pb$ ratios of the sulfide minerals from the Jiangyong Pb-Zn-Ag deposit range from 18.836 to 18.969, 15.712 to 15.875, and 38.997 to 39.535, respectively. Two pyrrhotite samples have $^{206}Pb/^{204}Pb$, $^{207}Pb/^{204}Pb$, and $^{208}Pb/^{204}Pb$ ratios of 18.921 – 18.932, 15.818 – 15.834, and 39.349 – 39.408, respectively. The $^{206}Pb/^{204}Pb$, $^{207}Pb/^{204}Pb$, and $^{208}Pb/^{204}Pb$ ratios of two sphalerite samples are 18.853 – 18.969, 15.727 – 15.875, and 39.055 – 39.535, respectively. Six galena samples show $^{206}Pb/^{204}Pb$, $^{207}Pb/^{204}Pb$, and $^{208}Pb/^{204}Pb$ ratios of 18.836 – 18.880, 15.712 – 15.752, and 38.997 – 39.143, respectively. The $^{206}Pb/^{204}Pb$, $^{207}Pb/^{204}Pb$, and $^{208}Pb/^{204}Pb$ ratios of one pyrrhotite sample from the Yulong Mo deposit are 18.772, 15.729, and 39.022, respectively.

In the $^{206}Pb/^{204}Pb$ vs. $^{208}Pb/^{204}Pb$ and $^{206}Pb/^{204}Pb$ vs. $^{207}Pb/^{204}Pb$ diagrams, the sulfide minerals from the Tongshanling Cu-Pb-Zn deposit, Jiangyong Pb-Zn-Ag deposit, and Yulong Mo deposit show similar Pb isotopic compositions on the whole and are plotted above the average upper crust evolution lines (Fig. 7-14a and b). Notably, except for three discrete points, all the sulfide minerals of different mineralization types from the Tongshanling Cu-Pb-Zn deposit construct perfect positive linear correlations in the $^{206}Pb/^{204}Pb$ vs. $^{208}Pb/^{204}Pb$ and $^{206}Pb/^{204}Pb$ vs. $^{207}Pb/^{204}Pb$ diagrams with high squared correlation coefficients (R^2) of 0.97 (Fig. 7-14c and d). In the same way, all the sulfide minerals of different mineralization types from the Jiangyong Pb-Zn-Ag deposit also construct perfect positive linear correlations ($R^2 = 0.99$) with similar but slightly steeper slopes and lower intercept values relative to those of the Tongshanling Cu-Pb-Zn deposit (Fig. 7-14c and d).

7.4.6. H-O isotopes

The analytical results of H-O isotopic compositions of the quartz from the Tongshanling

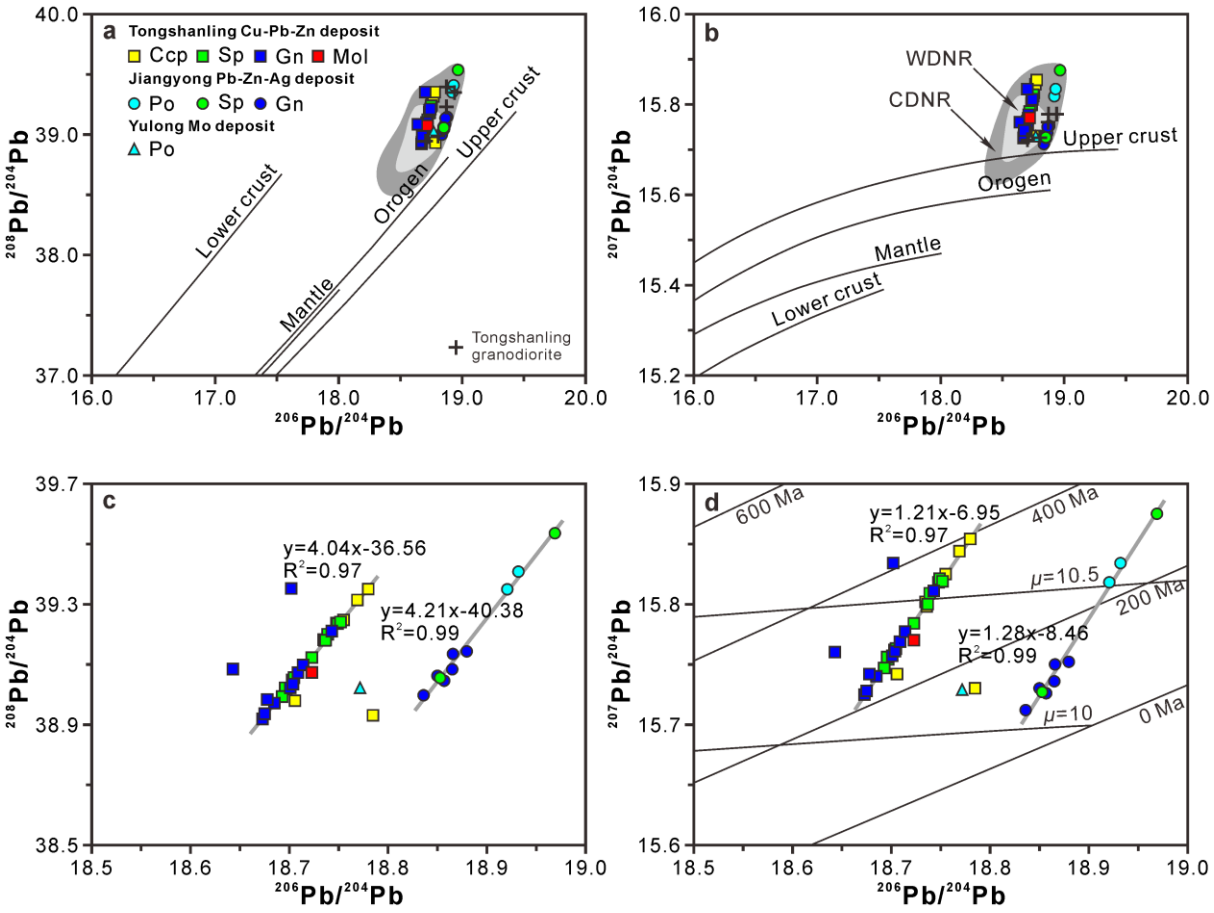

Figure 7-14. Pb isotopic compositions of sulfide minerals from the Tongshanling Cu-Pb-Zn deposit, Jiangyong Pb-Zn-Ag deposit, and Yulong Mo deposit plotted with the evolution curves generated by the plumbotectonics model of Zartman and Doe (1981) (a and b) and the two-stage model of Stacey and Kramers (1975) (d). The Pb isotopic compositions of the Tongshanling granodiorite are from Cai et al. (2015). The data sources of Pb isotopic compositions of sulfide minerals from the Middle-Late Jurassic Cu-Pb-Zn (CDNR) and W (WDNR) deposits in the Nanling Range are listed in Appendix 7-5.

Cu-Pb-Zn deposit, Jiangyong Pb-Zn-Ag deposit, and Yulong Mo deposit are listed in Appendix 7-6. The H isotopic compositions of the fluids hosted by quartz were directly obtained through the analyses by mass spectrometer and the O isotopic compositions of the fluids were calculated from the O isotopic compositions of quartz and the homogenization temperatures of fluid inclusions based on the quartz-water isotopic equilibrium equation of $1000\ \ln\alpha = 3.38\ (10^6\ T^{-2}) - 3.40$, $1000\ \ln\alpha \approx \delta^{18}O_{quartz} - \delta^{18}O_{H2O}$, T in K (Clayton et al., 1972). Nine quartz samples from the Tongshanling Cu-Pb-Zn deposit, one quartz sample from the Jiangyong Pb-Zn-Ag deposit, and three quartz samples from the Yulong Mo deposit have

respective δD_{H2O} values of –62 – –48 ‰, –70 ‰, and –58 – –53 ‰, respective $\delta^{18}O_{quartz}$ values of 11.7 – 14.0 ‰, 12.4 ‰, and 9.4 – 13.3 ‰, and respective $\delta^{18}O_{H2O}$ values of 1.6 – 4.8 ‰, 4.3 ‰, and 4.1 – 5.5 ‰. In the $\delta^{18}O_{H2O}$ vs. δD_{H2O} diagram, all the quartz samples from the three deposits show similar H-O isotopic compositions between the magmatic water and meteoric water on the whole (Fig. 7-15). Compared with the sulfide-quartz veins in the peripheral limestone from the Tongshanling Cu-Pb-Zn deposit, the quartz veins in granodiorite from the Tongshanling Cu-Pb-Zn deposit and Jiangyong Pb-Zn-Ag deposit and the quartz in skarn from the Yulong Mo deposit have slightly higher $\delta^{18}O_{H2O}$ and lower δD_{H2O} values and are closer to the field of magmatic water (Fig. 7-15).

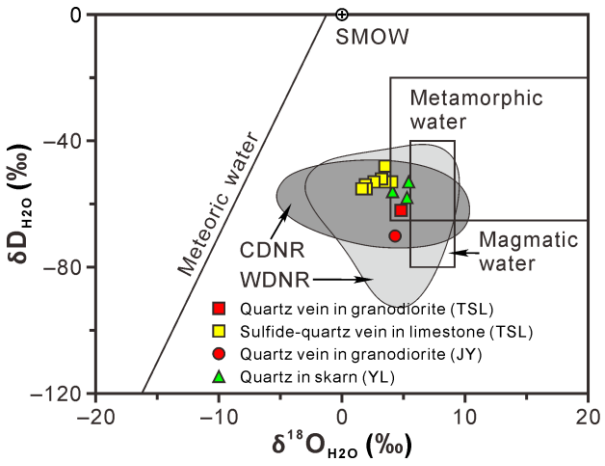

Figure 7-15. H-O isotopic compositions of the fluids hosted by quartz from the Tongshanling (TSL) Cu-Pb-Zn deposit, Jiangyong (JY) Pb-Zn-Ag deposit, and Yulong (YL) Mo deposit. The fields of primary magmatic and metamorphic waters and the meteoric water line are from Taylor (1997). SMOW = standard mean ocean water. The data sources of H-O isotopic compositions of ore-forming fluids of the Middle-Late Jurassic Cu-Pb-Zn (CDNR) and W (WDNR) deposits in the Nanling Range are listed in Appendix 7-7.

7.5. Discussion

7.5.1. Timing of mineralization

As a routine and effective method to directly constrain the metallogenic ages, molybdenite Re-Os dating has been widely used in the geochronological studies of

ore-forming process (e.g., Stein et al., 1997, 2001; Mao et al., 1999, 2008b, 2013c; Stein, 2014; Catchpole et al., 2015; Sillitoe et al., 2015). Several molybdenite Re-Os ages of the Tongshanling polymetallic ore district have been reported by previous studies. Lu et al. (2015) obtained a weighted average model age of 161 ± 1 Ma for the molybdenites from the sulfide-quartz veins of the Tongshanling Cu-Pb-Zn deposit. The weighted average Re-Os model ages of the molybdenites from the skarn ores of the Yulong Mo deposit published by Lu et al. (2015) and Zhao et al. (2016b) are 155 ± 3 Ma and 162.2 ± 1.6 Ma, respectively. However, the metallogenic ages of the dominant distal and proximal skarns in the Tongshanling Cu-Pb-Zn deposit are still not well constrained and the two molybdenite Re-Os model ages of the Yulong Mo deposit are not consistent and their corresponding ^{187}Re-^{187}Os isochron ages are unavailable or not precise (Lu et al., 2015; Zhao et al., 2016b).

In this study, the molybdenites from the proximal endoskarn, proximal exoskarn, and distal skarn of the Tongshanling Cu-Pb-Zn deposit yield consistent Re-Os model ages of 162.4 ± 2.2 – 163.1 ± 2.3 Ma, 160.2 ± 2.4 Ma, and 161.1 ± 2.4 – 163.5 ± 3.7 Ma (Appendix 7-2), respectively, with an integrated weighted average value of 161.9 ± 1.1 Ma (Fig. 7-11a). The ^{187}Re-^{187}Os isochron age of these molybdenites is 161.8 ± 1.7 Ma (Fig. 7-11a) and perfectly coincides with the weighted average model age. These geochronological results are in accordance to the metallogenic age of the sulfide-quartz veins (161 ± 1 Ma, Lu et al., 2015). Therefore, it is concluded that the proximal endoskarn, proximal exoskarn, sulfide-quartz veins, and distal skarn are temporally indistinguishable by molybdenite Re-Os dating and there are no obvious time intervals between these different mineralization types in the Tongshanling Cu-Pb-Zn deposit. The molybdenites from the skarn ores of the Yulong Mo deposit yield a ^{187}Re-^{187}Os isochron age of 160.0 ± 5.8 Ma (Fig. 7-11b) with a well consistent weighted average model age of 160.1 ± 0.8 Ma (Fig. 7-11b). These ages are consistent with the result of 162.2 ± 1.6 Ma published by Zhao et al. (2016b). Thus, the Tongshanling Cu-Pb-Zn deposit and Yulong Mo deposit were formed simultaneously with identical metallogenic ages of 160 – 162 Ma.

Except for the molybdenite Re-Os ages, two Sm-Nd isochron ages of 155 ± 8 Ma and 173 ± 3 Ma for the garnets from the skarn of the Yulong Mo deposit and the distal skarn of the

Tongshanling Cu-Pb-Zn deposit, respectively, were achieved by previous studies (Lu et al., 2015; Wang et al., 2017d). These geochronological results are quite dispersed relative to the molybdenite Re-Os ages. In order to determine the time interval between skarn formation and sulfide mineralization, LA-ICP-MS U-Pb dating of the garnet from the proximal exoskarn of the Tongshanling Cu-Pb-Zn deposit was carried out in this study and yields a concordia age of 162.0 ± 3.7 Ma with a consistent weighted average $^{206}Pb/^{238}U$ age of 162.4 ± 4.2 Ma (Fig. 7-10). These results are in accordance to the molybdenite Re-Os ages and reveal that there is no obvious time interval between skarn formation and sulfide mineralization.

The LA-ICP-MS U-Pb dating of the hydrothermal titanite in the altered granodiorite from the Tongshanling Cu-Pb-Zn deposit yields lower intercept ages of 155.5 ± 3.1 Ma and 155.6 ± 3.1 Ma in the Wetherill and Tera-Wasserburg U-Pb concordia diagrams, respectively (Fig. 7-12), with a consistent weighted average $^{206}Pb/^{238}U$ age of 154.4 ± 1.9 Ma (Fig. 7-12b). These titanite U-Pb ages are about 5 Ma younger than the molybdenite Re-Os and garnet U-Pb ages and may reflect a slightly later hydrothermal event after the dominant skarn and sulfide-quartz vein mineralization. However, the nature and role of the later hydrothermal event are still unknown and need to be further studied. A possibility is that the later hydrothermal event was genetically related to the later carbonate replacement mineralization in the Tongshanling polymetallic ore district.

For the Jiangyong Pb-Zn-Ag deposit, up to date, there is no available mineral found for geochronological study of metallogenesis. Zhao et al. (2016b) obtained two zircon U-Pb ages of 160.7 ± 0.5 Ma and 160.5±0.9 Ma for the ore-bearing Tongshanling granodiorite sampled from the underground galleries in the Jiangyong Pb-Zn-Ag deposit. It is dependable to conjecture that the Jiangyong Pb-Zn-Ag deposit was formed temporally consistent with or slightly later than the Tongshanling granodiorite.

In a word, the three ore deposits in the Tongshanling polymetallic ore district were almost contemporaneously formed at 160 – 162 Ma which is consistent with the zircon U-Pb age of the Tongshanling granodiorite (160 – 164 Ma, Jiang et al., 2009; Zhao et al., 2016b; Huang et al., 2017a). Except for the carbonate replacement mineralization which is still not well constrained by geochronology, there are no evident time intervals between the different

mineralization types in the Tongshanling ore district.

7.5.2. Sources of ore-forming materials

The sulfide minerals of the Tongshanling Cu-Pb-Zn deposit, Jiangyong Pb-Zn-Ag deposit, and Yulong Mo deposit show a narrow variation of $\delta^{34}S$ values from –0.3 ‰ to 6.3 ‰ (Fig. 7-13). Such S isotopic compositions are consistent with those of the sulfides derived from high-temperature magmas but are distinctly different from those of the sulfides precipitated from sea water and also the sulfides transformed from sulfate by organic reduction (Fig. 7-16). Therefore, the sulfur for sulfide mineralization in the Tongshanling polymetallic ore district is magmatic sulfur originated from the Tongshanling granodioritic intrusion, whereas, the carbonate wall rocks almost do not make a contribution of sulfur to the metallogenesis.

The Pb isotopic compositions of the sulfide minerals from the three ore deposits are similar on the whole and are identical to those of the Tongshanling granodiorite (Fig. 7-14a and b, Cai et al., 2015), indicating that the lead for sulfide mineralization in the Tongshanling polymetallic ore district was derived from the Tongshanling granodioritic intrusion. The sulfide minerals from the Tongshanling ore district show Pb isotopic compositions with upper crust affinities (Fig. 7-14a and b). Based on detailed geochronological, geochemical, petrographic, and mineralogical studies, Huang et al. (2017a) and Huang et al. (2018) demonstrated that the Tongshanling granodiorite was originated from partial melting of the mafic amphibolitic lower crust. Thus, the lead for the metallogenesis in the Tongshanling ore district was in all probability extracted from the upper crust by the ascending granodioritic magma. The positive linear correlations of Pb isotopic compositions made up by the sulfide minerals from the Tongshanling ore district show steep slopes and do not construct isochrons (Fig. 7-14c and d). Such Pb isotopic linear trends are probably indicative of a mixing between two different source-rock components (e.g., Anderson et al., 2002; Schneider et al., 2002; Cunha et al., 2007; Zeng et al., 2014). The mixing of a lower crust-derived magma with relatively low U/Pb and Th/Pb ratios and an upper crust-derived component with relatively high U/Pb and Th/Pb ratios may be the genesis of the Pb isotopic linear trends revealed by the sulfide minerals from the Tongshanling ore district.

It is noteworthy that, the mafic amphibolitic lower crust in South China has fertile Cu and Zn contents but a barren Pb content. For instance, the exposed amphibolites in the Tianjinping Formation and the Mayuan Group which are the lower-crust basement of the Cathaysia Block have Cu contents of 57.7 ppm and 66.5 ppm, Zn contents of 119 ppm and 118 ppm, and Pb contents of 7.39 ppm and 8.46 ppm, respectively (Li, 1997). Their Cu and Zn contents are distinctly higher than those of the upper crust (Cu: 29 ppm, Zn: 63 ppm) in Southeast China (Gao et al., 1998) and are also higher than those of the lower crust (Cu: 26 ppm, Zn: 78 ppm) reported by Rudnick and Fountain (1995). However, their Pb contents are distinctly lower than that of the upper crust (17 ppm) in Southeast China (Gao et al., 1998). Taylor and McLennan (1995) also reported a distinctly lower Pb content of the lower crust (4 ppm) than that of the upper crust (20 ppm). Therefore, the Cu and Zn of the Tongshanling ore district were most probably released from the mafic amphibolitic lower crust by partial melting, whereas, the Pb was extracted from the upper crust by the ascending granodioritic magma.

7.5.3. Nature of ore-forming fluids

The quartz veins in the granodiorite from the Tongshanling Cu-Pb-Zn deposit and Jiangyong Pb-Zn-Ag deposit and the quartz in the skarn of the Yulong Mo deposit show H-O isotopic compositions with evident magmatic water affinities (Fig. 7-15), indicating a magmatic origin of the ore-forming fluids. By contrast, the sulfide-quartz veins in the Tongshanling Cu-Pb-Zn deposit show a slight shift of oxygen isotope towards the meteoric water line (Fig. 7-15), indicating an additional influence of meteoric water during the migration of ore-bearing fluids from the granodiorite to the peripheral wall rocks with the temperature decreasing. However, the effect of meteoric water during mineralization was limited and did not change the magmatic water-dominant nature of the ore-forming fluids. In a word, the ore-forming fluids of the three ore deposits in the Tongshanling ore district are all dominated by magmatic water derived from the Tongshanling granodioritic intrusion.

7.5.4. Genetic links between different mineralization types and ore deposits

The Tongshanling Cu-Pb-Zn deposit exhibits a well-developed outward zonation from

the proximal endoskarn (Fig. 7-4a) through the proximal exoskarn (Fig. 7-4b) to the sulfide-quartz veins (Fig. 7-4g) and then to the distal skarn (Fig. 7-4c) with an extending distance of several hundred meters (Fig. 7-2). Besides, a few late Pb-Zn sulfide-quartz veins (Fig. 7-4h) and carbonate replacement Pb-Zn sulfide veins (Fig. 7-4i) occur in the granodiorite and proximal wall rocks, respectively. Previous studies argued that the distal skarn mineralization was caused by hydrothermal overprint and reworking of a pre-enriched syndepositional source bed and belongs to stratabound mineralization during which the strata have made a significant contribution of ore-forming materials (Long, 1983; Chen, 1986; Deng and Deng, 1991). However, the sulfide minerals from the distal skarn ores do not show any credible isotopic information supporting a wall-rock contribution of syndepositional ore-forming materials. They have similar magmatic $\delta^{34}S$ values to those of the other mineralization types (Fig. 7-13). The positive linear correlations made up by the sulfide Pb isotopic compositions of these different mineralization types in the Tongshanling Cu-Pb-Zn deposit (Fig. 7-14c and d) which show a consistent variation with those of the Tongshanling granodiorite (Fig. 7-14a) also indicate the same origin of ore-forming materials from the Tongshanling intrusion. According to the spatiotemporal evolution sequence from the irregular quartz within the proximal endoskarn (Fig. 7-4a) through the barren vein-like quartz in the center of the proximal exoskarn (Fig. 7-4b) or cutting the proximal exoskarn (Fig. 7-4e) to the sulfide-quartz veins in the peripheral limestone (Fig. 7-4g), the sulfide-quartz veins are considered as later productions of the evolved skarn system relative to the earlier skarn. Then, the carbonate replacement Pb-Zn sulfide veins were formed with lower temperatures than the sulfide-quartz veins (Table 7-1). The zonation of these different mineralization types results in the formation of a metal zonation from proximal Cu to distal Cu-Pb-Zn with a few late Pb-Zn orebodies in the proximal part. In summary, the different mineralization types of the Tongshanling Cu-Pb-Zn deposit are genetically connected in the same skarn system related to the Tongshanling granodioritic intrusion.

Similar to the Tongshanling Cu-Pb-Zn deposit, for the Jiangyong Pb-Zn-Ag deposit, the sulfide S and Pb isotopic compositions of the skarn and carbonate replacement mineralization types (Figs. 7-13 and 7-14) also indicate the same origin of ore-forming materials from the

Tongshanling intrusion. The temperature of carbonate replacement (237 – 331 °C, Table 7-1) calculated by the sulfur isotopic fractionation between sphalerite and galena is consistent with previous fluid inclusion microthermometric results (225 – 340 °C, Yi and Xu, 2006) and is similar to that of the Tongshanling Cu-Pb-Zn deposit (237 °C, Table 7-1), indicating a low-temperature and late mineralization. Notably, the Pb isotopic linear trends of the Jiangyong Pb-Zn-Ag deposit are almost parallel to those of the Tongshanling Cu-Pb-Zn deposit with lower intercept values (i.e., higher $^{206}Pb/^{204}Pb$ ratio) (Fig. 7-14c and d). Since the $^{206}Pb/^{204}Pb$ ratio of the ore-bearing magma was always in evolution by the decay of ^{238}U, the divergence of $^{206}Pb/^{204}Pb$ ratio between these two deposits may be indicative of a time interval between the non-simultaneous separations of ore-bearing fluids from magma to form these two deposits. Thus, the Jiangyong Pb-Zn-Ag deposit was formed slightly later than the Tongshanling Cu-Pb-Zn deposit. This is in accordance with the low-temperature carbonate replacement-dominant mineralization in the Jiangyong Pb-Zn-Ag deposit.

The southern contact zone between the Tongshanling granodiorite and country rocks, where the Yulong Mo deposit occurs (Fig. 3-1), shows distinctly stronger wall-rock marblization and deformation than the northeastern contact zone. Based on detailed field observations, structural analysis, RSCM thermometric and EBSD studies (shown in Chapter 6), it is concluded that the emplacement of the Tongshanling intrusion started from the southern part. Therefore, under a high-temperature condition, skarn molybdenite mineralization is the predominant mineralization type in the Yulong Mo deposit, whereas, the relatively low-temperature sulfide-quartz vein and carbonate replacement mineralization types are absent.

Geochronological and S, Pb, and H-O isotopic studies reveal that the Tongshanling Cu-Pb-Zn deposit, Jiangyong Pb-Zn-Ag deposit, and Yulong Mo deposits were almost contemporaneously formed with the ore-forming materials and fluids derived from the Tongshanling granodioritic intrusion. They are genetically linked in the same magmatic-hydrothermal system. The sulfide $\delta^{34}S$ values show a progressively decreasing trend from the Yulong Mo deposit through the Tongshanling Cu-Pb-Zn deposit to the Jiangyong Pb-Zn-Ag deposit (Fig. 7-13). This trend results from thermodynamic equilibrium

fractionation of S isotopes from the same magmatic sulfur source. Among these sulfide minerals, the molybdenite has the strongest chemical bond, thus, it has the highest $\delta^{34}S$ values (Fig. 7-13). The higher $\delta^{34}S$ values of the molybdenite from the Yulong Mo deposit than that from the Tongshanling Cu-Pb-Zn deposit (Fig. 7-13) indicate a relatively high ore-forming temperature of the Yulong Mo deposit. The lower $\delta^{34}S$ values of the galena from the Jiangyong Pb-Zn-Ag deposit than that from the Tongshanling Cu-Pb-Zn deposit (Fig. 7-13) result from the lower ore-forming temperature of the Jiangyong Pb-Zn-Ag deposit. A comparison of the paragenetic sequences of these three ore deposits (Figs. 7-7–7-9) indicates that the Yulong Mo deposit and Jiangyong Pb-Zn-Ag deposit are corresponding to the skarn stage and carbonate replacement stage of the Tongshanling Cu-Pb-Zn deposit, respectively. In conclusion, the different mineralization types and ore deposits in the Tongshanling ore district are genetically linked together and are the productions of evolution and zonation of the same skarn system associated with the Tongshanling granodioritic intrusion.

7.5.5. Ore-forming process

On the basis of the geological, geochronological, and geochemical studies and the discussion above, the ore-forming process of the Tongshanling polymetallic ore district is summarized as follows.

During Middle-Late Jurassic, partial melting of the fertile mafic amphibolitic lower crust produced a Cu and Zn enriched granodioritic magma. The ascending granodioritic magma extracted abundant Pb from the upper crust and intruded into the Devonian and Carboniferous carbonate strata. Then, the vein skarn of the Yulong Mo deposit and the proximal massive endoskarn and vein exoskarn of the Tongshanling Cu-Pb-Zn deposit were firstly formed by reaction between the granodioritic intrusion and carbonate rocks and followed by Mo, Cu, and Cu-Pb-Zn mineralization, respectively, with temperature decreasing. A great quantity of ore-bearing magmatic fluids were transported outward maybe along a major fault in the Tongshanling Cu-Pb-Zn deposit. The infiltration of ore-bearing magmatic fluids along the argillaceous limestone of the Xikuangshan Formation led to the formation of the stratiform distal skarn Cu-Pb-Zn orebodies. With the evolution of the skarn system, the outward migration of ore-bearing magmatic fluids along fractures from the proximal part resulted in the

formation of the sulfide-quartz veins in the peripheral limestone between the proximal and distal skarns. The Cu-dominant sulfide-quartz veins were formed earlier at more proximal locations than the Cu-Pb-Zn sulfide-quartz veins. After, with the temperature further decreasing, the carbonate replacement Pb-Zn sulfide orebodies were formed at the latest dominantly in the Jiangyong Pb-Zn-Ag deposit with a few in the Tongshanling Cu-Pb-Zn deposit.

7.5.6. Comparison with the Late Jurassic W deposits in the Nanling Range

A great number of previously published S, Pb, and H-O isotopic data and molybdenite Re-Os geochronological data of the Middle-Late Jurassic Cu-Pb-Zn and W deposits in the Nanling Range are collected to make a comparative study of these two different types of mineralization. The detailed data are listed in Appendices 7-5 and 7-7–7-9 and shown in Figures 7-14–7-18.

The S isotopic compositions of the sulfide minerals from the Middle-Late Jurassic Cu-Pb-Zn and W deposits in the Nanling Range predominantly show narrow variations ($\delta^{34}S$ values are –5.0 – 6.5 ‰ and –2.9 – 8.9 ‰, respectively) and are of an evident magmatic signature except for the Huangshaping Pb-Zn-W-Mo deposit (Fig. 7-16). Ding et al. (2016a) proposed that the sulfur for Pb-Zn mineralization in the Huangshaping deposit has a mixing origin of partial magmatic sulfur and partial sulfur reduced from evaporite. The H-O isotopic compositions of the quartz from the Cu-Pb-Zn and W deposits are similar and show trends of oxygen isotope shift from magmatic water to meteoric water (Fig. 7-15). These isotopic features indicate that granitoid magmas have played an important role in providing ore-forming materials and fluids for the Middle-Late Jurassic Cu-Pb-Zn and W mineralization in the Nanling Range. The Pb isotopic compositions of the sulfide minerals from these two types of mineral deposits are similar and show upper crust affinities (Fig. 7-14a and b). Huang et al. (2017a) proposed that the Middle-Late Jurassic Cu-Pb-Zn-bearing and W-bearing granitoids in the Nanling Range were derived from non-simultaneous partial melting of the mafic amphibolitic basement in the lower crust and the muscovite-rich metasedimentary basement in the upper-middle crust, respectively. Thus, the upper-crust Pb isotopic signatures of the W deposits were probably inherited from the magma source, whereas, those of the

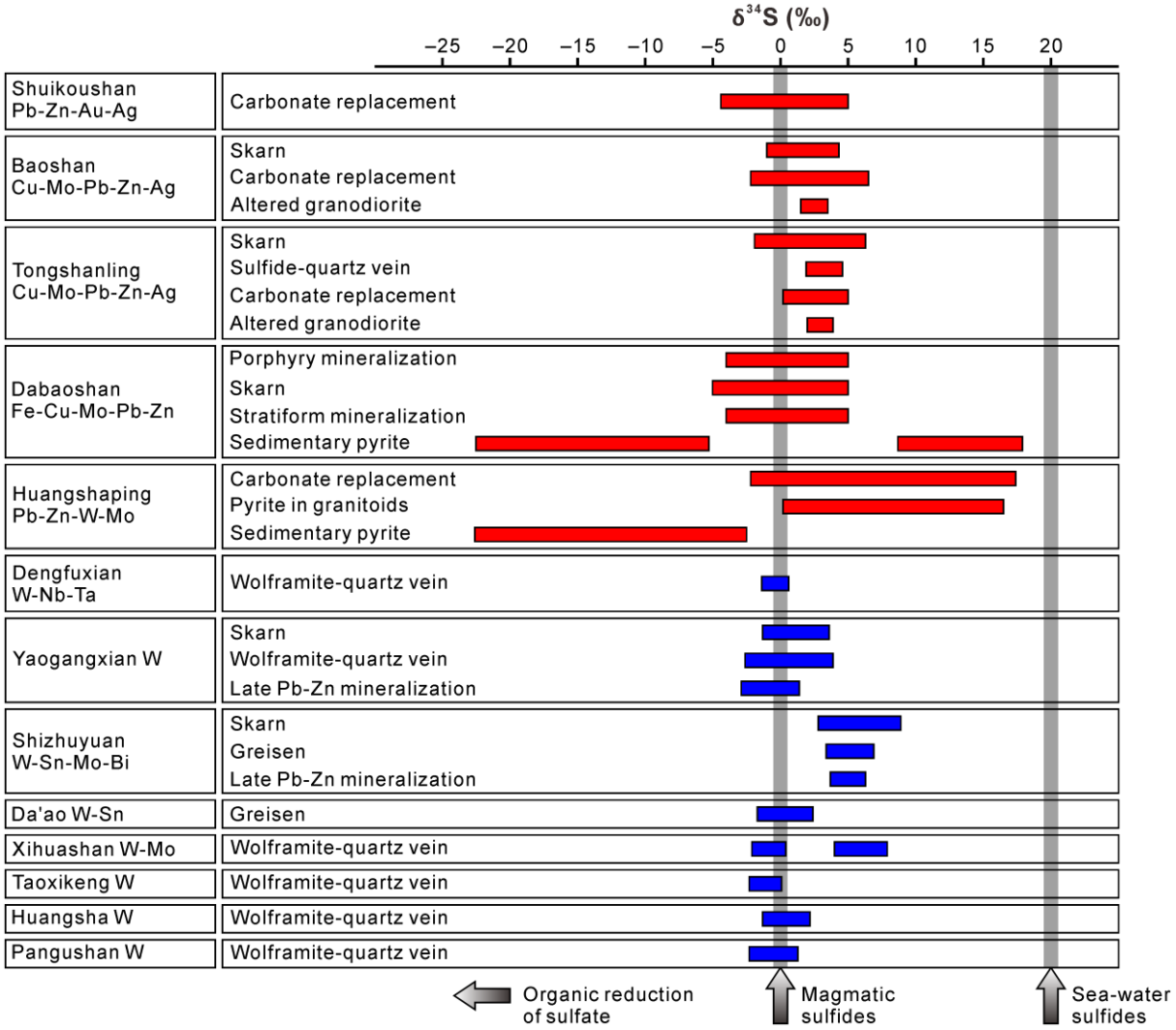

Figure 7-16. S isotopic compositions of sulfide minerals from the Middle-Late Jurassic Cu-Pb-Zn and W deposits in the Nanling Range. The data sources are listed in Appendix 7-8.

Cu-Pb-Zn deposits may be indicative of an extraction of Pb from the upper crust by the ascending lower crust-derived magmas as discuss before.

Notably, the molybdenite Re-Os ages revealed that the Cu-Pb-Zn deposits were formed mainly from 153.8 Ma to 166.0 Ma with a peak value of 159.9 Ma, whereas, the W deposits were formed mainly from 146.9 Ma to 160.0 Ma with a peak value of 154.5 Ma (Fig. 7-17). There is a time gap of about 5 Ma between the two different types of mineral deposits. This is highly consistent with the time gap of about 5 Ma between the Cu-Pb-Zn-bearing and W-bearing granitoids (Huang et al., 2017a) and further supports the petrogenetic model of non-simultaneous partial melting illustrating the origins of the Cu-Pb-Zn-bearing and

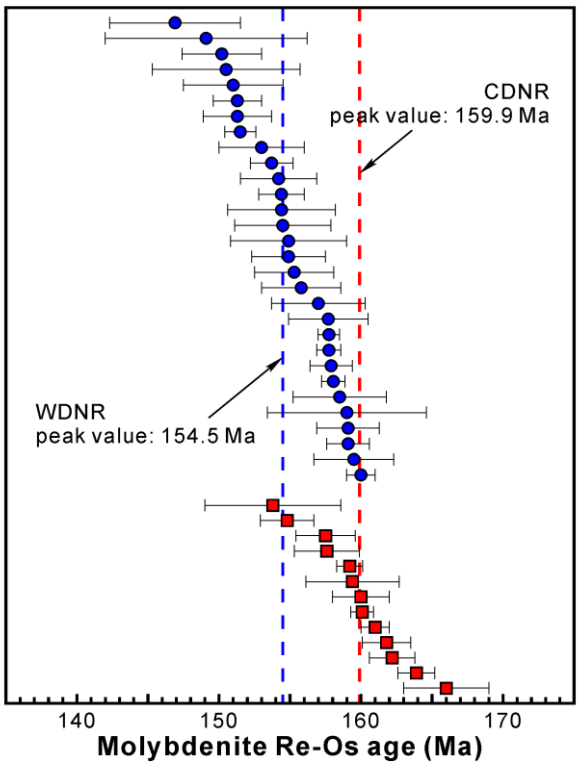

Figure 7-17. Molybdenite Re-Os ages of the Middle-Late Jurassic Cu-Pb-Zn (CDNR) and W (WDNR) deposits in the Nanling Range. The data sources are listed in Appendix 7-9.

W-bearing granitoids (Huang et al., 2017a). The molybdenite Re-Os ages of the Cu-Pb-Zn and W deposits are consistent with the zircon U-Pb ages of the Cu-Pb-Zn-bearing and W-bearing granitoids (Huang et al., 2017a), respectively, indicating that the Middle-Late Jurassic Cu-Pb-Zn and W deposits in the Nanling Range are genetically associated with the contemporaneous ore-bearing granitoids.

The molybdenites from the Middle-Late Jurassic Cu-Pb-Zn and W deposits in the Nanling Range have Re contents of 16.3 – 1841 ppm and 0.003 – 14.6 ppm, respectively (Fig. 7-18). Such distinctly different molybdenite Re contents are indicative of different sources of ore-forming materials for the Cu-Pb-Zn and W deposits. Mao et al. (1999) proposed that the Re contents of molybdenite progressively decrease from a mantle source ($n \times 10^{-4}$) through a crust-mantle mixing source ($n \times 10^{-5}$) to a crustal source ($n \times 10^{-6}$). The low Re contents of the molybdenites from the W deposits are consistent with their upper-middle crust-derived ore-bearing granites and ore-forming materials. The high Re contents of the molybdenites from the Cu-Pb-Zn deposits are widely considered as an indicator of crust-mantle

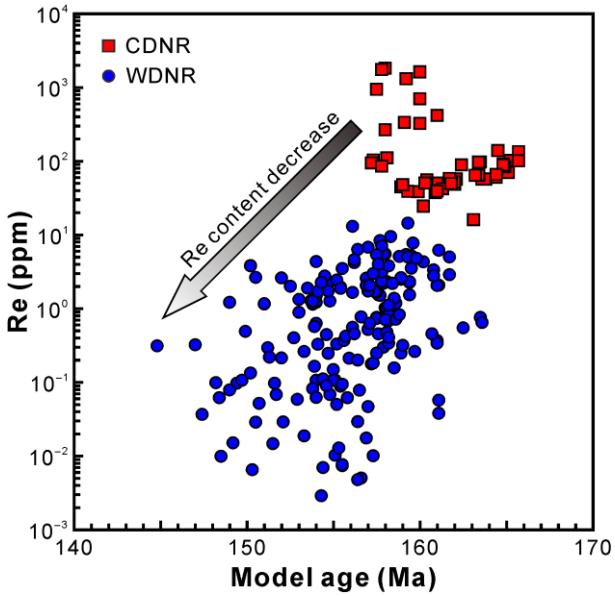

Figure 7-18. Re contents of molybdenites from the Middle-Late Jurassic Cu-Pb-Zn (CDNR) and W (WDNR) deposits in the Nanling Range. The data sources are the same as Figure 7-17.

mixing-derived ore-forming materials (e.g., Lu et al., 2006, 2015; Wang et al., 2011d; Huang et al., 2015). However, Stein et al. (2001) pointed that melting of mafic rocks may also be expected to produce high Re contents in associated molybdenites. Therefore, the high molybdenite Re contents of the Cu-Pb-Zn deposits can be well explained by the origin of the Cu-Pb-Zn-bearing granitoids, i.e., partial melting of the mafic amphibolitic lower crust, and the crust-mantle mixing source is not necessary. The progressively decreasing molybdenite Re contents from the earlier Cu-Pb-Zn deposits to the later W deposits (Fig. 7-18) reflect the non-simultaneous formation of the Cu-Pb-Zn-bearing and W-bearing granitoids by progressive partial melting from the mafic amphibolitic lower crust to the muscovite-rich metasedimentary upper-middle crust.

7.6. Summary

The Tongshanling Cu-Pb-Zn deposit shows a well-developed outward zonation from proximal endoskarn through proximal exoskarn to sulfide-quartz veins and then to distal skarn, additionally with a few late Pb-Zn sulfide-quartz veins and carbonate replacement Pb-Zn sulfide veins distributed in the proximal part. The Jiangyong Pb-Zn-Ag deposit and Yulong

Mo deposit are dominated by carbonate replacement and skarn mineralization, respectively.

Garnet U-Pb dating yields a $^{207}Pb/^{235}U$-$^{206}Pb/^{238}U$ concordia age of 162.0 ± 3.7 Ma with a weighted average $^{206}Pb/^{238}U$ age of 162.4 ± 4.2 Ma for the proximal exoskarn in the Tongshanling Cu-Pb-Zn deposit. Molybdenite Re-Os dating of the Tongshanling Cu-Pb-Zn deposit and Yulong Mo deposit yields ^{187}Re-^{187}Os isochron ages of 161.8 ± 1.7 Ma and 160.0 ± 5.8 Ma with weighted average model ages of 161.9 ± 1.1 Ma and 160.1 ± 0.8 Ma, respectively. U-Pb dating of the hydrothermal titanite in the altered granodiorite yields lower intercept ages of 155.5 ± 3.1 Ma and 155.6 ± 3.1 Ma in the Wetherill and Tera-Wasserburg U-Pb concordia plots, respectively, with a weighted average $^{206}Pb/^{238}U$ age of 154.4 ± 1.9 Ma.

S, Pb, and H-O isotopic studies reveal that the ore-forming materials and fluids of the Tongshanling polymetallic ore district were derived from the Tongshanling intrusion. The Cu and Zn were most probably released from the mafic amphibolitic lower crust by partial melting, whereas, the Pb was extracted from the upper crust by the ascending granodioritic magma.

Based on the geological, geochronological, and isotopic geochemical studies, it is concluded that the different mineralization types and ore deposits in the Tongshanling ore district are genetically linked together and are the productions of evolution and zonation of the same skarn system associated with the Tongshanling granodioritic intrusion.

A comparison of the Middle-Late Jurassic Cu-Pb-Zn and W deposits in the Nanling Range further supports the petrogenetic model of non-simultaneous partial melting illustrating the origins of the Cu-Pb-Zn-bearing and W-bearing granitoids.

Chapter 8. Ore-forming process of the Weijia scheelite skarn deposit

8.1. Introduction

About one-half of the world's tungsten resources are present as scheelite in skarn deposits (Werner et al., 2014). Essentially, all economic W skarns are calcic throughout the world (Kwak, 1987), such as the well-known MacTung (Canada), CanTung (Canada), Pine Creek (USA), King Island (Australia), Sangdong (South Korea), Nui Phao (Vietnam), Uludağ (Turkey), Salau (France), Los Santos (Spain), Xintianling (China), Shizhuyuan (China), and Yaogangxian (China) deposits (see details in the Appendix of Meinert et al., 2005). Especially, the recently discovered giant Zhuxi W-Cu deposit (2.86 Mt WO_3, Wang et al., 2017b) in northeastern Jiangxi Province of South China is also dominated by calcic skarn mineralization (Pan et al., 2017). In contrast, magnesian W skarns are uncommon and have been rarely reported. For instance, the Costabonne W deposit (France) (Guy, 1979; Kwak, 1987; Dubru et al., 1988), Carro del Diablo W-Sn deposit (Spain) (Casquet and Tornos, 1984), and Traversella Fe-W-Cu deposit (Italy) (Dubru et al., 1988; Vander Auwera and Andre, 1991) are several exceptional examples of magnesian W skarns. These latter are characterized by small-scale mineralization and are of less economic importance. Although dolomitic rocks are favorable hosts for some Fe, Sn, and Au skarns, general observations revealed that they tend to inhibit the development of W skarns (Zharikov, 1970; Einaudi et al., 1981; Kwak, 1987; Ray, 1998, 2013; Meinert et al., 2005).

The discovery of the super-large Weijia scheelite skarn deposit in South China that comprises predominant magnesian W skarn and subordinate calcic W skarn demonstrates and highlights the importance of magnesian skarn for W mineralization. The Weijia W deposit has a total WO_3 resource of ca. 300,000 t estimated by a cut-off grade of 0.12 wt.%, in which ca. 240,000 t are from the magnesian skarn with an average grade of ca. 0.18 wt.% and the rest ca. 60,000 t from the calcic skarn with an average grade of ca. 0.24 wt.% (No. 1 General Brigade of Hunan Geological and Mining Bureau for Nonferrous Metals, unpub. report, 2014; No. 418

Geological Team of Bureau of Geology and Mineral Exploration and Development of Hunan Province, unpub. report, 2016). Since the concealed Weijia W deposit is still unmined, however, very few studies have been carried out on its metallogenesis and mineralization process, except for some publications of deposit geology and ore-bearing granite (e.g., Li et al., 2012a; Hu et al., 2015; Zhao et al., 2016a, 2016b; Huang et al., 2017a). Scientifically the Weija deposit presents a special case of scheelite skarn deposit. Such unusual economic mineralization is of great interest to economic geologists and provides an excellent opportunity for further understanding of W mineralization. Two main particularities have been evocated in preceding publications. First, it is genetically related to a highly fractionated porphyritic granite with petrographic features similar to those of the subvolcanic granites (Huang et al., 2017a). Such an association differs from most other W skarn deposits that are commonly related to deep-emplaced and coarse-grained granitoids (Einaudi et al., 1981; Newberry and Swanson, 1986; Kwak, 1987; Ray and Webster, 1991; Meinert et al., 2005). Second, fluorite is abundant and is a potential economic resource of the Weijia W deposit (Hu et al., 2015). However, no genetic model has been proposed for this particular deposit.

In this study, based on detailed observations of surface outcrops and numerous drill cores, systematic petrographic study, Raman spectroscopy of carbonaceous material (RSCM) thermometry, whole-rock geochemical analysis of altered granite, and mineralogical analyses of micas, skarn minerals, and scheelite are carried out to constrain the process of magmatic to hydrothermal evolution and magnesian and calcic skarnization and mineralization of the Weijia W deposit. Some key processes that control tungsten mineralization are then discussed based on these results and previous studies. Finally, a comprehensive genetic model of the Weijia W deposit is proposed.

8.2. Deposit geology

8.2.1. Stratigraphy

In the Weijia W deposit, the exposed strata are mainly Middle-Upper Devonian carbonate rocks that include the Middle Devonian Qiziqiao and Upper Devonian Shetianqiao and Xikuangshan Formations, some of which are covered by Quaternary sediments (Fig. 8-1).

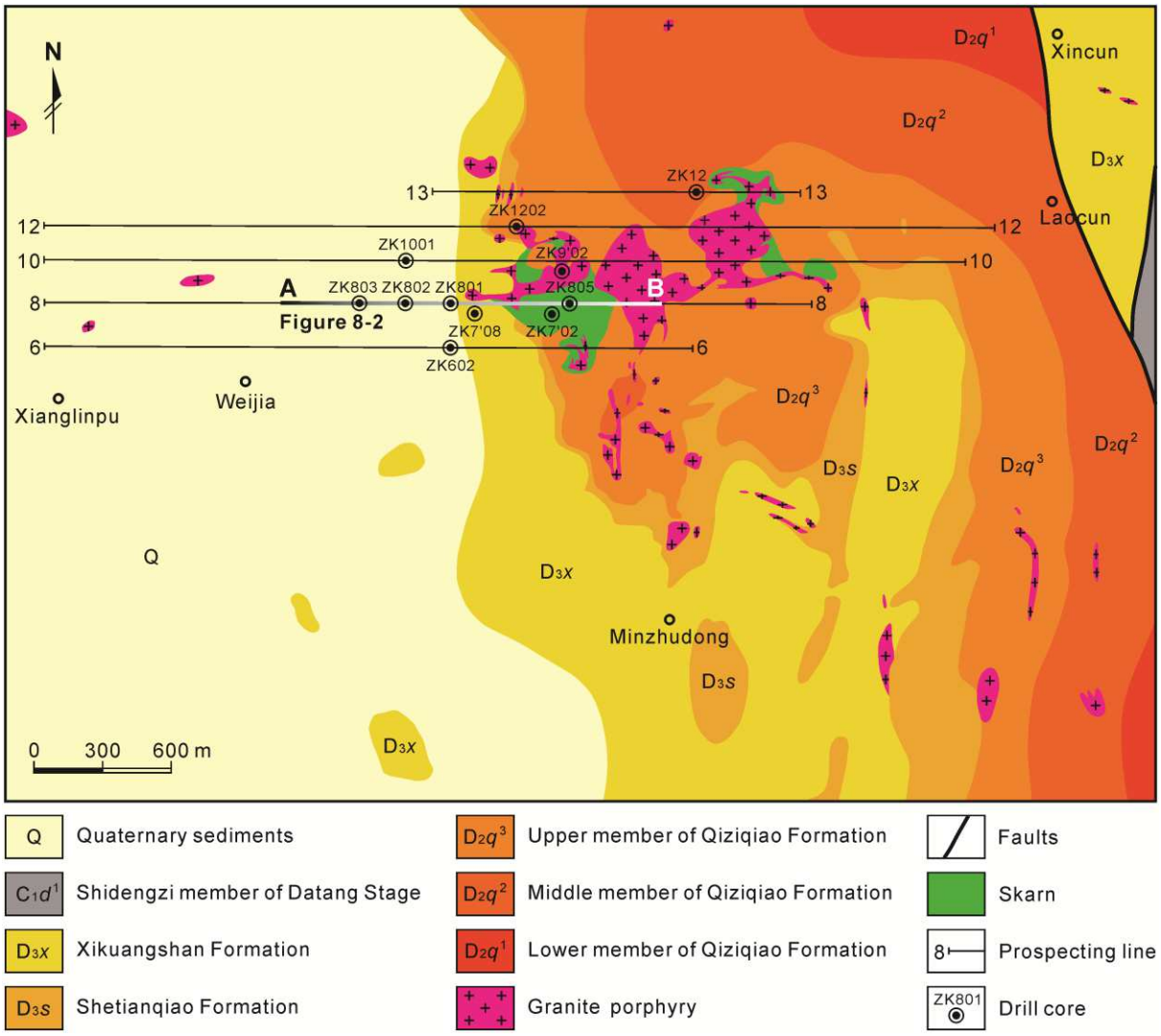

Figure 8-1. Geological map of the Weijia W deposit (modified after No. 418 Geological Team of Bureau of Geology and Mineral Exploration and Development of Hunan Province, unpub. report, 2016).

These strata have not been intensively deformed by regional folds and faults, and consistently strike northwest-southeast and dip 10 – 35 ° to southwest (Fig. 8-2). The Qiziqiao Formation is composed of a ca. 340-m-thick lower member of limestone, carbonaceous limestone, and marly limestone, a ca. 390-m-thick middle member of dolostone with intercalated dolomitic limestone, and a ca. 350-m-thick upper member of limestone with intercalated marly limestone. The Shetianqiao and Xikuangshan Formations dominantly consist of limestone, dolomitic limestone, and marly limestone. During Late Jurassic, the Qiziqiao Formation was intruded by the Weijia granite and the magnesian and calcic skarn scheelite orebodies were formed in the middle and upper members, respectively (Fig. 8-2).

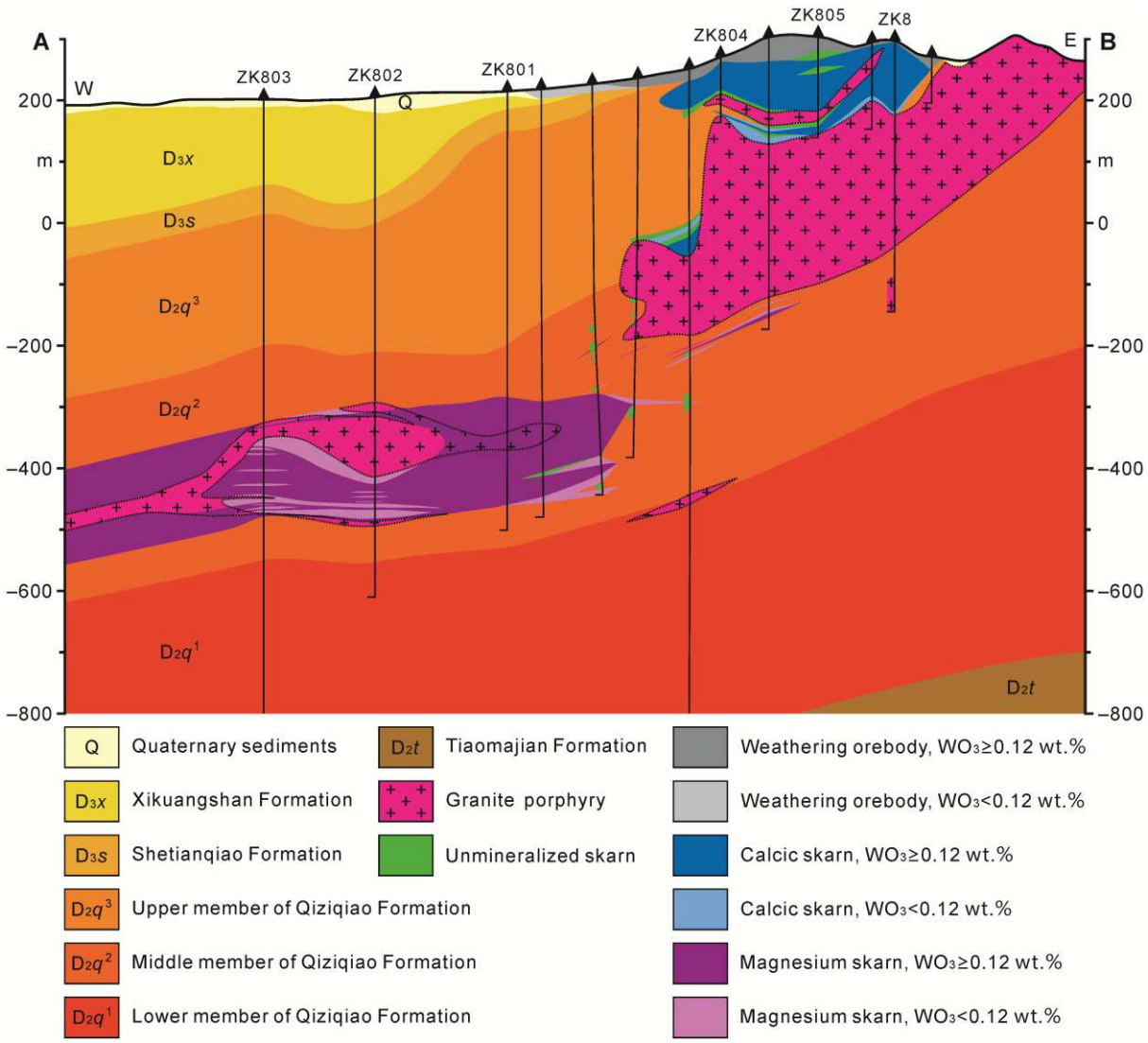

Figure 8-2. Cross section A-B (section line shown in Fig. 8-1) of the Weijia W deposit (modified after No. 1 General Brigade of Hunan Geological and Mining Bureau for Nonferrous Metals, unpub. report, 2014; No. 418 Geological Team of Bureau of Geology and Mineral Exploration and Development of Hunan Province, unpub. report, 2016).

8.2.2. Weijia granite

The Weijia granite was emplaced along the bedding (Fig. 8-2) and occurs as scattered bosses, ductoliths, apophyses, and dikes, with a total exposure area of ca. 1.3 km^2 (Fig. 8-1). A rough estimation shows that the total volume of the Weijia granite not exceeds 1 km^3. With a light red to off-white color, the fresh granite shows a typical porphyritic texture (Figs. 8-3a and 8-4a). The porphyritic Weijia granite contains 30 – 50 vol.% of phenocrysts mostly with a

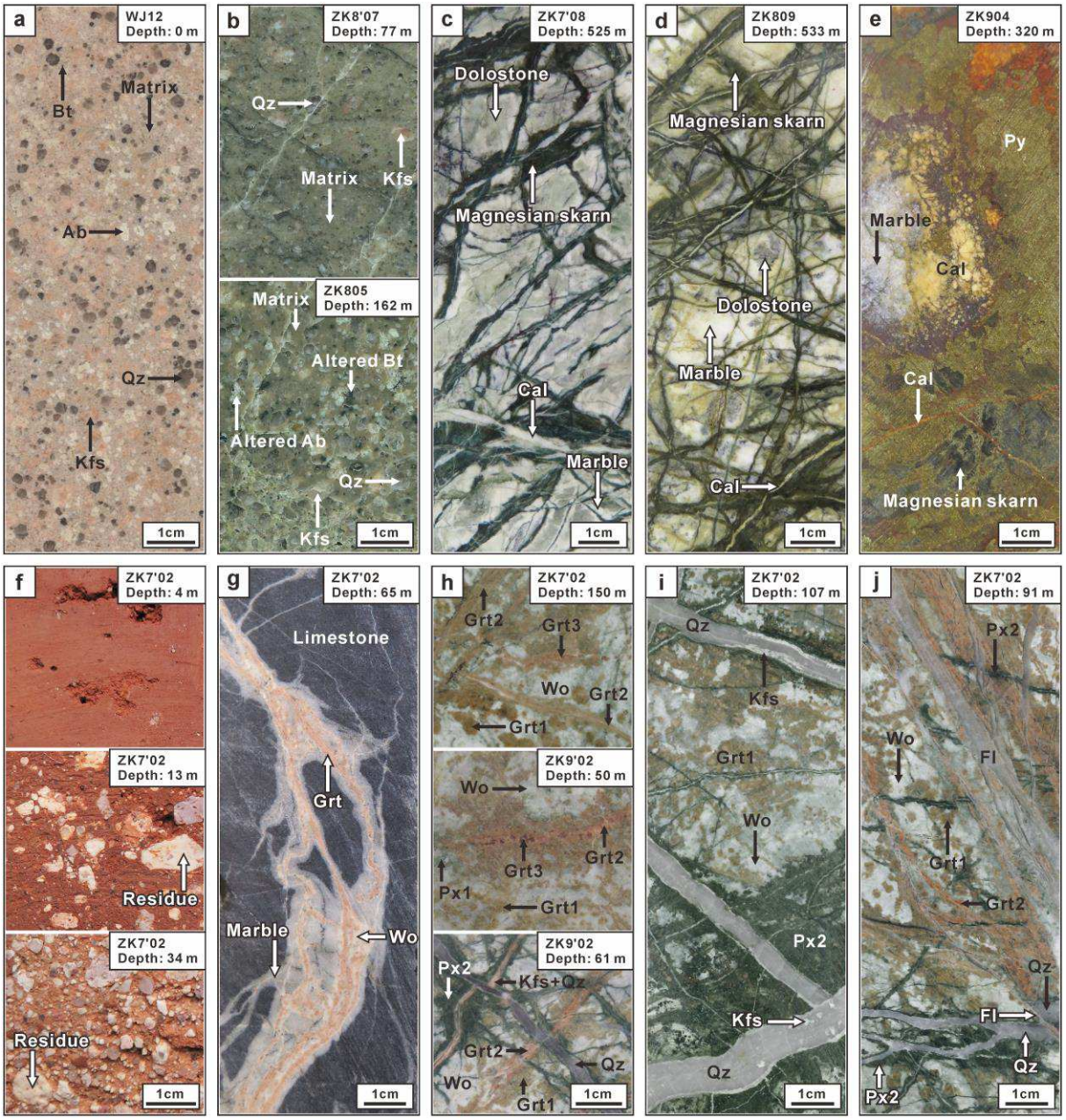

Figure 8-3. Petrographic photographs of the Weijia W deposit at hand-specimen scale. (a) Porphyritic texture of the Weijia granite. (b) Altered granite with a green color. (c and d) Stockwork magnesian skarn veinlets hosted by dolostone. (e) Sulfide ore from the bottom of magnesian skarn. (f) Secondary weathering orebody over the calcic skarn. (g) Reaction front of the calcic skarn. (h) Three generations of garnet, two generations of pyroxene, and K-feldspar-quartz and quartz veinlets in the calcic skarn. (i) The first-generation garnet, late pyroxene, and (K-feldspar)-quartz veins in the calcic skarn. (j) The latest fluorite veinlets cut across all the other minerals, include quartz, in the calcic skarn. Mineral abbreviations: Ab = albite, Bt = biotite, Cal = calcite, Fl = fluorite, Grt = garnet, Kfs = K-feldspar, Px = pyroxene, Py = pyrite, Qz = quartz, Wo = wollastonite.

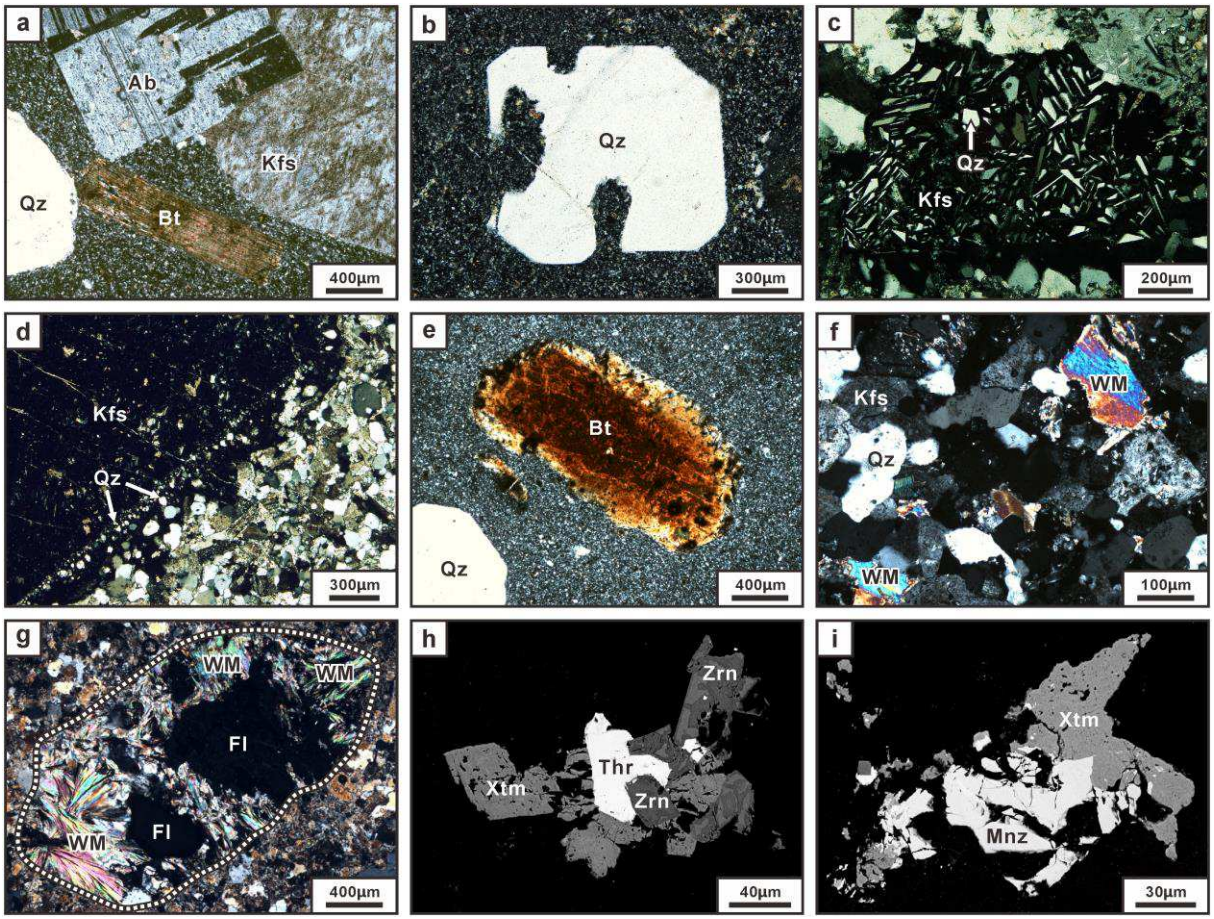

Figure 8-4. Petrographic photomicrographs (crossed-polarized light) and backscattered electron (BSE) images of the Weijia granite. (a) Porphyritic texture of the Weijia granite (b) Embayment texture of the hexagonal bipyramidal quartz phenocryst. (c) Micrographic texture in K-feldspar. (d) "Pearlitic border" texture of the K-feldspar phenocryst. (e) Bleached biotite phenocryst. (f) Interstitial white mica in the matrix. (g) Bubble-like aggregate of white mica and fluorite. (h) Intergrowth of zircon, thorite, and xenotime. (i) Intergrowth of monazite and xenotime. Mineral abbreviations: Ab = albite, Bt = biotite, Fl = fluorite, Kfs = K-feldspar, Mnz = monazite, Qz = quartz, Thr = thorite, WM = white mica, Xtm = xenotime, Zrn = zircon.

granularity of 0.5 – 5 mm and 50 – 70 vol.% of matrix with a felsitic to fine-grained texture (Figs. 8-3a and 8-4a–f). It is comprised of quartz (ca. 35 vol.%), K-feldspar (ca. 37 vol.%), albite (ca. 25 vol.%), and minor biotite (ca. 1 vol.%) and white mica (ca. 2 vol.%) (Figs. 8-3a and 8-4a–f). With a hexagonal bipyramidal shape, the quartz phenocrysts frequently exhibit an embayment texture (Fig. 8-4b). Micrographic texture is common in K-feldspar (Fig. 8-4c). In the rim of some K-feldspar phenocrysts, microgranular quartz (10 – 100 μm), with a gradually increased grain size outward, constitutes a "pearlitic border" texture (Fig. 8-4d).

Biotite crystals mainly occur as phenocrysts, a large proportion of which are bleached (Fig. 8-4e) in comparison to the fresh ones (Fig. 8-4a). White mica is distributed as interstitial crystals in the matrix (Fig. 8-4f) or coexists with fluorite as millimeter-sized bubble-like aggregates (Fig. 8-4g). Accessory minerals include fluorite, scheelite, zircon, thorite, xenotime, monazite (Fig. 8-4h and i), niobite, samarskite, fergusonite, parisite, ilmenite, etc.

The granite close to skarn orebodies has been widely altered and sometimes mineralized (Fig. 8-2) and is generally green-colored (Fig. 8-3b). The altered granite close to the magnesian skarn commonly shows a much stronger degree of alteration than that close to the calcic skarn. Serpentine, phlogopite, dolomite, and calcite are widespread in the altered granite near the magnesian skarn (Fig. 8-5). Serpentine usually cuts the granite as veinlets (Fig. 8-5a) or brecciates and replaces the phenocrysts (Fig. 8-5b). Phlogopite generally replaces the K-feldspar phenocrysts with a relict (Fig. 8-5c) or pseudomorph (Fig. 8-5d) texture or occurs as alteration mineral colts in the matrix that are frequently constituted by a core of dolomite or calcite with/without fluorite and a rim of phlogopite (Fig. 8-5e and f).

8.2.3. Stockwork veins

It is interesting to note that the apex of the Weijia granite has been mined for kaolin. Numerous stockwork veins and a few aplite veins are distributed at the apex of the Weijia granite. These stockwork veins are mostly northeast-southwest to north-south striking and steeply dip to northwest to west with some to southeast (Fig. 8-6). Three generations of stockwork veins have been distinguished according to their petrographic features. They are successivelly the first-generation K-feldspar-quartz pegmatite veins (Fig. 8-7a), the second-generation (K-feldspar)-quartz veins (Fig. 8-7b) or veinlets, and the third-generation stockwork quartz veinlets (Fig. 8-7c). The K-feldspar-quartz pegmatite veins are several centimeters in thickness and comprise dominantly K-feldspar and quartz that are similar in contents (Fig. 8-7a). Two generations of K-feldspar are recognized in the K-feldspar-quartz pegmatite veins (Fig. 8-7a). By contrast, the (K-feldspar)-quartz veins or veinlets contain obviously less K-feldspar which is corresponding to the late-generation K-feldspar in the K-feldspar-quartz pegmatite veins (Fig. 8-7a and b). The stockwork quartz veinlets have a thickness of several millimeters and are predominantly composed of quartz almost without

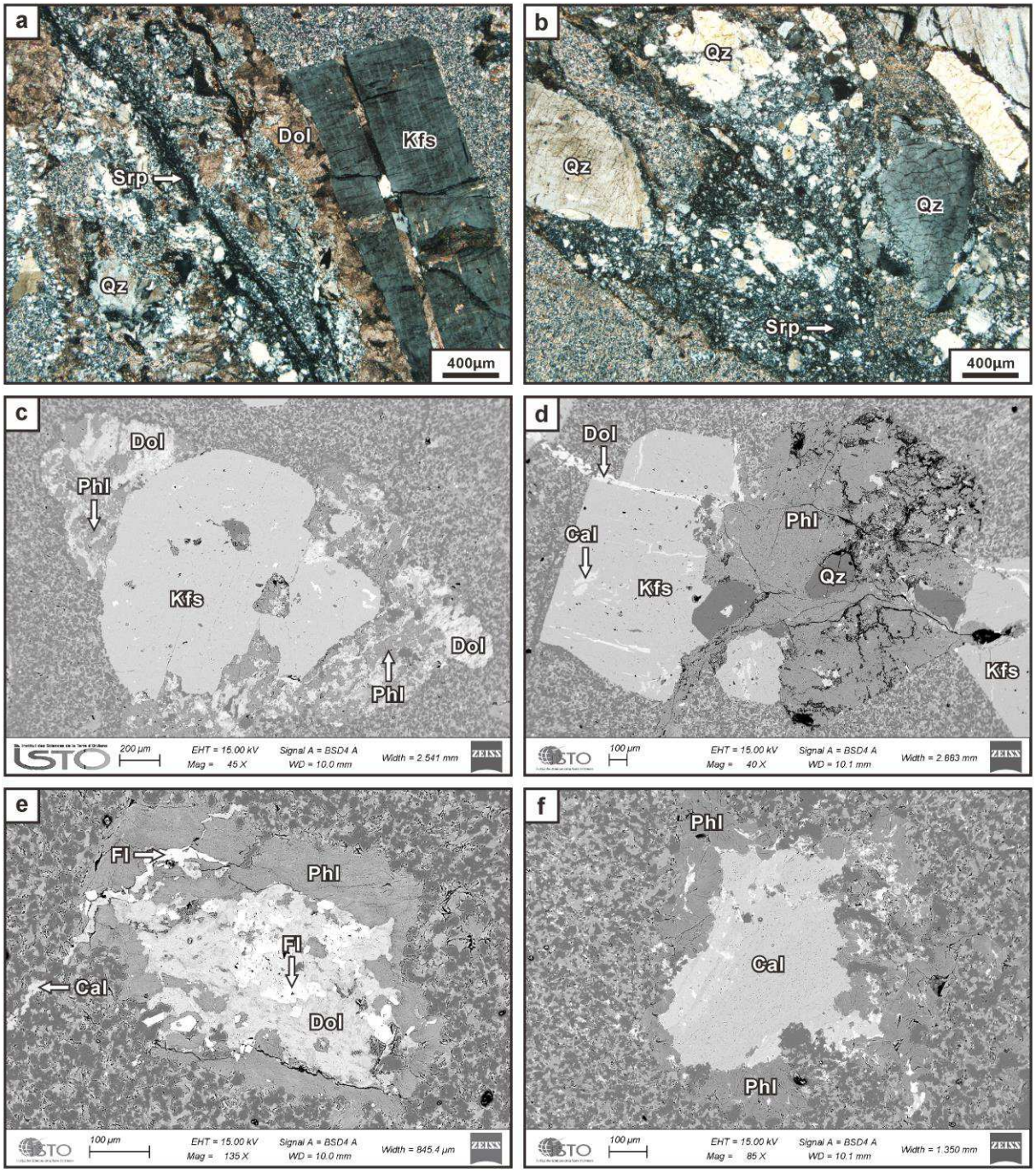

Figure 8-5. Petrographic photomicrographs (crossed-polarized light) and BSE images of the altered Weijia granite near the magnesian skarn. (a) Serpentine cuts the granite as veinlet coexisting with abundant dolomite. (b) Serpentine brecciates and replaces the quartz phenocryst. (c) K-felspar phenocryst replaced by phlogopite and dolomite with a residual core. (d) Pseudomorphic replacement of a K-felspar phenocryst by phlogopite. (e) Alteration mineral clot constituted by a core of dolomite and fluorite and a rim of phlogopite. (f) Alteration mineral clot constituted by a core of calcite and a rim of phlogopite. Mineral abbreviations: Cal = calcite, Dol = dolomite, Fl = fluorite, Kfs = K-feldspar, Phl = phlogopite, Qz = quartz, Srp = serpentine.

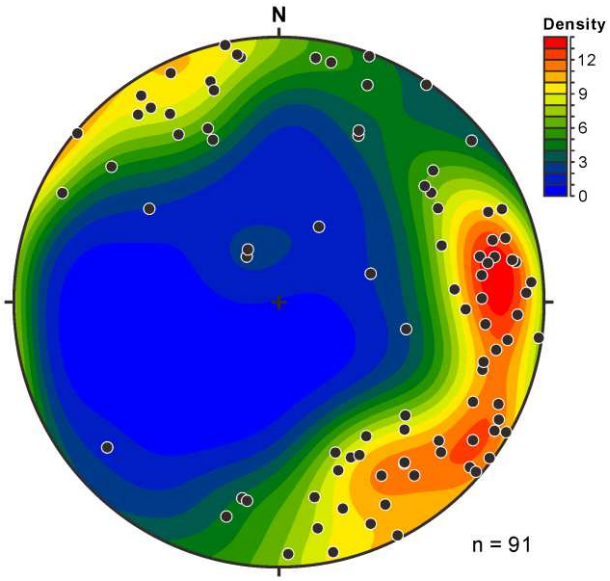

Figure 8-6. Equal-area lower hemisphere stereonet projection and density distribution of the poles of the stockwork veins at the apex of the Weijia granite.

K-feldspar (Fig. 8-7c). Notably, there is a bleached zone of granite enveloping the K-feldspar-quartz pegmatite veins and (K-feldspar)-quartz veins (Fig. 8-7a and b). Fe-Ti oxide halos and biotite occur in the periphery of the bleached zone but are absent in bleached zone (Fig. 8-7a and b). The granite surrounding the stockwork quartz veinlets is totally bleached without biotite and Fe-Ti oxide halos (Fig. 8-7c).

White mica commonly appears in the stockwork veins (Fig. 8-8a–c). The white mica in the K-feldspar-quartz pegmatite veins and (K-feldspar)-quartz veins or veinlets generally occurs as independent crystals and has a relatively large grain size of hundreds of microns (Fig. 8-8a and b), whereas, the white mica in the stockwork quartz veinlets is aggregated and is distinctly smaller with a grain size of several microns to dozens of microns (Fig. 8-8c). The biotite crystals in the granite with stockwork veins are widely bleached with the formation of abundant Fe-Ti oxides (Fig. 8-8d). White mica also appears in the matrix of granite with stockwork veins (Fig. 8-8e) and the bleached zone near stockwork veins (Fig. 8-8f).

8.2.4. Magnesian skarn

The magnesian skarn is distributed along the contact zone between the Weijia granite and dolostone (Fig. 8-2). With thicknesses of 85 – 182 m, the magnesian skarn orebodies mostly

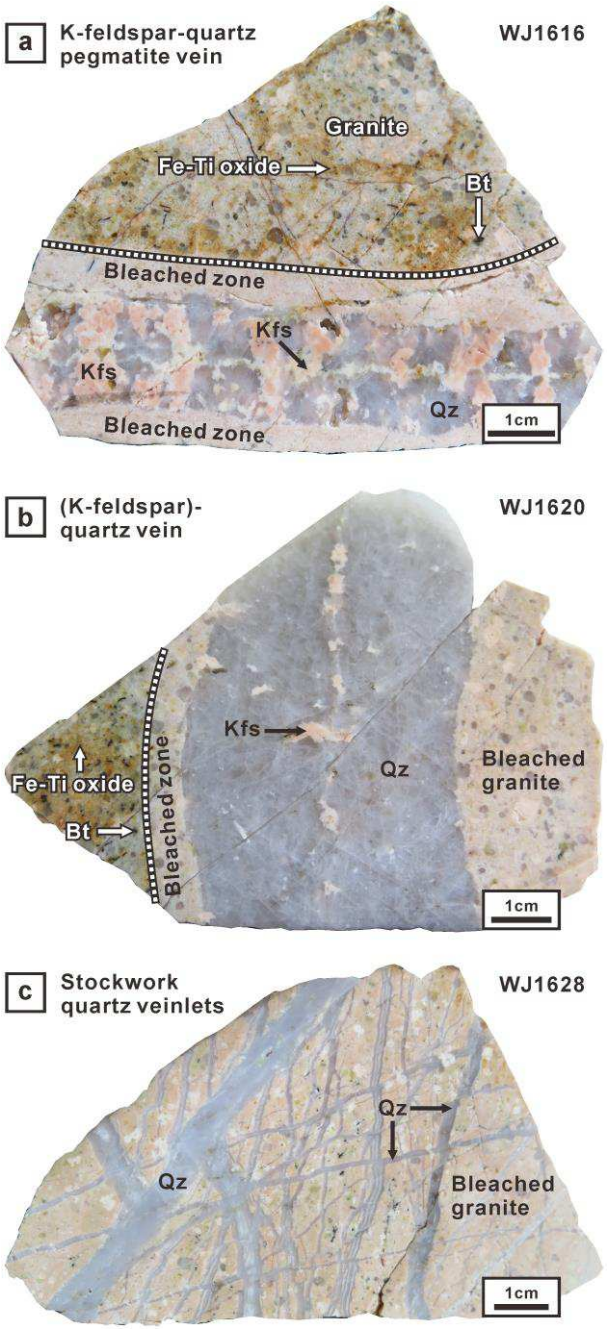

Figure 8-7. Petrographic photographs of the stockwork veins at the apex of the Weijia granite at hand-specimen scale. Mineral abbreviations are the same as Figure 8-3.

occur as stratiform within the dolostone of the middle member of the Qiziqiao Formation and have a consistent strike-dip with the host strata (Fig. 8-2). They are buried at the depths below the surface of 200 – 900 m (Fig. 8-2). The magnesian skarn generally occurs as green-colored stockwork veinlets in the fissures of dolostone with a millimeter-scale outward zonation from magnesian skarn through bleached marble to unaltered dolostone (Fig. 8-3c and d). This

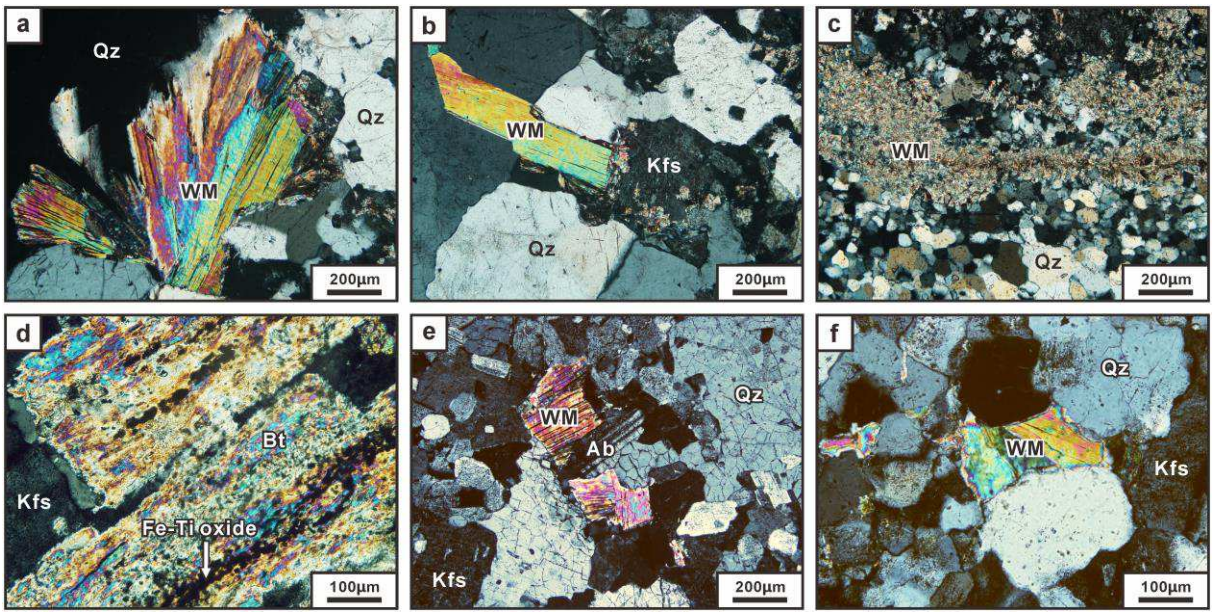

Figure 8-8. Petrographic photomicrographs (crossed-polarized light) of micas in the stockwork veins and their adjacent zone at the apex of the Weijia granite. (a) White mica in the K-feldspar-quartz pegmatite veins. (b) White mica in the (K-feldspar)-quartz veinlets. (c) White mica in the stockwork quartz veinlets. (d) Bleached biotite in the granite with stockwork veins. (e) White mica in the matrix of granite with stockwork veins. (f) White mica in the bleached zone near stockwork veins. Mineral abbreviations are the same as Figure 8-4.

zonation is particularly obvious in the dolostone enriched with carbonaceous materials (Fig. 8-9). At the bottom of the magnesian skarn orebodies, there is a 0.85-m-thick stratiform sulfide orebody. It is low-grade and has a dominant ore mineralogy of chalcopyrite, sphalerite, galena, pyrite (Fig. 8-3e), and arsenopyrite.

Serpentine and phlogopite are the predominant magnesian skarn minerals (Figs. 8-9 and 8-10a–d), however, forsterite and spinel which frequently occur in magnesian skarn as prograde minerals are absent. Abundant calcite was formed during the magnesian skarnization of dolostone. The calcite generally constructs the envelopes of the magnesian skarn veinlets (Figs. 8-9 and 8-10a and c–e), cross-cuts them as late veinlets (Figs. 8-3c and 8-10f), or occurs in the center of them (Figs. 8-3d and 8-10d). Abundant fluorite was formed together with the magnesian skarn minerals. The fluorite generally coexists with serpentine and phlogopite in the center of the magnesian skarn veinlets (Fig. 8-10b, c, and e) or constructs the envelopes of them (Fig. 8-10e and g). Some sellaite crystals appear in the calcite

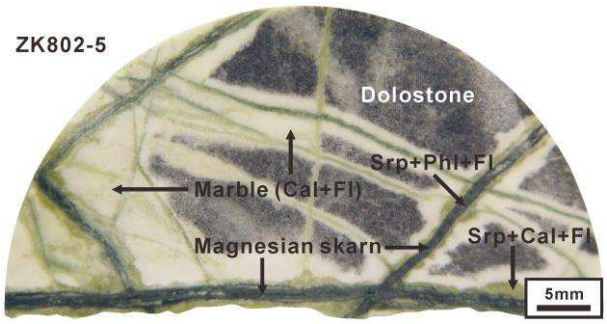

Figure 8-9. Stockwork magnesian skarn veinlets hosted by the dolostone enriched with carbonaceous materials in the Weijia W deposit. Mineral abbreviations are the same as Figure 8-5.

envelopes of the magnesian skarn veinlets (Fig. 8-10c–e). A few marialite (Fig. 8-10e and g), plagioclase, and K-feldspar (Fig. 8-10 g) were late formed in the center of the magnesian skarn veinlets. Garnet as en early prograde mineral occasionally appears in the magnesian skarn and may coexist with scheelite (Fig. 8-10f and h). Scheelite is mostly distributed in the magnesian skarn veinlets as disseminated grains and sometimes coexists with magnetite (Fig. 8-10c).

The paragenetic sequence of the magnesian skarn is shown in Figure 8-11. In the pre-ore stage, some prograde minerals, i.e., garnet and pyroxene, were formed firstly followed by the formation of a few chondrodite, fluoborite, magnetite, and scheelite. Fluorite also began to precipitate. The syn-ore stage was dominated by the formation of abundant serpentine, phlogopite, fluorite, scheelite, calcite, and dolomite, some talc, chlorite, and sellaite, and a few later marialite, plagioclase, K-feldspar, and quartz. In the post-ore stage, carbonate minerals, fluorite, and quartz were still continually formed with the disseminated precipitation of some sulfide minerals, such as pyrite, arsenopyrite, chalcopyrite, sphalerite, and galena.

8.2.5. Calcic skarn

The calcic skarn is distributed along the contact zone between the Weijia granite and limestone (Fig. 8-2). With thicknesses of 14 – 46 m, the calcic skarn orebodies mostly occur as massive or stratiform within the limestone of the upper member of the Qiziqiao Formation (Fig. 8-2). They have a buried depth shallower than 300 m and are partially exposed on the surface (Fig. 8-2). Surficial weathering of the calcic skarn led to the formation of a secondary

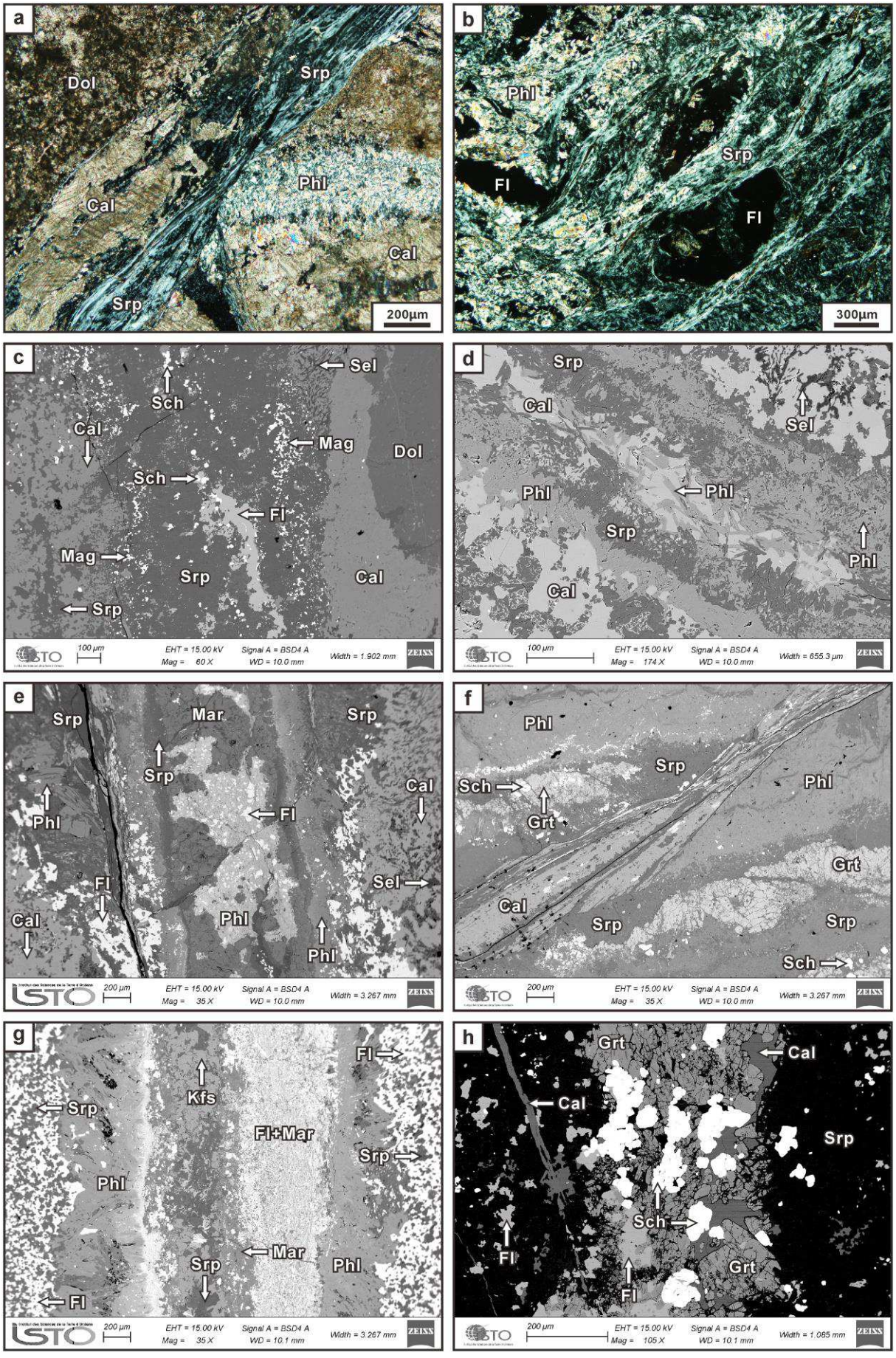
a
Dol
Srp
Phl
Cal
Cal
Srp
200μm
b
Phl
Srp
Fl
Fl
300μm
c
Sel
Sch
Cal
Mag
Dol
Sch
Fl
Mag
Srp
Cal
Srp
d
Srp
Cal
Sel
Phl
Phl
Srp
Phl
Cal
e
Srp
Mar
Srp
Srp
Cal
Phl
Fl
Fl
Sel
Cal
Phl
Phl
f
Phl
Srp
Sch
Phl
Grt
Grt
Cal
Srp
Srp
Sch
g
Fl
Kfs
Srp
Fl+Mar
Srp
Phl
Mar
Srp
Phl
Fl
h
Grt
Cal
Cal
Srp
Sch
Fl
Grt
Fl

Figure 8-10. Petrographic photomicrographs (crossed-polarized light) and BSE images of the magnesian skarn in the Weijia W deposit. (a) Phlogopite, serpentine, and calcite formed by skarnization of dolostone. (b) Coexistence of phlogopite, serpentine, and fluorite in the magnesian skarn. (c) Outward zonation of magnesian skarn from serpentine with scheelite and fluorite in the center and magnetite in the rim through calcite with a few sellaite to dolomite. (d) Outward zonation of magnesian skarn from phlogopite + calcite through serpentine to phlogopite and then to serpentine + calcite with a few sellaite. (e) Outward zonation of magnesian skarn from phlogopite + fluorite and marialite through serpentine to phlogopite and to serpentine and fluorite with some phlogopite and then to calcite and sellaite. (f) Earlier garnet, phlogopite, and serpentine with a few scheelite cut by later calcite. (g) Outward zonation of magnesian skarn from serpentine and K-feldspar through fluorite + marialite to phlogopite and then to fluorite + serpentine. (h) Scheelite coexisting with garnet, fluorite, and calcite enveloped by serpentine. Mineral abbreviations: Cal = calcite, Dol = dolomite, Fl = fluorite, Grt = garnet, Kfs = K-feldspar, Mag = magnetite, Mar = marialite, Phl = phlogopite, Sch = scheelite, Sel = sellaite, Srp = serpentine.

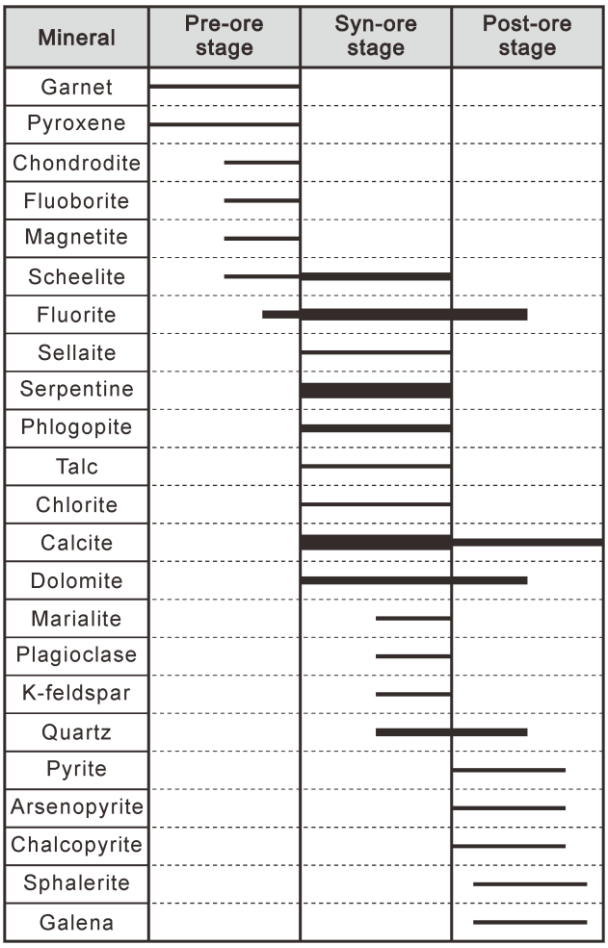

Figure 8-11. Paragenetic sequence of the magnesian skarn in the Weijia W deposit.

weathering orebody with a WO_3 resource of ca. 8,000 t and an enriched average grade of ca. 0.35 wt.% (No. 1 General Brigade of Hunan Geological and Mining Bureau for Nonferrous Metals, unpub. report, 2014). This weathering orebody is horizontally extended over the calcic skarn orebodies with a thickness of 3 – 40 m (Fig. 8-2). It is composed of Quaternary sediments in which the content of residues increases with depth (Fig. 8-3f).

Wollastonite, garnet, and pyroxene are the predominant calcic skarn minerals (Fig. 8-3g–j). At the reaction front of calcic skarn, marble was formed along the fluid pathways in limestone and overprinted by wollastonite and followed by garnet (Fig. 8-3g). Three generations of garnet have been distinguished in the calcic skarn, which are chronologically green-brown to yellow-brown disseminated or aggregated garnet, yellow-brown to red-brown vein-like garnet, and red-brown to dark brown vein-like or interstitial garnet (Fig. 8-3h–j). The first-generation garnet is commonly zoned with some pyroxene inclusions inside and has been partially replaced by later minerals (Fig. 8-12a). By contrast, the second-generation vein-like garnet does not show a zonal texture and cuts earlier pyroxene (Fig. 8-12b). The third-generation interstitial garnet has a well-developed zonal texture with the remaining interstice filled by calcite (Fig. 8-12c). The pyroxene can be divided into an early generation of light green disseminated pyroxene (Fig. 8-3h) and a late generation of dark green pyroxene dominated by veinlets (Fig. 8-3h–j) and sometimes aggregated masses (Fig. 8-3i). The wollastonite contains an early generation that coexists with garnet and pyroxene and shows an intergrowth texture with fluorite and a late generation that occurs as veinlets cutting the earlier garnet, pyroxene, wollastonite, and fluorite (Fig. 8-12d and e). The matrix of the calcic skarn frequently exhibits a complex intergrowth texture of skarn minerals, calcite, fluorite, and quartz (Fig. 8-12f). Some columnar vesuvianite crystals with a zonal texture appear in the calcic skarn (Fig. 8-12g). The calcic skarn is cross-cut by (K-feldspar)-quartz veins or veinlets which are commonly enveloped by the late pyroxene (Fig. 8-3h–j). Fluorite veinlets were formed later and cut across the quartz veinlets (Fig. 8-3j). Late K-feldspar and quartz may coexist with fluorite (Fig. 8-12h). Scheelite is distributed in the calcic skarn as disseminated grains (Fig. 8-12b and h).

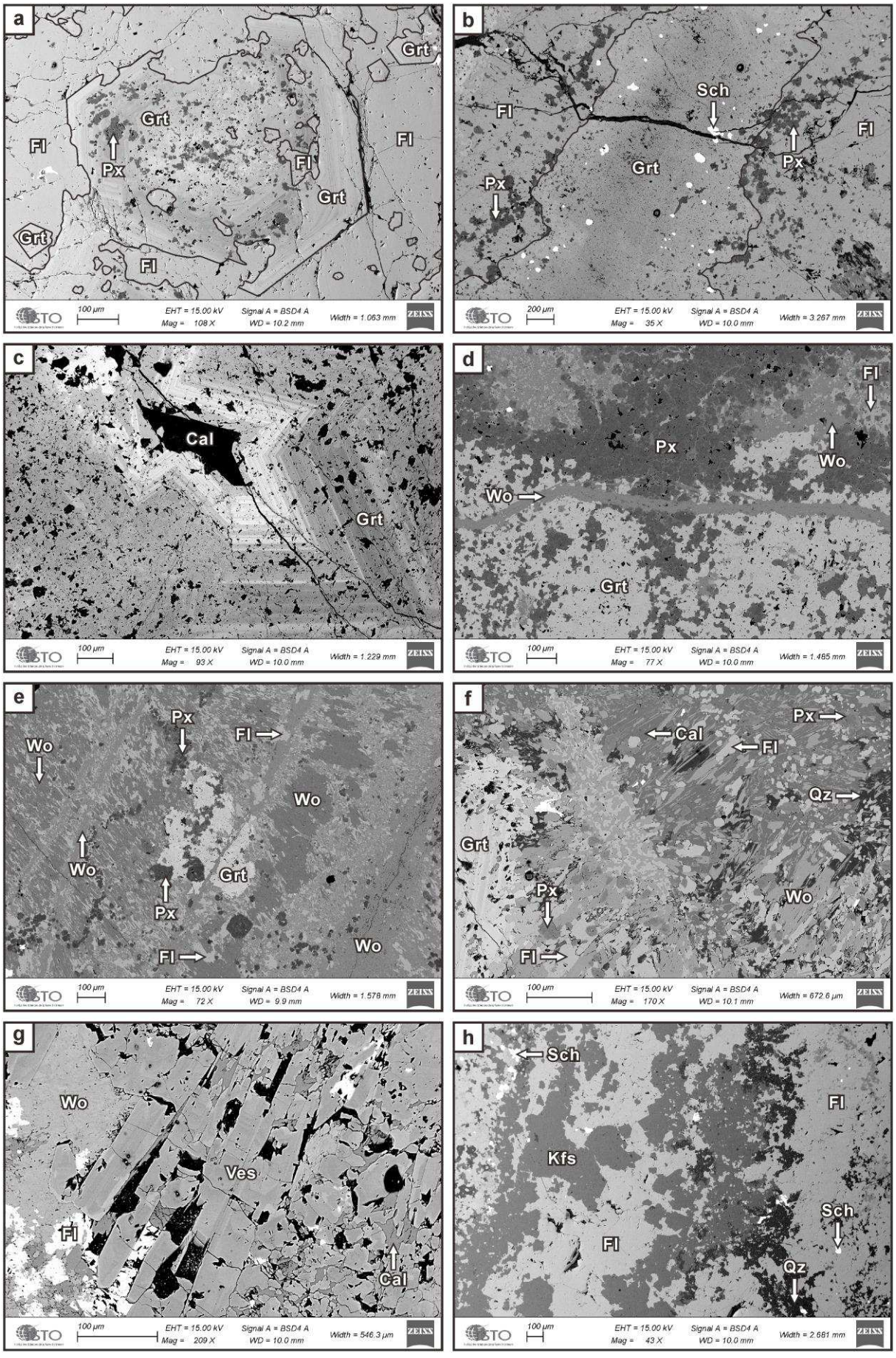
a
Grt
Grt
Fl
Px
Fl
Fl
Grt
Grt
Fl
100 μm EHT = 15.00 kV Signal A = BSD4 A Mag = 108 X WD = 10.2 mm Width = 1.063 mm ZEISS
b
Sch
Fl
Fl
Grt
Px
Px
200 μm EHT = 15.00 kV Signal A = BSD4 A Mag = 35 X WD = 10.0 mm Width = 3.267 mm ZEISS
c
Cal
Grt
100 μm EHT = 15.00 kV Signal A = BSD4 A Mag = 93 X WD = 10.0 mm Width = 1.229 mm ZEISS
d
Fl
Px
Wo
Wo
Grt
100 μm EHT = 15.00 kV Signal A = BSD4 A Mag = 77 X WD = 10.0 mm Width = 1.465 mm ZEISS
e
Px
Fl
Wo
Wo
Wo
Grt
Px
Fl
Wo
100 μm EHT = 15.00 kV Signal A = BSD4 A Mag = 72 X WD = 9.9 mm Width = 1.578 mm ZEISS
f
Px
Cal
Fl
Qz
Grt
Px
Wo
Fl
100 μm EHT = 15.00 kV Signal A = BSD4 A Mag = 170 X WD = 10.1 mm Width = 672.6 μm ZEISS
g
Wo
Ves
Fl
Cal
100 μm EHT = 15.00 kV Signal A = BSD4 A Mag = 209 X WD = 10.0 mm Width = 546.3 μm ZEISS
h
Sch
Fl
Kfs
Sch
Fl
Qz
100 μm EHT = 15.00 kV Signal A = BSD4 A Mag = 43 X WD = 10.0 mm Width = 2.681 mm ZEISS

Figure 8-12. BSE images of the calcic skarn in the Weijia W deposit. (a) The first-generation automorphic garnet with a zonal texture containing some pyroxene inclusions and enclosed and partially replaced by fluorite. (b) The second-generation vein-like garnet including some scheelite and enveloped by fluorite and pyroxene. (c) The third-generation interstitial garnet with a well-developed zonal texture. (d and e) Earlier garnet, pyroxene, wollastonite and fluorite cut by later wollastonite, the earlier wollastonite shows an intergrowth texture with fluorite and the later wollastonite occurs as veinlets. (f) Complex intergrowth texture of skarn minerals, calcite, fluorite, and quartz in the matrix of the calcic skarn. (g) Columnar vesuvianite with a zonal texture. (h) Late K-feldspar and quartz coexisting with fluorite. Mineral abbreviations: Cal = calcite, Fl = fluorite, Grt = garnet, Kfs = K-feldspar, Px = pyroxene, Qz = quartz, Sch = scheelite, Ves = vesuvianite, Wo = wollastonite.

The paragenetic sequence of the calcic skarn is shown in Figure 8-13. In the pre-ore stage, abundant prograde minerals, i.e., garnet, pyroxene, and wollastonite, were formed firstly followed by the formation of a few magnetite, vesuvianite, and scheelite. Fluorite also

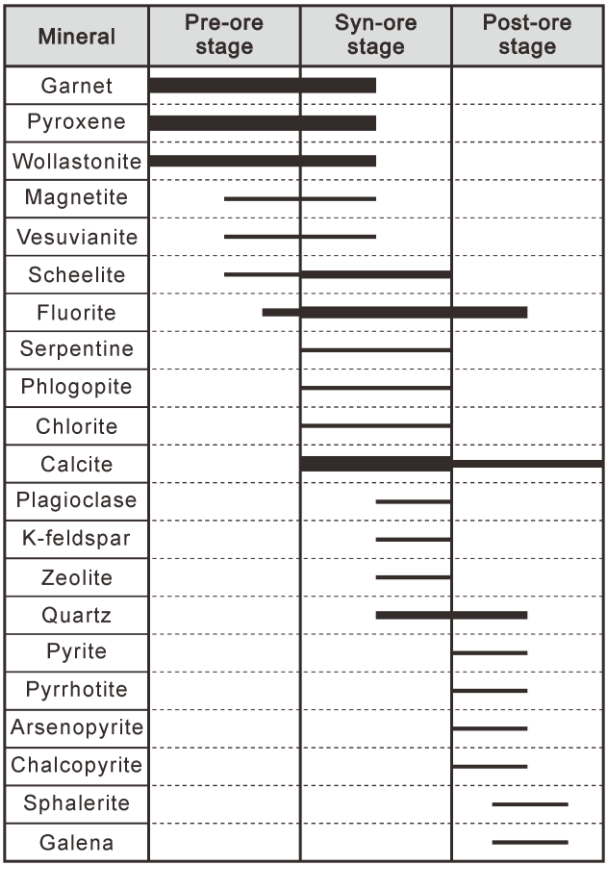

Figure 8-13. Paragenetic sequence of the calcic skarn in the Weijia W deposit.

began to precipitate. The skarn minerals were still continually formed in the syn-ore stage. Besides the skarn minerals, the syn-ore stage was dominated by the formation of abundant fluorite, scheelite, and calcite and a few serpentine, phlogopite, and chlorite followed by a few later plagioclase, K-feldspar, zeolite, and quartz. In the post-ore stage, calcite, fluorite, and quartz were still continually formed with the disseminated precipitation of some sulfide minerals, such as pyrite, pyrrhotite, arsenopyrite, chalcopyrite, sphalerite, and galena.

8.2.6. Relationship between WO_3 and CaF_2 grades

Both the magnesian and calcic skarn scheelite ores contain abundant fluorite (mostly 5 – 20 wt.%), and their WO_3 grades show an obvious positive correlation with fluorite contents (Figs. 8-14 and 8-15). The wall rocks (dolostone) near the magnesian skarn orebodies also have a high content of fluorite (mostly > 10 wt.%, Figs. 8-14 and 8-15), however, the wall rocks (limestone) near the calcic skarn orebodies show a distinctly lower fluorite content (mostly < 5 wt.%, Fig. 8-15). Weathering and leaching of the calcic skarn resulted in a sharp decrease of fluorite content to 0.4 – 0.8 wt.% (Figs. 8-14 and 8-15).

8.3. Sampling and analytical methods

Representative samples of the fresh and altered Weijia granite, stockwork veins at the apex of granite, and magnesian and calcic skarns and their adjacent carbonate wall rocks were collected from drill cores (numbered by ZK) and surface outcrops (numbered by WJ). They were firstly prepared as polished thin sections for petrographic studies under optical microscope and scanning electron microscope (SEM), and then for mineral composition analyses by SEM, electron microprobe (EMP), and laser ablation-inductively coupled plasma-mass spectrometry (LA-ICP-MS). Eleven polished thin sections of carbonate rocks close to the magnesian (six samples) and calcic (five samples) skarns were selected for RSCM thermometry. Twelve samples of altered granite spatially close to the magnesian (eight samples) and calcic (four samples) skarn orebodies were crushed to 200 mesh for whole-rock analyses of major and trace elements.

RSCM analysis was carried out by a Renishaw InVIA Reflex micro-spectrometer coupled to a DM2500 Leica microscope at Bureau de Recherches Géologiques et Minières

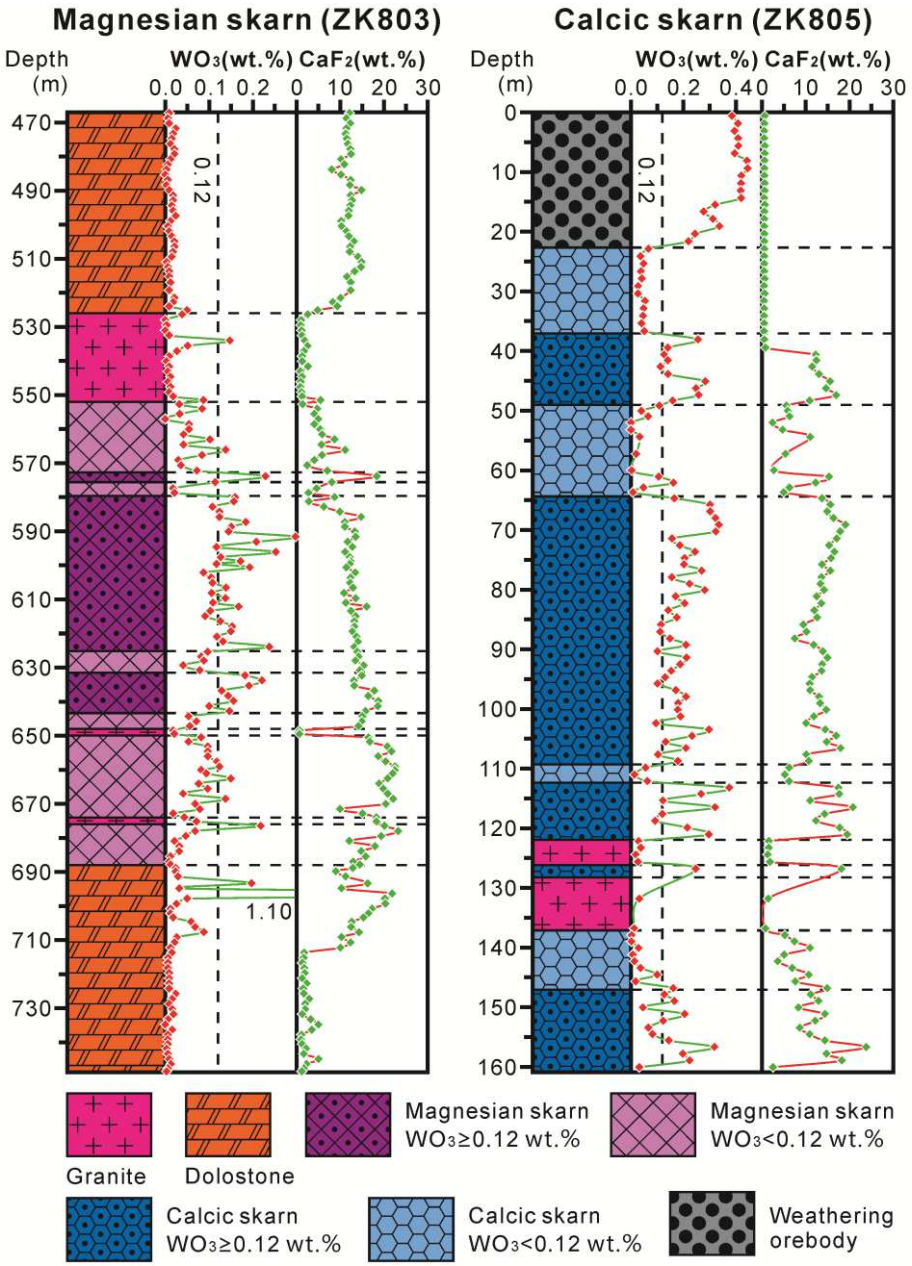

Figure 8-14. Variations of WO_3 and CaF_2 grades in representative drill cores of the magnesian and calcic skarns in the Weijia W deposit. The data are from No. 1 General Brigade of Hunan Geological and Mining Bureau for Nonferrous Metals, unpub. report (2014) and No. 418 Geological Team of Bureau of Geology and Mineral Exploration and Development of Hunan Province, unpub. report (2016).

(BRGM), Orléans, France. An argon laser with λ_0 = 514.5 nm was used as exciter. Instrument control and Raman measurements were performed by the Renishaw Wire 3.4 software. Before analysis, the spectrometer was calibrated using the 520.4 cm^{-1} line of silicon. To check within-sample structural heterogeneity, at least 10 spectra were recorded for each sample.

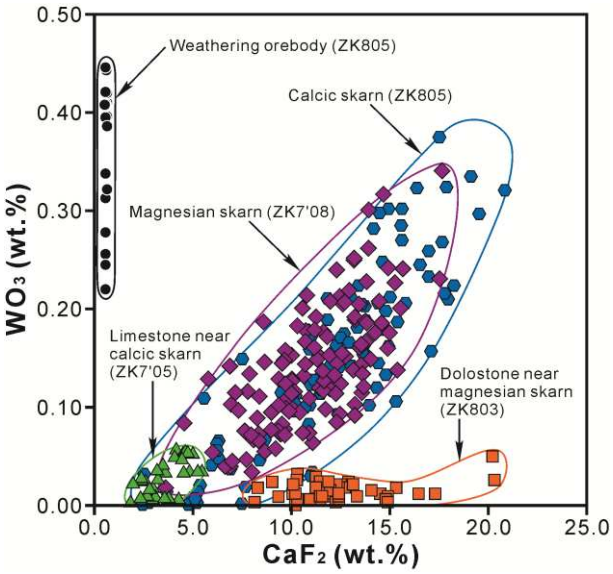

Figure 8-15. Binary plot of CaF_2 and WO_3 grades in representative drill cores of the magnesian and calcic skarns in the Weijia W deposit. The data sources are the same as Figure 8-14.

Each spectrum was acquired through 5 – 10 accumulations and an acquisition time of 10 – 20 s. The off-line data were processed using the program PeakFit v4.06 with a Voigt function.

Whole-rock major elements were measured using wet chemical methods at the Analysis Center of No. 230 Research Institute of the China National Nuclear Corporation, Changsha. The detailed procedures are described in the China National Standards GB/T 14506.3-2010 – GB/T 14506.14-2010. The analytical precisions for all elements were better than 5 %. Whole-rock trace and rare earth elements were determined by a Finnigan MAT Element II high resolution ICP-MS at the State Key Laboratory for Mineral Deposits Research (LAMD), Nanjing University (NJU), China. The analytical procedures and conditions followed Gao et al. (2003). The analytical precisions for most elements were better than 5 %.

Mineral discrimination, backscattered electron (BSE) imaging, and energy dispersive spectrometry (EDS) elemental mapping were performed by a ZEISS MERLIN Compact SEM equipped with a Gemini I electron column and a Bruker XFlash 6 | 30 silicon drift detector (SDD) at Institut des Sciences de la Terre d'Orléans (ISTO), France. The analytical conditions included an accelerating voltage of 15 kV, a current up to 100 nA with resolution up to 0.8 nm, and a work distance of 10 mm.

Major element analyses of micas and skarn minerals were carried out with a CAMECA SX50 EMP at ISTO, France. The analytical conditions included an accelerating voltage of 15 kV, a beam current of 10 nA with diameter of 1 μm, and counting times of 10 s for all elements and 5 s for background. The collected data were corrected by the ZAF procedures. Calibration was performed using natural minerals and synthetic compounds.

Trace elements of garnet and scheelite were analyzed by an Agilent 7700× ICP-MS coupled to an Excite 193 nm Photon Machines laser ablation system at Nanjing FocuMS Technology Co. Ltd., China. Each analysis was carried out by a 50-μm ablating spot at 8 Hz with energy of 4.5 mJ (transmittance 50%) for 40 s after measuring the gas blank for 15 s. NIST SRM 610 was used as the external standard for quantitative calibration of the time-dependent drift of sensitivity and mass discrimination. The off-line data processing was performed using a program called ICPMSDataCal (Liu et al., 2008b).

8.4. Results

8.4.1. RSCM thermometry

The Raman spectrum of carbonaceous material comprises a first-order region of 1100 – 1800 cm^{-1} and a second-order region of 2300 – 3500 cm^{-1} (Tuinstra and Koenig, 1970; Nemanich and Solin, 1979). All measurements were performed in the first-order domain. In the first-order region, the graphite (G) band occurs around 1580 cm^{-1} and corresponds to in-plane vibration of aromatic carbons in the graphitic structure (Tuinstra and Koenig, 1970; Lespade et al., 1984; Wopenka and Pasteris, 1993). The defect bands D1 and D2 occur around 1350 cm^{-1} and 1620 cm^{-1}, respectively, corresponding to physical and chemical defects in the aromatic skeleton of carbonaceous material (Wopenka and Pasteris, 1993; Ferrari and Robertson, 2000). Beyssac et al. (2002) defined the parameters R1 and R2 ratios, which are D1/G peak intensity (i.e., peak height) ratio and D1/(G + D1 + D2) peak area ratio, respectively, to evaluate the disorder degree of carbonaceous material. A negative linear correlation of the R2 ratio with the peak temperature of metamorphism in the range of 330 – 640 °C was established by Beyssac et al. (2002), i.e., $T\ (°C) = -445 \times R2 + 641$. The RSCM thermometer was extended towards low temperatures of 200 – 330 °C by Lahfid et al. (2010).

The Raman spectra of carbonaceous material in the carbonate rocks close to the magnesian and calcic skarns are shown in Figure 8-16. Some parameters of the Raman spectra, include the position and full width at half maximum (FWHM) of the G band, the R1 and R2 ratios, and the calculated temperature, are listed in Appendix 8-1. Compared with the Raman spectra of carbonaceous material in the carbonate rocks near the calcic skarn, the Raman spectra of carbonaceous material in the carbonate rocks near the magnesian skarn show higher R1 and R2 ratios, indicating higher degrees of disorder and corresponding to lower peak metamorphic temperatures (Appendix 8-1 and Fig. 8-16). The Raman spectra of carbonaceous material in the carbonate rocks close to the magnesian and calcic skarns have respective R1 ratios of 0.44 – 0.59 and 0.13 – 0.20, respective R2 ratios of 0.33 – 0.38 and 0.15 – 0.20, and respective calculated temperatures of 470 – 496 °C and 554 – 576 °C (Appendix 8-1 and Fig. 8-16). The RSCM thermometry reveals that the wall-rock metamorphic temperature of the magnesian skarn was about 80 °C lower than that of the calcic skarn.

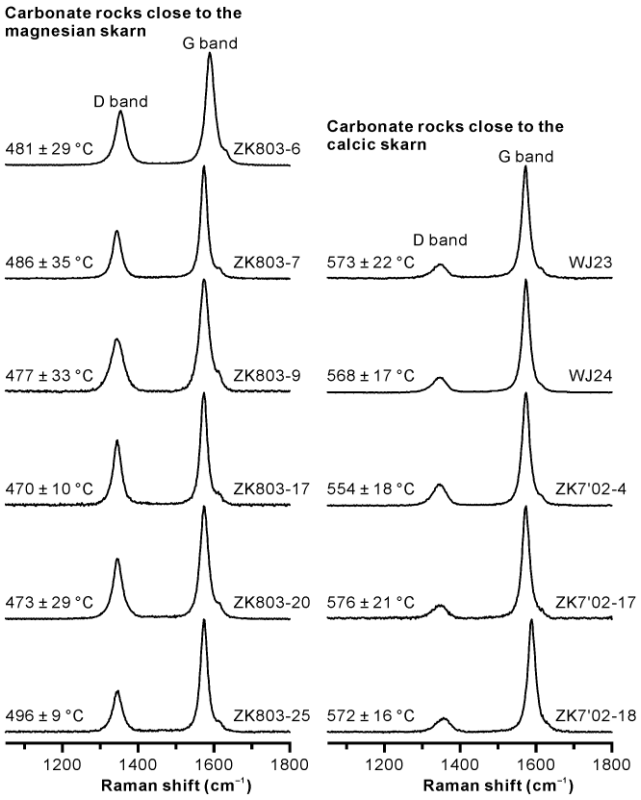

Figure 8-16. Raman spectra of carbonaceous material in carbonate rocks close to the magnesian and calcic skarns in the Weijia W deposit and temperatures calculated by the RSCM thermometry.

8.4.2. Altered granite

The fresh Weijia granite is predominantly composed of quartz, K-feldspar, and albite, containing high SiO_2 (73.86 – 76.73 wt.%), Al_2O_3 (13.06 – 14.27 wt.%), K_2O (4.84 – 6.78 wt.%), and Na_2O (3.01 – 3.72 wt.%) contents and low CaO (0.12 – 0.88 wt.%), MgO (0.01 – 0.17 wt.%), FeO_{Total} (0.12 – 0.54 wt.%), and MnO (0.00 – 0.01 wt.%) contents (Huang et al., 2017a). EDS elemental mapping of the altered granite close to the magnesian skarn shows that obvious Ca, Mg, Fe, and Mn gains happened during the hydrothermal alteration of granite (Fig. 8-17), corresponding to the formation of serpentine, phlogopite, dolomite, and calcite in the altered granite (Fig. 8-5). The matrix of the altered granite exhibits an evident Na loss (Fig. 8-18) relative to the fresh granite which may indicate a breakdown of albite during the hydrothermal alteration of granite.

The analytical results of whole-rock major and trace element compositions of the altered Weijia granite are listed in Appendix 8-2 and shown in Figures 8-19 and 8-20. For major elements, the altered granite close to the magnesian skarn has distinctly higher CaO (0.69 – 3.03 wt.%), MgO (0.11 – 0.90 wt.%), FeO_{Total} (0.27 – 1.57 wt.%), MnO (0.02 – 0.10 wt.%), and LOI (loss on ignition) (2.33 – 4.02 wt.%) contents and lower Na_2O contents (0.10 – 1.74 wt.%) than the fresh granite (Fig. 8-19a–d). In contrast, the altered granite close to the calcic skarn shows an obviously lower degree of mass transfer and has intermediate compositions between the fresh granite and the altered granite close to the magnesian skarn (Fig. 8-19a–d). The CaO, MgO, FeO_{Total}, MnO, LOI, and Na_2O contents of the altered granite close to the calcic skarn are 0.18 – 1.26 wt.%, 0.04 – 0.19 wt.%, 0.21 – 0.73 wt.%, 0.00 – 0.02 wt.%, 1.70 – 2.02 wt.%, and 1.59 – 3.19 wt.%, respectively (Fig. 8-19a–d). There are no strong Si, Ti, Al, and K (Fig. 8-19b) gains or losses during the hydrothermal alteration of granite.

For trace elements, the altered granite close to the magnesian skarn has distinctly higher LILE (large ion lithophile elements) such as Rb (412 – 619 ppm) and Ba (66 – 195 ppm) contents than the fresh granite (Rb: 260 – 356 ppm, Ba: 7 – 43 ppm, Huang et al., 2017a) (Fig. 8-19e). The altered granite close to the calcic skarn contains intermediate LILE contents (Rb: 309 – 409 ppm, Ba: 25 – 38 ppm) between the fresh granite and the altered granite close to the magnesian skarn (Fig. 8-19e). In contrast, the HFSE (high field strength elements) such as Th,

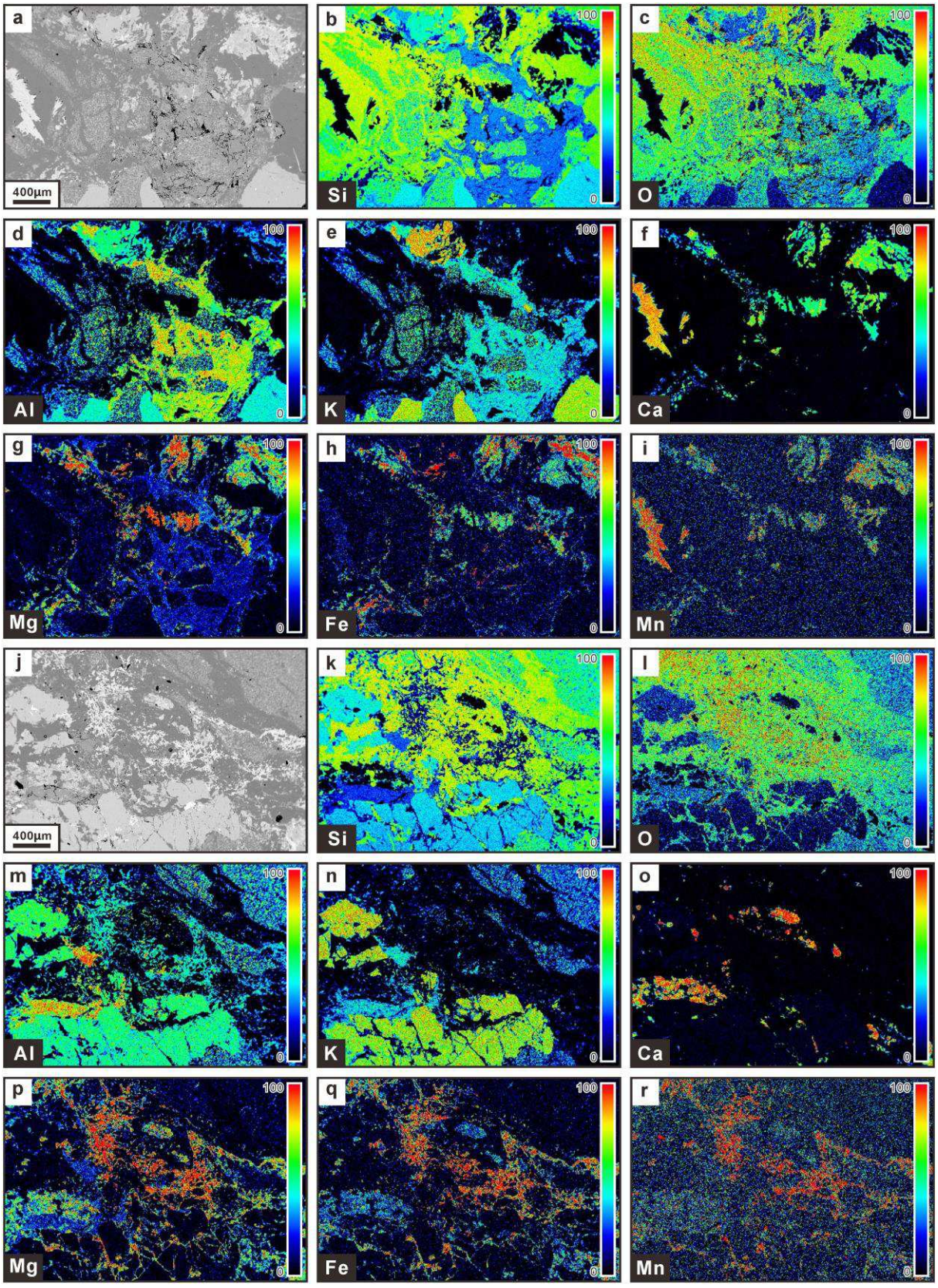

Figure 8-17. Energy dispersive spectrometry (EDS) elemental mapping of the altered Weijia granite close to the magnesian skarn.

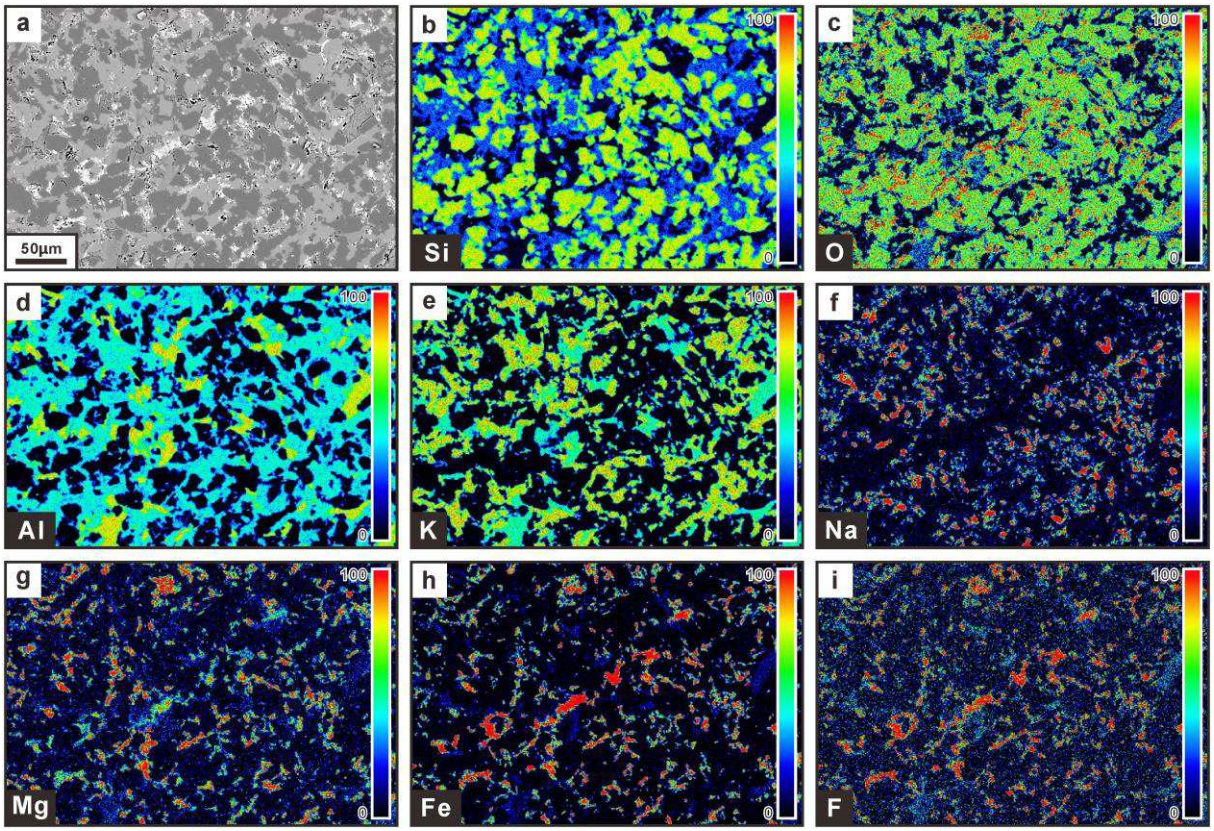

Figure 8-18. EDS elemental mapping of the matrix of the altered Weijia granite close to the magnesian skarn.

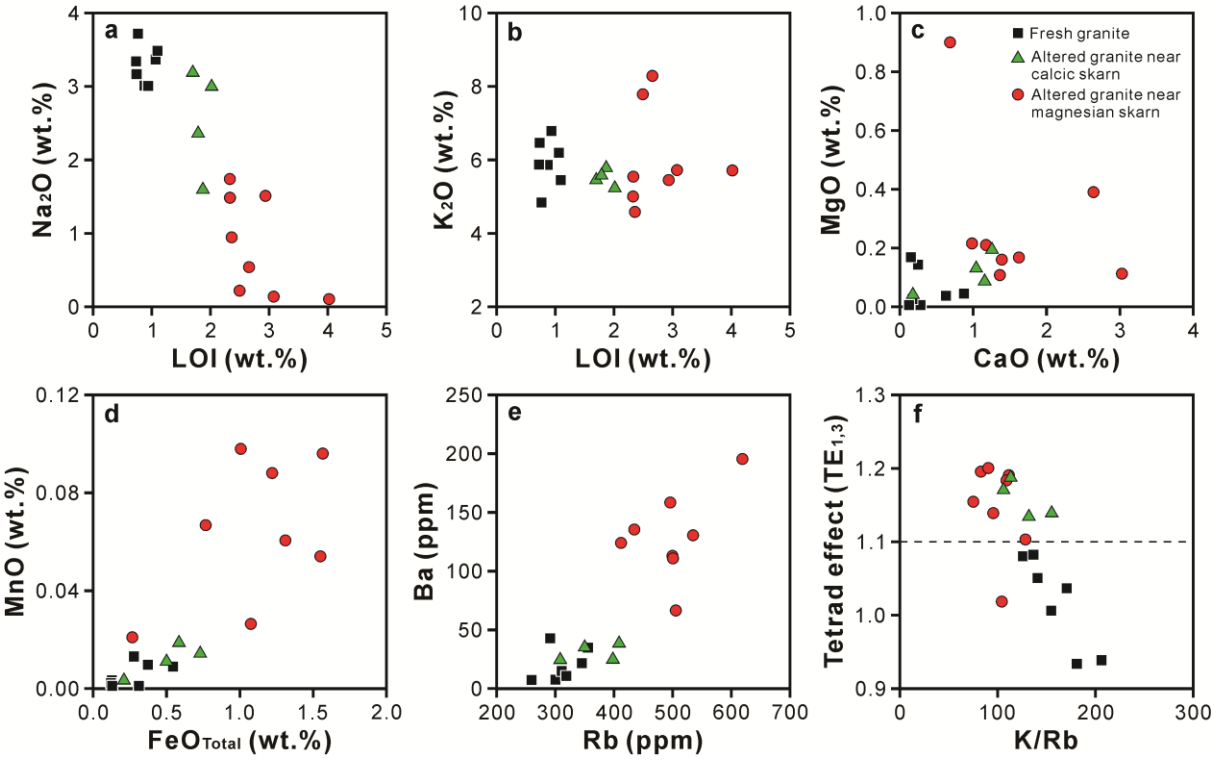

Figure 8-19. Binary plots of some major compositions, trace elements, and calculated parameters of the fresh and

altered Weijia granite. LOI = loss on ignition. $TE_{1,3} = \{[Ce_N/(La_N^{2/3} \times Nd_N^{1/3}) \times Pr_N/(La_N^{1/3} \times Nd_N^{2/3})]^{0.5} \times [Tb_N/(Gd_N^{2/3} \times Ho_N^{1/3}) \times Dy_N/(Gd_N^{1/3} \times Ho_N^{2/3})]^{0.5}\}^{0.5}$, it quantifies the degree of the tetrad effect (Irber, 1999). The data of fresh granite are from Huang et al. (2017a).

U, Nb, Ta, Zr, and Hf are more stable than the LILE and do not show strong gains or losses during the hydrothermal alteration of granite (Fig. 8-20a). Notably, the altered granite shows higher REE especially HREE contents and a stronger REE tetrad effect than the fresh granite (Figs. 8-19f and 8-20b). The altered granite close to the magnesian skarn has higher ΣREE (105 – 207 ppm) and LREE (59 – 150 ppm) contents, similar HREE contents (43 – 59 ppm), and slightly higher δEu values (0.04 – 0.08) than that close to the calcic skarn (ΣREE: 117 – 133 ppm, LREE: 51 – 80 ppm, HREE: 51 – 66 ppm, δEu: 0.02 – 0.04) (Fig. 8-20b).

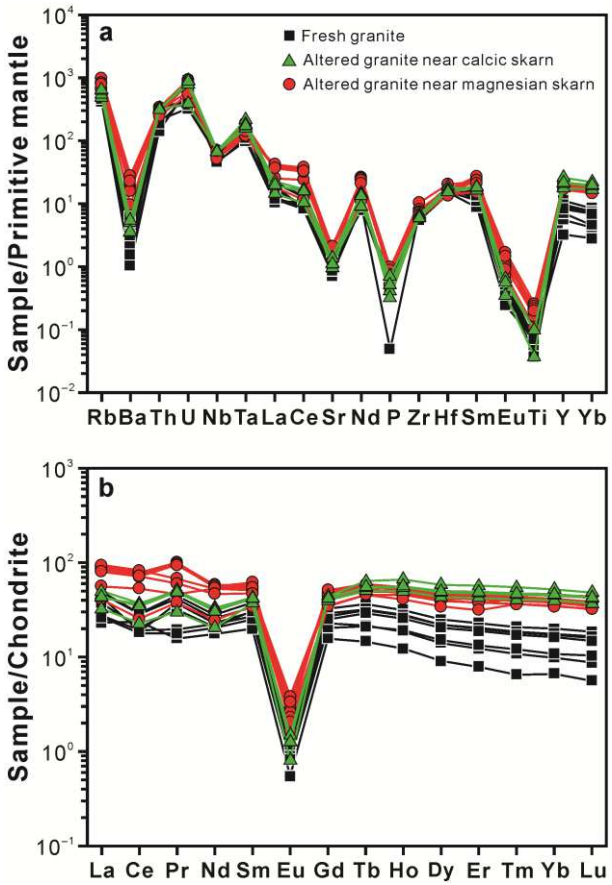

Figure 8-20. Primitive mantle-normalized (Sun and Mcdonough, 1989) spider diagrams and chondrite-normalized (Boynton, 1984) REE patterns of the fresh and altered Weijia granite. The data source of fresh granite is the same as Figure 8-19.

8.4.3. Biotite

EDS elemental mapping reveals that the fresh biotite in the Weijia granite is Fe-rich and F-bearing biotite (Fig. 8-21). Some fluorite crystals appear in the fresh biotite along the (001) plane (Fig. 8-21). By contrast, the bleached biotite in the Weijia granite shows obvious losses of K, Fe, Mg, and Ti and a gain of Ca (Fig. 8-22), probably resulting from the hydrothermal alteration of granite during which the fresh biotite was broken down.

Representative EMP analytical results and crystallochemical calculations of the fresh and bleached biotite in the Weijia granite are listed in Appendix 8-3. The fresh biotite in the granite without stockwork veins contains SiO_2 contents of 31.15 – 34.85 wt.%, TiO_2 contents

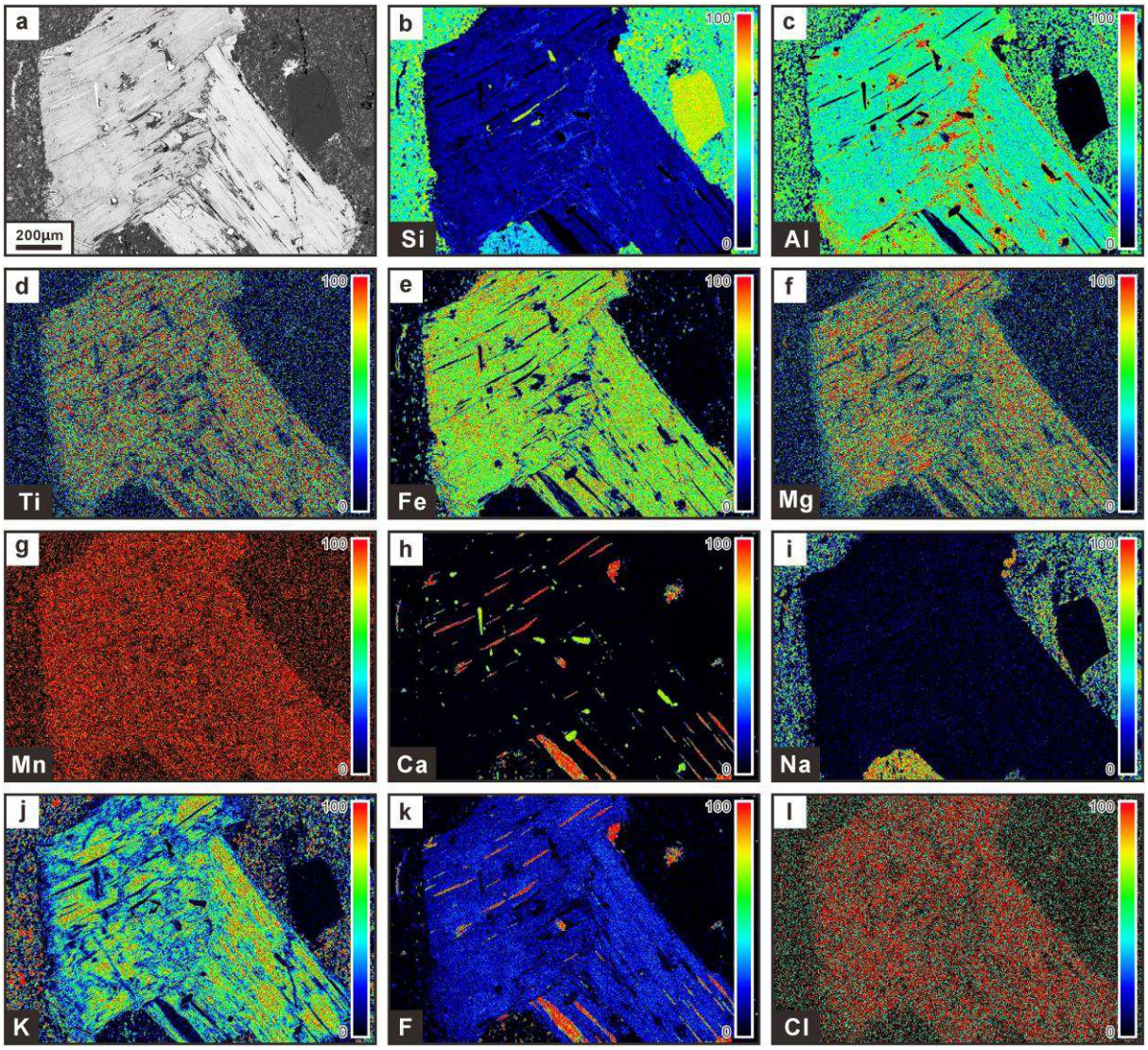

Figure 8-21. EDS elemental mapping of fresh biotite in the Weijia granite.

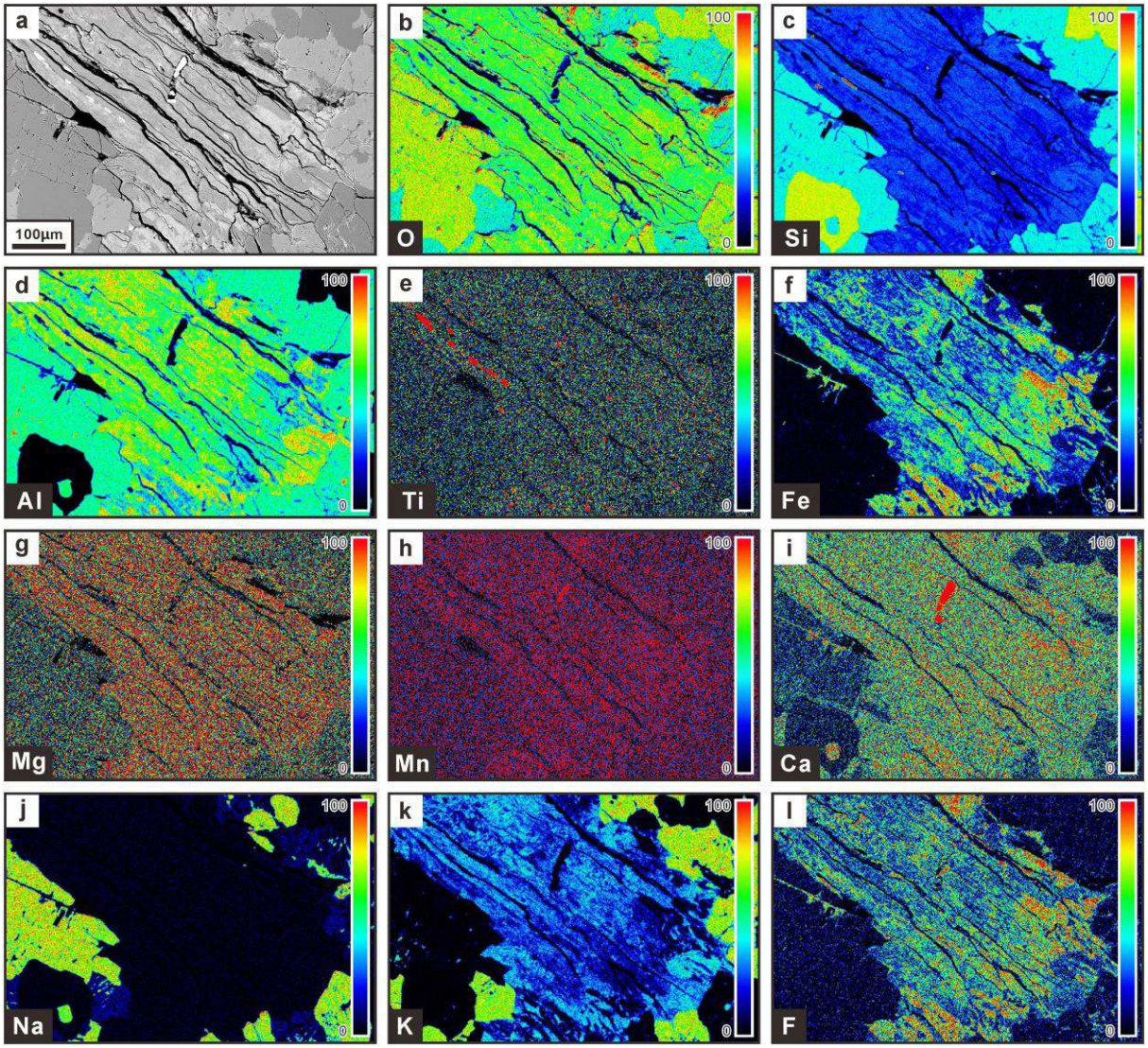

Figure 8-22. EDS elemental mapping of bleached biotite in the Weijia granite.

of 1.46 – 3.10 wt.%, Al_2O_3 contents of 14.70 – 16.46 wt.%, FeO contents of 29.27 – 35.39 wt.%, MnO contents of 0.53 – 1.10 wt.%, MgO contents of 0.87 – 2.97 wt.%, CaO contents of 0.00 – 0.20 wt.%, Na_2O contents of 0.25 – 0.44 wt.%, and K_2O contents of 5.95 – 8.92 wt.% and plots in the lepidomelane field of the [Fe_{Total}+Mn+Ti–^{VI}Al (apfu: atoms per formula unit)] vs. [Mg–Li (apfu)] classification diagram (Fig. 8-23a).

Compared with the fresh biotite, the bleached biotite in the granite without stockwork veins has distinctly lower K_2O contents of 0.32 – 7.42 wt.% (Fig. 8-24) and TiO_2 contents of 0.00 – 2.23 wt.% and higher Al_2O_3 contents of 15.62 – 25.44 wt.%, plotting in the lepidomelane and siderophyllite fields (Fig. 8-23a).

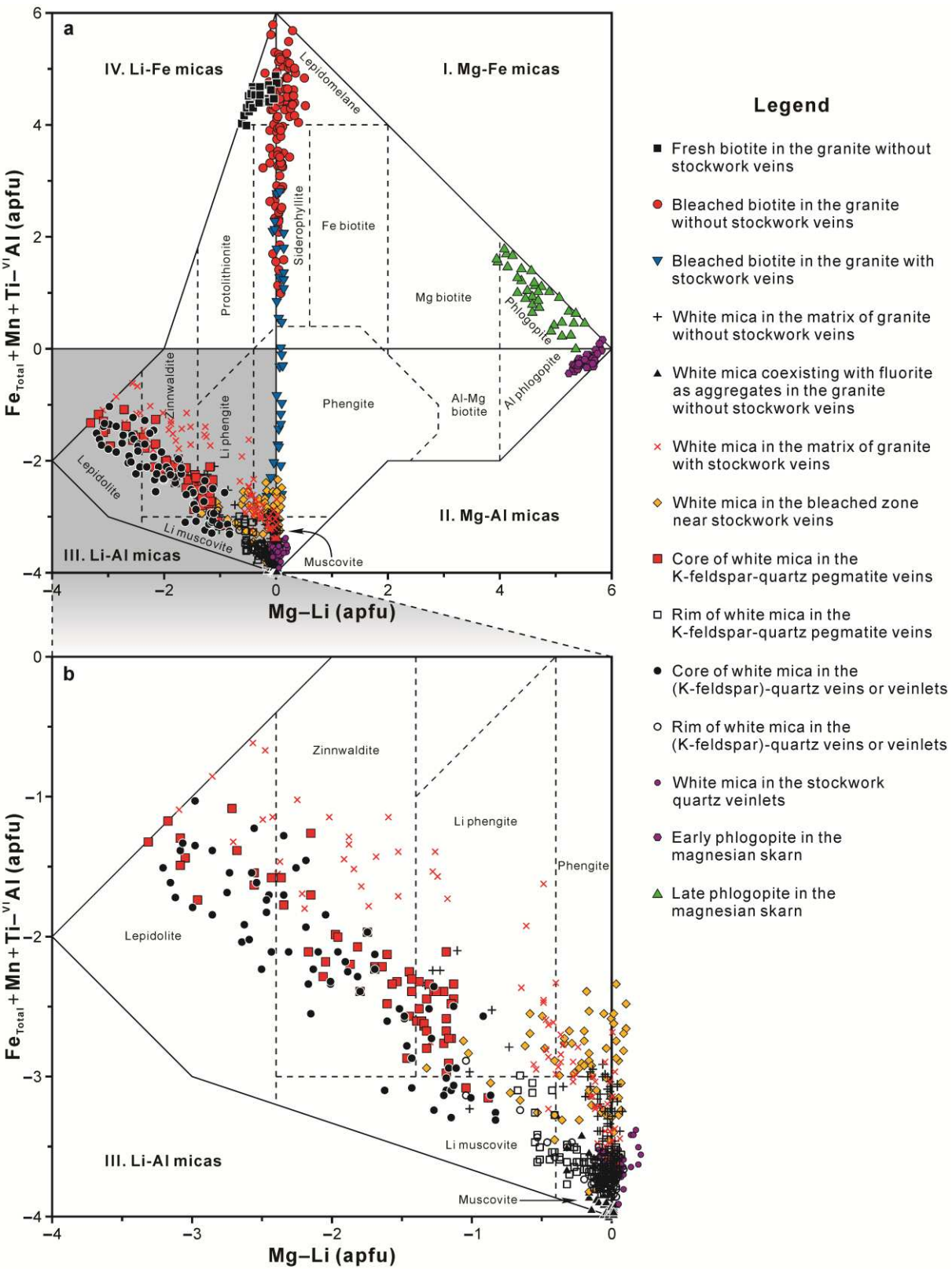

Figure 8-23. (Fe_{Total}+Mn+Ti–^{VI}Al) (apfu)-(Mg–Li) (apfu) classification diagram of micas (after Tischendorf et al., 1997) from the Weijia W deposit.

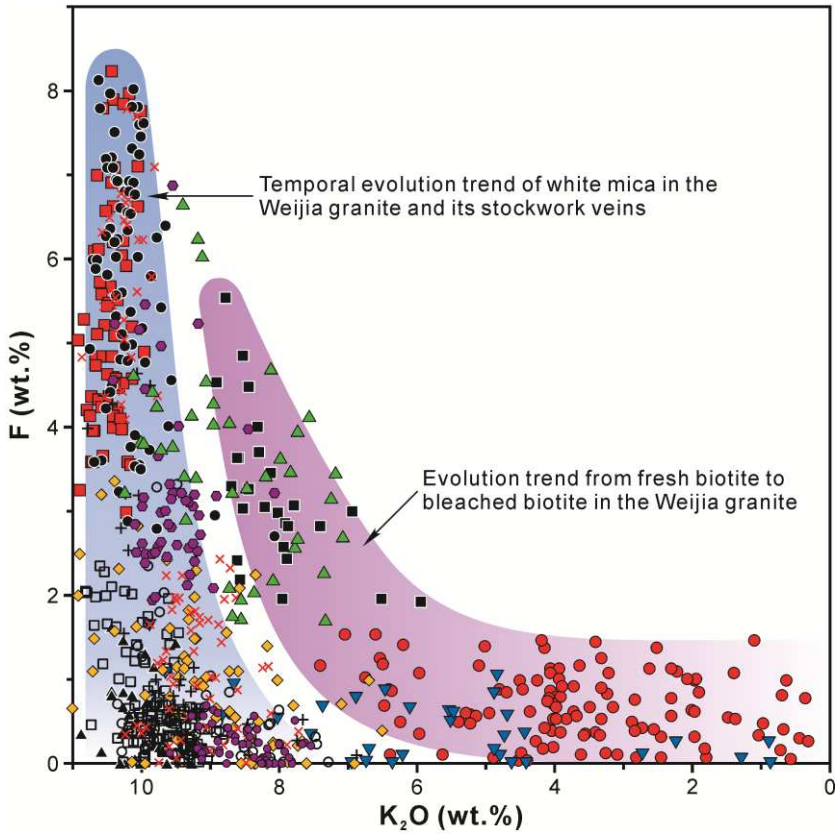

Figure 8-24. K_2O and F contents of micas from the Weijia W deposit. Legends are the same as Figure 8-23.

Notably, the bleached biotite in the granite with stockwork veins shows distinctly higher SiO_2 contents of 35.75 – 49.81 wt.%, Al_2O_3 contents of 16.71 – 30.81 wt.%, and CaO contents of 0.14 – 1.82 wt.% and lower TiO_2 contents of 0.00 – 1.40 wt.%, FeO contents of 4.40 – 27.43 wt.%, MnO contents of 0.00 – 0.87 wt.%, MgO contents of 0.13 – 0.69 wt.%, Na_2O contents of 0.00 – 0.19 wt.%, and K_2O contents of 0.88 – 9.90 wt.% (Fig. 8-24) than the fresh biotite in the granite without stockwork veins and is plotted in the siderophyllite and phengite fields (Fig. 8-23a).

To be exact, the bleached biotite is not true mica and is transforming into clay minerals. In addition to the large variation of the K_2O contents of the fresh and bleached biotite, the F contents of the fresh and bleached biotite also show a large variation (Fig. 8-24). The fresh and bleached biotite in the granite without stockwork veins and the bleached biotite in the granite with stockwork veins have progressively decreasing F contents of 1.93 – 5.54 wt.% with a peak value of 2.9 wt.%, 0.03 – 1.54 wt.% with a peak value of 0.5 wt.%, and 0.00 – 1.65 wt.% with a peak value of 0.1 wt.% (Figs. 8-24 and 8-25a–b).

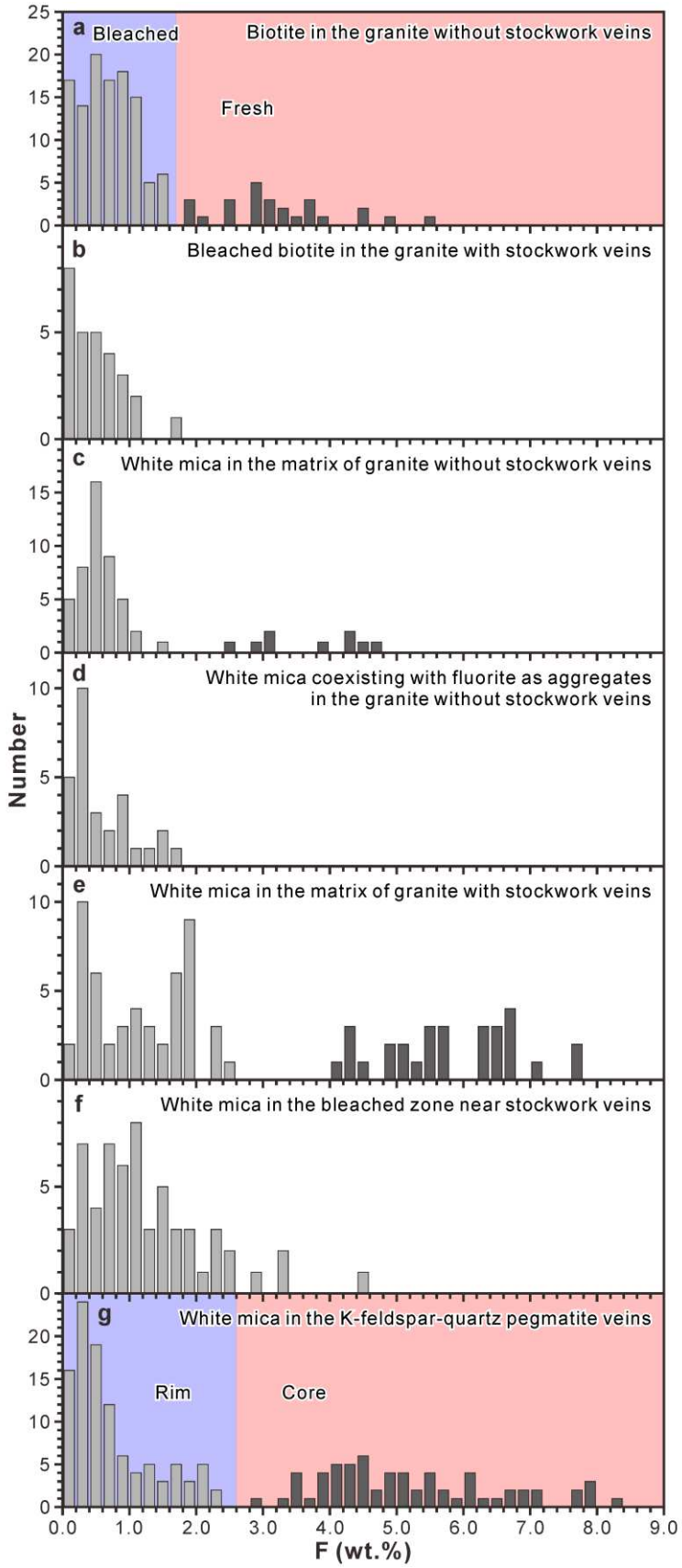

Figure 8-25. Histograms for F contents of different F-bearing minerals in the Weijia W deposit.

(*To be continued on the next page*)

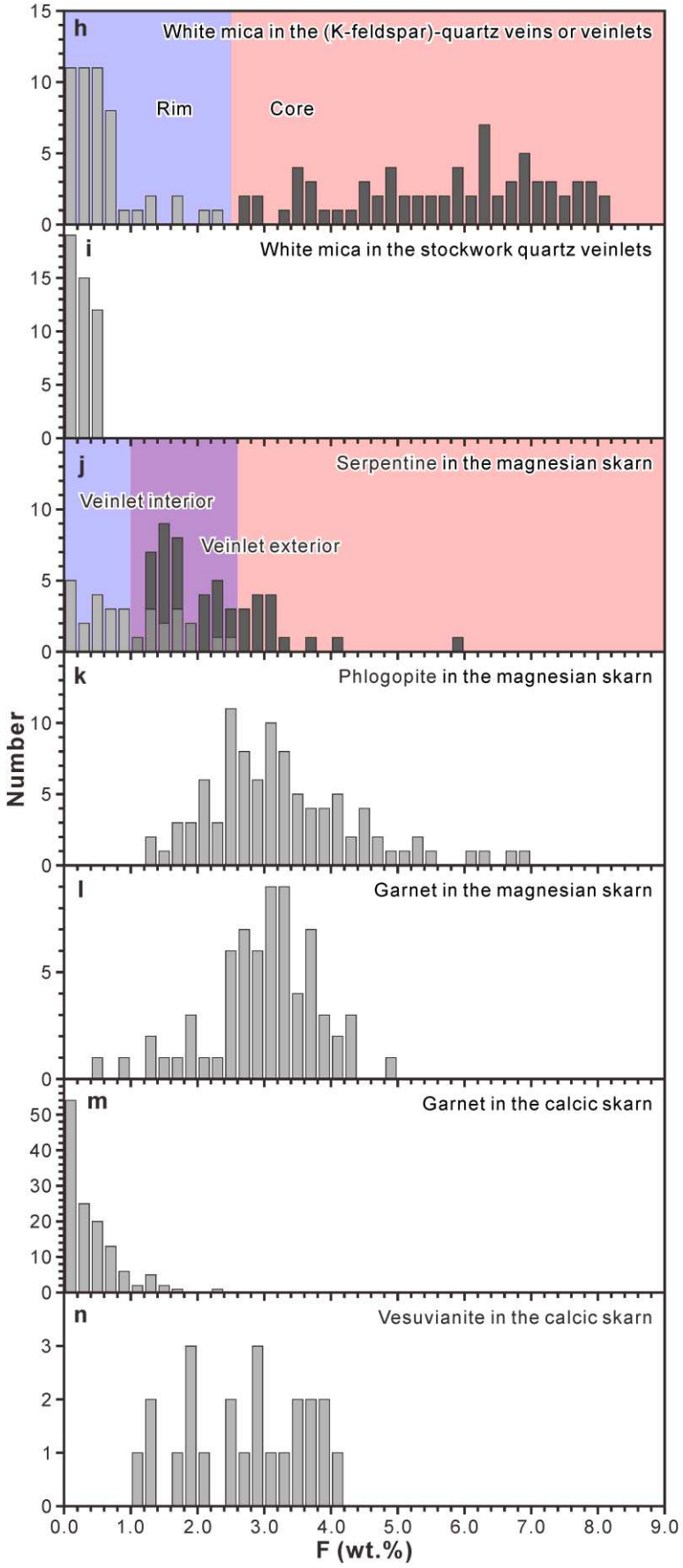

Figure 8-25. (*Continued*).

8.4.4. White mica

Representative EMP analytical results and crystallochemical calculations of the white mica in the Weijia granite and its stockwork veins are listed in Appendix 8-4. The white mica in the matrix of granite without stockwork veins contains SiO_2 contents of 43.00 – 51.00 wt.%, TiO_2 contents of 0.00 – 0.69 wt.%, Al_2O_3 contents of 28.81 – 33.75 wt.%, FeO contents of 1.02 – 7.37 wt.%, MnO contents of 0.00 – 0.32 wt.%, MgO contents of 0.02 – 0.37 wt.%, CaO contents of 0.00 – 0.31 wt.%, Na_2O contents of 0.02 – 0.38 wt.%, and K_2O contents of 6.89 – 10.78 wt.% (Fig. 8-24) and plots dominantly in the muscovite field with some in the Li muscovite, Li phengite, and phengite fields (Fig. 8-23b). This kind of white mica mostly has F contents of 0.09 – 1.54 wt.% with a peak value of 0.5 wt.% and some has F contents of 2.54 – 4.63 wt.% with peak values of 3.1 wt.% and 4.3 wt.% (Figs. 8-24 and 8-25c).

Compared with the white mica in the matrix of granite without stockwork veins, the white mica coexisting with fluorite as aggregates in the granite without stockwork veins shows distinctly higher Al_2O_3 contents of 33.76 – 37.69 wt.% and lower FeO contents of 0.00 – 1.87 wt.% and F contents of 0.00 – 1.62 wt.% with a peak value of 0.3 wt.% (Figs. 8-24 and 8-25d), all plotting in the muscovite field (Fig. 8-23b).

The white mica in the matrix of granite with stockwork veins can be divided into two groups with one group having relatively low SiO_2 contents of 42.32 – 46.28 wt.% and Al_2O_3 contents of 23.48 – 26.44 wt.% and high FeO contents of 7.15 – 12.14 wt.%, K_2O contents of 9.77 – 10.88 wt.% (Fig. 8-24), and F contents of 4.09 – 7.79 wt.% with a peak value of 6.7 wt.% (Figs. 8-24 and 8-25e) and the other group containing relatively high SiO_2 contents of 44.70 – 49.76 wt.% and Al_2O_3 contents of 26.39 – 32.91 wt.% and low FeO contents of 0.80 – 6.51 wt.%, K_2O contents of 7.59 – 10.25 wt.% (Fig. 8-24), and F contents of 0.00 – 2.43 wt.% with peak values of 0.3 wt.% and 1.9 wt.% (Figs. 8-24 and 8-25e). They are plotted in the muscovite, phengite, Li muscovite, and Li phengite fields and the Li phengite, zinnwaldite, and lepidolite fields, respectively (Fig. 8-23b).

The SiO_2, TiO_2, Al_2O_3, FeO, MnO, MgO, CaO, Na_2O, and K_2O contents of the white mica in the bleached zone near stockwork veins are 43.72 – 49.85 wt.%, 0.00 – 0.36 wt.%, 26.59 – 34.37 wt.%, 0.34 – 7.30 wt.%, 0.00 – 0.34 wt.%, 0.00 – 0.47 wt.%, 0.00 – 0.86 wt.%,

0.00 – 0.35 wt.%, and 6.52 – 11.01 wt.% (Fig. 8-24), respectively. This kind of white mica shows F contents of 0.00 – 4.51 wt.% with a peak value of 1.1 wt.% (Figs. 8-24 and 8-25f) and plots in the muscovite, phengite, Li muscovite, and Li phengite fields (Fig. 8-23b).

EDS elemental mapping reveals that the white mica in the K-feldspar-quartz pegmatite veins has a zonal texture with the core showing higher Fe, F, and K contents and lower Al contents than the rim (Fig. 8-26). EMP analyses show that the core contains SiO_2 contents of 44.16 – 49.59 wt.%, TiO_2 contents of 0.00 – 0.36 wt.%, Al_2O_3 contents of 25.73 – 31.20 wt.%, FeO contents of 2.12 – 9.79 wt.%, MnO contents of 0.00 – 0.52 wt.%, MgO contents of 0.00 – 0.27 wt.%, CaO contents of 0.00 – 0.10 wt.%, Na_2O contents of 0.03 – 0.37 wt.%, K_2O contents of 10.01 – 11.07 wt.% (Fig. 8-24), and F contents of 2.99 – 8.23 wt.% with a peak value of 4.5 wt.% (Figs. 8-24 and 8-25g), plotting in the lepidolite, zinnwaldite, Li phengite, and Li muscovite fields (Fig. 8-23b). Whereas, the rim contains distinctly higher Al_2O_3 contents of 30.44 – 35.56 wt.% and lower FeO contents of 0.17 – 3.39 wt.%, K_2O contents of 8.40 – 10.80 wt.% (Fig. 8-24), and F contents of 0.00 – 2.34 wt.% with a peak value of 0.3 wt.% (Figs. 8-24 and 8-25g), plotting in the muscovite and Li muscovite fields (Fig. 8-23b).

EDS elemental mapping reveals that the white mica in the (K-feldspar)-quartz veins or veinlets also has a zonal texture with the core showing higher Fe, F, and K contents and lower Al contents than the rim (Fig. 8-27). EMP analyses show that the core contains SiO_2 contents of 44.62 – 47.84 wt.%, TiO_2 contents of 0.00 – 0.28 wt.%, Al_2O_3 contents of 25.47 – 33.33 wt.%, FeO contents of 1.67 – 10.61 wt.%, MnO contents of 0.00 – 0.66 wt.%, MgO contents of 0.00 – 0.28 wt.%, CaO contents of 0.00 – 0.34 wt.%, Na_2O contents of 0.00 – 0.53 wt.%, K_2O contents of 9.57 – 10.75 wt.% (Fig. 8-24), and F contents of 2.71 – 8.12 wt.% with a peak value of 6.3 wt.% (Figs. 8-24 and 8-25h), plotting in the lepidolite, zinnwaldite, Li phengite, and Li muscovite fields (Fig. 8-23b). Whereas, the rim contains distinctly higher Al_2O_3 contents of 32.10 – 35.12 wt.% and lower FeO contents of 0.43 – 2.67 wt.%, K_2O contents of 7.29 – 10.35 wt.% (Fig. 8-24), and F contents of 0.00 – 2.34 wt.% with a peak value of 0.3 wt.% (Figs. 8-24 and 8-25h), plotting predominantly in the muscovite and Li muscovite fields (Fig. 8-23b).

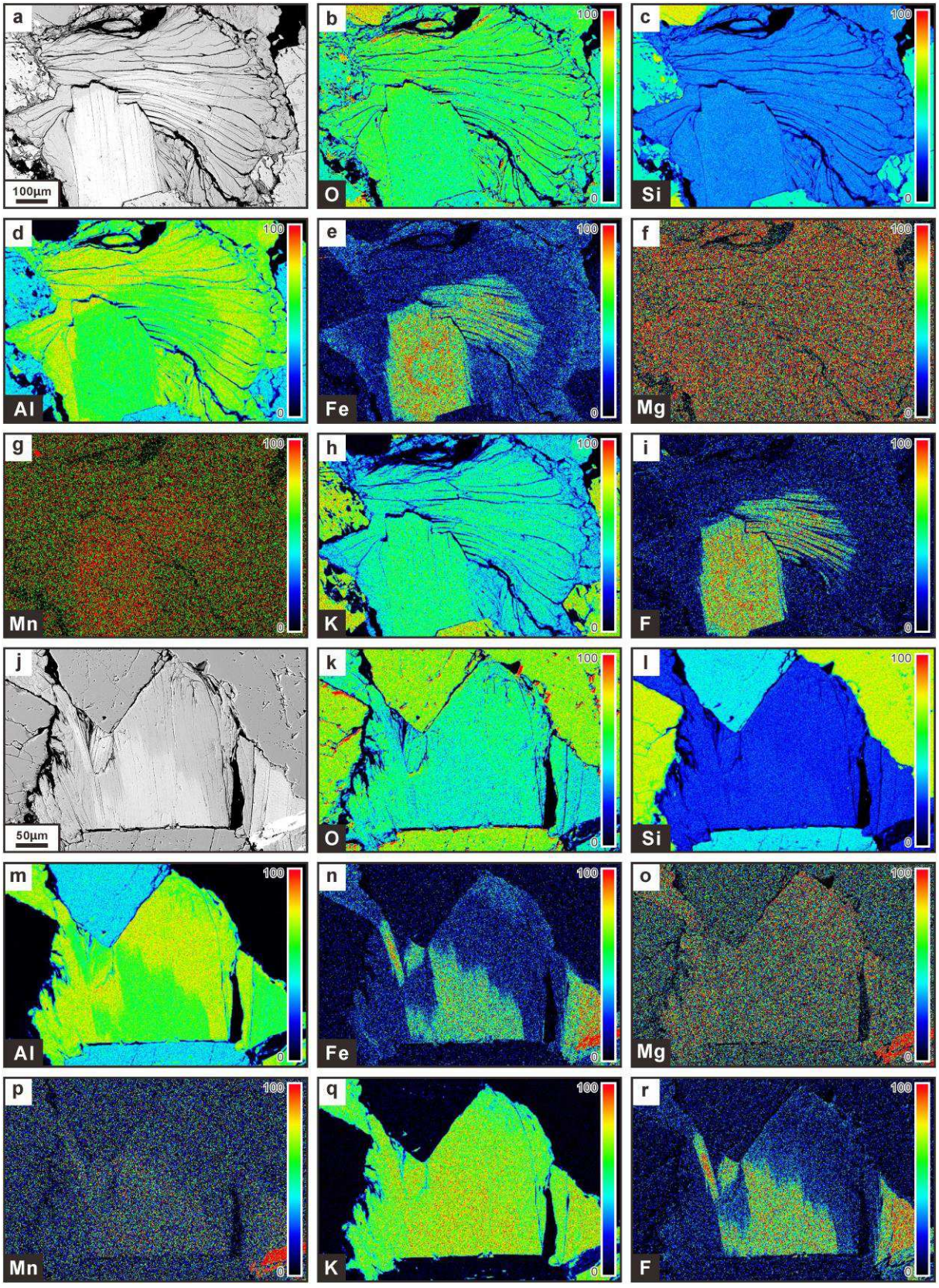

Figure 8-26. EDS elemental mapping of white mica in the K-feldspar-quartz pegmatite veins at the apex of the Weijia granite.

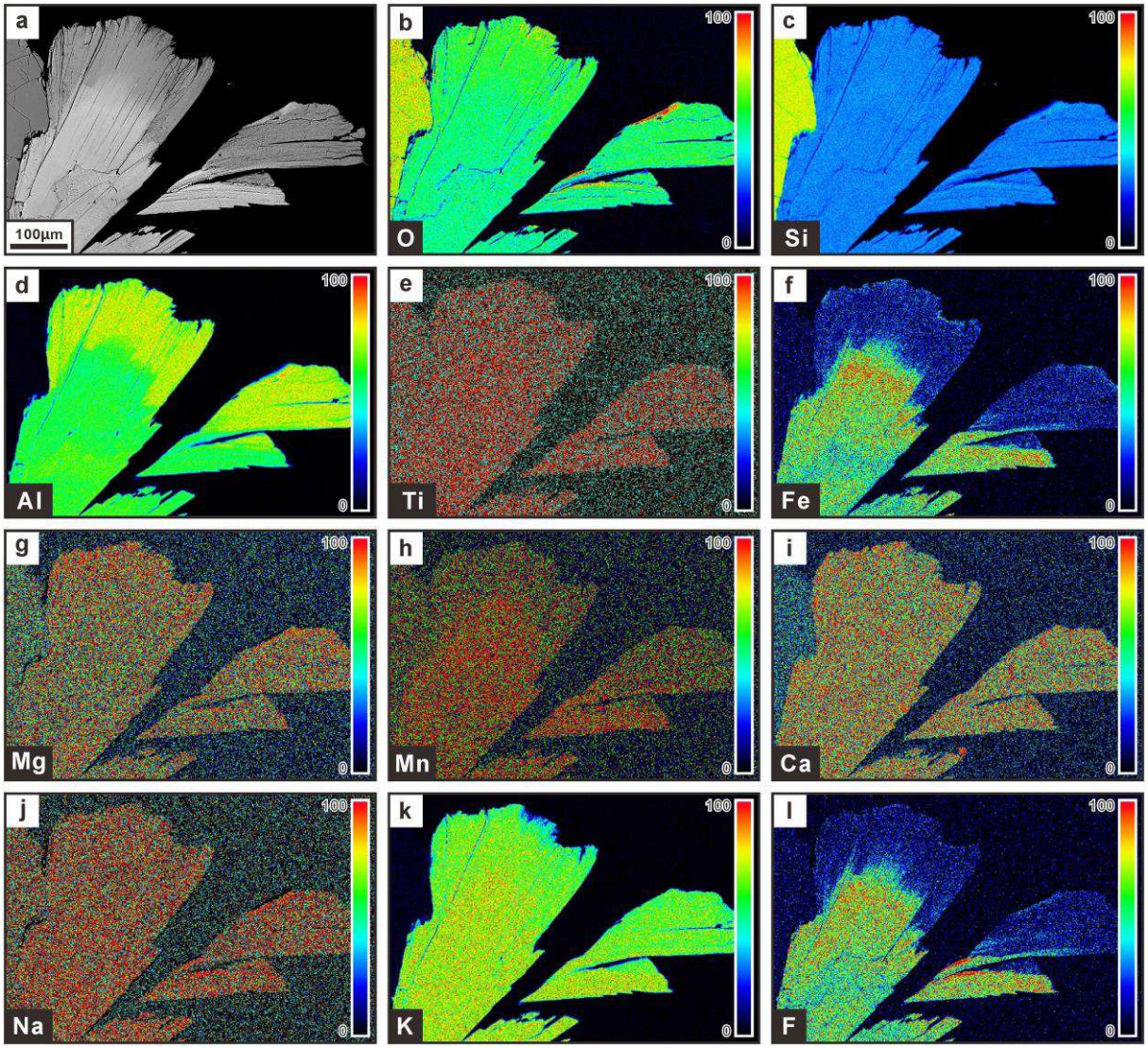

Figure 8-27. EDS elemental mapping of white mica in the (K-feldspar)-quartz veinlet at the apex of the Weijia granite.

The SiO_2, TiO_2, Al_2O_3, FeO, MnO, MgO, CaO, Na_2O, and K_2O contents of the white mica in the stockwork veinlets are 45.92 – 51.56 wt.%, 0.00 – 0.18 wt.%, 29.08 – 33.70 wt.%, 0.61 – 2.09 wt.%, 0.00 – 0.22 wt.%, 0.06 – 0.60 wt.%, 0.05 – 0.42 wt.%, 0.03 – 0.16 wt.%, and 7.55 – 9.60 wt.% (Fig. 8-24), respectively. This kind of white mica shows extremely low F contents of 0.00 – 0.69 wt.% with a peak value of 0.1 wt.% (Figs. 8-24 and 8-25i) and is all plotted in the muscovite field (Fig. 8-23b).

8.4.5. Serpentine

EDS elemental mapping reveals that, during the process of magnesian skarnization,

dolomite was decomposed to release Mg for the formation of serpentine firstly and then phlogopite, calcite and fluorite were formed contemporaneously (Fig. 8-28a–i). The serpentine in the magnesian skarn can be roughly divided into two types according to its occurrences. The first type of serpentine shows a disseminated distribution in the exteriors of the magnesian skarn veinlets and coexists with calcite and fluorite, whereas, the other type of serpentine occurs together with phlogopite and fluorite in the interiors of the magnesian skarn veinlets (Figs. 8-9, 8-10d–e and g, and 8-28). Reasonably, the serpentine in the veinlet interiors was formed later than that in the veinlet exteriors.

Representative EMP analytical results and crystallochemical calculations of the serpentine in the magnesian skarn of the Weijia W deposit are listed in Appendix 8-5. The serpentine in the magnesian skarn veinlet exteriors contains SiO_2 contents of 39.36 – 46.74 wt.%, TiO_2 contents of 0.00 – 0.13 wt.%, Al_2O_3 contents of 0.47 – 2.92 wt.%, FeO contents of 1.25 – 3.56 wt.%, MnO contents of 0.00 – 0.45 wt.%, MgO contents of 25.00 – 40.61 wt.%, CaO contents of 0.04 – 0.80 wt.%, Na_2O contents of 0.00 – 0.20 wt.%, K_2O contents of 0.00 – 0.31 wt.%, and F contents of 1.08 – 5.88 wt.% with a peak value of 1.5 wt.% (Fig. 8-25j). By contrast, the serpentine in the magnesian skarn veinlet interiors has distinctly lower SiO_2 contents of 33.33 – 42.38 wt.%, MgO contents of 20.93 – 36.09 wt.%, and F contents of 0.00 – 2.57 wt.% with a peak value of 0.1 wt.% (Fig. 8-25j) and higher Al_2O_3 contents of 0.79 – 6.83 wt.% and FeO contents of 3.67 – 8.12 wt.%.

8.4.6. Phlogopite

BSE imaging (Fig. 8-10e) and EDS elemental mapping (Fig. 8-28j–aa) reveal that the late-formed phlogopite has higher Fe and lower Mg contents than the early-formed phlogopite. In the individual zoned phlogopite crystals, the later rim parts also show higher Fe and lower Mg contents than the earlier core parts (Fig. 8-29).

Representative EMP analytical results and crystallochemical calculations of the phlogopite in the magnesian skarn of the Weijia W deposit are listed in Appendix 8-6. The phlogopite in the magnesian skarn contains SiO_2 contents of 36.01 – 43.85 wt.%, TiO_2 contents of 0.00 – 0.19 wt.%, Al_2O_3 contents of 9.96 – 17.45 wt.%, FeO contents of 0.75 – 22.26 wt.%, MnO contents of 0.00 – 1.49 wt.%, MgO contents of 11.47 – 31.57 wt.%, CaO

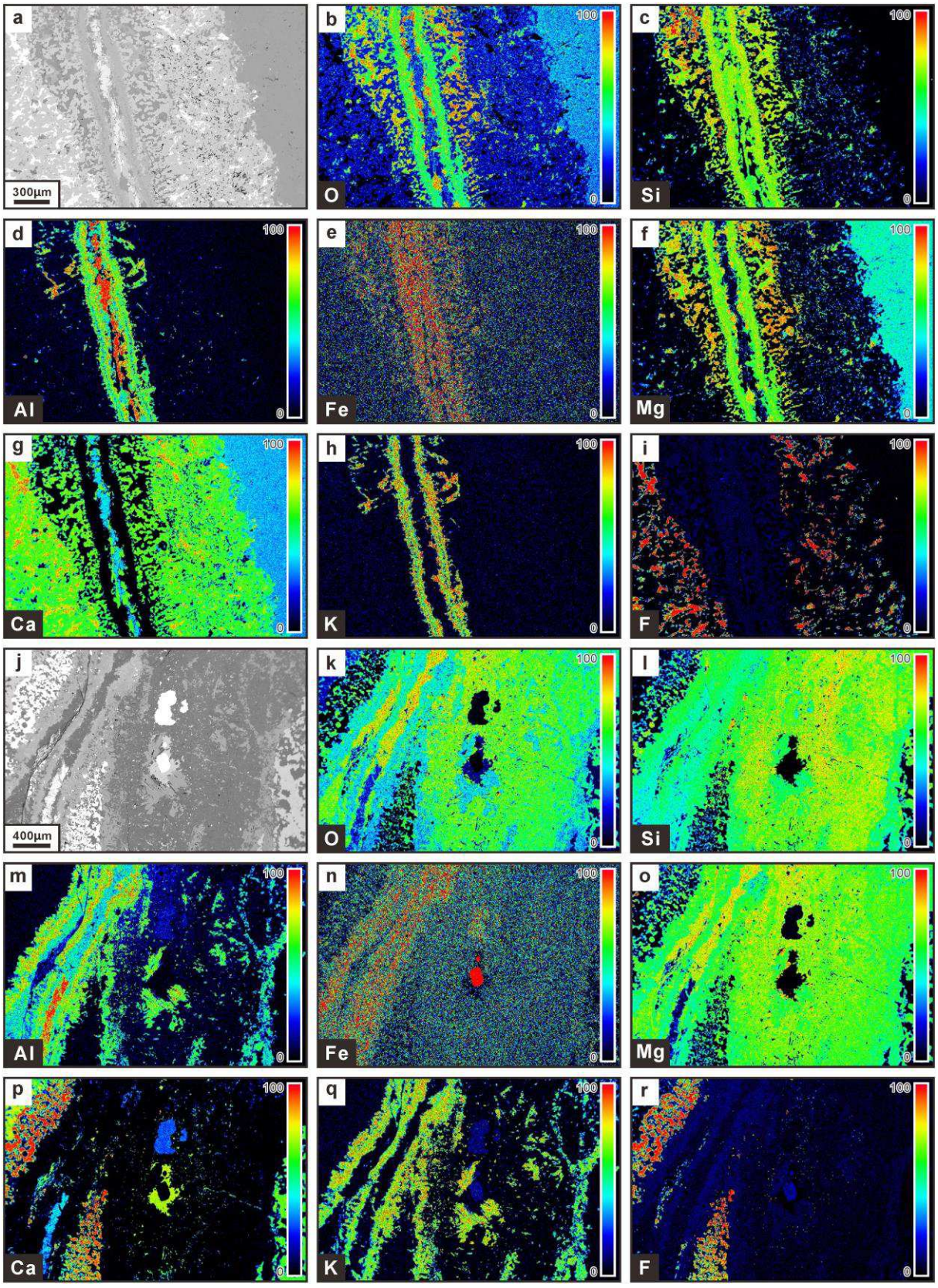

Figure 8-28. EDS elemental mapping of the magnesian skarn veinlets in the Weijia W deposit.

(*To be continued on the next page*)

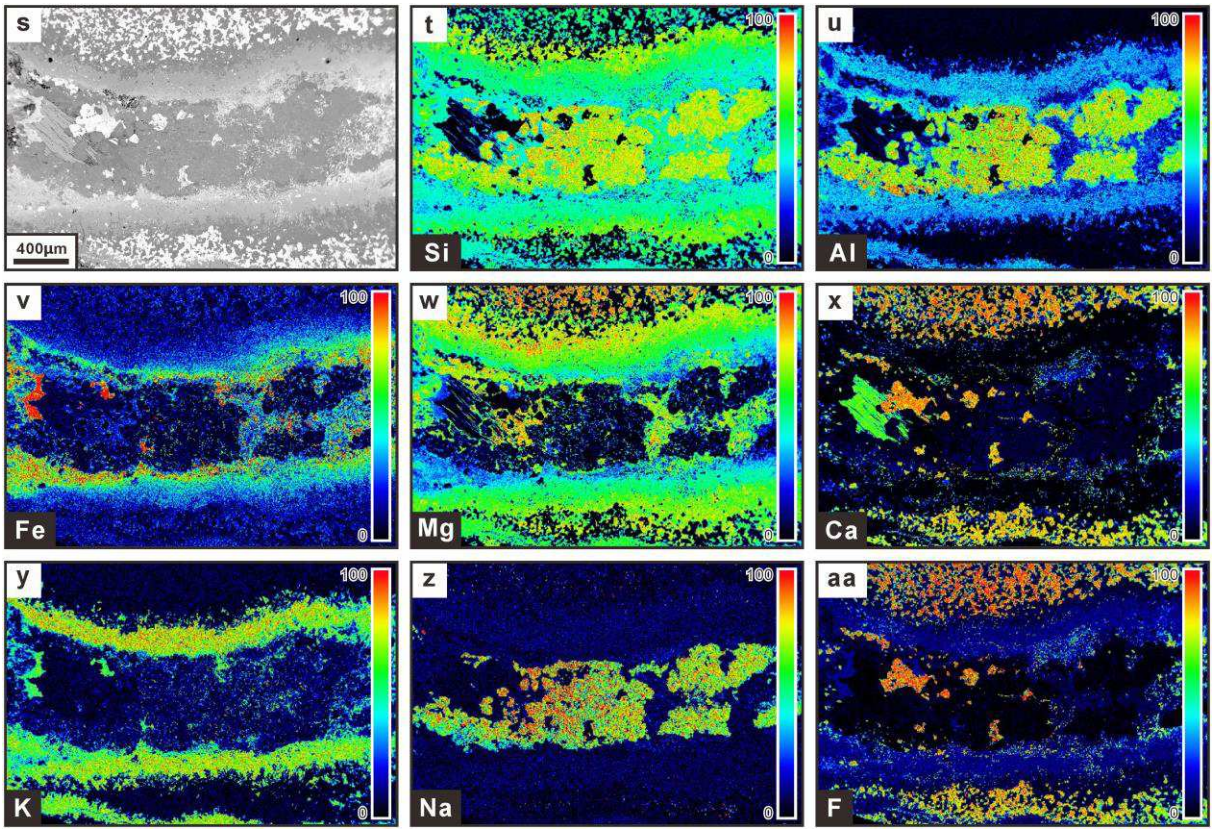

Figure 8-28. (*Continued*).

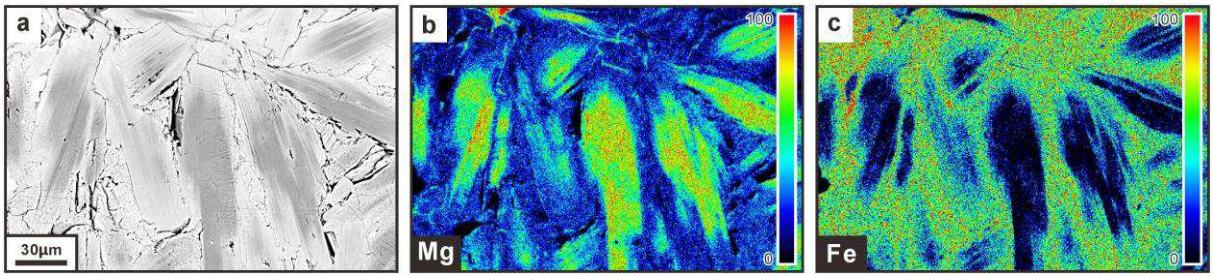

Figure 8-29. EDS elemental mapping of phlogopite in the magnesian skarn of the Weijia W deposit.

contents of 0.00 – 0.15 wt.%, Na_2O contents of 0.00 – 0.40 wt.%, K_2O contents of 7.04 – 10.41 wt.% (Fig. 8-24), and F contents of 1.25 – 6.88 wt.% with peak values of 2.5 wt.% and 3.1 wt.% (Figs. 8-24 and 8-25k). The late phlogopite shows distinctly higher FeO contents of 3.97 – 22.26 wt.% and lower MgO contents of 11.47 – 25.10 wt.% and slightly higher MnO contents of 0.07 – 1.49 wt.% and lower K_2O contents of 7.04 – 10.24 wt.% (Fig. 8-24) than the early phlogopite (FeO: 0.75 – 3.63 wt.%, MgO: 25.58 – 31.57 wt.%, MnO: 0.00 – 0.29 wt.%, K_2O: 8.07 – 10.41 wt.%). They have similar F contents 1.25 – 6.66 wt.% and 1.94 –

6.88 wt.%, respectively (Fig. 8-24). The early phlogopite plots predominantly in the Al phlogopite field of the [Fe_{Total}+Mn+Ti–^{VI}Al (apfu)] vs. [Mg–Li (apfu)] classification diagram, whereas, the late phlogopite is plotted in the phlogopite field (Fig. 8-23a).

8.4.7. Garnet

Representative EMP analytical results and crystallochemical calculations of the garnet in the magnesian and calcic skarns of the Weijia W deposit are listed in Appendix 8-7. The garnet in the magnesian skarn is grandite (Py+Al+Sp: 0.7 – 13.8 mol.%, mostly 8.0 – 13.8 mol.%) (Fig. 8-30a). It has SiO_2 contents of 34.48 – 37.81 wt.%, TiO_2 contents of 0.00 – 0.19 wt.%, Al_2O_3 contents of 14.68 – 20.37 wt.%, FeO contents of 2.11 – 9.33 wt.%, MnO contents of 0.22 – 3.96 wt.%, MgO contents of 0.05 – 3.13 wt.%, CaO contents of 30.39 – 36.29 wt.%, Na_2O contents of 0.00 – 0.24 wt.%, and K_2O contents of 0.00 – 0.08 wt.%, showing a compositional variation between $Gr_{67.4}Ad_{21.7}$ and $Gr_{86.3}Ad_{8.6}$ (Fig. 8-30a). Uncommonly, the garnet in the magnesian skarn contains very high F contents of 0.51 – 4.83 wt.% with a peak value of 3.2 wt.% (Fig. 8-25l).

EDS elemental mapping reveals that the first-generation garnet in the calcic skarn exhibits a well-developed compositional zonation with the later rim parts having higher Fe and lower Al contents than the earlier core parts (Fig. 8-31a–f) or an oscillatory compositional zoning of Al and Fe (Fig. 8-31g–r). However, the second-generation vein-like garnet in the

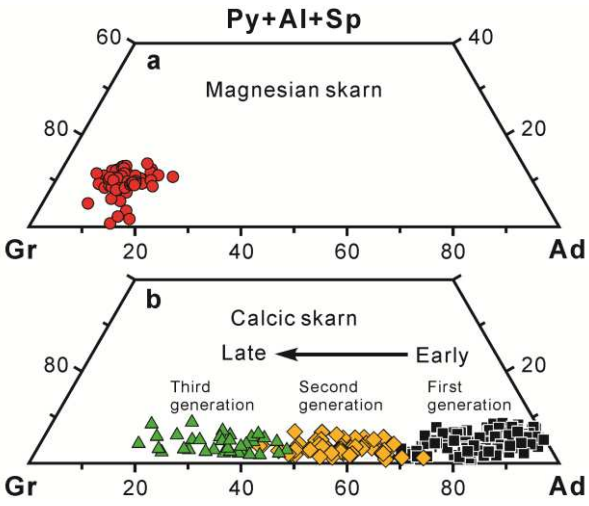

Figure 8-30. Compositions of garnets from the magnesian and calcic skarns in the Weijia W deposit. Mineral abbreviations: Ad = andradite, Al = almandine, Gr = grossularite, Py = pyrope, Sp = spessartine.

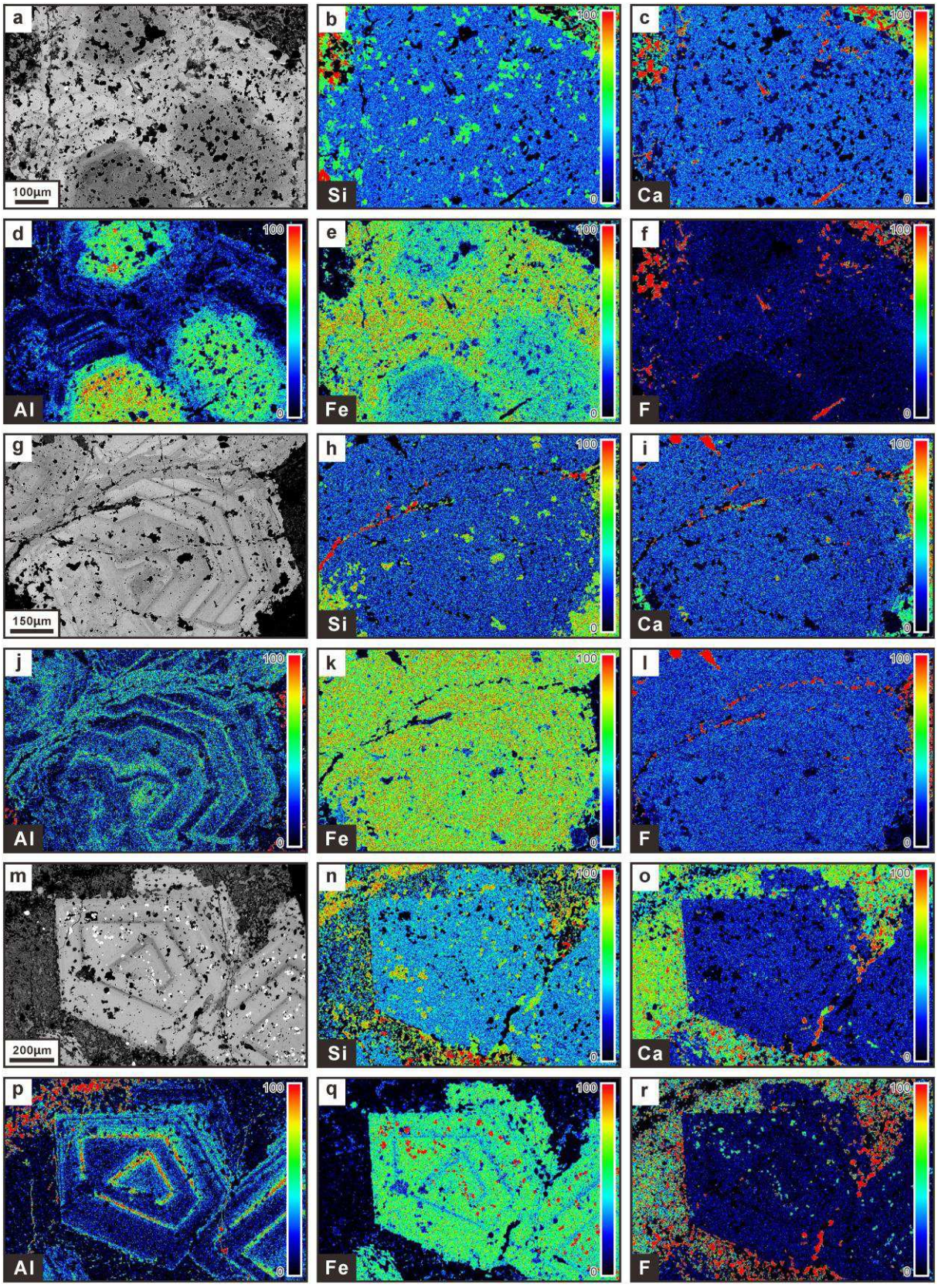

Figure 8-31. EDS elemental mapping of the first-generation garnet in the calcic skarn of the Weijia W deposit.

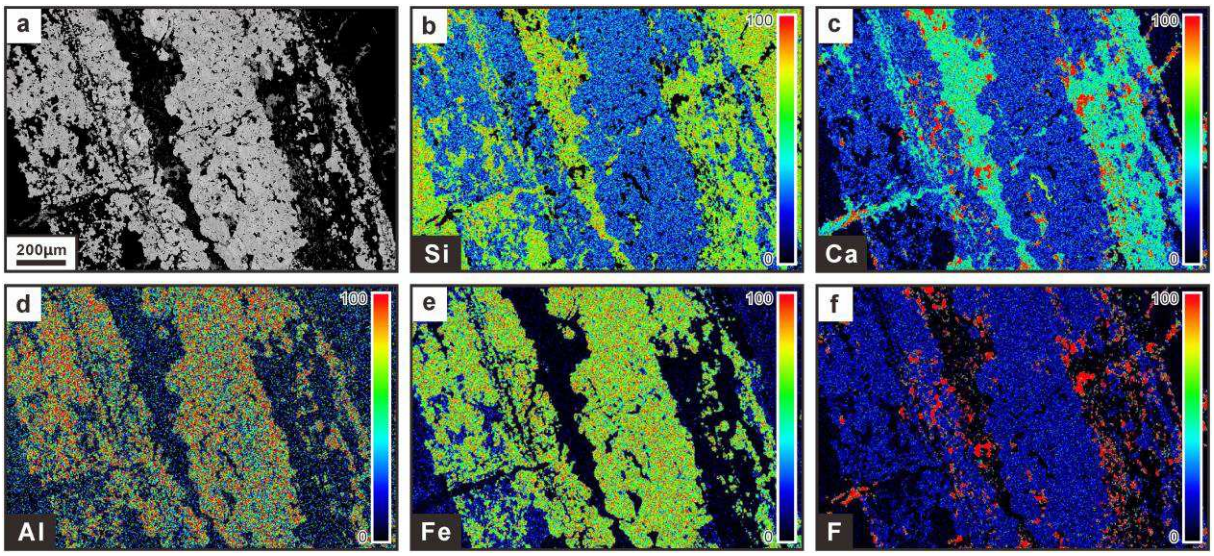

Figure 8-32. EDS elemental mapping of the second-generation garnet in the calcic skarn of the Weijia W deposit.

calcic skarn does not show a compositional zonation (Fig. 8-32). Like the first-generation garnet, the third-generation interstitial garnet in the calcic skarn also has an obvious compositional zonation with the later outer parts having higher Fe and lower Al contents than the earlier inner parts (Fig. 8-33).

All the three generations of garnets in the calcic skarn are grandite (Py+Al+Sp: 0.8 – 9.3 mol.%) (Fig. 8-30b). The first-generation garnet has SiO_2 contents of 34.19 – 36.87 wt.%, TiO_2 contents of 0.00 – 0.28 wt.%, Al_2O_3 contents of 0.06 – 6.91 wt.%, FeO contents of 20.15 – 29.38 wt.%, MnO contents of 0.02 – 1.89 wt.%, MgO contents of 0.00 – 0.54 wt.%, CaO contents of 31.24 – 34.38 wt.%, Na_2O contents of 0.00 – 0.06 wt.%, and K_2O contents of 0.00 – 0.10 wt.%, showing a compositional variation between $Gr_{0.3}Ad_{94.6}$ and $Gr_{32.4}Ad_{62.5}$ (Fig. 8-30b).

The second-generation garnet has SiO_2 contents of 35.57 – 37.56 wt.%, TiO_2 contents of 0.00 – 0.21 wt.%, Al_2O_3 contents of 5.17 – 13.57 wt.%, FeO contents of 12.31 – 21.57 wt.%, MnO contents of 0.07 – 1.40 wt.%, MgO contents of 0.01 – 0.36 wt.%, CaO contents of 31.99 – 35.10 wt.%, Na_2O contents of 0.00 – 0.05 wt.%, and K_2O contents of 0.00 – 0.08 wt.%, showing a compositional variation between $Gr_{25.0}Ad_{73.8}$ and $Gr_{59.4}Ad_{35.2}$ (Fig. 8-30b).

The third-generation garnet has SiO_2 contents of 36.36 – 38.13 wt.%, TiO_2 contents of 0.00 – 0.11 wt.%, Al_2O_3 contents of 10.69 – 19.78 wt.%, FeO contents of 7.14 – 15.64 wt.%,

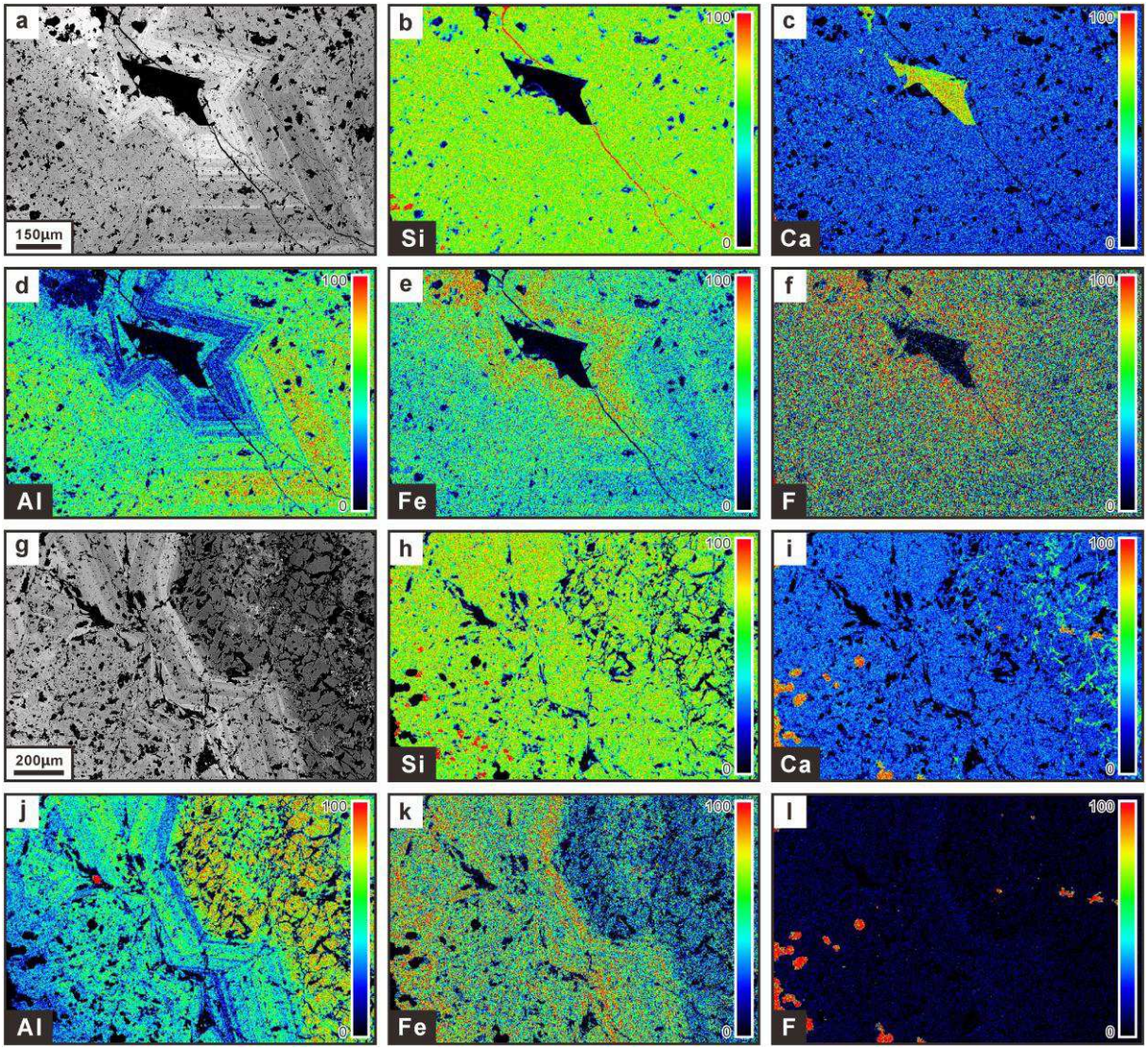

Figure 8-33. EDS elemental mapping of the third-generation garnet in the calcic skarn of the Weijia W deposit.

MnO contents of 0.57 – 2.29 wt.%, MgO contents of 0.00 – 0.17 wt.%, CaO contents of 31.41 – 35.01 wt.%, Na_2O contents of 0.00 – 0.03 wt.%, and K_2O contents of 0.00 – 0.06 wt.%, showing a compositional variation between $Gr_{49.7}Ad_{47.0}$ and $Gr_{73.7}Ad_{22.7}$ (Fig. 8-30b).

Although the Fe and Al contents gradually increase and decrease with time, respectively, in the individual generations (i.e., first generation and third generation) of garnets (Figs. 8-31a–f and 8-33), overall, the Fe and Al contents progressively decrease and increase, respectively, from the first-generation garnet through the second-generation garnet to the third-generation garnet (Fig. 8-30b). Compared with the garnet in the magnesian skarn, the three generations of garnets in the calcic skarn contain distinctly lower F contents of 0.00 – 2.37 wt.% with a peak value of 0.1 wt.% (Fig. 8-25m).

LA-ICP-MS analytical results of the garnet in the magnesian and calcic skarns of the Weijia W deposit are listed in Appendix 8-8 and shown in Figures 8-34 and 8-35. The garnet in the magnesian skarn shows rightward sloping REE patterns with $(La/Yb)_N$ values of 5.9 – 62.0 and obvious negative Eu anomalies with δEu values of 0.02 – 0.35 (Figs. 8-34a and 8-35a–b). It contains ΣREE contents of 10.8 – 73.7 ppm (Fig. 8-35b). The first-generation garnet in the calcic skarn also shows rightward sloping REE patterns with $(La/Yb)_N$ values of 0.6 – 62.8 but almost no Eu anomalies with δEu values of 0.44 – 1.79 (Figs. 8-34b and 8-35a–b). It contains ΣREE contents of 4.4 – 26.8 ppm (Fig. 8-35b). In contrast, the second-generation and third-generation garnets in the calcic skarn show relatively flat REE patterns with obvious LREE depletions and negative Eu anomalies (Fig. 8-34c and d). They have $(La/Sm)_N$ values of 0.06 – 0.19 and 0.02 – 0.08, $(La/Yb)_N$ values of 0.07 – 0.55 and 0.02 – 0.10, ΣREE contents of 5.9 – 36.4 ppm and 0.5 – 4.2 ppm, and δEu values of 0.11 – 0.40 and 0.16 – 0.59, respectively (Fig. 8-35a–b).

The garnet in the magnesian skarn and the third-generation garnet in the calcic skarn contain distinctly lower Ti and V contents than the first-generation and second-generation garnets in the calcic skarn (Fig. 8-35c). The HFSE (Zr, Hf, Th, and U) contents of the third-generation garnet in the calcic skarn are distinctly lower than those of the garnet in the magnesian skarn and the first-generation and second-generation garnets in the calcic skarn (Fig. 8-35d and e). The garnet in the magnesian skarn has distinctly lower W contents than the garnet in the calcic skarn (Fig. 8-35f). Among the three generations of garnets in the calcic skarn, the second-generation garnet contains the lowest W contents (Fig. 8-35f).

8.4.8. Pyroxene

Representative EMP analytical results and crystallochemical calculations of the pyroxene in the magnesian and calcic skarns of the Weijia W deposit are listed in Appendix 8-9. The pyroxene in the magnesian skarn is salite (Jo: 0.1 – 1.6 mol.%) (Fig. 8-36a). Its SiO_2, TiO_2, Al_2O_3, FeO, MnO, MgO, CaO, Na_2O, and K_2O contents are 52.84 – 55.58 wt.%, 0.00 – 0.06 wt.%, 0.14 – 0.92 wt.%, 0.88 – 2.67 wt.%, 0.05 – 0.50 wt.%, 17.13 – 19.94 wt.%, 24.14 – 26.16 wt.%, 0.00 – 0.09 wt.%, and 0.00 – 0.08 wt.%, respectively, showing a compositional variation between $Di_{98.4}Hd_{0.0}$ and $Di_{99.9}Hd_{0.0}$ (Fig. 8-36a).

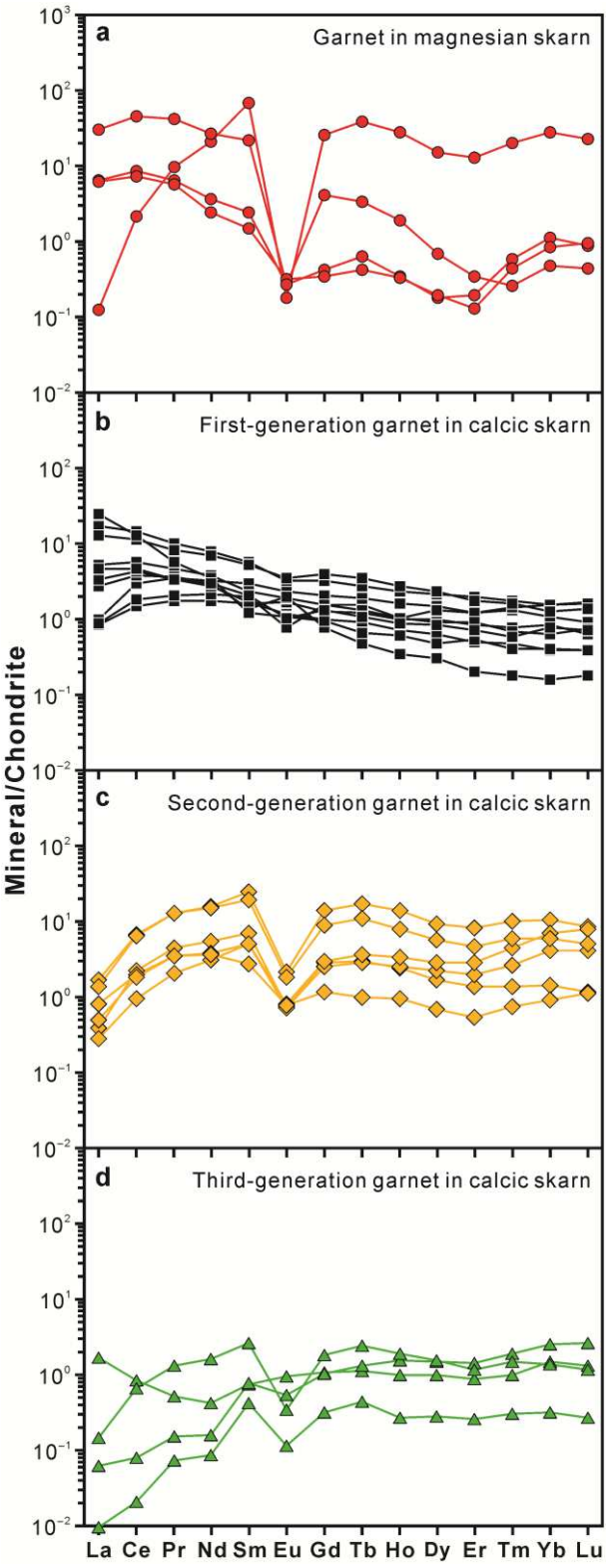

Figure 8-34. Chondrite-normalized (Boynton, 1984) REE patterns of garnets from the magnesian and calcic skarns in the Weijia W deposit.

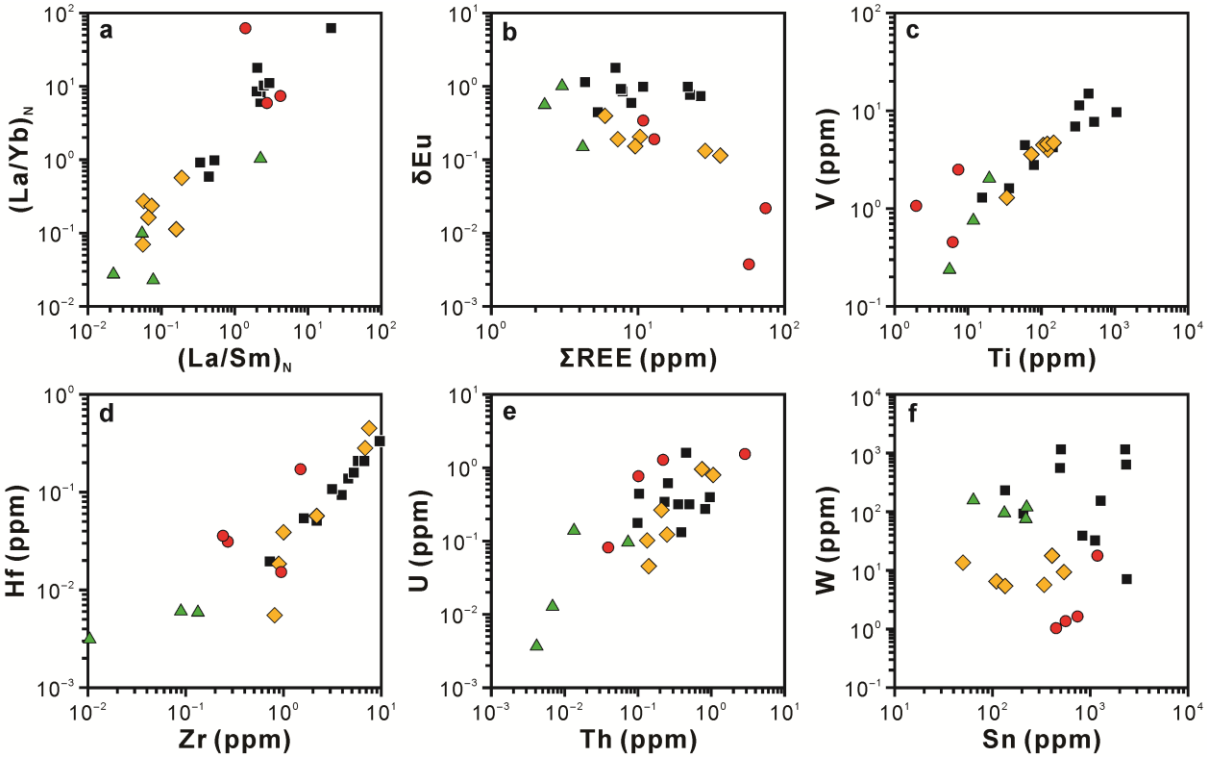

Figure 8-35. Trace element binary diagrams of garnets from the magnesian and calcic skarns in the Weijia W deposit. Legends are the same as Figure 8-34.

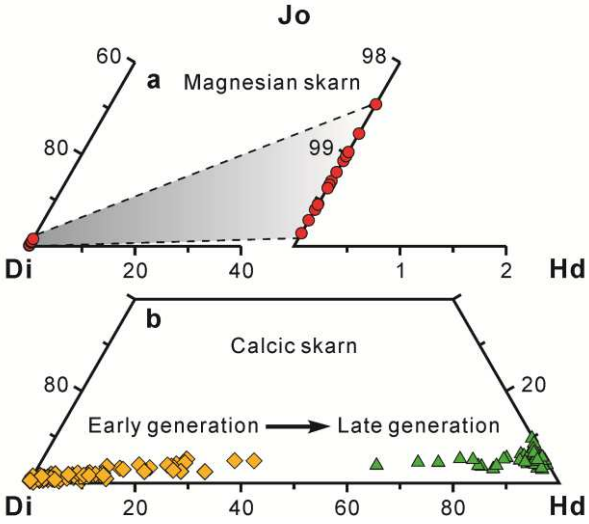

Figure 8-36. Compositions of pyroxenes from the magnesian and calcic skarns in the Weijia W deposit. Mineral abbreviations: Di = diopside, Hd = hedenbergite, Jo = johannsenite.

Both the early and late generations of pyroxenes in the calcic skarn are salite and the late-generation pyroxene contains slightly higher contents of johannsenite components (3.3 – 10.2 mol.%) than the early-generation pyroxene (0.2 – 5.2 mol.%) (Fig. 8-36b). The early-generation and late-generation pyroxenes show compositions close to the diopside and hedenbergite end members, respectively (Fig. 8-36b).

The early-generation pyroxene has SiO_2 contents of 48.91 – 54.97 wt.%, TiO_2 contents of 0.00 – 0.12 wt.%, Al_2O_3 contents of 0.04 – 1.81 wt.%, FeO contents of 1.60 – 13.50 wt.%, MnO contents of 0.05 – 1.54 wt.%, MgO contents of 9.09 – 17.98 wt.%, CaO contents of 23.42 – 25.98 wt.%, Na_2O contents of 0.00 – 0.11 wt.%, and K_2O contents of 0.00 – 0.07 wt.%, showing a compositional variation between $Di_{55.1}Hd_{40.1}$ and $Di_{99.6}Hd_{0.0}$ (Fig. 8-36b).

The late-generation pyroxene has SiO_2 contents of 46.22 – 49.92 wt.%, TiO_2 contents of 0.00 – 0.15 wt.%, Al_2O_3 contents of 0.03 – 2.31 wt.%, FeO contents of 20.61 – 30.04 wt.%, MnO contents of 0.88 – 2.84 wt.%, MgO contents of 0.00 – 5.28 wt.%, CaO contents of 21.51 – 23.47 wt.%, Na_2O contents of 0.04 – 0.40 wt.%, and K_2O contents of 0.00 – 0.10 wt.%, showing a compositional variation between $Di_{0.0}Hd_{94.6}$ and $Di_{32.3}Hd_{63.4}$ (Fig. 8-36b).

8.4.9. Wollastonite

Representative EMP analytical results and crystallochemical calculations of the wollastonite in the calcic skarn of the Weijia W deposit are listed in Appendix 8-10. The early-generation wollastonite has SiO_2 contents of 47.82 – 49.37 wt.%, TiO_2 contents of 0.00 – 0.03 wt.%, Al_2O_3 contents of 0.00 – 0.02 wt.%, FeO contents of 0.00 – 0.07 wt.%, MnO contents of 0.01 – 0.16 wt.%, CaO contents of 45.53 – 47.05 wt.%, Na_2O contents of 0.01 – 0.05 wt.%, and K_2O contents of 0.00 – 0.03 wt.%. Compared with the early-generation wollastonite, the late-generation wollastonite contains distinctly higher FeO contents of 0.20 – 1.49 wt.% and MnO contents of 0.24 – 1.31 wt.% (Fig. 8-37).

8.4.10. Vesuvianite

Representative EMP analytical results and crystallochemical calculations of the vesuvianite in the calcic skarn of the Weijia W deposit are listed in Appendix 8-11. The vesuvianite has SiO_2 contents of 33.45 – 36.55 wt.%, TiO_2 contents of 0.00 – 0.14 wt.%,

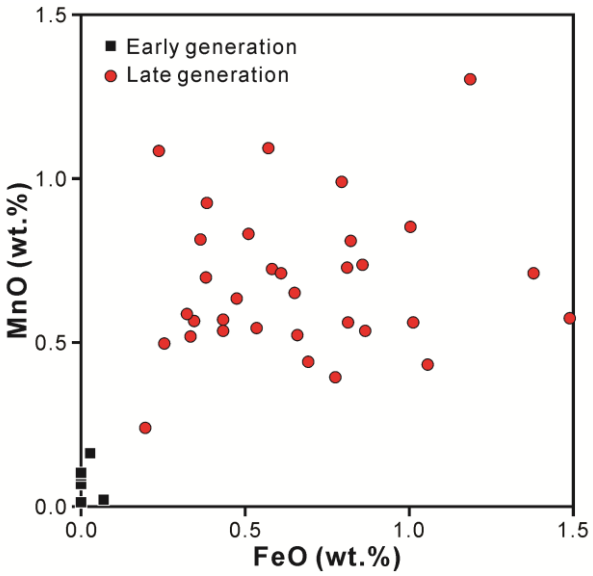

Figure 8-37. Binary plot of FeO (wt.%) vs. MnO (wt.%) contents of wollastonite in the calcic skarn of the Weijia W deposit.

Al_2O_3 contents of 14.23 – 17.31 wt.%, FeO contents of 3.09 – 6.72 wt.%, MnO contents of 0.07 – 0.49 wt.%, MgO contents of 1.06 – 3.25 wt.%, CaO contents of 35.25 – 36.38 wt.%, Na_2O contents of 0.00 – 0.08 wt.%, and K_2O contents of 0.00 – 0.07 wt.%. Notably, the vesuvianite contains high F contents of 1.04 – 4.03 wt.% with peak values of 1.9 wt.% and 2.9 wt.% (Fig. 8-25n).

8.4.11. Scheelite

Representative LA-ICP-MS analytical results of scheelite from the Weijia W deposit are listed in Appendix 8-12 and shown in Figures 8-38 and 8-39. The scheelite in the stockwork quartz veinlets shows flat REE patterns with $(La/Yb)_N$ values of 0.3 – 2.4 and $(La/Sm)_N$ values of 0.3 – 1.3 and strong negative Eu anomalies with low δEu values of 0.01 – 0.06 (Figs. 8-38a and 8-39a–b). It contains high ΣREE contents of 1255.0 – 4891.8 ppm (Fig. 8-39b).

Two generations of scheelites with distinctly different REE patterns have been distinguished in the magnesian skarn (Fig. 8-38b and c). The early-generation scheelite in the magnesian skarn shows flat to slightly rightward sloping REE patterns with $(La/Yb)_N$ values of 0.1 – 17.0 and $(La/Sm)_N$ values of 0.2 – 2.2 and strong negative Eu anomalies with low

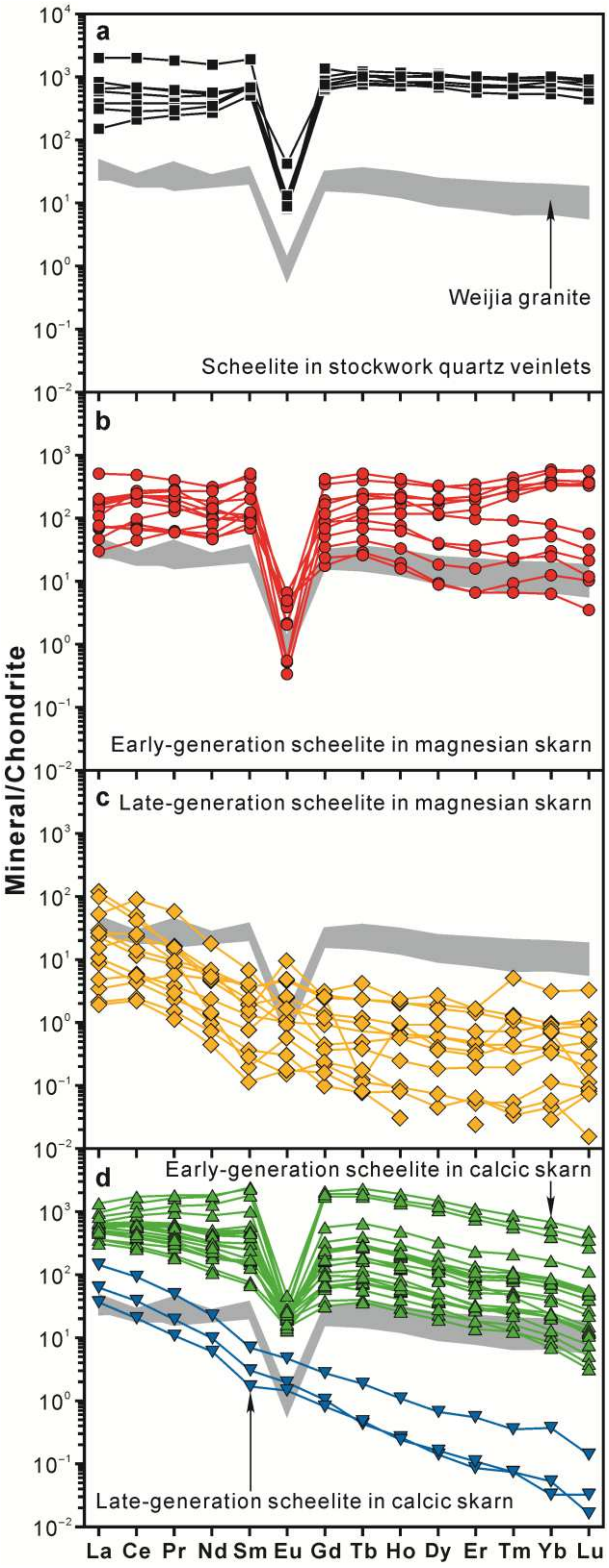

Figure 8-38. Chondrite-normalized (Boynton, 1984) REE patterns of scheelites from the stockwork quartz veinlets of granite and the magnesian and calcic skarns in the Weijia W deposit.

Figure 8-39. Trace element binary diagrams of scheelites from the stockwork quartz veinlets of granite and the magnesian and calcic skarns in the Weijia W deposit. Legends are the same as Figure 8-38.

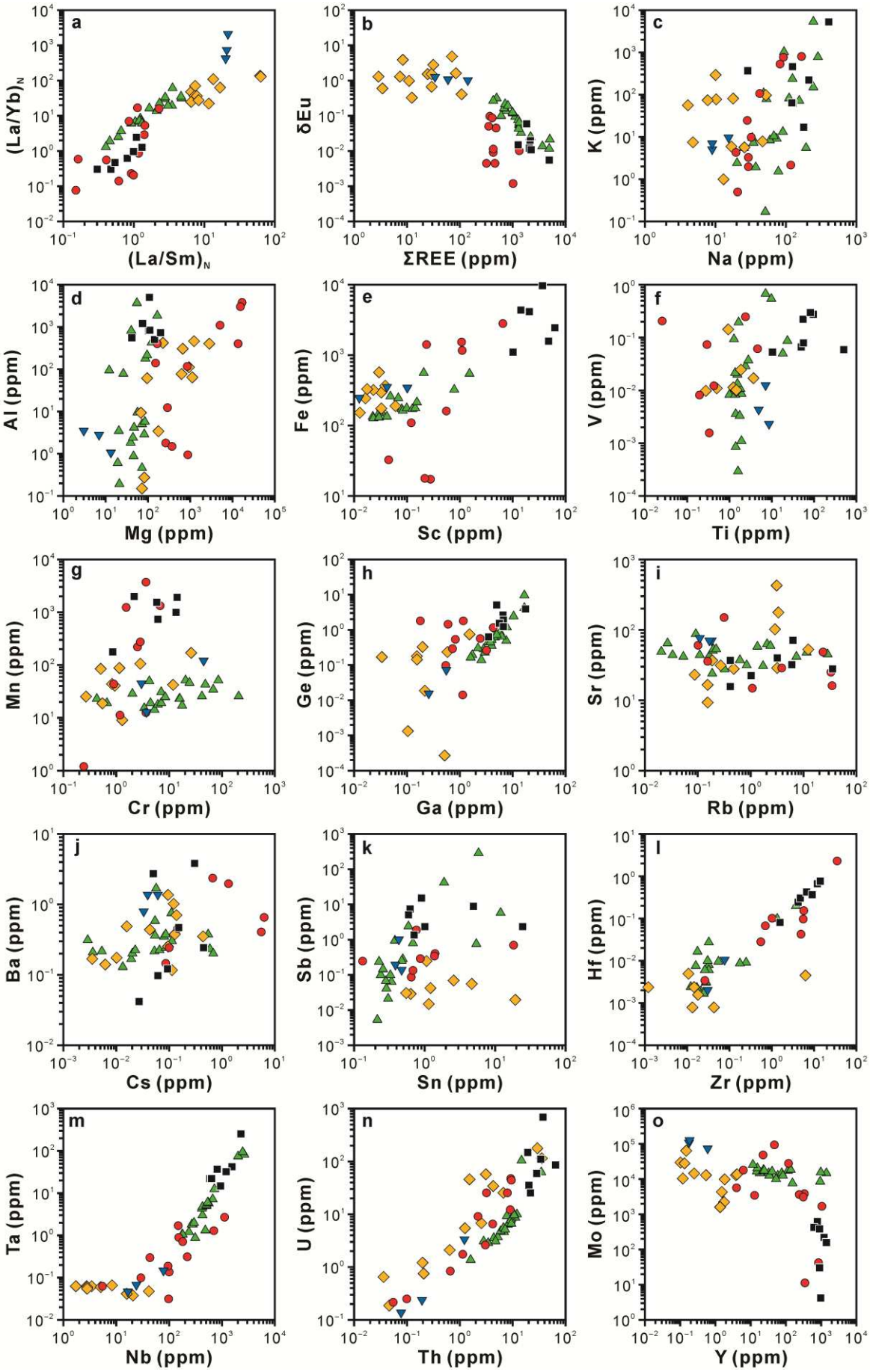
a
(La/Yb)N
(La/Sm)N
b
δEu
ΣREE (ppm)
c
K (ppm)
Na (ppm)
d
Al (ppm)
Mg (ppm)
e
Fe (ppm)
Sc (ppm)
f
V (ppm)
Ti (ppm)
g
Mn (ppm)
Cr (ppm)
h
Ge (ppm)
Ga (ppm)
i
Sr (ppm)
Rb (ppm)
j
Ba (ppm)
Cs (ppm)
k
Sb (ppm)
Sn (ppm)
l
Hf (ppm)
Zr (ppm)
m
Ta (ppm)
Nb (ppm)
n
U (ppm)
Th (ppm)
o
Mo (ppm)
Y (ppm)

δEu values of 0.00 – 0.15 (Figs. 8-38b and 8-39a–b). It contains high ΣREE contents of 313.8 – 1340.6 ppm (Fig. 8-39b). Whereas, the late-generation scheelite in the magnesian skarn shows steeper rightward sloping REE patterns with $(La/Yb)_N$ values of 21.7 – 138.0 and $(La/Sm)_N$ values of 6.5 – 63.3 and slightly negative to positive Eu anomalies with distinctly higher δEu values of 0.32 – 4.70 (Figs. 8-38c and 8-39a–b). It contains distinctly lower ΣREE contents of 2.9 – 108.0 ppm (Fig. 8-39b).

Like the magnesian skarn, the calcic skarn also contains two generations of scheelites which show distinctly different REE patterns (Fig. 8-38d). The early-generation scheelite in the calcic skarn shows slightly rightward sloping REE patterns with $(La/Yb)_N$ values of 1.4 – 67.4 and $(La/Sm)_N$ values of 0.4 – 4.8 and strong negative Eu anomalies with low δEu values of 0.01 – 0.34 (Figs. 8-38d and 8-39a–b). It contains high ΣREE contents of 426.7 – 5058.7 ppm (Fig. 8-39b). Whereas, the late-generation scheelite in the calcic skarn shows steeper rightward sloping REE patterns with $(La/Yb)_N$ values of 380.9 – 1947.3 and $(La/Sm)_N$ values of 19.9 – 21.4 and almost no Eu anomalies with distinctly higher δEu values of 0.94 – 1.17 (Figs. 8-38d and 8-39a–b). It contains distinctly lower ΣREE contents of 33.5 – 139.7 ppm (Fig. 8-39b).

Compared with the scheelite in the magnesian and calcic skarns, the scheelite in the stockwork quartz veinlets contains higher Na, K, Al, Sc, Fe, Ti, V, Mn, Ga, Ge, Sb, Zr, Hf, Nb, Ta, Th, U, REE, and Y contents and lower Mo contents (Fig. 8-39). The scheelite in the magnesian skarn shows distinctly higher Mg contents than the scheelite in the calcic skarn and stockwork quartz veinlets (Fig. 8-39d). Whether for the magnesian skarn or the calcic skarn, the early-generation scheelite has higher Na, Mg, Sc, Ga, Ge, Nb, Ta, REE, and Y contents and lower Mo contents than the late-generation scheelite (Fig. 8-39). Besides, for the magnesian skarn, the early-generation scheelite contains higher Cs, Sb, Zr, and Hf contents than the late-generation scheelite (Fig. 8-39j–l); for the calcic skarn, the early-generation scheelite contains higher Th and U contents and lower Ba contents than the late-generation scheelite (Fig. 8-39j and n).

8.5. Estimation of fluorine activity

The fluorine contents of the biotite in the Weijia granite, the white mica in the Weijia granite and its stockwork veins, the serpentine, phlogopite, and garnet in the magnesian skarn, and the garnet and vesuvianite in the calcic skarn are shown in Figures 8-24 and 8-25 and summarized in Table 8-1. Based on the occurrence of abundant fluorite and F-rich silicate minerals, especially the uncommon F-rich garnet, it is certain that the Weijia W deposit was formed in a special environment with high fluorine activity.

Munoz (1984) proposed the F intercept value [IV (F)] and F/Cl intercept value [IV (F/Cl)] of micas to quantitatively estimate the fluorine activities of magmatic and hydrothermal conditions. Both higher IV (F) and IV (F/Cl) numbers indicate a lower degree of fluorine enrichment. The calculated IV (F) numbers of biotite, white mica, and phlogopite and IV (F/Cl) numbers of biotite and phlogopite are summarized in Table 8-1 and shown in Figures 8-40–8-42. The fresh biotite in the granite shows obviously lower IV (F) numbers than the bleached biotite (Fig. 8-40a–c), however, they have similar IV (F/Cl) numbers (Fig. 8-41a–c). Except for the core parts of the white micas in the K-feldspar-quartz pegmatite veins and (K-feldspar)-quartz veins or veinlets and some white micas in the matrix of granite, which were formed with high fluorine activities, all the other white micas indicate relatively low fluorine activities (Fig. 8-40d–l). The phlogopite in the magnesian skarn has similar IV (F) numbers with the bleached biotite (Fig. 8-40m) and distinctly higher IV (F/Cl) numbers than the fresh and bleached biotite (Fig. 8-41d). In the IV (F) vs. IV (F/Cl) diagram (Fig. 8-42), the fresh biotite in the granite plots in the field of porphyry Mo deposits, indicating an extremely high fluorine activity, whereas, the bleached biotite and phlogopite with distinctly higher IV (F) numbers indicate lower fluorine activities.

Aksyuk (2000) proposed new biotite and phlogopite fluorimeters to estimate the fluorine concentrations in fluids associated with different skarn deposits, granitoids, pegmatites, and marble. Using the biotite fluorimeter, the HF concentrations calculated by the fresh biotite in the granite without stockwork veins are $10^{-1.46}$ – $10^{-0.71}$ mole/dm^3 with a peak value of $10^{-1.00}$ mole/dm^3. The temperatures (569 – 659 °C with a peak value of 635 °C) used in the biotite fluorimeter are calculated by the Ti-in-biotite geothermometer according to Henry et al.

Table 8-1. F contents and some related parameters of different F-bearing minerals in the Weijia W deposit

Host rock	Mineral	F content (wt.%)		IV (F)[a]		IV (F/Cl)[a]	
		Range	Peak value	Range	Peak value	Range	Peak value
Granite	Fresh biotite in the granite without stockwork veins	1.93 – 5.54	2.9	0.10 – 0.86	0.55	3.57 – 4.73	4.45
	Bleached biotite in the granite without stockwork veins	0.03 – 1.54	0.5	0.82 – 2.65	1.05	3.33 – 6.02	4.55
	Bleached biotite in the granite with stockwork veins	0.00 – 1.65	0.1	0.93 – 2.83	1.40	3.23 – 5.08	4.05
	White mica in the matrix of granite without stockwork veins	0.09 – 1.54 2.54 – 4.63	0.5 3.1, 4.3	0.82 – 2.33 0.04 – 0.43	1.45 0.05		
	White mica coexisting with fluorite as aggregates in the granite without stockwork veins	0.00 – 1.62	0.3	0.67 – 2.60	1.35		
	White mica in the matrix of granite with stockwork veins	0.06 – 2.43 4.09 – 7.79	0.3, 1.9 6.7	0.55 – 1.93 –0.73 to 0.10	0.75 –0.15		
	White mica in the bleached zone near stockwork veins	0.00 – 4.51	1.1	0.01 – 2.10	0.95		
Stockwork veins at the apex of granite	Core of white mica in the K-feldspar-quartz pegmatite veins	2.99 – 8.23	4.5	–0.85 to 0.32	0.05		
	Rim of white mica in the K-feldspar-quartz pegmatite veins	0.00 – 2.34	0.3	0.45 – 2.57	1.65		
	Core of white mica in the (K-feldspar)-quartz veins or veinlets	2.71 – 8.12	6.3	–0.76 to 0.44	–0.45, –0.15		
	Rim of white mica in the (K-feldspar)-quartz veins or veinlets	0.00 – 2.34	0.3	0.27 – 2.78	1.55		
	White mica in the stockwork quartz veinlets	0.00 – 0.69	0.1	1.19 – 2.65	1.90		
Magnesian skarn	Serpentine in the magnesian skarn veinlet exteriors	1.08 – 5.88	1.5				
	Serpentine in the magnesian skarn veinlet interiors	0.00 – 2.57	0.1				
	Phlogopite	1.25 – 6.88	2.5, 3.1	0.90 – 2.06	1.45, 1.85	4.08 – 5.88	5.45
	Garnet	0.51 – 4.83	3.2				
Calcic skarn	Garnet	0.00 – 2.37	0.1				
	Vesuvianite	1.04 – 4.03	1.9, 2.9				

Note: [a] F intercept value [IV (F)] and F/Cl intercept value [IV (F/Cl)] are quantitative parameters for F enrichment degree defined by Munoz (1984), both higher values indicate a lower F enrichment degree.

(2005). The bleached biotite in the granite without stockwork veins yields HF concentrations of $10^{-2.93}$ – $10^{-1.35}$ mole/dm^3 with a peak value of $10^{-1.75}$ mole/dm^3 (calculated by a constant

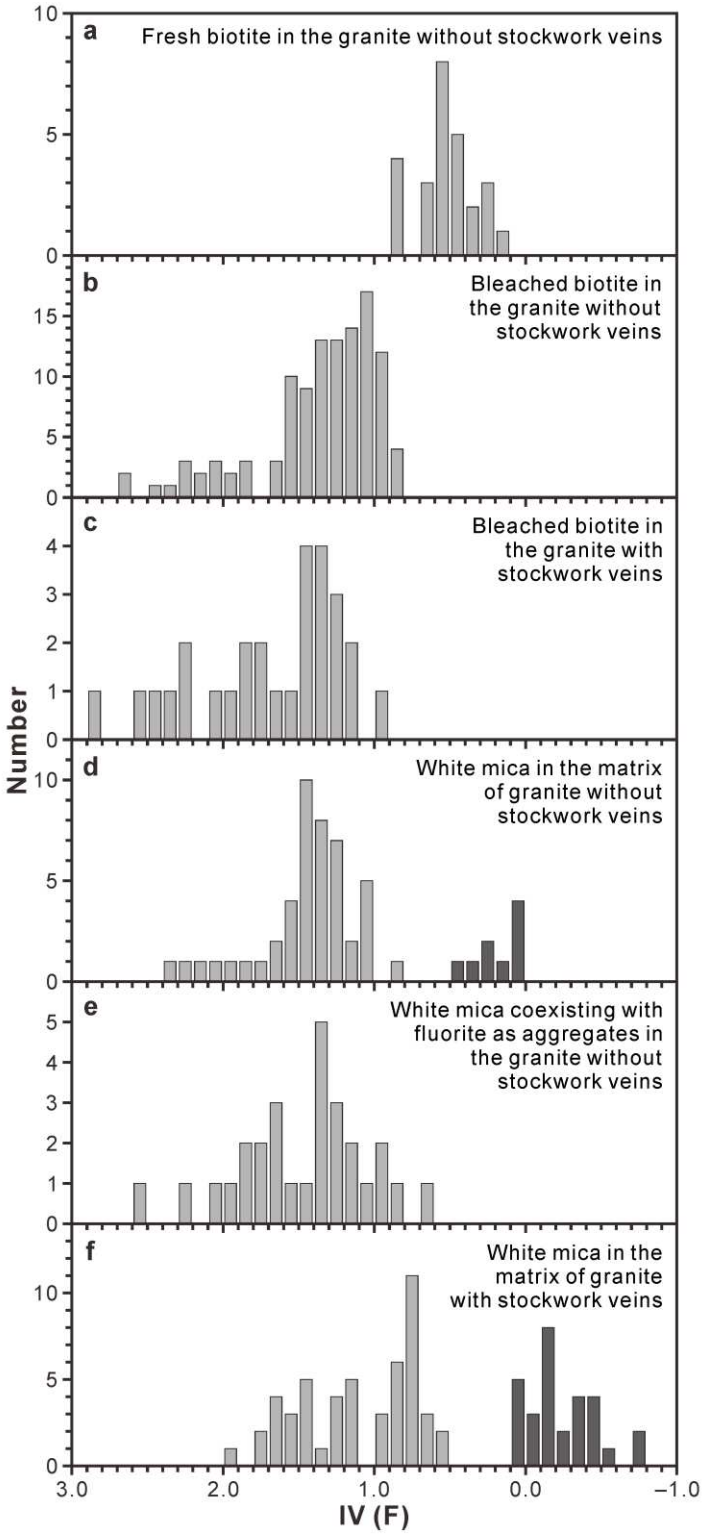

Figure 8-40. Histograms for F intercept value [IV (F)] of micas in the Weijia W deposit.

(*To be continued on the next page*)

temperature of 550 °C). The bleached biotite in the granite with stockwork veins yields HF concentrations of $10^{-2.91}$ – $10^{-1.49}$ mole/dm^3 with a peak value of $10^{-1.95}$ mole/dm^3 (using a

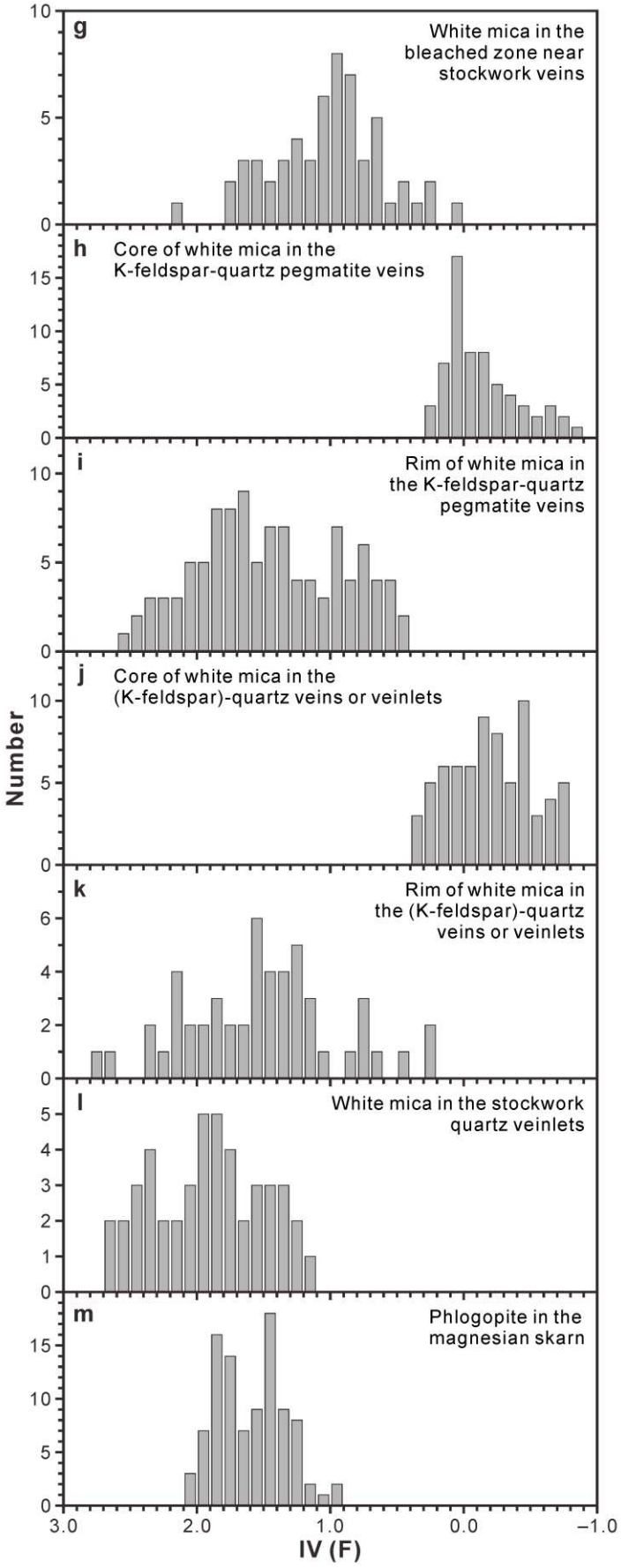

Figure 8-40. (*Continued*).

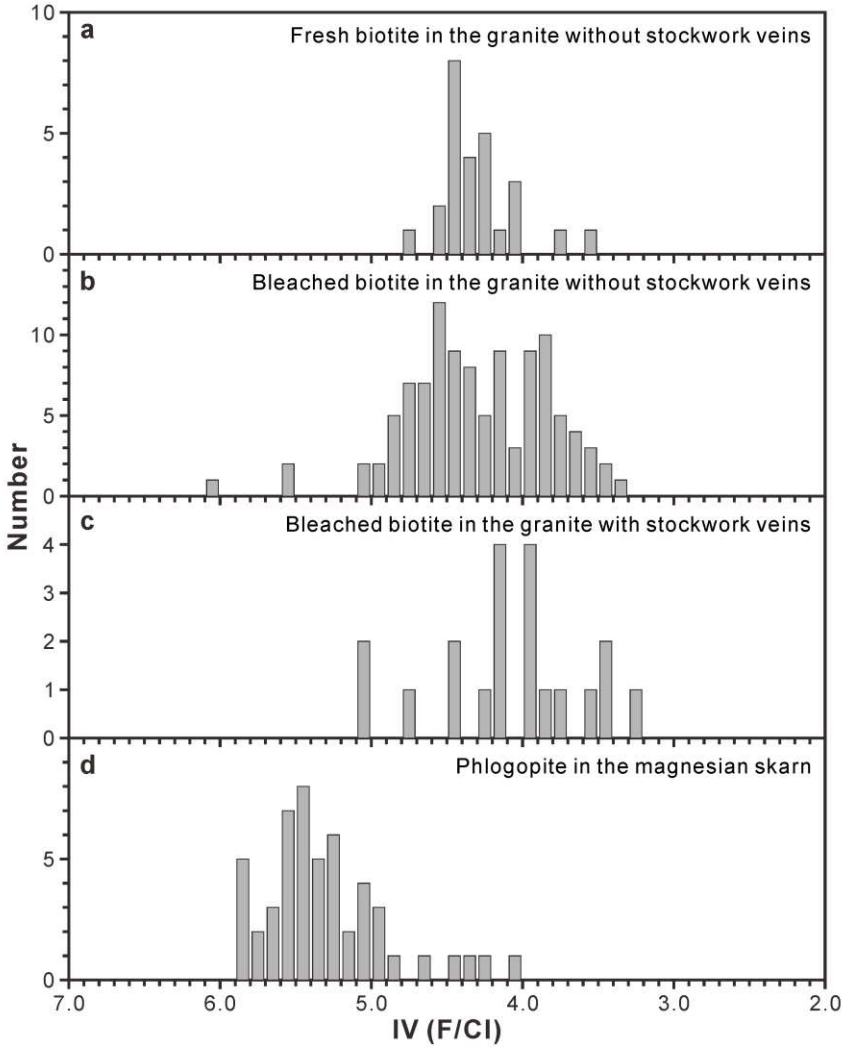

Figure 8-41. Histograms for F/Cl intercept value [IV (F/Cl)] of biotite and phlogopite in the Weijia W deposit.

constant temperature of 500 °C). Using the phlogopite fluorimeter, the HF concentrations calculated by the phlogopite in the magnesian skarn are $10^{-3.03}$ – $10^{-1.45}$ mole/dm^3 with a peak value of $10^{-2.75}$ mole/dm^3 (using a constant temperature of 450 °C). Therefore, a progressive decreasing trend of HF concentration (fluorine activity) from $10^{-1.00}$ mole/dm^3 through $10^{-1.75}$ mole/dm^3 to $10^{-1.95}$ mole/dm^3 and then to $10^{-2.75}$ mole/dm^3 is revealed by the fresh and bleached biotite and phlogopite.

8.6. Discussion

8.6.1. Fluorine promoting magmatic fractionation and tungsten enrichment

The fresh biotite in the Weijia granite has high F contents (Figs. 8-24 and 8-25a), shows

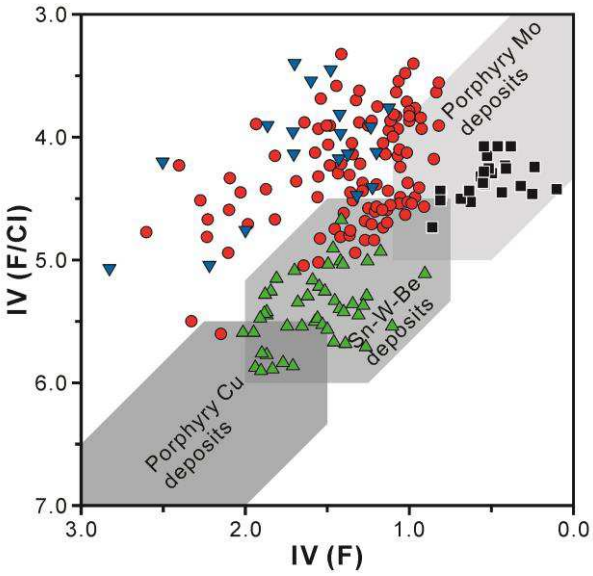

Figure 8-42. F intercept value [IV (F)] vs. F/Cl intercept value [IV (F/Cl)] diagram (after Munoz, 1984) for biotite and phlogopite in the Weijia W deposit. IV (F) and IV (F/Cl) are quantitative parameters for F enrichment degree defined by Munoz (1984), both higher values indicate a lower F enrichment degree. Legends are the same as Figure 8-23.

low IV (F) and IV (F/Cl) numbers (Figs. 8-40–8-42), and yields high HF concentrations ($10^{-1.5}$ – $10^{-0.7}$ mole/dm^3) by the biotite fluorimetry (Aksyuk, 2000), indicating that the Weijia granite was formed by crystallization of a F-rich magma. The HF concentration of the Weijia granitic magma is consistent with those of the other rare metal leucogranites and Li-F granites and pegmatites worldwide ($10^{-1.5}$ – 10^{-1} mole/dm^3, Aksyuk, 2000) and is significantly higher than those of the granitoids related to W-skarns in the western Cordillera ($10^{-2.8}$ – $10^{-1.8}$ mole/dm^3, Aksyuk, 2000) and also those of the porphyry Cu deposits (Fig. 8-42, Aksyuk, 2000).

The existence of abundant fluorine can dramatically reduce the viscosity and the minimum liquidus temperature of granitic melts by the formation of aluminofluoride ($A1F_6^{3-}$) complex anions that weaken the framework of aluminosilicate complexes (Manning et al., 1980; Manning, 1981). The minimum liquidus temperature of granitic melts at 1 kbar changes progressively from 730 °C (Tuttle and Bowen, 1958) for the F-free system to 630 °C for the system with 4 wt.% added fluorine (Manning, 1981). As a consequence, the low viscosity and minimum liquidus temperature will lead to the formation of highly fractionated granites by

protracting the process of crystallization differentiation. Such prolonged crystal fractionation will then result in the enrichment of the incompatible tungsten in the residual granitic melts especially at relatively low magmatic temperatures (Audétat et al., 2000; Linnen and Cuney, 2005), even though the tungsten solubility in granitic melts is nearly independent of the fluorine content (Linnen and Cuney, 2005; Che et al., 2013).

Huang et al. (2017a) carried out detailed geochemical study of the Weijia granite and pointed out that it is a highly fractionated peraluminous S-type granite. It has high SiO_2 contents and shows low $CaO/(Na_2O+K_2O)$ and high Rb/Sr ratios, low δEu values, and strong Ba, Sr, P, and Ti depletions (Huang et al., 2017a). The Ti-in-biotite thermometry of the fresh biotite in the Weijia granite yields a low temperature of 569 – 659 °C with a peak value of 635 °C. The RSCM thermometry of the carbonate rocks close to the magnesian and calcic skarns reveals that the peak metamorphic temperature of the wall rocks does not exceed 576 °C (Fig. 8-16). All these thermometric results indicate a low magmatic temperature of the Weijia granite. The highly fractionated and low-temperature features of the Weijia granite are genetically related to the high fluorine activity.

The porphyritic texture with a felsitic to fine-grained matrix in the Weijia granite (Figs. 8-3a and 8-4a), the embayment texture of the hexagonal bipyramidal quartz phenocrysts (Fig. 8-4b), the micrographic texture in K-feldspar (Fig. 8-4c), and the distinctive “pearlitic border” texture of some K-feldspar phenocrysts (Fig. 8-4d) seem to suggest a shallow emplacement depth. Zhou et al. (1999) reported the similar “pearlitic border” texture of the porphyroclastic K-feldspar in the Tonglu rhyodacite in Southeastern China and interpreted it as a result of boundary layer effect caused by compositional disequilibrium during a rapid crystallization process. However, the small grain size of matrix in porphyritic granites can also simply result from the crystallization under water-saturated conditions and is not necessarily produced by pressure quenching (Whitney, 1988; Audétat et al., 2000). The embayment texture of quartz phenocrysts could be formed by a primary growth in F-rich magmas and is not necessarily to be the result of resorption in shallow environments (Audétat et al., 2000). Notably, the Al-in-hornblende geobarometry of the contemporaneous Tongshanling granodiorite which is located 15 km to the southwest of the Weijia granite and emplaced in the same Middle-Upper

Devonian carbonate strata (i.e., the Qiziqiao, Shetianqiao, and Xikuangshan Formations) yields a deep emplacement depth of ca. 10 km (Huang et al., 2018). Thus, the Weijia porphyritic granite should not be formed in a subvolcanic environment and its felsitic to fine-grained matrix was crystallized from the highly fractionated F-rich and water-saturated melts.

In summary, the high fluorine activity of granitic melts results in a low magmatic viscosity to enable the prolonged crystal fractionation and tungsten enrichment of the granitic magma to a relatively low temperature, finally with the porphyritic Weijia granite formed under a water-saturated condition.

8.6.2. Magmatic to hydrothermal evolution

The Weijia granite and its later stockwork veins from K-feldspar-quartz pegmatite veins (Fig. 8-7a) through (K-feldspar)-quartz veins (Fig. 8-7b) or veinlets to stockwork quartz veinlets (Fig. 8-7c) reflect a process of magmatic to hydrothermal evolution. Especially, the white mica in the K-feldspar-quartz pegmatite veins and (K-feldspar)-quartz veins or veinlets shows a zonal texture with F-rich cores and F-poor rims, whereas, the white mica in the stockwork quartz veinlets has F-poor compositions without zonation (Figs. 8-24, 8-25g–i, 8-26, and 8-27). Such an evolution trend from early F-rich compositions to late F-poor compositions of white mica (Fig. 8-24) is indicative of the magmatic to hydrothermal evolution, because fluorine prefers to partition in melt and its fluid-melt partition coefficient ($D^{F}_{fluid/melt}$) is small even the melt contains a high fluorine concentration (e.g., $D^{F}_{fluid/melt}$ = 0.4 at 3 wt.% F in the melt) (London et al., 1988; Webster and Holloway, 1990; Carroll and Webster, 1994). The occurrence of two groups of white mica in the matrix of granite with respective higher and lower F contents (Figs. 8-24 and 8-25c and e) also reflects the evolution process from the earlier magmatic stage with a higher fluorine activity to the later hydrothermal stage with a lower fluorine activity (Fig. 8-40d and f). Thus, the F-poor white mica coexisting with fluorite as aggregates in the granite is hydrothermal mica (Figs. 8-24, 8-25d, and 8-40e).

Abundant fluorite and the other F-rich minerals occur in the magnesian and calcic skarns, whereas, the Weijia granite contains almost no fluorine, only with minor preserved in the micas, indicating that the majority of fluorine in the granitic magma has been transported into the wall rocks. Considering the small $D^{F}_{fluid/melt}$ value, it is speculated that the fluorine was

probably dominantly transported by F-rich concentrated hydrosaline melts rather than by dilute hydrothermal fluids. Such hydrosaline melts could be generated by silicate-hydrosaline liquid immiscibility which has been demonstrated by natural and experimental studies (Veksler et al., 2002; Badanina et al., 2004; Veksler, 2005). The enrichment of non-silicate anions, such as F^-, Cl^-, CO_3^{2-}, and BO_3^{3-}, is critical to the generation of the liquid immiscibility (Veksler, 2005). Veksler (2005) pointed out that the hydrosaline melts are likely to have Na, Li, and alkaline earths enriched and K and heavier rare alkalis depleted compositions. Using homogenized melt inclusions, Badanina et al. (2004) revealed the immiscibility between a Na-F-rich hydrosaline melt and a K-rich aluminosilicate melt in the most evolved units of the Orlovka granite complex. Between the silicate and hydrosaline melts, tungsten partitions strongly into the depolymerized hydrosaline liquids (Gramenitskiy et al., 1996), indicating the hydrosaline melts could be an important agent for tungsten enrichment and transportation from magma (Veksler, 2005).

Since the fluorine in the granitic magma has been mostly extracted into the immiscible hydrosaline melts, the later exsolved hydrothermal fluids from the residual aluminosilicate melts have a distinctly lower fluorine activity. Overprint of the later hydrothermal stage on the earlier magmatic stage led to the formation of the F-poor micas in the Weijia granite and its stockwork veins (Figs. 8-24 and 8-25a–i). This hydrothermal overprint is particularly evident in the bleached biotite of the granite which is transforming into clay minerals (Figs. 8-22 and 8-24), in the zonal white micas of the stockwork veins (Figs. 8-26 and 8-27), and in the peripheral bleached zone of the stockwork veins where biotite and F-rich white mica are absent (Figs. 8-7 and 8-25f). The occurrence of abundant kaolin at the apex of the Weijia granite, which is similar to that of the Beauvoir granite in the French Massif Central, may be genetically related to greisenization during the hydrothermal alteration (Cuney et al., 1992). Hydrothermal alteration of the marginal granite close to carbonate rocks resulted in the gains of Ca, Mg, Fe, and Mn from wall rocks and the loss of Na into fluids (Fig. 8-19a, c, and d). The released Na from the granite could be important for the transportation of tungsten in the hydrothermal fluids as $NaHWO_4^0$ and $NaWO_4^-$ (Wood and Samson, 2000). This may also be implicated by the formation of late Na-bearing aluminosilicate minerals in the magnesian and calcic skarns, such

as the marialite, zeolite, and plagioclase (Figs. 8-11, 8-13, and 8-28s–aa). To a certain extent, the different alteration degrees of the granites close to the magnesian and calcic skarns are corresponding to the different mineralization scales of the magnesian and calcic skarns, respectively.

To sum up, during the magmatic to hydrothermal evolution of the Weijia granite, F-rich hydrosaline melts were firstly separated from magma by liquid immiscibility followed by the exsolution of F-poor hydrothermal fluids. Both of the F-rich hydrosaline melts and F-poor hydrothermal fluids could be the agents for tungsten transportation from magma.

8.6.3. Magnesian and calcic skarn formation

The differential formation of the magnesian and calcic skarns respectively in the middle-member dolostone and upper-member limestone of the Qiziqiao Formation is dominantly controlled by the different lithologies of the host carbonate strata (Fig. 8-2). RSCM thermometry reveals that the magnesian skarn was formed under a distinctly lower temperature than the calcic skarn (Fig. 8-16). This is consistent with the contrary mineral associations of the magnesian and calcic skarns which are dominated by retrograde minerals (serpentine and phlogopite) and prograde minerals (garnet, pyroxene, and wollastonite), respectively (Figs. 8-11 and 8-13). Except for the serpentine and phlogopite, some other Mg-rich minerals, such as the sellaite, fluoborite, and chondrodite, occur in the magnesian skarn but are absent in the calcic skarn (Figs. 8-11 and 8-13). Compared with the garnet in the calcic skarn, the garnet in the magnesian skarn contains higher Mg contents (Appendix 8-7 and Fig. 8-33). The pyroxene in the magnesian skarn is almost pure diopside (Fig. 8-36). All these features of the magnesian skarn are genetically related to the high Mg activity during skarn formation. Different from the calcic skarnization during which a high Ca activity is expected, the magnesian skarnization should be developed with a relatively low Ca activity and a high Mg activity which will result in a relatively high F activity. Because Ca can easily combine with F to form fluorite and decrease the F activity, whereas, it seems more difficult for Mg to combine with F to form sellaite. This is demonstrated by the occurrence of abundant fluorite but minor sellaite in the magnesian skarn (Fig. 8-11). The relatively low temperature and high fluorine activity during magnesian skarnization are not favorable for the

development of anhydrous prograde skarn minerals, such as forsterite and spinel, and lead to the formation of the special F-rich garnet (Fig. 8-25l). By contrast, the garnet formed with relatively high temperature and low fluorine activity during calcic skarnization has normal F-poor compositions (Fig. 8-25m).

Both of the serpentine and phlogopite in the magnesian skarn show decreasing Mg and increasing Fe contents from early to late (Appendices 8-5 and 8-6 and Figs. 8-28j–aa and 8-29). In addition, the serpentine shows a decreasing trend of F contents with time (Appendix 8-5). These compositional variations indicate a coupled decreasing of F and Mg activities during magnesian skarn formation. F may have played an important role in releasing Mg from dolostone to form the magnesian skarn minerals. For the calcic skarn, the progressive changes of garnet compositions from andradite to grossularite (Fig. 8-33b) and pyroxene compositions from diopside to hedenbergite (Fig. 8-36b) indicate a decreasing trend of oxygen fugacity during skarn formation. This is also demonstrated by the evolution of negative Eu anomalies of the garnet REE patterns (Fig. 8-34b–d). The distinctly higher FeO and MnO contents of the late-generation wollastonite than those of the early-generation wollastonite (Fig. 8-37) implies a stronger contribution of components from wall rocks during the late stage of calcic skarn formation.

8.6.4. Calcium as the precipitant of fluorine and tungsten

The strong positive correlations between the WO_3 and CaF_2 grades of both the magnesian and calcic skarn ores (Figs. 8-14 and 8-15) seem to indicate a genetical link between tungsten and fluorine. However, previous experimental studies demonstrated that the tungsten solubilities in both silicate melts and aqueous fluids are almost independent of fluorine content (Manning and Henderson, 1984; Keppler and Wyllie, 1991; Linnen and Cuney, 2005; Che et al., 2013). Thus, the positive correlation between the WO_3 and CaF_2 grades is not derived from a direct link between tungsten and fluorine. Instead, calcium, which is the shared precipitant for fluorine and tungsten to form fluorite and scheelite, respectively, could be the critical factor to induce the positive correlation between the WO_3 and CaF_2 grades in the skarn ores.

It is noteworthy that the wall rocks (dolostone) close to the magnesian skarn orebodies contain significantly higher fluorite contents than those (limestone) close to the calcic skarn

orebodies (Figs. 8-14 and 8-15). This difference results from the higher calcium activity in the limestone than that in the dolostone which catches the fluorine in a relatively limited zone and prevents the outward escape of fluorine. To a certain extent, the high CaF_2 but low WO_3 grades of the dolostone close to the magnesian skarn (Figs. 8-14 and 8-15) are indicative of the independent relationship between tungsten and fluorine. During the process of skarn formation, the fluorine activity gradually decreases along with the precipitation of fluorite and the other F-bearing minerals.

Lecumberri-Sanchez et al. (2017) emphasized that fluid-rock interaction is decisive for the formation of tungsten deposits and the precipitation of the main tungsten minerals scheelite ($CaWO_4$) and wolframite [$(Fe, Mn)WO_4$] thus depends on the availability of Ca, Fe, or Mn. Wang et al., (2017e) demonstrated that the released Ca by plagioclase breakdown controlled the scheelite mineralization in the Dongyuan and Zhuxiling porphyritic granodiorites, southern Anhui Province, China. A model of Fe-Mn and Ca released from biotite and apatite respectively by alteration to form wolframite and scheelite in granodiorite was proposed by Zhang et al., (2018a) to explain the genesis of the giant Dahutang W deposit in northwestern Jiangxi Province, China. In the skarn deposits, such as the Weijia W deposit, scheelite is predominantly hosted by skarn in the carbonate wall rocks. Therefore, it is evident that the key factor controlling the occurrences of scheelite orebodies in granitoids or wall rocks is calcium activity. The higher WO_3 grades of the calcic skarn orebodies than those of the magnesian skarn ore bodies in the Weijia W deposit are controlled by the higher calcium activity during skarnization in limestone than that during skarnization in dolostone. This is also indicated by the distinctly lower Mg contents of the scheelite in the calcic skarn than those of the scheelite in the magnesian skarn (Fig. 8-39d).

8.6.5. Ore-forming process

Scheelite is a common mineral in various hydrothermal deposits and has been widely used as an indicator to trace ore-forming process (e.g., Li et al., 2018b; Zhang et al., 2018b; Zhao et al., 2018). The REE patterns of the scheelite from the Weijia W deposit can be divided into two different types on the whole, with one type of flat to slightly rightward sloping REE patterns with strong negative Eu anomalies and the other type of steeper

rightward sloping REE patterns almost without Eu anomalies (Fig. 8-38). These two different types of scheelite REE patterns are indicative of two generations of ore-forming liquids.

The scheelite in the stockwork quartz veinlets (Fig. 8-38a) and the early-generation scheelites in the magnesian and calcic skarns (Fig. 8-38b and d) were formed by the early-generation ore-forming liquids. Their REE patterns are similar to those of the Weijia granite but with distinctly higher REE contents (Fig. 8-38a, b, and d), indicating large REE partition coefficients between the liquids and granitic melts. The early-generation ore-forming liquids are in all probability the F-rich hydrosaline melts which have enriched incompatible elements and were earlier separated from magma by liquid immiscibility (Veksler, 2005). The similar REE patterns of the early-formed scheelites with the granite result from an inheritance from the magma.

The late-generation scheelites in the magnesian and calcic skarns (Fig. 8-38c and d) were formed by the late-generation ore-forming liquids. They have distinctly lower REE contents than the Weijia granite (Fig. 8-38c and d), indicating small REE partition coefficients between the liquids and granitic melts. Thus, the late-generation ore-forming liquids are the F-poor hydrothermal fluids which have relatively depleted incompatible elements and were later separated from magma by exsolution. The enrichment of LREE and the disappearance of negative Eu anomalies of the late-formed scheelites may result from the hydrothermal alteration of feldspars which are characterized by LREE enrichment and positive Eu anomalies.

Therefore, both of the earlier separated F-rich hydrosaline melts and the later exsolved F-poor hydrothermal fluids have transported tungsten from the magma into the wall rocks for subsequent skarn mineralization.

8.6.6. Metallogenic model

Except for the processes of magmatic fractionation, magmatic to hydrothermal evolution, magnesian and calcic skarnization, and ore formation discussed above, the magma origin is another key process that controls tungsten mineralization. Romer and Kroner (2015, 2016) emphasized that protolith enrichment, sedimentary and tectonic accumulation of enriched source rocks, and heat input from the mantle are prerequisite steps for the generation of W

enriched melts. The existence of an enriched source in the Nanling Range is widely accepted due to the occurrences of abundant large-scale W deposits. The subduction of the palaeo-Pacific plate in South China during Late Mesozoic induced asthenosphere upwelling and basaltic magma underplating to promote partial melting of the enriched source and then generate W-bearing melts (Zhou and Li, 2000; Zhou et al., 2006a; Huang et al., 2017a). Different source rocks may produce different types of ore-bearing melts. For instance, the partial melting of the lower-crust mafic amphibolitic rocks and the middle-upper-crust metasedimentary rocks in the Nanling Range during Middle-Late Jurassic produced W-bearing and Cu-Pb-Zn-bearing granitoids, respectively (Huang et al., 2017a). Notably, the S-type Weijia granite, the A-type Hehuaping granite, and the I-type Tongshanling granodiorite in the Nanling Range which were emplaced in the same Qiziqiao Formation at the same time during Middle-Late Jurassic but are genetically related to W, Sn, and Cu-Pb-Zn skarn mineralization, respectively (Yao et al., 2014b; Huang et al., 2017a). Thus, the nature of the enriched source is also a key factor controlling tungsten mineralization.

Based on the deposit geological, RSCM thermometric, whole-rock geochemical, and mineralogical studies and the discussion above, the comprehensive genetic model of the Weijia W deposit is summarized as follows. During Late Jurassic, with the subduction of the palaeo-Pacific plate, the underplated basaltic magmas heated and partially melted the enriched source in the Nanling Range to produce fluorine and tungsten enriched melts. The prolonged crystal fractionation of the fluorine-rich low-viscosity granitic magma to a relatively low temperature resulted in a strong enrichment of tungsten in the residual melts. During the magmatic to hydrothermal evolution, the earlier separated F-rich hydrosaline melts and the later exsolved F-poor hydrothermal fluids transported tungsten from the magma into the wall rocks. With the development of magnesian and calcic skarns, fluorine and tungsten were precipitated by calcium to form fluorite and scheelite, respectively. Fluorine was also involved in the formation of the other F-bearing minerals, such as serpentine and phlogopite. The relatively low temperature and high fluorine activity during magnesian skarnization prevented the development of anhydrous prograde skarn minerals, such as forsterite and spinel. The

higher calcium activity during skarnization in limestone than that in dolostone resulted in the higher WO_3 grades of calcic skarn than those of magnesian skarn.

8.7. Summary

The Weijia scheelite skarn deposit comprises dominant magnesian skarn and subordinate calcic skarn with abundant fluorite and is genetically related to a highly fractionated porphyritic granite with a felsitic to fine-grained matrix. The magnesian skarn generally occurs as stockwork veinlets in dolostone with a mineralogy dominated by serpentine and phlogopite. Wollastonite, garnet, and pyroxene are the main calcic skarn minerals. Scheelite is mostly distributed in the magnesian and calcic skarns as disseminated grains.

Biotite fluorimetry indicates that the Weijia granite was crystallized from a F-rich magma. The high fluorine activity of granitic melts results in a low magmatic viscosity to enable the prolonged crystal fractionation and tungsten enrichment of the granitic magma to a relatively low temperature, finally with the porphyritic Weijia granite formed under a water-saturated condition.

During the magmatic to hydrothermal evolution, F-rich hydrosaline melts were firstly separated from magma by liquid immiscibility followed by the exsolution of F-poor hydrothermal fluids. Both of the F-rich hydrosaline melts and F-poor hydrothermal fluids have transported tungsten from the magma into the wall rocks for subsequent skarn mineralization.

RSCM thermometry indicates a distinctly lower temperature of magnesian skarnization than calcic skarnization. The relatively low temperature and high fluorine activity during magnesian skarnization are not favorable for the development of anhydrous prograde skarn minerals, such as forsterite and spinel, and lead to the formation of the special F-rich garnet.

As the shared precipitant of fluorine and tungsten, calcium could be the critical factor to induce the positive correlation between the WO_3 and CaF_2 grades of skarn ores. The higher WO_3 grades of the calcic skarn than those of the magnesian skarn are controlled by the higher calcium activity during skarnization in limestone than that in dolostone.

The key factors controlling the occurrence of unusual magnesian skarn W mineralization during Late Jurassic in the Nanling Range mainly include an enriched source, a fluorine-rich magma, a strong crystal fractionation, and a fluorine-rich hydrosaline melt.

Chapter 9. Conclusions and perspectives

9.1. Conclusions

Main conclusions of this Ph.D. thesis are summarized as follows.

(1) The Middle-Late Jurassic Cu-Pb-Zn-bearing and W-bearing granitoids in the Nanling Range are dominated by weakly fractionated metaluminous I-type amphibole-bearing granodiorites and highly differentiated peraluminous S-type granites, respectively. They were mainly derived from non-simultaneous partial melting of the mafic amphibolitic basement in the lower crust and the muscovite-rich metasedimentary basement in the upper-middle crust, respectively. The compositional divergence between different sources accounted for the metallogenic specializations of ore-bearing granitoids and the non-simultaneous partial melting of one source followed by the other brought about a time gap of about 5 Ma between the Cu-Pb-Zn-bearing and W-bearing granitoids.

(2) Dark microgranular enclaves are commonly observed in the Middle-Late Jurassic Cu-Pb-Zn-bearing granodiorites in the Nanling Range. The microgranular enclaves in the Tongshanling granodiorite which contain abundant residual materials, such as mafic mineral clots, inherited and metamorphic zircon, and Ca-rich core plagioclase, are thought to be reworked restite enclaves formed by reaction of the restite with the host magma. The amphibole-rich clots are vestiges of residual pyroxene-rich precursors from the source. Consequently, the Tongshanling granodiorite was derived from dehydration melting of amphibolite in the mafic lower crust. The fertile amphibolitic source is beneficial to the formation of Cu-Pb-Zn-bearing granodiorites in the Nanling Range.

(3) In the Tongshanling area, the regional normal faults were in all probability formed during the Late Triassic to Early Jurassic decompression and are not related to the emplacement of the Middle-Late Jurassic Tongshanling granodiorite. Based on structural analysis, RSCM thermometry, and EBSD mapping, it is concluded that the emplacement of the Tongshanling granodiorite started from the southern part and induced wall-rock strong marbleization and deformation in the contact zone. The magma emplacement-induced

wall-rock deformation significantly increased the permeability of wall rocks to promote the infiltration of magmatic fluids along fractures and then structurally controlled the formation of exoskarn and sulfide-quartz veins.

(4) Geochronological studies reveal that the three ore deposits in the Tongshanling polymetallic ore district were almost contemporaneously formed at 160 – 162 Ma, consistent with the Tongshanling granodiorite (160 – 164 Ma). S, Pb, and H-O isotopic studies indicate that the ore-forming materials and fluids of the Tongshanling ore district were derived from the Tongshanling intrusion. The Cu and Zn were most probably released from the mafic amphibolitic lower crust by partial melting, whereas, the Pb was extracted from the upper crust by the ascending granodioritic magma. The different mineralization types and ore deposits in the Tongshanling ore district are genetically linked together and are the productions of evolution and zonation of the same skarn system associated with the Tongshanling granodioritic intrusion.

(5) The Weijia granite was crystallized from a F-rich low-viscosity magma which had experienced a prolonged crystal fractionation and tungsten enrichment. The separation of F-rich hydrosaline melts by liquid immiscibility during the magmatic to hydrothermal evolution is important for tungsten transportation from the magma into the wall rocks. The relatively low temperature and high fluorine activity during magnesian skarnization are not favorable for the development of anhydrous prograde skarn minerals. As the shared precipitant of fluorine and tungsten, calcium could be the critical factor to induce the positive correlation between the WO_3 and CaF_2 grades of skarn ores. The higher WO_3 grades of the calcic skarn than those of the magnesian skarn are controlled by the higher calcium activity during skarnization in limestone than that in dolostone.

9.2. Perspectives

Although a lot of new findings and conclusions are achieved through this Ph.D. thesis, some parts need to be further improved, such as the structural study of mineral deposits, and some other studies are still insufficient, such as the metallogenic age of the Jiangyong Pb-Zn-Ag deposit, the geochemical compositions of ore-forming fluids, and the detailed

physicochemical evolution during mineralization. In addition, the model of reworked restite enclaves should be further tested by the microgranular enclaves of the other Middle-Late Jurassic Cu-Pb-Zn-bearing granodiorites in the Nanling Range. A comparison between the microgranular enclaves of the Middle-Late Jurassic Cu-Pb-Zn-bearing granodiorites and Sn-bearing A_2-type granites in the Nanling Range is necessary for understanding the origins of different ore-bearing granitoids.

For further research of the multiple-aged granitoids and associated polymetallic mineral deposits in South China, besides the common geochronological, geochemical, and mineralogical studies, more attentions should be paid to structural controls on mineralization which are crucial to understanding the ore-forming process and can provide important information for prospecting and exploration. Many newly developed methods, such as the Raman spectroscopy of carbonaceous material thermometry (Beyssac et al., 2002; Lahfid et al., 2010), paleo-fluid flow orientation and velocity estimation (Sizaret et al., 2009; Launay et al., 2018), permeability experimentation (Coelho et al., 2015), and numerical modeling (Eldursi et al., 2009; Ingebritsen and Appold, 2012), should be introduced and applied to the further studies of metallogenesis in South China.

Acknowledgements

As the time flying away, the years shuttling again. With memory of the past and looking forward to the future, I am finally walking to the end of my career as a student. Since I firstly came to Nanjing at the beginning of September 2009, I have lived and studied here for nine years. Nanjing has become my second home town. During my five-year postgraduate period from September 2013 to December 2018, I was fortunate to have chances to study abroad in Orléans, France from February 2015 to July 2015 as a master student supported by an international student exchange program of Université d'Orléans and from February 2016 to February 2018 as a co-supervised Ph.D. student supported by the Sino-French Cai Yuanpei Program of China Scholarship Council. Here, at the end of the thesis, I would like to express my sincere gratitude to a lot of teachers, students, friends, technicians, and administration staff in NJU and ISTO and also many other persons who helped me a lot during my postgraduate study. Without their caring and help, I cannot finish this Ph.D. thesis.

First of all, special appreciation is expressed to my Chinese supervisor Prof. LU Jian-Jun in NJU. He aroused my interest in Geology and led me into the field of Mineral Deposit Geology. All stages of this thesis, include research topic selection, literature search, field observation, sample collection, processing and analysis, data interpretation, and scientific paper and thesis writing and revision, were accomplished under the meticulous guidance of Prof. LU. His rigorous academic attitude, sharp academic thinking, solid academic foundation, and strict academic criterion will benefit me all through my life. I have learned a lot from him, especially in the aspects of granitoid petrogenesis, deposit geology, and ore deposit geochemistry. In addition, Prof. LU is the role model for me also in his philosophy of life and particular personality charm. He encouraged and financially supported me to attend a number of international academic activities, such as the IAGOD2014, EGU2016, and SEG2017 conferences, and thus gave me an opportunity to visit the world famous Jiaodong Au deposits.

I also want to gratefully acknowledge the training, help, and support from my French supervisor Prof. Stanislas SIZARET in ISTO. He is not only a teacher but also a friend. In my two and a half years' study and life in Orléans, he was always taking care of me and thus I

could adapt myself to the new environment soon. He organized the Sino-French Cai Yuanpei Program. With Prof. SIZARET, I have learned many new skills and knowledge and conducted some new studies to better understand the ore-forming process, such as electrical prospecting, paleo-fluid flow orientation and velocity estimation, crystal growth experiment, numerical modeling, RSCM thermometry, and permeability experiment. Prof. SIZARET encouraged and financially supported me to participate various academic activities, include the W-Sn international workshop in Nancy (2016), SGA2017 and MPC2017 conferences, and skarn deposits short course in Freiberg (2017).

Prof. WANG Ru-Cheng and Prof. MA Dong-Sheng are the other two key members of our research group on granitoids and related mineralization in NJU. They are thanked for their general supervision and discussion on my research works. I have realized the importance of mineralogy in the study of metallogenesis from Prof. WANG and learned geochemistry from Prof. MA. I am also deeply grateful to CNRS Researcher Alain CHAUVET in Géosciences Montpellier and Associate Prof. Luc BARBANSON in ISTO. Working with Dr. CHAUVET in the field, I was trained by detailed field observation, geological sketching, and structural analysis. He helped me accomplish EBSD mapping in Géosciences Montpellier. Working with Dr. BARBANSON, I got new knowledge and skills on ore mineralogy and texture, paragenesis, and chemical exchange during metasomatic alteration.

Special gratitude is expressed to Prof. CHEN Yan in ISTO and his wife Mrs. CHEN Li-Li. Their caring, enthusiasm, and hospitality made me feel at home in Orléans. Prof. CHEN helped me a lot in my two and a half years' study and life abroad and was always caring about the progress of my research works. I have learned geophysical knowledge from Prof. CHEN, include electricity, magnetism, seismology, and gravity. The numerous times of discussion with him on the topic of granitic magmatism and related mineralization in South China greatly benefited me for my research. Prof. CHEN provided me precious opportunities to participate the field excursions in the French Massif Central and the Western Alps.

I am grateful to Prof. ZHOU Mei-Fu at The University of Hong Kong, Prof. SUN Xiao-Ming at Sun Yat-Sen University, and the other three anonymous reviewers for their valuable comments. The members of the examination board of my Ph.D. thesis defense,

including Prof. JIN Zhen-Min at China University of Geosciences, Wuhan, Prof. WANG Ru-Cheng, Prof. ZHOU Mei-Fu, Prof. NI Pei at Nanjing University, CAS Researcher XIONG Xiao-Lin at Guangzhou Institute of Geochemistry, Prof. CHEN Yan, CNRS Researcher Alain CHAUVET, and Prof. Stanislas SIZARET, are sincerely thanked for their attendance and constructive suggestions.

Academicians of Chinese Academy of Sciences Prof. CHEN Jun and Prof. WANG De-Zi are thanked for their recommendation letters for me to apply the Sino-French Cai Yuanpei Program. Prof. WANG Bo, Associate Prof. XIE Lei, CNRS Researcher Julien MERCADIER, and Ph.D. students ZHU Ze-Ying and Hélène LEGROS are thanked for their collaboration in executing the Sino-French Cai Yuanpei Program.

The following teachers who enlightened my academic thinking are also thanked. They are Prof. HU Wen-Xuan, Prof. SHU Liang-Shu, Prof. XU Xi-Sheng, Prof. QIU Jian-Sheng, Prof. NI Pei, Prof. LING Hong-Fei, Prof. JIANG Yao-Hui, Prof. LU Hua-Yu, Prof. Michel FAURE, Prof. Bruno SCAILLET, Prof. Eric MARCOUX, Prof. Michel PICHAVANT, and Prof. Nicole LE BRETON.

XING Gen-Sheng and ZHOU Pu-Cai at the Tongshanling Cu-Pb-Zn mine, OU Yue-Ming and CHANG Jia-Liang at the Jiangyong Pb-Zn-Ag mine, ZHU Xian and HE Li-Bin from the No. 418 Geological Team of Bureau of Geology and Mineral Exploration and Development of Hunan Province, and HE Zhong-Yuan from the No. 1 General Brigade of Hunan Geological and Mining Bureau for Nonferrous Metals are sincerely thanked for their kindly help and guidance during the fieldwork.

I would like to express my appreciation to the following teachers, students, and technicians for their technical assistance with sample processing and analysis. They are Sylvain JANIEC for sample polishing, thin section making, and SEM analysis; Gabriel BADIN and ZHANG Guang-Hui for sample polishing and thin section making; Patricia BENOIST for thin section carbon coating and SEM analysis; WU Bing for LA-ICP-MS zircon U-Pb dating; YANG Tao and BIAN Xiao-Peng for LA-MC-ICP-MS zircon Hf isotopic analysis; LIU Qian for whole-rock trace element analysis; PU Wei for whole-rock Sr-Nd isotopic analysis; Ida DI CARLO for SEM, EMP, and RSCM analyses; LI Juan, ZHAO Xu,

and ZHANG Rui for SEM analysis; ZHANG Wen-Lan, WU Bin, CHEN Wen-Di, YU Quan, XIANG Lu, and Saskia ERDMANN for EMP analysis; GAO Jian-Feng and LI Liang for LA-ICP-MS mineral trace element analysis and titanite U-Pb dating; HU Huan, ZHANG Rong-Qing, TIAN En-Nong, and SHAO Chun-Jing for the attempt of LA-ICP-MS calcite U-Pb dating; Thomas POITRENAUD, Hugues RAIMBOURG, and Romain AUGIER for RSCM analysis; Fabrice BAROU for EBSD mapping; Rémi CHAMPALLIER and Gaëtan LAUNAY for permeability experiment; DING Jun-Ying, LI Wen-Sheng, and LIU Zheng for fluid inclusion analysis.

WU Xue-Min and WANG Chun-Qiao at the Education Office of the Embassy of the People's Republic of China in the French Republic are thanked for their help with the applications for the field trip in China during October 2016 and the SGA2017 and SEG2017 conferences. LU Xian-Cai, TANG Xiao-Qian, ZHANG Xiao-Qin, Marie-Noëlle PAILHÈS, Dominique FRERE, and Amélie SCHNEUWLY are thanked for their administrative management. ZHU Ye, Virginie LANCELOT, and Olivier GAUDEFROY are thanked for their help with financial reimbursement.

I am also grateful to the other Ph.D. and master students of Prof. LU. They are ZHANG Rong-Qing, DING Teng, XIE Yin-Cai, ZHAO Zeng-Xia, ZHANG Shi-Tao, GAO Shou-Ye, ZHAO Xu, ZHANG Xue-Ai, ZHANG Qiang, LI Xiao-Yu, CHEN Guang-Hong, and ZHOU Wei-Fa. They greatly helped me with field works, sample collection, processing, and analysis, and some other daily works. We have similar research topics and frequently discussed with each other. Many new ideas in my research were derived from such general discussions.

During my two and a half years' study and life abroad, a number of Chinese students and friends in Orléans provided me their enthusiastic help and precious academic thinking. They are LIU Hong-Sheng, HUANG Fang-Fang, YAN Chao-Lei, XUE Zhen-Hua, CHEN Jin-Yu, XIANG Lu, ZHU Xin, WEI Wei, XIA Wen-Jing, LU Yun-Qiao, FANG Ting, LI Shuai, HAN Si-Yu, REN Yan-Gang, WANG Ren-Lei, WEN Liang, YAN Rui, XU Chen, SUN Wen-Yu, LI Qian, ZHANG Feng-Feng, and CAI Min. The French Ph.D. students Hugo BOURQUE, Gaëtan LAUNAY, Thomas POITRENAUD, and Florent CHEVAL-GARABEDIAN are also sincerely thanked for their daily academic discussions with me.

I want to thank my roommates in the office 433 of the Zhu Gongshan Building in NJU. They are WAN Ye, ZHANG Yang, CHEN Wen-Di, YU Quan, ZHU Shu-Qi, XIE Si-Wen, LIU Ding-Ding, BAI Li-Juan, LI Ming-Min, ZHAO Xu, XIANG Lu, ZHANG Yue-Xia, REN Qing-Qing, WANG Xiao-Yu, ZHU Qiang, LIU Chen, YANG Zhao-Yu, and QU Yang. I also deeply appreciate LI Lin and HAN Zhong who were my dormitory roommates during the master and doctoral stages, respectively.

Finally, I would like to particularly thank my family. It is impossible for me to finish my doctoral study and Ph.D. thesis without the caring, help, and support from my parents and sister and her husband. This Ph.D. thesis is dedicated to my family.

This Ph.D. thesis was financially supported by the National Natural Science Foundation of China (Grant No. 41273053, 41230315), the National Key Basic Research Program of China (Grant No. 2012CB416702, 2012CB416705), the China Geological Survey Program (Grant No. 1212011085407, 12120113067300), the French Labex Voltaire Project (Grant No. ANR-10-LABX-100-01), and the Sino-French Cai Yuanpei Program of China Scholarship Council.

Xu-Dong HUANG

November 14, 2018, Nanjing

References

Aksyuk, A.M., 2000. Estimation of fluorine concentrations in fluids of mineralized skarn systems. Economic Geology 95, 1339–1347.

Aleinikoff, J.N., Wintsch, R.P., Fanning, C.M., Dorais, M.J., 2002. U-Pb geochronology of zircon and polygenetic titanite from the Glastonbury Complex, Connecticut, USA: an integrated SEM, EMPA, TIMS, and SHRIMP study. Chemical Geology 188, 125–147.

Aleinikoff, J.N., Wintsch, R.P., Tollo, R.P., Unruh, D.M., Fanning, C.M., Schmitz, M.D., 2007. Ages and origins of rocks of Killingworth dome, South-Central Connecticut: Implications for the tectonic evolution of southern New England. American Journal of Science 307, 63–118.

Altherr, R., Holl, A., Hegner, E., Langer, C., Kreuzer, H., 2000. High-potassium, calc-alkaline I-type plutonism in the European Variscides: northern Vosges (France) and northern Schwarzwald (Germany). Lithos 50, 51–73.

Anderson, B.R., Gemmell, J.B., Nelson, D.R., 2002. Lead isotope evolution of mineral deposits in the Proterozoic Throssell Group, Western Australia. Economic Geology 97, 897–911.

Anderson, J.L., Smith, D.R., 1995. The effects of temperature and f_{O2} on the Al-in-hornblende barometer. American Mineralogist 80, 549–559.

Arth, J.G., 1976. Behaviour of trace elements during magmatic processes–a summary of theoretical models and their applications. Journal of Research of the U.S. Geological Survey 4, 41–47.

Audétat, A., Günther, D., Heinrich, C.A., 2000. Magmatic-hydrothermal evolution in a fractionating granite: A microchemical study of the Sn-W-F-mineralized Mole Granite (Australia). Geochimica et Cosmochimica Acta 64, 3373–3393.

Badanina, E.V., Veksler, I.V., Thomas, R., Syritso, L.F., Trumbull, R.B., 2004. Magmatic evolution of Li-F, rare metal granites: a case study of melt inclusions in the Khangilay complex, Eastern Transbaikalia (Russia). Chemical Geology 210, 113–133.

Ballouard, C., Poujol, M., Boulvais, P., Branquet, Y., Tartèse, R., Vigneresse, J.L., 2016. Nb-Ta fractionation in peraluminous granites: A marker of the magmatic-hydrothermal transition. Geology 44, 231–234.

Bao, T., Ye, L., Yang, Y.L., Li, Z.L., 2014. Characteristics of sulfur isotope geochemistry of Baoshan Cu-Mo-Pb-Zn-Ag polymetallic deposit, Hunan Province and its geological significance. Acta Mineralogica Sinica 34, 261–266 (in Chinese with English abstract).

Barbarin, B., 2005. Mafic magmatic enclaves and mafic rocks associated with some granitoids of the central Sierra Nevada batholith, California: nature, origin, and relations with the hosts. Lithos 80, 155–177.

Barnhoorn, A., Bystricky, M., Burlini, L., Kunze, K., 2004. The role of recrystallisation on the deformation behaviour of calcite rocks: large strain torsion experiments on Carrara marble. Journal of Structural Geology 26, 885–903.

Barnhoorn, A., Bystricky, M., Burlini, L., Kunze, K., 2005. Post-deformational annealing of calcite rocks. Tectonophysics 403, 167–191.

Beard, J.S., Lofgren, G.E., 1991. Dehydration melting and water-saturated melting of basaltic and andesitic greenstones and amphibolites at 1, 3, and 6.9 kb. Journal of Petrology 32, 365–401.

Berger, A., Ebert, A., Ramseyer, K., Gnos, E., Decrouez, D., 2016. Dolomite microstructures between 390° and 700 °C: Indications for deformation mechanisms and grain size evolution. Journal of Structural Geology 89, 144–152.

Beyssac, O., Goffé, B., Chopin, C., Rouzaud, J.N., 2002. Raman spectra of carbonaceous material in metasediments: a new geothermometer. Journal of Metamorphic Geology 20, 859–871.

Bi, C.S., Wu, J.S., Wang, M.Y., Ai, S.Z., 1988. Stable isotope geology of the Xintianling scheelite deposit. Mineral Deposits 7, 39–48 (in Chinese with English abstract).

Blundy, J.D., Holland, T.J.B., 1990. Calcic amphibole equilibria and a new amphibole-plagioclase geothermometer. Contributions to Mineralogy and Petrology 104, 208–224.

Blundy, J.D., Sparks, R.S.J., 1992. Petrogenesis of mafic inclusions in granitoids of the Adamello Massif, Italy. Journal of Petrology 33, 1039–1104.

Boynton, W.V., 1984. Cosmochemistry of the rare earth elements: meteorite studies, in: Henderson, P. (Ed.), Rare Earth Element Geochemistry. Elsevier, Amsterdam, pp. 63–114.

Cai, J.H., Liu, J.Q., 1993. Research and its application on the inclusions characteristics in the Dabaoshan polymetallic deposit, Northern Guangdong. Journal of Mineralogy and Petrology 13, 33–40 (in Chinese with English abstract).

Cai, J.X., Zhang, K.J., 2009. A new model for the Indochina and South China collision during the Late Permian to the Middle Triassic. Tectonophysics 467, 35–43.

Cai, Y., 2013. The study on Dengfuxian granite and its mineralization in Hunan Province. (Ph.D. thesis). Nanjing University, Nanjing, pp. 1–138 (in Chinese with English abstract).

Cai, Y., Ma, D.S., Lu, J.J., Huang, H., Zhang, R.Q., Qu, W.J., 2012. Re-Os geochronology and S isotope geochemistry of Dengfuxian tungsten deposit, Hunan Province, China. Acta Petrologica Sinica 28, 3798–3808 (in Chinese with English abstract).

Cai, Y.X., Tan, J.J., Yang, H.M., Lu, S.S., Duan, R.C., Qiu, X.F., Cheng, S.B., Yang, X.L., 2015. The origin of ore-forming material in the Tongshanling Cu-polymetallic ore field in Hunan Province: Constraints from S-Pb-C isotopes. Acta Geologica Sinica 89, 1792–1803 (in Chinese with English abstract).

Carroll, M.R., Webster, J.D., 1994. Solubilities of sulfur, noble gases, nitrogen, chlorine, and fluorine in magmas. Reviews in Mineralogy 30, 231-279.

Carter, A., Clift, P.D., 2008. Was the Indosinian orogeny a Triassic mountain building or a thermotectonic reactivation event? Comptes Rendus Geoscience 340, 83–93.

Carter, A., Roques, D., Bristow, C., Kinny, R., 2001. Understanding Mesozoic accretion in Southeast Asia: Significance of Triassic thermotectonism (Indosinian orogeny) in Vietnam. Geology 29, 211–214.

Casquet, C., Tornos, F., 1984. El skarn de W-Sn del Carro del Diablo (Sistema Central Español). Boletín Geológico y Minero CXV-I, 58–79 (in Spanish with English abstract).

Castro, A., Stephens, W.E., 1992. Amphibole-rich polycrystalline clots in calc-alkaline granitic rocks and their enclaves. Canadian Mineralogist 30, 1093–1112.

Catchpole, H., Kouzmanov, K., Bendezú, A., Ovtcharova, M., Spikings, R., Stein, H., Fontboté, L., 2015. Timing of porphyry (Cu-Mo) and base metal (Zn-Pb-Ag-Cu) mineralisation in a magmatic-hydrothermal system-Morococha district, Peru. Mineralium Deposita 50, 895–22.

Cawood, P.A., Wang, Y.J., Xu, Y.J., Zhao, G.C., 2013. Locating South China in Rodinia and Gondwana: A fragment of greater India lithosphere? Geology 41, 903–906.

Černý, P., Blevin, P.L., Cuney, M., London, D., 2005. Granite-related ore deposits. Economic Geology 100th Anniversary Volume, 337–370.

Chappell, B.W., 1996. Magma mixing and the production of compositional variation within granite suites: evidence from the granites of southeastern Australia. Journal of Petrology 37, 449–470.

Chappell, B.W., 1999. Aluminium saturation in I- and S-type granites and the characterization of fractionated haplogranites. Lithos 46, 535–551.

Chappell, B.W., White, A.J.R., 1991. Restite enclaves and the restite model, in: Didier, J., Barbarin, B. (Eds.), Enclaves and Granite Petrology. Elsevier, Amsterdam, pp. 375–381.

Chappell, B.W., White, A.J.R., Williams, I.S., Wyborn, D., Wyborn, L.A.I., 2000. Lachlan Fold Belt granites revisited: high- and low-temperature granites and their implications. Australian Journal of Earth Sciences 47, 123–138.

Chappell, B.W., White, A.J.R., Wyborn, D., 1987. The importance of residual source material (restite) in granite petrogenesis. Journal of Petrology 28, 1111–1138.

Chappell, B.W., Wyborn, D., 2012. Origin of enclaves in S-type granites of the Lachlan Fold Belt. Lithos 154, 235–247.

Charvet, J., 2013. The Neoproterozoic-Early Paleozoic tectonic evolution of the South China Block: An overview. Journal of Asian Earth Sciences 74, 198–209.

Charvet, J., Shu, L.S., Faure, M., Choulet, F., Wang, B., Lu, H.F., Le Breton, N., 2010. Structural development of the Lower Paleozoic belt of South China: Genesis of an intracontinental orogen. Journal of Asian Earth Sciences 39, 309–330.

Che, X.D., Linnen, R.L., Wang, R.C., Aseri, A., Thibault, Y., 2013. Tungsten solubility in evolved granitic melt: An evaluation of magmatic wolframite. Geochimica et Cosmochimica Acta 106, 84–98.

Che, X.D., Wang, R.C., Wu, F.Y., Zhu, Z.Y., Zhang, W.L., Hu, H., Xie, L., Lu, J.J., Zhang, D., 2018. Multi-aged mineralization of niobium and tantalum in South China: Constrained by in situ columbite-tantalite U-Pb LA-ICP-MS dating. Submitted to Ore Geology Reviews (in press).

Chen, G.H., Shu, L.S., Shu, L.M., Zhang, C., Ouyang, Y.P., 2015b. Geological characteristics and mineralization setting of the Zhuxi tungsten (copper) polymetallic deposit in the Eastern Jiangnan Orogen. Science China Earth Sciences 59, 803–823.

Chen, J., Lu, J.J., Chen, W.F., Wang, R.C., Ma, D.S., Zhu, J.C., Zhang, W.L., Ji, J.F., 2008. W-Sn-Nb-Ta-bearing granites in the Nanling Range and their relationship to metallogengesis. Geological Journal of China Universities 14, 459–473 (in Chinese with English abstract).

Chen, J., Wang, R.C., Zhu, J.C., Lu, J.J., Ma, D.S., 2013. Multiple-aged granitoids and related tungsten-tin mineralization in the Nanling Range, South China. Science China Earth Sciences 56, 2045–2055.

Chen, L., Wang, Z.Q., Yan, Z., Gong, J.H., Ma, S.X., 2018. Zircon and cassiterite U-Pb ages, petrogeochemistry and metallogenesis of Sn deposits in the Sibao area, northern Guangxi: constraints on the neoproterozoic granitic magmatism and related Sn mineralization in the western Jiangnan Orogen, South China. Mineralogy and Petrology 112, 437–463.

Chen, W.D., Zhang, W.L., Wang, R.C., Chu, Z.Y., Xiao, R., Zhang, D., Che, X.D., 2016. A study on the Dushiling tungsten-copper deposit in the Miao'ershan-Yuechengling area, Northern Guangxi, China: Implications for variations in the mineralization of multi-aged composite granite plutons. Science China Earth Sciences 59, 2121–2141.

Chen, X., Zhang, Y.D., Fan, J.X., Cheng, J.F., Li, Q.J., 2010. Ordovician graptolite-bearing strata in southern Jiangxi with a special reference to the Kwangsian Orogeny. Science China Earth Sciences 53, 1602–1610.

Chen, X.Y., Wang, Y.J., Fan, W.M., Zhang, F.F., Peng, T.P., Zhang, Y.Z., 2011. Zircon LA-ICP-MS U-Pb dating of granitic gneisses from Wuzhishan area, Hainan, and geological significances. Geochimica 40, 454–463 (in Chinese with English abstract).

Chen, Y.C., Pei, R.F., Zhang, H.L., Lin, X.D., Bai, G., Li, C.Y., Hu, Y.J., Liu, G.Q., Xian, B.Q., 1989a. The geology of non-ferrous and rare metal deposits related to Mesozoic granitoids in Nanling Region. Geological Publishing House, Beijing (in Chinese with English abstract).

Chen, Y.D., Chappell, B.W., White, A.J.R., 1991. Mafic enclaves of some I-type granites of the Palaeozoic Lachlan Fold Belt, southeastern Australia, in: Didier, J., Barbarin, B. (Eds.), Enclaves and Granite Petrology. Elsevier, Amsterdam, pp. 113–124.

Chen, Y.D., Price, R.C., White, A.J.R., 1989b. Inclusions in three S-type granites from southeastern Australia. Journal of Petrology 30, 1181–1218.

Chen, Y.D., Price, R.C., White, A.J.R., Chappell, B.W., 1990. Mafic inclusions from the Glenbog and Blue Gum granite suites, southeastern Australia. Journal of Geophysical Research 95, 17757–17785.

Chen, Z., 1986. An investigation into the genesis of the Tongshanling "interformational skarn type" polymetallic deposit. Mineral Deposits 5, 36–43 (in Chinese with English abstract).

Chen, Z.H., Wang, D.H., Sheng, J.F., Ying, L.J., Liang, T., Wang, C.H., Liu, L.J., Wang, Y.L., 2015a. The metallogenic regularity of tin deposits in China. Acta Geologica Sinica 89, 1026–1037 (in Chinese with English abstract).

Cheng, Y.B., Spandler, C., Mao, J.W., Rusk, B.G., 2012. Granite, gabbro and mafic microgranular enclaves in the Gejiu area, Yunnan Province, China: a case of two-stage mixing of crust- and mantle-derived magmas. Contributions to Mineralogy and Petrology 164, 659–676.

Cheng, Y.B., Tong, X., Wu, J.D., Mo, G.P., 2010. Geochronology framework of the W-Sn mineralization granites in western South China and their geological significance. Acta Petrologica Sinica 26, 809–818 (in Chinese with English abstract).

Chiaradia, M., Vallance, J., Fontboté, L., Stein, H., Schaltegger, U., Coder, J., Richards, J., Villeneuve, M., Gendall, I., 2009. U-Pb, Re-Os, and $^{40}Ar/^{39}Ar$ geochronology of the Nambija Au-skarn and Pangui porphyry Cu deposits, Ecuador: implications for the Jurassic metallogenic belt of the Northern Andes. Mineralium Deposita 44, 371–387.

Chu, Y., Faure, M., Lin, W., Wang, Q.C., 2012b. Early Mesozoic tectonics of the South China block: Insights from the Xuefengshan intracontinental orogen. Journal of Asian Earth Sciences 61, 199–220.

Chu, Y., Faure, M., Lin, W., Wang, Q.C., Ji, W.B., 2012a. Tectonics of the Middle Triassic intracontinental Xuefengshan Belt, South China: new insights from structural and chronological constraints on the basal déollement zone. International Journal of Earth Sciences 101, 2125–2150.

Clayton, R.N., O'Neil, J.R., Mayeda, T.K., 1972. Oxygen isotope exchange between quartz and water. Journal of Geophysical Research 77, 3057–3067.

Coelho, G., Branquet, Y., Sizaret, S., Arbaret, L., Champallier, R., Rozenbaum, O., 2015. Permeability of sheeted dykes beneath oceanic ridges: Strain experiments coupled with 3D numerical modeling of the Troodos Ophiolite, Cyprus. Tectonophysics 644–645, 138–150.

Corfu, F., 1996. Multistage zircon and titanite growth and inheritance in Archean gneiss complex, Winnipeg River Subprovince, Ontario. Earth and Planetary Science Letters 141, 175–186.

Corfu, F., Hanchar, J.M., Hoskin, P.W.O., Kinny, P., 2003. Atlas of zircon textures. Reviews in Mineralogy and Geochemistry 53, 469–500.

Cuney, M., Marignac, C., Weisbrod, A., 1992. The Beauvoir topaz-lepidolite albite granite (Massif Central, France): the disseminated magmatic Sn-Li-Ta-Nb-Be mineralization. Economic Geology 87, 1766–1794.

Cunha, I.A., Misi, A., Babinski, M., Iyer, S.S.S., 2007. Lead isotope constraints on the genesis of Pb-Zn deposits in the Neoproterozoic Vazante Group, Minas Gerais, Brazil. Gondwana Research 11, 382–395.

Dai, B.Z., Jiang, S.Y., Jiang, Y.H., Zhao, K.D., Liu, D.Y., 2008. Geochronology, geochemistry and Hf-Sr-Nd isotopic compositions of Huziyan mafic xenoliths, southern Hunan Province, South China: Petrogenesis and implications for lower crust evolution. Lithos 102, 65–87.

Dai, T.G., Yin, X.L., Zhang, D.X., 2015. Ore-forming model of Dabaoshan poly-metal deposit in Guangdong Province. Journal of Central South University (Science and Technology) 46, 2693–2700 (in Chinese with

English abstract).

Deng, H.X., Deng, Q., 1991. The geological characteristics and genesis of Tongshanling polymetallic deposits, Hunan. Journal of Guilin College of Geology 11, 139–149 (in Chinese with English abstract).

Deng, X.D., Li, J.W., Luo, T., Wang, H.Q., 2017. Dating magmatic and hydrothermal processes using andradite-rich garnet U-Pb geochronometry. Contributions to Mineralogy and Petrology 172, 71.

Deng, X.G., Chen, Z.G., Li, X.H., Liu, D.Y., 2004. SHRIMP U-Pb zircon dating of the Darongshan-Shiwandashan granitoid belt in southeastern Guangxi, China. Geological Review 50, 426–432 (in Chinese with English abstract).

Department of Geology, NJU (Nanjing University), 1981. Granitoids of different ages in South China and their relationship with mineralization. Science Press, Beijing (in Chinese).

Deprat, J., 1914. Étude des plissements et des zones d'écrasement de la Moyenne et de la Basse Rivière Noire. Mémoires du Service Géologique de l'Indochine 3, 1–59.

Deprat, J., 1915. Études géologiques sur la région septentrionale du Haut-Tonkin (feuilles de Pa Kha, Ha Giang, Ma-Li-Po, Yen Minh). Mémoires du Service Géologique de l'Indochine 4, 1–174.

Didier, J., 1973. Granites and Their Enclaves. Elsevier, Amsterdam.

Didier, J., Barbarin, B., 1991. Enclaves and Granite Petrology. Elsevier, Amsterdam.

Ding, T., Ma, D.S., Lu, J.J., Zhang, R.Q., Xie, Y.C., 2016c. Sulfur and lead isotopic compositions of granitoids and fluid inclusions in Baoshan deposit, Hunan Province. Mineral Deposits 35, 663–676 (in Chinese with English abstract).

Ding, T., Ma, D.S., Lu, J.J., Zhang, R.Q., Zhang, S.T., 2016a. S, Pb, and Sr isotope geochemistry and genesis of Pb-Zn mineralization in the Huangshaping polymetallic ore deposit of southern Hunan Province, China. Ore Geology Reviews 77, 117–132.

Ding, T., Ma, D.S., Lu, J.J., Zhang, R.Q., Zhang, S.T., Gao, S.Y., 2016b. Petrogenesis of Late Jurassic granitoids and relationship to polymetallic deposits in southern China: The Huangshaping example. International Geology Review 58, 1646–1672.

Dong, S.H., Bi, X.W., Hu, R.Z., Chen, Y.W., 2014. Petrogenesis of the Yaogangxian granites and implications for W mineralization, Hunan Province. Acta Petrologica Sinica 30, 2749–2765 (in Chinese with English abstract).

Dorais, M.J., Whitney, J.A., Roden, M.F., 1990. Origin of mafic enclaves in the Dinkey Creek pluton, Central Sierra Nevada Batholith, California. Journal of Petrology 31, 853–881.

Droop, G.T.R., 1987. A general equation for estimating Fe^{3+} concentrations in ferromagnesian silicates and oxides from microprobe analyses, using stoichiometric criteria. Mineralogical Magazine 51, 431–435.

Du, A.D., Wu, S.Q., Sun, D.Z., Wang, S.X., Qu, W.J., Markey, R., Stain, H., Morgan, J., Malinovskiy, D., 2004. Preparation and certification of Re-Os dating reference materials: molybdenites HLP and JDC. Geostandards and Geoanalytical Research 28, 41–52.

Duan, D.F., Jiang, S.Y., 2017. In situ major and trace element analysis of amphiboles in quartz monzodiorite porphyry from the Tonglvshan Cu–Fe (Au) deposit, Hubei Province, China: insights into magma evolution and related mineralization. Contributions to Mineralogy and Petrology 172, 36.

Dubru, M., Vander Auwera, J., van Marcke de Lummen, G., Verkaeren, J., 1988. Distribution of scheelite in magnesian skarns at Traversella (Piemontese Alps, Italy) and Costabonne (Eastern Pyrenees, France): Nature of the associated magmatism and influence of fluid composition, in: Boissonnas, J., Omenetto, P. (Eds.), Mineral deposits within the European community. Springer, Berlin, pp. 117–134.

Ducoux, M., Branquet, Y., Jolivet, L., Arbaret, L., Grasemann, B., Rabillard, A., Gumiaux, C., Drufin, S., 2017. Synkinematic skarns and fluid drainage along detachments: The West Cycladic Detachment System on Serifos Island (Cyclades, Greece) and its related mineralization. Tectonophysics 695, 1–26.

Einaudi, M.T., Meinert, L.D., Newberry, R.J., 1981. Skarn deposits. Economic Geology 75th Anniversary Volume, 317–391.

Eldursi, K., Branquet, Y., Guillou-Frottier, L., Marcoux, E., 2009. Numerical investigation of transient hydrothermal processes around intrusions: Heat-transfer and fluid-circulation controlled mineralization patterns. Earth and Planetary Science Letters 288, 70–83.

Ernst, W.G., Liu, J., 1998. Experimental phase-equilibrium study of Al- and Ti-contents of calcic amphibole in MORB–A semiquantitative thermobarometer. American Mineralogist 83, 952–969.

Fan, W.M., Zhang, C.H., Wang, Y.J., Guo, F., Peng, T.P., 2008. Geochronology and geochemistry of Permian basalts in western Guangxi Province, Southwest China: Evidence for plume-lithosphere interaction. Lithos 102, 218–236.

Fang, G.C., Tong, Q.Q., Sun, J., Zhu, G.H., Chen, Z.H., Zeng, Z.L., Liu, K.L., 2014. Stable isotope geochemical characteristics of Pangushan tungsten deposit in southern Jiangxi Province. Mineral Deposits 33, 1391–1399 (in Chinese with English abstract).

Faure, M., Chen, Y., Feng, Z.H., Shu, L.S., Xu, Z.Q., 2017. Tectonics and geodynamics of South China: An introductory note. Journal of Asian Earth Sciences 141, 1–6.

Faure, M., Lepvrier, C., Nguyen, V.V., Vu, T.V., Lin, W., Chen, Z.C., 2014. The South China Block-Indochina collision: Where, when, and how? Journal of Asian Earth Sciences 79, 260–274.

Faure, M., Lin, W., Chu, Y., Lepvrier, C., 2016a. Triassic tectonics of the southern margin of the South China Block. Comptes Rendus Geoscience 348, 5–14.

Faure, M., Lin, W., Chu, Y., Lepvrier, C., 2016b. Triassic tectonics of the Ailaoshan Belt (SW China): Early Triassic collision between the South China and Indochina Blocks, and Middle Triassic intracontinental shearing. Tectonophysics 683, 27–42.

Faure, M., Lin, W., Monié, P., Meffre, S., 2008. Palaeozoic collision between the North and South China blocks, Triassic intracontinental tectonics, and the problem of the ultrahigh-pressure metamorphism. Comptes Rendus Geoscience 340, 139–150.

Faure, M., Shu, L.S., Wang, B., Charvet, J., Choulet, F., Monie, P., 2009. Intracontinental subduction: a possible mechanism for the Early Palaeozoic Orogen of SE China. Terra Nova 21, 360–368.

Feng, C.Y., Feng, Y.D., Xu, J.X., Zeng, Z.L., She, H.Q., Zhang, D.Q., Qu, W.J., Du, A.D., 2007b. Isotope chronological evidence for Upper Jurassic petrogenesis and mineralization of altered granite-type tungsten deposits in the Zhangtiantang area, southern Jiangxi. Geology in China 34, 642–650 (in Chinese with English abstract).

Feng, C.Y., Huang, F., Qu, W.J., Zeng, Z.L., Ding, M., 2011b. Molybdenite Re-Os isotopic dating on different types of tungsten deposits in southeast of Jiulongnao orefield and its geological significances. China Tungsten Industry 26, 6–11 (in Chinese with English abstract).

Feng, C.Y., Xu, J.X., Zeng, Z.L., Zhang, D.Q., Qu, W.J., She, H.Q., Li, J.W., Li, D.X., Du, A.D., Dong, Y.J., 2007a. Zircon SHRIMP U-Pb and molybdenite Re-Os dating in Tianmenshan-Hongtaoling tungsten-tin orefield, southern Jiangxi Province, China and its geological implication. Acta Geologica Sinica 81, 952–963 (in Chinese with English abstract).

Feng, C.Y., Zeng, Z.L., Zhang, D.Q., Qu, W.J., Du, A.D., Li, D.X., She, H.Q., 2011a. SHRIMP zircon U-Pb and molybdenite Re-Os isotopic dating of the tungsten deposits in the Tianmenshan-Hongtaoling W-Sn orefield, southern Jiangxi Province, China, and geological implications. Ore Geology Reviews 43, 8–25.

Feng, C.Y., Zhao, Z., Qu, W.J., Zeng, Z.L., 2015. Temporal consistency between granite evolution and tungsten mineralization in Huamei'ao, southern Jiangxi Province, China: Evidence from precise zircon U-Pb, molybdenite Re-Os, and muscovite ^{40}Ar-^{39}Ar isotope geochronology. Ore Geology Reviews 65, 1005–1020.

Feng, Z.H., Kang, Z.Q., Yang, F., Liao, J.F., Wang, C.Z., 2013. Geochronology of the Limu W-Sn-Nb-Ta-bearing granite pluton in South China. Resource Geology 63, 320–329.

Feng, Z.W., Xia, W.H., Zhang, J.T., Chen, Z.Y., 1989. Geological characteristics of the Huangsha vein-type tungsten deposit and a discussion on the property of its ore-forming fluid, Jiangxi. Earth Science-Journal of China University of Geosciences 14, 424–432 (in Chinese with English abstract).

Förster, H.-J., Tischendorf, G., Trumbull, R.B., 1997. An evaluation of the Rb vs. (Y + Nb) discrimination diagram to infer tectonic setting of silicic igneous rocks. Lithos 40, 261–293.

Fromaget, J., 1932. Sur la structure des Indosinides. Comptes Rendus de l'Académie des Sciences 195, 1–538.

Fromaget, J., 1941. L'Indochine française, sa structure géologique, ses roches, ses mines et leurs relations possibles avec la tectonique. Bulletin du Service Géologique de l'Indochine 26, 1–140.

Frost, B.R., Chamberlain, K.R., Schumacher, J.C., 2000. Sphene (titanite): phase relations and role as a geochronometer. Chemical Geology 172, 131–148.

Fu, J.M., Li, H.Q., Qu, W.J., Ma, L.Y., Yang, X.J., Wei, J.Q., Liu, G.Q., 2008. Determination of mineralization epoch of quartz-vein type tungsten deposits in Shixing region, northern Guangdong and its geological significance. Geotectonica et Metallogenia 32, 57–62 (in Chinese with English abstract).

Fu, J.M., Li, H.Q., Qu, W.J., Yang, X.J., Wei, J.Q., Liu, G.Q., Ma, L.Y., 2007. Re-Os isotope dating of the Da'ao tungsten-tin deposit in the Jiuyi Mountains, southern Hunan Province. Geology in China 34, 651–656 (in

Chinese with English abstract).

Fu, J.M., Ma, L.Y., Cheng, S.B., Lu, Y.Y., 2013. Metallogenesis of W(Sn) deposits and their exploration in Nanling Range, China. Geological Journal of China Universities 19, 202–212 (in Chinese with English abstract).

Fu, L.B., Wei, J.H., Tan, J., Santosh, M., Zhang, D.H., Chen, J.J., Li, Y.J., Zhao, S.Q., Peng, L.N., 2016. Magma mixing in the Kalaqin core complex, northern North China Craton: Linking deep lithospheric destruction and shallow extension. Lithos 260, 390–412.

Fujimaki, H., Tatsumoto, M., Aoki, K.-i., 1984. Partition coefficients of Hf, Zr, and REE between phenocrysts and groundmasses. Journal of Geophysical Research 89 (suppl.), B662–B672.

Gao, J.F., Lu, J.J., Lai, M.Y., Lin, Y.P., Pu, W., 2003. Analysis of trace elements in rock samples using HR-ICPMS. Journal of Nanjing University (Natural Sciences) 39, 844–850 (in Chinese with English abstract).

Gao, P., Zheng, Y.F., Zhao, Z.F., 2016. Distinction between S-type and peraluminous I-type granites: Zircon versus whole-rock geochemistry. Lithos 258–259, 77–91.

Gao, S., Luo, T.C., Zhang, B.R., Zhang, H.F., Han, Y.W., Zhao, Z.D., Hu, Y.K., 1998. Chemical composition of the continental crust as revealed by studies in East China. Geochimica et Cosmochimica Acta 62, 1959–1975.

Gardien, V., Thompson, A.B., Grujic, D., Ulmer, P., 1995. Experimental melting of biotite + plagioclase + quartz ± muscovite assemblages and implications for crustal melting. Journal of Geophysical Research 100, 15581–15591.

Ge, X.Y., 2003. Mesozoic magmatism in Hainan Island (SE China) and its tectonic significance: geochronology, geochemistry and Sr-Nd isotope evidences. (Ph.D. thesis). Guangzhou Institute of Geochemistry, Chinese Academy of Sciences, Guangzhou, pp. 1–87 (in Chinese with English abstract).

Grabau, A., 1924. Stratigraphy of China, Part I, Paleozoic and Older. Geological Survey of Agriculture and Commerce, Peking.

Gramenitskiy, Ye.N., Shekina, T.I., Romanenko, I.M., 1996. The nature of W-specialised granites in the light of experimental data. Doklady, Transactions of Russian Academy of Sciences 343, 171–176.

Gu, X.X., Liu, J.M., Zheng, M.H., Tang, J.X., Qi, L., 2002. Provenance and tectonic setting of the Proterozoic turbidites in Hunan, South China: Geochemical evidence. Journal of Sedimentary Research 72, 393–407.

Guo, C.L., Mao, J.W., Bierlein, F., Chen, Z.H., Chen, Y.C., Li, C.B., Zeng, Z.L., 2011. SHRIMP U-Pb (zircon), Ar-Ar (muscovite) and Re-Os (molybdenite) isotopic dating of the Taoxikeng tungsten deposit, South China Block. Ore Geology Reviews 43, 26–39.

Guy, B., 1979. Pétrologie et géochimie isotopique (S, C, O) des skarns à scheelite de Costabonne (Pyrénées orientales, France). (Ph.D. thesis). Ecole Nationale Supérieure des Mines de Paris, Paris, pp. 1–238 (in French with English abstract).

Harley, S.L., Kelly, N.M., Möller, A., 2007. Zircon behaviour and the thermal histories of mountain chains. Elements 3, 25–30.

Hawthorne, F.C., Oberti, R., Harlow, G.E., Maresch, W.V., Martin, R.F., Schumacher, J.C., Welch, M.D., 2012. IMA report: Nomenclature of the amphibole supergroup. American Mineralogist 97, 2031–2048.

He, X.L., Zhang, D., Chen, G.H., Di, Y.J., Huo, H.L., Li, N., Zhang, Z.H., Rao, J.F., Wei, J., Ouyang, Y.P., 2018. Genesis of Zhuxi copper-tungsten deposit in Jiangxi Province: Insights from mineralogy and chronology. Journal of Jilin University (Earth Science Edition) 48, 1050–1070 (in Chinese with English abstract).

He, Z.Y., Xu, X.S., Niu, Y.L., 2010. Petrogenesis and tectonic significance of a Mesozoic granite-syenite-gabbro association from inland South China. Lithos 119, 621–641.

Henry, D.J., Guidotti, C.V., Thomson, J.A., 2005. The Ti-saturation surface for low-to-medium pressure metapelitic biotites: Implications for geothermometry and Ti-substitution mechanisms. American Mineralogist 90, 316–328.

Hine, R., Williams, I.S., Chappell, B.W., White, A.J.R., 1978. Contrasts between I-and S-type granitoids of the Kosciusko batholith. Journal of the Geological Society of Australia 25, 219–234.

Holland, T., Blundy, J., 1994. Non-ideal interactions in calcic amphiboles and their bearing on amphibole-plagioclase thermometry. Contributions to Mineralogy and Petrology 116, 433–447.

Hoskin, P.W.O., Black, L.P., 2000. Metamorphic zircon formation by solid-state recrystallization of protolith igneous zircon. Journal of Metamorphic Geology 18, 423–439.

Hsu, K.C., 1943. Tungsten deposits of southern Kiangsi, China. Economic Geology 38, 431–474.

Hsu, K.C., Liu, Y.J., Yu, S.Y., Wang, H.N., Wei, X.Z., 1960. Discovery of granites of the Caledonian age in southern Kiangsi. Geological Review 20, 112–114 (in Chinese).

Hsu, K.C., Sun, N., Wang, T.T., Hu, S.C., 1963a. Investigation on the polycyclic granite intrusions of southern China, with special notice on their ages of intrusions, distribution, characteristics, and their genetic relations to mineral deposits. Acta Geologica Sinica 43, 1–26 (in Chinese with English abstract).

Hsu, K.C., Sun, N., Wang, T.T., Hu, S.C., 1963b. Investigation on the polycyclic granite intrusions of southern China, with special notice on their ages of intrusions, distribution, characteristics, and their genetic relations to mineral deposits. Acta Geologica Sinica 43, 141–155 (in Chinese with English abstract).

Hsü, K.J., Li, J.L., Chen, H.H., Wang, Q.C., Sun, S., Sengor, A.M.C., 1990. Tectonics of South China: Key to understanding West Pacific geology. Tectonophysics 183, 9–39.

Hsü, K.J., Sun, S., Li, J.L., Chen, H.H., Pen, H.P., Sengor, A.M.C., 1988. Mesozoic overthrust tectonics in south China. Geology 16, 418–421.

Hu, R.Z., Chen, W.T., Xu, D.R., Zhou, M.F., 2017. Reviews and new metallogenic models of mineral deposits in South China: An introduction. Journal of Asian Earth Sciences 137, 1–8.

Hu, R.Z., Fu, S.L., Xiao, J.F., 2016. Major scientific problems on low-temperature metallogenesis in South China. Acta Petrologica Sinica 32, 3239–3251 (in Chinese with English abstract).

Hu, R.Z., Wei, W.F., Bi, X.W., Peng, J.T., Qi, Y.Q., Wu, L.Y., Chen, Y.W., 2012. Molybdenite Re-Os and muscovite $^{40}Ar/^{39}Ar$ dating of the Xihuashan tungsten deposit, central Nanling district, South China. Lithos 150, 111–118.

Hu, R.Z., Zhou, M.F., 2012. Multiple Mesozoic mineralization events in South China–an introduction to the thematic issue. Mineralium Deposita 47, 579–588.

Hu, X.Y., Wu, Y.C., Kang, R.H., Ning, Y.Y., He, W.H., 2015. Ore controlling factors and metallogenic regularity of concealed tungsten-fluorite deposits in Weijia of Hunan. Mineral Resources and Geology 4, 434–437 (in Chinese with English abstract).

Hua, R.M., Chen, P.R., Zhang, W.L., Liu, X.D., Lu, J.J., Lin, J.F., Yao, J.M., Qi, H.W., Zhang, Z.S., Gu, S.Y., 2003. Metallogenic systems related to Mesozoic and Cenozoic granitoids in South China. Science in China Series D: Earth Sciences 46, 816–829.

Hua, R.M., Chen, P.R., Zhang, W.L., Lu, J.J., 2005. Three major metallogenic events in Mesozoic in South China. Mineral Deposits 24, 99–107 (in Chinese with English abstract).

Hua, R.M., Mao, J.W., 1999. A preliminary discussion on the Mesozoic metallogenic explosion in East China. Mineral Deposits 18, 300–308 (in Chinese with English abstract).

Huang, F., Feng, C.Y., Chen, Y.C., Ying, L.J., Chen, Z.H., Zeng, Z.L., Qu, W.J., 2011. Isotopic chronological study of the Huangsha-Tieshanlong quartz vein-type tungsten deposit and timescale of molybdenum mineralization in southern Jiangxi Province, China. Acta Geologica Sinica (English Edition) 85, 1434–1447.

Huang, J.C., Peng, J.T., Yang, J.H., Zhang, B.L., Xu, C.X., 2015. Precise zircon U-Pb and molybdenite Re-Os dating of the Shuikoushan granodiorite-related Pb-Zn mineralization, southern Hunan, South China. Ore Geology Reviews 71, 305–317.

Huang, L.C., Jiang, S.Y., 2014. Highly fractionated S-type granites from the giant Dahutang tungsten deposit in Jiangnan Orogen, Southeast China: geochronology, petrogenesis and their relationship with W-mineralization. Lithos 202–203, 207–226.

Huang, W.T., Liang, H.Y., Wu, J., Zou, Y.Q., Zhang, J., 2017b. Formation of porphyry Mo deposit in a deep fault zone, example from the Dabaoshan porphyry Mo deposit in northern Guangdong, South China. Ore Geology Reviews 81, 940–952.

Huang, X.D., Lu, J.J., 2014. Geological characteristics and Re-Os geochronology of Tongshanling polymetallic ore field, South Hunan, China. Acta Geologica Sinica (English Edition) 88 (suppl. 2), 1626–1629.

Huang, X.D., Lu, J.J., Sizaret, S., Wang, R.C., Ma, D.S., Zhang, R.Q., Zhao, X., Wu, J.W., 2017a. Petrogenetic differences between the Middle-Late Jurassic Cu-Pb-Zn-bearing and W-bearing granites in the Nanling Range, South China: A case study of the Tongshanling and Weijia deposits in southern Hunan Province. Science China Earth Sciences 60, 1220–1236.

Huang, X.D., Lu, J.J., Sizaret, S., Wang, R.C., Wu, J.W., Ma, D.S., 2018. Reworked restite enclave: Petrographic and mineralogical constraints from the Tongshanling intrusion, Nanling Range, South China. Journal of Asian Earth Sciences 166, 1–18.

Hulsbosch, N., Boiron, M.C., Dewaele, S., Muchez, P., 2016. Fluid fractionation of tungsten during granite-pegmatite differentiation and the metal source of peribatholitic W quartz veins: Evidence from the Karagwe-Ankole Belt (Rwanda). Geochimica et Cosmochimica Acta 175, 299–318.

Ingebritsen, S.E., Appold, M.S., 2012. The physical hydrogeology of ore deposits. Economic Geology 107, 559–584.

Ingebritsen, S.E., Manning, C.E., 1999. Geological implications of a permeability-depth curve for the continental crust. Geology 27, 1107–1110.

Institute of Geochemistry, CAS (Chinese Academy of Sciences), 1979. Geochemistry of granitoids in South China. Science Press, Beijing (in Chinese).

Irber, W., 1999. The lanthanide tetrad effect and its correlation with K/Rb, Eu/Eu*, Sr/Eu, Y/Ho, and Zr/Hf of evolving peraluminous granite suites. Geochimica et Cosmochimica Acta 63, 489–508.

Jiang, S.Y., Zhao, K.D., Jiang, Y.H., Dai, B.Z., 2008. Characteristics and genesis of Mesozoic A-type granites and associated mineral deposits in the Southern Hunan and Northern Guangxi provinces along the Shi-Hang Belt, South China. Geological Journal of China Universities 14, 496–509 (in Chinese with English abstract).

Jiang, Y.H., Jiang, S.Y., Dai, B.Z., Liao, S.Y., Zhao, K.D., Ling, H.F., 2009. Middle to late Jurassic felsic and mafic magmatism in southern Hunan province, southeast China: Implications for a continental arc to rifting. Lithos 107, 185–204.

Jiang, Y.H., Zhu, S.Q., 2017. Petrogenesis of the Late Jurassic peraluminous biotite granites and muscovite-bearing granites in SE China: geochronological, elemental and Sr-Nd-O-Hf isotopic constraints. Contributions to Mineralogy and Petrology 172, 101.

Jin, R.L., 1986. Sulfur-lead isotopes and fluid inclusion characteristics of the main Pb-Zn deposits in South Hunan Province and their applications in prospecting. Geology and Prospecting 22, 29–35 (in Chinese).

Johannes, W., Holtz, F., 1996. Petrogenesis and Experimental Petrology of Granitic Rocks. Springer, Berlin.

Keppler, H., Wyllie, P.J., 1991. Partitioning of Cu, Sn, Mo, W, U and Th between melt and aqueous fluid in the systems haplogranite-H_2O-HCl and haplogranite-H_2O-HF. Contributions to Mineralogy and Petrology 109, 139–150.

Kong, H., Jin, Z.M., Lin, Y.X., 2000. Petrology and chronology of granulite xenolith in Daoxian county, Hunan Province. Journal of Changchun University of Science and Technology 30, 115–119 (in Chinese with English abstract).

Korges, M., Weis, P., Lüders, V., Laurent O., 2018. Depressurization and boiling of a single magmatic fluid as a mechanism for tin-tungsten deposit formation. Geology 46, 75–78.

Kushnir, A.R.L., Kennedy, L.A., Misra, S., Benson, P., White, J.C., 2015. The mechanical and microstructural behaviour of calcite-dolomite composites: An experimental investigation. Journal of Structural Geology 70, 200–216.

Kwak, T.A.P., 1987. W-Sn skarn deposits and related metamorphic skarns and granitoids. Developments in Economic Geology 24, Elsevier, Amsterdam.

Lahfid, A., Beyssac, O., Deville, E., Negro, F., Chopin, C., Goffé, B., 2010. Evolution of the Raman spectrum of carbonaceous material in low-grade metasediments of the Glarus Alps (Switzerland). Terra Nova 22, 354–360.

Lan, C.Y., Chung, S.L., Shen, J.J.S., Lo, C.H., Wang, P.L., Hoa, T.T., Thanh, H.H., Mertzman, S.A., 2000. Geochemical and Sr-Nd isotopic characteristics of granitic rocks from northern Vietnam. Journal of Asian Earth Sciences 18, 267–280.

Laumonier, M., Scaillet, B., Arbaret, L., Andújar, J., Champallier, R., 2015. Experimental mixing of hydrous magmas. Chemical Geology 418, 158–170.

Laumonier, M., Scaillet, B., Arbaret, L., Champallier, R., 2014a. Experimental simulation of magma mixing at high pressure. Lithos 196–197, 281–300.

Laumonier, M., Scaillet, B., Pichavant, M., Champallier, R., Andujar, J., Arbaret, L., 2014b. On the conditions of magma mixing and its bearing on andesite production in the crust. Nature Communications 5, 5607.

Launay, G., Sizaret, S., Guillou-Frottier, L., Gloaguen, E., Pinto, F., 2018. Deciphering fluid flow at the magmatic-hydrothermal transition: A case study from the world-class Panasqueira W-Sn-(Cu) ore deposit (Portugal). Earth and Planetary Science Letters 499, 1–12.

Leake, B.E., Woolley, A.R., Arps, C.E.S., Birch, W.D., Gilbert, M.C., Grice, J.D., Hawthorne, F.C., Kato, A., Kisch, H.J., Krivovichev, V.G., Linthout, K., Laird, J., Mandarino, J.A., Maresch, W.V., Nickel, E.H., Rock, N.M.S., Schumacher, J.C., Smith, D.C., Stephenson, N.C.N., Ungaretti, L., Whittaker, E.J.W., Guo, Y.Z., 1997. Nomenclature of amphiboles: Report of the subcommittee on amphiboles of the International Mineralogical Association, Commission on New Minerals and Mineral Names. Canadian Mineralogist 35, 219–246.

Lecumberri-Sanchez, P., Vieira, R., Heinrich, C.A., Pinto, F., Wälle, M., 2017. Fluid-rock interaction is decisive for the formation of tungsten deposits. Geology 45, 579–582.

Lei, Z.H., Chen, F.W., Chen, Z.H., Xu, Y.M., Gong, S.Q., Li, H.Q., Mei, Y.P., Qu, W.J., Wang, D.H., 2010. Petrogenetic and metallogenic age determination of the Huangshaping lead-zinc polymetallic deposit and its geological significance. Acta Geoscientica Sinica 31, 532–541 (in Chinese with English abstract).

Lepvrier, C., Maluski, H., Tich, V.V., Leyreloup, A., Thi, P.T., Vuong, N.V., 2004. The Early Triassic Indosinian orogeny in Vietnam (Truong Son Belt and Kontum Massif); implications for the geodynamic evolution of Indochina. Tectonophysics 393, 87–118.

Li, C.Y., Zhang, H., Wang, F.Y., Liu, J.Q., Sun, Y.L., Hao, X.L., Li, Y.L., Sun, W.D., 2012b. The formation of the Dabaoshan porphyry molybdenum deposit induced by slab rollback. Lithos 150, 101–110.

Li, F.S., Kang, R.H., Hu, X.Y., Ma, W.L., Huang, X.H., Zeng, Y.H., Tang, J.B., Zhu, X., Qin, Z.W., Zhao, J., He, L.B., 2012a. Geological characteristics and ore-search prospect of the Weijia tungsten deposit in Nanling region. Geology in China 39, 445–457 (in Chinese with English abstract).

Li, G.R., Sizaret, S., Branquet, Y., Barbanson, L., Chen, Y., Wang, B., Wu, C.Z., Gu, L.X., Shu, L.S., 2014a. Initial geometry and paleoflow reconstruction of the Yamansu skarn-related iron deposit of eastern Tianshan (China) from paleomagnetic and magnetic fabrics investigations. Journal of Asian Earth Sciences 93, 1–14.

Li, H.Y., Mao, J.W., Sun, Y.L., Zhou, X.Q., He, H.M., Du, A.D., 1996. Re-Os isotopic chronology of molybdenites in the Shizhuyuan polymetallic tungsten deposit, Southern Hunan. Geological Review 42, 261–267 (in Chinese with English abstract).

Li, J.H., Dong, S.W., Zhang, Y.Q., Zhao, G.C., Johnston, S.T., Cui, J.J., Xin, Y.J., 2016. New insights into Phanerozoic tectonics of south China: Part 1, polyphase deformation in the Jiuling and Lianyunshan domains of the central Jiangnan Orogen. Journal of Geophysical Research: Solid Earth 121, 3048–3080.

Li, J.H., Zhang, Y.Q., Zhao, G.C., Johnston, S.T., Dong, S.W., Koppers, A., Miggins, D.P., Sun, H.S., Wang, W.B, Xin, Y.J., 2017. New insights into Phanerozoic tectonics of South China: Early Paleozoic sinistral and Triassic dextral transpression in the east Wuyishan and Chencai domains, NE Cathaysia. Tectonics 36, 819–853.

Li, L.X., Chen, Z.H., Shi, G.H., Zhang, S.M., Qu, W.J., Ying, L.J., Qin, Y., Ding, Q., 2014c. Metallogenic epoch and geological characteristics of the Kuimeishan tungsten deposit, Jiangxi Province. Rock and Mineral Analysis 33, 287–295 (in Chinese with English abstract).

Li, S.G., 1942. Where is the Nanling Range? Geological Review 7, 253–266 (in Chinese).

Li, S.T., Wang, J.B., Zhu, X.Y., Wang, Y.L., Han, Y., Guo, N.N., 2011. Chronological characteristics of the Yaogangxian composite pluton in Hunan Province. Geology and Exploration 47, 143–150 (in Chinese with English abstract).

Li, S.X., Yun, P., Fan, Y., Zhou, J.B., 2005. Zircon U-Pb age and its geological significance for Qiongzhong pluton in Qiongzhong area, Hainan Island. Geotectonica et Metallogenia 29, 227–233, 241 (in Chinese with English abstract).

Li, S.Z., Suo, Y.H., Li, X.Y., Wang, Y.M., Cao, X.Z., Wang, P.C., Guo, L.L., Yu, S.Y., Lan, H.Y., Li, S.J., Zhao, S.J., Zhou, Z.Z., Zhang, Z., Zhang, G.W., 2018a. Mesozoic plate subduction in West Pacific and tectono-magmatic response in the East Asian ocean-continent connection zone. Chinese Science Bulletin 63, 1550–1593 (in Chinese with English abstract).

Li, W.X., Li, X.H., Li, Z.X., Lou, F.S., 2008. Obduction-type granites within the NE Jiangxi Ophiolite: Implications for the final amalgamation between the Yangtze and Cathaysia Blocks. Gondwana Research 13, 288–301.

Li, X.F., Hu, R.Z., Hua, R.M., Ma, D.S., Wu, L.Y., Qi, Y.Q., Peng, J.T., 2013. The Mesozoic syntexis type granite-related Cu-Pb-Zn mineralization in South China. Acta Petrologica Sinica 29, 4037–4050 (in Chinese with English abstract).

Li, X.H., 1997. Timing of the Cathaysia Block formation: Constraints from SHRIMP U-Pb zircon geochronology. Episodes 20, 188–192.

Li, X.H., Chung, S.L., Zhou, H.W., Lo, C.H., Liu, Y., Chen, C.H., 2004. Jurassic intraplate magmatism in southern Hunan-eastern Guangxi: $^{40}Ar/^{39}Ar$ dating, geochemistry, Sr-Nd isotopes and implications for tectonic evolution of SE China, in: Malpas, J., Fletcher, C.J.N., Ali, J.R., Aitchison, J.C. (Eds.), Aspects of the tectonic evolution of China. Geological Society, London, Special Publications 226, 193–216.

Li, X.H., Li, W.X., Li, Z.X., 2007a. On the genetic classification and tectonic implications of the Early Yanshanian granitoids in the Nanling Range, South China. Chinese Science Bulletin 52, 1873–1885.

Li, X.H., Li, W.X., Li, Z.X., Lo, C.H., Wang, J., Ye, M.F., Yang, Y.H., 2009. Amalgamation between the Yangtze and Cathaysia Blocks in South China: Constraints from SHRIMP U-Pb zircon ages, geochemistry and Nd-Hf isotopes of the Shuangxiwu volcanic rocks. Precambrian Research 174, 117–128.

Li, X.H., Li, Z.X., Ge, W.C., Zhou, H.W., Li, W.X., Liu, Y., Wingate, M.T.D., 2003. Neoproterozoic granitoids in South China: crustal melting above a mantle plume at ca. 825 Ma? Precambrian Research 122, 45–83.

Li, X.H., Li, Z.X., Li, W.X., 2014b. Detrital zircon U-Pb age and Hf isotope constrains on the generation and reworking of Precambrian continental crust in the Cathaysia Block, South China: A synthesis. Gondwana Research 25, 1202–1215.

Li, X.H., Li, Z.X., Li, W.X., Wang, Y.J., 2006. Initiation of the Indosinian orogeny in South China: evidence for a Permian magmatic arc on Hainan Island. The Journal of Geology 114, 341–353.

Li, X.Y., Gao, J.F., Zhang, R.Q., Lu, J.J., Chen, W.H., Wu, J.W., 2018b. Origin of the Muguayuan veinlet-disseminated tungsten deposit, South China: Constraints from in-situ trace element analyses of scheelite. Ore Geology Reviews 99, 180–194.

Li, Z.X., Li, X.H., 2007. Formation of the 1300-km-wide intracontinental orogen and postorogenic magmatic province in Mesozoic South China: A flat-slab subduction model. Geology 35, 179–182.

Li, Z.X., Li, X.H., Wartho, J.A., Clark, C., Li, W.X., Zhang, C.L., Bao, C.M., 2010. Magmatic and metamorphic events during the early Paleozoic Wuyi-Yunkai orogeny, southeastern South China: New age constraints and pressure-temperature conditions. Geological Society of America Bulletin 122, 772–793.

Li, Z.X., Li, X.H., Zhou, H.W., Kinny, P.D., 2002. Grenvillian continental collision in south China: New SHRIMP U-Pb zircon results and implications for the configuration of Rodinia. Geology 30, 163–166.

Li, Z.X., Wartho, J.A., Occhipinti, S., Zhang, C.L., Li, X.H., Wang, J., Bao, C.M., 2007b. Early history of the eastern Sibao Orogen (South China) during the assembly of Rodinia: New mica $^{40}Ar/^{39}Ar$ dating and SHRIMP U-Pb detrital zircon provenance constraints. Precambrian Research 159, 79–94.

Lin, W., Wang, Q.C., Chen, K., 2008. Phanerozoic tectonics of south China block: New insights from the polyphase deformation in the Yunkai massif. Tectonics 27, TC6004, doi:10.1029/2007TC002207.

Linnen, R.L., Cuney, M., 2005. Granite-related rare-element deposits and experimental constraints on Ta-Nb-W-Sn-Zr-Hf mineralization, in: Linnen, R.L., Samson, I.M. (Eds.), Rare-element geochemistry and mineral deposits. Geological Association of Canada Short Course Notes 17, 45–68.

Liu, H.S., Martelet, G., Wang, B., Erdmann, S., Chen, Y., Faure, M., Huang, F.F., Scaillet, B., le-Breton, N., Wang, R.C., Zhu, J.C., 2018. Incremental emplacement of the late Jurassic mid-crustal, lopolith-like Qitianling pluton, South China, revealed by AMS and Bouguer gravity data. Journal of Geophysical Research: Solid Earth (in press).

Liu, J., Mao, J.W., Ye, H.S., Xie, G.Q., Yang, G.Q., Zhang, W., 2008a. Zircon LA-ICPMS U-Pb dating of Hukeng granite in Wugongshan area, Jiangxi Province and its geochemical characteristics. Acta Petrologica Sinica 24, 1813–1822 (in Chinese with English abstract).

Liu, J.X., Chen, H.W., Liu, X.C., Wang, G., Li, C., Zhang, J.G., 2015. Isotopic age dating of Huashandong tungsten deposit in Xiushui County, Jiangxi Province and its geological significance. Resources Survey and Environment 36, 1–9 (in Chinese with English abstract).

Liu, L., Qiu, J.S., Li, Z., 2013. Origin of mafic microgranular enclaves (MMEs) and their host quartz monzonites from the Muchen pluton in Zhejiang Province, Southeast China: Implications for magma mixing and crust-mantle interaction. Lithos 160–161, 145–163.

Liu, L., Yang, Y.J., Li, Y.G., Wang, C.Z., Lin, Z.Y., 2016b. Metallogenic regularity and pattern of the Nanjia tungsten-copper polymetallic deposits, Congjiang area, Guizhou Province. Guizhou Geology 33, 265–271 (in Chinese with English abstract).

Liu, L., Yang, Y.J., Li, Y.G., Wu, S.N., Zhang, Y., 2016a. Geochemical characteristics and genesis of the Wuya tungsten deposit in Congjiang area, Guizhou Province. Guizhou Geology 33, 205–212 (in Chinese with English abstract).

Liu, S.B., Chen, Y.C., Fan, S.X., Xu, J.X., Qu, W.J., Ying, L.J., 2010. The second ore-prospecting space in the eastern and central parts of the Nanling metallogenic belt: evidence from isotopic chronology. Geology in China 37, 1034–1049 (in Chinese with English abstract).

Liu, S.B., Liu, Z.Q., Wang, C.H., Wang, D.H., Zhao, Z., Hu, Z.H., 2017. Geochemical characteristics of REEs and trace elements and Sm-Nd dating of scheelite from the Zhuxi giant tungsten deposit in northeast Jiangxi. Earth Science Frontiers 24, 17–30 (in Chinese with English abstract).

Liu, S.S., Zeng, Z.F., Zhao, Y.X., 2007. Geological characteristics and genesis of the Da'ao intrusion-type tungsten-tin deposit, Daoxian County, Hunan. Geology in China 34, 657–667 (in Chinese with English abstract).

Liu, W., 1994. Nature, source and convection path of the ore-bearing fluid in the Shuikoushan Pb-Zn-Au ore field. Geotectonica et Metallogenia 18, 209–218 (in Chinese with English abstract).

Liu, W.H., Xu, W.X., Dai, T.G., Li, H., 2006. Isotope geochemistry of the Yejiwei deposit in the Shizhuyuan W-Sn ore field in Hunan Province. Acta Petrologica Sinica 22, 2517–2524 (in Chinese with English abstract).

Liu, X.F., Yuan, S.D., Shuang, Y., Yuan, Y.B., Mi, J.R., Xuan, Y.S., 2014. In situ LA-ICP-MS REE analyses of the skarn garnets from the Jinchuantang tin-bismuth deposit in Hunan Province, and their significance. Acta Petrologica Sinica 30, 163–177 (in Chinese with English abstract).

Liu, Y.S., Hu, Z.C., Gao, S., Günther, D., Xu, J., Gao, C.G., Chen, H.H., 2008b. In situ analysis of major and trace elements of anhydrous minerals by LA-ICP-MS without applying an internal standard. Chemical Geology 257, 34–43.

London, D., Hervig, R.L., Morgan, G.B.VI., 1988. Melt-vapor solubilities and elemental partitioning in peraluminous granite-pegmatite systems: experimental results with Macusani glass at 200 MPa. Contributions to Mineralogy and Petrology 99, 360–373.

Long, H.C., 1983. Genetic characteristics and material sources of poly metallic deposit in Tongshanling. Geotectonica et Metallogenia 7, 198–208 (in Chinese with English abstract).

Love, D.A., Clark, A.H., Glover, J.K., 2004. The lithologic, stratigraphic, and structural setting of the giant Antamina copper-zinc skarn deposit, Ancash, Peru. Economic Geology 99, 887–916.

Lu, R., Xu, Z.W., Lu, J.J., Wang, R.C., Zuo, C.H., Zhao, Z.X., Miao, B.H., 2013. Genesis of the Shuikoushan lead-zinc deposit, Changning City, Hunan Province. Journal of Nanjing University (Natural Sciences) 49, 732–746 (in Chinese with English abstract).

Lu, Y.F., Ma, L.Y., Qu, W.J., Mei, Y.P., Chen, X.Q., 2006. U-Pb and Re-Os isotope geochronology of Baoshan Cu-Mo polymetallic deposit in Hunan province. Acta Petrologica Sinica 22, 2483–2492 (in Chinese with English abstract).

Lu, Y.Y., Fu, J.M., Cheng, S.B., Liu, S.S., Li, C.B., Zhang, L.G., Ma, L.Y., 2015. Rock-forming and ore-forming ages of Tongshanling copper polymetallic ore-field in southern Hunan Province. Geotectonica et Metallogenia 39, 1061–1071 (in Chinese with English abstract).

Ludwig, K.R., 2012. User's manual for Isoplot 3.75: A geochronology toolkit for Microsoft Excel. Berkeley Geochronology Center Special Publication No.5, 1–75.

Luo, B.J., Zhang, H.F., Xu, W.C., Guo, L., Pan, F.B., Yang, H., 2015. The Middle Triassic Meiwu batholith, West Qinling, Central China: implications for the evolution of compositional diversity in a composite batholith. Journal of Petrology 56, 1139–1172.

Ma, D.S., 2008. Metallogenetic characteristics of the important deposits in South China. Bulletin of Mineralogy, Petrology and Geochemistry 27, 209–217 (in Chinese with English abstract).

Ma, L.Y., Lu, Y.F., Mei, Y.P., Chen, X.Q., 2006. Zircon SHRIMP U-Pb dating of granodiorite from Shuikoushan ore-field, Hunan province and its geological significance. Acta Petrologica Sinica 22, 2475–2482 (in Chinese with English abstract).

Ma, L.Y., Lu, Y.F., Qu, W.J., Fu, J.M., 2007. Re-Os isotopic chronology of molybdenites in Huangshaping lead-zinc deposit, southeast Hunan, and its geological implications. Mineral Deposits 26, 425–431 (in Chinese with English abstract).

Mahjoubi, E.M., Chauvet, A., Badra, L., Sizaret, S., Barbanson, L., Maz, A.E., Chen, Y., Amann, M., 2016. Structural, mineralogical, and paleoflow velocity constraints on Hercynian tin mineralization: the Achmmach prospect of the Moroccan Central Massif. Mineralium Deposita 51, 431–451.

Manning, D.A.C., 1981. The effect of fluorine on liquidus phase relationships in the system Qz-Ab-Or with

excess water at 1kb. Contributions to Mineralogy and Petrology 76, 206–215.

Manning, D.A.C., Hamilton, D.L., Henderson, C.M.B., Dempsey, M.J., 1980. The probable occurrence of interstitial Al in hydrous, F-bearing and F-free aluminosilicate melts. Contributions to Mineralogy and Petrology 75, 257–262.

Manning, D.A.C., Henderson, P., 1984. The behaviour of tungsten in granitic melt-vapour systems. Contributions to Mineralogy and Petrology 86, 286–293.

Mao, J.W., Chen, M.H., Yuan, S.D., Guo, C.L., 2011b. Geological characteristics of the Qinhang (or Shihang) metallogenic belt in South China and spatial-temporal distribution regularity of mineral deposits. Acta Geologica Sinica 85, 636–658 (in Chinese with English abstract).

Mao, J.W., Cheng, Y.B., Chen, M.H., Pirajno, F., 2013a. Major types and time-space distribution of Mesozoic ore deposits in South China and their geodynamic settings. Mineralium Deposita 48, 267–294.

Mao, J.W., Pirajno, F., Cook, N., 2011a. Mesozoic metallogeny in East China and corresponding geodynamic settings–An introduction to the special issue. Ore Geology Reviews 43, 1–7.

Mao, J.W., Shao, Y.J., Xie, G.Q., Zhang, J.D., Chen, Y.C., 2009b. Mineral deposit model for porphyry-skarn polymetallic copper deposits in Tongling ore dense district of Middle-Lower Yangtze Valley metallogenic belt. Mineral Deposits 28, 109–119 (in Chinese with English abstract).

Mao, J.W., Xie, G.Q., Bierlein, F., Qu, W.J., Du, A.D., Ye, H.S., Pirajno, F., Li, H.M., Guo, B.J., Li, X.F., Yang, Z.Q., 2008b. Tectonic implications from Re-Os dating of Mesozoic molybdenum deposits in the East Qinling-Dabie orogenic belt. Geochimica et Cosmochimica Acta 72, 4607–4626.

Mao, J.W., Xie, G.Q., Cheng, Y.B., Chen, Y.C., 2009a. Mineral deposit models of Mesozoic ore deposits in South China. Geological Review 55, 347–354 (in Chinese with English abstract).

Mao, J.W., Xie, G.Q., Guo, C.L., Chen, Y.C., 2007. Large-scale tungsten-tin mineralization in the Nanling region, South China: Metallogenic ages and corresponding geodynamic processes. Acta Petrologica Sinica 23, 2329–2338 (in Chinese with English abstract).

Mao, J.W., Xie, G.Q., Guo, C.L., Yuan, S.D., Cheng, Y.B., Chen, Y.C., 2008a. Spatial-temporal distribution of Mesozoic ore deposits in South China and their metallogenic settings. Geological Journal of China Universities 14, 510–526 (in Chinese with English abstract).

Mao, J.W., Zhang, Z.C., Zhang, Z.H., Du, A.D., 1999. Re-Os isotopic dating of molybdenites in the Xiaoliugou W (Mo) deposit in the northern Qilian mountains and its geological significance. Geochimica et Cosmochimica Acta 63, 1815–1818.

Mao, W., Li, X.F., Yang, F.C., 2013b. Zircon LA-ICP-MS U-Pb ages of granites at Dabaoshan polymetallic deposit and its geological significance, Guangdong, South China. Acta Petrologica Sinica 29, 4104–4120 (in Chinese with English abstract).

Mao, W., Rusk, B., Yang, F.C., Zhang, M.J., 2017. Physical and chemical evolution of the Dabaoshan porphyry Mo deposit, South China: Insights from fluid inclusions, cathodoluminescence, and trace elements in quartz. Economic Geology 112, 889–918.

Mao, Z.H., Cheng, Y.B., Liu, J.J., Yuan, S.D., Wu, S.H., Xiang, X.K., Luo, X.H., 2013c. Geology and molybdenite Re-Os age of the Dahutang granite-related veinlets-disseminated tungsten ore field in the Jiangxi Province, China. Ore Geology Reviews 53, 422–433.

Mao, Z.H., Liu, J.J., Mao, J.W., Deng, J., Zhang, F., Meng, X.Y., Xiong, B.K., Xiang, X.K., Luo, X.H., 2015. Geochronology and geochemistry of granitoids related to the giant Dahutang tungsten deposit, middle Yangtze River region, China: Implications for petrogenesis, geodynamic setting, and mineralization. Gondwana Research 28, 816–836.

Martin, R.F., 2007. Amphiboles in the igneous environment. Reviews in Mineralogy and Geochemistry 67, 323–358.

Mazdab, F.K., 2009. Characterization of flux-grown trace-element-doped titanite using the high-mass-resolution ion microprobe (SHRIMP-RG). The Canadian Mineralogist 47, 813–831.

Meinert, L.D., Dipple, G.M., Nicolescu, S., 2005. World skarn deposits. Economic Geology 100th Anniversary Volume, 299–336.

Metcalfe, I., 2013. Gondwana dispersion and Asian accretion: Tectonic and palaeogeographic evolution of eastern Tethys. Journal of Asian Earth Sciences 66, 1–33.

Mezger, K., Hanson, G.N., Bohlen, S.R., 1989. U-Pb systematics of garnet: dating the growth of garnet in the late Archean Pikwitonei granulite domain at Cauchon and Natawahunan Lakes, Manitoba, Canada. Contributions to Mineralogy and Petrology 101, 136–148.

Miao, B.H., Zuo, C.H., Zhao, Z.X., Xu, Z.W., Lu, J.J., Lu, R., Chen, J.Q., 2014. Forming age and material source of the Zhoujialing granite in Qingshuitang orefield, Qidong County, Hunan Province. Geological Review 60, 611–623 (in Chinese with English abstract).

Middlemost, E.A.K., 1994. Naming materials in the magma/igneous rock system. Earth-Science Reviews 37, 215–224.

Miller, C.F., Meschter McDowell, S., Mapes, R.W., 2003. Hot and cold granites? Implications of zircon saturation temperatures and preservation of inheritance. Geology 31, 529–532.

Mo, Z.S., Ye, B.D., Pan, W.Z., Wang, S.N., Zhuang, J.L., Gao, B.Z., Liu, J.Q., Liu, W.Z., 1980. Geology of granitoids in the Nanling Range. Geological Publishing House, Beijing (in Chinese).

Molina, J.F., Moreno, J.A., Castro, A., Rodríguez, C., Fershtater, G.B., 2015. Calcic amphibole thermobarometry in metamorphic and igneous rocks: New calibrations based on plagioclase/amphibole Al-Si partitioning and amphibole/liquid Mg partitioning. Lithos 232, 286–305.

Munoz, J.L., 1984. F-OH and Cl-OH exchange in micas with applications to hydrothermal ore deposits. Reviews in Mineralogy 13, 469–493.

Mutch, E.J.F., Blundy, J.D., Tattitch, B.C., Cooper, F.J., Brooker, R.A., 2016. An experimental study of amphibole stability in low-pressure granitic magmas and a revised Al-in-hornblende geobarometer. Contributions to Mineralogy and Petrology 171, 85.

Naranjo, A., Horner, J., Jahoda, R., Diamond, L.W., Castro, A., Uribe, A., Perez, C., Paz, H., Mejia, C., Weil, J., 2018. La Colosa Au porphyry deposit, Colombia: Mineralization styles, structural controls, and age constraints. Economic Geology 113, 553–578.

Newberry, R.J., Swanson, S.E., 1986. Scheelite skarn granitoids: An evaluation of the roles of magmatic source and process. Ore Geology Reviews 1, 57–81.

Oesterling, N., Heilbronner, R., Stünitz, H., Barnhoorn, A., Molli, G., 2007. Strain dependent variation of microstructure and texture in naturally deformed Carrara marble. Journal of Structural Geology 29, 681–696.

Ohmoto, H., Rye, R.O., 1979. Isotopes of sulfur and carbon, in: Barnes, H.L. (Ed.), Geochemistry of hydrothermal ore deposits, second ed. Wiley, New York, pp. 509–567.

Pan, G.S., Hu, G.M., 2014. Basic geological characteristics and its genesis of Wuya scheelite deposit in Congjiang. Guizhou Geology 31, 286–290 (in Chinese with English abstract).

Pan, X.F., Hou, Z.Q., Li, Y., Chen, G.H., Zhao, M., Zhang, T.F., Zhang, C., Wei, J., Kang, C., 2017. Dating the giant Zhuxi W-Cu deposit (Taqian-Fuchun Ore Belt) in South China using molybdenite Re-Os and muscovite Ar-Ar system. Ore Geology Reviews 86, 719–733.

Pearce, J.A., Harris, N.B.W., Tindle, A.G., 1984. Trace element discrimination diagrams for the tectonic interpretation of granitic rocks. Journal of Petrology 25, 956–983.

Pei, R.F., Wang, Y.L., Li, L., Wang, H.L., 2008. South China great granite province and its metallogenic series of tungsten-tin poly-metallics. China Tungsten Industry 23, 10–13 (in Chinese with English abstract).

Peng, B.X., Wang, Y.J., Fan, W.M., Peng, T.P., Liang, X.Q., 2006a. LA-ICPMS zircon U-Pb dating for three Indosinian granitic plutons from central Hunan and western Guangdong Provinces and its petrogenetic implications. Acta Geologica Sinica (English Edition) 80, 660–669.

Peng, J.T., Zhou, M.F., Hu, R.Z., Shen, N.P., Yuan, S.D., Bi, X.W., Du, A.D., Qu, W.J., 2006b. Precise molybdenite Re-Os and mica Ar-Ar dating of the Mesozoic Yaogangxian tungsten deposit, central Nanling district, South China. Mineralium Deposita 41, 661–669.

Perugini, D., Poli, G., 2012. The mixing of magmas in plutonic and volcanic environments: Analogies and differences. Lithos 153, 261–277.

Pieri, M., Burlini, L., Kunze, K., Stretton, I., Olgaard, D.L., 2001. Rheological and microstructural evolution of Carrara marble with high shear strain: results from high temperature torsion experiments. Journal of Structural Geology 23, 1393–1413.

Pirajno, F., 2013. The geology and tectonic settings of China's mineral deposits. Springer, Dordrecht.

Pirajno, F., Zhou, T.F., 2015. Intracontinental porphyry and porphyry-skarn mineral systems in Eastern China: Scrutiny of a special case "Made-in-China". Economic Geology 110, 603–629.

Poli, G.E., Tommasini, S., 1991. Model for the origin and significance of microgranular enclaves in calc-alkaline granitoids. Journal of Petrology 32, 657–666.

Pu, W., Gao, J.F., Zhao, K.D., Ling, H.F., Jiang, S.Y., 2005. Separation method of Rb-Sr, Sm-Nd using DCTA and HIBA. Journal of Nanjing University (Natural Sciences) 41, 445–450 (in Chinese with English abstract).

Putirka, K., 2016. Amphibole thermometers and barometers for igneous systems and some implications for eruption mechanisms of felsic magmas at arc volcanoes. American Mineralogist 101, 841–858.

Putirka, K.D., 2005. Igneous thermometers and barometers based on plagioclase + liquid equilibria: Tests of some existing models and new calibrations. American Mineralogist 90, 336–346.

Putirka, K.D., 2008. Thermometers and barometers for volcanic systems. Reviews in Mineralogy and Geochemistry 69, 61–120.

Qi, H.W., Hu, R.Z., Wang, X.F., Qu, W.J., Bi, X.W., Peng, J.T., 2012. Molybdenite Re-Os and muscovite $^{40}Ar/^{39}Ar$ dating of quartz vein-type W-Sn polymetallic deposits in Northern Guangdong, South China. Mineralium Deposita 47, 607–622.

Qu, H.Y., Chen, M.H., Yang, F.C., Gao, Z.H., Wang, Y.W., Zhao, H.J., Yu, Z.F., 2014. Metallogenic chronology of the stratiform Cu orebody in the Dabaoshan Cu polymetallic deposit, northern Guangdong Province and its geological significance. Acta Petrologica Sinica 30, 152–162 (in Chinese with English abstract).

Quan, T.J., Wang, G., Zhong, J.L., Fei, L.D., Kong, H., Liu, S.J., Zhao, Z.Q., Guo, B.Y., 2013. Petrogenesis of granodiorites in Tongshanling deposit of Hunan Province: Constraints from petrogeochemistry, zircon U-Pb chronology and Hf isotope. Journal of Mineralogy and Petrology 33, 43–52 (in Chinese with English abstract).

Ray, G.E., 1998. Skarns and skarn deposits in the Canadian Cordillera. B.C. Geological Survey Open File 1998-8, M3–73.

Ray, G.E., 2013. A review of skarns in the Canadian Cordillera. B.C. Geological Survey Open File 2013-08.

Ray, G.E., Webster, I.C.L., 1991. An overview of skarn deposits. B.C. Geological Survey Paper Series 1991-4, 213–252.

Regional Geological Survey Team of Hunan Geology Bureau, 1975a. Geology map of the People's Republic of China: Daoxian (G-49-XXII, scale 1:200000) (in Chinese).

Regional Geological Survey Team of Hunan Geology Bureau, 1975b. Geology map of the People's Republic of China: Jiangyong (G-49-XXVIII, scale 1:200000) (in Chinese).

Ren, J.S., 1991. On the geotectonics of southern China. Acta Geologica Sinica (English Edition) 4, 111–130.

Ridolfi, F., Renzulli, A., 2012. Calcic amphiboles in calc-alkaline and alkaline magmas: thermobarometric and chemometric empirical equations valid up to 1,130 °C and 2.2 GPa. Contributions to Mineralogy and Petrology 163, 877–895.

Ridolfi, F., Renzulli, A., Puerini, M., 2010. Stability and chemical equilibrium of amphibole in calc-alkaline magmas: an overview, new thermobarometric formulations and application to subduction-related volcanoes. Contributions to Mineralogy and Petrology 160, 45–66.

Roberts, N.M.W., Rasbury, E.T., Parrish, R.R., Smith, C.J., Horstwood, M.S.A., Condon, D.J., 2017. A calcite reference material for LA-ICP-MS U-Pb geochronology. Geochemistry, Geophysics, Geosystems 18, 2807–2814.

Romer, R.L., Kroner, U., 2015. Sediment and weathering control on the distribution of Paleozoic magmatic tin-tungsten mineralization. Mineralium Deposita 50, 327–338.

Romer, R.L., Kroner, U., 2016. Phanerozoic tin and tungsten mineralization-Tectonic controls on the distribution of enriched protoliths and heat sources for crustal melting. Gondwana Research 31, 60–95.

Rudnick, R.L., Fountain, D.M., 1995. Nature and composition of the continental crust: A lower crustal perspective. Reviews of Geophysics 33, 267–309.

Sato, E., Sato, H., 2009. Study of effect of magma pocket on mixing of two magmas with different viscosities and densities by analogue experiments. Journal of Volcanology and Geothermal Research 181, 115–123.

Schmidt, C., 2018. Formation of hydrothermal tin deposits: Raman spectroscopic evidence for an important role of aqueous Sn(IV) species. Geochimica et Cosmochimica Acta 220, 499–511.

Schmidt, M.W., 1992. Amphibole composition in tonalite as a function of pressure: an experimental calibration of the Al-in-hornblende barometer. Contributions to Mineralogy and Petrology 110, 304–310.

Schneider, J., Boni, M., Lapponi, F., Bechstädt, T., 2002. Carbonate-hosted zinc-lead deposits in the Lower Cambrian of Hunan, South China: a radiogenic (Pb, Sr) isotope study. Economic Geology 97, 1815–1827.

Schöpa, A., Annen, C., Dilles, J.H., Sparks, R.S.J., Blundy, J.D., 2017. Magma emplacement rates and porphyry copper deposits: Thermal modeling of the Yerington batholith, Nevada. Economic Geology 112, 1653–1672.

Schumacher, J.C., 2007. Metamorphic amphiboles: composition and coexistence. Reviews in Mineralogy and Geochemistry 67, 359–416.

Seaton, N.C.A., Whitney, D.L., Teyssier, C., Toraman, E., Heizler, M.T., 2009. Recrystallization of high-pressure marble (Sivrihisar, Turkey). Tectonophysics 479, 241–253.

Seedorff, E., Dilles, J.H., Proffett, J.M., Jr., Einaudi, M.T., Zurcher, L., Stavast, W.J.A., Johnson, D.A., Barton, M.D., 2005. Porphyry deposits: Characteristics and origin of hypogene features. Economic Geology 100th Anniversary Volume, 251–298.

Seman, S., Stockli, D.F., McLean, N.M., 2017. U-Pb geochronology of grossular-andradite garnet. Chemical Geology 460, 106–116.

Sheng, J.F., Chen, Z.H., Liu, L.J., Ying, L.J., Huang, F., Wang, D.H., Wang, J.H., Zeng, L., 2015. Outline of metallogeny of tungsten deposits in China. Acta Geologica Sinica 89, 1038–1050 (in Chinese with English abstract).

Shi, M.K., Xiong, C.Y., Jia, D.Y., Lu, Y.F., Li, B., 1993. Comprehensive prognosis for the concealed nonferrous metallic deposits in Hunan-Guangxi-Guangdong-Jiangxi area. Geological Publishing House, Beijing (in Chinese with English abstract).

Shirey, S.B., Walker, R.J., 1995. Carius tube digestion for low-blank rhenium-osmium analysis. Analytical Chemistry 67, 2136–2141.

Shu, L.S., 2012. An analysis of principal features of tectonic evolution in South China Block. Geological Bulletin of China 31, 1035–1053 (in Chinese with English abstract).

Shu, L.S., Faure, M., Jiang, S.Y., Yang, Q., Wang, Y.J., 2006a. SHRIMP zircon U-Pb age, litho- and biostratigraphic analyses of the Huaiyu Domain in South China–Evidence for a Neoproterozoic orogen, not Late Paleozoic-Early Mesozoic collision. Episodes 29, 244–252.

Shu, L.S., Faure, M., Wang, B., Zhou, X.M., Song, B., 2008. Late Paleozoic-Early Mesozoic geological features of South China: Response to the Indosinian collision event in Southeast Asia. Comptes Rendus Geoscience 340, 151–165.

Shu, L.S., Faure, M., Yu, J.H., Jahn, B.M., 2011. Geochronological and geochemical features of the Cathaysia block (South China): New evidence for the Neoproterozoic breakup of Rodinia. Precambrian Research 187, 263–276.

Shu, L.S., Jahn, B.M., Charvet, J., Santosh, M., Wang, B., Xu, X.S., Jiang, S.Y., 2014. Early Paleozoic depositional environment and intraplate tectono-magmatism in the Cathaysia Block (South China): Evidence from stratigraphic, structural, geochemical and geochronological investigations. American Journal of Science 314, 154–186.

Shu, L.S., Lu, H.F., Jia, D., Charvet, J., Faure, M., 1999. Study of the $^{40}Ar/^{39}Ar$ isotopic age for the Early Paleozoic tectonothermal event in the Wuyishan region, South China. Journal of Nanjing University (Natural Sciences) 35, 668–674 (in Chinese with English abstract).

Shu, L.S., Wang, B., Cawood, P.A., Santosh, M., Xu, Z.Q., 2015. Early Paleozoic and Early Mesozoic intraplate tectonic and magmatic events in the Cathaysia Block, South China. Tectonics 34, 1600–1621.

Shu, L.S., Zhou, X.M., 2002. Late Mesozoic tectonism of southeast China. Geological Review 48, 249–260 (in Chinese with English abstract).

Shu, L.S., Zhou, X.M., Deng, P., Wang, B., Jiang, S.Y., Yu, J.H., Zhao, X.X., 2009. Mesozoic tectonic evolution of the Southeast China Block: New insights from basin analysis. Journal of Asian Earth Sciences 34, 376–391.

Shu, L.S., Zhou, X.M., Deng, P., Yu, X.Q., 2006b. Principal geological features of Nanling Tectonic Belt, South China. Geological Review 52, 251–265 (in Chinese with English abstract).

Shu, Q.H., Lai, Y., Sun, Y., Wang, C., Meng, S., 2013. Ore genesis and hydrothermal evolution of the Baiyinnuo'er zinc-lead skarn deposit, Northeast China: Evidence from isotopes (S, Pb) and fluid inclusions. Economic Geology 108, 835–860.

Shuang, Y., Gong, Y.C., Li, H., Tian, X.F., Mao, L.L., Chen, W., 2016. Fluid-inclusion geochemistry of the large-sized Xintianling tungsten deposit, Hunan Province, China. Geochimica 45, 569–581 (in Chinese with English abstract).

Sial, A.N., Ferreira, V.P., Fallick, A.E., Cruz, M.J.M., 1998. Amphibole-rich clots in calc-alkalic granitoids in the Borborema province, northeastern Brazil. Journal of South American Earth Sciences 11, 457–471.

Sillitoe, R.H., 2010. Porphyry copper systems. Economic Geology 105, 3–41.

Sillitoe, R.H., Perelló, J., Creaser, R.A., Wilton, J., Dawborn, T., 2015. Two ages of copper mineralization in the Mwombezhi Dome, northwestern Zambia: Metallogenic implications for the Central African Copperbelt. Economic Geology 110, 1917–1923.

Simons, B., Andersen, J.C.Ø., Shail, R.K., Jenner, F.E., 2017. Fractionation of Li, Be, Ga, Nb, Ta, In, Sn, Sb, W and Bi in the peraluminous Early Permian Variscan granites of the Cornubian Batholith: Precursor processes to magmatic-hydrothermal mineralisation. Lithos 278–281, 491–512.

Simons, B., Shail, R.K., Andersen, J.C.Ø., 2016. The petrogenesis of the Early Permian Variscan granites of the Cornubian Batholith: Lower plate post-collisional peraluminous magmatism in the Rhenohercynian Zone of SW England. Lithos 260, 76–94.

Sizaret, S., Branquet, Y., Gloaguen, E., Chauvet, A., Barbanson, L., Arbaret, L., Chen, Y., 2009. Estimating the local paleo-fluid flow velocity: New textural method and application to metasomatism. Earth and Planetary Science Letters 280, 71–82.

Smoliar, M.I., Walker, R.J., Morgan, J.W., 1996. Re-Os ages of group IIA, IIIA, IVA and IVB iron meteorites. Science 271, 1099–1102.

Soloviev, S.G., 2011. Geology, mineralization, and fluid inclusion characteristics of the Kensu W-Mo skarn and Mo-W-Cu-Au alkalic porphyry deposit, Tien Shan, Kyrgyzstan. Economic Geology 106, 193–222.

Soloviev, S.G., 2015. Geology, mineralization, and fluid inclusion characteristics of the Kumbel oxidized W-Cu-Mo skarn and Au-W stockwork deposit in Kyrgyzstan, Tien Shan. Mineralium Deposita 50, 187–220.

Soloviev, S.G., Kryazhev, S.G., 2017. Geology, mineralization, and fluid inclusion characteristics of the Skrytoe reduced-type W skarn and stockwork deposit, Sikhote-Alin, Russia. Mineralium Deposita 52, 903–928.

Soloviev, S.G., Kryazhev, S.G., Dvurechenskaya, S.S., 2013. Geology, mineralization, stable isotope geochemistry, and fluid inclusion characteristics of the Novogodnee-Monto oxidized Au-(Cu) skarn and porphyry deposit, Polar Ural, Russia. Mineralium Deposita 48, 603–627.

Song, S.Q., Hu, R.Z., Bi, X.W., Wei, W.F., Shi, S.H., 2011. Hydrogen, oxygen and sulfur isotope geochemical characteristics of Taoxikeng tungsten deposit in Chongyi County, Southern Jiangxi Province. Mineral Deposits 30, 1–10 (in Chinese with English abstract).

Stacey, J.S., Kramers, J.D., 1975. Approximation of terrestrial lead isotope evolution by a two-stage model. Earth and Planetary Science Letters 26, 207–221.

Stein, H.J., 2014. Dating and tracing the history of ore formation, in: Holland, H.D., Turekian, K.K. (Eds.), Treatise on geochemistry, second ed. Elsevier, Oxford, pp. 87–118.

Stein, H.J., Markey, R.J., Morgan, J.W., 1997. Highly precise and accurate Re-Os ages for molybdenite from the

East Qinling molybdenum belt, Shanxi Province, China. Economic Geology 92, 827–835.

Stein, H.J., Markey, R.J., Morgan, J.W., Hannah, J.L., Scherstén, A., 2001. The remarkable Re-Os chronometer in molybdenite: how and why it works. Terra Nova 13, 479–486.

Stephens, W.E., 2001. Polycrystalline amphibole aggregates (clots) in granites as potential I-type restite: an ion microprobe study of rare-earth distributions. Australian Journal of Earth Sciences 48, 591–601.

Stern, R.A., 1997. The GSC sensitive high resolution ion microprobe (SHRIMP): analytical techniques of zircon U-Th-Pb age determinations and performance evaluation. Radiogenic Age and Isotopic Studies: Report 10. Geological Survey of Canada Current Research 1997-F, 1–31.

Sun, S.-S., Mcdonough, W.F., 1989. Chemical and isotopic systematics of oceanic basalts: Implications for mantle composition and processes, in: Saunders, A.D., Norry, M.J. (Eds.), Magmatism in the ocean basins. Geological Society, London, Special Publications 42, 313–345.

Sun, T., 2006. A new map showing the distribution of granites in South China and its explanatory notes. Geological Bulletin of China 25, 332–335 (in Chinese with English abstract).

Sun, T., Zhou, X.M., Chen, P.R., Li, H.M., Zhou, H.Y., Wang, Z.C., Shen, W.Z., 2005. Strongly peraluminous granites of Mesozoic in Eastern Nanling Range, southern China: Petrogenesis and implications for tectonics. Science in China Series D: Earth Sciences 48, 165–174.

Tartèse, R., Boulvais, P., 2010. Differentiation of peraluminous leucogranites “en route” to the surface. Lithos 114, 353–368.

Taylor, H.P., 1997. Oxygen and hydrogen isotope relationships in hydrothermal mineral deposits, in: Barnes, H.L. (Ed.), Geochemistry of hydrothermal ore deposits, third ed. Wiley, New York, pp. 229–302.

Taylor, S.R., McLennan, S.M., 1995. The geochemical evolution of the continental crust. Reviews of Geophysics 33, 241–265.

The Granitoid Research Group of the Nanling Project, MGMR (Ministry of Geology and Mineral Resources of P.R. China), 1989. Geology of granitoids of Nanling Region and their petrogenesis and mineralization. Geological Publishing House, Beijing (in Chinese with English abstract).

Thompson, A.B., 1982. Dehydration melting of pelitic rocks and the generation of H_2O-undersaturated granitic liquids. American Journal of Science 282, 1567–1595.

Ting, V.K., 1929. The orogenic movements in China. Bulletin of the Geological Society of China 8, 151–170.

Tischendorf, G., Gottesmann, B., Förster, H.-J., Trumbull, R.B., 1997. On Li-bearing micas: estimating Li from electron microprobe analyses and an improved diagram for graphical representation. Mineralogical Magazine 61, 809–834.

Tong, Q.M., Wu, R.H., Peng, J.L., Wang, S.M., 1995. Metallogeny of W, Sn, Pb-Zn, Au, and Ag deposits in the Chenxian-Guiyang region, south Hunan, China. Geological Publishing House, Beijing (in Chinese with English abstract).

Tuttle, O.F., Bowen, N.L., 1958. Origin of granite in the light of experimental studies in the system $NaAlSi_3O_8$-$KAlSi_3O_8$-SiO_2-H_2O. Geological Society of America Memoirs 74, 907–921.

Vallance, J., Fontboté, L., Chiaradia, M., Markowski, A., Schmidt, S., Vennemann, T., 2009. Magmatic-dominated fluid evolution in the Jurassic Nambija gold skarn deposits (southeastern Ecuador). Mineralium Deposita 44, 389–413.

Vander Auwera, J., Andre, L., 1991. Trace elements (REE) and isotopes (O, C, Sr) to characterize the metasomatic fluid sources: evidence from the skarn deposit (Fe, W, Cu) of Traversella (Ivrea, Italy). Contributions to Mineralogy and Petrology 106, 325–339.

Veksler, I.V., 2005. Element enrichment and fractionation by magmatic aqueous fluids: Experimental constraints on fluid-melt immiscibility and element partitioning, in: Linnen, R.L., Samson, I.M. (Eds.), Rare-element geochemistry and mineral deposits. Geological Association of Canada Short Course Notes 17, 69–85.

Veksler, I.V., Thomas, R., Schmidt, C., 2002. Experimental evidence of three coexisting immiscible fluids in synthetic granitic pegmatite. American Mineralogist 87, 775–779.

Vernon, R.H., 1984. Microgranitoid enclaves in granites-globules of hybrid magma quenched in a plutonic environment. Nature 309, 438–439.

Vernon, R.H., 1991. Interpretation of microstructures of microgranitoid enclaves, in: Didier, J., Barbarin, B. (Eds.), Enclaves and Granite Petrology. Elsevier, Amsterdam, pp. 277–291.

Vielzeuf, D., Montel, J.M., 1994. Partial melting of metagreywackes. Part I. Fluid-absent experiments and phase relationship. Contributions to Mineralogy and Petrology 117, 375–393.

Wan, T.F., 2010. The tectonics of China: data, maps and evolution. Higher Education Press, Beijing and Springer, Heidelberg.

Wang, C.B., Rao, J.F., Chen, J.G., Ouyang, Y.P., Qi, S.J., Li, Q., 2017b. Prospectivity mapping for ‘‘Zhuxi-type” copper-tungsten polymetallic deposits in the Jingdezhen region of Jiangxi Province, South China. Ore Geology Reviews 89, 1–14.

Wang, D.Z., Shu, L.S., 2012. Late Mesozoic basin and range tectonics and related magmatism in Southeast China. Geoscience Frontiers 3, 109–124.

Wang, D.Z., Zhou, X.M., 2002. Petrogenesis of the Late Mesozoic granitic volcanic-intrusive complexes and crustal evolution in Southeastern China. Science Press, Beijing (in Chinese).

Wang, F.Y., Li, C.Y., Ling, M.X., Zhang, H., Sun, Y.L., Sun, W.D., 2011c. Geochronology of the Xihuashan tungsten deposit in southeastern China: Constraints from Re-Os and U-Pb dating. Resource Geology 61, 414–423.

Wang, J., Li, Z.X., 2003. History of Neoproterozoic rift basins in South China: implications for Rodinia break-up. Precambrian Research 122, 141–158.

Wang, L., 2010. Metallogenic model and prospecting potential in Dabaoshan molybdenum polymetallic ore deposit, North Guangdong Province. (Ph.D. thesis). China University of Geosciences, Wuhan, pp. 1–119 (in Chinese with English abstract).

Wang, L., Hu, M.A., Yang, Z., Qu, W.J., Xia, J.L., Chen, K.X., 2011d. U-Pb and Re-Os geochronology and geodynamic setting of the Dabaoshan polymetallic deposit, northern Guangdong Province, South China. Ore Geology Reviews 43, 40–49.

Wang, M., Dai, C.G., Wang, X.H., Chen, J.S., Ma, H.Z., 2011b. In-situ zircon geochronology and Hf isotope of muscovite-bearing leucogranites from Fanjingshan, Guizhou Province, and constraints on continental growth of the Southern China block. Earth Science Frontiers 18, 213–223 (in Chinese with English abstract).

Wang, Q., Li, J.W., Jian, P., Zhao, Z.H., Xiong, X.L., Bao, Z.W., Xu, J.F., Li, C.F., Ma, J.L., 2005b. Alkaline syenites in eastern Cathaysia (South China): link to Permian-Triassic transtension. Earth and Planetary Science Letters 230, 339– 354.

Wang, R.C., Xie, L., Lu, J.J., Zhu, J.C., Chen, J., 2017c. Diversity of Mesozoic tin-bearing granites in the Nanling and adjacent regions, South China: Distinctive mineralogical patterns. Science China Earth Sciences 60, 1909–1919.

Wang, X.F., Qi, H.W., Hu, R.Z., Qu, W.J., Peng, J.T., Bi, X.W., 2010b. Re-Os isotopic chronology of molybdenites from Hongling tungsten deposit of Guangdong Province and its geological significance. Mineral Deposits 29, 415–426 (in Chinese with English abstract).

Wang, X.L., Zhou, J.C., Chen, X., Zhang, F.F., Sun, Z.M., 2017a. Formation and evolution of the Jiangnan Orogen. Bulletin of Mineralogy, Petrology and Geochemistry 36, 714–735 (in Chinese with English abstract).

Wang, X.L., Zhou, J.C., Griffin, W.L., Wang, R.C., Qiu, J.S., O'Reilly, S.Y., Xu, X.S., Liu, X.M., Zhang, G.L., 2007a. Detrital zircon geochronology of Precambrian basement sequences in the Jiangnan orogen: Dating the assembly of the Yangtze and Cathaysia Blocks. Precambrian Research 159, 117–131.

Wang, Y.F., Yang, H.M., Zhang, L.G., Lu, S.S., Yang, Z.F., Qiu, X.F., Liu, Z.P., 2017d. Metallogenic epoch and ore-forming material source of the Tongshanling Pb-Zn polymetallic deposit in southern Hunan Province: Evidence from Sm-Nd isochron age and Pb isotope. Geological Bulletin of China 36, 875–884 (in Chinese with English abstract).

Wang, Y.J., Fan, W.M., Guo, F., 2003a. Geochemistry of early Mesozoic potassium-rich diorites-granodiorites in southeastern Hunan Province, South China: Petrogenesis and tectonic implications. Geochemical Journal 37, 427–448.

Wang, Y.J., Fan, W.M., Guo, F., Li, H.M., Liang, X.Q., 2002b. U-Pb dating of early Mesozoic granodioritic intrusions in southeastern Hunan Province, South China and its petrogenetic implications. Science in China Series D: Earth Sciences 45, 280–288.

Wang, Y.J., Fan, W.M., Guo, F., Peng, T.P., Li, C.W., 2003b. Geochemistry of Mesozoic mafic rocks adjacent to the Chenzhou-Linwu fault, South China: Implications for the lithospheric boundary between the Yangtze and Cathaysia blocks. International Geology Review 45, 263–286.

Wang, Y.J., Fan, W.M., Sun, M., Liang, X.Q., Zhang, Y.H., Peng, T.P., 2007b. Geochronological, geochemical and geothermal constraints on petrogenesis of the Indosinian peraluminous granites in the South China Block: A case study in the Hunan Province. Lithos 96, 475–502.

Wang, Y.J., Fan, W.M., Zhang, G.W., Zhang, Y.H., 2013. Phanerozoic tectonics of the South China Block: Key observations and controversies. Gondwana Research 23, 1273–1305.

Wang, Y.J., Zhang, A.M., Fan, W.M., Zhao, G.C., Zhang, G.W., Zhang, Y.Z., Zhang, F.F., Li, S.Z., 2011a. Kwangsian crustal anatexis within the eastern South China Block: Geochemical, zircon U-Pb geochronological and Hf isotopic fingerprints from the gneissoid granites of Wugong and Wuyi-Yunkai Domains. Lithos 127, 239–260.

Wang, Y.J., Zhang, F.F., Fan, W.M., Zhang, G.W., Chen, S.Y., Cawood, P.A., Zhang, A.M., 2010a. Tectonic setting of the South China Block in the early Paleozoic: Resolving intracontinental and ocean closure models from detrital zircon U-Pb geochronology. Tectonics 29, TC6020, doi:10.1029/2010TC002750.

Wang, Y.J., Zhang, Y., Fan, W.M., Xi, X.W., Guo, F., Lin, G., 2002a. Numerical modeling of the formation of Indo-Sinian peraluminous granitoids in Hunan Province: Basaltic underplating versus tectonic thickening. Science in China Series D: Earth Sciences 45, 1042–1056.

Wang, Y.J., Zhang, Y.H., Fan, W.M., Peng, T.P., 2005a. Structural signatures and $^{40}Ar/^{39}Ar$ geochronology of the Indosinian Xuefengshan tectonic belt, South China Block. Journal of Structural Geology 27, 985–998.

Wang, Y.L., Pei, R.F., Li, J.W., Wang, H.L., Liu, X.F., 2009. Geochemical characteristics of granites from the Jiangjunzhai tungsten deposit of southeast Hunan Province and its Re-Os isotopic dating. Rock and Mineral Analysis 28, 274–278 (in Chinese with English abstract).

Wang, Y.Y., van den Kerkhof, A., Xiao, Y.L., Sun, H., Yang, X.Y., Lai, J.Q., Wang, Y.G., 2017e. Geochemistry and fluid inclusions of scheelite-mineralized granodiorite porphyries from southern Anhui Province, China. Ore Geology Reviews 89, 988–1005.

Webster, J.D., Holloway, J.R., 1990. Partitioning of F and Cl between magmatic hydrothermal fluids and highly evolved granitic magmas, in: Stein, H.J., Hannah, J.L. (Eds.), Ore-bearing granite systems; Petrogenesis and mineralizing processes. Geological Society of America Special Paper 246, 21–34.

Wei, D.F., Bao, Z.Y., Fu, J.M., 2007. Geochemical characteristics and zircon SHRIMP U-Pb dating of the Tongshanling granite in Hunan province, South China. Geotectonica et Metallogenia 31, 482–489 (in Chinese with English abstract).

Wei, W., Chen, Y., Faure, M., Martelet, G., Lin, W., Wang, Q.C., Yan, Q.R., Hou, Q.L., 2016. An early extensional event of the South China Block during the Late Mesozoic recorded by the emplacement of the Late Jurassic syntectonic Hengshan Composite Granitic Massif (Hunan, SE China). Tectonophysics 672–673, 50–67.

Wei, W., Chen, Y., Faure, M., Shi, Y.H., Martelet, G., Hou, Q.L., Lin, W., Le Breton, N., Wang, Q.C., 2014a. A multidisciplinary study on the emplacement mechanism of the Qingyang-Jiuhua Massif in Southeast China and its tectonic bearings. Part I: Structural geology, AMS and paleomagnetism. Journal of Asian Earth Sciences 86, 76–93.

Wei, W., Martelet, G., Le Breton, N., Shi, Y.H., Faure, M., Chen, Y., Hou, Q.L., Lin, W., Wang, Q.C., 2014b. A multidisciplinary study of the emplacement mechanism of the Qingyang-Jiuhua massif in Southeast China and its tectonic bearings. Part II: Amphibole geobarometry and gravity modeling. Journal of Asian Earth Sciences 86, 94–105.

Wei, W.F., Hu, R.Z., Peng, J.T., Bi, X.W., Song, S.Q., Shi, S.H., 2011. Fluid mixing in Xihuashan tungsten deposit, Southern Jiangxi Province: Hydrogen and oxygen isotope simulation analysis. Geochimica 40, 45–55 (in Chinese with English abstract).

Werner, A.B.T., Sinclair, W.D., Amey, E.B., 2014. International strategic mineral issues summary report-Tungsten (U.S. Geological Survey Circular 930-O, ver. 1.1, November 2014). U.S. Government Printing Office, Washington.

White, A.J.R., Chappell, B.W., 1977. Ultrametamorphism and granitoid genesis. Tectonophysics 43, 7–22.

White, A.J.R., Chappell, B.W., Wyborn, D., 1999. Application of the restite model to the Deddick granodiorite and its enclaves–a reinterpretation of the observations and data of Maas et al. (1997). Journal of Petrology 40, 413–421.

Whitney, J.A., 1988. The origin of granites: The role and source of water in the evolution of granitic magmas. Geological Society of America Bulletin 100, 1886–1997.

Wiedenbeck, M., AllÉ, P., Corfu, F., Griffin, W.L., Meier, M., Oberli, F., Von Quadt, A., Roddick, J.C., Spiegel, W., 1995. Three natural zircon standards for U-Th-Pb, Lu-Hf, trace element and REE analyses. Geostandards Newsletter 19, 1–23.

Wolf, M., Romer, R.L., Franz, L., López-Moro, F.J., 2018. Tin in granitic melts: The role of melting temperature and protolith composition. Lithos 310–311, 20–30.

Wolf, M.B., Wyllie, P.J., 1994. Dehydration-melting of amphibolite at 10 kbar: the effects of temperature and time. Contributions to Mineralogy and Petrology 115, 369–383.

Wood, S.A., Samson, I.M., 2000. The hydrothermal geochemistry of tungsten in granitoid environments: I. Relative solubilities of ferberite and scheelite as a function of T, P, pH, and m_{NaCl}. Economic Geology 95, 143–182.

Wright, J.B., 1969. A simple alkalinity ratio and its application to questions of non-orogenic granite genesis. Geological Magazine 106, 370–384.

Wu, F.Y., Li, X.H., Yang, J.H., Zheng, Y.F., 2007. Discussions on the petrogenesis of granites. Acta Petrologica Sinica 23, 1217–1238 (in Chinese with English abstract).

Wu, F.Y., Liu, X.C., Ji, W.Q., Wang, J.M., Yang, L., 2017. Highly fractionated granites: Recognition and research. Science China Earth Sciences 60, 1201–1219.

Wu, G.Y., Ma, T.Q., Bai, D.Y., Li, J.D., Che, Q.J., Wang, X.H., 2005. Petrological and geochemical characteristics of granodioritic cryptoexplosion breccia and zircon SHRIMP dating in the Baoshan area, Hunan Province. Geoscience 19, 198–204 (in Chinese with English abstract).

Wu, G.Y., Ma, T.Q., Feng, Y.F., Yan, Q.R., Liu, F.G., Bo, D.Y., 2008. Geological and geochemical characteristics and genesis of the Caledonian Wanyangshan granite in the Nanling Mountains, South China. Geology in China 35, 608–617 (in Chinese with English abstract).

Wu, J., Liang, H.Y., Huang, W.T., Wang, C.L., Sun, W.D., Sun, Y.L., Li, J., Mo, J.H., Wang, X.Z., 2012. Indosinian isotope ages of plutons and deposits in southwestern Miaoershan-Yuechengling, northeastern Guangxi and implications on Indosinian mineralization in South China. Chinese Science Bulletin 57, 1024–1035.

Wu, S.H., Dai, P., Wang, X.D., 2016. C, H, O, Pb isotopic geochemistry of W polymetallic skarn-greisen and Pb-Zn-Ag veins in Shizhuyuan orefield, Hunan Province. Mineral Deposits 35, 633–647 (in Chinese with English abstract).

Wu, Y.B., Zheng, Y.F., 2004. Genesis of zircon and its constraints on interpretation of U-Pb age. Chinese Science Bulletin 49, 1554–1569.

Xi, C.Z., Dai, T.G., Liu, W.H., 2009. Lead and sulfur isotope geochemistry of the Huangshaping lead-zinc Deposit, Hunan Province. Acta Geoscientica Sinica 30, 89–94 (in Chinese with English abstract).

Xia, Y., 1985. The geochemical features and genesis of Heiwan River W-Sn deposit in Guizhou. Guizhou Geology 3, 253–262 (in Chinese with English abstract).

Xiang, L., Wang, R.C., Erdmann, S., Sizaret, S., Lu, J.J., Zhang, W.L., Xie, L., Che, X.D., Zhang, R.Q., 2018. Neoproterozoic mineralization in a hydrothermal cassiterite-sulfide deposit at Jiumao, northern Guangxi, South China: Mineral-scale constraints on metal origins and ore-forming processes. Ore Geology Reviews 94, 172–192.

Xie, G.Q., Mao, J.W., Bagas, L., Fu, B., Zhang, Z.Y., 2018. Mineralogy and titanite geochronology of the Caojiaba W deposit, Xiangzhong metallogenic province, southern China: implications for a distal reduced skarn W formation. Mineralium Deposita, doi: https://doi.org/10.1007/s00126-018-0816-2.

Xie, Y.C., Lu, J.J., Ma, D.S., Zhang, R.Q., Gao, J.F., Yao, Y., 2013. Origin of granodiorite porphyry and mafic microgranular enclave in the Baoshan Pb-Zn polymetallic deposit, southern Hunan Province: Zircon U-Pb chronological, geochemical and Sr-Nd-Hf isotopic constraints. Acta Petrologica Sinica 29, 4186–4214 (in Chinese with English abstract).

Xie, Y.C., Lu, J.J., Yang, P., Ma, D.S., Xu, Z.W., Zhang, R.Q., Cai, Y., Ding, T., 2015. S, Pb, C and O isotopic characteristics and sources of metallogenic materials of Baoshan Pb-Zn deposit, southern Hunan province. Mineral Deposits 34, 333–351 (in Chinese with English abstract).

Xu, K.Q., Hu, S.X., Sun, M.Z., Ye, J., 1982. On the two genetic series of granites in southeastern China and their metallogenetic characteristics. Mineral Deposits 1, 1–14 (in Chinese with English abstract).

Xu, K.Q., Hu, S.X., Sun, M.Z., Zhang, J.R., Ye, J., 1983. On the genetic series of granites, as exemplified by the Mesozoic granites of South China. Acta Geologica Sinica 57, 107–118 (in Chinese with English abstract).

Xu, T., Wang, Y., 2014. Sulfur and lead isotope composition on tracing ore-forming materials of the Xihuashan tungsten deposit in Southern Jiangxi. Bulletin of Mineralogy, Petrology and Geochemistry 33, 342–347 (in Chinese with English abstract).

Xu, W.X., Li, H., Chen, M.Y., Huang, D.X., Zhang, F.T., Wang, L.M., 2008. Isotope evidence of material sources of the Dabaoshan polymetallic deposit. Acta Geoscientica Sinica 29, 684–690 (in Chinese with English abstract).

Xu, Y.G., Chung, S.L., Jahn, B.M., Wu, G.Y., 2001. Petrologic and geochemical constraints on the petrogenesis of Permian–Triassic Emeishan flood basalts in southwestern China. Lithos 58, 145–168.

Yan, J., Hou, T.J., Wang, A.G., Wang, D.E., Zhang, D.Y., Weng, W.F., Liu, J.M., Liu, X.Q., Li, Q.Z., 2017. Petrogenetic contrastive studies on the Mesozoic early stage ore-bearing and late stage ore-barren granites from the southern Anhui Province. Science China Earth Sciences 60, 1920–1941.

Yang, J.H., Peng, J.T., Zhao, J.H., Fu, Y.Z., Yang, C., Hong, Y.L., 2012. Petrogenesis of the Xihuashan granite in southern Jiangxi Province, South China: Constraints from zircon U-Pb geochronology, geochemistry and Nd isotopes. Acta Geologica Sinica (English Edition) 86, 131–152.

Yang, J.H., Peng, J.T., Zheng, Y.F., Hu, R.Z., Bi, X.W., Zhao, J.H., Huang, J.C., Zhang, B.L., 2016. Petrogenesis of the Mesozoic Shuikoushan peraluminous I-type granodioritic intrusion in Hunan Province, South China: Middle-lower crustal reworking in an extensional tectonic setting. Journal of Asian Earth Sciences 123, 224–242.

Yang, J.H., Wu, F.Y., Chung, S.L., Wilde, S.A., Chu, M.F., 2004. Multiple sources for the origin of granites: Geochemical and Nd/Sr isotopic evidence from the Gudaoling granite and its mafic enclaves, northeast China. Geochimica et Cosmochimica Acta 68, 4469–4483.

Yang, J.H., Wu, F.Y., Wilde, S.A., Xie, L.W., Yang, Y.H., Liu, X.M., 2007. Tracing magma mixing in granite genesis: in situ U-Pb dating and Hf-isotope analysis of zircons. Contributions to Mineralogy and Petrology 153, 177–190.

Yang, L., Zhao, R., Wang, Q.F., Liu, X.F., Carranza, E.J.M., 2018. Fault geometry and fluid-rock reaction: Combined controls on mineralization in the Xinli gold deposit, Jiaodong Peninsula, China. Journal of Structural Geology 111, 14–26.

Yang, Z., Wang, R.C., Zhang, W.L., Chu, Z.Y., Chen, J., Zhu, J.C., Zhang, R.Q., 2014. Skarn-type tungsten mineralization associated with the Caledonian (Silurian) Niutangjie granite, northern Guangxi, China. Science China Earth Sciences 57, 1551–1566.

Yang, Z., Zhang, W.L., Wang, R.C., Lu, J.J., Xie, L., Che, X.D., 2013. Geochronology and geochemical characteristics of metallogenetic pluton in the Youmaling tungsten mining area, northern Guangxi Province, and its geological significance. Geological Journal of China Universities 19, 159–172 (in Chinese with English abstract).

Yao, J.L., Shu, L.S., Santosh, M., Zhao, G.C., 2014a. Neoproterozoic arc-related mafic-ultramafic rocks and syn-collision granite from the western segment of the Jiangnan Orogen, South China: Constraints on the Neoproterozoic assembly of the Yangtze and Cathaysia Blocks. Precambrian Research 243, 39–62.

Yao, J.M., Hua, R.M., Lin, J.F., 2006. REE, Pb-S isotope geochemistry, and Rb-Sr isochron age of pyrites in the Baoshan deposit, South Hunan Province, China. Acta Geologica Sinica 80, 1045–1054 (in Chinese with English abstract).

Yao, J.M., Hua, R.M., Qu, W.J., Qi, H.W., Lin, J.F., Du, A.D., 2007. Re-Os isotope dating of molybdenites in the Huangshaping Pb-Zn-W-Mo polymetallic deposit, Hunan Province, South China and its geological significance. Science in China Series D: Earth Sciences 50, 519–526.

Yao, Y., Chen, J., Lu, J.J., Wang, R.C., Zhang, R.Q., 2014b. Geology and genesis of the Hehuaping magnesian skarn-type cassiterite-sulfide deposit, Hunan Province, Southern China. Ore Geology Reviews 58, 163–184.

Yi, H., Xu, S.Y., 2006. Geochemical characteristics of Antangling lead-zinc deposit in the Tongshanling orefield. Geology and Prospecting 42, 20–24 (in Chinese with English abstract).

Yuan, S.D., Williams-Jones, A.E., Mao, J.W., Zhao, P.L., Yan, C., Zhang, D.L., 2018. The origin of the Zhangjialong tungsten deposit, South China: Implications for W-Sn mineralization in large granite batholiths. Economic Geology 113, 1193–1208.

Yuan, Y.B., Yuan, S.D., Chen, C.J., Huo, R., 2014. Zircon U-Pb ages and Hf isotopes of the granitoids in the Huangshaping mining area and their geological significance. Acta Petrologica Sinica 30, 64–78 (in Chinese with English abstract).

Zartman, R.E., Doe, B.R., 1981. Plumbotectonics-the model. Tectonophysics 75, 135–162.

Zaw, K., Peters, S.G., Cromie, P., Burrett, C., Hou, Z.Q., 2007. Nature, diversity of deposit types and metallogenic relations of South China. Ore Geology Reviews 31, 3–47.

Zeng, Q.D., Wang, Z.C., He, H.Y., Wang, Y.B., Zhang, S., Liu, J.M., 2014. Multiple isotope composition (S, Pb, H, O, He, and Ar) and genetic implications for gold deposits in the Jiapigou gold belt, Northeast China. Mineralium Deposita 49, 145–164.

Zeng, Z.L., Zhang, Y.Z., Chen, Z.H., Chen, Y.C., Zhu, X.P., Tong, Q.Q., Zheng, B.H., Zhou, Y., 2011. Geological characteristics and metallogenic epoch of Pangushan W-Bi(Te) ore deposit in Yudu County, Jiangxi province. Mineral Deposits 30, 949–958 (in Chinese with English abstract).

Zeng, Z.L., Zhang, Y.Z., Zhu, X.P., Chen, Z.H., Wang, C.H., Qu, W.J., 2009. Re-Os isotopic dating of molybdenite from the Maoping tungsten-tin deposit in Chongyi County of southern Jiangxi Province and its geological significance. Rock and Mineral Analysis 28, 209–214 (in Chinese with English abstract).

Zhang, D., Zhang, W.L., Wang, R.C., Chu, Z.Y., Gong, M.W., Jiang, G.X., 2015b. Quartz-vein type tungsten mineralization associated with the Indosinian (Triassic) Gaoling granite, Miao'ershan area, northern Guangxi. Geological Review 61, 817–834 (in Chinese with English abstract).

Zhang, F.F., Wang, Y.J., Fan, W.M., Zhang, A.M., Zhang, Y.Z., 2010. LA-ICPMS zircon U-Pb geochronology of late Early Paleozoic granites in eastern Hunan and western Jiangxi provinces, South China. Geochimica 39, 414–426 (in Chinese with English abstract).

Zhang, F.F., Wang, Y.J., Zhang, A.M., Fan, W.M., Zhang, Y.Z., Zi, J.W., 2012. Geochronological and geochemical constraints on the petrogenesis of Middle Paleozoic (Kwangsian) massive granites in the eastern South China Block. Lithos 150, 188–208.

Zhang, G.W., Guo, A.L., Wang, Y.J., Li, S.Z., Dong, Y.P., Liu, S.F., He, D.F., Cheng, S.Y., Lu, R.K., Yao, A.P., 2013. Tectonics of South China Continent and its implications. Science China Earth Sciences 56, 1804–1828.

Zhang, H.F., Lu, J.J., Wang, R.C., Ma, D.S., Zhu, J.C., Zhang, R.Q., 2014. Petrogenesis of the concealed Daqiling intrusion in Guangxi and its tectonic significance: Constraints from geochemistry, zircon U-Pb dating and Nd-Hf isotopic compositions. Science China Earth Sciences 57, 1723–1740.

Zhang, J.J., Wang, T., Castro, A., Zhang, L., Shi, X.J., Tong, Y., Zhang, Z.C., Guo, L., Yang, Q.D., Iaccheri, L.M., 2016b. Multiple mixing and hybridization from magma source to final emplacement in the Permian Yamatu pluton, the Northern Alxa Block, China. Journal of Petrology 57, 933–980.

Zhang, K.J., Cai, J.X., 2009. NE-SW-trending Hepu-Hetai dextral shear zone in southern China: Penetration of the Yunkai Promontory of South China into Indochina. Journal of Structural Geology 31, 737–748.

Zhang, L.G., 1989. Stable isotope geochemistry of the Qianlishan granites and tungsten-polymetallic deposits in Dongpo area, Hunan. Journal of Guilin College of Geology 9, 259–267 (in Chinese with English abstract).

Zhang, Q., Zhang, R.Q., Gao, J.F., Lu, J.J., Wu, J.W., 2018b. In-situ LA-ICP-MS trace element analyses of scheelite and wolframite: Constraints on the genesis of veinlet-disseminated and vein-type tungsten deposits, South China. Ore Geology Reviews 99, 166–179.

Zhang, R.Q., 2014. Petrogenesis and metallogeny of the W- and Sn-bearing granites in southern Hunan province: Case study from Wangxianling and Xintianling. (Ph.D. thesis). Nanjing University, Nanjing, pp. 1–193 (in Chinese with English abstract).

Zhang, R.Q., Lehmann, B., Seltmann, R., Sun, W.D., Li, C.Y., 2017c. Cassiterite U-Pb geochronology constrains magmatic-hydrothermal evolution in complex evolved granite systems: The classic Erzgebirge tin province (Saxony and Bohemia). Geology 45, 1095–1098.

Zhang, R.Q., Lu, J.J., Lehmann, B., Li, C.Y., Li, G.L., Zhang, L.P., Guo, J., Sun, W.D., 2017b. Combined zircon and cassiterite U-Pb dating of the Piaotang granite related tungsten-tin deposit, southern Jiangxi tungsten district, China. Ore Geology Reviews 82, 268–284.

Zhang, R.Q., Lu, J.J., Wang, R.C., Yang, P., Zhu, J.C., Yao, Y., Gao, J.F., Li, C., Lei, Z.H., Zhang, W.L., Guo, W.M., 2015a. Constraints of in situ zircon and cassiterite U-Pb, molybdenite Re-Os and muscovite ^{40}Ar-^{39}Ar ages on multiple generations of granitic magmatism and related W-Sn mineralization in the Wangxianling area, Nanling Range, South China. Ore Geology Reviews 65, 1021–1042.

Zhang, S.M., Chen, Z.H., Shi, G.H., Li, L.X., Qu, W.J., Li, C., 2011b. Re-Os isotopic dating of molybdenite

from Dajishan tungsten deposit in Jiangxi Province. Mineral Deposits 30, 1113–1121 (in Chinese with English abstract).

Zhang, S.T., Ma, D.S., Lu, J.J., Zhang, R.Q., Cai, Y., Ding, C.C., 2016a. Geochronology, Hf isotopic compositions and geochemical characteristics of the Pingying granite pluton in Northern Guangxi, South China, and its geological significance. Geological Journal of China Universities 22, 92–104 (in Chinese with English abstract).

Zhang, W.L., 2004. Study on the characteristics, origin and related metallogeny of granites in Dajishan and Piaotang, Southern Jiangxi Province. (Ph.D. thesis). Nanjing University, Nanjing, pp. 1–159 (in Chinese with English abstract).

Zhang, W.L., Hua, R.M., Wang, R.C., Chen, P.R., Li, H.M., 2006. New dating of the Dajishan granite and related tungsten mineralization in southern Jiangxi. Acta Geologica Sinica 80, 956–962 (in Chinese with English abstract).

Zhang, W.L., Hua, R.M., Wang, R.C., Li, H.M., Qu, W.J., Ji, J.Q., 2009. New dating of the Piaotang granite and related tungsten mineralization in southern Jiangxi. Acta Geologica Sinica 83, 659–670 (in Chinese with English abstract).

Zhang, W.L., Wang, R.C., Lei, Z.H., Hua, R.M., Zhu, J.C., Lu, J.J., Xie, L., Che, X.D., Zhang, R.Q., Yao, Y., Chen, J., 2011a. Zircon U-Pb dating confirms existence of a Caledonian scheelite-bearing aplitic vein in the Penggongmiao granite batholith, South Hunan. Chinese Science Bulletin 56, 2031–2036.

Zhang, X.S., Xu, X.S., Xia, Y., Liu, L., 2017d. Early Paleozoic intracontinental orogeny and post-orogenic extension in the South China Block: Insights from volcanic rocks. Journal of Asian Earth Sciences 141, 24–42.

Zhang, Y., Gao, J.F., Ma, D.S., Pan, J.Y., 2018a. The role of hydrothermal alteration in tungsten mineralization at the Dahutang tungsten deposit, South China. Ore Geology Reviews 95, 1008–1027.

Zhang, Y., Yang, J.H., Chen, J.Y., Wang, H., Xiang, Y.X., 2017a. Petrogenesis of Jurassic tungsten-bearing granites in the Nanling Range, South China: Evidence from whole-rock geochemistry and zircon U-Pb and Hf-O isotopes. Lithos 278–281, 166–180.

Zhao, G.C., Cawood, P.A., 2012. Precambrian geology of China. Precambrian Research 222–223, 13–54.

Zhao, K.D., Jiang, S.Y., Zhu, J.C., Li, L., Dai, B.Z., Jiang, Y.H., Ling, H.F., 2010. Hf isotopic composition of zircons from the Huashan-Guposhan intrusive complex and their mafic enclaves in northeastern Guangxi: Implication for petrogenesis. Chinese Science Bulletin 55, 509–519.

Zhao, P.L., Yuan, S.D., Mao, J.W., Santosh, M., Li, C., Hou, K.J., 2016b. Geochronological and petrogeochemical constraints on the skarn deposits in Tongshanling ore district, southern Hunan Province: Implications for Jurassic Cu and W metallogenic events in South China. Ore Geology Reviews 78, 120–137.

Zhao, P.L., Yuan, S.D., Yuan, Y.B., 2016a. Zircon LA-MC-ICP-MS U-Pb dating of the Xianglinpu granites from the Weijia tungsten deposit in southern Hunan Province and its implications for the Late Jurassic tungsten

metallogenesis in the westernmost Nanling W-Sn metallogenic belt. Geology in China 43, 120–131 (in Chinese with English abstract).

Zhao, W.W., Zhou, M.F., 2018. Mineralogical and metasomatic evolution of the Jurassic Baoshan scheelite skarn deposit, Nanling, South China. Ore Geology Reviews 95, 182–194.

Zhao, W.W., Zhou, M.F., Li, Y.H.M., Zhao, Z., Gao, J.F., 2017. Genetic types, mineralization styles, and geodynamic settings of Mesozoic tungsten deposits in South China. Journal of Asian Earth Sciences 137, 109–140.

Zhao, W.W., Zhou, M.F., Williams-Jones, A.E., Zhao, Z., 2018. Constraints on the uptake of REE by scheelite in the Baoshan tungsten skarn deposit, South China. Chemical Geology 477, 123–136.

Zhao, Z., Chen, Y.C., Zeng, Z.L., Chen, Z.H., Wang, D.H., Zhao, B., Zhang, J.J., 2013. Geological characteristics and petrogenic & metallogenic ages of the Yanqian tungsten deposit in eastern Nanling region. Journal of Jilin University (Earth Science Edition) 43, 1828–1839 (in Chinese with English abstract).

Zharikov, V.A., 1970. Skarns. International Geology Review 12, 541–559, 619–647, 760–775.

Zheng, Q.R., 1983. Calculation of the Fe^{3+} and Fe^{2+} contents in silicate and Ti-Fe oxide minerals from EMPA data. Acta Mineralogica Sinica 3, 55–62 (in Chinese with English abstract).

Zhong, Y.F., Ma, C.Q., She, Z.B., Lin, G.C., Xu, H.J., Wang, R.J., Yang, K.G., Liu, Q., 2005. SHRIMP U-Pb zircon geochemistry of the Jiuling granitic complex batholith in Jiangxi Province. Earth Science-Journal of China University of Geosciences 30, 685–691 (in Chinese with English abstract).

Zhou, J.C., Jiang, S.Y., Wang, X.L., Ying, J.H., Zhang, M.Q., 2006c. Re-Os isotopic compositions of late Mesozoic mafic rocks from southeastern coast of China. Acta Petrologica Sinica 22, 407–413 (in Chinese with English abstract).

Zhou, J.C., Wang, D.Z., Wang, X., Chen, X.M., 1999. An understanding of the origin of the Tonglu Early Cretaceous volcanic-intrusive rocks. Acta Petrologica Sinica 15, 263–271 (in Chinese with English abstract).

Zhou, L.Q., Li, G.L., Tang, A., Su, Y., 2016. Ore-forming fluids characteristics of quartz-vein tungsten deposits in southern Jiangxi Province. East China Geology 37, 136–146 (in Chinese with English abstract).

Zhou, M.F., Arndt, N.T., Malpas, J., Wang, C.Y., Kennedy, A.K., 2008. Two magma series and associated ore deposit types in the Permian Emeishan large igneous province, SW China. Lithos 103, 352–368.

Zhou, M.F., Gao, J.F., Zhao, Z., Zhao, W.W., 2018. Introduction to the special issue of Mesozoic W-Sn deposits in South China. Ore Geology Reviews, doi: https://doi.org/10.1016/j.oregeorev.2018.07.023.

Zhou, M.F., Ma, Y.X., Yan, D.P., Xia, X.P., Zhao, J.H., Sun, M., 2006b. The Yanbian Terrane (Southern Sichuan Province, SW China): A Neoproterozoic arc assemblage in the western margin of the Yangtze Block. Precambrian Research 144, 19–38.

Zhou, X., Yu, J.H., 2001. Geochemistry of the granitoids in Mesozoic metamorphic belt of coastal Fujian Province. Geochimica 30, 282–292 (in Chinese with English abstract).

Zhou, X.M., 2003. My thinking about granite geneses of South China. Geological Journal of China Universities 9, 556–565 (in Chinese with English abstract).

Zhou, X.M., 2007. Petrogenesis of the Late Mesozoic granitoids and lithosphere dynamic evolution in the Nanling Range. Science Press, Beijing (in Chinese).

Zhou, X.M., Li, W.X., 2000. Origin of Late Mesozoic igneous rocks in Southeastern China: implications for lithosphere subduction and underplating of mafic magmas. Tectonophysics 326, 269–287.

Zhou, X.M., Sun, T., Shen, W.Z., Shu, L.S., Niu, Y.L., 2006a. Petrogenesis of Mesozoic granitoids and volcanic rocks in South China: a response to tectonic evolution. Episodes 29, 26–33.

Zhou, Y.Z., Li, X.Y., Zheng, Y., Shen, W.J., He, J.G., Yu, P.P., Niu, J., Zeng, C.Y., 2017. Geological settings and metallogenesis of Qinzhou Bay-Hangzhou Bay orogenic juncture belt, South China. Acta Petrologica Sinica 33, 667–681 (in Chinese with English abstract).

Zhu, J.C., Chen, J., Wang, R.C., Lu, J.J., Xie, L., 2008. Early Yanshanian NE trending Sn/W-bearing A-type granites in the western-middle part of the Nanling Mts region. Geological Journal of China Universities 14, 474–484 (in Chinese with English abstract).

Zhu, X.Y., Wang, J.B., Wang, Y.L., Cheng, X.Y., Fu, Q.B., 2012. Sulfur and lead isotope constraints on ore formation of the Huangshaping W-Mo-Bi-Pb-Zn polymetallic ore deposit, Hunan Province, South China. Acta Petrologica Sinica 34, 261–266 (in Chinese with English abstract).

Zhu, X.Y., Wang, J.B., Wang, Y.L., Cheng, X.Y., Fu, Q.B., Fu, M., Yu, Z.F., 2014. Characteristics of stable isotopes S, Pb, O, and H in the Yaogangxian tungsten deposits, Hunan Province. Geology and Exploration 50, 947–960 (in Chinese with English abstract).

Zhu, Y.H., 2010. Geological character and ore-controlling factors of Biaoshuiyan tin (tungsten) deposit in Fanjing Mountain. Geology and Exploration 46, 244–251 (in Chinese with English abstract).

Zuo, C.H., Lu, R., Zhao, Z.X., Xu, Z.W., Lu, J.J., Wang, R.C., Chen, J.Q., 2014. Characterization of element geochemistry, LA-ICP-MS zircon U-Pb age, and Hf isotope of granodiorite in the Shuikoushan deposit, Changning, Hunan Province. Geological Review 60, 811–823 (in Chinese with English abstract).

Appendices

Appendix 4-1. LA-ICP-MS zircon U-Pb isotope analyses of granitoids from the Tongshanling-Weijia area

Spot	Elements (ppm)			Isotopic ratios						Ages (Ma)					
	^{232}Th	^{238}U	Th/U	^{207}Pb/^{206}Pb	1σ	^{207}Pb/^{235}U	1σ	^{206}Pb/^{238}U	1σ	^{207}Pb/^{206}Pb	1σ	^{207}Pb/^{235}U	1σ	^{206}Pb/^{238}U	1σ
Tongshanling granodiorite porphyry															
TSL001-01	453	2476	0.18	0.04859	0.00184	0.16772	0.00588	0.02503	0.00036	128	88	157	5	159	2
TSL001-02	365	1482	0.25	0.04931	0.00205	0.17024	0.00710	0.02504	0.00044	163	97	160	6	159	3
TSL001-03	299	827	0.36	0.05178	0.00106	0.17960	0.00396	0.02516	0.00041	276	48	168	3	160	3
TSL001-04	349	1157	0.30	0.04984	0.00203	0.17294	0.00692	0.02517	0.00047	188	96	162	6	160	3
TSL001-05	368	648	0.57	0.04929	0.00123	0.17108	0.00441	0.02518	0.00039	162	60	160	4	160	2
TSL001-06	745	1396	0.53	0.04899	0.00106	0.17053	0.00391	0.02525	0.00045	147	52	160	3	161	3
TSL001-07	262	588	0.45	0.04926	0.00117	0.17134	0.00426	0.02523	0.00039	160	57	161	4	161	2
TSL001-08	510	1579	0.32	0.04936	0.00171	0.17181	0.00610	0.02526	0.00045	165	83	161	5	161	3
TSL001-09	266	330	0.80	0.05226	0.00172	0.18349	0.00602	0.02547	0.00042	297	77	171	5	162	3
TSL001-10	228	469	0.49	0.05149	0.00123	0.18077	0.00450	0.02546	0.00040	263	56	169	4	162	3
TSL001-11	365	954	0.38	0.04932	0.00095	0.17464	0.00367	0.02568	0.00039	163	46	163	3	163	2
TSL001-12	255	1091	0.23	0.04931	0.00104	0.17400	0.00390	0.02559	0.00039	163	50	163	3	163	2
TSL001-13	255	1160	0.22	0.04933	0.00215	0.17424	0.00763	0.02562	0.00047	164	101	163	7	163	3
TSL001-14	409	1243	0.33	0.05258	0.00222	0.18724	0.00741	0.02583	0.00038	311	98	174	6	164	2
TSL001-15	825	2320	0.36	0.04936	0.00084	0.17513	0.00335	0.02573	0.00039	165	41	164	3	164	2
TSL001-16	678	1856	0.37	0.05468	0.00091	0.19425	0.00363	0.02577	0.00038	399	38	180	3	164	2
TSL001-17	532	1508	0.35	0.05585	0.00127	0.19821	0.00478	0.02574	0.00042	446	52	184	4	164	3
TSL001-18	401	1941	0.21	0.04945	0.00121	0.17624	0.00460	0.02585	0.00045	169	58	165	4	165	3
TSL001-19	345	755	0.46	0.04950	0.00222	0.17702	0.00773	0.02593	0.00051	172	104	165	7	165	3
TSL001-20	594	2406	0.25	0.04953	0.00116	0.17755	0.00447	0.02600	0.00046	173	56	166	4	165	3
TSL001-21	1119	2485	0.45	0.04930	0.00125	0.17679	0.00468	0.02601	0.00050	162	61	165	4	166	3
TSL001-22	578	1221	0.47	0.04945	0.00091	0.17935	0.00363	0.02631	0.00041	169	44	168	3	167	3
TSL001-23	583	2082	0.28	0.05313	0.00091	0.26407	0.00514	0.03605	0.00058	334	40	238	4	228	4
TSL001-24	168	371	0.45	0.05165	0.00139	0.25717	0.00712	0.03612	0.00063	270	63	232	6	229	4
TSL001-25	369	1176	0.31	0.06830	0.00210	0.66895	0.02115	0.07105	0.00122	878	65	520	13	442	7
TSL001-26	735	1128	0.65	0.07765	0.00223	0.93747	0.02796	0.08757	0.00147	1138	58	672	15	541	9
TSL001-27	119	96	1.23	0.06503	0.00479	1.13255	0.08199	0.12634	0.00283	775	160	769	39	767	16
TSL001-28	355	451	0.79	0.07094	0.00235	1.44505	0.04864	0.14776	0.00254	956	69	908	20	888	14
TSL001-29	239	303	0.79	0.06985	0.00204	1.43373	0.04349	0.14895	0.00259	924	61	903	18	895	15
TSL001-30	130	373	0.35	0.06977	0.00230	1.43448	0.04821	0.14916	0.00267	922	69	903	20	896	15
TSL001-31	256	99	2.58	0.07596	0.00410	1.63620	0.08734	0.15625	0.00328	1094	111	984	34	936	18

(*To be continued on the next page*)

Appendix 4-1. (*Continued*)

Spot	Elements (ppm)			Isotopic ratios						Ages (Ma)					
	^{232}Th	^{238}U	Th/U	^{207}Pb/^{206}Pb	1σ	^{207}Pb/^{235}U	1σ	^{206}Pb/^{238}U	1σ	^{207}Pb/^{206}Pb	1σ	^{207}Pb/^{235}U	1σ	^{206}Pb/^{238}U	1σ
TSL001-32	332	460	0.72	0.07027	0.00189	1.51324	0.04276	0.15622	0.00259	936	56	936	17	936	14
TSL001-33	318	1011	0.31	0.07324	0.00104	1.72992	0.02909	0.17133	0.00250	1021	29	1020	11	1019	14
TSL001-34	309	179	1.72	0.10088	0.00458	3.74683	0.16915	0.26940	0.00531	1640	86	1581	36	1538	27
TSL001-35	224	1285	0.17	0.14227	0.00651	7.15118	0.32685	0.36459	0.00729	2255	81	2130	41	2004	34
TSL001-36	874	402	2.17	0.15994	0.00497	9.76820	0.31243	0.44301	0.00760	2455	54	2413	29	2364	34
TSL001-37	421	449	0.94	0.16071	0.00421	7.55281	0.21014	0.34108	0.00603	2463	45	2179	25	1892	29
TSL001-38	248	536	0.46	0.16357	0.00410	6.94630	0.18542	0.30809	0.00514	2493	43	2105	24	1731	25
Dioritic dark enclaves															
JY55-01	1261	2438	0.52	0.05016	0.00177	0.17134	0.00608	0.02478	0.00043	202	84	161	5	158	3
JY55-02	602	2214	0.27	0.05069	0.00141	0.17303	0.00500	0.02476	0.00041	227	66	162	4	158	3
JY55-03	138	344	0.40	0.04936	0.00385	0.16964	0.01314	0.02493	0.00050	165	177	159	11	159	3
JY55-04	374	522	0.72	0.04917	0.00350	0.16976	0.01189	0.02505	0.00052	156	161	159	10	159	3
JY55-05	430	1750	0.25	0.04746	0.00138	0.16379	0.00494	0.02504	0.00040	72	65	154	4	159	3
JY55-06	658	2115	0.31	0.05037	0.00152	0.17391	0.00541	0.02505	0.00041	212	72	163	5	159	3
JY55-07	488	1725	0.28	0.05045	0.00154	0.17485	0.00544	0.02514	0.00040	216	72	164	5	160	3
JY55-08	977	2158	0.45	0.04938	0.00132	0.17075	0.00474	0.02508	0.00039	166	64	160	4	160	2
JY55-09	208	415	0.50	0.04932	0.00325	0.17215	0.01130	0.02533	0.00049	163	150	161	10	161	3
JY55-10	834	1569	0.53	0.04933	0.00168	0.17243	0.00592	0.02535	0.00041	164	81	162	5	161	3
JY55-11	824	2049	0.40	0.04928	0.00147	0.17143	0.00524	0.02523	0.00040	161	71	161	5	161	3
JY55-12	481	1722	0.28	0.05349	0.00141	0.18722	0.00515	0.02540	0.00040	350	61	174	4	162	3
JY55-13	59	210	0.28	0.04734	0.00545	0.16568	0.01894	0.02538	0.00056	66	238	156	16	162	4
JY55-14	953	505	1.89	0.05569	0.00313	0.19547	0.01092	0.02550	0.00050	440	129	181	9	162	3
JY55-15	3821	2517	1.52	0.04931	0.00168	0.17352	0.00601	0.02554	0.00045	163	81	162	5	163	3
JY55-16	536	1212	0.44	0.04932	0.00170	0.17440	0.00612	0.02565	0.00043	163	82	163	5	163	3
JY55-17	491	1666	0.29	0.05019	0.00151	0.17783	0.00551	0.02570	0.00041	204	71	166	5	164	3
JY55-18	333	1464	0.23	0.05562	0.00188	0.25475	0.00870	0.03323	0.00056	437	77	230	7	211	3
JY55-19	513	531	0.96	0.05519	0.00169	0.51161	0.01610	0.06731	0.00113	420	70	420	11	420	7
JY55-20	899	544	1.65	0.05643	0.00162	0.53298	0.01578	0.06852	0.00110	469	65	434	10	427	7
JY55-21	110	2117	0.05	0.06687	0.00196	0.93484	0.02807	0.10176	0.00177	834	63	670	15	625	10
JY55-22	83	232	0.36	0.07508	0.00310	1.64143	0.06688	0.15859	0.00281	1071	85	986	26	949	16
JY55-23	639	796	0.80	0.07566	0.00168	1.75299	0.04171	0.16814	0.00262	1086	46	1028	15	1002	14
JY55-24	220	485	0.45	0.08013	0.00247	1.89245	0.05919	0.17132	0.00276	1200	62	1078	21	1019	15

(*To be continued on the next page*)

Appendix 4-1. (*Continued*)

Spot	Elements (ppm)			Isotopic ratios						Ages (Ma)					
	^{232}Th	^{238}U	Th/U	^{207}Pb/^{206}Pb	1σ	^{207}Pb/^{235}U	1σ	^{206}Pb/^{238}U	1σ	^{207}Pb/^{206}Pb	1σ	^{207}Pb/^{235}U	1σ	^{206}Pb/^{238}U	1σ
Tongshanling granite porphyry															
TSL138-01	230	1258	0.18	0.05021	0.00217	0.17069	0.00720	0.02467	0.00044	205	102	160	6	157	3
TSL138-02	743	1639	0.45	0.04933	0.00201	0.16719	0.00665	0.02460	0.00044	164	95	157	6	157	3
TSL138-03	880	1881	0.47	0.04782	0.00160	0.16299	0.00557	0.02473	0.00039	90	76	153	5	157	2
TSL138-04	410	1421	0.29	0.05079	0.00171	0.17277	0.00591	0.02468	0.00041	231	80	162	5	157	3
TSL138-05	667	1660	0.40	0.04713	0.00179	0.16049	0.00618	0.02470	0.00040	56	83	151	5	157	3
TSL138-06	483	683	0.71	0.04918	0.00361	0.16852	0.01209	0.02486	0.00054	156	166	158	11	158	3
TSL138-07	670	1229	0.55	0.04919	0.00235	0.16827	0.00784	0.02484	0.00047	157	110	158	7	158	3
TSL138-08	657	1723	0.38	0.05252	0.00216	0.18023	0.00740	0.02489	0.00048	308	96	168	6	158	3
TSL138-09	1120	1992	0.56	0.04932	0.00188	0.16929	0.00629	0.02490	0.00045	163	89	159	5	159	3
TSL138-10	325	1044	0.31	0.04992	0.00249	0.17166	0.00834	0.02497	0.00048	191	116	161	7	159	3
TSL138-11	935	1844	0.51	0.05323	0.00170	0.18275	0.00598	0.02491	0.00040	339	74	170	5	159	3
TSL138-12	735	1806	0.41	0.04926	0.00201	0.16893	0.00674	0.02490	0.00045	160	95	158	6	159	3
TSL138-13	676	1553	0.44	0.05074	0.00190	0.17426	0.00655	0.02492	0.00041	229	89	163	6	159	3
TSL138-14	525	1411	0.37	0.04932	0.00177	0.16970	0.00615	0.02496	0.00041	163	85	159	5	159	3
TSL138-15	598	1822	0.33	0.05236	0.00224	0.18015	0.00765	0.02495	0.00047	301	100	168	7	159	3
TSL138-16	245	620	0.39	0.04924	0.00342	0.17052	0.01162	0.02512	0.00052	159	158	160	10	160	3
TSL138-17	393	1110	0.35	0.04914	0.00335	0.17067	0.01127	0.02520	0.00057	155	155	160	10	160	4
TSL138-18	789	1600	0.49	0.04921	0.00225	0.16995	0.00756	0.02509	0.00048	158	106	159	7	160	3
TSL138-19	834	1899	0.44	0.04961	0.00156	0.17155	0.00555	0.02508	0.00042	177	75	161	5	160	3
TSL138-20	902	2107	0.43	0.04935	0.00168	0.17139	0.00593	0.02519	0.00043	164	81	161	5	160	3
TSL138-21	635	688	0.92	0.04922	0.00309	0.17113	0.01052	0.02523	0.00051	158	143	160	9	161	3
TSL138-22	659	1600	0.41	0.05005	0.00153	0.17407	0.00547	0.02523	0.00042	197	73	163	5	161	3
TSL138-23	610	1604	0.38	0.04931	0.00155	0.17153	0.00552	0.02523	0.00042	163	75	161	5	161	3
TSL138-24	188	437	0.43	0.06932	0.00215	1.39889	0.04419	0.14638	0.00248	908	65	888	19	881	14
TSL138-25	444	940	0.47	0.07284	0.00146	1.50132	0.03312	0.14951	0.00231	1010	42	931	13	898	13
TSL138-26	729	552	1.32	0.07108	0.00206	1.53689	0.04540	0.15684	0.00251	960	61	945	18	939	14
TSL138-27	292	245	1.19	0.07779	0.00181	2.05875	0.05104	0.19200	0.00302	1142	47	1135	17	1132	16
TSL138-28	287	151	1.90	0.07851	0.00265	2.02175	0.06929	0.18684	0.00316	1160	69	1123	23	1104	17
TSL138-29	386	446	0.87	0.07943	0.00200	2.08608	0.05485	0.19054	0.00297	1183	51	1144	18	1124	16
TSL138-30	538	284	1.90	0.10423	0.00238	4.13516	0.10124	0.28778	0.00475	1701	43	1661	20	1630	24
TSL138-31	159	326	0.49	0.14988	0.00418	4.88191	0.14065	0.23626	0.00393	2345	49	1799	24	1367	20
TSL138-32	1319	537	2.46	0.15273	0.00393	6.18107	0.16762	0.29356	0.00473	2377	45	2002	24	1659	24
TSL138-33	288	409	0.70	0.15826	0.00397	8.98428	0.23580	0.41175	0.00649	2437	43	2336	24	2223	30

(*To be continued on the next page*)

Appendix 4-1. (*Continued*)

Spot	Elements (ppm)			Isotopic ratios						Ages (Ma)					
	^{232}Th	^{238}U	Th/U	^{207}Pb/^{206}Pb	1σ	^{207}Pb/^{235}U	1σ	^{206}Pb/^{238}U	1σ	^{207}Pb/^{206}Pb	1σ	^{207}Pb/^{235}U	1σ	^{206}Pb/^{238}U	1σ
Weijia granite porphyry															
WJ5-01	183	223	0.82	0.05617	0.00488	0.19085	0.01641	0.02464	0.00053	459	199	177	14	157	3
WJ5-02	975	942	1.03	0.05974	0.00276	0.20360	0.00931	0.02472	0.00046	594	103	188	8	157	3
WJ5-03	388	534	0.73	0.04923	0.00324	0.16797	0.01091	0.02476	0.00052	159	150	158	9	158	3
WJ5-04	99	136	0.73	0.04937	0.00955	0.16876	0.03239	0.02479	0.00077	165	357	158	28	158	5
WJ5-05	83	99	0.84	0.04922	0.01522	0.16889	0.05186	0.02489	0.00103	158	525	158	45	158	6
WJ5-06	47	66	0.71	0.04947	0.01829	0.16894	0.06209	0.02479	0.00110	170	633	158	54	158	7
WJ5-07	686	2573	0.27	0.04924	0.00185	0.16956	0.00635	0.02499	0.00042	159	88	159	6	159	3
WJ5-08	139	201	0.69	0.04940	0.00698	0.16972	0.02373	0.02492	0.00065	167	286	159	21	159	4
WJ5-09	257	215	1.20	0.07385	0.00670	0.25373	0.02247	0.02492	0.00067	1037	190	230	18	159	4
WJ5-10	257	501	0.51	0.04932	0.00343	0.17073	0.01174	0.02513	0.00052	163	158	160	10	160	3
WJ5-11	574	595	0.96	0.06024	0.00272	0.22010	0.00984	0.02656	0.00050	612	100	202	8	169	3
WJ5-12	136	208	0.65	0.04951	0.00611	0.18297	0.02231	0.02681	0.00070	172	262	171	19	171	4
WJ5-13	101	141	0.72	0.10832	0.01572	0.45749	0.06498	0.03063	0.00091	1771	281	383	45	194	6
WJ5-14	406	535	0.76	0.05117	0.00227	0.27302	0.01207	0.03873	0.00069	248	104	245	10	245	4
WJ5-15	484	868	0.56	0.06603	0.00286	0.55699	0.02360	0.06119	0.00110	807	93	450	15	383	7
WJ5-16	307	182	1.69	0.06361	0.00234	1.04873	0.03886	0.11962	0.00209	729	80	728	19	728	12
WJ5-17	61	66	0.92	0.06878	0.00272	1.98580	0.07835	0.20972	0.00379	892	84	1111	27	1227	20
WJ5-18	294	977	0.30	0.15223	0.00406	5.18185	0.14516	0.24692	0.00422	2371	47	1850	24	1423	22
WJ5-19	77	84	0.92	0.16010	0.00463	10.19107	0.29969	0.46186	0.00782	2457	50	2452	27	2448	34

Appendix 4-2. LA-ICP-MS zircon Hf isotope analyses of granitoids from the Tongshanling-Weijia area

Spot	Age (Ma)	$^{176}Lu/^{177}Hf$	2σ	$^{176}Hf/^{177}Hf$	2σ	$(^{176}Hf/^{177}Hf)_i$	$\varepsilon_{Hf}(t)$	$T_{DM}(Hf)$ (Ga)	$T^{C}_{DM}(Hf)$ (Ga)
Tongshanling granodiorite porphyry									
TSL001-01	159	0.001143	0.000013	0.282389	0.000020	0.282385	–10.2	1.23	1.85
TSL001-02	160	0.001599	0.000046	0.282438	0.000026	0.282434	–8.5	1.17	1.74
TSL001-03	160	0.000934	0.000003	0.282463	0.000022	0.282460	–7.5	1.12	1.68
TSL001-04	160	0.000774	0.000016	0.282397	0.000031	0.282395	–9.8	1.20	1.83
TSL001-05	161	0.001337	0.000011	0.282354	0.000023	0.282350	–11.4	1.28	1.92
TSL001-06	161	0.000443	0.000026	0.282345	0.000026	0.282344	–11.6	1.26	1.94
TSL001-07	162	0.001349	0.000040	0.282460	0.000024	0.282456	–7.6	1.13	1.69
TSL001-08	162	0.001151	0.000017	0.282453	0.000029	0.282449	–7.9	1.14	1.70
TSL001-09	163	0.000831	0.000023	0.282465	0.000021	0.282462	–7.4	1.11	1.67
TSL001-10	163	0.001320	0.000018	0.282449	0.000024	0.282445	–8.0	1.15	1.71
TSL001-11	163	0.000999	0.000006	0.282441	0.000019	0.282438	–8.2	1.15	1.73
TSL001-12	164	0.001893	0.000057	0.282499	0.000022	0.282493	–6.3	1.09	1.60
TSL001-13	164	0.001569	0.000020	0.282478	0.000024	0.282473	–7.0	1.11	1.65
TSL001-14	165	0.001592	0.000017	0.282428	0.000023	0.282423	–8.7	1.19	1.76
TSL001-15	167	0.001293	0.000009	0.282421	0.000025	0.282417	–8.9	1.19	1.77
TSL001-16	442	0.000790	0.000032	0.282107	0.000024	0.282100	–14.0	1.61	2.30
TSL001-17	541	0.001396	0.000021	0.282587	0.000020	0.282573	4.9	0.95	1.19
TSL001-18	767	0.000261	0.000003	0.281978	0.000024	0.281974	–11.3	1.76	2.37
TSL001-19	888	0.000694	0.000016	0.282342	0.000024	0.282330	4.0	1.28	1.51
TSL001-20	895	0.000190	0.000021	0.282206	0.000023	0.282202	–0.4	1.45	1.79
TSL001-21	896	0.001093	0.000015	0.282250	0.000023	0.282232	0.7	1.42	1.73
TSL001-22	936	0.000867	0.000032	0.282355	0.000022	0.282340	5.4	1.26	1.46
TSL001-23	936	0.000721	0.000016	0.282188	0.000036	0.282175	–0.4	1.49	1.83
TSL001-24	1021	0.000511	0.000002	0.282024	0.000024	0.282014	–4.2	1.71	2.13
TSL001-25	1640	0.000847	0.000009	0.281873	0.000023	0.281846	3.7	1.93	2.11
Dioritic dark enclaves									
JY55-01	158	0.002067	0.000019	0.282463	0.000024	0.282457	–7.7	1.15	1.69
JY55-02	158	0.001549	0.000009	0.282470	0.000022	0.282466	–7.4	1.12	1.67
JY55-03	159	0.001662	0.000037	0.282447	0.000021	0.282442	–8.2	1.16	1.72
JY55-04	159	0.001383	0.000026	0.282461	0.000024	0.282457	–7.7	1.13	1.69
JY55-05	159	0.001722	0.000060	0.282470	0.000029	0.282465	–7.4	1.13	1.67
JY55-06	160	0.001339	0.000020	0.282482	0.000022	0.282478	–6.9	1.10	1.64
JY55-07	160	0.001843	0.000030	0.282414	0.000022	0.282409	–9.3	1.21	1.79
JY55-08	161	0.001094	0.000018	0.282476	0.000021	0.282473	–7.1	1.10	1.65

(*To be continued on the next page*)

Appendix 4-2. (*Continued*)

Spot	Age (Ma)	$^{176}Lu/^{177}Hf$	2σ	$^{176}Hf/^{177}Hf$	2σ	$(^{176}Hf/^{177}Hf)_i$	$\varepsilon_{Hf}(t)$	$T_{DM}(Hf)$ (Ga)	$T^{C}_{DM}(Hf)$ (Ga)
JY55-09	161	0.001723	0.000006	0.282453	0.000031	0.282447	–8.0	1.15	1.71
JY55-10	161	0.002152	0.000033	0.282476	0.000035	0.282470	–7.2	1.13	1.66
JY55-11	162	0.001205	0.000018	0.282424	0.000028	0.282421	–8.9	1.18	1.77
JY55-12	162	0.001468	0.000043	0.282451	0.000029	0.282446	–8.0	1.15	1.71
JY55-13	163	0.001454	0.000053	0.282445	0.000027	0.282441	–8.2	1.16	1.72
JY55-14	164	0.001419	0.000030	0.282448	0.000020	0.282444	–8.0	1.15	1.71
JY55-15	420	0.001284	0.000015	0.282313	0.000023	0.282303	–7.4	1.34	1.87
JY55-16	427	0.000830	0.000011	0.282434	0.000021	0.282427	–2.8	1.15	1.59
JY55-17	625	0.001375	0.000020	0.282187	0.000021	0.282171	–7.5	1.52	2.03
JY55-18	949	0.001815	0.000083	0.282275	0.000021	0.282243	2.3	1.41	1.67
JY55-19	1086	0.001182	0.000056	0.282299	0.000040	0.282275	6.4	1.35	1.51
JY55-20	1200	0.001281	0.000040	0.282244	0.000028	0.282215	6.9	1.43	1.57
Tongshanling granite porphyry									
TSL138-01	157	0.001435	0.000012	0.282535	0.000028	0.282531	–5.1	1.03	1.53
TSL138-02	157	0.001202	0.000027	0.282559	0.000033	0.282556	–4.2	0.99	1.47
TSL138-03	158	0.002067	0.000013	0.282612	0.000027	0.282606	–2.4	0.93	1.36
TSL138-04	158	0.002170	0.000048	0.282224	0.000035	0.282217	–16.1	1.50	2.22
TSL138-05	159	0.000894	0.000022	0.282387	0.000039	0.282384	–10.2	1.22	1.85
TSL138-06	159	0.002494	0.000019	0.282442	0.000054	0.282435	–8.4	1.19	1.74
TSL138-07	159	0.001451	0.000029	0.282517	0.000033	0.282512	–5.7	1.06	1.57
TSL138-08	159	0.001330	0.000036	0.282549	0.000038	0.282545	–4.5	1.01	1.49
TSL138-09	159	0.001231	0.000026	0.282670	0.000031	0.282666	–0.2	0.83	1.22
TSL138-10	159	0.000874	0.000012	0.282546	0.000027	0.282544	–4.6	1.00	1.50
TSL138-11	159	0.001635	0.000039	0.282519	0.000030	0.282514	–5.6	1.06	1.56
TSL138-12	160	0.001433	0.000014	0.282613	0.000020	0.282609	–2.3	0.92	1.35
TSL138-13	160	0.001663	0.000018	0.282518	0.000025	0.282513	–5.7	1.06	1.56
TSL138-14	160	0.000634	0.000039	0.282387	0.000031	0.282385	–10.2	1.21	1.85
TSL138-15	160	0.000482	0.000030	0.282597	0.000029	0.282596	–2.7	0.92	1.38
TSL138-16	161	0.001269	0.000011	0.282539	0.000022	0.282535	–4.9	1.02	1.51
TSL138-17	161	0.001147	0.000012	0.282560	0.000022	0.282557	–4.1	0.99	1.46
TSL138-18	161	0.002161	0.000009	0.282636	0.000028	0.282629	–1.5	0.90	1.30
TSL138-19	881	0.001075	0.000018	0.282306	0.000018	0.282288	2.3	1.34	1.61
TSL138-20	898	0.001502	0.000017	0.281938	0.000026	0.281912	–10.6	1.88	2.43
TSL138-21	1142	0.001484	0.000079	0.282366	0.000032	0.282334	9.8	1.27	1.34
TSL138-22	1160	0.001377	0.000055	0.282169	0.000034	0.282139	3.3	1.55	1.77

(*To be continued on the next page*)

Appendix 4-2. (*Continued*)

Spot	Age (Ma)	$^{176}Lu/^{177}Hf$	2σ	$^{176}Hf/^{177}Hf$	2σ	$(^{176}Hf/^{177}Hf)_i$	$\varepsilon_{Hf}(t)$	$T_{DM}(Hf)$ (Ga)	$T^{C}_{DM}(Hf)$ (Ga)
TSL138-23	1183	0.001369	0.000025	0.282004	0.000038	0.281973	–2.1	1.78	2.12
TSL138-24	1701	0.001505	0.000029	0.281952	0.000033	0.281904	7.2	1.85	1.94
TSL138-25	2377	0.000746	0.000008	0.281489	0.000029	0.281455	6.7	2.45	2.50
TSL138-26	2437	0.000623	0.000024	0.281424	0.000033	0.281395	5.9	2.53	2.59
Weijia granite porphyry									
WJ5-01	157	0.000868	0.000007	0.282582	0.000027	0.282579	–3.4	0.95	1.42
WJ5-02	157	0.001934	0.000087	0.282634	0.000027	0.282628	–1.7	0.90	1.31
WJ5-03	158	0.000578	0.000015	0.282554	0.000030	0.282552	–4.3	0.98	1.48
WJ5-04	158	0.000792	0.000011	0.282571	0.000027	0.282569	–3.7	0.96	1.44
WJ5-05	158	0.000697	0.000007	0.282597	0.000029	0.282595	–2.8	0.92	1.38
WJ5-06	159	0.001100	0.000014	0.282577	0.000047	0.282574	–3.5	0.96	1.43
WJ5-07	159	0.001082	0.000006	0.282621	0.000019	0.282617	–2.0	0.90	1.33
WJ5-08	159	0.000856	0.000017	0.282624	0.000024	0.282622	–1.8	0.89	1.32
WJ5-09	160	0.000645	0.000005	0.282543	0.000025	0.282542	–4.6	0.99	1.50
WJ5-10	383	0.001379	0.000088	0.282547	0.000024	0.282537	0.1	1.01	1.37
WJ5-11	892	0.001141	0.000029	0.282420	0.000033	0.282401	6.6	1.18	1.35
WJ5-12	2457	0.000886	0.000056	0.281501	0.000046	0.281459	8.7	2.44	2.44

Note: Zircons with $\varepsilon_{Hf}(t) > 0$ using single-stage model ages $T_{DM}(Hf)$ (Ga); Zircons with $\varepsilon_{Hf}(t) < 0$ using two-stage model ages $T^{C}_{DM}(Hf)$ (Ga).

Appendix 4-3. Major elements (wt.%), trace elements (ppm) and Sr-Nd isotopes of granitoids from the Tongshanling-Weijia area

Sample	Tongshanling granodiorite porphyry								
	TSL58	TSL59	TSL60	JY23	JY36	JY38	JY40	YL49	YL50
SiO_2	68.23	68.12	65.94	65.74	63.71	65.02	65.84	68.21	70.09
TiO_2	0.37	0.43	0.47	0.52	0.52	0.56	0.48	0.44	0.37
Al_2O_3	14.38	14.90	15.68	15.97	16.66	15.84	15.24	14.37	13.68
Fe_2O_3	0.70	0.97	1.26	1.17	1.33	1.22	0.95	1.00	0.99
FeO	2.15	2.04	2.18	2.45	2.62	2.60	2.36	2.28	1.85
MnO	0.08	0.06	0.05	0.09	0.09	0.11	0.09	0.08	0.07
MgO	1.16	1.29	1.41	1.64	1.81	1.69	1.63	1.30	1.08
CaO	3.16	2.78	3.42	3.58	4.15	3.75	3.75	3.14	2.35
Na_2O	2.77	2.89	3.19	2.89	3.03	2.95	3.14	2.94	2.57
K_2O	4.63	4.64	3.97	3.97	3.92	4.22	4.42	4.20	4.79
P_2O_5	0.13	0.15	0.18	0.19	0.21	0.20	0.18	0.18	0.15
LOI	2.56	2.52	2.08	1.48	2.02	2.01	1.44	1.20	1.32
Total	100.32	100.80	99.82	99.69	100.08	100.16	99.53	99.35	99.31
Ga	16.80	15.71	17.41	16.29	15.75	16.73	16.24	17.30	17.05
Rb	194.25	187.97	179.67	169.97	177.11	164.65	162.50	228.55	256.48
Sr	267.48	302.14	308.22	339.80	291.38	310.89	332.43	268.47	205.93
Y	18.41	24.32	21.85	18.33	19.42	20.25	19.90	17.49	18.26
Zr	123.44	138.31	154.91	129.48	142.41	152.77	143.96	118.88	127.29
Nb	14.43	21.02	23.52	14.65	15.05	15.79	13.55	17.93	16.85
Ba	601.26	858.21	749.22	1795.75	916.95	845.02	872.38	246.68	213.69
Hf	3.93	4.02	4.55	4.08	4.49	4.68	4.43	3.72	4.16
Ta	1.60	1.48	1.78	1.74	1.69	1.57	1.45	1.95	2.52
Th	23.21	15.19	16.62	13.47	13.26	13.78	14.75	15.12	20.42
U	10.55	4.56	5.59	5.91	5.78	5.46	5.18	11.88	15.17
La	17.91	22.42	23.88	20.80	21.13	22.12	21.19	13.40	16.00
Ce	34.69	42.22	40.23	40.83	39.83	42.56	41.09	29.51	34.78
Pr	4.77	5.16	5.03	5.71	5.96	5.97	5.82	4.61	5.17
Nd	16.80	19.42	19.41	19.92	20.80	20.88	20.23	17.92	19.11
Sm	3.42	3.76	4.01	4.01	4.22	4.31	4.25	3.82	3.90
Eu	1.01	1.17	1.21	1.47	1.21	1.20	1.20	0.85	0.78
Gd	3.26	3.53	3.80	3.81	3.89	3.84	3.95	3.40	3.41
Tb	0.53	0.55	0.62	0.59	0.62	0.64	0.65	0.54	0.54
Dy	3.16	3.16	3.64	3.40	3.58	3.72	3.74	3.00	3.01
Ho	0.63	0.61	0.71	0.66	0.69	0.72	0.72	0.58	0.59
Er	1.91	1.88	2.19	1.99	2.06	2.14	2.15	1.72	1.84
Tm	0.30	0.28	0.33	0.30	0.31	0.32	0.32	0.26	0.29
Yb	2.05	1.94	2.27	2.06	2.11	2.17	2.15	1.85	2.14
Lu	0.32	0.31	0.36	0.32	0.32	0.33	0.33	0.29	0.35
ASI[a]	0.94	1.00	0.99	1.03	0.99	0.97	0.91	0.95	1.00
DI[b]	76.08	76.88	72.69	70.80	67.52	70.24	72.74	75.51	79.64
ΣREE	90.76	106.42	107.69	105.87	106.73	110.92	107.79	81.75	91.91
HFSE[c]	190.97	225.86	240.51	203.29	216.71	231.37	218.50	183.81	197.18
T_{Zr}[d] (°C)	749	764	770	758	758	764	752	747	761
$^{87}Rb/^{86}Sr$	2.10	1.80		1.45	1.76	1.53	1.41	2.46	3.60
$^{87}Sr/^{86}Sr$	0.715467	0.714273		0.714026	0.713045	0.714132	0.713807	0.714646	0.717641
2σ	0.000008	0.000006		0.000006	0.000009	0.000007	0.000014	0.000008	0.000008
$(^{87}Sr/^{86}Sr)_i$	0.710612	0.710114		0.710682	0.708982	0.710592	0.710539	0.708955	0.709315
$^{147}Sm/^{144}Nd$	0.12	0.12		0.12	0.12	0.12	0.13	0.13	0.12
$^{143}Nd/^{144}Nd$	0.512208	0.512209		0.512231	0.512258	0.512212	0.512214	0.512351	0.512329
2σ	0.000006	0.000005		0.000008	0.000007	0.000006	0.000005	0.000006	0.000006
$\varepsilon_{Nd}(t)$	–6.9	–6.7		–6.4	–5.9	–6.8	–6.8	–4.2	–4.5
T^{c}_{DM}(Nd) (Ga)	1.51	1.50		1.47	1.43	1.51	1.51	1.29	1.32

(*To be continued on the next page*)

Appendix 4-3. (*Continued*)

Sample	Dioritic dark enclaves						
	JY41	JY42	JY43	JY44	JY52	JY55	JY65
SiO_2	55.70	48.61	59.35	53.38	55.13	58.79	57.56
TiO_2	0.85	1.00	0.80	1.16	0.90	0.85	0.86
Al_2O_3	16.18	16.48	16.49	18.54	16.82	17.05	17.20
Fe_2O_3	1.30	4.80	1.27	1.18	1.71	1.58	1.48
FeO	6.95	4.62	4.88	7.01	6.80	5.13	5.26
MnO	0.30	0.29	0.18	0.17	0.32	0.20	0.19
MgO	3.99	4.47	2.77	3.25	4.09	3.09	3.13
CaO	5.87	6.62	4.92	4.46	6.00	4.80	5.36
Na_2O	3.27	3.38	3.08	3.23	3.46	3.48	3.26
K_2O	2.52	2.03	3.17	2.99	2.87	3.39	2.85
P_2O_5	0.26	0.24	0.29	0.34	0.30	0.33	0.32
LOI	2.57	6.72	2.03	3.43	1.23	1.57	1.77
Total	99.77	99.26	99.25	99.13	99.63	100.26	99.24
Ga	16.03	22.42	20.01	24.99	21.60	21.07	20.53
Rb	125.83	135.10	221.60	213.96	185.59	224.96	210.82
Sr	192.90	267.18	350.11	271.46	246.51	256.45	391.37
Y	53.29	58.85	30.82	38.47	61.81	47.11	24.09
Zr	105.97	134.91	121.57	144.20	146.16	190.58	133.43
Nb	19.80	24.34	19.16	33.14	23.37	23.24	21.06
Ba	268.94	400.17	592.37	428.28	479.41	515.45	617.02
Hf	3.67	4.48	3.89	4.51	4.71	6.09	4.06
Ta	2.12	2.50	1.73	3.83	2.67	2.80	0.88
Th	11.77	15.20	15.26	12.61	10.01	24.09	13.13
U	5.67	7.29	4.57	10.16	5.81	10.34	3.24
La	15.24	19.65	28.17	18.42	16.70	35.53	26.87
Ce	39.92	52.09	59.63	30.46	43.81	73.46	57.18
Pr	7.98	10.15	9.32	5.55	8.58	11.06	8.58
Nd	30.98	39.66	32.17	21.47	36.21	40.21	31.52
Sm	8.76	10.59	6.66	5.94	10.27	9.02	6.33
Eu	1.04	1.37	1.28	1.06	1.35	1.22	1.46
Gd	8.32	9.72	6.07	5.82	9.64	8.49	5.65
Tb	1.58	1.77	0.97	1.07	1.79	1.43	0.85
Dy	9.86	10.81	5.66	6.68	11.14	8.56	4.78
Ho	1.93	2.12	1.11	1.33	2.20	1.68	0.91
Er	5.69	6.30	3.35	4.05	6.57	5.08	2.70
Tm	0.86	0.96	0.50	0.63	0.99	0.76	0.38
Yb	5.63	6.46	3.40	4.25	6.65	5.06	2.55
Lu	0.82	0.97	0.51	0.67	0.99	0.77	0.39
ASI[a]	0.86	0.83	0.94	1.11	0.85	0.94	0.94
DI[b]	48.05	41.68	57.26	50.02	48.78	58.07	53.66
ΣREE	138.60	172.62	158.80	107.38	156.90	202.33	150.15
HFSE[c]	218.97	270.19	231.19	246.27	275.15	334.40	235.77
T_{Zr}[d] (°C)	702	702	732	755	721	764	735
$^{87}Rb/^{86}Sr$	1.89				2.18		1.56
$^{87}Sr/^{86}Sr$	0.714602				0.714997		0.714759
2σ	0.000005				0.000006		0.000005
$(^{87}Sr/^{86}Sr)_i$	0.710293				0.710023		0.711200
$^{147}Sm/^{144}Nd$	0.17				0.17		0.12
$^{143}Nd/^{144}Nd$	0.512270				0.512291		0.512290
2σ	0.000004				0.000005		0.000006
$\varepsilon_{Nd}(t)$	–6.7				–6.3		–5.2
T^c_{DM}(Nd) (Ga)	1.49				1.46		1.38

(*To be continued on the next page*)

Appendix 4-3. (*Continued*)

Sample	Tongshanling granite porphyry							
	TSL89	TSL90	TSL138	TSL139	TSL141	TSL142	TSL143	TSL146
SiO_2	71.57	71.35	72.29	73.07	71.80	72.17	72.68	74.34
TiO_2	0.22	0.24	0.21	0.23	0.22	0.22	0.22	0.22
Al_2O_3	13.83	14.01	12.72	13.61	13.56	13.69	13.66	13.04
Fe_2O_3	0.57	0.67	0.43	0.44	0.52	0.54	0.36	0.44
FeO	1.36	1.10	1.18	1.31	1.24	1.32	1.38	1.21
MnO	0.08	0.07	0.10	0.07	0.09	0.09	0.07	0.08
MgO	0.56	0.60	0.60	0.51	0.54	0.61	0.42	0.56
CaO	1.23	0.73	2.15	0.93	1.25	1.83	0.85	1.03
Na_2O	2.95	2.62	2.73	2.82	3.21	2.44	3.98	4.04
K_2O	5.16	5.81	4.30	4.94	4.87	5.04	4.41	3.98
P_2O_5	0.10	0.09	0.08	0.08	0.08	0.08	0.08	0.08
LOI	2.17	1.77	2.84	1.63	2.27	2.47	1.27	1.22
Total	99.79	99.05	99.63	99.63	99.63	100.52	99.38	100.23
Ga	15.53	14.80	14.95	16.93	16.91	16.68	15.65	12.32
Rb	208.19	220.83	204.94	228.28	224.03	232.93	186.58	163.39
Sr	228.16	184.64	167.17	308.94	293.35	277.23	277.33	323.44
Y	12.64	10.95	13.02	14.07	13.35	13.13	13.81	13.88
Zr	137.78	130.61	127.83	134.44	143.31	132.92	142.62	134.92
Nb	35.00	32.91	34.68	38.50	37.15	37.30	37.15	38.42
Ba	635.01	556.30	633.86	650.21	650.26	679.25	611.55	778.21
Hf	4.39	4.76	3.95	4.21	4.39	4.18	4.35	4.19
Ta	2.70	2.91	2.46	2.71	2.67	2.70	2.68	2.65
Th	17.15	17.71	21.80	24.65	24.12	24.55	24.64	24.01
U	6.30	11.07	13.83	9.14	7.31	7.51	9.55	9.26
La	32.45	31.68	33.56	40.95	40.33	39.32	39.04	37.77
Ce	51.93	54.02	55.92	68.35	66.82	66.01	65.07	63.39
Pr	6.55	7.25	8.10	9.74	9.45	9.18	8.94	8.60
Nd	20.40	22.27	20.43	24.77	24.52	24.12	23.90	23.37
Sm	3.35	3.55	3.40	3.89	3.95	3.85	3.80	3.76
Eu	0.87	0.86	0.86	1.02	1.04	0.99	0.98	0.88
Gd	3.06	3.26	3.21	3.55	3.65	3.56	3.48	3.48
Tb	0.40	0.42	0.43	0.45	0.48	0.46	0.45	0.45
Dy	2.00	2.07	2.16	2.16	2.37	2.26	2.17	2.22
Ho	0.37	0.38	0.40	0.39	0.43	0.41	0.40	0.41
Er	1.12	1.17	1.22	1.20	1.34	1.28	1.24	1.28
Tm	0.17	0.17	0.18	0.18	0.20	0.19	0.18	0.19
Yb	1.20	1.24	1.28	1.23	1.38	1.33	1.28	1.34
Lu	0.19	0.20	0.20	0.20	0.22	0.21	0.21	0.22
ASI[a]	1.09	1.17	0.97	1.16	1.06	1.07	1.06	1.02
DI[b]	86.12	87.64	82.50	87.48	86.43	83.74	89.23	89.73
ΣREE	124.06	128.54	131.34	158.06	156.19	153.17	151.15	147.36
HFSE[c]	237.35	228.49	231.44	255.35	260.63	249.35	258.65	250.61
T_{Zr}[d] (°C)	778	781	763	784	779	774	779	771
$^{87}Rb/^{86}Sr$	2.64	3.46	2.61					
$^{87}Sr/^{86}Sr$	0.713635	0.714824	0.714022					
2σ	0.000007	0.000006	0.000009					
$(^{87}Sr/^{86}Sr)_i$	0.707674	0.707011	0.708124					
$^{147}Sm/^{144}Nd$	0.10	0.10	0.10					
$^{143}Nd/^{144}Nd$	0.512431	0.512409	0.512391					
2σ	0.000006	0.000006	0.000005					
$\varepsilon_{Nd}(t)$	–2.1	–2.4	–2.8					
T^c_{DM}(Nd) (Ga)	1.12	1.15	1.18					

(*To be continued on the next page*)

Appendix 4-3. (*Continued*)

Sample	Weijia granite porphyry						
	WJ-2	WJ-10	WJ-11	WJ-12	WJ-15	WJ-18	WJ-22
SiO_2	73.86	74.06	74.60	76.69	76.12	75.73	76.73
TiO_2	0.01	0.01	0.01	0.01	0.01	0.01	0.02
Al_2O_3	13.84	14.27	14.08	13.30	13.70	13.69	13.06
Fe_2O_3	0.07	0.29	0.11	0.02	0.00	0.01	0.22
FeO	0.22	0.28	0.27	0.11	0.13	0.11	0.11
MnO	0.01	0.01	0.01	0.00	0.00	0.00	0.00
MgO	0.04	0.17	0.04	0.01	0.01	0.03	0.14
CaO	0.88	0.15	0.63	0.28	0.12	0.17	0.25
Na_2O	3.36	3.01	3.17	3.72	3.34	3.01	3.48
K_2O	6.19	6.78	6.46	4.84	5.87	5.86	5.44
P_2O_5	0.02	0.01	0.00	0.01	0.01	0.01	0.01
LOI	1.06	0.94	0.74	0.77	0.73	0.88	1.10
Total	99.57	99.98	100.12	99.74	100.04	99.51	100.57
Ga	17.08	22.24	16.06	28.72	25.08	27.43	21.03
Rb	300.62	310.95	259.64	318.89	345.79	355.98	291.60
Sr	27.20	19.93	15.97	14.77	17.69	21.75	28.45
Y	14.67	25.12	31.97	51.27	39.88	43.33	37.28
Zr	74.78	83.19	74.06	60.61	81.13	71.77	80.14
Nb	33.06	41.78	32.31	41.81	40.47	41.16	39.75
Ba	7.46	15.02	7.32	10.62	21.52	34.84	42.60
Hf	4.67	5.56	4.75	4.34	4.80	4.84	5.13
Ta	4.04	6.12	4.49	7.53	5.39	5.97	5.54
Th	12.04	18.05	15.83	26.76	27.31	27.78	27.60
U	13.69	6.78	11.44	18.79	7.79	9.16	8.69
La	7.14	8.52	8.12	15.20	11.55	14.67	13.33
Ce	19.16	15.58	14.47	23.48	16.45	22.77	14.81
Pr	1.92	2.38	2.17	5.49	3.85	5.08	4.54
Nd	10.51	13.48	12.24	16.73	12.34	15.34	13.57
Sm	3.86	5.26	4.89	7.40	5.97	6.61	5.88
Eu	0.04	0.07	0.06	0.09	0.09	0.10	0.10
Gd	4.05	5.88	5.26	8.32	7.02	7.45	6.49
Tb	0.69	1.02	0.99	1.71	1.48	1.52	1.37
Dy	3.91	5.96	6.13	10.11	8.83	8.95	8.25
Ho	0.65	1.01	1.08	1.78	1.56	1.57	1.46
Er	1.65	2.56	2.78	4.77	4.15	4.23	3.94
Tm	0.21	0.35	0.39	0.67	0.59	0.59	0.55
Yb	1.38	2.06	2.26	4.14	3.58	3.68	3.38
Lu	0.18	0.28	0.33	0.59	0.51	0.53	0.47
ASI[a]	1.00	1.13	1.05	1.12	1.13	1.18	1.08
DI[b]	93.59	95.46	94.85	95.93	96.82	95.44	96.58
ΣREE	55.35	64.41	61.17	100.47	77.97	93.08	78.14
HFSE[c]	141.67	165.67	152.81	177.17	177.93	179.02	171.97
T_{Zr}[d] (°C)	722	741	726	718	741	735	737
$^{87}Rb/^{86}Sr$							
$^{87}Sr/^{86}Sr$							
2σ							
$(^{87}Sr/^{86}Sr)_i$							
$^{147}Sm/^{144}Nd$	0.22	0.24	0.24				
$^{143}Nd/^{144}Nd$	0.512424	0.512446	0.512406				
2σ	0.000006	0.000013	0.000009				
$\varepsilon_{Nd}(t)$	–4.7	–4.5	–5.4				
T^c_{DM}(Nd) (Ga)	1.33	1.32	1.39				

Notes: [a] ASI: aluminum saturation index, $n(Al_2O_3)/n(CaO+Na_2O+K_2O)$. [b] DI: differentiation index, the sum of CIPW normative minerals Q, Or, Ab, Ne, Lc, and Kp. [c] HFSE: high field strength elements (Zr+Nb+Ce+Y). [d] T_{Zr}: zircon saturation temperature.

Appendix 4-4. Zircon U-Pb ages of the Middle-Late Jurassic Cu-Pb-Zn-bearing and W-bearing granitoids in the Nanling Range, South China

Intrusion/Deposit	Metal association	Lithology	Analytical method	Age (Ma)	Reference
Cu-Pb-Zn-bearing granites					
Shuikoushan	Pb-Zn-Au-Ag	Granodiorite	SHRIMP	163.0 ± 2.0	Ma et al. (2006)
			LA-ICP-MS	156.0 ± 1.0	Zuo et al. (2014)
			SIMS	158.8 ± 1.8	Huang et al. (2015)
			SIMS	158.3 ± 1.2	Yang et al. (2016)
Baoshan	Cu-Mo-Pb-Zn-Ag	Granodiorite porphyry	SHRIMP	158.0 ± 2.0	Lu et al. (2006)
			LA-ICP-MS	156.7 ± 1.4	Xie et al. (2013)
				157.7 ± 1.1	
		Granodioritic cryptoexplosion breccia	SHRIMP	164.1 ± 1.9	Wu et al. (2005)
				162.2 ± 1.6	
Tongshanling	Cu-Mo-Pb-Zn-Ag	Granodiorite porphyry	SHRIMP	163.6 ± 2.1	Jiang et al. (2009)
			LA-ICP-MS	160.7 ± 0.5	Zhao et al. (2016b)
				160.5 ± 0.9	
				159.7 ± 0.8	
			LA-ICP-MS	162.5 ± 1.0	This study
Dabaoshan	Fe-Cu-Mo-Pb-Zn	Granodiorite porphyry	LA-ICP-MS	167.0 ± 2.5	Li et al. (2012b)
		Granodiorite porphyry	LA-ICP-MS	162.2 ± 0.7	Mao et al. (2013b)
				161.0 ± 0.9	
		Granodiorite		160.2 ± 0.9	
Huangshaping	Pb-Zn-W-Mo	Dacite porphyry	LA-ICP-MS	158.5 ± 0.9	Yuan et al. (2014)
		Quartz porphyry		160.8 ± 1.0	
		Granite porphyry		155.2 ± 0.4	
		Quartz porphyry	LA-ICP-MS	160.5 ± 1.3	Ding et al. (2016b)
W-bearing granites					
Dengfuxian	W-Nb-Ta	Medium-fine-grained two-mica granite	LA-ICP-MS	154.4 ± 2.2	Cai (2013)
		Medium-grained porphyritic two-mica granite		151.1 ± 2.3	
Yaogangxian	W	Coarse-grained biotite granite	SHRIMP	155.4 ± 2.2	Li et al. (2011)
		Fine-grained porphyritic granite		157.6 ± 2.6	
		Quartz porphyry		158.4 ± 2.1	
Weijia	W	Granite porphyry	LA-ICP-MS	157.8 ± 0.9	Zhao et al. (2016a)
		Quartz porphyry		158.3 ± 1.4	
		Granite porphyry	LA-ICP-MS	158.3 ± 2.2	This study
Baxiannao	W-Sn	Medium-coarse-grained biotite granite	SHRIMP	157.2 ± 2.2	Feng et al. (2011a)
Maoping	W-Sn	Porphyritic biotite granite		151.8 ± 2.9	
Taoxikeng	W	Biotite granite	SHRIMP	158.7 ± 3.9	Guo et al. (2011)
				157.6 ± 3.5	
Piaotang	W-Sn	Medium-fine-grained porphyritic biotite granite	Single-grain zircon dating	161.8 ± 1.0	Zhang et al. (2009)
Muziyuan	W-Mo	Medium-fine-grained biotite-bearing granite		153.3 ± 1.9	
Xihuashan	W-Mo	Coarse-grained porphyritic biotite granite	LA-ICP-MS	155.7 ± 2.2	Wang et al. (2011c)
		Medium-grained porphyritic biotite granite	LA-ICP-MS	155.5 ± 0.4	Yang et al. (2012)
		Medium-grained biotite granite		153.0 ± 0.6	
		Fine-grained two-mica granite		152.8 ± 0.9	
Hukeng	W	Muscovite granite	LA-ICP-MS	151.6 ± 2.6	Liu et al. (2008a)
Hongtaoling	W	Biotite granite	SHRIMP	151.4 ± 3.1	Feng et al. (2007a)
Zhangtiantang	W	Fine-grained porphyritic muscovite granite	SHRIMP	156.9 ± 1.7	Feng et al. (2007b)
Huamei'ao	W	Biotite granite	LA-ICP-MS	159.9 ± 1.2	Feng et al. (2015)
Kuimeishan	W	Biotite granite	SHRIMP	157.7 ± 2.7	Li et al. (2014c)
Dajishan	W-Nb-Ta	Fine-grained muscovite granite	Single-grain zircon dating	151.7 ± 1.6	Zhang et al. (2006)

Appendix 5-1. Representative EMP analyses of plagioclase (wt.%) from the Tongshanling granodiorite and its microgranular enclaves

	Tongshanling granodiorite							Microgranular enclaves						
Sample No.	TSL009	TSL016	YL49					JY55						
			From core to rim in the same grain					From core to rim in the same grain						
Type	Rim	Rim	Core	Rim	Rim	Rim	Rim	Core	Core	Core	Rim	Rim	Rim	Rim
SiO_2	61.19	60.92	49.89	51.51	54.34	57.42	61.14	49.72	48.75	52.02	57.85	60.47	61.05	62.69
TiO_2	0.04	0.01	0.00	0.00	0.00	0.05	0.00	0.00	0.00	0.00	0.06	0.00	0.00	0.03
Al_2O_3	23.40	24.06	30.89	29.81	28.70	26.51	23.26	31.74	32.17	29.32	25.63	23.93	23.85	22.43
FeO[a]	0.48	0.22	0.22	0.44	0.04	0.08	0.17	0.02	0.21	0.05	0.07	0.01	0.14	0.15
MnO	0.03	0.00	0.04	0.00	0.00	0.01	0.03	0.06	0.11	0.00	0.06	0.05	0.00	0.02
MgO	0.00	0.02	0.01	0.04	0.00	0.01	0.03	0.00	0.00	0.01	0.00	0.00	0.01	0.00
CaO	5.55	6.32	14.56	12.80	11.03	8.52	6.49	14.74	15.22	13.70	8.51	6.75	6.18	4.81
Na_2O	8.46	7.55	3.03	3.84	4.93	6.11	7.76	2.95	2.71	3.95	6.95	7.93	8.26	8.96
K_2O	0.21	0.25	0.13	0.12	0.20	0.49	0.33	0.05	0.06	0.13	0.11	0.16	0.22	0.29
Total	99.36	99.33	98.77	98.57	99.23	99.19	99.22	99.28	99.24	99.19	99.24	99.31	99.70	99.37
Cations based on 8 oxygen														
Si	2.742	2.725	2.304	2.373	2.467	2.592	2.743	2.282	2.246	2.384	2.613	2.713	2.726	2.798
Al	1.236	1.269	1.681	1.618	1.536	1.410	1.230	1.717	1.747	1.584	1.364	1.265	1.255	1.180
Ti	0.001	0.000	0.000	0.000	0.000	0.002	0.000	0.000	0.000	0.000	0.002	0.000	0.000	0.001
Fe	0.018	0.008	0.009	0.017	0.001	0.003	0.006	0.001	0.008	0.002	0.003	0.000	0.005	0.006
Mn	0.001	0.000	0.001	0.000	0.000	0.000	0.001	0.002	0.004	0.000	0.002	0.002	0.000	0.001
Mg	0.000	0.001	0.001	0.003	0.000	0.001	0.002	0.000	0.000	0.001	0.000	0.000	0.001	0.000
Ca	0.267	0.303	0.720	0.632	0.537	0.412	0.312	0.725	0.751	0.673	0.412	0.324	0.296	0.230
Na	0.735	0.655	0.271	0.343	0.434	0.535	0.675	0.262	0.242	0.351	0.609	0.690	0.716	0.776
K	0.012	0.014	0.008	0.007	0.012	0.028	0.019	0.003	0.003	0.008	0.006	0.009	0.013	0.016
End members[b] (%)														
An	26.30	31.16	72.08	64.33	54.63	42.27	31.00	73.24	75.36	65.20	40.08	31.69	28.90	22.50
Ab	72.49	67.39	27.15	34.94	44.18	54.85	67.12	26.48	24.31	34.04	59.29	67.41	69.88	75.91
Or	1.21	1.45	0.77	0.74	1.20	2.88	1.89	0.28	0.32	0.76	0.63	0.90	1.22	1.59

Notes: [a] All Fe as Fe^{2+}. [b] An = anorthite, Ab = albite, Or = orthoclase.

Appendix 5-2. Representative EMP analyses of amphibole (wt.%) from the Tongshanling granodiorite and its microgranular enclaves

	Tongshanling granodiorite							Microgranular enclaves						
Sample No.	TSL016	YL49			JY40			JY55						
			Same grain		Same grain					Same grain			Same grain	
Type[a]	MI	MI	II	OI	CA	RA	OI	I	I	CCI	RCI	RCI	CCE	RCE
SiO_2	42.69	40.85	43.69	45.47	50.54	45.80	47.53	49.56	44.80	52.68	46.55	48.09	48.38	45.59
TiO_2	1.55	1.82	1.22	0.90	0.40	0.94	0.89	0.62	1.32	0.16	0.64	0.55	0.42	1.14
Al_2O_3	9.67	11.52	8.59	7.53	3.68	7.66	5.89	4.76	8.12	2.48	6.86	5.81	4.57	7.25
FeO	19.02	17.69	19.23	18.70	16.97	18.78	19.60	17.56	18.66	16.81	18.82	17.94	17.74	18.13
MnO	0.59	0.41	0.72	0.56	1.07	0.94	0.89	0.63	0.64	0.98	0.71	0.96	0.87	0.52
MgO	8.39	10.37	9.74	10.36	12.34	10.22	10.27	11.76	9.39	12.75	10.11	10.57	11.46	10.23
CaO	11.74	9.18	11.17	11.07	11.25	11.22	10.90	11.26	11.10	11.88	11.72	11.85	11.26	11.14
Na_2O	1.49	1.32	1.42	1.40	0.62	1.28	0.89	0.81	1.16	0.41	1.00	0.85	0.66	1.16
K_2O	1.14	3.23	1.12	0.75	0.34	0.82	0.59	0.45	0.77	0.21	0.64	0.63	0.44	0.74
F	0.14	0.61	0.43	0.49	0.14	0.15	0.21	0.20	0.24	0.08	0.17	0.17	0.32	0.21
Cl	0.39	0.12	0.12	0.10	0.06	0.10	0.06	0.07	0.08	0.06	0.16	0.12	0.05	0.12
Total	96.81	97.11	97.45	97.34	97.41	97.91	97.72	97.69	96.28	98.49	97.36	97.54	96.14	96.23
Ions based on 23 oxygen														
T_Si	6.604	6.263	6.652	6.877	7.479	6.871	7.121	7.337	6.850	7.687	7.021	7.217	7.299	6.945
T_Al	1.396	1.737	1.348	1.123	0.521	1.129	0.879	0.663	1.150	0.313	0.979	0.783	0.701	1.055
ΣT	**8.000**	**8.000**	**8.000**	**8.000**	**8.000**	**8.000**	**8.000**	**8.000**	**8.000**	**8.000**	**8.000**	**8.000**	**8.000**	**8.000**
C_Al	0.368	0.345	0.192	0.220	0.121	0.225	0.161	0.166	0.313	0.113	0.240	0.245	0.111	0.247
C_Ti	0.180	0.210	0.140	0.102	0.045	0.106	0.100	0.069	0.152	0.017	0.072	0.062	0.047	0.130
C_Fe^{3+}[b]	0.068	0.441	0.430	0.363	0.256	0.373	0.402	0.298	0.257	0.146	0.293	0.153	0.411	0.271
C_Mg	1.934	2.370	2.210	2.337	2.722	2.286	2.293	2.596	2.140	2.773	2.273	2.364	2.578	2.323
C_Fe^{2+}	2.393	1.634	2.018	1.979	1.845	1.984	2.044	1.871	2.129	1.905	2.081	2.098	1.827	2.029
C_Mn	0.058	0.000	0.010	0.000	0.012	0.027	0.000	0.000	0.010	0.045	0.040	0.078	0.026	0.000
ΣC	**5.000**	**5.000**	**5.000**	**5.000**	**5.000**	**5.000**	**5.000**	**5.000**	**5.000**	**5.000**	**5.000**	**5.000**	**5.000**	**5.000**
B_Mg	0.000	0.000	0.000	0.000	0.000	0.000	0.000	0.000	0.000	0.000	0.000	0.000	0.000	0.000
B_Fe^{2+}	0.000	0.193	0.000	0.025	0.000	0.000	0.010	0.006	0.000	0.000	0.000	0.000	0.000	0.010
B_Mn	0.019	0.053	0.083	0.072	0.122	0.092	0.113	0.079	0.073	0.076	0.050	0.043	0.084	0.067
B_Ca	1.946	1.508	1.822	1.794	1.784	1.803	1.749	1.787	1.819	1.857	1.893	1.904	1.819	1.817
B_Na	0.035	0.246	0.095	0.110	0.094	0.105	0.128	0.128	0.108	0.067	0.057	0.052	0.096	0.105
ΣB	**2.000**	**2.000**	**2.000**	**2.000**	**2.000**	**2.000**	**2.000**	**2.000**	**2.000**	**2.000**	**2.000**	**2.000**	**2.000**	**2.000**
A_Na	0.411	0.147	0.323	0.301	0.084	0.268	0.130	0.104	0.234	0.048	0.235	0.194	0.097	0.238
A_K	0.225	0.631	0.218	0.145	0.065	0.157	0.113	0.085	0.150	0.039	0.123	0.120	0.084	0.145
ΣA	**0.636**	**0.777**	**0.541**	**0.446**	**0.149**	**0.424**	**0.243**	**0.189**	**0.384**	**0.087**	**0.357**	**0.314**	**0.181**	**0.382**
OH[c]	1.831	1.671	1.763	1.735	1.921	1.902	1.884	1.888	1.861	1.952	1.880	1.889	1.837	1.867
F	0.068	0.298	0.207	0.238	0.065	0.072	0.100	0.095	0.119	0.035	0.079	0.080	0.152	0.103
Cl	0.102	0.031	0.030	0.026	0.014	0.027	0.016	0.017	0.020	0.014	0.041	0.032	0.012	0.030
Mg/(Mg+Fe)	0.44	0.51	0.47	0.50	0.56	0.49	0.48	0.54	0.47	0.57	0.49	0.51	0.54	0.50
$Fe^{3+}/(Fe^{2+}+Fe^{3+})$	0.03	0.19	0.21	0.15	0.14	0.19	0.16	0.14	0.11	0.07	0.12	0.07	0.18	0.12

Notes: General formula: $A_{0-1}B_2C_5T_8O_{22}(OH, F, Cl)_2$. [a] MI: mineral inclusion; II: inner of isolated amphibole; OI: outer of isolated amphibole; CA: core of aggregated amphibole grains; RA: rim of aggregated amphibole grains; I: isolated amphibole; CCI: core of clot interior amphibole grains; RCI: rim of clot interior amphibole grains; CCE: core of clot exterior amphibole grains; RCE: rim of clot exterior amphibole grains. [b] Fe^{3+} was calculated using the average estimation after Leake et al. (1997). [c] The estimation of OH was based on OH+F+Cl = 2.

Appendix 5-3. LA-ICP-MS analyses of amphibole and biotite (ppm) from the Tongshanling granodiorite and its microgranular enclaves

	Amphibole														Biotite					
	Tongshanling granodiorite						Microgranular enclaves								Tongshanling granodiorite			Microgranular enclaves		
Sample No.	TSL009			T1512			JY55								TSL009			JY55		
Type	Isolated amphibole			Isolated amphibole			Isolated amphibole		Core of clot interior amphibole grains			Rim of clot interior amphibole grains								
Trace elements																				
Sc	228.07	218.18	202.13	222.79	128.34	243.36	173.68	169.95	15.66	14.57	24.45	75.92	100.27	196.03	27.93	24.99	24.23	15.26	15.90	18.89
V	341.09	326.39	426.10	420.57	407.28	397.12	436.33	528.56	42.44	37.63	73.41	163.36	243.60	414.63	413.87	424.33	429.83	517.65	509.53	445.61
Cr	87.74	77.66	70.34	413.10	1006.91	391.54	77.45	86.36	368.61	390.45	278.45	783.18	382.77	143.75	94.59	86.13	101.01	88.78	84.95	80.90
Co	34.07	34.93	32.90	29.65	29.95	25.25	28.89	28.93	33.53	33.63	32.99	31.23	29.87	32.44	51.66	50.80	49.38	42.64	43.09	45.10
Ni	22.43	23.80	20.46	22.38	17.97	23.61	15.55	14.31	128.30	128.04	48.73	52.97	40.82	18.73	38.01	40.16	38.55	20.56	24.63	25.76
Zn	282.42	299.29	303.45	266.58	262.78	225.39	232.00	232.38	220.78	225.22	207.41	218.74	217.52	230.96	355.49	387.97	397.94	314.71	323.71	316.08
Ga	20.76	18.55	22.57	15.34	18.74	14.48	17.51	20.24	6.19	5.63	8.11	15.12	19.39	17.91	39.14	41.42	42.06	38.79	37.99	36.03
Rb	4.09	4.00	3.86	6.83	4.20	13.65	5.66	12.26	0.88	0.53	0.80	2.93	2.56	10.47	858.82	902.22	923.82	961.43	988.88	722.87
Sr	6.42	8.75	33.66	21.98	42.61	75.44	14.91	28.60	8.90	8.25	9.14	11.35	26.16	13.48	2.45	1.80	2.11	1.22	0.63	1.23
Y	505.48	470.00	299.36	278.26	210.98	268.25	337.02	234.40	78.69	69.43	91.37	255.97	180.42	419.30	8.15	0.90	0.94	0.38	0.77	0.01
Zr	41.60	33.06	48.20	19.98	43.93	17.53	45.21	64.16	6.84	5.73	9.73	26.51	31.42	37.40	2.02	1.67	2.04	1.44	2.13	3.37
Nb	56.33	60.42	45.91	21.55	18.57	20.31	34.89	29.20	3.99	3.42	6.16	25.98	26.61	37.54	94.81	93.38	98.80	94.73	94.59	72.71
In	0.80	0.76	0.92	0.89	0.79	0.88	0.73	0.79	0.29	0.24	0.39	0.71	0.77	0.77	0.16	0.13	0.14	0.11	0.11	0.13
Sn	20.01	19.53	16.85	17.15	11.85	14.98	19.07	17.88	5.11	4.25	6.45	17.90	12.22	25.56	7.81	8.20	8.64	9.83	9.68	9.73
Cs	0.00	0.37	0.00	3.04	0.95	5.78	0.98	2.53	0.08	0.00	0.05	0.43	0.10	1.87	35.64	18.72	21.48	27.00	57.32	17.68
Ba	1.78	5.14	35.25	4.66	31.29	5.74	10.64	31.46	0.69	1.06	2.05	6.09	16.95	8.58	1188.67	2485.56	2333.86	1400.97	1057.79	1013.68
Hf	5.14	4.16	3.30	2.22	2.67	2.13	4.08	4.42	0.33	0.13	0.67	1.91	1.90	5.03	0.18	0.23	0.21	0.13	0.24	0.25
Ta	9.33	12.51	2.75	3.52	1.07	4.10	4.74	1.69	0.23	0.19	0.31	2.68	1.26	7.29	8.24	6.44	8.14	13.13	12.14	4.43
W	0.65	0.46	0.31	0.31	0.11	0.45	0.20	0.17	0.00	0.04	0.13	0.25	0.12	0.37	1.72	2.03	2.14	0.95	0.96	0.84

(*To be continued on the next page*)

Appendix 5-3. (*Continued*)

	Amphibole														Biotite					
	Tongshanling granodiorite						Microgranular enclaves								Tongshanling granodiorite			Microgranular enclaves		
Sample No.	TSL009			T1512			JY55								TSL009			JY55		
Type	Isolated amphibole			Isolated amphibole			Isolated amphibole		Core of clot interior amphibole grains			Rim of clot interior amphibole grains								
Pb	2.93	3.03	4.24	4.14	2.88	8.78	2.63	3.16	0.94	0.84	0.87	2.03	2.22	2.77	3.48	3.52	3.85	2.42	1.88	2.43
Th	0.36	0.26	0.34	0.41	0.53	1.37	0.16	0.16	0.01	0.00	0.07	0.13	0.16	0.17	0.03	0.00	0.00	0.00	0.00	0.00
U	0.54	0.39	0.59	0.74	0.28	1.22	0.22	0.21	0.00	0.04	0.09	0.17	0.21	0.20	0.11	0.00	0.13	0.01	0.00	0.00
Rare earth elements (REE)																				
La	31.01	25.14	27.74	10.55	17.24	11.10	21.73	28.24	4.24	3.51	5.58	15.16	14.28	17.80	2.72	1.51	1.40	0.08	0.02	0.00
Ce	140.42	120.56	120.00	47.91	70.80	40.50	99.85	117.29	20.04	17.40	28.98	74.08	65.06	87.82	5.64	0.59	0.60	0.27	0.13	0.01
Pr	28.72	25.52	22.36	10.64	12.93	8.63	20.42	21.84	4.26	3.66	5.95	15.35	13.31	19.21	1.05	0.32	0.33	0.05	0.03	0.00
Nd	173.15	151.32	127.07	67.25	75.05	56.13	123.02	118.72	25.09	22.03	35.02	93.68	71.57	119.02	5.48	1.44	1.35	0.07	0.38	0.01
Sm	67.69	60.99	48.42	30.19	24.54	26.54	46.98	38.14	9.62	8.80	13.09	34.83	26.58	50.44	1.73	0.19	0.32	0.03	0.13	0.05
Eu	1.95	1.80	3.69	1.49	2.64	1.39	1.96	3.03	0.81	0.83	1.07	1.76	2.67	2.21	0.11	0.09	0.09	0.04	0.03	0.03
Gd	75.10	67.75	51.66	38.10	28.54	34.96	50.46	36.73	8.31	8.87	13.08	37.90	28.10	56.27	3.86	5.15	4.68	2.13	1.85	1.76
Tb	13.37	12.55	9.40	6.91	4.96	6.66	8.82	6.20	1.85	1.61	2.22	6.29	4.94	10.47	0.21	0.01	0.01	0.01	0.01	0.00
Dy	87.79	84.58	58.71	47.82	34.59	45.79	56.67	39.98	13.97	10.62	15.25	43.61	32.93	68.27	1.15	0.05	0.15	0.02	0.08	0.00
Ho	18.09	17.10	11.64	9.86	7.39	9.33	11.63	8.42	2.54	2.27	3.12	9.01	6.56	14.38	0.23	0.02	0.04	0.01	0.00	0.00
Er	54.83	53.50	33.61	30.26	24.14	29.19	36.34	26.39	9.09	7.45	9.28	27.13	20.73	44.45	0.71	0.05	0.06	0.04	0.04	0.00
Tm	7.73	7.47	4.56	4.15	3.59	4.10	5.08	3.92	1.29	1.23	1.36	3.73	2.79	6.50	0.07	0.00	0.01	0.01	0.02	0.01
Yb	56.06	55.59	31.84	30.35	26.39	28.04	36.70	31.11	11.57	9.23	10.84	27.48	24.15	45.39	0.56	0.00	0.06	0.08	0.09	0.00
Lu	7.76	7.89	4.29	4.39	3.73	4.21	5.13	4.50	1.74	1.25	1.57	4.03	3.42	6.74	0.10	0.03	0.00	0.02	0.00	0.02

Appendix 5-4. Representative EMP analyses of biotite (wt.%) from the Tongshanling granodiorite and its microgranular enclaves

	Tongshanling granodiorite								Microgranular enclaves			
Sample No.	TSL009		TSL016		TSL58		YL49		JY55			
SiO_2	36.12	35.76	36.13	35.90	35.57	36.30	35.78	35.02	35.44	36.09	35.61	35.31
TiO_2	3.44	3.49	3.83	3.76	3.58	3.40	3.87	4.12	3.78	3.67	3.68	3.74
Al_2O_3	13.20	13.43	13.49	13.03	14.30	14.99	13.11	13.82	13.70	14.28	13.75	13.91
FeO	21.09	20.26	21.20	22.51	21.02	20.55	22.70	23.47	22.16	21.41	21.76	22.83
MnO	0.47	0.31	0.48	0.33	0.54	0.36	0.52	0.59	0.48	0.47	0.44	0.40
MgO	9.42	10.03	9.12	9.20	10.68	9.85	9.37	8.96	9.84	9.96	9.83	10.48
CaO	0.01	0.08	0.00	0.00	0.00	0.00	0.00	0.00	0.00	0.00	0.00	0.00
Na_2O	0.12	0.20	0.10	0.10	0.09	0.06	0.09	0.07	0.10	0.12	0.06	0.04
K_2O	9.23	8.95	9.39	9.30	9.67	9.70	9.27	9.61	8.95	9.52	9.30	9.09
F	0.12	0.20	0.13	0.32	0.61	0.81	0.60	0.61	0.50	0.97	0.70	0.59
Cl	0.73	0.64	0.36	0.33	0.18	0.13	0.09	0.14	0.23	0.19	0.20	0.21
Total	93.94	93.35	94.24	94.78	96.24	96.16	95.39	96.40	95.20	96.68	95.33	96.57
Ions based on 22 oxygen												
T_Si	5.671	5.622	5.642	5.609	5.433	5.544	5.562	5.416	5.501	5.518	5.523	5.409
T_Al	2.329	2.378	2.358	2.391	2.567	2.456	2.402	2.519	2.499	2.482	2.477	2.511
T_Fe^{3+a}	0.000	0.000	0.000	0.000	0.000	0.000	0.036	0.065	0.000	0.000	0.000	0.080
ΣT	**8.000**	**8.000**	**8.000**	**8.000**	**8.000**	**8.000**	**8.000**	**8.000**	**8.000**	**8.000**	**8.000**	**8.000**
M_Al	0.114	0.110	0.125	0.009	0.008	0.242	0.000	0.000	0.007	0.092	0.035	0.000
M_Ti	0.406	0.412	0.450	0.442	0.411	0.391	0.453	0.479	0.442	0.422	0.429	0.431
M_Fe^{3+}	0.401	0.407	0.369	0.456	0.612	0.432	0.450	0.524	0.473	0.489	0.491	0.503
M_Mg	2.206	2.350	2.124	2.143	2.431	2.243	2.172	2.065	2.277	2.269	2.273	2.393
M_Fe^{2+}	2.368	2.256	2.400	2.485	2.073	2.193	2.465	2.446	2.403	2.248	2.331	2.342
M_Mn	0.062	0.041	0.064	0.044	0.070	0.047	0.068	0.078	0.063	0.060	0.057	0.052
ΣM	**5.556**	**5.577**	**5.532**	**5.579**	**5.606**	**5.547**	**5.608**	**5.592**	**5.666**	**5.581**	**5.617**	**5.720**
I_Ca	0.002	0.014	0.000	0.000	0.000	0.000	0.000	0.001	0.000	0.000	0.000	0.000
I_Na	0.037	0.060	0.031	0.030	0.027	0.018	0.027	0.020	0.031	0.036	0.019	0.012
I_K	1.848	1.795	1.870	1.854	1.884	1.890	1.838	1.897	1.772	1.858	1.839	1.776
ΣI	**1.888**	**1.869**	**1.901**	**1.884**	**1.911**	**1.908**	**1.865**	**1.917**	**1.803**	**1.893**	**1.858**	**1.787**
OH^b	3.872	3.864	3.920	3.876	3.827	3.785	3.840	3.831	3.845	3.737	3.798	3.828
F	0.030	0.051	0.033	0.079	0.150	0.198	0.148	0.151	0.124	0.238	0.175	0.144
Cl	0.098	0.086	0.048	0.045	0.023	0.016	0.013	0.018	0.031	0.025	0.027	0.027
Mg/(Mg+Fe)	0.44	0.47	0.43	0.42	0.48	0.46	0.42	0.40	0.44	0.45	0.45	0.45
$Fe^{3+}/(Fe^{2+}+Fe^{3+})$	0.14	0.15	0.13	0.16	0.23	0.16	0.16	0.19	0.16	0.18	0.17	0.20

Notes: General formula: $IM_3T_4O_{10}(OH, F, Cl)_2$. [a] Fe^{3+} was calculated by the surplus oxygen method after Zheng (1983). [b] The estimation of OH was based on OH+F+Cl = 2.

Appendix 5-5. Representative EMP analyses of magmatic zircon (wt.%) in the Tongshanling granodiorite and its microgranular enclaves

	Tongshanling granodiorite				Microgranular enclaves							
Sample No.	TSL001				JY55							
Type					Inner				Outer			
SiO_2	33.93	33.33	32.84	33.83	32.87	33.20	33.45	33.12	32.93	32.94	32.92	32.60
ZrO_2	65.08	65.24	66.07	65.06	66.64	66.35	65.85	66.48	65.60	66.22	66.08	66.08
HfO_2	1.38	1.29	1.53	1.46	1.15	1.09	1.03	1.12	1.44	1.53	1.51	1.35
UO_2	0.13	0.33	0.13	0.09	0.10	0.07	0.08	0.00	0.19	0.12	0.10	0.28
ThO_2	0.02	0.10	0.07	0.04	0.08	0.00	0.05	0.00	0.02	0.01	0.09	0.04
P_2O_5	0.00	0.14	0.00	0.00	0.00	0.00	0.28	0.00	0.07	0.00	0.00	0.00
Nb_2O_5	0.00	0.00	0.07	0.06	0.11	0.06	0.00	0.00	0.04	0.03	0.02	0.00
Ta_2O_5	0.00	0.00	0.03	0.00	0.00	0.00	0.00	0.00	0.14	0.00	0.00	0.15
Y_2O_3	0.00	0.38	0.00	0.00	0.00	0.00	0.00	0.00	0.00	0.00	0.00	0.16
Sc_2O_3	0.11	0.09	0.07	0.08	0.00	0.13	0.05	0.00	0.08	0.04	0.02	0.00
Total	100.65	100.90	100.81	100.62	100.95	100.90	100.79	100.73	100.49	100.88	100.74	100.66
Cations based on 4 oxygen												
Si	1.026	1.007	1.001	1.024	0.999	1.006	1.010	1.006	1.005	1.002	1.003	0.996
Zr	0.959	0.961	0.982	0.960	0.988	0.980	0.970	0.984	0.976	0.982	0.982	0.985
Hf	0.012	0.011	0.013	0.013	0.010	0.009	0.009	0.010	0.013	0.013	0.013	0.012
U	0.001	0.002	0.001	0.001	0.001	0.000	0.001	0.000	0.001	0.001	0.001	0.002
Th	0.000	0.001	0.001	0.000	0.001	0.000	0.000	0.000	0.000	0.000	0.001	0.000
P	0.000	0.004	0.000	0.000	0.000	0.000	0.007	0.000	0.002	0.000	0.000	0.000
Nb	0.000	0.000	0.001	0.001	0.002	0.001	0.000	0.000	0.001	0.000	0.000	0.000
Ta	0.000	0.000	0.000	0.000	0.000	0.000	0.000	0.000	0.001	0.000	0.000	0.001
Y	0.000	0.006	0.000	0.000	0.000	0.000	0.000	0.000	0.000	0.000	0.000	0.003
Sc	0.003	0.002	0.002	0.002	0.000	0.003	0.001	0.000	0.002	0.001	0.001	0.000
ThO_2+UO_2	0.15	0.44	0.21	0.13	0.17	0.07	0.13	0.00	0.20	0.12	0.18	0.32
Zr/Hf	80.62	86.33	73.86	76.01	99.07	103.70	109.52	101.04	77.71	73.93	74.66	83.62

Appendix 6-1. Some parameters for Raman spectra of carbonaceous material in carbonate rocks from the Tongshanling Cu-Pb-Zn deposit and its adjacent area and temperatures calculated by the RSCM thermometry (mean value and standard deviation)

Sample No.	Formation[a] [Depth (m)]	Number of spectra	G position[b]		G FWHM[c]		R1 ratio[d]		R2 ratio[e]		Temperature[f] (°C)	
			Mean	SD	Mean	SD	Mean	SD	Mean	SD	Mean	SD
Regional carbonate samples collected from the surface far away from the Tongshanling intrusion												
D1509	D_3x	16	1574.24	1.77	54.48	0.01	0.57	0.02	1.31	0.09	238	22
D1512	D_2q	16	1566.77	1.46	54.48	0.01	0.66	0.01	1.96	0.11	347	16
D1515	D_3s	11	1576.18	2.45	54.48	0.01	0.60	0.01	1.51	0.09	282	18
D1522	D_3s	11	1574.51	2.55	54.48	0.01	0.68	0.00	2.10	0.03	340	4
D1524	C_1y	13	1578.66	3.09	54.46	0.01	0.57	0.01	1.33	0.08	244	18
D1531	D_3x	10	1603.38	2.01	50.17	4.18	0.66	0.02	1.96	0.16	347	21
T1610	C_1y	14	1561.64	10.18	53.21	3.30	0.61	0.02	1.57	0.14	293	27
T1613	C_1y	15	1579.77	10.86	59.89	6.25	0.62	0.02	1.64	0.16	305	28
T1615	D_3s	17	1574.81	4.76	80.61	7.40	0.66	0.01	1.92	0.06	348	9
T1637A	D_3s	15	1599.22	11.34	40.30	3.89	0.63	0.01	1.74	0.06	324	10
Metamorphosed carbonate samples collected from the surface and a drill core (ZK1001) in the Tongshanling ore district												
D1507B	C_1d	11	1579.94	1.45	18.05	1.45	0.11	0.05	0.16	0.07	570	29
T1532	C_1d	15	1579.67	0.73	18.51	1.83	0.06	0.02	0.09	0.05	599	20
T1533	C_1d	24	1579.33	1.30	19.68	2.16	0.11	0.04	0.15	0.05	572	21
T1641	C_1d	20	1580.51	0.55	18.26	0.90	0.07	0.02	0.11	0.03	593	14
T1645	C_1y	22	1580.63	0.37	22.56	1.32	0.09	0.03	0.12	0.04	587	18
ZK1001-08	C_1d [1146]	15	1579.25	0.57	17.03	1.35	0.06	0.03	0.09	0.05	601	24
ZK1001-10	C_1d [1110]	11	1579.12	1.45	18.53	1.41	0.15	0.05	0.17	0.07	564	30
ZK1001-15	C_1d [980]	16	1579.21	0.91	20.91	0.92	0.20	0.05	0.22	0.06	544	27
ZK1001-18	C_1d [851]	18	1579.38	0.69	21.94	1.31	0.23	0.12	0.24	0.09	532	39
ZK1001-22	C_1d [651]	10	1580.46	0.49	25.05	2.23	0.28	0.10	0.28	0.06	516	27
ZK1001-23	C_1d [601]	16	1581.33	0.54	22.97	0.75	0.56	0.15	0.36	0.05	480	21
ZK1001-24	C_1d [550]	20	1580.88	2.05	23.58	2.11	1.19	0.66	0.49	0.10	421	43
ZK1001-25	C_1d [500]	20	1582.92	4.75	39.44	6.47	1.75	0.36	0.60	0.07	372	29
ZK1001-26	C_1d [404]	18	1587.09	5.77	51.14	8.45	1.96	0.31	0.67	0.04	343	17
ZK1001-29	C_1d [203]	16	1596.68	2.63	53.22	4.95	2.21	0.17	0.71	0.02	326	10
ZK1001-31	C_1d [42]	17	1586.72	3.84	37.39	5.31	2.26	0.40	0.72	0.03	320	15
Metamorphosed carbonate samples collected from the underground adits of the Tongshanling Cu-Pb-Zn deposit												
Samples close to the proximal endoskarn												
TSL1403	D_2q	20	1580.48	0.61	17.20	1.68	0.03	0.02	0.04	0.02	624	11
TSL1410	D_2q	18	1577.42	4.41	17.94	2.84	0.04	0.03	0.05	0.04	618	17
Samples close to the proximal exoskarn												
TSL1404	D_2q	24	1579.89	2.73	18.39	3.41	0.08	0.04	0.10	0.05	595	21
TSL1407	D_2q	22	1579.81	2.88	18.20	6.98	0.05	0.03	0.07	0.05	610	22
T1534A	D_2q	20	1580.51	0.95	18.16	1.52	0.04	0.03	0.05	0.04	619	17
Samples close to the sulfide-quartz vein												
TSL1411	D_3s	21	1580.92	0.45	24.58	2.13	0.33	0.06	0.32	0.04	500	18
TSL1412	D_2q	17	1580.71	0.72	25.00	1.23	0.23	0.05	0.23	0.04	539	16
TSL1413	D_2q	20	1579.81	1.39	22.74	0.90	0.19	0.04	0.21	0.04	547	16
Samples close to the distal skarn												
T1507	D_3x	15	1580.87	1.04	26.91	0.94	0.30	0.06	0.28	0.04	515	17
T1530A	D_3x	13	1581.06	1.12	27.48	1.47	0.52	0.14	0.41	0.06	461	25

Notes: [a] The abbreviations and lithologies of different Formations refer to Huang et al. (2017a). [b] Raman shift center of the graphite band. [c] Full width at half maximum of the graphite band. [d] R1 = (D1 + D4) / (D1 + D2 + D3 + D4 + G) area ratio and D1 / G height ratio for samples with temperatures of 200 – 320 °C and 330 – 650 °C, respectively. [e] R2 = (D1 + D4) / (D2 + D3 + G) and D1 / (G + D1 + D2) area ratios for samples with temperatures of 200 – 320 °C and 330 – 650 °C, respectively. [f] T (°C) = 1250 × R1–469.75 (Lahfid et al., 2010) and –445 × R2 + 641 (Beyssac et al., 2002) for samples with temperatures of 200 – 320 °C and 330 – 650 °C, respectively.

Appendix 6-2. Representative EMP analyses of garnets (wt.%) from the proximal endoskarn and exoskarn of the Tongshanling Cu-Pb-Zn deposit

Skarn	Proximal endoskarn						Proximal exoskarn													
Generation							First generation						Second generation				Third generation			
Point No.	1	2	3	4	5	6	7	8	9	10	11	12	13	14	15	16	17	18	19	20
SiO_2	36.93	36.66	36.85	36.92	36.18	36.53	35.09	34.92	34.87	35.14	35.17	35.17	35.04	35.03	35.26	35.42	37.41	37.23	37.23	37.39
TiO_2	0.02	0.08	0.01	0.10	0.00	0.01	0.00	0.00	0.03	0.06	0.00	0.00	0.00	0.00	0.00	0.01	0.03	0.05	0.00	0.04
Al_2O_3	16.11	15.17	15.98	15.80	14.47	16.50	2.30	2.06	3.73	4.44	3.81	4.34	5.75	4.95	6.54	6.37	17.24	14.41	16.46	16.93
FeO	12.01	12.56	11.70	11.64	13.65	10.79	27.49	27.56	25.35	24.73	24.70	23.38	23.32	24.39	22.35	22.25	10.27	12.50	12.17	10.45
MnO	1.66	1.65	1.65	1.66	1.56	1.96	0.38	0.44	0.20	0.24	0.31	0.33	0.64	0.53	0.59	0.74	0.84	0.69	1.36	0.88
MgO	0.02	0.00	0.00	0.00	0.01	0.01	0.05	0.06	0.10	0.10	0.16	0.15	0.02	0.03	0.00	0.01	0.09	0.07	0.04	0.05
CaO	33.32	33.58	33.71	33.51	33.81	33.45	34.24	34.28	34.70	34.67	34.20	34.50	34.01	33.79	34.35	34.02	34.38	35.76	33.64	34.56
Na_2O	0.00	0.00	0.00	0.00	0.00	0.00	0.00	0.00	0.00	0.00	0.00	0.00	0.09	0.09	0.08	0.08	0.00	0.00	0.00	0.00
K_2O	0.03	0.04	0.02	0.02	0.01	0.00	0.00	0.02	0.01	0.00	0.00	0.00	0.00	0.01	0.01	0.02	0.01	0.01	0.00	0.01
F	0.00	0.00	0.00	0.00	0.00	0.00	0.00	0.00	0.00	0.00	0.00	0.00	0.00	0.00	0.00	0.00	0.00	0.00	0.00	0.00
Cl	0.04	0.04	0.03	0.04	0.03	0.03	0.04	0.02	0.03	0.03	0.03	0.03	0.05	0.04	0.05	0.05	0.03	0.03	0.03	0.04
Total	100.09	99.74	99.92	99.65	99.68	99.26	99.55	99.35	98.99	99.38	98.34	97.87	98.88	98.83	99.18	98.93	100.27	100.71	100.89	100.31
Ions based on 12 oxygen																				
T_Si	2.868	2.867	2.868	2.880	2.844	2.860	2.889	2.885	2.872	2.874	2.907	2.915	2.868	2.875	2.869	2.887	2.880	2.888	2.865	2.881
T_Al	0.132	0.133	0.132	0.120	0.156	0.140	0.111	0.115	0.128	0.126	0.093	0.085	0.132	0.125	0.131	0.113	0.120	0.112	0.135	0.119
ΣT	**3.000**	**3.000**	**3.000**	**3.000**	**3.000**	**3.000**	**3.000**	**3.000**	**3.000**	**3.000**	**3.000**	**3.000**	**3.000**	**3.000**	**3.000**	**3.000**	**3.000**	**3.000**	**3.000**	**3.000**
B_Al	1.342	1.266	1.334	1.332	1.185	1.382	0.113	0.086	0.234	0.302	0.277	0.338	0.423	0.354	0.495	0.499	1.443	1.206	1.358	1.419
B_Ti	0.001	0.005	0.001	0.006	0.000	0.000	0.000	0.000	0.002	0.003	0.000	0.000	0.000	0.000	0.000	0.000	0.001	0.003	0.000	0.002
B_Fe^{3+a}	0.773	0.822	0.762	0.759	0.898	0.707	1.881	1.904	1.746	1.691	1.707	1.620	1.596	1.674	1.520	1.517	0.661	0.811	0.760	0.674

(*To be continued on the next page*)

Appendix 6-2. (*Continued*)

Skarn	Proximal endoskarn						Proximal exoskarn													
Generation							First generation						Second generation				Third generation			
Point No.	1	2	3	4	5	6	7	8	9	10	11	12	13	14	15	16	17	18	19	20
B_Mg	0.000	0.000	0.000	0.000	0.000	0.000	0.006	0.007	0.012	0.004	0.016	0.019	0.000	0.000	0.000	0.000	0.000	0.000	0.000	0.000
B_Fe^{2+}	0.000	0.000	0.000	0.000	0.000	0.000	0.000	0.000	0.000	0.000	0.000	0.000	0.000	0.000	0.000	0.000	0.000	0.000	0.000	0.000
B_Mn	0.000	0.000	0.000	0.000	0.000	0.000	0.000	0.003	0.006	0.000	0.000	0.023	0.000	0.000	0.000	0.000	0.000	0.000	0.000	0.000
ΣB	**2.116**	**2.092**	**2.096**	**2.098**	**2.083**	**2.089**	**2.000**	**2.000**	**2.000**	**2.000**	**2.000**	**2.000**	**2.019**	**2.028**	**2.016**	**2.017**	**2.106**	**2.020**	**2.118**	**2.095**
A_Mg	0.002	0.000	0.000	0.000	0.001	0.002	0.000	0.000	0.000	0.009	0.004	0.000	0.003	0.004	0.000	0.001	0.010	0.008	0.005	0.005
A_Fe^{2+}	0.007	0.000	0.000	0.000	0.000	0.000	0.011	0.000	0.000	0.000	0.000	0.000	0.000	0.000	0.000	0.000	0.000	0.000	0.023	0.000
A_Mn	0.109	0.109	0.109	0.110	0.104	0.130	0.027	0.028	0.009	0.017	0.022	0.000	0.045	0.037	0.041	0.051	0.055	0.045	0.089	0.057
A_Ca	2.772	2.814	2.811	2.800	2.848	2.805	3.021	3.034	3.063	3.037	3.029	3.063	2.983	2.972	2.994	2.971	2.835	2.972	2.774	2.853
A_Na	0.000	0.000	0.000	0.000	0.000	0.000	0.000	0.000	0.000	0.000	0.000	0.000	0.015	0.014	0.013	0.013	0.000	0.000	0.000	0.000
A_K	0.003	0.004	0.002	0.002	0.001	0.000	0.000	0.003	0.001	0.000	0.000	0.000	0.000	0.001	0.001	0.002	0.001	0.000	0.000	0.001
ΣA	**2.891**	**2.927**	**2.922**	**2.912**	**2.953**	**2.935**	**3.058**	**3.064**	**3.072**	**3.054**	**3.051**	**3.063**	**3.042**	**3.024**	**3.049**	**3.038**	**2.891**	**3.018**	**2.886**	**2.911**
F	0.000	0.000	0.000	0.000	0.000	0.000	0.000	0.000	0.000	0.000	0.000	0.000	0.000	0.000	0.000	0.000	0.000	0.000	0.000	0.000
Cl	0.003	0.003	0.002	0.003	0.002	0.002	0.003	0.001	0.002	0.002	0.002	0.002	0.003	0.003	0.003	0.004	0.002	0.002	0.002	0.002
End members[b] (%)																				
Gr	62.92	60.63	63.34	63.20	57.77	65.24	10.47	9.41	17.02	19.99	17.60	20.44	25.37	21.95	28.79	28.25	68.71	60.82	63.59	68.05
Ad	32.99	35.63	32.92	33.04	38.67	30.28	88.11	89.35	82.14	79.05	81.05	78.22	73.06	76.72	69.87	70.02	29.06	37.43	32.37	29.81
Py + Al + Sp	4.09	3.74	3.74	3.76	3.56	4.48	1.42	1.24	0.84	0.95	1.35	1.34	1.57	1.33	1.34	1.73	2.23	1.74	4.04	2.14

Notes: General formula: $A_3B_2T_3O_{12}$. [a] Fe^{3+} was calculated based on the stoichiometric criteria after Droop (1987). [b] Mineral abbreviations: Ad = andradite, Al = almandine, Gr = grossularite, Py = pyrope, Sp = spessartine.

Appendix 7-1. LA-ICP-MS U-Pb dating results of garnet in the proximal exoskarn from the Tongshanling Cu-Pb-Zn deposit

Spot	Elements (ppm)			Isotopic ratios						Ages (Ma)					
	Pb	Th	U	$^{207}Pb/^{206}Pb$	1σ	$^{207}Pb/^{235}U$	1σ	$^{206}Pb/^{238}U$	1σ	$^{207}Pb/^{206}Pb$	1σ	$^{207}Pb/^{235}U$	1σ	$^{206}Pb/^{238}U$	1σ
1-2-01	0.26	0.03	9.72	0.048939	0.019178	0.223433	0.100543	0.026977	0.001657	146.4	725.8	204.8	83.4	171.6	10.4
1-2-02	0.38	0.03	9.50	0.096833	0.024945	0.448277	0.152093	0.029738	0.002805	1564.8	500.0	376.1	106.6	188.9	17.6
1-2-03	0.37	0.03	10.29	0.054834	0.019057	0.204357	0.075525	0.026576	0.001561	405.6	633.3	188.8	63.7	169.1	9.8
1-2-04	0.18	0.02	7.25	0.012337	0.007236	0.202635	0.103736	0.024695	0.001777			187.4	87.6	157.3	11.2
1-2-05	0.44	0.11	14.56	0.035332	0.010679	0.208372	0.117544	0.026316	0.001677			192.2	98.8	167.5	10.5
1-2-06	0.41	0.08	13.38	0.046970	0.013289	0.219194	0.085812	0.026908	0.001432	55.7	557.3	201.2	71.5	171.2	9.0
1-2-07	0.45	0.12	15.08	0.052511	0.016047	0.184665	0.069402	0.026084	0.001374	309.3	577.7	172.1	59.5	166.0	8.6
1-2-08	0.31	0.05	7.53	0.122815	0.032590	0.609241	0.183162	0.029443	0.001852	1998.2	487.5	483.1	115.6	187.1	11.6
1-2-09	0.39	0.19	12.50	0.065390	0.019121	0.259003	0.056590	0.027293	0.001422	787.0	646.2	233.9	45.6	173.6	8.9
1-2-10	0.51	0.18	16.77	0.080256	0.018175	0.224366	0.044099	0.028541	0.001349	1203.4	459.4	205.5	36.6	181.4	8.5
1-2-11	0.50	0.16	14.49	0.071699	0.021054	0.206117	0.058539	0.028077	0.001605	977.5	625.0	190.3	49.3	178.5	10.1
1-2-12	0.61	0.19	15.71	0.073554	0.014188	0.279307	0.047431	0.027565	0.001355	1029.3	394.0	250.1	37.6	175.3	8.5
1-2-13	0.59	0.17	15.97	0.090933	0.023792	0.255400	0.072031	0.023547	0.001180	1455.6	516.7	231.0	58.3	150.0	7.4
1-2-14	0.42	0.14	15.72	0.053655	0.016171	0.165985	0.042760	0.026614	0.001352	366.7	557.4	155.9	37.2	169.3	8.5
1-2-15	0.44	0.13	14.06	0.085756	0.022678	0.244963	0.070105	0.025858	0.001392	1332.4	531.2	222.5	57.2	164.6	8.7
1-2-16	0.39	0.15	15.37	0.089366	0.024653	0.284113	0.105711	0.023639	0.001177	1413.0	550.0	253.9	83.6	150.6	7.4
1-2-17	0.30	0.07	10.46	0.026099	0.009569	0.177004	0.085985	0.024113	0.001568			165.5	74.2	153.6	9.9
1-2-18	0.24	0.06	9.71	0.043009	0.016189	0.220661	0.089927	0.023937	0.001480			202.5	74.8	152.5	9.3
1-2-19	0.33	0.07	10.81	0.040697	0.012388	0.196150	0.060537	0.025212	0.001469			181.9	51.4	160.5	9.2
1-2-20	0.43	0.16	14.94	0.077035	0.022432	0.213394	0.056517	0.024789	0.001317	1121.9	609.7	196.4	47.3	157.9	8.3
1-2-21	0.48	0.15	16.06	0.090418	0.019451	0.303659	0.080001	0.023926	0.001317	1435.2	415.7	269.3	62.3	152.4	8.3
1-2-22	0.50	0.19	17.19	0.072609	0.020124	0.207200	0.056798	0.025658	0.001214	1002.8	588.9	191.2	47.8	163.3	7.6
1-2-23	0.49	0.19	15.45	0.091629	0.026971	0.246048	0.055312	0.025958	0.001400	1461.1	585.3	223.4	45.1	165.2	8.8
1-2-24	0.46	0.20	13.79	0.114048	0.031148	0.372318	0.123122	0.027943	0.001567	1865.1	506.0	321.4	91.1	177.7	9.8
1-2-25	0.44	0.07	12.34	0.041993	0.012332	0.303210	0.057434	0.027684	0.001758			268.9	44.7	176.0	11.0

Appendix 7-2. Re-Os dating results of molybdenites from the Tongshanling Cu-Pb-Zn deposit and Yulong Mo deposit

Sample No.	Weight (g)	Re (ppb)		Common Os (ppb)		^{187}Re (ppb)		^{187}Os (ppb)		Model age (Ma)	
		Measured	2σ	Measured	2σ	Measured	2σ	Measured	2σ	Measured	2σ
Tongshanling Cu-Pb-Zn deposit											
Proximal endoskarn											
TSL20	0.01504	16281	129	2.7618	0.0615	10233	81	27.84	0.23	163.1	2.3
TSL32	0.01960	89506	680	27.5608	0.2776	56257	427	152.45	1.26	162.4	2.2
Proximal exoskarn											
TSL25-1	0.02073	24604	222	1.7207	0.0527	15464	140	41.32	0.36	160.2	2.4
Distal skarn											
TSL29-1	0.02047	47972	444	3.2672	0.0765	30152	279	81.02	0.64	161.1	2.4
TSL31	0.04999	98234	1900	10.5649	0.1255	61742	1194	168.46	1.48	163.5	3.7
Yulong Mo deposit											
YL08-1	0.02029	39083	291	0.3933	0.0625	24564	183	65.30	0.59	159.3	2.3
YL08-2	0.02076	45294	334	0.3870	0.0308	28468	210	75.44	0.68	158.9	2.3
YL09-2	0.02017	38827	321	3.5533	0.0594	24404	201	65.12	0.64	159.9	2.4
YL12	0.02015	37900	282	7.2538	0.0846	23821	177	63.93	0.58	160.9	2.3
YL19-1	0.02056	39333	292	0.7386	0.0589	24722	184	66.41	0.61	161.0	2.3
YL19-2	0.02042	49801	394	6.3257	0.0564	31301	248	84.48	0.71	161.8	2.3
YL19-4	0.02025	48309	365	0.6849	0.0610	30363	229	80.56	0.70	159.0	2.2
YL22	0.02034	50815	453	0.7244	0.0509	31938	285	85.39	0.78	160.3	2.4

Appendix 7-3. LA-ICP-MS U-Pb dating results of hydrothermal titanite in the altered granodiorite from the Tongshanling Cu-Pb-Zn deposit

Spot	Elements (ppm)			Isotopic ratios						Ages (Ma)					
	Pb	Th	U	$^{207}Pb/^{206}Pb$	1σ	$^{207}Pb/^{235}U$	1σ	$^{206}Pb/^{238}U$	1σ	$^{207}Pb/^{235}U$	1σ	$^{206}Pb/^{238}U$	1σ	$^{206}Pb/^{238}U^{*a}$	1σ
T1511-01	8.6	190.1	282.5	0.085678	0.001746	0.307062	0.006331	0.026084	0.000233	271.9	4.9	166.0	1.5	156.0	1.5
T1511-02	5.3	115.4	157.5	0.111566	0.002456	0.405767	0.008640	0.026777	0.000284	345.8	6.2	170.3	1.8	152.8	1.8
T1511-03	3.5	48.3	92.2	0.146566	0.003705	0.569599	0.013901	0.028694	0.000343	457.8	9.0	182.4	2.2	153.0	2.2
T1511-04	2.3	22.3	40.6	0.240957	0.006790	1.109653	0.029336	0.034629	0.000536	758.0	14.1	219.5	3.3	149.9	3.3
T1511-05	4.0	72.3	100.0	0.152320	0.003824	0.596640	0.013411	0.029174	0.000349	475.1	8.5	185.4	2.2	153.8	2.2
T1511-06	2.2	27.5	52.6	0.177440	0.006053	0.686225	0.018989	0.030032	0.000479	530.5	11.4	190.7	3.0	150.3	3.0
T1511-07	2.1	21.1	41.6	0.225677	0.007948	0.961289	0.027863	0.033166	0.000564	684.0	14.4	210.3	3.5	148.9	3.5
T1511-08	4.3	75.8	104.9	0.153664	0.003749	0.606192	0.014528	0.029044	0.000340	481.2	9.2	184.6	2.1	152.7	2.1
T1511-09	10.2	228.6	350.0	0.080016	0.001645	0.278568	0.005713	0.025346	0.000258	249.5	4.5	161.4	1.6	153.1	1.6
T1511-10	8.3	184.4	260.7	0.095849	0.002182	0.343503	0.007520	0.026265	0.000284	299.8	5.7	167.1	1.8	154.2	1.8
T1511-11	8.0	166.1	274.4	0.081790	0.002092	0.284642	0.006853	0.025621	0.000280	254.3	5.4	163.1	1.8	154.3	1.8
T1511-12	10.0	104.3	404.4	0.070981	0.001690	0.236849	0.005345	0.024529	0.000285	215.8	4.4	156.2	1.8	150.6	1.8
T1511-13	4.0	51.5	96.9	0.164386	0.004785	0.653694	0.018112	0.029627	0.000446	510.7	11.1	188.2	2.8	152.4	2.8
T1511-14	7.0	49.4	89.9	0.295930	0.008572	1.833193	0.063727	0.043285	0.000904	1057.4	22.9	273.2	5.6	161.8	5.6
T1511-15	12.4	249.1	391.2	0.086929	0.001854	0.317984	0.006593	0.026884	0.000375	280.4	5.1	171.0	2.4	160.3	2.4
T1511-16	2.6	28.9	65.9	0.173843	0.006048	0.655088	0.019371	0.028880	0.000519	511.6	11.9	183.5	3.3	145.7	3.3
T1511-17	2.7	28.9	57.6	0.198502	0.006853	0.806138	0.023689	0.031272	0.000582	600.3	13.3	198.5	3.6	149.5	3.6
T1511-18	9.6	146.2	309.3	0.090529	0.002128	0.342463	0.008829	0.027414	0.000396	299.0	6.7	174.3	2.5	162.4	2.5
T1511-19	9.2	168.4	286.4	0.086536	0.001804	0.323680	0.006563	0.027420	0.000365	284.7	5.0	174.4	2.3	163.6	2.3
T1511-20	3.3	38.5	63.0	0.216300	0.006615	0.964200	0.026053	0.033919	0.000612	685.5	13.5	215.0	3.8	155.6	3.8
T1511-21	4.0	47.6	92.0	0.165419	0.004588	0.702422	0.018261	0.031660	0.000512	540.2	10.9	200.9	3.2	162.3	3.2

Note: [a] $^{206}Pb/^{238}U$ age corrected by ^{207}Pb method.

Appendix 7-4. S and Pb isotopic compositions of sulfide minerals from the Tongshanling Cu-Pb-Zn deposit, Jiangyong Pb-Zn-Ag deposit, and Yulong Mo deposit

Sample No.	Mineralization type	Level	Mineral[a]	$\delta^{34}S_{CDT}$ (‰)	$^{206}Pb/^{204}Pb$	2σ	$^{207}Pb/^{204}Pb$	2σ	$^{208}Pb/^{204}Pb$	2σ
Tongshanling Cu-Pb-Zn deposit										
TSL60	Altered granodiorite	30 m	Po	3.9						
TSL25-1	Proximal endoskarn	30 m	Mol	3.6	18.723	0.001	15.770	0.001	39.073	0.002
TSL34	Proximal endoskarn	00 m	Mol	3.2						
TSL120	Proximal endoskarn	00 m	Po	2.0						
TSL121	Proximal endoskarn	00 m	Po	2.1						
TSL121	Proximal endoskarn	00 m	Ccp	2.4	18.785	0.002	15.730	0.002	38.931	0.004
TSL122	Proximal endoskarn	00 m	Po	1.9						
TSL122	Proximal endoskarn	00 m	Ccp	2.2	18.706	0.003	15.742	0.002	38.979	0.006
TSL98	Proximal exoskarn	00 m	Ccp	3.4	18.780	0.003	15.854	0.003	39.350	0.008
TSL98	Proximal exoskarn	00 m	Sp	2.8						
TSL98	Proximal exoskarn	00 m	Gn	2.5						
TSL123	Proximal exoskarn	00 m	Ccp	4.4						
TSL123	Proximal exoskarn	00 m	Sp	3.9						
TSL123	Proximal exoskarn	00 m	Gn	2.8	18.704	0.002	15.761	0.002	39.034	0.005
TSL04-1	Sulfide-quartz vein	60 m	Ccp	3.0						
TSL04-1	Sulfide-quartz vein	60 m	Sp	3.7	18.697	0.002	15.754	0.002	39.018	0.004
TSL04-1	Sulfide-quartz vein	60 m	Gn	2.1						
TSL04-5	Sulfide-quartz vein	60 m	Ccp	4.0	18.736	0.003	15.798	0.003	39.179	0.008
TSL04-5	Sulfide-quartz vein	60 m	Sp	3.8						
TSL04-5	Sulfide-quartz vein	60 m	Gn	2.7	18.701	0.003	15.757	0.003	39.022	0.007
TSL04-6	Sulfide-quartz vein	60 m	Ccp	3.5	18.769	0.003	15.844	0.003	39.314	0.008
TSL04-6	Sulfide-quartz vein	60 m	Sp	3.3						
TSL04-6	Sulfide-quartz vein	60 m	Gn	2.3						
TSL04-7	Sulfide-quartz vein	60 m	Ccp	3.6	18.755	0.002	15.825	0.002	39.247	0.004
TSL04-9	Sulfide-quartz vein	60 m	Ccp	4.2	18.735	0.002	15.802	0.001	39.182	0.004
TSL04-9	Sulfide-quartz vein	60 m	Sp	4.0						
TSL04-12	Sulfide-quartz vein	60 m	Ccp	4.6	18.703	0.003	15.762	0.002	39.048	0.005
TSL04-12	Sulfide-quartz vein	60 m	Sp	3.7						
TSL04-15	Sulfide-quartz vein	60 m	Ccp	3.5	18.748	0.003	15.818	0.003	39.237	0.007
TSL04-15	Sulfide-quartz vein	60 m	Sp	4.5						
TSL25-2	Sulfide-quartz vein	90 m	Ccp	3.1						
TSL25-2	Sulfide-quartz vein	90 m	Sp	2.9	18.752	0.003	15.819	0.003	39.240	0.006
TSL25-2	Sulfide-quartz vein	90 m	Gn	1.9						
TSL25-3	Sulfide-quartz vein	90 m	Ccp	2.9						
TSL25-3	Sulfide-quartz vein	90 m	Sp	2.9						
TSL25-3	Sulfide-quartz vein	90 m	Gn	2.1	18.743	0.002	15.811	0.002	39.210	0.004
TSL26-1	Sulfide-quartz vein	120 m	Ccp	3.0						

(*To be continued on the next page*)

Appendix 7-4. (*Continued*)

Sample No.	Mineralization type	Level	Mineral[a]	$\delta^{34}S_{CDT}$ (‰)	$^{206}Pb/^{204}Pb$	2σ	$^{207}Pb/^{204}Pb$	2σ	$^{208}Pb/^{204}Pb$	2σ
TSL26-1	Sulfide-quartz vein	120 m	Sp	3.2						
TSL26-1	Sulfide-quartz vein	120 m	Gn	2.2	18.685	0.002	15.740	0.002	38.971	0.005
TSL28-1	Sulfide-quartz vein	120 m	Ccp	3.9						
TSL28-1	Sulfide-quartz vein	120 m	Sp	3.6	18.737	0.002	15.800	0.002	39.180	0.004
TSL28-2	Sulfide-quartz vein	120 m	Ccp	3.5						
TSL28-2	Sulfide-quartz vein	120 m	Sp	3.3	18.693	0.001	15.747	0.001	38.993	0.004
TSL28-2	Sulfide-quartz vein	120 m	Gn	2.5						
TSL28-3	Sulfide-quartz vein	120 m	Ccp	3.5						
TSL28-3	Sulfide-quartz vein	120 m	Sp	3.7	18.705	0.003	15.763	0.002	39.056	0.005
TSL28-3	Sulfide-quartz vein	120 m	Gn	2.5	18.709	0.002	15.769	0.002	39.072	0.004
TSL29-2	Sulfide-quartz vein	180 m	Ccp	3.4						
TSL29-2	Sulfide-quartz vein	180 m	Sp	3.3	18.723	0.002	15.784	0.002	39.122	0.005
TSL29-2	Sulfide-quartz vein	180 m	Gn	3.1						
TSL66	Sulfide-quartz vein	60 m	Ccp	3.1						
TSL71	Sulfide-quartz vein	60 m	Ccp	3.6						
TSL78	Sulfide-quartz vein	150 m	Ccp	3.7						
TSL79	Sulfide-quartz vein	150 m	Ccp	3.3						
TSL81	Sulfide-quartz vein	150 m	Ccp	2.7						
TSL85	Sulfide-quartz vein	205 m	Ccp	2.8						
TSL95	Sulfide-quartz vein	231 m	Ccp	3.3						
TSL109	Sulfide-quartz vein	231 m	Ccp	3.5						
TSL03	Distal skarn	205 m	Gn	1.4	18.673	0.001	15.725	0.001	38.919	0.003
TSL27-1	Distal skarn	260 m	Gn	1.5	18.714	0.002	15.777	0.003	39.098	0.007
TSL29-1	Distal skarn	290 m	Mol	4.5						
TSL33-2	Distal skarn	290 m	Gn	0.2						
TSL91	Distal skarn	231 m	Ccp	3.1						
TSL91	Distal skarn	231 m	Sp	3.0	18.749	0.002	15.821	0.002	39.235	0.005
TSL91	Distal skarn	231 m	Gn	1.7	18.675	0.003	15.728	0.002	38.936	0.006
TSL93	Distal skarn	231 m	Sp	3.4	18.696	0.002	15.756	0.002	39.022	0.004
TSL93	Distal skarn	231 m	Gn	1.8	18.678	0.002	15.742	0.002	38.983	0.005
TSL145	Distal skarn	231 m	Ccp	3.6						
TSL145	Distal skarn	231 m	Sp	3.1	18.739	0.002	15.809	0.002	39.200	0.004
TSL17	Carbonate replacement	60 m	Sp	5.0						
TSL17	Carbonate replacement	60 m	Gn	2.2	18.702	0.002	15.834	0.002	39.352	0.004
TSL40	Carbonate replacement	231 m	Sp	4.7						
TSL40	Carbonate replacement	231 m	Gn	1.9	18.643	0.002	15.760	0.002	39.084	0.004
Jiangyong Pb-Zn-Ag deposit										
JY23	Altered granodiorite	160 m	Po	2.5						
JY27	Altered granodiorite	160 m	Po	2.0						

(*To be continued on the next page*)

Appendix 7-4. (*Continued*)

Sample No.	Mineralization type	Level	Mineral[a]	$\delta^{34}S_{CDT}$ (‰)	$^{206}Pb/^{204}Pb$	2σ	$^{207}Pb/^{204}Pb$	2σ	$^{208}Pb/^{204}Pb$	2σ
JY64	Skarn	160 m	Po	1.2	18.921	0.002	15.818	0.002	39.349	0.005
JY54	Skarn	200 m	Po	2.1	18.932	0.003	15.834	0.003	39.408	0.007
JY48	Skarn	240 m	Po	2.2						
JY48	Skarn	240 m	Sp	2.6	18.853	0.002	15.727	0.002	39.055	0.004
JY59	Carbonate replacement	200 m	Py	1.9						
JY59	Carbonate replacement	200 m	Sp	2.6	18.969	0.002	15.875	0.003	39.535	0.006
JY47	Carbonate replacement	160 m	Py	1.8						
JY47	Carbonate replacement	160 m	Sp	2.8						
JY47	Carbonate replacement	160 m	Gn	0.3	18.850	0.002	15.730	0.002	39.062	0.006
JY63	Carbonate replacement	160 m	Py	2.3						
JY63	Carbonate replacement	160 m	Sp	2.7						
JY63	Carbonate replacement	160 m	Gn	0.2	18.836	0.002	15.712	0.002	38.997	0.004
JY50	Carbonate replacement	240 m	Py	2.4						
JY50	Carbonate replacement	240 m	Sp	3.3						
JY50	Carbonate replacement	240 m	Gn	0.5	18.880	0.002	15.752	0.002	39.143	0.004
JY56	Carbonate replacement	200 m	Py	2.6						
JY56	Carbonate replacement	200 m	Sp	3.2						
JY56	Carbonate replacement	200 m	Gn	0.8	18.857	0.002	15.726	0.002	39.045	0.005
JY58	Carbonate replacement	200 m	Py	2.4						
JY58	Carbonate replacement	200 m	Sp	3.3						
JY58	Carbonate replacement	200 m	Gn	1.1	18.865	0.003	15.736	0.003	39.083	0.008
JY66	Carbonate replacement	240 m	Py	2.3						
JY66	Carbonate replacement	240 m	Sp	2.4						
JY66	Carbonate replacement	240 m	Gn	0.4	18.866	0.003	15.750	0.002	39.134	0.005
Yulong Mo deposit										
YL02	Skarn	395 m	Mol	5.6						
YL08-1	Skarn	480 m	Mol	5.9						
YL08-2	Skarn	480 m	Mol	6.3						
YL09-1	Skarn	480 m	Mol	6.1						
YL09-2	Skarn	480 m	Mol	6.3						
YL12	Skarn	480 m	Mol	4.9						
YL19	Skarn	435 m	Mol	5.3						
YL19-1A	Skarn	435 m	Mol	4.9						
YL19-1B	Skarn	435 m	Mol	5.0						
YL19-2A	Skarn	435 m	Mol	5.4						
YL19-2B	Skarn	435 m	Mol	5.8						
YL22	Skarn	520 m	Mol	5.6						
YL67	Skarn	520 m	Po	–0.3	18.772	0.003	15.729	0.002	39.022	0.006

Note: [a] Mineral abbreviations: Ccp = chalcopyrite, Gn = galena, Mol = molybdenite, Po = pyrrhotite, Py = pyrite, Sp = sphalerite.

Appendix 7-5. Pb isotopic compositions of sulfide minerals from the Middle-Late Jurassic Cu-Pb-Zn and W deposits in the Nanling Range of South China

Deposit	Metal association	Related intrusion	$^{206}Pb/^{204}Pb$	$^{207}Pb/^{204}Pb$	$^{208}Pb/^{204}Pb$	Reference
Cu-Pb-Zn deposits						
Shuikoushan	Pb-Zn-Au-Ag	Granodiorite	18.444 – 18.538	15.654 – 15.783	38.627 – 39.066	Lu et al. (2013)
Baoshan	Cu-Mo-Pb-Zn-Ag	Granodiorite porphyry	18.188 – 18.844	15.675 – 15.768	38.562 – 39.149	Yao et al. (2006)
			18.602 – 18.672	15.693 – 15.780	38.901 – 39.186	Zhu et al. (2012)
			18.485 – 18.753	15.661 – 15.843	38.737 – 39.395	Xie et al. (2015)
			18.479 – 18.767	15.684 – 15.722	38.790 – 39.104	Ding et al. (2016c)
Tongshanling	Cu-Mo-Pb-Zn-Ag	Granodiorite porphyry	18.256 – 18.856	15.726 – 15.877	38.878 – 39.430	Cai et al. (2015)
			18.165 – 18.707	15.649 – 15.798	38.114 – 39.000	Wang et al. (2017d)
			18.673 – 18.969	15.712 – 15.875	38.919 – 39.535	This study
Dabaoshan	Cu-Pb-Zn-Mo-W-Fe	Granodiorite porphyry	18.330 – 18.785	15.491 – 15.772	38.518 – 39.088	Xu et al. (2008)
Huangshaping	Pb-Zn-W-Mo	Dacite porphyry,	18.315 – 18.841	15.450 – 16.000	38.441 – 39.571	Xi et al. (2009)
		quartz porphyry,	18.498 – 18.658	15.672 – 15.792	38.770 – 39.260	Zhu et al. (2012)
		granite porphyry	18.525 – 18.652	15.686 – 15.845	38.821 – 39.345	Ding et al. (2016a)
W deposits						
Yaogangxian	W	Biotite granite	18.548 – 18.701	15.691 – 15.811	38.809 – 39.212	Zhu et al. (2014)
Shizhuyuan	W-Sn-Mo-Bi	Biotite monzogranite	18.504 – 18.834	15.598 – 15.786	38.711 – 39.354	Zhang (1989)
			18.565 – 18.622	15.694 – 15.738	38.819 – 38.986	Wu et al. (2016)
Da'ao	W-Sn	Biotite granite	18.599 – 18.857	15.685 – 15.762	38.822 – 39.077	Liu et al. (2007)
Xihuashan	W-Mo	Biotite granite,	18.640 – 18.849	15.697 – 15.941	38.902 – 39.134	Xu and Wang (2014)
		two-mica granite				

Appendix 7-6. H-O isotopic compositions of quartz from the Tongshanling Cu-Pb-Zn deposit, Jiangyong Pb-Zn-Ag deposit, and Yulong Mo deposit

Sample No.	Occurrence of quartz	T_h[a] (°C)	$\delta D_{H2O\ (V\text{-}SMOW)}$ (‰)	$\delta^{18}O_{quartz\ (V\text{-}SMOW)}$ (‰)	$\delta^{18}O_{H2O\ (V\text{-}SMOW)}$[b] (‰)
Tongshanling Cu-Pb-Zn deposit					
TSL011	Quartz vein in granodiorite	300	–62	11.7	4.8
TSL04-1	Sulfide-quartz vein in limestone	200	–55	13.7	2.0
TSL04-5	Sulfide-quartz vein in limestone	220	–53	14.0	3.5
TSL04-6	Sulfide-quartz vein in limestone	235	–53	12.3	2.6
TSL04-7	Sulfide-quartz vein in limestone	250	–53	13.0	4.1
TSL04-10	Sulfide-quartz vein in limestone	220	–48	14.0	3.5
TSL12-1	Quartz cement of brecciated limestone	215	–52	14.0	3.2
TSL13	Quartz vein in limestone	200	–55	13.3	1.6
TSL28-3	Sulfide-quartz vein in limestone	215	–54	12.7	1.9
Jiangyong Pb-Zn-Ag deposit					
JY51	Quartz vein in granodiorite	270	–70	12.4	4.3
Yulong Mo deposit					
YL5	Vein-like quartz in skarn	275	–53	13.3	5.5
YL63	Vein-like quartz in skarn	275	–58	13.1	5.3
YL64	Massive quartz in skarn	350	–56	9.4	4.1

Notes: [a] Homogenization temperature obtained from fluid inclusions in quartz. [b] $\delta^{18}O_{H2O}$ values are calculated based on the quartz-water isotopic equilibrium equation of Clayton et al. (1972).

Appendix 7-7. H-O isotopic compositions of ore-forming fluids of the Middle-Late Jurassic Cu-Pb-Zn and W deposits in the Nanling Range of South China

Deposit	Metal association	Related intrusion	Mineral	δD_{H2O} (‰)	$\delta^{18}O_{H2O}$ (‰)	Reference
Cu-Pb-Zn deposits						
Shuikoushan	Pb-Zn-Au-Ag	Granodiorite	Quartz	–54 – –49	–6.3 – 2.5	Liu (1994)
Baoshan	Cu-Mo-Pb-Zn-Ag	Granodiorite porphyry	Fluorite	–48	2.0 – 8.4	Shi et al. (1993)
						Tong et al. (1995)
Tongshanling	Cu-Mo-Pb-Zn-Ag	Granodiorite porphyry	Quartz	–70 – –48	1.6 – 5.5	This study
Dabaoshan	Cu-Pb-Zn-Mo-W-Fe	Granodiorite porphyry	Quartz	–56 – –51	–2.9 – 11.3	Cai and Liu (1993)
						Mao et al. (2017)
Huangshaping	Pb-Zn-W-Mo	Dacite porphyry,	Quartz	–75	5.5	Shi et al. (1993)
		quartz porphyry,	Calcite	–55	6.5 – 8.7	Tong et al. (1995)
		granite porphyry				
W deposits						
Xintianling	W	Biotite granite	Quartz	–97 – –43	4.7 – 8.2	Bi et al. (1988)
						Shuang et al. (2016)
Da'ao	W-Sn	Biotite granite	Quartz	–92 – –54	3.2 – 5.9	Liu et al. (2007)
			Cassiterite	–86	–1.6	
Maoping	W-Sn	Biotite granite	Quartz	–60	7.0 – 8.0	Zhou et al. (2016)
Piaotang	W-Sn	Biotite granite	Quartz	–72 – –52	4.9 – 8.9	Zhou et al. (2016)
			Wolframite	–89 – –50	4.9 – 8.9	
Muziyuan	W-Mo	Biotite-bearing granite	Quartz	–99 – –46		Zhou et al. (2016)
Xihuashan	W-Mo	Biotite granite,	Quartz	–91 – –43	–2.4 – 8.3	Wei et al. (2011)
		two-mica granite	Wolframite	–55 – –43	6.3 – 8.4	Zhou et al. (2016)
Dalongshan	W-Mo	Biotite granite	Quartz	–85 – –50		Zhou et al. (2016)
Taoxikeng	W	Biotite granite	Quartz	–77 – –45	–3.1 – 1.2	Song et al. (2011)
Huangsha	W	Biotite granite	Quartz	–68 – –56	5.0 – 7.1	Zhou et al. (2016)
Pangushan	W-Bi	Biotite granite,	Quartz	–90 – –58	3.0 – 6.5	Fang et al. (2014)
		two-mica granite				Zhou et al. (2016)
Dajishan	W-Nb-Ta	Muscovite granite	Quartz	–53 – –49	2.8 – 7.4	Zhou et al. (2016)

Appendix 7-8. S isotopic compositions of sulfide minerals from the Middle-Late Jurassic Cu-Pb-Zn and W deposits in the Nanling Range of South China

Deposit	Metal association	Related intrusion	Occurrences of sulfide minerals	$\delta^{34}S_{CDT}$ (‰)	Reference
Cu-Pb-Zn deposits					
Shuikoushan	Pb-Zn-Au-Ag	Granodiorite	Carbonate replacement	–4.4 – 5.0	Jin et al. (1986)
					Lu et al. (2013)
Baoshan	Cu-Mo-Pb-Zn-Ag	Granodiorite porphyry	Skarn	–1.0 – 4.3	Yao et al. (2006)
			Carbonate replacement	–2.2 – 6.5	Zhu et al. (2012)
			Altered granodiorite	1.5 – 3.5	Bao et al. (2014)
					Xie et al. (2015)
					Ding et al. (2016c)
Tongshanling	Cu-Mo-Pb-Zn-Ag	Granodiorite porphyry	Skarn	–1.9 – 6.3	Cai et al. (2015)
			Sulfide-quartz vein	1.9 – 4.6	This study
			Carbonate replacement	0.2 – 5.0	
			Altered granodiorite	2.0 – 3.9	
Dabaoshan	Cu-Pb-Zn-Mo-W-Fe	Granodiorite porphyry	Porphyry mineralization	–4.0 – 5.0	Xu et al. (2008)
			Skarn	–5.0 – 5.0	Dai et al. (2015)
			Stratiform mineralization	–4.0 – 5.0	
			Sedimentary pyrite	–22.5 – –5.3	
				8.7 – 17.9	
Huangshaping	Pb-Zn-W-Mo	Dacite porphyry,	Carbonate replacement	–2.2 – 17.4	Xi et al. (2009)
		quartz porphyry,	Pyrite in granitoids	0.2 – 16.5	Zhu et al. (2012)
		granite porphyry	Sedimentary pyrite	–22.6 – –2.5	Ding et al. (2016a)
W deposits					
Dengfuxian	W-Nb-Ta	Two-mica granite	Wolframite-quartz vein	–1.4 – 0.6	Cai et al. (2012)
Yaogangxian	W	Biotite granite	Skarn	–1.3 – 3.6	Zhu et al. (2014)
			Wolframite-quartz vein	–2.6 – 3.9	
			Late Pb-Zn mineralization	–2.9 – 1.4	
Shizhuyuan	W-Sn-Mo-Bi	Biotite monzogranite	Skarn	2.8 – 8.9	Liu et al. (2006)
			Greisen	3.4 – 6.9	
			Late Pb-Zn mineralization	3.7 – 6.3	
Da'ao	W-Sn	Biotite granite	Greisen	–1.7 – 2.4	Liu et al. (2007)
Xihuashan	W-Mo	Biotite granite,	Wolframite-quartz vein	–2.1 – 0.4	Xu and Wang (2014)
		two-mica granite		4.0 – 7.9	
Taoxikeng	W	Biotite granite	Wolframite-quartz vein	–2.3 – 0.1	Song et al. (2011)
Huangsha	W	Biotite granite	Wolframite-quartz vein	–1.3 – 2.2	Feng et al. (1989)
Pangushan	W-Bi	Biotite granite,	Wolframite-quartz vein	–2.3 – 1.3	Fang et al. (2014)
		two-mica granite			

Appendix 7-9. Re contents and Re-Os ages of molybdenites from the Middle-Late Jurassic Cu-Pb-Zn and W deposits in the Nanling Range of South China

Deposit	Metal association	Related intrusion	Mineralization types	Re content (ppm) of molybdenite	Molybdenite Re-Os age (Ma) Isochron age (weighted average model age)	Reference
Cu-Pb-Zn deposits						
Shuikoushan	Pb-Zn-Au-Ag	Granodiorite	Skarn, carbonate replacement	419.9 – 1841	157.8 ± 1.4 (159.21 ± 0.91)	Huang et al. (2015)
Baoshan	Cu-Mo-Pb-Zn-Ag	Granodiorite porphyry	Skarn, carbonate replacement	86.3 – 338.6	160 ± 2 (158 ± 1)	Lu et al. (2006)
Tongshanling	Cu-Mo-Pb-Zn-Ag	Granodiorite porphyry	Skarn,	16.3 – 98.2	161.8 ± 1.7 (161.9 ± 1.1)	This study
			sulfide-quartz vein,	37.9 – 50.8	160.0 ± 5.8 (160.1 ± 0.8)	This study
			carbonate replacement	48.9 – 52.6	161 ± 45 (161 ± 1)	Lu et al. (2015)
				42.5 – 61.1	167 ± 15 (162.2 ± 1.6)	Zhao et al. (2016b)
Dabaoshan	Cu-Pb-Zn-Mo-W-Fe	Granodiorite porphyry	Porphyry, skarn,	64.7 – 102.4	168.3 ± 5.8 (163.9 ± 1.3)	Wang et al. (2011d)
			stratiform mineralization	66.4 – 139.7	166 ± 3 (164.83 ± 0.80)	Qu et al. (2014)
Huangshaping	Pb-Zn-W-Mo	Dacite porphyry,	Skarn,	0.46 – 25.9	154.8 ± 1.9 (154.6 ± 2.5)	Yao et al. (2007)
		quartz porphyry,	carbonate replacement	3.1 – 46.8	153.8 ± 4.8 (159 ± 8)	Ma et al. (2007)
		granite porphyry		0.43 – 20.2	159.4 ± 3.3 (157.1 ± 2.9)	Lei et al. (2010)
				1.2 – 11.9	157.5 ± 2.1 (156.6 ± 0.9)	Lei et al. (2010)
				0.59 – 17.4	157.6 ± 2.3 (156.5 ± 1.0)	Lei et al. (2010)
W deposits						
Dengfuxian	W-Nb-Ta	Two-mica granite	Quartz vein	0.0029 – 0.098	150.5 ± 5.2 (152.4 ± 3.3)	Cai et al. (2012)
Yaogangxian	W	Biotite granite	Quartz vein, skarn	0.010 – 2.6	154.9 ± 2.6 (155.5 ± 2.5)	Peng et al. (2006b)
Shizhuyuan	W-Sn-Mo-Bi	Biotite monzogranite	Skarn	1.0 – 1.3	151.0 ± 3.5	Li et al. (1996)
Weijia	W	Granite porphyry	Skarn	0.15 – 5.5	159 ± 8 (159.0 ± 5.6)	Zhao et al. (2016b)
Da'ao	W-Sn	Biotite granite	Greisen, quartz vein	0.029 – 1.2	151.3 ± 2.4 (153.3 ± 3.2)	Fu et al. (2007)
Yaolanzhai	W	Muscovite granite	Altered granite, greisen	0.030 – 0.079	155.8 ± 2.8 (156.0 ± 1.1)	Feng et al. (2011a)
Maoping	W-Sn	Biotite granite	Greisen, quartz vein	0.083 – 0.21	155.3 ± 2.8 (155.0 ± 0.9)	Feng et al. (2011a)
				0.037 – 0.11	150.2 ± 2.8 (148.7 ± 1.2)	Zeng et al. (2009)
Baxiannao	W-Sn	Biotite granite	Fractured zone	0.69 – 2.6	157.9 ± 1.5 (158.1 ± 1.0)	Feng et al. (2011a)
Niuling	W	Biotite granite	Quartz vein	0.029 – 0.64	154.9 ± 4.1 (155.1 ± 4.6)	Feng et al. (2011a)
Zhangdou	W	Biotite granite	Quartz vein	0.21 – 0.52	149.1 ± 7.1 (159.1 ± 5.0)	Feng et al. (2011a)
Muziyuan	W-Mo	Biotite-bearing granite	Quartz vein	0.30 – 2.7	151.1 ± 8.5 (146.9 ± 4.6)	Zhang et al. (2009)

(*To be continued on the next page*)

Appendix 7-9. (*Continued*)

Deposit	Metal association	Related intrusion	Mineralization types	Re content (ppm) of molybdenite	Molybdenite Re-Os age (Ma) Isochron age (weighted average model age)	Reference
Xihuashan	W-Mo	Biotite granite, two-mica granite	Quartz vein	0.052 – 1.5	157.75 ± 0.85 (156.3 ± 2.6)	Hu et al. (2012)
Taoxikeng	W	Biotite granite	Quartz vein	0.0049 – 0.013	154.4 ± 3.8 (155.5 ± 1.1)	Guo et al. (2011)
Hongshuizhai	W	Biotite granite	Greisen	0.047 – 0.30	157.0 ± 3.3 (156.3 ± 1.3)	Feng et al. (2011b)
Jiulongnao	W	Biotite granite	Quartz vein	0.22 – 0.49	150 ± 11 (151.5 ± 1.1)	Feng et al. (2011b)
Zhangdongkeng	W	Biotite granite	Quartz vein	0.010 – 0.14	153.6 ± 7.8 (151.3 ± 1.7)	Feng et al. (2011b)
Yanqian	W	Biotite granite	Quartz vein	3.4 – 6.8	154.5 ± 3.4 (159.2 ± 2.3)	Zhao et al. (2013)
Huamei'ao	W-Sn	Biotite granite	Quartz vein	0.20 – 1.7	158.5 ± 3.3 (158.6 ± 1.8)	Feng et al. (2015)
Huangsha	W	Biotite granite	Quartz vein	2.0 – 3.9	145.7 ± 5.7 (153 ± 3)	Huang et al. (2011)
Pangushan	W-Bi	Biotite granite, two-mica granite	Quartz vein	0.091 – 4.2	157.75 ± 0.76 (157.49 ± 0.82)	Zeng et al. (2011)
				5.4 – 9.6	158.8 ± 5.7 (158.06 ± 0.82)	Zeng et al. (2011)
Anqiantan	W-Bi	Two-mica granite	Quartz vein	0.78 – 3.5	154.4 ± 1.6 (155.17 ± 0.99)	Liu et al. (2010)
Baiyunxian	W	Amphibole-bearing biotite granite	Quartz vein	0.22 – 0.66	(157.4 ± 9.1)	Wang et al. (2009)
Hongling	W	Biotite granite, muscovite granite	Quartz vein	1.4 – 14.6	159.1 ± 1.5 (158.80 ± 0.88)	Wang et al. (2010b)
Yaoling	W	Monzogranite	Quartz vein	0.46 – 6.2	159.5 ± 2.8 (158.9 ± 3.0)	Qi et al. (2012)
Meiziwo	W-Sn	Monzogranite	Quartz vein	0.72 – 4.7	157.7 ± 2.8 (158.0 ± 2.1)	Qi et al. (2012)
Shigushan	W-Bi	Two-mica granite, muscovite granite	Quartz vein	0.58 – 1.5	154.2 ± 2.7 (154 ± 2)	Fu et al. (2008)
Shirenzhang	W	Monzogranite, two-mica granite	Quartz vein	0.48 – 5.0	159.1 ± 2.2 (157.6 ± 1.6)	Fu et al. (2008)
Kuimeishan	W	Biotite granite	Quartz vein	0.41 – 4.4	153.7 ± 1.5 (155.2 ± 1.7)	Li et al. (2014c)
Dajishan	W-Nb-Ta	Muscovite granite	Quartz vein	0.32 – 2.8	161.0 ± 1.3 (160 ± 1)	Zhang et al. (2011b)

Appendix 8-1. Some parameters for Raman spectra of carbonaceous material in carbonate rocks close to the magnesian and calcic skarns in the Weijia W deposit and temperatures calculated by the RSCM thermometry (mean value and standard deviation)

Sample No.	Formation[a] [Depth (m)]	Number of spectra	G position[b]		G FWHM[c]		R1 ratio[d]		R2 ratio[e]		Temperature[f] (°C)	
			Mean	SD	Mean	SD	Mean	SD	Mean	SD	Mean	SD
Carbonate rocks close to the magnesian skarn												
ZK803-6	D_2q [601]	21	1580.10	3.01	24.00	2.46	0.51	0.17	0.36	0.07	481	29
ZK803-7	D_2q [624]	22	1580.30	2.11	22.32	1.94	0.46	0.17	0.35	0.08	486	35
ZK803-9	D_2q [565]	20	1581.36	0.57	22.77	1.50	0.59	0.20	0.37	0.07	477	33
ZK803-17	D_2q [615]	14	1579.81	2.64	24.36	3.71	0.54	0.08	0.38	0.02	470	10
ZK803-20	D_2q [628]	25	1580.66	2.55	25.35	2.75	0.55	0.17	0.38	0.06	473	29
ZK803-25	D_2q [666]	12	1580.90	0.61	22.35	2.74	0.44	0.04	0.33	0.02	496	9
Carbonate rocks close to the calcic skarn												
WJ23	D_2q [0]	16	1579.94	0.82	23.55	2.06	0.13	0.05	0.15	0.05	573	22
WJ24	D_2q [0]	15	1579.93	0.65	23.01	1.50	0.14	0.04	0.16	0.04	568	17
ZK7'02-4	D_2q [42]	18	1580.11	0.26	21.42	1.05	0.20	0.05	0.20	0.04	554	18
ZK7'02-17	D_2q [176]	18	1579.71	0.75	20.33	3.20	0.15	0.07	0.15	0.05	576	21
ZK7'02-18	D_2q [180]	18	1579.89	0.45	21.35	6.13	0.16	0.13	0.16	0.04	572	16

Notes: [a] D_2q: The Middle Devonian Qiziqiao Formation. [b] Raman shift center of the graphite band. [c] Full width at half maximum of the graphite band. [d] R1 = D1 / G height ratio. [e] R2 = D1 / (G + D1 + D2) area ratio. [f] T (°C) = –445 × R2 + 641 (Beyssac et al., 2002).

Appendix 8-2. Whole-rock major and trace element compositions of the altered Weijia granite

Sample No.	ZK802-6	ZK803-29	ZK1001-2	ZK1001-3	ZK1001-5	ZK1001-6	ZK1001-7	ZK1001-9	WJ29	WJ35	ZK706-1	ZK706-2
Depth (m)	565	548	642	634	616	604	594	573	0	0	286	279
Major elements (wt.%)												
SiO_2	73.85	72.81	71.19	74.62	75.38	74.93	73.10	74.98	76.82	75.82	73.87	74.12
TiO_2	0.06	0.02	0.05	0.05	0.05	0.04	0.05	0.04	0.01	0.02	0.02	0.02
Al_2O_3	12.79	12.40	13.52	13.85	12.92	12.88	13.58	12.53	12.72	12.74	13.46	13.65
Fe_2O_3	0.31	0.12	0.83	0.26	0.72	0.81	0.31	0.25	0.15	0.21	0.15	0.24
FeO	0.49	0.16	0.81	0.84	0.66	0.83	0.73	1.00	0.07	0.40	0.36	0.51
MnO	0.07	0.02	0.05	0.03	0.06	0.10	0.10	0.09	0.00	0.02	0.01	0.01
MgO	0.90	0.11	0.39	0.21	0.22	0.16	0.17	0.11	0.04	0.19	0.09	0.13
CaO	0.69	3.03	2.64	1.18	0.98	1.39	1.62	1.36	0.18	1.26	1.16	1.04
Na_2O	0.22	0.54	0.10	0.14	1.48	0.94	1.51	1.74	1.59	2.36	3.19	3.00
K_2O	7.78	8.28	5.71	5.72	5.54	4.58	5.45	5.00	5.78	5.57	5.45	5.23
P_2O_5	0.02	0.01	0.02	0.02	0.02	0.02	0.02	0.02	0.02	0.01	0.01	0.01
LOI	2.49	2.66	4.02	3.08	2.33	2.36	2.94	2.33	1.87	1.79	1.70	2.02
Total	99.66	100.16	99.32	99.98	100.36	99.05	99.57	99.43	99.26	100.38	99.46	99.99
Trace elements (ppm)												
Li	18.62	5.16	20.13	22.08	30.96	39.19	31.28	35.35	5.84	12.23	9.98	13.18
Be	6.25	10.84	12.01	7.69	5.67	18.03	4.70	18.13	2.17	9.47	5.12	9.36
Sc	8.13	5.35	15.74	10.76	10.15	13.99	10.17	10.26	4.14	8.53	9.70	9.69
Ti	386.31	196.16	1094.95	443.71	399.34	1073.45	446.10	313.66	73.19	197.55	177.25	192.69
Mn	691.13	186.83	539.26	217.43	469.80	898.70	753.27	701.25	64.31	215.16	118.50	153.76
Cu	2.34	1.55	2.90	0.54	0.49	2.48	1.13	0.45	0.27	0.55	1.47	2.40
Zn	99.28	31.82	62.91	65.14	62.75	100.14	75.16	67.18	16.04	25.82	16.70	22.64
Ga	26.88	25.84	33.73	28.24	26.24	32.24	29.18	27.92	28.38	28.54	27.98	30.58
Rb	619.16	535.09	496.16	435.02	412.27	505.75	499.94	500.77	308.68	350.27	398.48	409.01
Sr	37.72	25.92	43.58	25.35	40.99	44.24	41.68	26.60	23.85	29.16	20.03	23.01
Y	82.26	75.98	96.69	92.15	89.36	85.41	90.29	97.53	118.23	79.59	96.44	99.10
Zr	115.45	65.52	81.35	84.82	89.35	74.42	83.39	78.29	69.41	75.16	69.64	65.42
Nb	36.99	49.47	50.49	41.33	40.23	48.15	39.64	36.20	49.09	47.96	49.23	46.65
Sn	55.04	3.00	6.46	8.62	9.81	13.44	13.66	24.88	0.79	1.76	4.63	10.30
Cs	13.10	15.22	13.80	13.39	14.41	12.99	15.03	13.56	7.90	14.90	7.91	9.52
Ba	195.34	130.39	158.30	135.26	123.84	66.38	112.91	110.79	24.50	35.00	24.75	38.41
Hf	6.25	4.34	4.31	5.05	5.19	4.07	4.98	5.03	5.72	5.13	4.87	4.76

(*To be continued on the next page*)

Appendix 8-2. (*Continued*)

Sample No.	ZK802-6	ZK803-29	ZK1001-2	ZK1001-3	ZK1001-5	ZK1001-6	ZK1001-7	ZK1001-9	WJ29	WJ35	ZK706-1	ZK706-2
Depth (m)	565	548	642	634	616	604	594	573	0	0	286	279
Ta	4.79	7.64	4.95	5.05	5.11	5.82	5.96	7.20	8.91	7.42	6.47	7.04
W	14.16	38.83	3.88	4.42	3.73	4.69	5.38	4.86	5.43	264.89	3.42	3.01
Pb	39.36	37.42	56.34	38.93	40.49	51.87	36.57	36.53	20.27	37.68	43.90	42.19
Th	26.63	23.09	25.61	28.60	27.43	20.91	25.19	22.87	26.71	27.79	26.28	26.39
U	15.89	16.27	12.72	19.41	18.92	11.42	18.05	17.22	8.14	16.32	18.95	18.32
Rare earth elements (REE)												
La	17.32	12.62	28.98	28.30	27.30	25.04	26.59	24.89	9.96	15.39	13.10	13.50
Ce	42.72	20.49	66.29	63.72	61.92	57.66	60.05	57.32	18.26	29.85	29.26	27.88
Pr	5.60	4.63	8.29	12.21	12.00	7.30	11.65	11.48	3.64	6.14	6.24	5.93
Nd	31.67	14.65	31.95	34.98	34.18	28.01	32.76	33.47	12.24	19.82	19.35	18.30
Sm	9.86	6.63	10.49	11.08	10.99	9.16	10.43	11.98	7.26	8.29	8.33	8.06
Eu	0.28	0.12	0.25	0.21	0.19	0.15	0.19	0.17	0.06	0.11	0.09	0.09
Gd	11.30	8.90	10.46	12.65	12.42	9.01	11.97	13.21	11.38	10.23	10.90	10.83
Tb	2.34	2.16	2.48	2.66	2.61	2.17	2.56	2.78	2.99	2.38	2.57	2.61
Dy	15.80	14.53	15.15	17.26	16.90	13.18	16.60	17.59	21.32	16.00	17.58	18.00
Ho	3.05	2.80	2.91	3.34	3.24	2.46	3.17	3.29	4.18	3.11	3.45	3.56
Er	8.60	7.97	7.79	9.53	9.23	6.61	9.07	9.49	11.89	8.85	9.95	10.21
Tm	1.27	1.17	1.34	1.39	1.35	1.17	1.35	1.46	1.76	1.31	1.48	1.53
Yb	7.89	7.32	7.96	8.61	8.44	7.13	8.63	9.57	10.90	8.28	9.36	9.63
Lu	1.11	1.03	1.15	1.24	1.21	1.04	1.24	1.40	1.55	1.18	1.35	1.38
ΣREE	158.81	105.02	195.47	207.19	201.98	170.08	196.26	198.11	117.40	130.93	133.01	131.51
La/Yb	2.20	1.72	3.64	3.29	3.23	3.51	3.08	2.60	0.91	1.86	1.40	1.40
K/Rb	104.28	128.46	95.50	109.09	111.47	75.14	90.41	82.87	155.32	132.02	113.39	106.00
Y/Ho	26.97	27.10	33.24	27.55	27.57	34.70	28.52	29.60	28.31	25.63	27.92	27.84
Zr/Hf	18.47	15.09	18.90	16.79	17.23	18.28	16.73	15.57	12.13	14.66	14.29	13.75
Sr/Eu	134.71	213.20	177.14	120.09	220.93	296.91	218.62	159.17	407.80	267.52	216.07	248.60
δEu[a]	0.08	0.05	0.07	0.05	0.05	0.05	0.05	0.04	0.02	0.04	0.03	0.03
$TE_{1,3}$[b]	1.02	1.10	1.14	1.18	1.19	1.15	1.20	1.20	1.14	1.13	1.19	1.17

Notes: ZK802-6, ZK803-29, ZK1001-2, ZK1001-3, ZK1001-5, ZK1001-6, ZK1001-7, and ZK1001-9 were sampled from altered granite spatially close to the magnesian skarn orebodies; WJ29, WJ35, ZK706-1, and ZK706-2 were sampled from altered granite spatially close to the calcic skarn orebodies. [a] $\delta Eu = 2Eu_N/(Sm_N + Gd_N)$. [b] $TE_{1,3} = \{[Ce_N/(La_N^{2/3} \times Nd_N^{1/3}) \times Pr_N/(La_N^{1/3} \times Nd_N^{2/3})]^{0.5} \times [Tb_N/(Gd_N^{2/3} \times Ho_N^{1/3}) \times Dy_N/(Gd_N^{1/3} \times Ho_N^{2/3})]^{0.5}\}^{0.5}$, it quantifies the degree of the tetrad effect (Irber, 1999).

Appendix 8-3. Representative EMP analyses of fresh and bleached biotite in the Weijia granite

Occurrence	Biotite in the granite without stockwork veins												Biotite in the granite with stockwork veins							
Sample No.	WJ2						ZK902-1						WJ1616B				WJ1617B			
Type	Fresh		Bleached				Fresh			Bleached			Bleached				Bleached			
SiO_2 (wt.%)	32.30	31.94	31.42	32.36	32.21	29.65	33.84	33.76	33.46	30.45	30.44	30.01	37.14	40.38	37.95	42.61	45.14	45.72	43.34	41.65
TiO_2	0.59	0.30	0.19	0.35	0.43	0.36	2.45	2.60	2.41	2.91	2.95	0.85	1.40	0.64	0.44	1.17	0.18	0.00	0.09	0.04
Al_2O_3	18.64	19.04	20.56	20.66	21.78	19.35	15.09	15.35	15.51	16.79	16.98	20.31	17.93	18.04	16.71	18.71	24.03	22.58	19.39	15.27
FeO	28.51	30.41	31.66	31.95	30.60	35.15	29.89	33.19	33.53	36.24	34.27	35.54	23.02	22.29	25.55	18.16	12.02	13.96	17.12	25.49
MnO	0.86	0.96	0.94	0.93	0.87	1.34	0.60	0.66	0.60	0.65	0.82	0.65	0.31	0.29	0.24	0.33	0.10	0.21	0.21	0.06
MgO	0.27	0.36	0.37	0.64	0.34	0.33	2.97	1.03	1.27	1.48	2.48	1.18	0.34	0.52	0.46	0.69	0.36	0.40	0.48	0.58
CaO	0.00	0.00	0.10	0.05	0.04	0.08	0.11	0.00	0.00	0.00	0.02	0.28	0.44	0.67	0.74	1.03	0.61	0.98	1.31	1.70
Na_2O	0.19	0.10	0.06	0.07	0.06	0.08	0.37	0.37	0.40	0.18	0.11	0.06	0.06	0.11	0.08	0.05	0.00	0.02	0.10	0.10
K_2O	8.62	7.89	5.30	5.23	4.40	3.89	8.54	8.21	8.62	5.10	4.07	3.32	6.10	5.47	4.85	4.45	6.35	4.63	2.74	0.88
F	3.64	2.42	0.59	0.48	0.03	0.91	4.84	3.06	2.42	1.17	0.85	0.53	0.65	0.60	1.04	0.35	0.00	0.00	0.11	0.24
Cl	0.13	0.12	0.10	0.08	0.02	0.06	0.44	0.29	0.47	0.26	0.27	0.16	0.17	0.04	0.05	0.03	0.04	0.00	0.00	0.00
Total	93.75	93.55	91.28	92.80	90.78	91.19	99.15	98.51	98.68	95.23	93.25	92.88	87.55	89.04	88.10	87.58	88.84	88.48	84.87	86.00
Li_2O^a	1.74	0.93	0.11	0.08	0.00	0.21	2.71	1.33	0.92	0.30	0.19	0.09	0.12	0.11	0.25	0.10	0.00	0.00	0.02	0.03
Ions based on 22 oxygen																				
T_Si	5.360	5.333	5.274	5.319	5.316	5.092	5.343	5.434	5.407	5.072	5.093	5.007	6.155	6.447	6.286	6.660	6.691	6.805	6.831	6.781
T_Al	2.640	2.667	2.726	2.681	2.684	2.908	2.657	2.566	2.593	2.928	2.907	2.993	1.845	1.553	1.714	1.340	1.309	1.195	1.169	1.219
ΣT	**8.000**	**8.000**	**8.000**	**8.000**	**8.000**	**8.000**	**8.000**	**8.000**	**8.000**	**8.000**	**8.000**	**8.000**	**8.000**	**8.000**	**8.000**	**8.000**	**8.000**	**8.000**	**8.000**	**8.000**

(*To be continued on the next page*)

Appendix 8-3. (*Continued*)

Occurrence	Biotite in the granite without stockwork veins												Biotite in the granite with stockwork veins							
Sample No.	WJ2						ZK902-1						WJ1616B				WJ1617B			
Type	Fresh		Bleached				Fresh			Bleached			Bleached				Bleached			
M_Al	1.005	1.078	1.342	1.322	1.551	1.007	0.151	0.347	0.360	0.368	0.442	0.999	1.656	1.841	1.548	2.107	2.889	2.765	2.433	1.712
M_Ti	0.073	0.038	0.024	0.043	0.054	0.047	0.290	0.314	0.293	0.365	0.371	0.107	0.174	0.077	0.055	0.137	0.020	0.000	0.011	0.005
M_Fe	3.956	4.246	4.445	4.392	4.224	5.048	3.947	4.467	4.531	5.050	4.796	4.958	3.190	2.977	3.539	2.374	1.490	1.738	2.257	3.470
M_Mg	0.066	0.090	0.093	0.157	0.083	0.083	0.699	0.247	0.305	0.367	0.619	0.293	0.083	0.123	0.112	0.161	0.080	0.088	0.112	0.141
M_Mn	0.120	0.136	0.133	0.129	0.122	0.195	0.080	0.090	0.082	0.092	0.117	0.091	0.043	0.039	0.033	0.043	0.013	0.026	0.027	0.008
M_Li	1.162	0.624	0.072	0.050	0.001	0.142	1.720	0.861	0.601	0.201	0.125	0.059	0.081	0.069	0.168	0.062	0.000	0.000	0.013	0.017
ΣM	**6.383**	**6.212**	**6.109**	**6.093**	**6.034**	**6.522**	**6.887**	**6.326**	**6.172**	**6.443**	**6.468**	**6.508**	**5.228**	**5.126**	**5.456**	**4.885**	**4.492**	**4.618**	**4.853**	**5.353**
I_Ca	0.000	0.000	0.018	0.009	0.007	0.014	0.018	0.000	0.000	0.000	0.003	0.050	0.077	0.114	0.130	0.173	0.097	0.155	0.221	0.297
I_Na	0.061	0.033	0.021	0.023	0.018	0.027	0.114	0.114	0.127	0.059	0.037	0.018	0.020	0.035	0.027	0.016	0.000	0.005	0.030	0.033
I_K	1.825	1.680	1.134	1.096	0.926	0.851	1.720	1.685	1.776	1.084	0.869	0.707	1.290	1.113	1.024	0.887	1.201	0.879	0.550	0.182
ΣI	**1.886**	**1.713**	**1.173**	**1.128**	**0.951**	**0.892**	**1.853**	**1.799**	**1.903**	**1.143**	**0.908**	**0.775**	**1.388**	**1.262**	**1.181**	**1.076**	**1.299**	**1.039**	**0.800**	**0.512**
OH[b]	2.054	2.687	3.657	3.729	3.978	3.487	1.462	2.365	2.638	3.313	3.473	3.675	3.612	3.687	3.442	3.818	3.990	4.000	3.946	3.878
F	1.910	1.279	0.315	0.247	0.017	0.495	2.419	1.556	1.234	0.614	0.451	0.279	0.341	0.301	0.545	0.175	0.000	0.000	0.054	0.122
Cl	0.036	0.034	0.028	0.023	0.005	0.018	0.119	0.079	0.128	0.073	0.075	0.046	0.047	0.011	0.013	0.008	0.010	0.000	0.000	0.000
Fe^{3+c}	1.386	0.892	0.000	0.000	0.000	0.157	2.063	1.180	1.108	0.406	0.104	0.000	0.000	0.000	0.000	0.000	0.000	0.000	0.000	0.000
Fe^{2+}	2.570	3.353	4.445	4.392	4.224	4.891	1.883	3.287	3.423	4.644	4.692	4.958	3.190	2.977	3.539	2.374	1.490	1.738	2.257	3.470

Notes: General formula: $IM_{2-3}T_4O_{10}(OH, F, Cl)_2$. [a] Li_2O is estimated using the equations $Li_2O = 0.237 \times F^{1.544}$ (trioctahedral micas) and $Li_2O = 0.3935 \times F^{1.326}$ (dioctahedral micas) after Tischendorf et al. (1997). [b] The estimation of OH is based on OH + F + Cl = 2. [c] Fe^{3+} is calculated based on the surplus oxygen method after Zheng (1983).

Appendix 8-4. Representative EMP analyses of white mica in the Weijia granite and its stockwork veins

Occurrence	White mica in the matrix of granite without stockwork veins				White mica coexisting with fluorite as aggregates in the granite without stockwork veins				White mica in the matrix of granite with stockwork veins				White mica in the bleached zone near stockwork veins				White mica in the K-feldspar-quartz pegmatite veins			
Sample No.	WJ2		ZK706-2		WJ13				WJ1616B				WJ1617B				WJ1616A			
Type																	Core	Core	Core	Rim
SiO_2 (wt.%)	44.48	47.33	48.57	49.27	48.28	46.13	46.57	46.48	44.43	42.72	47.81	49.06	46.03	49.03	48.71	49.85	45.55	47.35	49.22	49.17
TiO_2	0.00	0.31	0.29	0.27	0.00	0.00	0.17	0.10	0.04	0.18	0.08	0.04	0.06	0.13	0.20	0.07	0.00	0.03	0.01	0.00
Al_2O_3	28.98	30.41	32.42	31.43	37.39	36.98	33.76	36.41	25.16	27.72	28.98	32.46	31.57	28.08	28.03	30.88	26.37	27.63	28.84	34.07
FeO	6.04	3.05	3.24	3.58	0.08	0.32	1.19	0.67	8.83	9.61	4.00	2.14	2.60	4.54	4.08	2.67	8.74	6.12	5.48	1.07
MnO	0.29	0.00	0.07	0.00	0.00	0.00	0.10	0.01	0.06	0.18	0.14	0.10	0.03	0.03	0.07	0.04	0.22	0.39	0.21	0.04
MgO	0.08	0.19	0.22	0.26	0.01	0.02	0.40	0.09	0.16	0.16	0.33	0.06	0.02	0.29	0.31	0.39	0.07	0.03	0.07	0.05
CaO	0.09	0.00	0.03	0.00	0.00	0.00	0.00	0.10	0.00	0.01	0.09	0.21	0.01	0.15	0.10	0.40	0.00	0.00	0.00	0.00
Na_2O	0.32	0.04	0.04	0.08	0.20	0.26	0.40	0.42	0.20	0.23	0.03	0.08	0.30	0.03	0.02	0.05	0.20	0.05	0.06	0.07
K_2O	10.55	10.27	9.52	9.88	10.15	10.58	9.83	9.99	9.81	10.53	9.17	8.82	10.32	9.60	9.06	8.31	10.41	10.59	10.20	9.94
F	4.38	1.54	0.70	0.40	0.81	0.15	1.14	0.35	7.09	4.36	1.67	0.22	2.32	1.61	1.03	0.49	7.90	5.58	3.59	0.38
Cl	0.01	0.00	0.00	0.00	0.00	0.02	0.00	0.00	0.00	0.00	0.00	0.00	0.00	0.00	0.00	0.01	0.00	0.00	0.02	0.02
Total	95.21	93.13	95.09	95.17	96.92	94.45	93.55	94.62	95.75	95.69	92.28	93.19	93.26	93.48	91.61	93.16	99.43	97.77	97.69	94.80
Li_2O[a]	2.32	0.69	0.24	0.12	0.30	0.03	0.47	0.10	4.88	2.30	0.77	0.05	1.20	0.74	0.41	0.15	5.76	3.37	2.14	0.11
Ions based on 22 oxygen																				
T_Si	6.217	6.520	6.491	6.589	6.248	6.151	6.311	6.188	6.214	6.075	6.638	6.599	6.349	6.744	6.785	6.714	6.121	6.404	6.556	6.509
T_Al	1.783	1.480	1.509	1.411	1.752	1.849	1.689	1.812	1.786	1.925	1.362	1.401	1.651	1.256	1.215	1.286	1.879	1.596	1.444	1.491
ΣT	**8.000**	**8.000**	**8.000**	**8.000**	**8.000**	**8.000**	**8.000**	**8.000**	**8.000**	**8.000**	**8.000**	**8.000**	**8.000**	**8.000**	**8.000**	**8.000**	**8.000**	**8.000**	**8.000**	**8.000**

(*To be continued on the next page*)

Appendix 8-4. (*Continued*)

Occurrence	White mica in the matrix of granite without stockwork veins				White mica coexisting with fluorite as aggregates in the granite without stockwork veins				White mica in the matrix of granite with stockwork veins				White mica in the bleached zone near stockwork veins				White mica in the K-feldspar-quartz pegmatite veins			
Sample No.	WJ2		ZK706-2		WJ13				WJ1616B				WJ1617B				WJ1616A			
Type																	Core	Core	Core	Rim
M_Al	2.991	3.458	3.597	3.543	3.950	3.962	3.702	3.899	2.361	2.721	3.381	3.744	3.481	3.297	3.387	3.616	2.297	2.808	3.083	3.824
M_Ti	0.000	0.032	0.029	0.027	0.000	0.000	0.018	0.010	0.004	0.019	0.009	0.004	0.006	0.013	0.021	0.007	0.000	0.003	0.001	0.000
M_Fe	0.706	0.351	0.362	0.401	0.009	0.035	0.135	0.074	1.033	1.142	0.464	0.241	0.300	0.522	0.476	0.301	0.982	0.692	0.610	0.118
M_Mg	0.016	0.038	0.045	0.052	0.002	0.005	0.080	0.018	0.032	0.034	0.068	0.012	0.004	0.059	0.065	0.078	0.013	0.006	0.014	0.010
M_Mn	0.035	0.000	0.008	0.000	0.000	0.000	0.011	0.001	0.007	0.022	0.016	0.012	0.003	0.003	0.008	0.004	0.024	0.045	0.023	0.005
M_Li	1.301	0.385	0.131	0.062	0.154	0.016	0.255	0.053	2.743	1.315	0.432	0.029	0.667	0.409	0.229	0.084	3.112	1.831	1.147	0.058
ΣM	**5.049**	**4.264**	**4.172**	**4.085**	**4.115**	**4.019**	**4.201**	**4.055**	**6.179**	**5.253**	**4.370**	**4.041**	**4.462**	**4.303**	**4.185**	**4.091**	**6.429**	**5.386**	**4.879**	**4.015**
I_Ca	0.013	0.000	0.004	0.000	0.000	0.000	0.000	0.015	0.000	0.001	0.013	0.031	0.001	0.022	0.015	0.058	0.000	0.000	0.000	0.000
I_Na	0.086	0.011	0.010	0.020	0.049	0.067	0.105	0.108	0.053	0.063	0.007	0.020	0.080	0.009	0.006	0.012	0.052	0.012	0.015	0.017
I_K	1.881	1.804	1.622	1.686	1.676	1.799	1.699	1.697	1.750	1.909	1.624	1.514	1.817	1.684	1.610	1.427	1.785	1.827	1.733	1.678
ΣI	**1.981**	**1.816**	**1.636**	**1.707**	**1.725**	**1.866**	**1.804**	**1.819**	**1.803**	**1.973**	**1.643**	**1.564**	**1.898**	**1.715**	**1.631**	**1.498**	**1.837**	**1.840**	**1.748**	**1.695**
OH^{b}	2.063	3.330	3.705	3.832	3.670	3.935	3.511	3.852	0.864	2.041	3.269	3.906	2.987	3.300	3.546	3.788	0.644	1.615	2.484	3.837
F	1.934	0.669	0.295	0.168	0.329	0.062	0.489	0.148	3.136	1.959	0.731	0.094	1.013	0.700	0.454	0.210	3.356	2.385	1.512	0.158
Cl	0.002	0.001	0.000	0.000	0.001	0.004	0.000	0.000	0.000	0.000	0.000	0.000	0.000	0.001	0.000	0.001	0.000	0.000	0.004	0.005
Fe^{3+c}	0.000	0.000	0.000	0.000	0.000	0.000	0.000	0.000	0.974	0.000	0.000	0.000	0.000	0.000	0.000	0.000	0.982	0.000	0.000	0.000
Fe^{2+}	0.706	0.351	0.362	0.401	0.009	0.035	0.135	0.074	0.058	1.142	0.464	0.241	0.300	0.522	0.476	0.301	0.000	0.692	0.610	0.118

(*To be continued on the next page*)

Appendix 8-4. (*Continued*)

Occurrence	White mica in the K-feldspar-quartz pegmatite veins						White mica in the (K-feldspar)-quartz veins or veinlets										White mica in the stockwork quartz veinlets			
Sample No.	WJ1617A						WJ3				WJ1620						WJ1628A		WJ1628B	
Type	Core	Core	Core	Rim	Rim	Rim	Core	Core	Core	Rim	Core	Core	Core	Core	Rim	Rim				
SiO_2 (wt.%)	45.45	47.18	45.97	45.52	46.23	46.85	45.89	45.82	47.39	49.40	46.94	46.65	45.27	45.43	46.86	47.79	49.24	49.47	49.26	48.30
TiO_2	0.00	0.18	0.21	0.06	0.00	0.04	0.05	0.11	0.00	0.00	0.04	0.13	0.15	0.00	0.00	0.00	0.03	0.01	0.00	0.00
Al_2O_3	25.99	27.82	30.14	31.73	34.40	34.65	27.19	26.12	30.04	33.37	25.54	30.23	32.02	31.82	32.88	34.65	31.93	32.33	32.50	32.10
FeO	7.36	4.87	3.80	2.85	0.50	0.24	6.94	8.91	2.67	1.09	8.19	4.95	2.81	2.47	1.57	0.43	1.22	1.31	1.13	1.00
MnO	0.27	0.19	0.07	0.09	0.27	0.11	0.26	0.18	0.92	0.19	0.52	0.24	0.21	0.12	0.31	0.04	0.00	0.10	0.00	0.11
MgO	0.03	0.02	0.02	0.01	0.05	0.05	0.04	0.09	0.05	0.29	0.07	0.11	0.03	0.02	0.02	0.02	0.19	0.38	0.49	0.60
CaO	0.00	0.00	0.00	0.00	0.05	0.06	0.00	0.12	0.00	0.12	0.01	0.14	0.00	0.00	0.00	0.02	0.13	0.24	0.23	0.28
Na_2O	0.17	0.15	0.30	0.28	0.22	0.09	0.14	0.13	0.06	0.06	0.14	0.25	0.47	0.43	0.11	0.07	0.06	0.05	0.04	0.08
K_2O	10.62	10.92	10.73	10.60	10.21	10.19	10.13	9.78	9.78	9.21	9.65	9.57	10.59	10.21	9.98	9.82	8.36	9.14	8.30	8.25
F	6.11	5.04	3.59	2.34	1.31	0.33	8.02	6.25	3.28	0.34	6.39	4.55	3.60	2.87	1.25	0.27	0.57	0.13	0.24	0.00
Cl	0.00	0.00	0.01	0.00	0.00	0.01	0.00	0.00	0.00	0.01	0.02	0.04	0.05	0.00	0.02	0.00	0.02	0.02	0.03	0.01
Total	96.01	96.36	94.84	93.49	93.24	92.60	98.65	97.51	94.18	94.09	97.51	96.84	95.19	93.36	93.01	93.11	91.74	93.17	92.21	90.74
Li_2O^a	3.88	2.88	2.14	1.22	0.57	0.09	5.90	4.02	1.90	0.10	4.15	2.46	2.15	1.59	0.53	0.07	0.18	0.02	0.06	0.00
Ions based on 22 oxygen																				
T_Si	6.328	6.449	6.311	6.292	6.282	6.354	6.139	6.289	6.472	6.564	6.409	6.301	6.168	6.268	6.404	6.421	6.679	6.635	6.634	6.607
T_Al	1.672	1.551	1.689	1.708	1.718	1.646	1.861	1.711	1.528	1.436	1.591	1.699	1.832	1.732	1.596	1.579	1.321	1.365	1.366	1.393
ΣT	**8.000**	**8.000**	**8.000**	**8.000**	**8.000**	**8.000**	**8.000**	**8.000**	**8.000**	**8.000**	**8.000**	**8.000**	**8.000**	**8.000**	**8.000**	**8.000**	**8.000**	**8.000**	**8.000**	**8.000**

(*To be continued on the next page*)

Appendix 8-4. (*Continued*)

Occurrence	White mica in the K-feldspar-quartz pegmatite veins						White mica in the (K-feldspar)-quartz veins or veinlets										White mica in the stockwork quartz veinlets			
Sample No.	WJ1617A						WJ3				WJ1620						WJ1628A		WJ1628B	
Type	Core	Core	Core	Rim	Rim	Rim	Core	Core	Core	Rim	Core	Core	Core	Core	Rim	Rim				
M_Al	2.593	2.930	3.188	3.460	3.791	3.893	2.425	2.515	3.308	3.790	2.518	3.113	3.309	3.443	3.699	3.907	3.785	3.745	3.793	3.783
M_Ti	0.000	0.018	0.021	0.006	0.000	0.004	0.005	0.011	0.000	0.000	0.004	0.013	0.015	0.000	0.000	0.000	0.003	0.001	0.000	0.000
M_Fe	0.856	0.557	0.437	0.329	0.057	0.027	0.777	1.022	0.305	0.121	0.935	0.559	0.320	0.285	0.180	0.048	0.138	0.147	0.128	0.115
M_Mg	0.007	0.003	0.005	0.003	0.009	0.011	0.008	0.019	0.010	0.058	0.015	0.022	0.005	0.005	0.004	0.004	0.038	0.077	0.097	0.122
M_Mn	0.031	0.022	0.008	0.011	0.031	0.012	0.029	0.021	0.106	0.022	0.060	0.028	0.024	0.014	0.036	0.005	0.000	0.011	0.000	0.013
M_Li	2.172	1.583	1.184	0.676	0.309	0.050	3.175	2.218	1.044	0.051	2.281	1.337	1.179	0.885	0.292	0.037	0.101	0.013	0.033	0.000
ΣM	**5.659**	**5.113**	**4.842**	**4.485**	**4.197**	**3.996**	**6.419**	**5.805**	**4.773**	**4.042**	**5.813**	**5.072**	**4.853**	**4.632**	**4.210**	**4.001**	**4.065**	**3.994**	**4.051**	**4.033**
I_Ca	0.000	0.000	0.000	0.000	0.007	0.008	0.000	0.018	0.000	0.018	0.002	0.020	0.000	0.000	0.000	0.003	0.019	0.034	0.033	0.041
I_Na	0.047	0.039	0.079	0.074	0.058	0.023	0.035	0.034	0.015	0.016	0.037	0.065	0.124	0.114	0.028	0.017	0.016	0.013	0.011	0.022
I_K	1.887	1.904	1.879	1.869	1.770	1.763	1.728	1.712	1.704	1.561	1.681	1.649	1.841	1.797	1.740	1.683	1.447	1.563	1.425	1.440
ΣI	**1.934**	**1.942**	**1.958**	**1.943**	**1.834**	**1.794**	**1.763**	**1.764**	**1.718**	**1.595**	**1.719**	**1.733**	**1.965**	**1.911**	**1.768**	**1.703**	**1.482**	**1.610**	**1.470**	**1.503**
OH[b]	1.308	1.821	2.437	2.976	3.435	3.855	0.606	1.285	2.584	3.854	1.236	2.047	2.438	2.746	3.452	3.885	3.753	3.943	3.890	3.997
F	2.692	2.179	1.560	1.024	0.565	0.143	3.394	2.715	1.416	0.144	2.759	1.945	1.551	1.254	0.542	0.114	0.242	0.053	0.104	0.000
Cl	0.000	0.000	0.003	0.000	0.000	0.001	0.000	0.000	0.000	0.002	0.005	0.008	0.011	0.000	0.006	0.000	0.004	0.004	0.006	0.003
Fe^{3+}[c]	0.414	0.000	0.000	0.000	0.000	0.000	0.777	0.380	0.000	0.000	0.327	0.000	0.000	0.000	0.000	0.000	0.000	0.000	0.000	0.000
Fe^{2+}	0.442	0.557	0.437	0.329	0.057	0.027	0.000	0.642	0.305	0.121	0.608	0.559	0.320	0.285	0.180	0.048	0.138	0.147	0.128	0.115

Notes: General formula: $IM_{2-3}T_4O_{10}(OH, F, Cl)_2$. [a] Li_2O is estimated using the equations $Li_2O = 0.237 \times F^{1.544}$ (trioctahedral micas) and $Li_2O = 0.3935 \times F^{1.326}$ (dioctahedral micas) after Tischendorf et al. (1997). [b] The estimation of OH is based on OH + F + Cl = 2. [c] Fe^{3+} is calculated based on the surplus oxygen method after Zheng (1983).

Appendix 8-5. Representative EMP analyses of serpentine in the magnesian skarn of the Weijia W deposit

Sample No.	ZK7'08-7			ZK7'08-9								ZK803-5					ZK803-14		ZK1202-1	
Occurrence[a]	Exterior	Exterior	Exterior	Interior	Interior	Interior	Interior	Interior	Interior	Interior	Interior	Exterior	Exterior	Exterior	Exterior	Exterior	Exterior	Exterior	Interior	Interior
Point No.	1	2	3	1	2	3	4	5	6	7	8	1	2	3	4	5	1	2	1	2
SiO_2 (wt.%)	41.04	40.49	41.03	41.83	42.27	39.42	40.36	40.07	41.63	40.41	39.55	45.81	46.22	45.39	41.90	43.76	43.03	44.28	38.43	39.95
TiO_2	0.00	0.00	0.00	0.00	0.02	0.00	0.00	0.00	0.06	0.01	0.00	0.00	0.00	0.00	0.02	0.00	0.10	0.07	0.00	0.00
Al_2O_3	2.00	2.04	2.43	0.91	0.93	3.33	5.90	3.34	1.11	4.10	6.08	2.49	2.29	0.65	0.89	0.72	1.07	0.47	3.29	1.71
FeO[b]	3.40	3.17	1.60	6.61	5.34	5.73	6.55	5.54	5.70	5.81	5.53	2.58	2.46	3.18	2.27	3.38	1.35	1.25	4.53	4.86
MnO	0.14	0.24	0.07	0.28	0.19	0.31	0.21	0.15	0.39	0.29	0.15	0.04	0.11	0.08	0.00	0.01	0.09	0.00	0.43	0.39
MgO	39.54	40.03	40.61	32.15	32.62	34.84	34.01	36.09	33.83	36.03	35.29	32.56	34.42	32.96	30.30	31.55	31.65	36.26	30.92	30.39
CaO	0.11	0.11	0.11	0.41	0.29	0.06	0.02	0.07	0.26	0.09	0.04	0.38	0.22	0.30	0.48	1.34	0.46	0.26	0.14	0.12
Na_2O	0.01	0.03	0.00	0.03	0.03	0.02	0.04	0.06	0.04	0.07	0.00	0.05	0.05	0.00	0.00	0.00	0.00	0.03	0.04	0.00
K_2O	0.00	0.00	0.00	0.00	0.00	0.00	1.53	0.05	0.07	0.02	0.03	0.01	0.14	0.00	0.04	0.02	0.01	0.00	0.00	0.00
F	1.57	2.42	3.01	1.88	2.31	0.66	1.29	1.91	1.27	1.54	0.20	2.36	3.25	2.50	2.92	3.04	1.52	2.13	0.00	0.68
Cl	0.00	0.01	0.00	0.00	0.00	0.00	0.03	0.00	0.00	0.01	0.00	0.00	0.00	0.02	0.00	0.01	0.00	0.00	0.01	0.00
Total	87.82	88.54	88.86	84.10	84.00	84.36	89.95	87.29	84.35	88.36	86.86	86.27	89.15	85.07	78.83	83.83	79.28	84.76	77.80	78.10
Ions based on 14 oxygen																				
T_Si	3.891	3.849	3.871	4.200	4.233	3.892	3.804	3.875	4.128	3.847	3.760	4.356	4.305	4.410	4.410	4.373	4.398	4.278	4.042	4.213
T_Al	0.109	0.151	0.129	0.000	0.000	0.108	0.196	0.125	0.000	0.153	0.240	0.000	0.000	0.000	0.000	0.000	0.000	0.000	0.000	0.000
ΣT	**4.000**	**4.000**	**4.000**	**4.200**	**4.233**	**4.000**	**4.000**	**4.000**	**4.128**	**4.000**	**4.000**	**4.356**	**4.305**	**4.410**	**4.410**	**4.373**	**4.398**	**4.278**	**4.042**	**4.213**

(*To be continued on the next page*)

Appendix 8-5. (*Continued*)

Sample No.	ZK7'08-7			ZK7'08-9								ZK803-5					ZK803-14		ZK1202-1	
Occurrence[a]	Exterior	Exterior	Exterior	Interior	Interior	Interior	Interior	Interior	Interior	Interior	Interior	Exterior	Exterior	Exterior	Exterior	Exterior	Exterior	Exterior	Interior	Interior
Point No.	1	2	3	1	2	3	4	5	6	7	8	1	2	3	4	5	1	2	1	2
M_Al	0.115	0.078	0.140	0.108	0.110	0.280	0.459	0.256	0.129	0.307	0.441	0.280	0.251	0.074	0.111	0.085	0.129	0.053	0.407	0.212
M_Ti	0.000	0.000	0.000	0.000	0.001	0.000	0.000	0.000	0.004	0.001	0.000	0.000	0.000	0.000	0.002	0.000	0.007	0.005	0.000	0.000
M_Fe	0.269	0.252	0.126	0.555	0.447	0.473	0.516	0.448	0.473	0.462	0.440	0.205	0.192	0.258	0.200	0.282	0.116	0.101	0.399	0.429
M_Mg	5.589	5.674	5.711	4.813	4.869	5.128	4.778	5.203	5.001	5.114	5.002	4.616	4.780	4.773	4.753	4.700	4.823	5.223	4.848	4.778
M_Mn	0.011	0.020	0.005	0.024	0.016	0.026	0.017	0.012	0.033	0.023	0.012	0.003	0.009	0.007	0.000	0.001	0.008	0.000	0.039	0.035
M_Ca	0.011	0.011	0.011	0.045	0.031	0.006	0.002	0.008	0.028	0.009	0.004	0.039	0.022	0.031	0.054	0.143	0.050	0.027	0.016	0.013
M_Na	0.003	0.005	0.000	0.005	0.006	0.003	0.007	0.011	0.008	0.012	0.000	0.008	0.008	0.000	0.000	0.000	0.000	0.006	0.008	0.000
M_K	0.000	0.000	0.000	0.000	0.000	0.000	0.184	0.007	0.008	0.002	0.003	0.001	0.017	0.000	0.005	0.003	0.001	0.000	0.000	0.000
ΣM	**5.998**	**6.039**	**5.994**	**5.550**	**5.481**	**5.916**	**5.964**	**5.943**	**5.684**	**5.930**	**5.902**	**5.152**	**5.278**	**5.144**	**5.126**	**5.214**	**5.133**	**5.416**	**5.717**	**5.468**
OH[c]	7.528	7.271	7.102	7.402	7.268	7.794	7.611	7.415	7.602	7.535	7.941	7.290	7.042	7.230	7.028	7.036	7.508	7.349	7.998	7.773
F	0.472	0.727	0.898	0.598	0.732	0.206	0.384	0.584	0.398	0.463	0.059	0.710	0.958	0.767	0.972	0.962	0.492	0.651	0.000	0.227
Cl	0.000	0.002	0.000	0.000	0.000	0.000	0.005	0.000	0.000	0.001	0.000	0.000	0.000	0.003	0.000	0.002	0.000	0.000	0.002	0.000

Notes: General formula: $M_6T_4O_{10}(OH, F, Cl)_8$. [a] Interior and exterior represent that serpentine occurs in the interiors and exteriors of the magnesian skarn veinlets, respectively. [b] All Fe as Fe^{2+}. [c] The estimation of OH is based on OH + F + Cl = 8.

Appendix 8-6. Representative EMP analyses of phlogopite in the magnesian skarn of the Weijia W deposit

Sample No.	ZK7'08-7				ZK7'08-9					ZK7'08-10					ZK803-5				ZK803-14	
Sequence	Early	Early	Late	Late	Late	Late	Late	Late	Late	Late	Late	Late	Late	Late	Early	Early	Early	Early	Early	Early
Point No.	1	2	3	4	1	2	3	4	5	1	2	3	4	5	1	2	3	4	1	2
SiO_2 (wt.%)	41.90	42.87	40.20	37.07	40.11	37.97	39.07	39.45	36.25	41.85	41.00	39.03	37.29	37.57	40.45	41.58	42.57	41.72	43.41	42.33
TiO_2	0.00	0.00	0.06	0.04	0.00	0.00	0.01	0.00	0.00	0.00	0.03	0.00	0.04	0.00	0.00	0.00	0.19	0.13	0.00	0.01
Al_2O_3	12.05	8.99	9.46	15.93	13.30	13.42	13.41	12.47	13.93	11.15	11.48	11.31	11.79	11.96	16.28	14.69	13.21	12.55	12.20	13.22
FeO	2.15	3.45	4.26	7.58	5.03	7.35	9.61	11.19	15.44	9.91	12.02	20.10	21.86	22.06	1.95	2.64	1.98	1.53	1.02	1.89
MnO	0.10	0.10	0.08	0.41	0.16	0.38	0.37	0.33	0.36	0.64	0.52	0.66	1.24	1.49	0.29	0.01	0.10	0.12	0.00	0.13
MgO	27.89	30.80	31.57	23.20	25.10	25.00	21.34	19.95	17.73	20.99	20.65	15.22	12.56	11.88	25.58	26.59	27.60	27.36	28.01	26.97
CaO	0.00	0.00	0.04	0.03	0.06	0.03	0.08	0.08	0.07	0.02	0.05	0.02	0.06	0.04	0.02	0.00	0.00	0.10	0.02	0.00
Na_2O	0.17	0.14	0.09	0.13	0.17	0.16	0.17	0.23	0.10	0.15	0.10	0.02	0.10	0.00	0.29	0.35	0.22	0.25	0.27	0.31
K_2O	10.41	6.94	7.04	8.00	9.84	8.74	9.79	9.36	7.33	9.72	9.28	8.48	8.36	8.55	9.63	9.58	9.43	9.47	9.73	9.95
F	4.57	5.23	6.27	3.65	4.45	4.06	4.27	2.93	1.72	3.75	4.15	3.29	2.05	1.74	2.46	2.81	3.21	4.02	3.00	2.40
Cl	0.00	0.01	0.00	0.00	0.03	0.00	0.00	0.00	0.01	0.01	0.03	0.01	0.04	0.04	0.01	0.00	0.01	0.00	0.00	0.00
Total	99.24	98.52	99.06	96.02	98.26	97.10	98.13	95.98	92.95	98.20	99.30	98.14	95.39	95.32	96.96	98.24	98.53	97.26	97.66	97.20
Ions based on 22 oxygen																				
T_Si	5.933	6.082	5.799	5.478	5.805	5.600	5.787	5.921	5.632	6.142	6.026	5.981	5.901	5.938	5.700	5.811	5.931	5.945	6.064	5.947
T_Al	2.011	1.503	1.609	2.522	2.195	2.332	2.213	2.079	2.368	1.858	1.974	2.019	2.099	2.062	2.300	2.189	2.069	2.055	1.936	2.053
ΣT	**7.943**	**7.585**	**7.407**	**8.000**	**8.000**	**7.932**	**8.000**	**8.000**	**8.000**	**8.000**	**8.000**	**8.000**	**8.000**	**8.000**	**8.000**	**8.000**	**8.000**	**8.000**	**8.000**	**8.000**

(*To be continued on the next page*)

Appendix 8-6. (*Continued*)

Sample No.	ZK7'08-7				ZK7'08-9					ZK7'08-10					ZK803-5				ZK803-14	
Sequence	Early	Early	Late	Late	Late	Late	Late	Late	Late	Late	Late	Late	Late	Late	Early	Early	Early	Early	Early	Early
Point No.	1	2	3	4	1	2	3	4	5	1	2	3	4	5	1	2	3	4	1	2
M_Al	0.000	0.000	0.000	0.252	0.074	0.000	0.128	0.126	0.181	0.071	0.016	0.023	0.100	0.165	0.404	0.230	0.100	0.053	0.072	0.136
M_Ti	0.000	0.000	0.006	0.004	0.000	0.000	0.001	0.000	0.000	0.000	0.003	0.000	0.005	0.000	0.000	0.000	0.020	0.014	0.000	0.001
M_Fe	0.255	0.409	0.513	0.936	0.609	0.907	1.191	1.405	2.006	1.216	1.477	2.576	2.892	2.915	0.230	0.308	0.231	0.182	0.120	0.222
M_Mg	5.887	6.514	6.788	5.110	5.415	5.498	4.713	4.464	4.107	4.592	4.524	3.478	2.962	2.800	5.373	5.539	5.733	5.812	5.833	5.649
M_Mn	0.012	0.012	0.010	0.051	0.020	0.047	0.047	0.042	0.047	0.079	0.064	0.086	0.166	0.200	0.034	0.001	0.011	0.015	0.000	0.015
ΣM	**6.154**	**6.935**	**7.317**	**6.354**	**6.118**	**6.452**	**6.079**	**6.037**	**6.341**	**5.958**	**6.085**	**6.163**	**6.126**	**6.080**	**6.040**	**6.078**	**6.096**	**6.077**	**6.025**	**6.024**
I_Ca	0.000	0.000	0.006	0.004	0.010	0.005	0.012	0.012	0.011	0.003	0.007	0.003	0.010	0.006	0.003	0.000	0.000	0.015	0.003	0.000
I_Na	0.047	0.038	0.026	0.038	0.047	0.045	0.049	0.065	0.030	0.043	0.027	0.007	0.029	0.000	0.078	0.096	0.060	0.069	0.073	0.084
I_K	1.881	1.257	1.294	1.507	1.818	1.644	1.850	1.791	1.453	1.820	1.740	1.657	1.688	1.724	1.731	1.707	1.677	1.721	1.734	1.784
ΣI	**1.929**	**1.295**	**1.327**	**1.550**	**1.874**	**1.694**	**1.912**	**1.869**	**1.494**	**1.867**	**1.774**	**1.667**	**1.727**	**1.730**	**1.813**	**1.803**	**1.736**	**1.806**	**1.811**	**1.868**
OH[a]	1.954	1.651	1.142	2.294	1.958	2.105	2.002	2.611	3.150	2.255	2.060	2.404	2.963	3.120	2.900	2.758	2.582	2.187	2.674	2.934
F	2.046	2.345	2.858	1.706	2.036	1.895	1.998	1.389	0.846	1.742	1.931	1.595	1.026	0.869	1.097	1.242	1.416	1.813	1.326	1.066
Cl	0.000	0.003	0.000	0.000	0.007	0.000	0.000	0.000	0.004	0.003	0.008	0.001	0.012	0.012	0.003	0.000	0.002	0.000	0.001	0.000
Fe^{3+}[b]	0.255	0.409	0.513	0.862	0.609	0.907	0.987	0.864	0.763	0.749	0.797	0.755	0.789	0.728	0.230	0.308	0.231	0.182	0.120	0.222
Fe^{2+}	0.000	0.000	0.000	0.075	0.000	0.000	0.204	0.541	1.243	0.467	0.680	1.821	2.104	2.187	0.000	0.000	0.000	0.000	0.000	0.000

Notes: General formula: $IM_3T_4O_{10}(OH, F, Cl)_2$. [a] The estimation of OH is based on OH + F + Cl = 2. [b] Fe^{3+} is calculated based on the surplus oxygen method after Zheng (1983).

Appendix 8-7. Representative EMP analyses of garnet in the magnesian and calcic skarns of the Weijia W deposit

Skarn	Magnesian skarn												Calcic skarn							
Sample No.	ZK7'08-7		ZK7'08-9		ZK803-14		ZK803-15		ZK803-16		ZK1202-1		ZK7'02-1		ZK9'02-3					
Generation													First generation		First generation		Second generation		Third generation	
Point No.	1	2	1	2	1	2	1	2	1	2	1	2	1	2	1	2	1	2	1	2
SiO_2 (wt.%)	35.82	35.29	35.87	35.88	36.46	35.75	35.50	35.88	37.04	36.70	36.84	36.42	35.97	35.46	36.62	36.31	37.46	36.95	37.21	36.89
TiO_2	0.00	0.03	0.04	0.00	0.00	0.01	0.06	0.03	0.04	0.00	0.14	0.00	0.10	0.02	0.00	0.03	0.03	0.15	0.00	0.00
Al_2O_3	16.72	17.15	17.15	16.80	17.01	17.99	17.58	17.03	19.49	17.34	16.02	16.08	2.57	1.53	4.87	2.84	14.11	9.44	16.46	16.03
FeO	3.15	2.96	4.04	3.78	2.48	3.11	3.10	2.96	6.21	4.01	4.49	4.61	26.60	27.72	22.46	25.43	12.34	16.93	7.14	9.00
MnO	1.12	1.02	0.51	0.80	0.94	0.30	0.97	1.00	0.55	0.43	0.39	0.37	0.53	0.56	0.37	0.58	1.87	1.04	1.52	1.50
MgO	2.81	2.87	2.73	2.92	2.07	2.22	2.50	2.40	0.12	2.13	2.28	2.26	0.26	0.05	0.10	0.04	0.05	0.05	0.06	0.02
CaO	34.44	34.51	35.61	35.51	35.07	35.75	35.31	35.43	35.09	35.94	34.31	34.32	33.42	32.98	33.93	32.74	32.61	33.45	34.84	33.82
Na_2O	0.02	0.00	0.04	0.04	0.04	0.00	0.01	0.01	0.00	0.12	0.01	0.00	0.05	0.01	0.00	0.00	0.00	0.00	0.00	0.00
K_2O	0.02	0.05	0.00	0.04	0.01	0.00	0.00	0.01	0.00	0.00	0.04	0.00	0.05	0.00	0.00	0.00	0.00	0.00	0.03	0.03
F	3.82	4.83	2.96	3.92	2.45	3.76	2.44	3.74	2.71	4.09	2.65	4.24	0.09	0.18	0.03	0.09	1.23	1.36	2.37	1.22
Cl	0.07	0.06	0.18	0.12	0.00	0.06	0.02	0.03	0.00	0.02	0.06	0.05	0.01	0.02	0.00	0.00	0.00	0.00	0.01	0.02
Total	98.00	98.76	99.14	99.81	96.54	98.96	97.49	98.51	101.24	100.76	97.22	98.33	99.65	98.51	98.37	98.05	99.69	99.37	99.63	98.54
Ions based on 12 oxygen																				
T_Si	2.920	2.885	2.872	2.883	2.964	2.878	2.870	2.909	2.875	2.912	2.980	2.963	2.951	2.964	3.003	3.023	2.970	2.988	2.953	2.932
T_Al	0.080	0.115	0.128	0.117	0.036	0.122	0.130	0.091	0.125	0.088	0.020	0.037	0.049	0.036	0.000	0.000	0.030	0.012	0.047	0.068
ΣT	**3.000**	**3.000**	**3.000**	**3.000**	**3.000**	**3.000**	**3.000**	**3.000**	**3.000**	**3.000**	**3.000**	**3.000**	**3.000**	**3.000**	**3.003**	**3.023**	**3.000**	**3.000**	**3.000**	**3.000**
B_Al	1.526	1.537	1.490	1.474	1.594	1.584	1.545	1.536	1.658	1.533	1.507	1.505	0.199	0.115	0.470	0.278	1.288	0.888	1.493	1.434
B_Ti	0.000	0.002	0.002	0.000	0.000	0.001	0.004	0.002	0.002	0.000	0.009	0.000	0.006	0.001	0.000	0.002	0.002	0.009	0.000	0.000

(*To be continued on the next page*)

Appendix 8-7. (*Continued*)

Skarn	Magnesian skarn												Calcic skarn							
Sample No.	ZK7'08-7		ZK7'08-9		ZK803-14		ZK803-15		ZK803-16		ZK1202-1		ZK7'02-1		ZK9'02-3					
Generation													First generation		First generation		Second generation		Third generation	
Point No.	1	2	1	2	1	2	1	2	1	2	1	2	1	2	1	2	1	2	1	2
B_Fe^{3+a}	0.215	0.202	0.270	0.254	0.169	0.209	0.210	0.201	0.403	0.266	0.304	0.313	1.751	1.813	1.457	1.591	0.724	1.070	0.474	0.598
B_Mg	0.259	0.259	0.237	0.272	0.237	0.206	0.242	0.262	0.000	0.201	0.181	0.181	0.031	0.006	0.012	0.005	0.000	0.006	0.008	0.000
B_Fe^{2+}	0.000	0.000	0.000	0.000	0.000	0.000	0.000	0.000	0.000	0.000	0.000	0.000	0.012	0.066	0.060	0.125	0.000	0.027	0.000	0.000
B_Mn	0.000	0.000	0.000	0.000	0.000	0.000	0.000	0.000	0.000	0.000	0.000	0.000	0.000	0.000	0.000	0.000	0.000	0.000	0.026	0.000
ΣB	**2.000**	**2.000**	**2.000**	**2.000**	**2.000**	**2.000**	**2.000**	**2.000**	**2.063**	**2.000**	**2.000**	**2.000**	**2.000**	**2.000**	**2.000**	**2.000**	**2.013**	**2.000**	**2.000**	**2.032**
A_Mg	0.082	0.091	0.089	0.077	0.013	0.060	0.059	0.029	0.014	0.051	0.094	0.092	0.000	0.000	0.000	0.000	0.005	0.000	0.000	0.003
A_Fe^{2+}	0.000	0.000	0.000	0.000	0.000	0.000	0.000	0.000	0.000	0.000	0.000	0.000	0.062	0.059	0.023	0.055	0.094	0.048	0.000	0.000
A_Mn	0.078	0.071	0.035	0.055	0.065	0.021	0.066	0.068	0.036	0.029	0.026	0.025	0.037	0.040	0.025	0.041	0.126	0.071	0.076	0.101
A_Ca	3.007	3.022	3.055	3.057	3.055	3.083	3.058	3.077	2.917	3.056	2.973	2.991	2.937	2.954	2.982	2.921	2.770	2.898	2.962	2.880
A_Na	0.003	0.000	0.007	0.007	0.006	0.001	0.001	0.002	0.000	0.018	0.001	0.000	0.008	0.001	0.000	0.000	0.000	0.000	0.000	0.000
A_K	0.002	0.005	0.000	0.004	0.001	0.000	0.000	0.001	0.000	0.000	0.004	0.000	0.006	0.000	0.000	0.000	0.000	0.000	0.003	0.003
ΣA	**3.090**	**3.097**	**3.096**	**3.122**	**3.127**	**3.104**	**3.126**	**3.148**	**2.954**	**3.102**	**3.005**	**3.017**	**3.050**	**3.054**	**3.030**	**3.017**	**2.989**	**3.017**	**3.041**	**2.984**
F	0.497	0.629	0.379	0.503	0.317	0.483	0.315	0.483	0.338	0.518	0.343	0.552	0.013	0.026	0.004	0.013	0.159	0.182	0.303	0.157
Cl	0.005	0.004	0.012	0.008	0.000	0.004	0.002	0.002	0.000	0.001	0.004	0.004	0.001	0.001	0.000	0.000	0.000	0.000	0.000	0.001
End members[b] (%)																				
Gr	77.43	78.20	76.64	76.17	82.14	81.48	79.35	79.72	80.19	78.69	75.74	75.55	11.84	7.25	23.45	13.83	59.70	43.41	73.74	69.02
Ad	10.35	9.58	12.79	12.16	8.51	10.00	9.92	9.84	18.12	12.91	15.06	15.36	83.53	87.29	72.64	79.01	32.79	51.62	22.70	27.50
Py + Al + Sp	12.23	12.22	10.56	11.67	9.35	8.53	10.72	10.44	1.69	8.40	9.19	9.09	4.63	5.46	3.91	7.16	7.51	4.97	3.57	3.49

(*To be continued on the next page*)

Appendix 8-7. (*Continued*)

Skarn	Calcic skarn																			
Sample No.	ZK9'02-4				ZK9'02-7			ZK9'02-9-1						ZK9'02-9-2				ZK9'02-10		
Generation	First generation		Third generation		First generation			First generation		Second generation		Third generation		First generation		Second generation		First generation		
Point No.	1	2	1	2	1	2	3	1	2	1	2	1	2	1	2	1	2	1	2	3
SiO_2 (wt.%)	35.63	35.64	37.18	36.81	36.13	35.34	35.35	35.91	36.08	37.98	37.47	37.93	38.32	35.49	35.56	36.49	36.72	36.50	35.63	35.63
TiO_2	0.00	0.06	0.05	0.00	0.16	0.00	0.04	0.03	0.12	0.00	0.03	0.13	0.00	0.16	0.02	0.00	0.01	0.00	0.00	0.05
Al_2O_3	4.74	4.03	16.74	13.32	4.28	3.03	2.63	1.30	1.20	12.98	10.68	18.40	17.00	3.23	2.96	11.25	9.68	5.39	3.33	2.56
FeO	23.62	24.11	12.24	15.15	23.02	24.87	25.36	26.38	27.21	13.05	17.00	6.45	8.60	24.52	25.57	15.44	17.28	22.14	24.44	25.47
MnO	0.43	0.74	1.45	0.81	0.27	0.16	0.18	0.31	0.29	0.78	0.54	1.79	1.17	0.28	0.41	0.83	1.28	0.06	0.14	0.29
MgO	0.03	0.06	0.00	0.03	0.13	0.21	0.12	0.50	0.45	0.00	0.02	0.03	0.00	0.20	0.23	0.05	0.05	0.19	0.31	0.32
CaO	32.31	31.82	31.67	32.64	33.36	33.64	33.45	33.03	32.94	34.20	33.91	33.84	33.64	33.94	33.52	34.28	33.58	34.15	33.81	33.78
Na_2O	0.02	0.00	0.00	0.00	0.02	0.00	0.00	0.00	0.04	0.03	0.05	0.00	0.00	0.00	0.01	0.00	0.03	0.04	0.01	0.00
K_2O	0.00	0.00	0.00	0.00	0.04	0.00	0.03	0.00	0.00	0.01	0.00	0.03	0.00	0.00	0.02	0.00	0.02	0.00	0.00	0.00
F	0.00	0.00	0.34	0.21	0.00	0.14	0.00	0.00	0.00	1.44	0.99	1.74	0.68	0.24	0.00	0.93	0.15	0.28	0.00	0.18
Cl	0.00	0.00	0.00	0.01	0.00	0.00	0.03	0.02	0.00	0.00	0.00	0.00	0.00	0.01	0.00	0.00	0.00	0.00	0.00	0.00
Total	96.79	96.45	99.66	98.97	97.40	97.38	97.18	97.47	98.33	100.47	100.69	100.34	99.41	98.05	98.30	99.27	98.81	98.74	97.68	98.27
Ions based on 12 oxygen																				
T_Si	2.981	3.003	2.908	2.923	3.000	2.956	2.966	3.013	3.006	2.995	2.968	2.948	2.989	2.949	2.947	2.924	2.951	2.981	2.960	2.959
T_Al	0.019	0.000	0.092	0.077	0.000	0.044	0.034	0.000	0.000	0.005	0.032	0.052	0.011	0.051	0.053	0.076	0.049	0.019	0.040	0.041
ΣT	**3.000**	**3.003**	**3.000**	**3.000**	**3.000**	**3.000**	**3.000**	**3.013**	**3.006**	**3.000**	**3.000**	**3.000**	**3.000**	**3.000**	**3.000**	**3.000**	**3.000**	**3.000**	**3.000**	**3.000**
B_Al	0.449	0.400	1.452	1.170	0.419	0.254	0.226	0.129	0.118	1.202	0.965	1.633	1.553	0.265	0.236	0.986	0.868	0.500	0.286	0.210
B_Ti	0.000	0.004	0.003	0.000	0.010	0.000	0.002	0.002	0.008	0.000	0.002	0.008	0.000	0.010	0.001	0.000	0.001	0.000	0.000	0.003

(*To be continued on the next page*)

Appendix 8-7. (*Continued*)

Skarn	Calcic skarn																			
Sample No.	ZK9'02-4				ZK9'02-7			ZK9'02-9-1						ZK9'02-9-2				ZK9'02-10		
Generation	First generation		Third generation		First generation			First generation		Second generation		Third generation		First generation		Second generation		First generation		
Point No.	1	2	1	2	1	2	3	1	2	1	2	1	2	1	2	1	2	1	2	3
B_Fe^{3+a}	1.501	1.515	0.623	0.883	1.497	1.697	1.711	1.743	1.760	0.790	1.038	0.402	0.452	1.675	1.722	1.035	1.147	1.457	1.666	1.728
B_Mg	0.004	0.007	0.000	0.000	0.015	0.026	0.015	0.062	0.056	0.000	0.000	0.000	0.000	0.024	0.029	0.000	0.000	0.023	0.039	0.040
B_Fe^{2+}	0.046	0.075	0.000	0.000	0.059	0.023	0.046	0.064	0.059	0.009	0.000	0.000	0.000	0.025	0.012	0.000	0.000	0.020	0.009	0.020
B_Mn	0.000	0.000	0.000	0.000	0.000	0.000	0.000	0.000	0.000	0.000	0.000	0.000	0.000	0.000	0.000	0.000	0.000	0.000	0.000	0.000
ΣB	**2.000**	**2.000**	**2.078**	**2.053**	**2.000**	**2.000**	**2.000**	**2.000**	**2.000**	**2.000**	**2.005**	**2.043**	**2.005**	**2.000**	**2.000**	**2.021**	**2.015**	**2.000**	**2.000**	**2.000**
A_Mg	0.000	0.000	0.000	0.003	0.000	0.000	0.000	0.000	0.000	0.000	0.002	0.003	0.000	0.000	0.000	0.006	0.006	0.000	0.000	0.000
A_Fe^{2+}	0.106	0.109	0.177	0.123	0.043	0.020	0.023	0.044	0.077	0.063	0.088	0.017	0.109	0.004	0.038	0.000	0.014	0.035	0.023	0.021
A_Mn	0.031	0.053	0.096	0.055	0.019	0.011	0.013	0.022	0.020	0.052	0.036	0.118	0.077	0.019	0.029	0.057	0.087	0.004	0.010	0.020
A_Ca	2.897	2.872	2.655	2.778	2.967	3.015	3.008	2.970	2.940	2.890	2.878	2.818	2.812	3.022	2.977	2.943	2.891	2.989	3.010	3.007
A_Na	0.002	0.000	0.000	0.000	0.002	0.000	0.000	0.000	0.006	0.004	0.007	0.000	0.000	0.000	0.002	0.001	0.004	0.006	0.002	0.000
A_K	0.000	0.000	0.000	0.000	0.004	0.000	0.003	0.000	0.000	0.001	0.000	0.003	0.000	0.000	0.003	0.000	0.002	0.000	0.000	0.000
ΣA	**3.036**	**3.034**	**2.928**	**2.955**	**3.036**	**3.047**	**3.047**	**3.036**	**3.044**	**3.009**	**3.010**	**2.957**	**2.998**	**3.045**	**3.048**	**3.000**	**2.998**	**3.034**	**3.045**	**3.048**
F	0.000	0.000	0.043	0.027	0.000	0.020	0.000	0.000	0.000	0.186	0.130	0.217	0.085	0.033	0.000	0.123	0.021	0.039	0.000	0.026
Cl	0.000	0.000	0.000	0.000	0.000	0.000	0.002	0.001	0.000	0.000	0.000	0.000	0.000	0.001	0.000	0.000	0.000	0.000	0.000	0.000
End members[b] (%)																				
Gr	22.32	19.24	64.58	54.96	20.91	14.57	12.76	6.45	5.86	57.98	46.92	76.96	72.76	15.51	13.87	49.60	42.83	25.55	15.96	12.24
Ad	71.62	72.94	26.08	38.93	74.71	82.84	84.12	87.45	87.41	37.94	48.87	18.36	21.02	82.13	82.65	48.33	53.58	71.78	81.44	84.51
Py + Al + Sp	6.06	7.82	9.34	6.11	4.37	2.59	3.12	6.10	6.74	4.08	4.21	4.68	6.22	2.35	3.48	2.07	3.59	2.68	2.60	3.25

Notes: General formula: $A_3B_2T_3O_{12}$. [a] Fe^{3+} is calculated based on the stoichiometric criteria after Droop (1987). [b] Mineral abbreviations: Ad = andradite, Al = almandine, Gr = grossularite, Py = pyrope, Sp = spessartine.

Appendix 8-8. LA-ICP-MS analyses of garnet in the magnesian and calcic skarns of the Weijia W deposit

Skarn	Magnesian skarn				Calcic skarn							
Generation					First generation							
Sample No.	ZK803-15		ZK803-16		ZK7'02-1				ZK9'02-3			ZK9'02-9-1
Type					Core	Core	Rim	Rim				Core
Major elements (wt.%)												
SiO_2	39.42	39.44	40.16	39.75	39.18	35.98	38.13	37.84	39.77	37.70	39.14	40.18
CaO	35.35	35.05	32.01	35.00	35.66	40.06	34.29	34.89	34.58	36.28	34.29	35.57
Al_2O_3	19.23	19.18	19.65	19.02	2.77	3.83	1.38	2.45	4.41	4.42	2.81	0.82
FeO	2.23	2.19	5.80	3.18	19.34	17.82	23.53	22.14	17.71	20.09	22.23	21.72
MnO	0.98	1.04	1.79	0.31	0.90	0.60	1.89	1.78	0.61	0.31	0.58	0.30
MgO	2.61	2.89	0.13	2.21	1.25	0.75	0.04	0.18	2.15	0.22	0.15	0.31
Trace elements (ppm)												
Na	107.32	157.90	21.39	427.92	99.94	56.33	14.19	18.55	90.69	64.69	67.63	20.49
P	82.34	85.21	28.22	46.93	69.38	22.77	39.56	30.49	14.90	27.58	23.20	28.89
K	24.99	125.44	704.12	37.31	26.53	28.63	15.84	2.49	53.65	62.45	58.59	14.22
Sc	6.69	6.11	16.48	2.82	2.54	2.30	1.42	1.91	1.95	1.97	1.23	1.73
Ti	1.94	0.01	7.31	6.17	518.66	1068.36	36.31	287.47	330.02	443.70	141.52	78.23
V	1.07	0.73	2.47	0.45	7.79	9.53	1.60	6.88	11.35	14.73	4.19	2.78
Cr	0.03	1.14	0.00	0.00	105.84	108.80	0.29	3.12	33.68	12.09	16.93	22.75
Co	0.33	0.24	0.13	0.23	0.59	0.39	0.23	0.34	0.44	0.14	0.16	0.25
Ni	0.00	0.61	0.38	0.68	3.12	1.90	0.15	0.56	2.70	0.55	0.61	0.65
Cu	0.57	0.35	0.09	0.66	0.58	0.89	0.11	0.24	0.41	0.61	0.54	0.22
Zn	105.61	142.51	138.26	1872.47	542.07	56.00	36.62	70.15	162.38	15.02	30.65	16.24
Ga	13.79	12.84	43.35	33.54	34.82	37.66	34.89	36.72	48.62	31.76	57.87	52.21
Ge	25.88	25.57	34.91	20.80	28.80	31.05	22.43	24.12	61.43	64.30	48.02	40.98
Rb	0.54	3.50	19.10	1.05	0.35	0.57	0.29	0.03	0.95	1.14	1.10	0.26
Sr	23.53	27.83	0.54	145.36	2.33	2.54	1.48	1.72	1.40	0.29	0.80	1.63
Y	0.19	0.31	21.44	0.60	3.95	4.08	1.09	1.43	1.80	2.68	2.33	2.33
Zr	0.24	0.27	1.50	0.94	5.78	3.96	2.17	4.59	5.22	6.74	9.71	3.16
Nb	19.99	14.72	14.19	1.39	3.69	2.10	2.71	2.14	3.78	8.57	3.24	0.54

(*To be continued on the next page*)

Appendix 8-8. (*Continued*)

Skarn	Magnesian skarn				Calcic skarn							
Generation					First generation							
Sample No.	ZK803-15		ZK803-16		ZK7'02-1				ZK9'02-3			ZK9'02-9-1
Type					Core	Core	Rim	Rim				Core
Mo	0.74	0.67	0.84	0.17	17.03	33.96	4.50	3.13	1.08	1.06	4.19	79.44
Sn	446.29	553.60	1179.39	742.80	491.85	496.95	133.28	206.78	1115.17	2385.19	825.67	2294.44
Sb	4.64	4.64	0.10	10.51	8.58	0.88	0.02	0.23	0.78	0.10	0.15	0.01
Cs	0.16	1.41	0.36	0.29	0.07	0.10	0.05	0.00	0.14	0.19	0.34	0.04
Ba	0.11	0.43	7.88	0.89	0.08	0.05	0.00	0.01	0.07	0.07	0.02	0.05
Hf	0.04	0.03	0.17	0.02	0.21	0.09	0.05	0.14	0.16	0.21	0.33	0.11
Ta	0.07	0.04	0.08	0.02	0.05	0.05	0.01	0.02	0.04	0.11	0.05	0.04
W	1.00	1.33	17.56	1.65	551.36	1180.95	236.02	91.14	32.30	7.09	37.77	1128.32
Pb	5.54	5.93	0.22	47.28	8.46	2.17	0.18	0.34	5.28	2.46	1.49	0.94
Th	0.22	0.10	0.04	2.90	0.95	0.83	0.35	0.39	0.10	0.23	0.50	0.45
U	1.29	0.77	0.08	1.54	0.39	0.27	0.32	0.13	0.18	0.34	0.32	1.59
Rare earth elements (REE)												
La	2.03	1.94	0.04	9.33	5.27	4.00	7.75	1.45	0.26	0.31	0.27	1.61
Ce	6.84	5.89	1.73	36.75	11.53	9.12	10.33	3.77	1.21	2.41	1.48	4.54
Pr	0.80	0.69	1.19	5.15	1.22	1.02	0.71	0.40	0.21	0.43	0.25	0.56
Nd	2.15	1.45	12.64	16.24	4.64	4.17	2.06	1.76	1.05	1.93	1.29	2.29
Sm	0.47	0.29	13.20	4.19	1.13	1.00	0.24	0.41	0.32	0.58	0.38	0.45
Eu	0.02	0.02	0.01	0.02	0.24	0.26	0.08	0.07	0.12	0.17	0.06	0.14
Gd	0.11	0.09	6.74	1.07	0.83	1.03	0.25	0.34	0.33	0.53	0.40	0.40
Tb	0.03	0.02	1.82	0.16	0.13	0.16	0.03	0.05	0.06	0.09	0.07	0.06
Dy	0.11	0.10	8.93	0.60	0.76	0.88	0.19	0.28	0.33	0.51	0.33	0.33
Ho	0.01	0.01	1.10	0.05	0.15	0.16	0.03	0.06	0.07	0.11	0.09	0.07
Er	0.04	0.03	2.72	0.07	0.42	0.36	0.11	0.15	0.18	0.25	0.25	0.19
Tm	0.02	0.01	0.65	0.01	0.06	0.05	0.01	0.02	0.02	0.04	0.05	0.02
Yb	0.23	0.18	5.83	0.10	0.32	0.27	0.08	0.16	0.18	0.23	0.32	0.13
Lu	0.03	0.03	0.72	0.01	0.05	0.04	0.01	0.02	0.02	0.03	0.05	0.02

(*To be continued on the next page*)

Appendix 8-8. (*Continued*)

Skarn	Calcic skarn											
Generation	First generation		Second generation						Third generation			
Sample No.	ZK9'02-9-1		ZK9'02-3						ZK9'02-3	ZK9'02-9-1		
Type	Rim	Rim										
Major elements (wt.%)												
SiO_2	40.09	40.31	37.52	37.63	38.60	39.99	38.80	40.06	39.13	38.63	38.15	38.21
CaO	34.99	35.39	34.94	35.27	34.23	34.15	32.34	32.92	33.54	33.01	34.01	34.11
Al_2O_3	1.40	0.74	10.51	9.25	14.28	11.08	14.26	11.86	17.03	21.30	19.76	19.91
FeO	21.92	22.12	14.99	16.00	11.14	12.60	11.81	12.85	8.44	4.57	6.19	5.98
MnO	0.27	0.25	1.51	1.28	1.17	0.94	2.38	1.09	1.51	2.28	1.54	1.34
MgO	0.30	0.20	0.05	0.04	0.11	0.65	0.03	0.74	0.04	0.03	0.04	0.04
Trace elements (ppm)												
Na	63.40	68.38	47.54	50.35	212.62	378.87	9.78	137.39	8.61	13.17	252.84	303.98
P	25.65	29.79	24.71	17.86	20.68	21.53	25.73	16.97	15.17	27.84	26.19	39.65
K	27.07	1216.34	32.79	35.25	173.23	359.77	1.29	122.03	2.85	0.36	224.56	953.09
Sc	1.80	1.76	2.23	3.19	1.42	23.15	1.05	13.45	1.21	1.53	1.41	1.52
Ti	60.27	15.47	72.58	147.68	33.35	122.21	106.87	120.81	19.28	0.00	5.57	11.87
V	4.38	1.29	3.59	4.70	1.28	3.97	4.41	4.63	2.08	0.00	0.25	0.78
Cr	67.71	111.52	18.03	6.45	116.29	68.87	9.01	25.63	166.29	2.90	63.93	62.38
Co	0.20	0.17	0.19	0.18	0.16	0.24	0.23	0.35	0.18	0.29	0.24	0.31
Ni	0.69	0.58	0.29	0.26	0.41	1.23	0.23	1.81	0.38	0.41	0.63	0.57
Cu	0.28	0.48	0.34	0.39	1.37	2.33	0.20	0.68	0.16	0.00	1.02	1.30
Zn	12.45	11.50	21.40	16.63	32.27	75.68	32.71	63.02	18.61	33.98	46.31	40.62
Ga	34.93	32.14	52.21	51.78	48.92	49.62	55.88	49.82	50.53	31.90	61.73	63.31
Ge	36.55	22.94	34.22	38.50	20.66	23.60	25.36	20.59	28.46	30.31	23.37	26.73
Rb	0.43	11.05	0.60	0.62	2.96	7.05	0.00	2.12	0.06	0.04	3.77	7.96
Sr	0.76	1.72	0.33	0.46	0.64	1.23	0.29	1.05	0.21	0.10	3.94	11.84
Y	0.55	1.27	6.09	10.28	0.52	1.89	2.18	2.05	2.07	0.49	2.01	3.35
Zr	0.72	1.60	0.89	2.17	1.00	7.52	0.81	6.89	0.33	0.01	0.09	0.13
Nb	1.76	0.25	6.60	13.76	6.79	9.18	21.45	12.95	2.35	1.83	6.26	5.35

(*To be continued on the next page*)

Appendix 8-8. (*Continued*)

Skarn	Calcic skarn											
Generation	First generation		Second generation						Third generation			
Sample No.	ZK9'02-9-1		ZK9'02-3						ZK9'02-3	ZK9'02-9-1		
Type	Rim	Rim										
Mo	28.25	10.88	1.36	1.46	37.03	1.66	1.40	1.13	2.86	1.49	1.72	2.32
Sn	2331.71	1271.10	108.69	135.31	406.54	538.79	50.08	334.52	63.71	131.56	220.51	224.95
Sb	0.61	0.09	0.26	0.00	1.51	0.71	0.08	0.30	0.00	0.10	0.43	1.21
Cs	0.08	1.18	0.08	0.07	0.54	1.12	0.00	0.34	0.00	0.01	0.58	1.00
Ba	0.10	0.08	0.04	0.78	0.14	0.11	0.03	0.07	0.00	0.02	0.13	0.45
Hf	0.02	0.05	0.02	0.06	0.04	0.45	0.01	0.28	0.00	0.00	0.01	0.01
Ta	0.02	0.01	0.12	0.25	0.13	0.42	0.08	0.35	0.02	0.00	0.02	0.02
W	630.04	149.44	6.32	5.36	17.57	9.08	13.37	5.60	167.70	100.97	80.44	126.53
Pb	1.44	1.03	7.56	0.91	45.98	12.11	0.04	7.89	0.18	0.05	2.84	3.11
Th	0.10	0.25	0.74	1.06	0.13	0.25	0.21	0.14	0.07	0.00	0.01	0.01
U	0.43	0.62	0.94	0.80	0.10	0.12	0.26	0.05	0.10	0.00	0.15	0.01
Rare earth elements (REE)												
La	0.87	1.06	0.43	0.52	0.16	0.25	0.12	0.09	0.05	0.00	0.52	0.02
Ce	3.06	3.48	5.29	5.41	1.49	1.58	1.82	0.76	0.54	0.02	0.68	0.06
Pr	0.44	0.41	1.55	1.58	0.42	0.42	0.55	0.25	0.16	0.01	0.06	0.02
Nd	1.77	1.67	9.11	9.63	2.22	2.32	3.26	1.88	0.95	0.05	0.25	0.10
Sm	0.27	0.33	3.75	4.90	0.53	0.98	1.35	0.99	0.52	0.08	0.15	0.15
Eu	0.14	0.08	0.14	0.16	0.06	0.06	0.05	0.05	0.03	0.01	0.07	0.04
Gd	0.20	0.26	2.33	3.57	0.30	0.77	0.75	0.66	0.47	0.08	0.28	0.26
Tb	0.02	0.04	0.52	0.82	0.05	0.17	0.14	0.14	0.12	0.02	0.05	0.06
Dy	0.11	0.23	2.57	4.57	0.31	1.07	0.77	0.82	0.62	0.09	0.32	0.50
Ho	0.02	0.05	0.41	0.68	0.05	0.21	0.12	0.16	0.11	0.02	0.07	0.11
Er	0.04	0.11	0.99	1.72	0.11	0.59	0.28	0.42	0.24	0.06	0.18	0.30
Tm	0.01	0.02	0.19	0.33	0.02	0.14	0.04	0.09	0.05	0.01	0.03	0.06
Yb	0.03	0.08	1.24	2.20	0.19	1.48	0.30	0.86	0.29	0.07	0.32	0.54
Lu	0.01	0.01	0.16	0.27	0.04	0.26	0.04	0.13	0.04	0.01	0.04	0.09

Appendix 8-9. Representative EMP analyses of pyroxene in the magnesian and calcic skarns of the Weijia W deposit

Skarn	Magnesian skarn						Calcic skarn													
Generation							Early generation					Late generation								
Sample No.	ZK7'08-10						ZK9'02-4		ZK9'02-5			ZK9'02-6			ZK9'02-7			ZK9'02-9-2		
Point No.	1	2	3	4	5	6	1	2	1	2	3	1	2	3	1	2	3	1	2	3
SiO_2 (wt.%)	53.07	53.74	53.82	53.73	53.68	53.94	51.74	52.75	53.27	52.90	52.73	48.05	47.75	48.38	46.72	48.17	47.63	48.26	48.45	48.12
TiO_2	0.05	0.00	0.00	0.00	0.05	0.01	0.00	0.02	0.00	0.00	0.00	0.00	0.01	0.00	0.07	0.01	0.00	0.00	0.00	0.00
Al_2O_3	0.38	0.47	0.22	0.26	0.83	0.43	1.64	0.75	0.25	0.17	0.36	0.53	0.89	0.30	0.54	0.30	0.47	0.10	0.24	0.59
FeO	2.01	2.67	1.82	1.01	1.46	1.16	4.73	2.24	2.99	3.61	6.17	25.89	26.62	26.69	27.80	26.68	27.34	25.66	24.22	23.68
MnO	0.31	0.39	0.15	0.15	0.09	0.23	0.31	0.26	0.28	0.32	0.65	2.84	0.88	1.29	1.60	1.38	1.23	1.59	1.15	1.31
MgO	17.13	17.23	17.66	17.97	18.38	18.77	15.84	17.07	16.50	16.25	14.65	0.01	0.23	0.51	0.09	0.26	0.56	1.23	2.05	3.09
CaO	25.95	25.75	26.02	25.73	25.58	25.69	25.33	25.52	25.95	25.82	25.17	22.32	22.51	22.49	22.28	22.76	22.27	22.38	22.86	23.23
Na_2O	0.09	0.09	0.05	0.00	0.02	0.00	0.02	0.04	0.01	0.01	0.02	0.06	0.32	0.16	0.27	0.22	0.29	0.07	0.16	0.15
K_2O	0.00	0.02	0.05	0.02	0.01	0.00	0.00	0.00	0.00	0.00	0.00	0.10	0.00	0.02	0.00	0.03	0.00	0.00	0.05	0.00
Total	98.99	100.35	99.78	98.88	100.10	100.22	99.61	98.63	99.24	99.08	99.75	99.80	99.20	99.84	99.37	99.81	99.79	99.28	99.18	100.16
Cations based on 6 oxygen																				
T_Si	1.952	1.950	1.961	1.969	1.944	1.952	1.904	1.945	1.960	1.954	1.958	1.984	1.971	1.988	1.936	1.981	1.957	1.987	1.980	1.934
T_Al	0.017	0.020	0.009	0.011	0.035	0.018	0.071	0.033	0.011	0.007	0.016	0.016	0.029	0.012	0.026	0.015	0.023	0.005	0.012	0.028
T_Fe^{3+a}	0.031	0.030	0.030	0.019	0.020	0.030	0.024	0.022	0.029	0.039	0.026	0.000	0.000	0.000	0.038	0.004	0.020	0.008	0.008	0.038
ΣT	**2.000**	**2.000**	**2.000**	**2.000**	**2.000**	**2.000**	**2.000**	**2.000**	**2.000**	**2.000**	**2.000**	**2.000**	**2.000**	**2.000**	**2.000**	**2.000**	**2.000**	**2.000**	**2.000**	**2.000**
B_Al	0.000	0.000	0.000	0.000	0.000	0.000	0.000	0.000	0.000	0.000	0.000	0.009	0.014	0.003	0.000	0.000	0.000	0.000	0.000	0.000
B_Ti	0.001	0.000	0.000	0.000	0.001	0.000	0.000	0.000	0.000	0.000	0.000	0.000	0.000	0.000	0.002	0.000	0.000	0.000	0.000	0.000

(*To be continued on the next page*)

Appendix 8-9. (*Continued*)

Skarn	Magnesian skarn						Calcic skarn														
Generation							Early generation					Late generation									
Sample No.	ZK7'08-10						ZK9'02-4		ZK9'02-5			ZK9'02-6			ZK9'02-7			ZK9'02-9-2		
Point No.	1	2	3	4	5	6	1	2	1	2	3	1	2	3	1	2	3	1	2	3
B_Fe^{3+}	0.031	0.051	0.025	0.012	0.024	0.005	0.096	0.047	0.040	0.047	0.043	0.017	0.040	0.023	0.080	0.037	0.065	0.018	0.035	0.077
B_Mg	0.939	0.932	0.959	0.982	0.975	0.994	0.869	0.938	0.905	0.895	0.811	0.000	0.014	0.031	0.006	0.016	0.034	0.075	0.125	0.185
B_Fe^{2+}	0.000	0.000	0.000	0.000	0.000	0.000	0.025	0.000	0.022	0.026	0.122	0.876	0.879	0.894	0.845	0.877	0.855	0.858	0.785	0.681
B_Mn	0.010	0.012	0.004	0.005	0.000	0.000	0.010	0.008	0.009	0.010	0.020	0.097	0.031	0.045	0.056	0.048	0.043	0.049	0.040	0.044
ΣB	**0.981**	**0.995**	**0.989**	**0.998**	**1.000**	**1.000**	**1.000**	**0.994**	**0.976**	**0.977**	**0.997**	**1.000**	**0.979**	**0.996**	**0.990**	**0.978**	**0.997**	**1.000**	**0.984**	**0.988**
A_Mg	0.000	0.000	0.000	0.000	0.018	0.018	0.000	0.000	0.000	0.000	0.000	0.000	0.000	0.000	0.000	0.000	0.000	0.000	0.000	0.000
A_Fe^{2+}	0.000	0.000	0.000	0.000	0.000	0.000	0.000	0.000	0.000	0.000	0.000	0.000	0.000	0.000	0.000	0.000	0.000	0.000	0.000	0.000
A_Mn	0.000	0.000	0.000	0.000	0.003	0.007	0.000	0.000	0.000	0.000	0.000	0.002	0.000	0.000	0.000	0.000	0.000	0.007	0.000	0.000
A_Ca	1.023	1.001	1.015	1.011	0.993	0.996	0.999	1.008	1.023	1.022	1.002	0.987	0.996	0.990	0.989	1.003	0.981	0.988	1.001	1.000
A_Na	0.007	0.007	0.004	0.000	0.001	0.000	0.002	0.003	0.001	0.001	0.002	0.005	0.026	0.013	0.022	0.017	0.023	0.005	0.012	0.012
A_K	0.000	0.001	0.002	0.001	0.000	0.000	0.000	0.000	0.000	0.000	0.000	0.005	0.000	0.001	0.000	0.001	0.000	0.000	0.003	0.000
ΣA	**1.029**	**1.009**	**1.021**	**1.011**	**1.015**	**1.021**	**1.001**	**1.011**	**1.024**	**1.023**	**1.003**	**1.000**	**1.022**	**1.004**	**1.010**	**1.022**	**1.004**	**1.000**	**1.016**	**1.012**
End members[b] (%)																				
Di	98.99	98.74	99.54	99.53	99.71	99.31	96.17	99.16	96.67	96.13	85.02	0.04	1.52	3.24	0.63	1.72	3.66	7.63	13.17	20.34
Hd	0.00	0.00	0.00	0.00	0.00	0.00	2.76	0.00	2.40	2.79	12.84	89.80	95.16	92.12	93.18	93.18	91.75	86.75	82.65	74.78
Jo	1.01	1.26	0.46	0.47	0.29	0.69	1.07	0.84	0.93	1.08	2.14	10.16	3.33	4.63	6.20	5.10	4.59	5.62	4.19	4.88

Notes: General formula: ABT_2O_6. [a] Fe^{3+} is calculated based on the stoichiometric criteria after Droop (1987). [b] Mineral abbreviations: Di = diopside, Hd = hedenbergite, Jo = johannsenite.

Appendix 8-10. Representative EMP analyses of wollastonite in the calcic skarn of the Weijia W deposit

Sample No.	ZK9'02-4						ZK9'02-5					
Generation	Early generation		Late generation				Early generation		Late generation			
Point No.	1	2	1	2	3	4	1	2	1	2	3	4
SiO_2 (wt.%)	48.82	48.40	49.49	50.07	49.09	50.68	48.23	48.42	49.52	49.43	49.35	49.37
TiO_2	0.00	0.00	0.00	0.03	0.00	0.02	0.01	0.03	0.09	0.00	0.00	0.00
Al_2O_3	0.02	0.01	0.00	0.04	0.02	0.01	0.02	0.02	0.04	0.04	0.03	0.02
FeO[a]	0.00	0.03	0.34	0.82	1.01	1.19	0.00	0.07	0.38	0.65	0.86	1.49
MnO	0.09	0.16	0.52	0.81	0.85	1.31	0.10	0.02	0.70	0.65	0.74	0.58
MgO	0.00	0.00	0.00	0.04	0.04	0.06	0.00	0.00	0.04	0.00	0.00	0.05
CaO	45.99	46.66	47.59	46.56	46.18	46.06	46.89	45.53	47.08	46.48	46.47	46.11
Na_2O	0.05	0.05	0.02	0.00	0.06	0.00	0.04	0.01	0.05	0.02	0.02	0.01
K_2O	0.00	0.03	0.00	0.00	0.00	0.01	0.00	0.00	0.00	0.02	0.00	0.00
Total	94.98	95.36	97.96	98.37	97.25	99.33	95.54	94.09	97.89	97.30	97.46	97.62
Cations based on 18 oxygen												
T_Si	5.975	5.925	5.911	5.946	5.916	5.965	5.911	5.978	5.915	5.937	5.926	5.924
T_Al	0.003	0.002	0.000	0.006	0.003	0.001	0.002	0.003	0.005	0.006	0.004	0.003
ΣT	**5.978**	**5.927**	**5.911**	**5.952**	**5.919**	**5.966**	**5.913**	**5.981**	**5.920**	**5.943**	**5.929**	**5.927**
A_Ti	0.000	0.000	0.000	0.002	0.000	0.002	0.001	0.003	0.008	0.000	0.000	0.000
A_Fe	0.000	0.003	0.033	0.082	0.101	0.117	0.000	0.007	0.038	0.065	0.086	0.150
A_Mg	0.000	0.000	0.000	0.006	0.006	0.010	0.000	0.000	0.008	0.000	0.001	0.008
A_Mn	0.010	0.017	0.052	0.082	0.087	0.130	0.010	0.002	0.071	0.066	0.075	0.059
A_Ca	6.031	6.119	6.090	5.924	5.962	5.808	6.158	6.024	6.025	5.981	5.978	5.929
A_Na	0.012	0.013	0.005	0.000	0.015	0.000	0.009	0.002	0.010	0.005	0.006	0.003
A_K	0.000	0.005	0.000	0.000	0.000	0.002	0.000	0.000	0.000	0.004	0.000	0.000
ΣA	**6.043**	**6.137**	**6.095**	**5.924**	**5.977**	**5.810**	**6.167**	**6.026**	**6.035**	**5.990**	**5.984**	**5.932**

Notes: General formula: ATO_3. [a] All Fe as Fe^{2+}.

Appendix 8-11. Representative EMP analyses of vesuvianite in the calcic skarn of the Weijia W deposit

Sample No.	ZK9'02-5											
Point No.	1	2	3	4	5	6	7	8	9	10	11	12
SiO_2 (wt.%)	35.66	34.73	34.50	34.60	35.36	34.71	35.30	35.18	35.67	35.96	35.14	36.55
TiO_2	0.01	0.03	0.00	0.03	0.00	0.00	0.00	0.02	0.03	0.14	0.06	0.00
Al_2O_3	14.59	16.91	16.66	15.92	16.08	17.07	16.48	16.13	15.20	14.98	16.36	16.05
FeO[a]	5.44	3.92	3.96	5.09	4.25	3.09	4.81	5.94	4.99	6.09	6.36	6.72
MnO	0.22	0.07	0.32	0.38	0.23	0.37	0.26	0.49	0.13	0.42	0.35	0.34
MgO	2.57	2.12	1.71	1.71	2.37	1.78	1.88	1.06	2.76	2.30	1.39	1.30
CaO	35.56	35.44	35.33	35.54	35.46	35.42	35.34	35.82	35.96	36.01	35.57	35.77
Na_2O	0.02	0.04	0.01	0.02	0.01	0.04	0.03	0.08	0.01	0.01	0.07	0.01
K_2O	0.00	0.00	0.00	0.00	0.00	0.00	0.00	0.00	0.01	0.00	0.00	0.00
F	1.04	1.37	1.86	1.97	2.58	2.77	2.92	3.04	3.43	3.62	3.84	4.03
Cl	0.20	0.22	0.17	0.16	0.15	0.16	0.17	0.22	0.20	0.15	0.23	0.21
Total	95.31	94.84	94.52	95.43	96.50	95.40	97.18	97.99	98.39	99.66	99.35	100.97
Ions based on 73 oxygen												
T_Si	18.101	17.616	17.681	17.710	17.873	17.702	17.812	17.792	17.936	17.970	17.672	18.073
T_Al	0.000	0.384	0.319	0.290	0.127	0.298	0.188	0.208	0.064	0.030	0.328	0.000
ΣT	**18.101**	**18.000**	**18.000**	**18.000**	**18.000**	**18.000**	**18.000**	**18.000**	**18.000**	**18.000**	**18.000**	**18.073**
M_Al	8.730	9.729	9.743	9.315	9.451	9.964	9.614	9.410	8.941	8.792	9.369	9.351
M_Ti	0.004	0.011	0.000	0.011	0.000	0.000	0.000	0.009	0.011	0.052	0.022	0.000
M_Fe	2.308	1.664	1.695	2.179	1.797	1.316	2.031	2.512	2.097	2.545	2.673	2.777
M_Mg	1.945	1.602	1.309	1.306	1.789	1.353	1.413	0.800	2.066	1.711	1.044	0.955
M_Mn	0.094	0.031	0.139	0.164	0.097	0.158	0.111	0.208	0.053	0.176	0.149	0.141
ΣM	**13.081**	**13.037**	**12.886**	**12.975**	**13.134**	**12.791**	**13.169**	**12.938**	**13.168**	**13.276**	**13.256**	**13.224**
I_Ca	19.339	19.261	19.397	19.491	19.200	19.354	19.105	19.412	19.372	19.285	19.167	18.948
I_Na	0.018	0.036	0.009	0.021	0.009	0.041	0.025	0.079	0.013	0.012	0.067	0.012
I_K	0.000	0.000	0.000	0.000	0.000	0.003	0.000	0.000	0.008	0.000	0.000	0.000
ΣI	**19.357**	**19.297**	**19.406**	**19.511**	**19.209**	**19.397**	**19.130**	**19.492**	**19.392**	**19.297**	**19.234**	**18.961**
OH[b]	8.159	7.611	6.834	6.664	5.744	5.395	5.195	4.945	4.366	4.161	3.695	3.521
F	1.669	2.203	3.020	3.195	4.127	4.467	4.663	4.864	5.460	5.716	6.111	6.304
Cl	0.172	0.186	0.147	0.141	0.129	0.138	0.142	0.190	0.174	0.124	0.194	0.175

Notes: General formula: $I_{19}M_{13}T_{18}O_{68}(OH, F, Cl)_{10}$. [a] All Fe as Fe^{2+}. [b] The estimation of OH is based on OH + F + Cl = 10.

Appendix 8-12. Representative LA-ICP-MS analyses of scheelite from the Weijia W deposit

Occurrence	Scheelite in the stockwork quartz veinlets			Scheelite in the magnesian skarn								
Generation				Early generation						Late generation		
Sample No.	WJ35	WJ35	WJ35	ZK801-27	ZK801-33	ZK801-41	ZK802-15	ZK802-17	ZK803-2	ZK801-39	ZK801-40	ZK802-9
Major elements (wt.%)												
WO_3	70.01	79.72	80.91	79.27	78.67	78.34	74.47	62.96	77.17	80.21	75.21	78.75
CaO	27.62	16.84	16.28	20.19	20.50	20.45	20.98	22.23	18.00	18.87	21.88	20.38
MoO_3	0.02	0.03	0.09	0.01	0.50	0.86	4.25	14.39	0.47	0.64	1.49	0.00
Trace elements (ppm)												
Na	120.47	124.56	213.01	116.49	29.49	31.89	6.11	20.63	42.60	16.96	52.37	7.71
Mg	105.21	73.44	201.77	285.76	366.90	265.29	33.00	165.51	5027.73	80.58	2798.11	1224.54
Al	804.14	1220.50	741.54	12.20	1.49	1.80	0.00	398.91	1086.17	0.28	396.91	462.45
Si	3562.27	5424.47	2231.54	688.08	679.72	957.68	927.13	723.19	6317.25	1071.16	3462.98	2105.52
P	12.89	19.62	22.44	38.39	42.13	34.41	24.40	35.71	9.16	9.47	17.74	35.11
K	62.50	454.14	223.19	2.18	1.98	9.62	0.00	0.49	107.42	5.77	97.37	74.97
Sc	20.59	133.34	36.72	0.27	0.55	0.22	0.00	0.12	176.04	0.01	0.03	0.04
Ti	56.39	96.37	82.76	0.00	0.00	0.00	2.08	0.30	4.65	0.49	1.43	0.00
V	0.08	0.28	0.30	0.13	0.00	0.32	0.00	0.07	0.06	0.01	0.01	0.09
Cr	13.24	14.16	2.14	0.90	0.00	0.00	0.00	3.61	3.61	0.00	0.50	0.00
Mn	996.97	1936.14	1976.93	43.62	241.25	96.82	32.40	12.50	3743.52	5.16	84.08	4.23
Fe	4182.01	7348.49	9663.02	17.37	161.14	17.47	0.00	110.13	8829.23	153.26	576.20	370.15
Co	3.53	0.11	0.09	0.03	0.00	0.15	0.00	0.00	0.07	0.05	0.09	0.00
Ni	0.62	0.10	0.12	1.68	0.00	0.00	0.53	0.00	0.13	0.14	0.17	1.08
Cu	1.03	7.16	0.43	0.68	0.00	0.00	0.17	0.11	0.30	0.24	1.32	0.51
Zn	12.26	16.94	18.72	0.00	0.00	0.76	0.96	542.47	33.50	6.81	7.47	0.87
Ga	5.00	6.47	6.57	1.11	0.82	0.59	0.18	0.53	1.15	0.03	0.58	0.39
Ge	5.14	2.60	1.22	0.01	0.54	1.46	1.80	0.10	1.80	0.17	0.24	0.00
Rb	1.02	6.05	3.20	0.00	0.00	0.10	0.15	0.00	3.83	0.09	0.48	3.10
Sr	21.98	31.46	40.23	49.77	16.64	59.56	35.81	42.07	28.23	22.65	28.02	420.77
Y	1414.39	1221.18	774.84	824.54	12.76	4.01	117.44	47.52	313.78	1.53	1.84	1.34

(*To be continued on the next page*)

Appendix 8-12. (*Continued*)

Occurrence	Scheelite in the stockwork quartz veinlets			Scheelite in the magnesian skarn								
Generation				Early generation						Late generation		
Sample No.	WJ35	WJ35	WJ35	ZK801-27	ZK801-33	ZK801-41	ZK802-15	ZK802-17	ZK803-2	ZK801-39	ZK801-40	ZK802-9
Zr	8.97	12.07	4.80	6.23	5.17	7.30	5.61	4.94	35.16	0.02	0.02	6.63
Nb	1212.42	1535.87	584.69	148.32	43.36	97.70	98.62	94.54	1104.77	2.71	40.52	0.90
Sn	0.90	4.91	1.00	0.00	0.64	0.33	0.86	0.13	18.12	4.68	2.56	1.06
Sb	15.37	8.55	2.27	0.16	0.08	0.00	0.29	0.24	0.68	0.05	0.07	0.25
Cs	0.15	0.45	0.06	0.00	0.09	0.10	0.00	0.00	1.33	0.01	0.09	0.12
Ba	0.46	0.25	0.10	0.00	0.14	0.25	0.00	0.00	1.94	0.14	1.33	1.01
Hf	0.37	0.66	0.30	0.00	0.00	0.00	0.15	0.04	2.32	0.00	0.00	0.00
Ta	32.60	42.42	21.98	1.72	0.29	0.03	0.14	0.19	2.73	0.06	0.05	0.00
Pb	17.62	13.14	13.92	10.67	12.39	12.74	7.15	4.14	19.58	21.52	6.27	0.15
Th	36.95	34.03	21.92	8.84	3.05	2.21	0.10	0.65	9.24	0.63	4.29	0.04
U	703.35	108.24	25.38	12.37	2.58	9.00	0.25	0.83	47.44	2.11	34.51	0.65
Rare earth elements (REE)												
La	120.52	180.44	259.92	156.79	50.02	60.81	14.70	45.26	9.30	2.70	37.45	1.08
Ce	312.40	422.20	542.81	388.15	180.71	185.56	78.63	145.05	35.26	3.53	41.04	3.52
Pr	46.12	59.09	71.05	48.00	24.03	21.50	16.19	18.74	7.63	0.29	1.70	0.70
Nd	232.62	300.18	320.31	189.07	74.09	61.27	89.75	58.44	46.77	0.82	2.70	2.84
Sm	142.22	141.86	126.08	84.79	22.08	17.08	57.17	20.52	39.04	0.15	0.37	0.81
Eu	0.74	0.61	0.72	0.29	0.00	0.37	0.16	0.29	0.15	0.18	0.19	0.08
Gd	254.97	225.84	170.56	90.70	8.90	4.62	48.51	13.44	42.13	0.12	0.35	0.79
Tb	57.21	51.37	35.97	18.72	2.07	1.38	11.23	3.20	11.84	0.02	0.05	0.20
Dy	367.79	331.12	232.50	115.20	10.66	6.30	63.79	20.13	73.79	0.18	0.30	0.76
Ho	81.51	74.49	53.06	22.67	1.30	0.66	8.16	2.86	13.86	0.04	0.07	0.19
Er	202.80	194.17	140.08	72.28	3.40	1.42	19.82	7.65	39.84	0.10	0.15	0.35
Tm	28.75	30.76	22.16	13.98	0.70	0.31	3.01	1.45	9.23	0.01	0.02	0.16
Yb	178.35	201.06	140.40	121.59	6.26	2.66	16.97	10.61	84.01	0.08	0.20	0.64
Lu	22.79	28.30	20.35	18.40	0.69	0.33	1.83	1.02	12.29	0.02	0.04	0.10

(*To be continued on the next page*)

Appendix 8-12. (*Continued*)

Occurrence	Scheelite in the magnesian skarn			Scheelite in the calcic skarn								
Generation	Late generation			Early generation						Late generation		
Sample No.	ZK803-14	ZK803-14	ZK803-14	ZK7'04-2	ZK9'02-3	ZK9'02-3	ZK9'02-9-2	ZK9'02-10	ZK9'02-10	ZK9'02-7	ZK9'02-7	ZK9'02-7
Major elements (wt.%)												
WO_3	75.36	75.99	77.78	75.74	77.18	75.37	78.54	76.15	76.38	61.32	60.92	66.49
CaO	19.77	21.75	19.72	19.93	20.23	20.10	19.32	20.06	20.22	22.09	21.35	23.14
MoO_3	4.15	1.88	2.12	2.54	2.01	4.15	1.23	3.04	2.70	15.14	17.43	9.92
Trace elements (ppm)												
Na	10.01	13.06	4.79	246.11	90.21	20.16	124.70	52.82	58.89	15.22	9.02	9.04
Mg	664.29	175.33	68.55	121.11	71.46	20.73	95.40	11.92	86.54	6.88	3.00	13.07
Al	302.84	3.44	9.40	469.14	0.48	0.20	227.88	101.52	191.81	2.62	3.26	0.98
Si	1948.26	1298.26	1532.69	1916.45	1444.70	1238.32	1781.92	1325.96	1322.85	6321.01	960.28	1622.53
P	189.25	12.51	9.80	15.56	9.27	7.95	10.46	13.08	6.31	11.77	17.31	16.03
K	296.76	0.97	7.29	162.74	13.91	2.59	251.91	85.39	8.96	8.74	6.43	4.57
Sc	0.03	0.06	0.00	0.77	0.04	0.03	0.08	0.04	0.03	0.10	0.01	0.04
Ti	1.87	1.25	1.01	18.11	1.64	1.81	1.29	7.16	9.89	7.07	8.50	4.87
V	0.02	0.01	0.00	0.05	0.20	0.00	0.10	0.73	0.58	0.01	0.00	0.00
Cr	11.87	2.80	0.26	84.80	0.66	5.20	48.48	4.39	208.88	44.48	3.75	2.95
Mn	42.35	105.94	25.38	53.76	20.05	15.23	45.49	19.86	27.02	114.88	11.90	42.41
Fe	293.71	189.53	159.62	335.08	137.89	134.95	167.70	1568.35	1260.58	331.18	235.82	340.23
Co	0.06	0.04	0.05	1.25	0.05	0.03	0.05	0.07	0.06	0.05	0.07	0.08
Ni	0.02	0.05	0.06	0.48	0.09	0.04	0.04	0.12	0.16	0.22	0.15	0.17
Cu	0.08	0.06	0.05	2.80	0.12	0.05	0.09	0.60	0.17	0.18	0.22	0.04
Zn	17.77	0.57	0.55	0.44	0.88	0.08	0.18	2.39	6.12	1.04	0.92	0.44
Ga	0.11	0.51	0.10	16.65	4.56	1.60	7.61	3.78	3.41	0.26	0.12	0.55
Ge	0.00	0.00	0.00	4.59	0.68	0.17	1.30	0.49	0.47	0.01	0.00	0.07
Rb	12.32	0.00	0.27	2.39	0.22	0.03	1.73	0.62	0.19	0.18	0.17	0.11
Sr	52.21	33.91	30.63	61.83	55.40	66.61	31.77	38.96	52.30	66.53	66.48	72.75
Y	0.13	0.54	0.25	961.20	33.54	11.54	155.73	134.86	41.06	0.17	0.18	0.59

(*To be continued on the next page*)

Appendix 8-12. (*Continued*)

Occurrence	Scheelite in the magnesian skarn			Scheelite in the calcic skarn								
Generation	Late generation			Early generation						Late generation		
Sample No.	ZK803-14	ZK803-14	ZK803-14	ZK7'04-2	ZK9'02-3	ZK9'02-3	ZK9'02-9-2	ZK9'02-10	ZK9'02-10	ZK9'02-7	ZK9'02-7	ZK9'02-7
Zr	0.02	0.01	0.01	1.36	0.01	0.02	0.02	0.25	0.18	0.08	0.01	0.03
Nb	3.40	2.81	2.82	2480.59	420.02	180.68	721.06	477.04	308.49	24.06	16.29	77.11
Sn	0.79	0.63	0.54	1.87	0.21	0.28	0.34	12.03	5.42	0.47	0.43	0.38
Sb	0.00	0.03	0.03	45.96	0.01	0.07	0.07	6.15	0.81	0.13	0.90	0.18
Cs	0.43	0.00	0.01	0.11	0.09	0.00	0.02	0.11	0.05	0.06	0.04	0.03
Ba	0.35	0.16	0.18	0.31	0.39	0.32	0.23	0.78	0.37	1.32	1.33	0.74
Hf	0.00	0.00	0.00	0.11	0.00	0.00	0.02	0.01	0.01	0.01	0.00	0.00
Ta	0.06	0.06	0.05	101.96	4.53	1.09	13.17	1.41	0.94	0.06	0.04	0.14
Pb	14.53	10.94	9.69	335.08	5.23	3.07	7.55	8.02	3.43	39.29	232.47	12.71
Th	1.25	6.61	0.19	35.05	9.26	6.62	5.22	4.34	1.59	0.19	0.08	1.23
U	5.38	24.98	1.20	67.09	6.89	5.87	3.88	3.73	1.46	0.22	0.13	3.17
Rare earth elements (REE)												
La	1.53	15.83	4.76	420.74	180.12	97.17	207.46	177.43	148.54	19.70	11.14	43.84
Ce	4.59	72.12	18.16	1380.33	514.90	204.95	704.46	394.84	357.29	30.17	16.68	73.72
Pr	0.36	7.19	1.88	220.59	73.77	21.79	116.89	49.18	43.48	2.35	1.29	5.82
Nd	0.58	10.56	3.21	1108.41	273.61	63.59	512.06	187.21	158.33	5.80	3.55	13.24
Sm	0.07	1.34	0.46	444.27	92.88	13.25	199.95	48.63	34.05	0.58	0.33	1.38
Eu	0.02	0.12	0.07	3.45	1.49	1.03	1.59	2.02	2.12	0.14	0.11	0.34
Gd	0.03	0.30	0.09	494.53	59.06	8.24	142.81	44.50	25.17	0.27	0.20	0.71
Tb	0.00	0.04	0.02	91.86	12.76	1.70	30.76	8.55	4.35	0.02	0.02	0.09
Dy	0.03	0.18	0.08	489.41	61.75	8.46	156.10	45.42	21.63	0.08	0.08	0.34
Ho	0.00	0.03	0.01	87.30	8.87	1.36	23.51	7.89	3.61	0.01	0.01	0.05
Er	0.01	0.06	0.04	180.31	17.79	2.92	48.22	14.62	6.54	0.02	0.02	0.12
Tm	0.00	0.01	0.01	21.33	2.63	0.40	6.75	1.46	0.72	0.00	0.00	0.01
Yb	0.01	0.15	0.07	104.41	13.05	1.72	34.82	4.90	2.75	0.01	0.01	0.08
Lu	0.00	0.02	0.01	11.74	1.28	0.13	3.63	0.34	0.24	0.00	0.00	0.00

Xu-Dong HUANG

Les granitoïdes du jurassique moyen et les skarns à Cu-Pb-Zn et à W associées dans la région de Nanling (Chine du Sud): les gisements de Tongshanling et de Weijia

Les granitoïdes associés aux skarn à Cu-Pb-Zn et au W, dérivent, respectivement, de la fusion partielle de roches mafiques à amphiboles dans la croute inférieure et de roches métas-édimentaires riches en muscovite dans la croute moyenne-supérieure. Ces sources fertiles mobilisées pour la formation de ces plutons a permis la formation de gisements à Cu-Pb-Zn, et W au cours du Jurassique moyen. L'origine dans la croûte moyenne de la granodiorite de Tongshanling, associée aux minéralisations à Cu-Pb-Zn, a été montrée par l'étude des enclaves microgranulaires dioritiques qui sont des restites remaniées issues de la fusion partielle des amphibolites de la croûte inférieure. Le Cu et le Zn associées à ces plutons sont probablement issus de la croûte inférieure et ces métaux ont probablement étés remobilisés au cours de la fusion partielle. Le Pb issue de la croute supérieur a été collecté lors de l'ascension du magma qui a donné la granodiorite. Lors de leur mise en place ces granitoïdes ont exprimé leur potentiel minéralisateur. L'étude structural montre que la géométrie des corps minéralisés et en lien avec la déformation induite par la mise en place des plutons. Les différentes expressions de la minéralisation dans le district à Cu-Mo-Pb-Zn-Ag de Tongshanling sont génétiquement lié à l'hydrothermalisme et à son évolution lors du développement du skarn. Le granite de Weijia a cristallisé à partir d'un magma saturé en eau et riche en Fluor. Les facteurs qui ont contrôlé la formation de ce skarn magnésien riche en W, suppose l'existence d'une source enrichie en W dans les sources métasédimentaires et d'un magma riche en Fluor très différentia par cristallisation fractionnée.

Mots clés: Granitoïdes; Skarns; Enclave; Contrôle structuraux; Petrogènèse; Métallognénèse; Jurassique Moyen; Tongshanling; Weijia; Nanling

Middle-Late Jurassic Cu-Pb-Zn-bearing and W-bearing granitoids and their skarn mineralization in the Nanling Range, South China: the Tongshanling and Weijia deposits

The Middle-Late Jurassic Cu-Pb-Zn-bearing and W-bearing granitoids in the Nanling Range were mainly derived from non-simultaneous partial melting of the mafic amphibolitic rocks in the lower crust and the muscovite-rich metasedimentary rocks in the upper-middle crust, respectively. The fertile sources in the Nanling Range are beneficial to the formation of Cu-Pb-Zn and W deposits during Middle-Late Jurassic. The lower-crust origin of the Cu-Pb-Zn-bearing granodiorites is further demonstrated by the dioritic microgranular enclaves in the Tongshanling granodiorite which are reworked restite enclaves derived from partial melting of the mafic amphibolitic source. The Cu and Zn associated with these intrusions were most probably released from the mafic amphibolitic lower crust by partial melting, whereas, Pb was extracted from the upper crust by ascending granodioritic magmas. The emplacement of these ore-bearing granitoid magmas may have a structural connection with the subsequent polymetallic mineralization in some way. For instance, the exoskarn and sulfide-quartz veins in the Tongshanling Cu-Pb-Zn deposit are evidently controlled by magma emplacement-induced wall-rock deformation. The different mineralization types and ore deposits in the Tongshanling Cu-Mo-Pb-Zn-Ag ore district are genetically linked together in the same skarn system as the productions of evolution and zonation. The Weijia granite was crystallized from a F-rich and water-saturated magma. The key factors controlling the occurrence of unusual magnesian skarn W mineralization during Late Jurassic in the Nanling Range mainly include a W enriched metasedimentary source, a fluorine-rich magma, a strong crystal fractionation, and a fluorine-rich hydrosaline melt.

Keywords: Cu-Pb-Zn-bearing granitoids; W-bearing granites; Microgranular enclaves; Skarn; Structural control; Petrogenesis; Metallogenesis; Middle-Late Jurassic; Nanling Range

UNIVERSITE D'ORLEANS

Institut des Sciences de la Terre d'Orléans, Orléans 45071, France

School of Earth Sciences and Engineering, Nanjing University, Nanjing 210023, China

NANJING UNIVERSITY 1902